

# Oceanologia

Official Journal of the Polish Academy of Sciences



## EDITOR-IN-CHIEF

Prof. Jacek Piskozub  
Institute of Oceanology, Polish Academy of Sciences, Sopot, Poland

## MANAGING EDITOR

Agata Bielecka – abielecka@iopan.pl

## Editorial Office Address

Institute of Oceanology, Polish Academy of Sciences (IO PAN)  
Powstańców Warszawy 55  
81–712 Sopot, Poland  
Mail: editor@iopan.pl

## ADVISORY BOARD

**Prof. Xosé Antón Álvarez Salgado**  
Marine Research Institute, Spanish Research Council (CSIC), Vigo, Spain

**Prof. Mirosław Darecki**  
Institute of Oceanology, Polish Academy of Sciences, Sopot, Poland

**Prof. Jerzy Dera**  
Institute of Oceanology, Polish Academy of Sciences, Sopot, Poland

**Prof. Jan Harff**  
University of Szczecin, Poland; Leibniz-Institute for Baltic Sea Research, Warnemünde, Germany

**Prof. Agnieszka Herman**  
Institute of Oceanography, University of Gdańsk, Gdynia, Poland

**Prof. Genrik Sergey Karabashev**  
P.P. Shirshov Institute of Oceanology, Russian Academy of Sciences, Moscow, Russia

**Prof. Alicja Kosakowska**  
Institute of Oceanology, Polish Academy of Sciences, Sopot, Poland

**Prof. Matti Leppäranta**  
Institute of Atmospheric and Earth Sciences, University of Helsinki, Finland

## THEMATIC EDITORS

Dr. Katarzyna Błachowiak-Samolyk – Institute of Oceanology, Polish Academy of Sciences, Sopot, Poland

Dr. Artur Burzyński – Institute of Oceanology, Polish Academy of Sciences, Sopot, Poland

Prof. Piotr Kowalczyk – Institute of Oceanology, Polish Academy of Sciences, Sopot, Poland

Prof. Krzysztof Opaliński – Institute of Ecology and Bioethics, Warsaw, Poland

Prof. Żaneta Polkowska – Gdańsk University of Technology, Gdańsk, Poland

Dr. hab. Krzysztof Rychert – Pomeranian University in Słupsk, Poland

Prof. Marek Zajączkowski – Institute of Oceanology, Polish Academy of Sciences, Sopot, Poland

**Prof. Ewa Lupikasza**  
Faculty of Earth Sciences, University of Silesia, Sosnowiec, Poland

**Prof. Hanna Mazur-Marzec**  
Institute of Oceanography, University of Gdańsk, Gdynia, Poland

**Prof. David McKee**  
University of Strathclyde, Glasgow, Scotland, United Kingdom

**Prof. Dag Myrhaug**  
Norwegian University of Science and Technology (NTNU), Trondheim, Norway

**Prof. Tarmo Soomere**  
Tallinn University of Technology, Estonia

**Prof. Hans von Storch**  
Institute of Coastal Research, Helmholtz Center Geesthacht, Germany

**Prof. Piotr Szefer**  
Department of Food Sciences, Medical University of Gdańsk, Poland

**Prof. Muhammet Türkoğlu**  
Çanakkale Onsekiz Mart University, Turkey

**Prof. Jan Marcin Węślawski**  
Institute of Oceanology, Polish Academy of Sciences, Sopot, Poland

---

This journal is supported by the Ministry of Science and Higher Education, Warsaw, Poland

---

Indexed in: ISI Journal Master List, Science Citation Index Expanded, Scopus, Current Contents, Zoological Record, Thomson Scientific SSCI, Aquatic Sciences and Fisheries Abstracts, DOAJ

---

IMPACT FACTOR ANNOUNCED FOR 2020 IN THE 'JOURNAL CITATION REPORTS' IS 2.427; 5-year IF is 2.671. CITESCORE ANNOUNCED FOR 2020 IS 4.3

---

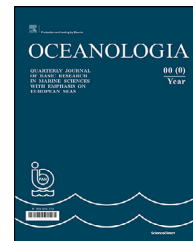
**Publisher**  
Elsevier B.V.  
Radarweg 29  
1043 NX Amsterdam  
The Netherlands

**Senior Publisher**  
Tobias Wesselius  
+31 6 5370 3539

ISSN 0078-3234

Available online at [www.sciencedirect.com](http://www.sciencedirect.com)

ScienceDirect

journal homepage: [www.journals.elsevier.com/oceanologia](http://www.journals.elsevier.com/oceanologia)

## ORIGINAL RESEARCH ARTICLE

# Striped texture of submesoscale fields in the northeastern Baltic Proper: Results of very high-resolution modelling for summer season

Victor Zhurbas<sup>a</sup>, Germo Väli<sup>b,\*</sup>, Natalia Kuzmina<sup>a</sup><sup>a</sup> Shirshov Institute of Oceanology, Russian Academy of Sciences, Moscow, Russia<sup>b</sup> Tallinn University of Technology, Tallinn, Estonia

Received 22 May 2021; accepted 17 August 2021

Available online 28 August 2021

**KEYWORDS**

Baltic Sea;  
Elongated  
submesoscale  
structures  
– stripes;  
Modelling;  
Symmetric  
instability;  
McIntyre instability;  
Frontogenesis;  
Stirring

**Abstract** Very high-resolution modelling of the northeastern Baltic Proper shows that preferentially elongated along the flow, submesoscale inhomogeneities of hydrodynamic fields or stripes of the order of 10–20 km in length and 1 km in width, are typical for summer season both in surface mixed layer and for interior layers which are not directly exposed to atmospheric forcing. In surface layer, the presence of stripes is supported by the remote sensing imagery and their vertical extension is comparable with the mixed layer depth (approx. 5–8 m). In the interior layers, the vertical extension of stripes is considerably larger (approx. 10–50 m) and their slopes exceed the isopycnal slope. Four competitive mechanisms of formation of the mesoscale striped texture are considered: stirring of large-scale inhomogeneities by the eddy field, the classic, inviscid adiabatic fluid symmetric instability, the McIntyre instability, and the strain-induced frontogenesis. Based on the instability criteria and the growth rates and geometry of the disturbances, the classic symmetric instability and the strain-induced frontogenesis are probably responsible for the formation of submesoscale striped texture in the

\* Corresponding author at: Department of Marine Systems, Tallinn University of Technology, Akadeemia tee 15A, 12618 Tallinn, Estonia.

E-mail address: [germo.vali@taltech.ee](mailto:germo.vali@taltech.ee) (G. Väli).

Peer review under the responsibility of the Institute of Oceanology of the Polish Academy of Sciences.



surface layer, while in the interior layers, the strain-induced frontogenesis and hypothetically the McIntyre instability can be essential. Stirring of large-scale inhomogeneities by the eddy field could be responsible for formation of striped texture in a passive tracer concentration and in temperature and salinity in the presence of thermohaline gradients on isopycnic surfaces (thermoclinicity), but it does not imply formation of stripes in dynamically active tracers, such as vertical vorticity, horizontal gradients of buoyancy, etc.

© 2021 Institute of Oceanology of the Polish Academy of Sciences. Production and hosting by Elsevier B.V. This is an open access article under the CC BY-NC-ND license (<http://creativecommons.org/licenses/by-nc-nd/4.0/>).

## 1. Introduction

High resolution images of the sea surface both provided by remote sensing and simulated by very high-resolution circulation models display a variety of elongated submesoscale structures – thin filaments or stripes of the order of 1 km wide and 10–20 km long (e.g. Barkan et al., 2019; Brannigan et al., 2017; Capet et al., 2008; Choi et al., 2017; D’Asaro et al., 2018; Gula et al., 2016; Jing et al., 2021; Karimova et al., 2012; McWilliams, 2016; Munk et al., 2000; Onken et al., 2020; Qiu et al., 2014; Schubert et al., 2020; Väli et al., 2017, 2018; Yu et al., 2019; Zhurbas et al., 2019a,b). Such elongated structures seem natural to associate with symmetric instabilities (SI) which are geometrically typified by overturning circulations about an axis aligned with the basic geostrophic flow – rolls (i.e. the disturbances are two-dimensional (2D) – they do not depend on the along-flow coordinate) (Bachman et al., 2017). The SI occurs in baroclinic flows when the Ertel potential vorticity  $q$  is opposite in sign of the Coriolis parameter  $f$  (Thomas et al., 2013):

$$\begin{aligned}fq < 0, q = (f\mathbf{k} + \nabla \times \mathbf{u}) \cdot \nabla b = q_{vert} + q_{bc} \\q_{vert} = (f - u_y + v_x)b_z = \zeta_{abs}b_z \\q_{bc} = (w_y - v_z)b_x + (u_z - w_x)b_y\end{aligned}\quad (1)$$

Here  $\mathbf{u}$  is the velocity,  $\mathbf{k}$  is the vertical unit vector,  $b = -g(\rho - \rho_0)/\rho_0$  is the buoyancy defined in terms of the gravitational acceleration  $g$ , potential density  $\rho$  and constant reference density  $\rho_0$ ,  $\zeta_{abs} = f - u_y + v_x$  is the absolute vertical vorticity. In more detail, the instability condition  $f q < 0$  implies a variety of instabilities such as (Bachman et al., 2017)

$$\text{Gravitational instability: } b_z < 0 \quad (2)$$

$$\text{Inertial instability: } f\zeta_{abs} < 0, b_z > 0 \quad (3)$$

$$\begin{aligned}\text{Symmetric instability:} \\fq_{bc} < 0, |fq_{bc}| > fq_{vert}, fq_{vert} > 0, b_z > 0\end{aligned}\quad (4)$$

If the flow is in geostrophic balance, we can apply the thermal wind relation ( $u_z = -b_y/f$ ,  $v_z = b_x/f$ ,  $w = 0$ ) and rewrite the expression for  $q_{bc}$  in Eq. (1) as

$$q_{bc} = -(b_x^2 + b_y^2)/f \quad (5)$$

and further the SI condition as (Haine and Marshall, 1998; Hoskins, 1974)

$$Ri \frac{\zeta_{abs}}{f} = Ri(1 + Ro) < 1, Ro > -1, b_z > 0 \quad (6)$$

where  $Ri = N^2/(u_z^2 + v_z^2) = f^2N^2/(b_x^2 + b_y^2)$  is the geostrophic Richardson number,  $Ro = (-u_y + v_x)/f$  is the gradient Rossby number defined as the ratio of vertical relative vorticity  $\zeta = -u_y + v_x$  to the planetary vorticity  $f$ , and  $N^2 = b_z$  is the buoyancy frequency squared.

Eq. (5) says that the baroclinicity of the fluid always works to reduce the potential vorticity and the SI occurs when the baroclinicity term  $q_{bc}$  of the Ertel potential vorticity  $q$  becomes prevalent over the vertical stratification and vorticity term  $q_{vert}$ . Such a prevalence is more likely to occur in the upper mixed layer where the vertical stratification is commonly weak and can be further weakened relative to the baroclinicity term that can increase due to atmospheric forcing (e.g. due to cross-front advection of dense water over light by Ekman transport driven by winds with down-front component (Thomas, 2005) – the situation that was revealed within the Northern Wall of the Gulf Stream (Thomas et al., 2013)).

The SI growth rate  $\omega_i$  and horizontal lengthscale  $L$  can be estimated for constant shear and stratification (see Eq. (1.4), (2.28), and (2.29) of Stone (1966)) as

$$\omega_i = f \frac{\sqrt{1 - Ri}}{\sqrt{Ri}}, L < 2 \frac{U}{f} \sqrt{1 - Ri} \quad (7)$$

where  $U$  is the velocity of the basic geostrophic flow. In accordance to Eq. (7), for typical ocean parameters,  $U = 0.1$  m/s,  $f = 1 \cdot 10^{-4}$  s<sup>-1</sup>, and SI favoring condition,  $Ri = 0.25 - 0.95$ , the SI time ( $1/\omega_i$ ) and length ( $L$ ) scales are in the range of  $(0.58 - 4.35)/f$  or 1.6–12 hours and below 0.45–1.7 km, respectively.

Favorable conditions for SI are also expected in the bottom boundary layer over sloping seabed where a cross-flow advection of dense water over light water by Ekman transport driven by bottom friction can reduce vertical stratification and increase baroclinicity (e.g. Garrett et al., 1993; Umlauf and Arneborg, 2009; Zhurbas et al., 2012).

The possibility to meet the SI condition Eq. (4) in well stratified interior layers of the sea that are not directly exposed to the atmospheric forcing and bottom friction seems questionable and should be additionally tested. However, one has to keep in mind that this instability condition is formulated in terms of the Ertel potential vorticity of inviscid adiabatic fluid and does not account for effects of vertical eddy viscosity and diffusion. If vertical eddy viscosity and diffusion is taken into account (see Eq. (3.3.a) and an unnumbered equation next to (3.5) in McIntyre (1970) and Appendix 1 for details), the SI condition Eq. (6) will change

for

$$Ri(1 + Ro) < \frac{(1 + Pr)^2}{4Pr}, Ro > -1, b_z > 0 \quad (8)$$

where  $Pr$  is the Prandtl number defined as the ratio of apparent vertical viscosity to diffusion of buoyancy. For this reason, diffusive destabilization of baroclinic geostrophic flow relative to 2D (symmetric) disturbances at  $1 \leq Ri < (1 + Pr)^2/(4Pr)$  is referred as the McIntyre instability (Ruddick, 1992). In stratified ocean the  $Pr$  value can be much larger than 1 because e.g. the low (near-inertial) frequency internal waves (Lappe and Umlauf, 2016; Thomas et al., 2016) can effectively contribute to the vertical transport of momentum without contributing to the vertical transport of mass/buoyancy. Comparing growth rates of symmetric disturbances in viscous non-adiabatic and inviscid adiabatic cases, the corresponding inviscid adiabatic modes usually have the numerically highest growth rates (McIntyre, 1970).

Apart from the diffusive destabilization, the baroclinic geostrophic flow in the ocean is subject to double-diffusive destabilization relative to 2D (symmetric) disturbances (Kuzmina and Rodionov, 1992; Kuzmina and Zhurbas, 2000; May and Kelley, 1997) caused by the differences in vertical apparent diffusivities for scalar quantities that determine the sea water density/buoyancy – temperature and salinity, in accordance with parameterization by Stern (1967). Therefore, there are at least three types of symmetric instability of baroclinic geostrophic flows: classic or inviscid adiabatic SI (SI), diffusive SI (DSI or McIntyre instability), and double-diffusive SI (DDSI). The DSI can exist at a wider range of  $Ri$  than SI (cf. Eq. (6) and (8) while DDSI is possible at any large value of  $Ri$  (Kuzmina and Zhurbas, 2000). The maximum growing SI disturbance is aligned to the isopycnal slope and gains the kinetic energy (KE) from the mean sheared flow, while the submesoscale and mesoscale currents/eddies gain KE primarily through the release of available potential energy stored in baroclinic fluid (Thomas et al. 2013, 2016). In contrast to SI, the maximum growing DSI and DDSI disturbances at  $Pr > 1$  have a smaller slope than the isopycnal slope and gain KE through the release of available potential energy of baroclinic fluid (Kuzmina and Zhurbas, 2000; McIntyre 1970). The SI, DSI and DDSI are characterized not only by different  $Ri$  ranges, but also by different growth timescales: the timescales for DSI and DDSI are larger than the timescale for SI (Kuzmina and Zhurbas, 2000; McIntyre, 1970; see also Appendix 1).

Apart from the symmetric instabilities, the elongated submesoscale features seen in the horizontal plane view of the vertical vorticity, temperature, material concentration  $c$ , etc. can be generated by strain-induced frontogenesis (McWilliams, 2016; Munk et al., 2000). Frontogenesis is a classical dynamical process in meteorology (Hoskins and Bretherton, 1972; Hoskins, 1982) and ocean (Kuzmina, 1981; Macvean and Woods, 1980) where a background horizontal deformation flow such as  $u_d = \alpha x$ ,  $v_d = -\alpha y$ ,  $w_d = 0$ ,  $\alpha > 0$  with a uniform strain rate

$$\alpha = \left( \frac{\partial u_d}{\partial x} - \frac{\partial v_d}{\partial y} \right) / 2 \quad (9)$$

provides a rapid growth of  $y$ -aligned surface horizontal gradients of buoyancy  $b_y$ , velocity  $u_y$  and passive tracer

concentration,  $c_y$ . The growth is exponential for passive tracer ( $c_y \sim \exp(\alpha t)$ ) and can be even super-exponential for the dynamically active  $b$  (Hoskins and Bretherton, 1972; Hoskins, 1982). In the course of strain-induced frontogenesis in inviscid adiabatic fluid, the frontal jet symmetry is violated towards a strong cyclonic shear and a weak anti-cyclonic shear: at time  $2.5\alpha^{-1}$  the associated Rossby numbers are  $Ro^+ = 1$  and  $Ro^- = -0.3$ , respectively. Soon afterwards, at  $2.89\alpha^{-1}$ , the singularity is achieved with  $Ro^+ = +\infty$  while the anticyclonic shear remains at  $Ro^- = -0.3$  (Macvean and Woods, 1980; Munk 2001; Ou, 1984). Remarkable that the modelled filamentous submesoscale features in the surface ocean layer are characterized by very high cyclonic shear at  $Ro > 1$  (McWilliams, 2016; Onken et al., 2020; Väli et al. 2017). In context of filamentous submesoscale features, the primary background strain can be from mesoscale currents and eddies as well as from submesoscale coherent vortices, while the seed buoyancy gradients are created either by the quasigeostrophic chaotic advection of the mesoscale  $b$  field or by the mixed layer instabilities (McWilliams, 2016).

In the general case the horizontal strain rate is defined as (e.g. Gula et al. (2014))

$$S = \sqrt{(u_x - v_y)^2 + (v_x + u_y)^2} \quad (10)$$

The principal strain axis, given by the angle  $\theta_p$  such that

$$\tan(2\theta_p) = \frac{v_x + u_y}{u_x - v_y} \quad (11)$$

corresponds to the direction of the maximum stretching, while its perpendicular direction corresponds to the maximum contraction. The straining will induce frontogenesis if the principal strain axis is aligned with the axis of the front. There is a link between the strain-induced frontogenesis and SI, namely, the enhancement of lateral buoyancy gradients due to frontogenesis in conjunction with atmospheric forced surface buoyancy loss can produce a negative Ertel potential vorticity  $q$  and thereby trigger SI (Jing et al., 2021).

There is another possibility of the striped texture formation, which can be considered as a null hypothesis. This refers to stirring of large-scale inhomogeneities by the eddy field (e.g. Villermaux (2019)). Smith and Ferrari (2009) have shown that temperature and salinity filaments with slopes much steeper than the isopycnal slope can be generated through lateral stirring of large-scale thermohaline gradients on isopycnal surfaces (thermoclinicity) by a vigorous geostrophic eddy field developed through baroclinic instability in the framework of a quasi-geostrophic model. Effect of stirring is demonstrated in Appendix 2 where the evolution of a constant gradient of the tracer concentration in a time-dependent, non-divergent 2D velocity field, consisting of two gyres that conversely expand and contract periodically in the  $x$ -direction, is considered. It is shown that for the advection time much longer than the period of eddy rotation and expansion-contraction, the constant gradient tracer concentration transforms into a striped texture, while the velocity and vorticity fields remain free of any strip-like irregularities.

Baltic Sea (Figure 1) is known for summer cyanobacteria blooming (e.g. Finni et al. (2001)) which provides outstanding ability to visualize filamentous submesoscale

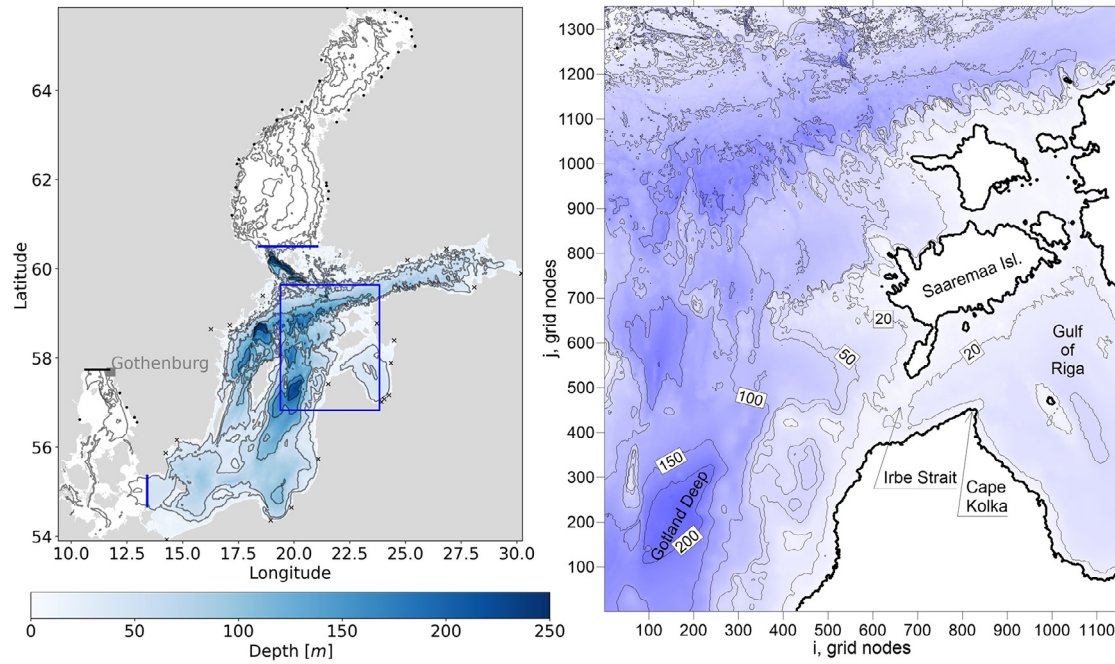


**Figure 1** Bathymetric map of the Baltic Sea. Left panel: The high resolution model domain (filled colors) with the open boundary locations (bold blue lines). The coarse resolution model domain (blank contours + filled colors) has an open boundary close to Gothenburg (bold black line). Right panel: Close-up of the northeastern Baltic Proper (the study area). The river mouth locations in the coarse model setup and in both setups are marked with dots and crosses, respectively.

structures and coherent vortices in remote sensing optical images of the sea surface. Such images were even used in review articles to demonstrate submesoscale phenomena (e.g. McWilliams (2016)). Several attempts were done to reproduce submesoscale features seen on remote sensing images of the Baltic Sea using very high-resolution circulation models (Laanemets et al., 2011; Onken et al., 2020; Vankevich et al., 2016; Zhurbas et al., 2008; 2019a,b). Statistics of submesoscale coherent vortices simulated in the surface layer of the Baltic Sea was accessed in Vortmeyer-Kley et al. (2019). Rotation of floating particulate matter in submesoscale vortices and its aggregation into filamentous features was studied by means of numerical modelling of the Baltic Sea circulation (Giudici et al., 2021; Kalda et al., 2014; Väli et al., 2018; Zhurbas et al., 2019a,b). Diagnosis of mixed layer instabilities as applied to the surface layer of the Baltic Sea was performed by Onken et al. (2020) and Chrysagi et al. (2021) based on submesoscale simulations. In summer, the SI condition (Eq. (4)) was found to be satisfied in 1.8–4.8% of the grid cells in the surface layer of a 100 km × 100 km model domain to the south of the Bornholm Island (Onken et al., 2020). Negative values of the Ertel potential vorticity consistent with SI were found in the down-wind flank of a frontal filament emerged during a storm event in the Eastern Gotland Basin (Chrysagi et al., 2021). Seasonality of submesoscale coherent vortices in different layers of the Baltic Sea was addressed in Väli and Zhurbas (2021) based on very high-resolution modelling. Kuzmina et al. (2005) showed that DDSI was probably responsible for generation of thermohaline intrusions observed in the permanent halocline of the Eastern Gotland Basin after the 1993 Major Inflow.

Almost all of the above cited studies of submesoscale processes were focused on the surface mixed layer. Meanwhile, submesoscale processes are not limited to the surface mixed layer, where they are probably most intensive, but can also be active in the interior sea layers (McWilliams, 2016; Smith and Ferrari, 2009; Yu et al., 2019). The objective of this work is to simulate submesoscale flows typical for summer season in the northeastern Baltic Proper based on a very high-resolution circulation model, compare the submesoscale filaments of the surface layer with those in the interior layers, and provide diagnosis of formation mechanisms based on the above listed criteria.

## 2. Material and methods

### 2.1. Model description

The General Estuarine Transport Model (GETM) (Burchard and Bolding, 2002) was applied to simulate the meso- and submesoscale variability of temperature, salinity, currents, and overall dynamics in the northeastern Baltic Proper. GETM is a primitive equation, 3-dimensional, free surface, hydrostatic model with the embedded vertically adaptive coordinate scheme (Hofmeister et al., 2010) which reduces the artificial numerical mixing in the simulations (Gräwe et al., 2015). The vertical mixing is parametrized by two equation  $k$ - $\epsilon$  turbulence model coupled with an algebraic second-moment closure (Burchard and Bolding, 2001; Canuto et al., 2001). The implementation of the turbulence model is performed via General Ocean Turbulence Model (GOTM) (Umlauf and Burchard, 2005).

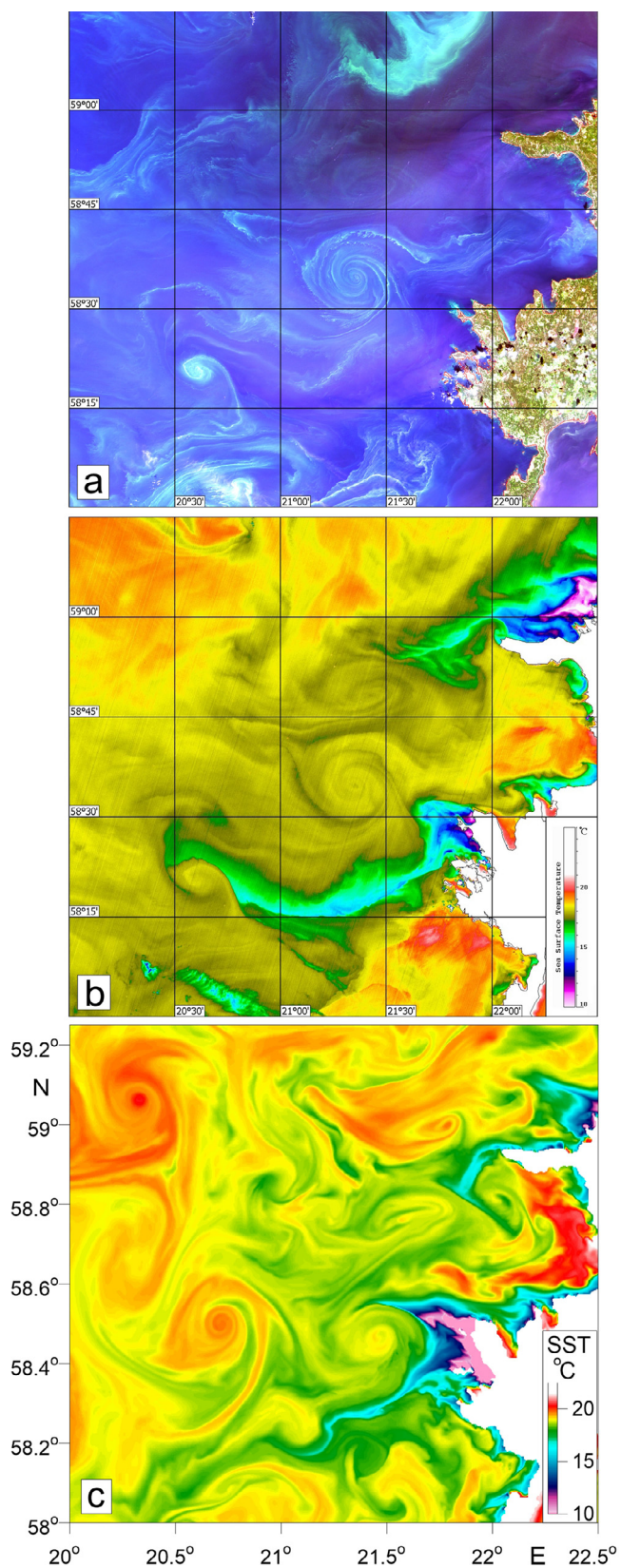


**Figure 2** Colour snapshot (a) and infrared SST map (b) of an area west of the Moonsund from Operational Land Imager (OLI) and Thermal Infrared Sensor (TIRS) of the Landsat 8 satellite on 2018/07/18 19:00 UTC versus modelled SST (GETM, 0.125 NM grid) on 2018/07/18 07:07 UTC (c).

For the horizontal and vertical transport of momentum and tracers, a second-order total variation diminishing (TVD)-scheme with Superbee limiter with reduced spurious mixing (Klingbeil et al., 2014 and 2018) is applied.

The coarse resolution model covers the entire Baltic Sea with an open boundary in the Kattegat and has the horizontal resolution of 0.5 nautical miles (926 m) over the whole model domain. The coarse resolution model run is started from 1 April 2010 with initial thermohaline conditions taken from the Baltic Sea reanalysis for the 1989–2015 by the Copernicus Marine service. More detailed information about the model setups is available in Zhurbas et al. (2018 and 2019a) and for the coarse resolution model in Liblik et al. (2020).

The horizontal grid of the high-resolution nested model with uniform step of 0.125 nautical miles (approximately 232 m) all over the computational domain, which covers the central Baltic Sea along with the Gulf of Finland and Gulf of Riga (Figure 1), is applied while 60 adaptive layers in the vertical direction are used, and the cell thickness in the surface layer within the study area does not exceed 1.8 m. The digital topography of the Baltic Sea with the resolution of 500 m (approximately 0.25 nautical miles) is obtained from the Baltic Sea Bathymetry Database (<http://data.bshc.pro/>) and interpolated bi-linearly to 232 m resolution.

Nested model simulation run is performed from 1 April to 20 September 2018. The model domain has the western open boundary in the Arkona Basin and the northern open boundary at the entrance to the Bothnian Sea (see Figure 1 for details). For the open boundary conditions the one-way nesting approach is used and the coarse resolution model results along the open boundaries are utilized. Sea-level fluctuations with 1-hourly resolution and temperature, salinity and current velocity profiles with 3-hourly resolution are interpolated using the nearest neighbour method in space to the higher resolution grid. In addition, the profiles are vertically interpolated to 2 m resolution and extended to the bottom of the high resolution model. Flather (1994) radiation condition is used for the obtained sea-level fluctuation data and relaxation towards obtained profiles with sponge layer factors according to the method of Martinsen and Engedahl (1987) during simulations at the boundary.

The atmospheric forcing (the wind stress and surface heat flux components) is calculated with bulk formulae from the wind components, solar radiation, air temperature, total cloudiness and relative humidity data generated by the operational model HIRLAM (High Resolution Limited Area Model) maintained by the Estonian Weather Service with the spatial resolution of 11 km and temporal resolution of 1 hour (Männik and Merilain, 2007). The wind velocity components at the 10 m level along with other HIRLAM meteorological parameters are bi-linearly interpolated to the model grid.

The freshwater input from 54 largest Baltic Sea rivers together with their inter-annual variability is taken into account in the coarse resolution model. The original dataset consists of daily climatological values of discharge for each river, but inter-annual variability is added by adjusting the freshwater input to different basins of the sea to match the values reported annually by HELCOM (Johansson, 2018).

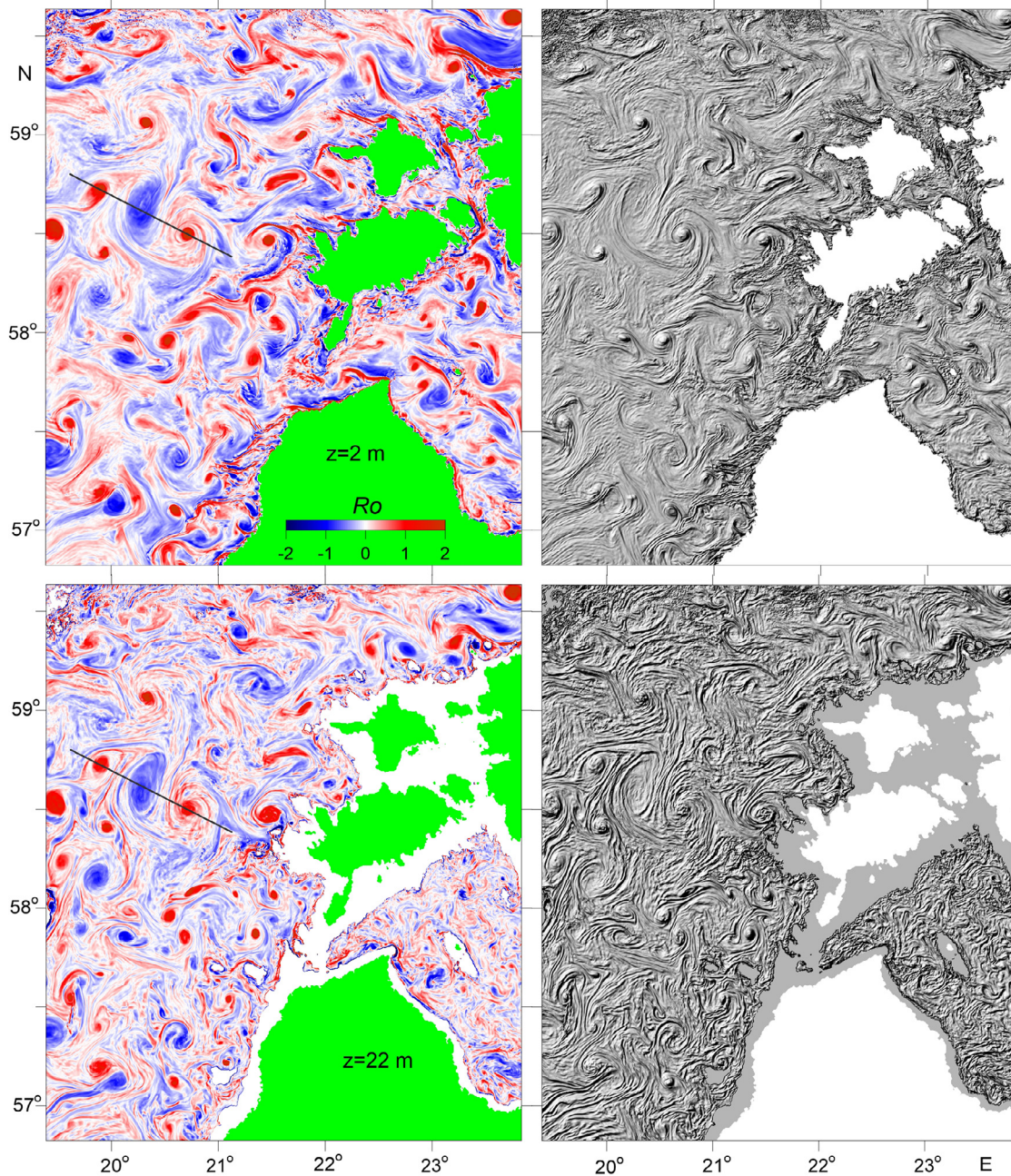


**Figure 3** Left panels: gradient Rossby number  $Ro = \zeta / f$  simulated on 2018/7/18 07:07 UTC at 2 m (top) and 22 m (bottom) levels. A black line on the left panels is the location of a transect to be analyzed in Figure 5 and 12. Right panels are the same but in the shaded relief form to highlight the striped texture.

The initial temperature and salinity fields are obtained from the coarse resolution model for 1 April 2018 and interpolated using the nearest neighbour method to the high-resolution model grid. In addition, as the adaptive vertical coordinates are used in both setups, the T/S profiles from coarse resolution are linearly interpolated to fixed 10 m vertical resolution before interpolation to the high resolution and extended to the maximum depth of high-resolution model. The model runs are started from motionless state and zero sea surface elevation. The spin-up time of the Baltic Sea model under the atmospheric forcing is expected to be within 10 days (Krauss and Brüggge, 1991; Lips et al., 2016), while the model output for comparison with the re-

spective satellite imagery was obtained after 108 days of simulation.

## 2.2. Model validation

The coarse-resolution model (926 m grid), whose output was used as the initial and open boundary conditions in the nested, high-resolution model (232 m grid), has been thoroughly tested by means of comparison of the simulated and observed current velocity variance and timeseries of sea-level fluctuations, temperature and salinity in the surface, intermediate and bottom layers for a number of monitor-

ing stations of the Baltic Sea (see Zhurbas et al. (2018) for details).

The ability of the nested, high-resolution model to reproduce the observed submesoscale structures is demonstrated in Figure 2 where the optical and infrared sea surface temperature (SST) snapshots of an area west of the Saaremaa and Hiiumaa islands (Moonsund), Estonia, from Landsat-8 mission is presented versus the modelled SST for 2018/07/18. The snapshots were taken during the period of summer blooming of cyanobacteria, when the submesoscale motions have assembled the phytoplankton material into filaments winded up into spirals thereby visualizing coherent submesoscale vortices. Note that the cyclonic vortices/spirals are visualized better than the anticyclonic ones which can be explained by larger rotation frequency and more pronounced differential rotation (Zhurbas et al., 2019b). Similar pattern of submesoscale filaments and eddies is seen in the simulated SST map; the difference is that the simulated pattern is more densely populated with submesoscale features in comparison to the remote sensing optical image which can be probably explained by the lack of visualizing tracer (phytoplankton) in some parts of the study area. The remote sensing SST is in good agreement with the modelled SST, displaying almost identical areas of pronounced coastal upwelling and many submesoscale eddies. Of course, one cannot expect that the model will reproduce the mutual arrangement of vortices in remote sensing images, since it is impossible to simulate the individual realization of a random process of the formation of submesoscale vortices.

### 3. Results

The simulated submesoscale filaments – stripes occurred to be found in different tracer fields not only in the surface layer but also in the interior layers. To illustrate this, we calculated patterns of the gradient Rossby number  $Ro = \zeta / f$  (Figure 3) and the horizontal temperature gradient modulus  $|\Delta_H T| = \sqrt{T_x^2 + T_y^2}$  (Figure 4) in the surface layer ( $z = 2$  m) and in an interior layer at depth  $z = 22$  m which is located in or just below the seasonal thermocline (cf. Figure 5d). Note that all of the gradient variables shown in Figure 3 and subsequent figures were calculated through the finite differences with a step of 2 m vertically and 232 m horizontally. Both the  $Ro$  and  $|\Delta_H T|$  maps display a variety of submesoscale stripes of the order 10 km in length and 1 km in width. The most prominent stripes are found on the periphery of submesoscale coherent vortices (cf. Figures 3, 4 and 5), and they display a tendency to be vertically inclined towards the center of the vortex with increasing depth (see Figure 5).

Vertical/side view of the submesoscale stripes is demonstrated in Figure 5 where the Rossby number fluctuations  $Ro' = Ro - \langle Ro \rangle$  and the horizontal gradient modulus of temperature and density,  $|\Delta_H T|$  and  $|\Delta_H \rho|$ , respectively, are plotted versus distance and depth;  $\langle Ro \rangle$  is the running mean value of  $Ro$  over 11 bins horizontally-neighbouring along the section (i.e. the smoothing window is  $11 \times 231.5$  m  $\approx$  2.5 km). The stripes seen in the interior layers have vertical extension of 10–50 m and do not penetrate into the surface

mixed layer whose thickness is only 5–8 m (cf. Figure 5b, c and d). The surface mixed layer has its own system of stripes, the vertical extension of which is probably determined by the thickness of the mixed layer but cannot be accurately estimated from Figure 5. To estimate the vertical extension of stripes in the mixed layer accurately, we calculated the correlation coefficient between the Rossby number fluctuations  $Ro'$  in the uppermost z-level (0.5 m depth) and that of 1.5, 2.5, ..., 10.5 m depth. Since the correlation dropped to 0.21 for the 0.5 m and 6.5 m series and became negative (-0.013) for the 0.5 m and 7.5 m series, the vertical extension of stripes in the surface mixed layer was estimated as 6–7 m.

To diagnose the possibility of formation of submesoscale striped texture in the Baltic Sea by stirring of large-scale inhomogeneities by the eddy field, we carried out a numerical experiment with floating Lagrangian particles, similar to that described in Appendix 2. Instead of the eddy field specified by the analytical forms (A26)–(A27), we took the time-dependent  $(u, v)$ –components of currents in the surface layer of the Baltic Sea, generated by the high-resolution model. The initial concentration of floating particles was taken either homogeneous with  $C_0 = 900$  particles per a  $232$  m  $\times$   $232$  m model bin, randomly seeded within the bin, or obeying a constant meridional gradient with 1000 particles per bin at the northern boundary of the study region and 800 particles per bin at the southern boundary. Keeping in mind that the typical period of rotation of coherent submesoscale vortices in the Baltic Sea is  $T_{CSV} = 4\pi / f \approx 28$  hours, we calculated the normalized concentration  $C/C_0$  for 2018/7/18 07:07 UTC formed from the homogeneous and constant meridional gradient states during the preceding time span of  $t = 8$  hours (which corresponds to the case of small advection time  $t/T_{CSV} = 0.29 \ll 1$ ) and  $t = 3$  days (which corresponds to the case of large advection time  $t/T_{CSV} = 2.6 \gg 1$ ) (Figure 6).

In contrast to the case of non-divergent, time-dependent, 2D eddy field where the formation of striped texture by stirring of the large scale inhomogeneities took place only at  $t/T_{CSV} \gg 1$  (see Appendix 2), in the case of the modelled  $(u, v)$ –components of surface currents of the Baltic Sea the striped texture in the floating particles concentration is already formed at  $t/T_{CSV} \ll 1$  starting from both the homogenous and constant meridional gradient state (cf. Figures 6 and 14). Moreover, the striped texture formed from initially homogeneous and constant gradient concentration is almost identical which means that the stripes are generated by the horizontal velocity divergence/convergence rather than by stirring of the large-scale horizontal gradients by the eddy field.

The striped texture is also seen in the field of horizontal velocity divergence, but it has no simple linear relationship with the striped texture of the floating tracer (cf. Figures 6 and 7). The dissimilarity of the texture in the fields of concentration of the floating tracer and horizontal divergence is associated with a complex integral relationship between these fields (Väli et al., 2018).

$$C(\mathbf{x}, t) = C(t - \tau | \mathbf{x}, t) \exp \left[ \int_t^{t-\tau} \text{div}(\mathbf{u}(t' | \mathbf{x}, t)) dt' \right] \quad (12)$$

where  $\mathbf{u} = (u, v)$  and  $A(t' | \mathbf{x}, t)$  denotes the value of a property  $A$  at time moment  $t'$  for a Lagrangian particle/parcel



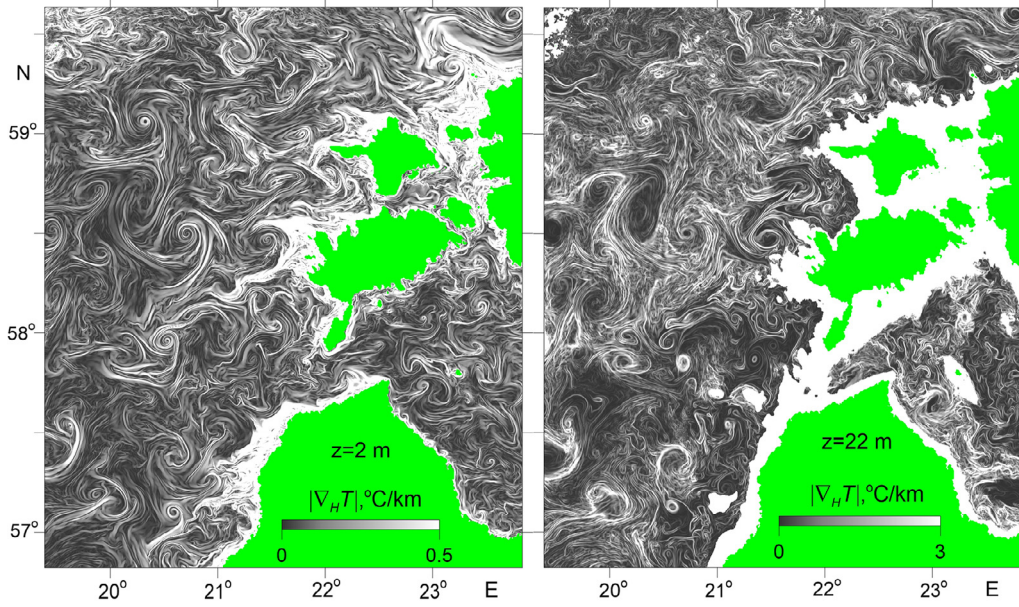


**Figure 4** Horizontal temperature gradient modulus  $|\nabla_H T|$  simulated on 2018/7/18 07:07 UTC at 2 m (left) and 22 m (right) levels.

that had the position  $\mathbf{x} = (x, y)$  at time moment  $t$ . The quadrature solution (12) shows that concentration of floating stuff at a material point  $(\mathbf{x}, t)$  is equal to the concentration at the same material point in the preceding time moment  $t - \tau$  multiplied by the exponent of the backward time integral of the Lagrangian velocity divergence for the time interval  $[t, t - \tau]$ .

To diagnose the classic symmetric instability using the results of simulation, we tested the fulfillment of the criterion Eq. (4) and the condition  $q < 0$  in the same layers as shown in Figures 2–4. A logical maps presented in Figure 8 show that the criterion Eq. (4) is satisfied in numerous elongated spots occupying approx. 20.1% of the study area in the surface layer, while at  $z = 22$  m the instability percentage falls to 0.6%. Moreover, even the rare, would-be instability spots at  $z = 22$  m level are not uniformly distributed within the study area but mostly located in the vicinity of the same contour of the sea depth, 22 m, i.e. they are actually in the bottom boundary layer. As to the gravitational (Eq. (2)) and inertial (Eq. (3)) instability, it is possible only in areas less than 1% of the total study area both at  $z = 2$  m and  $z = 22$  m (i.e. the likelihood to meet gravitational and inertial instabilities is insignificant both in the surface and interior layers).

To diagnose the McIntyre instability, we calculated parameter  $Ri(1 + Ro)$  at  $z = 2$  and 22 m levels (Figure 9). It was conventionally assumed that the McIntyre instability is possible at  $1 \leq Ri(1 + Ro) < 10$  when in accordance to Eq. (8) the Prandtl number is not too large,  $1 < Pr < 40$ , or not too small,  $1/40 < Pr < 1$ . The parameter  $Ri(1 + Ro)$  was in the  $1 \leq Ri(1 + Ro) < 10$  range (the would-be McIntyre instability) in 39.4% and 14.0% of the study area at  $z = 2$  and 22 m levels, respectively, and in the  $0 < Ri(1 + Ro) < 1$  range (classic symmetric instability) in 12.6% and 0.7%, respectively. Note that the criteria Eq. (4) and Eq. (6) provide nearly the same small value for the symmetric instability percentage in the interior layer (0.6% vs 0.7%) while in the surface layer, Eq. (4) gives considerably larger value of the

symmetric instability percentage relative to Eq. (6) (20.1% vs 12.6%). The discrepancy is likely caused by the vertical shear in the wind-driven Ekman currents which, being ignored in Eq. (6), can enlarge the absolute value of  $q_{bc}$  in the surface layer.

To diagnose the possibility of horizontally elongated submesoscale features to be generated by strain-induced frontogenesis, a frontogenetic strain rate was defined as  $S \cos(2\theta)$ , where  $\theta = \theta_p - \theta_\rho$  is the angle between the density front axis  $\theta_\rho$  and the principal strain axis  $\theta_p$ . At  $|\theta| < \pi/4$  we have  $S \cos(2\theta) > 0$  which corresponds to frontogenetic situation, and at  $|\theta| > \pi/4$  we have  $S \cos(2\theta) < 0$  which corresponds to frontolytic situation (Hoskins, 1982, Gula et al., 2014). The horizontal strain rate  $S$  defined by Eq. (11) and the angle  $\theta$  was calculated from the model output. Maps of the normalized frontogenetic strain rate  $S \cos(2\theta)/f$  (Figure 10) show that positive values of this parameter of the order of 1 frequently encounter both in the surface and interior layers. The cumulative distribution function  $PF$  of the  $S \cos(2\theta)/f$  parameter (Figure 11) show that the frontogenetic case is more probable than the frontolytic case ( $1 - PF(0) = 0.62$  and  $0.58$ ), and the 90% quantile of  $PF$  (i.e. the value of  $S \cos(2\theta)/f$  for which  $PF(S \cos(2\theta)/f) = 0.9$ ) is 0.41 and 0.33 at  $z = 2$  m and 22 m, respectively.

Distribution of the same parameters as in Figures 8–10 versus distance and depth (Figure 12) confirms that the ideal fluid SI criterion (Eq. (4)) is satisfied in numerous spots in the surface and bottom layers and not satisfied in the interior. In the surface layer, the spots do not exceed 5 m in depth. In contrast, there is some possibility for the McIntyre instability to exist both in the boundary and interior layers especially within the anticyclonic eddy (see Figure 12c). Similar to Figures 10–11, Figure 12d shows the presence of relatively high values of  $S \cos(2\theta)/f$  throughout the water column.

Vertical section of the SI logical parameter,  $q$ ,  $Ri(1 + Ro)$ , and  $S \cos(2\theta)/f$  (Figure 12) confirms that conditions favourable for SI are satisfied only in a localized spots in the

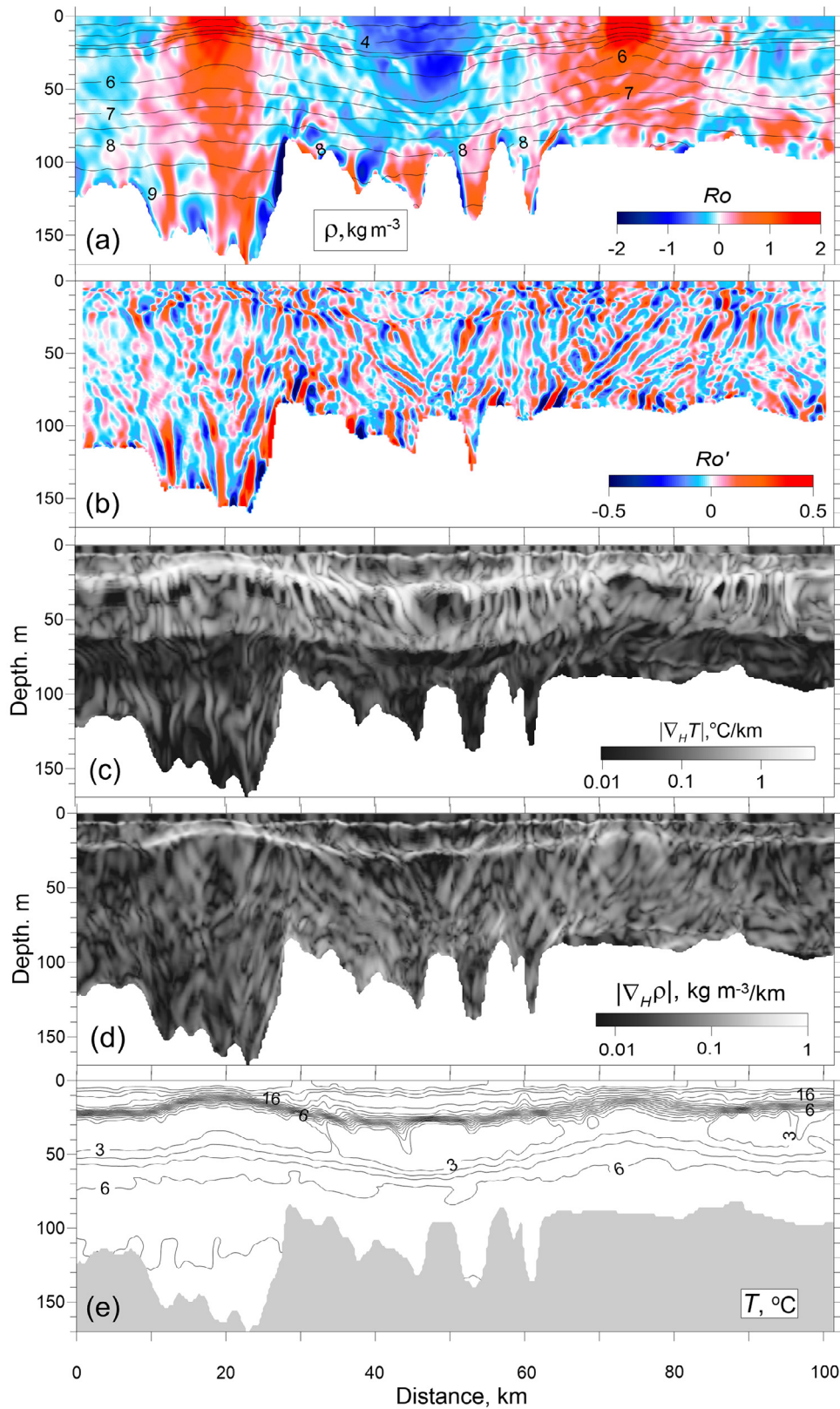


**Figure 5** Vertical section through an anticyclonic and two cyclonic eddies (simulation, 2018/7/18 07:07 UTC). The position of the section is shown in Figure 3. (a) Potential density anomaly  $\rho$  (contours) and Rossby number  $Ro$  (colours), (b) Rossby number fluctuations  $Ro'$ , (c) horizontal temperature gradient modulus  $|\nabla_H T|$ , (d) horizontal density gradient modulus  $|\nabla_H \rho|$ , and (e) temperature  $T$  versus distance and depth.

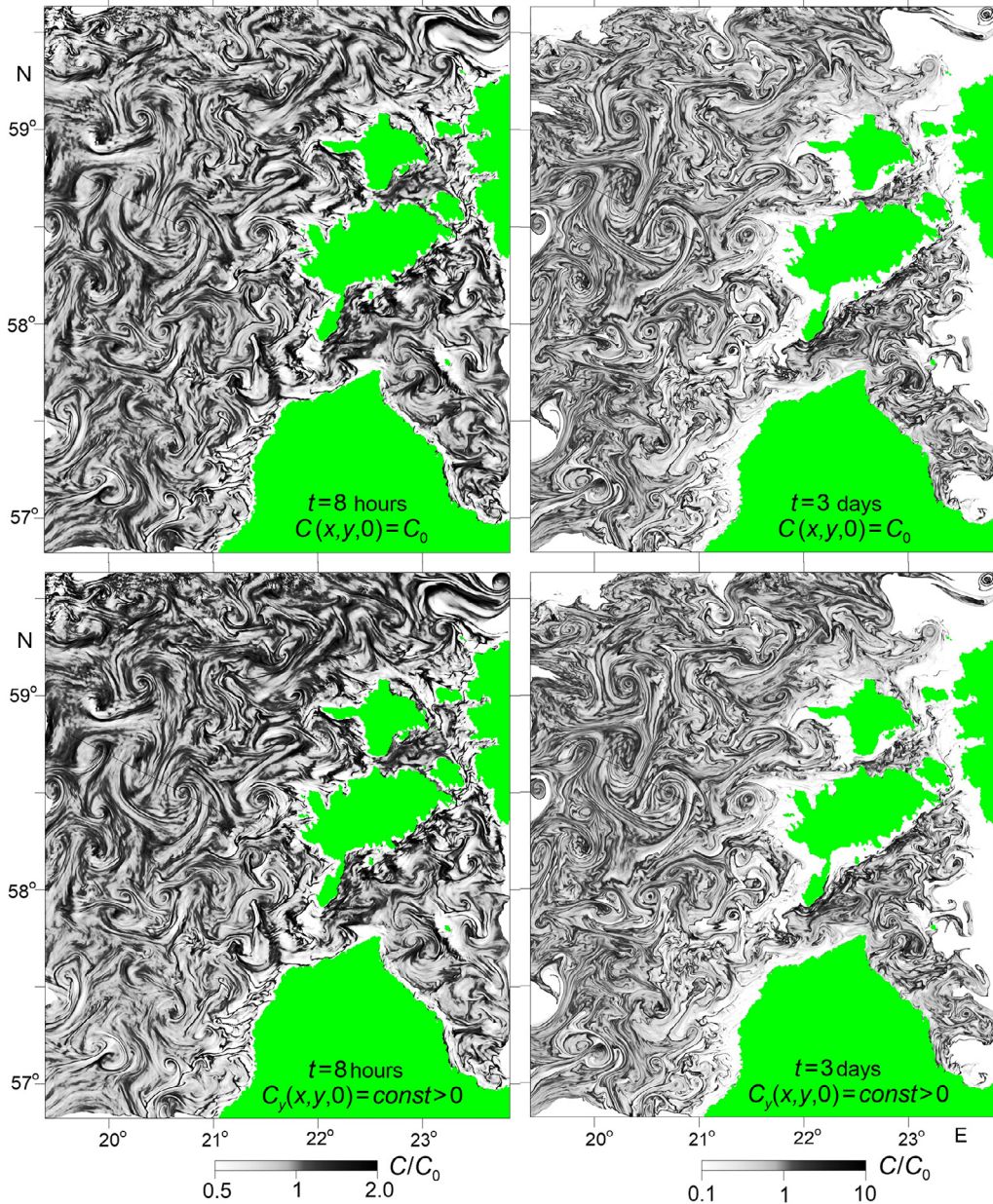


**Figure 6** Normalized concentration of floating particles on 2018/7/18 07:07 UTC formed by the modelled surface layer currents during the preceding time span of  $t = 8$  hours (left panels) and  $t = 3$  days (right panels) from the initially homogeneous (top panels) and constant meridional gradient (bottom panels) state.

surface and bottom layers while the high positive values of the horizontal frontogenetic strain rate  $S \cos(2\theta)$  of the order of  $f$  are frequently encountered everywhere throughout the water column. Note that there are some spots of negative  $q$  and  $Ri(1 + Ro)$  values in the core of the anticyclonic eddy and in the bottom layer which are not confirmed by the SI logical parameter and therefore relate to the inertial instability condition  $Ro < -1$ .

#### 4. Discussion and conclusions

The very high-resolution modelling of the northeastern Baltic Proper shows that preferentially along-flow elongated

submesoscale inhomogeneities or stripes of the order of 10–20 km in length and 1 km in width, are quite typical for summer season both in the surface layer and the interior layers. The difference lies in the vertical scale of the stripes: it does not exceed 6–7 m in the surface layer which is comparable with the upper mixed layer depth (see Figure 5) to 10–50 m in the interior layers. In the vertical plane, the stripes display a tendency to be inclined towards the center of submesoscale coherent vortices with increasing depth. The difference in vertical size of the stripes simulated in the surface and interior layers hints at different generation mechanisms, the diagnosis of which has become the main focus of this study.

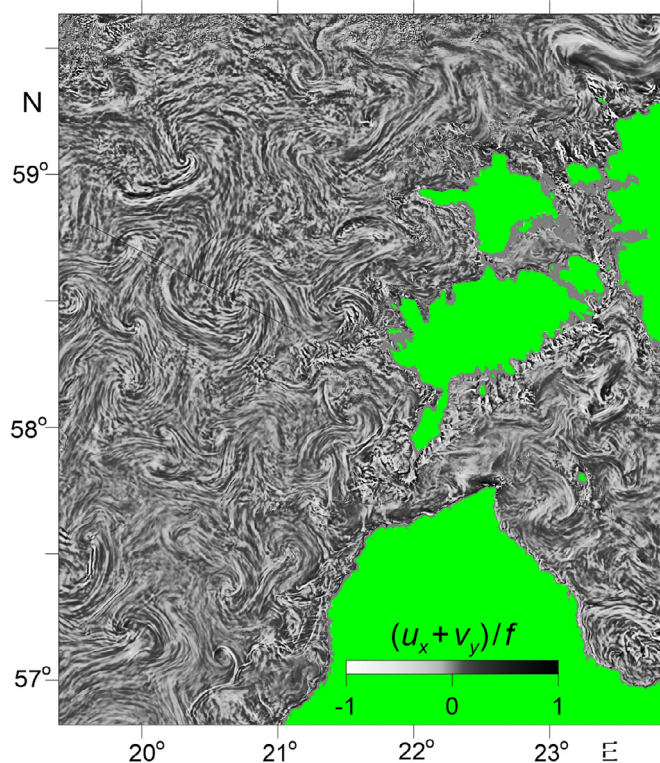


**Figure 7** Normalized horizontal divergence of the surface layer velocity simulated for 2018/7/18 07:07 UTC.

Stirring of large-scale inhomogeneities by the eddy field was chosen a null hypothesis for the striped texture formation. To test this, we performed a number of numerical experiments simulating horizontal advection of Lagrangian particles by the surface currents generated by the high-resolution model of the Baltic Sea and by the 2D non-divergent, time-dependent, two-gyre velocity field specified by analytical forms (A26)–(A27) for comparison. As a result, the null hypothesis was declined for the next two reasons.

First, the stirring of large-scale horizontal gradients of a passive tracer by the eddy field was found to form the striped texture for the advection time much larger than the period of eddy rotation,  $t/T_{CSV} \gg 1$ , while, in particular, the aggregation of floating particles in stripes by the modelled surface currents of the Baltic Sea took place already at  $t/T_{CSV} \ll 1$  even when the particles were uniformly seeded throughout the study region. The latter proves that the non-uniform horizontal divergence rather than stirring of large-scale horizontal gradients matters.

Second (and more principal), stirring of large scale inhomogeneities by eddies in its narrow sense implies the possibility of striped texture formation in the passive tracer concentration (e.g. Villermaux, 2019) or in temperature and salinity provided that there are thermohaline gradients on isopycnal surfaces, i.e. thermoclinicity (Smith and Ferrari, 2009). However, the high-resolution ocean modelling forecasts the striped texture also in the dynamically active tracers such as the vertical vorticity, modulus of horizontal gradient of buoyancy, horizontal divergence, etc. Therefore, one has to seek for other mechanisms responsible for strip-like submesoscale disturbances of the velocity and buoyancy fields.

**Table 1** Normalized growth rate  $\omega_i/f$  of the maximum growing mode of the classic symmetric instability versus the Richardson and Rossby numbers, calculated from Eq. (A10).

$Ro \backslash Ri$	0.25	0.5	0.95
-0.5	1.87	1.22	0.74
0	1.73	1	0.23
0.5	1.58	0.71	NONE

The classic SI criterion (Eq. (4)) is shown to be satisfied in numerous elongated spots occupying approximately 20% of the study area in the surface layer and the vertical extension of SI layer does not exceed 5 m and has the typical value of 4 m which is a part of the mixed layer of 6–8 m in depth (cf. Figures 5 and 12). The thermal wind velocity  $U$  in Eq. (A25) can be estimated from the model output as the product of the root mean square of the vertical velocity gradient at  $z = 2$  m (which is  $0.027 \text{ s}^{-1}$  for the time moment 2018/7/18 07:07 UTC) and the height of SI layer:  $U = 0.027 \times 4 \approx 0.1 \text{ m s}^{-1}$ . If one takes  $U = 0.1 \text{ m s}^{-1}$ ,  $f = 1.24 \cdot 10^{-4} \text{ s}^{-1}$  (at  $58.2^\circ\text{N}$ , the mid-latitude of the study area),  $Ri = 0.25\text{--}0.5$ , and  $Ro = -0.5\text{--}0.5$ , according to Eqs. (A10) and (A25) the SI growth timescale  $T = 1/\omega_i$  will be estimated as  $T = 1.2\text{--}3.2$  hours, while the upper limit for the lengthscale of growing disturbances varies within  $L = 540\text{--}3020$  m (see Tables 1 and 2). These estimates of  $T$  and  $L$  seem quite reasonable, because the former is much smaller than the formation time of the submesoscale coherent vortices (McWilliams, 2016), and the latter satisfacto-

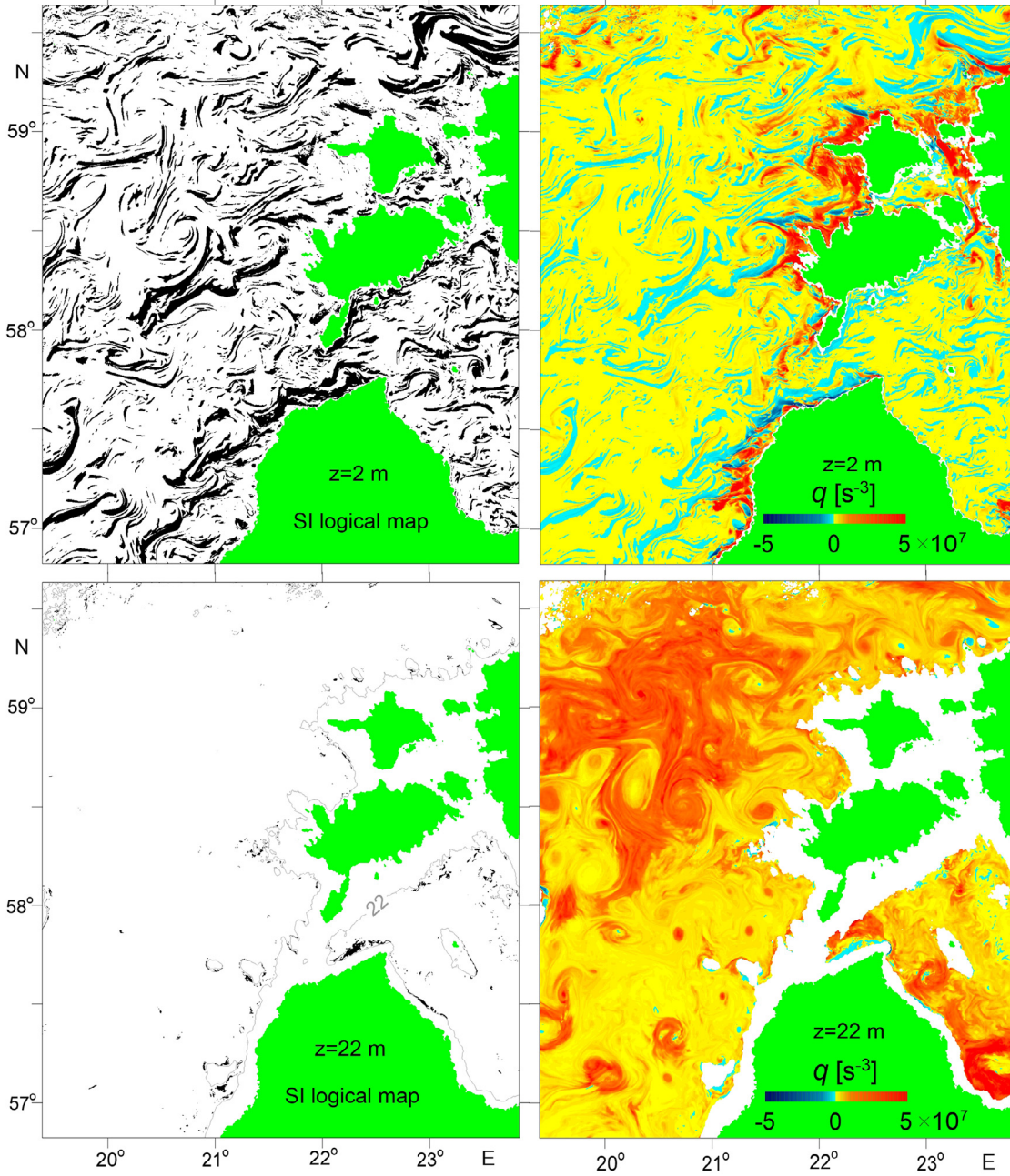


**Figure 8** Logical maps (left panels) indicating where the condition for symmetric instability (Eq. (4)) is satisfied (black spots) and Ertel potential vorticity  $q$  (right panels) in the surface layer (top panels) and the interior (bottom panels) layers (simulation, 2018/7/18 07:07 UTC).

rily corresponds to the width of the simulated filaments: in accordance to Figure 5b, the horizontal wavelength of the stripes in the surface layer varies between 2 km and 3 km which is close to the upper limit of the horizontal length-scale of the unstable SI modes. Given the uncertainties both in theory and in the simulation results, a more detailed comparison of the theory with the simulation results does not seem appropriate. Therefore, symmetric instability in inviscid adiabatic fluid may be considered as a probable generation mechanism for the submesoscale stripes in the surface layer of the Baltic Sea. To the contrast, the SI criterion

Eq. (4) is not satisfied in the interior layer, and alternative generation mechanisms of submesoscale stripes has to be suggested.

One of the competitive generation mechanisms of the submesoscale stripes in the interior layers of the Baltic Sea could be the McIntyre instability which is a form of symmetric instability in a viscous, non-adiabatic fluid accounting for the difference between vertical eddy viscosity and vertical eddy diffusion of buoyancy (McIntyre, 1970; Ruddick, 1992). Indeed, if we conditionally suppose that the Prandtl number  $Pr$  is as large as  $Pr = 40$  or as small as  $Pr = 1/40$  (so

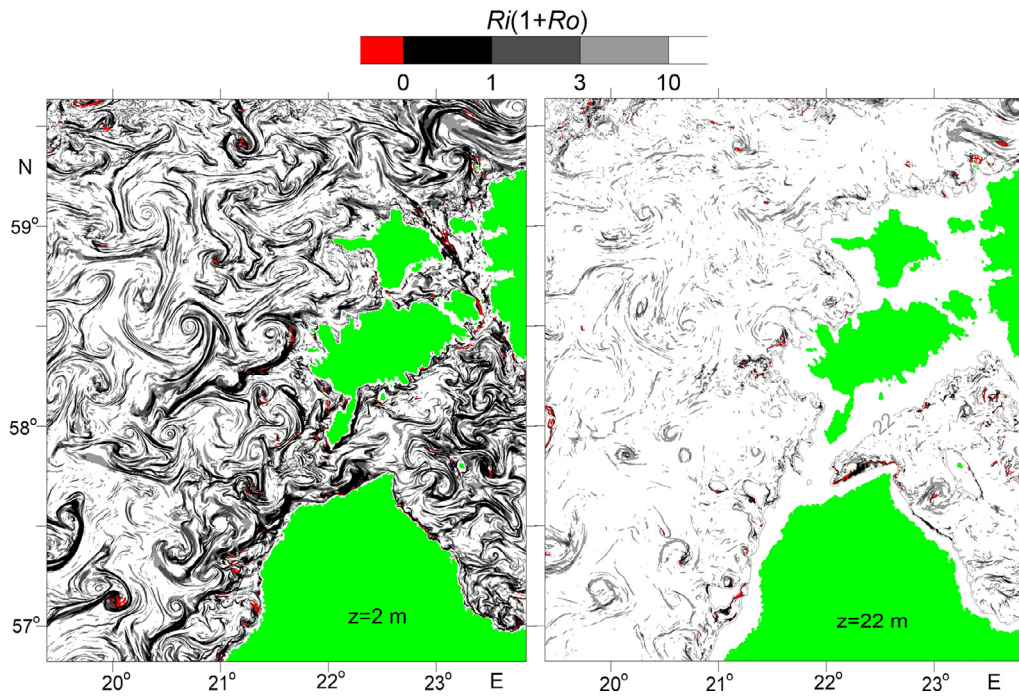


**Figure 9** Parameter  $Ri(1 + Ro)$  in the surface and the interior layers (simulation, 2018/7/18 07:07 UTC) indicating the possibility of different instabilities:  $Ri(1 + Ro) < 0$  – inertial instability,  $0 < Ri(1 + Ro) < 1$  – symmetric instability,  $1 \leq Ri(1 + Ro) < (1 + Pr)^2/4Pr = 10$  – McIntyre instability.

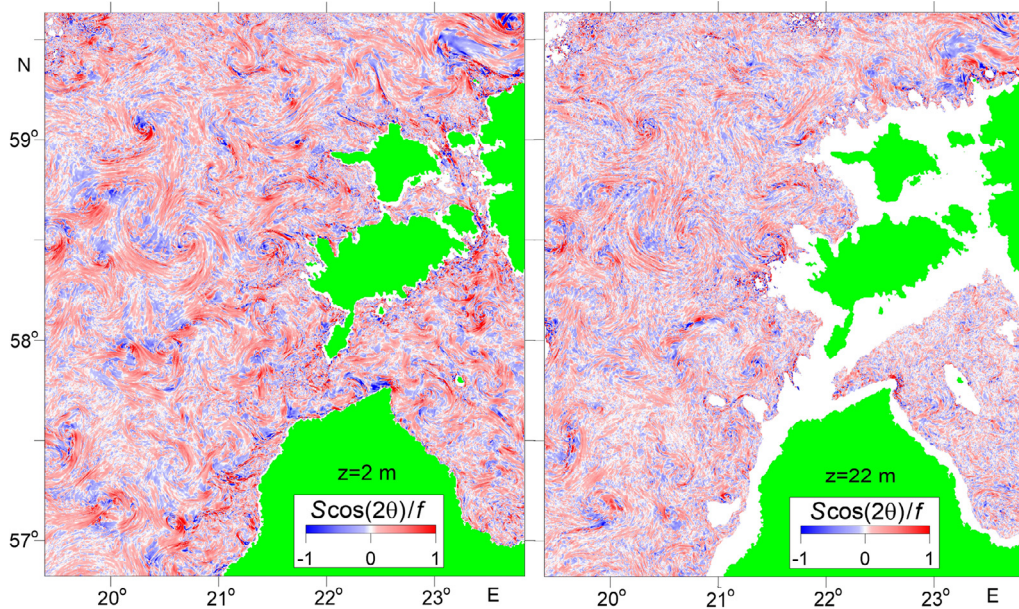


**Figure 10** Normalized frontogenetic strain rate  $S \cos(2\theta)/f$  in the surface (left) and interior (right) layers (simulation, 2018/7/18 07:07 UTC).

that  $(1 + Pr)^2/4Pr \approx 10$ ), the McIntyre instability criterion  $1 < Ri(1 + Ro) < (1 + Pr)^2/4Pr$  will be satisfied in approx. 39% of the study area in the surface layer, while in the interior layers, the percentage falls to 14% (see [Figures 9](#) and [12c](#)). The latter percentage value, 14%, being considerably

smaller than in the surface layer, is still large enough to consider the McIntyre instability as a competitive generation mechanism for submesoscale stripes in the interior layers. As to the growth time of the McIntyre instability, it is considerably larger than respective estimates for the clas-

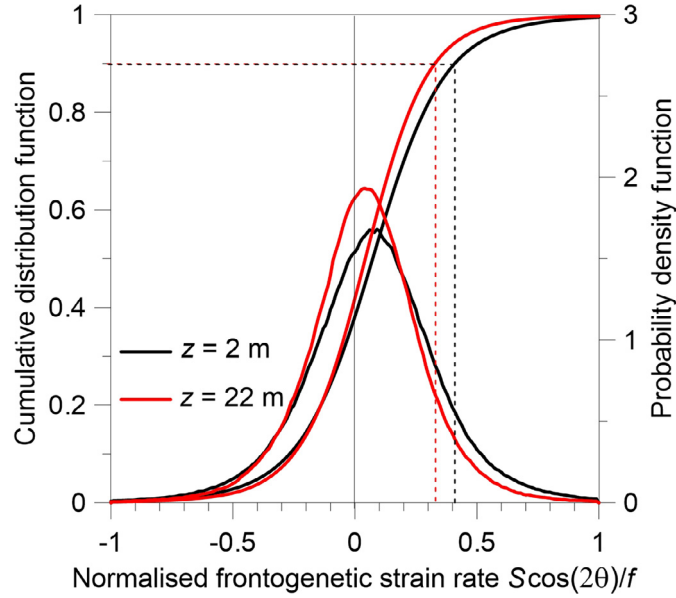


**Figure 11** Cumulative distribution functions and probability density functions of the normalized frontogenetic strain rate  $S \cos(2\theta)/f$  in the surface layer (black curves) and the interior (red curves) calculated from the model output on 2018/7/18 07:07 UTC. Dotted lines point at 90% quantile of the  $S \cos(2\theta)/f$  distributions.

**Table 2** Limitation for the horizontal length scale of disturbances  $L$  growing due to the classic symmetric instability, calculated from Eq. (A25) at  $U = 0.1 \text{ m s}^{-1}$ ,  $f = 1.24 \cdot 10^{-4} \text{ s}^{-1}$ , and different values of the Richardson and Rossby numbers.

$Ro \setminus Ri$	0.25	0.5	0.95
-0.5	<3020 m	<2800 m	<2340 m
0	<1400 m	<1140 m	<360 m
0.5	<860 m	<540 m	NONE

sic SI (cf. Tables 1 and 3). There is some doubt that the McIntyre instability at  $Pr > 1$  (viscous destabilization) can be responsible for generation of submesoscale stripes simulated in the interior layer of the Baltic Sea for two reasons. First, the typical value of the growth time  $1/\omega_i$ , achieved when  $Ri(1 + Ro)$  is in the middle of the instability range ( $1, (1 + Pr)^2/4Pr > 1$ ), is estimated at 3 days (see Table 3) which is comparable with the formation time of the submesoscale coherent vortices. Second, the slope of simulated stripes clearly exceeds the isopycnal slope (see Figure 5), while the theory forecasts the opposite (see Eq. (A18)).

Despite the fact that now we have no physical reason to believe that the Prandtl number in the ocean can be less than one, it still seems interesting to consider the McIntyre instability under the condition  $Pr < 1$  (diffusive destabilization). In this case, in accordance to Eq. (A18), the slope of growing disturbances is larger than the isopycnal slope which is consistent with the slopes of stripes simulated in the interior layers (see Figure 5b and c). Moreover, the growth rates of the maximum growing disturbances calculated from Eq. (A15) at  $Pr < 1$  are found to be much larger than that of  $Pr > 1$  (see Table 3). For example, at

**Table 3** Normalized growth rate  $\omega_i/f$  of the maximum growing mode of the McIntyre instability versus the Richardson, Rossby, and Prandtl numbers ( $Ri$ ,  $Ro$ , and  $Pr$ , respectively), calculated as the maximum positive root of the polynomial (A15). The choice of  $Pr$  values, 6, 1/6, 10, 1/10, 40 and 1/40, is motivated by the desire to have approx. 2, 3, and 10 for the respective values of  $(1 + Pr)^2/4Pr$  (see Eq. (8) and Figures 9 and 12c). Note that the case of  $Ri = 1$ ,  $Ro = -0.5$  does not correspond to the McIntyre instability because  $Ri(1 + Ro) = 0.5 < 1$ .

$Ro = 0$			
$Pr \setminus Ri$	1.1	2	5
6 (1/6)	0.096 (0.28)	0.00032 (0.0017)	<0
10 (1/10)	0.12 (0.45)	0.018 (0.13)	<0
40 (1/40)	0.15 (1.1)	0.055 (0.69)	0.0095 (0.23)
$Ro = 0.5$			
$Pr \setminus Ri$	1.1	2.2	5
6 (1/6)	-	0.066 (0.20)	<0
10 (1/10)	-	0.084 (0.32)	0.0035 (0.029)
40 (1/40)	-	0.11 (0.77)	0.027 (0.40)

$Ro = 1$ ,  $Ri = 2$ ,  $Pr = 14$  we have  $\omega_i/f = 0.031$  (the growth time is  $1/\omega_i \approx 3$  days) versus  $\omega_i/f = 0.24$  (the growth time is  $1/\omega_i \approx 9$  hours) at  $Ro = 1$ ,  $Ri = 2$ ,  $Pr = 1/14$ .

The credibility of generation of submesoscale stripes by strain-induced frontogenesis, can be evaluated by considering the 90% quantile of the probability function of the normalized frontogenetic strain rate  $PF(S \cos(2\theta)/f)$ . The high-resolution modelling show that the condition  $PF(S \cos(2\theta)/f) = 0.9$  is satisfied at  $[S \cos(2\theta)/f]_{0.9} = 0.41$  and 0.33 at  $z = 2 \text{ m}$  and  $22 \text{ m}$ , respectively. In this case,

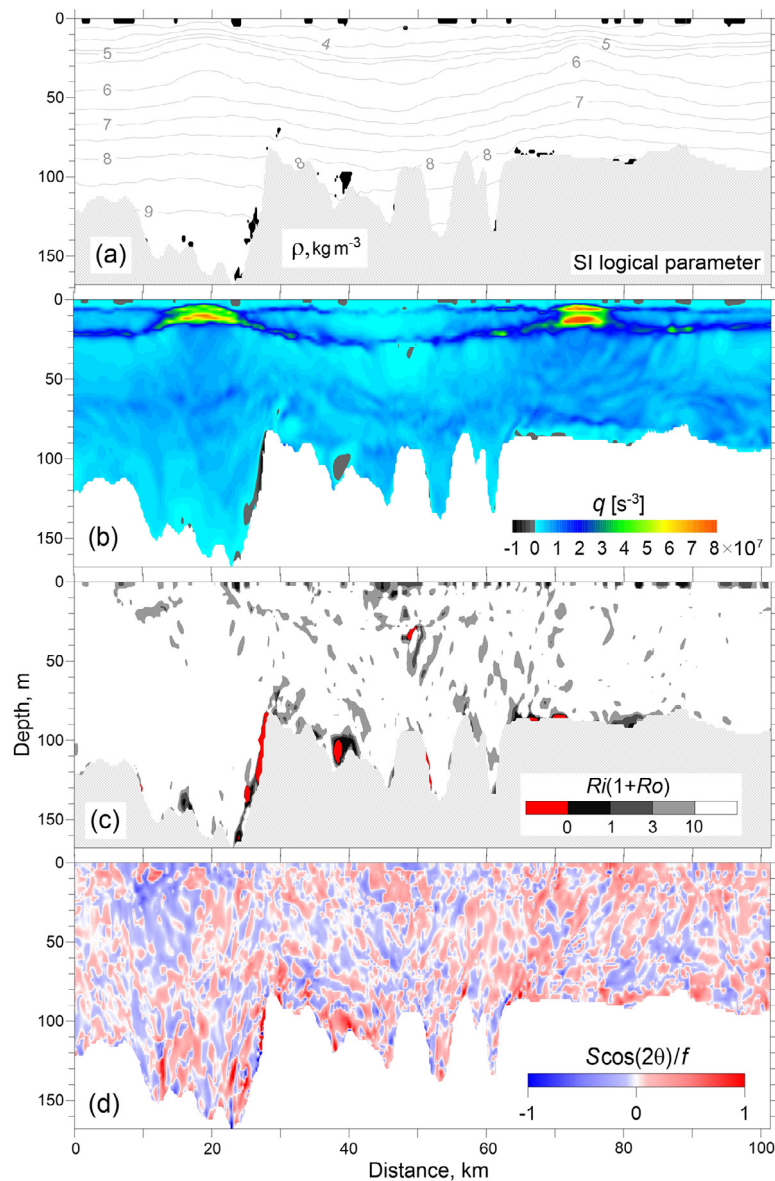


**Figure 12** Vertical section through an anticyclonic and two cyclonic eddies (simulation, 2018/7/18 07:07 UTC). The position of the section is shown in Figures 2 and 3. (a) Potential density anomaly  $\sigma_\theta$  (contours) and SI logical parameter based on Eq. (4) criterion (black spots), (b) Ertel potential vorticity  $q$  calculated using Eq. (1), (c) instability parameter  $Ri(1+Ro)$ , and (d) normalized frontogenetic rate  $S \cos(2\theta)/f$  versus distance and depth.

a characteristic growth time of submesoscale stripes due to frontogenesis can be estimated as  $1/(0.41f) = 5.5$  hours and  $1/(0.33f) = 6.8$  hours in the surface and interior layers, respectively, which is 2–4 times longer than the above mentioned SI growth times in the mixed layer.

Summarizing the above consideration, we admit that three of four processes considered (the classic symmetric instability, the McIntyre instability, and the strain-induced frontogenesis) could contribute to generation of the submesoscale striped texture in the surface layer of the Baltic Sea, while in the interior layers, the classic symmetric instability is excluded. Taking into account the fact that out of several competing processes, the fastest survives, we conclude that the classic symmetric instability and the strain-induced frontogenesis are the most probable mechanisms respon-

sible for the formation of submesoscale striped texture in the surface mixed layer of the Baltic Sea. In the interior layers, the strain-induced frontogenesis and hypothetically the McIntyre instability can be essential, but it takes further effort to draw a more definite conclusions. Stirring of large-scale inhomogeneities by the eddy field could be responsible for formation of striped texture in a passive tracer concentration and in temperature and salinity in the presence of thermoclinicity, but it does not imply formation of stripes in dynamically active tracers, such as vertical vorticity, horizontal gradients of buoyancy, etc. The DDSI is excluded from a list of possible mechanisms of formation of submesoscale stripes because the study area in the period considered was almost free of thermoclinicity, and double diffusion was therefore unable to generate alternating hor-



horizontal pressure gradients. Note that the presence of sub-mesoscale striped structures in the surface layer is backed up by remote sensing images, while the simulated deeper-layer filaments do not yet have such a strong observational support.

All the above-described processing and analysis of the model output was performed for one point in the simulation time – 2018/07/18, and therefore the question arises as to how typical the obtained results are. The same processing of the model output was carried out for two more points in time – 2018/07/27 and 2018/08/03 for which we have the remote sensing images similar to Figure 2, a and b (not shown in the article). Since no significant differences were found, the above results can be considered apparently typical for the summer season in the Baltic Sea.

## Declaration of competing interest

The authors declare that they have no known competing financial interests or personal relationships that could have appeared to influence the work reported in this paper.

## Acknowledgements

The allocation of computing time on High Performance Computing cluster by the Tallinn University of Technology and by the University of Tartu is gratefully acknowledged. The GETM community in Leibniz Institute of Baltic Sea Research (IOW) is acknowledged for their technical support and the maintenance of model code. Dmitry Solov'ev from Marine Hydrophysical Institute, Sevastopol, is acknowledged for presenting the remote sensing images. Germo Väli (submesoscale circulation modelling, discussing the results) was supported by the Estonian Research Council (grant no. PRG602 and grant no. IUT19-6). Victor Zhurbas (processing and interpreting the simulation data, preparation of the manuscript) and Natalia Kuzmina (instability analysis, discussing the results) were supported by budgetary financing of the Shirshov Institute of Oceanology RAS (Project No. 0128-2021-0001).

## Appendix 1. Instability analysis

Let us perform a simple analysis of the instability of a geostrophic flow with a linear vertical velocity profile in the framework of a 2D problem, that is, when the perturbations do not depend on the along-flow coordinate  $x$  (symmetric instability). The basic flow equations are

$$fU = -\frac{\partial \bar{P}}{\partial y}; \quad V = 0; \quad W = 0, \quad \frac{\partial \bar{P}}{\partial z} = -g\bar{\rho}$$

where  $\bar{P}$  and  $\bar{\rho}$  are the pressure and density divided by the reference density  $\rho_0$ ; the vertical shear of the basic flow is taken constant:  $\frac{\partial U}{\partial z} = \frac{g}{f} \frac{\partial \bar{\rho}}{\partial y} = \text{const}$ . We take into account also a constant barotropic shear of the basic flow:  $\frac{\partial U}{\partial y} = \text{const}$ .

Equations for disturbances with allowance for viscosity and diffusion of buoyancy are

$$\frac{\partial u}{\partial t} - fv + v \frac{\partial u}{\partial y} + w \frac{\partial u}{\partial z} = Pr \cdot K \frac{\partial^2 u}{\partial z^2} \quad (\text{A1})$$

$$\frac{\partial v}{\partial t} + fu = -\frac{\partial p}{\partial y} + Pr \cdot K \frac{\partial^2 v}{\partial z^2} \quad (\text{A2})$$

$$\frac{\partial w}{\partial t} + gw = -\frac{\partial p}{\partial z} \quad (\text{A3})$$

$$\frac{\partial v}{\partial y} + \frac{\partial w}{\partial z} = 0 \quad (\text{A4})$$

$$\frac{\partial \rho}{\partial t} + v \frac{\partial \bar{\rho}}{\partial y} + w \frac{\partial \bar{\rho}}{\partial z} = K \frac{\partial^2 \rho}{\partial z^2} \quad (\text{A5})$$

where  $u$ ,  $v$ , and  $w$  are components of velocity disturbances,  $p$  and  $\rho$  are disturbances of pressure and density divided by  $\rho_0$ , and  $K$  is the vertical diffusion of buoyancy.

In the case of infinite depth layer, the solution of system Eq. (A1)–(A5) is sought in the form

$$\psi = \psi_0 \exp(\omega t + imz + ily) \quad (\text{A6})$$

where  $\psi$  is any disturbed variable from Eq. (A1)–(A5). Note that with this form of solution, the tangent of the angle of inclination of the disturbances relative to the horizontal (slope) is

$$\tan(\gamma) = -\frac{l}{m}$$

Let's consider different cases of the Eq. (A1)–(A6) solutions.

### A1. Inviscid adiabatic fluid in hydrostatic approximation, infinite depth layer

After removing the last term in the right hand part of Eq. (A1), (A2), and (A5) and substituting Eq. (A6) to Eq. (A1)–(A5) the following equation for the growth rate  $\omega$  is obtained

$$\omega^2 + ff^* + 2\tan(\gamma_\rho)N^2 \frac{l}{m} + N^2 \frac{l^2}{m^2} = 0 \quad (\text{A7})$$

where  $\tan(\gamma_\rho) = \frac{g\bar{\rho}_y}{N^2}$  is the slope of isopycnals relative to the horizontal,  $f^* = f - \frac{\partial U}{\partial y}$ . For a small isopycnal slope,  $\gamma_\rho \ll 1$ ,  $\tan(\gamma_\rho) \approx \gamma_\rho$ , and Eq. (A7) re-writes as

$$\omega^2 + ff^* + N^2(l/m + \gamma_\rho)^2 - N^2\gamma_\rho^2 = 0 \quad (\text{A7a})$$

It follows from Eq. (A7a)' that instability (i.e.,  $\omega > 0$ ) is possible only when  $\gamma_\rho^2 - \frac{ff^*}{N^2} > 0$  or

$$Ri(1 + Ro) < 1 \quad (\text{A8})$$

where  $Ri = \frac{f^2}{N^2\gamma_\rho^2}$  is the geostrophic Richardson number and  $Ro = -\frac{\partial U/\partial y}{f}$  is the gradient Rossby number. Note that Eq. (A8) fits the classic SI instability condition Eq. (6). Based on the results of Ooyama (1966) Eq. (A8) was probably first obtained by Hoskins (1974).

According to Eq. (A7a)', the slope of the maximum growing disturbances,  $\gamma_i$ , is

$$\gamma_i = -\left(\frac{l}{m}\right)_i = \gamma_\rho \quad (\text{A9})$$

i.e., the maximum growing disturbance does not cross the isopycnal surfaces (see also Kuznima and Zhurbas, 2000; McIntyre, 1970; Taylor and Ferrari, 2009). The growth rate of the maximum growing disturbances,  $\omega_i$ , is

$$\omega_i = f \left( \frac{1 - Ri(1 + Ro)}{Ri} \right)^{1/2} \quad (A10)$$

Note that Eq. (A10) coincides the well-known formula by Stone (1966), provided that  $Ro = 0$  (cf. Eq. (7) which was derived in Stone (1966) for the no barotropic shear case). Eq. (A10) was also derived in Haine and Marshall (1998) from energy analysis of the thermal wind.

### A2. Inviscid adiabatic fluid, non-hydrostatic case, infinite depth layer

In this case, the equation for the growth rate is

$$\omega^2 \left( 1 + \frac{l^2}{m^2} \right) + f f^* + 2 \tan(\gamma_\rho) N^2 \frac{l}{m} + N^2 \frac{l^2}{m^2} = 0 \quad (A11)$$

It can be easily shown by analogy with the previous analysis, that the instability condition and the slope of the maximum growing mode remain the same as in the hydrostatic case (see Eq. (A8) and (A9)). However, the growth rate for the maximum growing disturbances is expressed in this case by the formula:

$$\omega_i = \left( \frac{(\tan(\gamma_\rho))^2 N^2}{1 + (\tan(\gamma_\rho))^2} - \frac{f f^*}{1 + (\tan(\gamma_\rho))^2} \right)^{1/2} \quad (A12)$$

For small isopycnal slopes  $\tan(\gamma_\rho) \ll 1$  Eq. (A12) reduces to Eq. (A10), while for large isopycnal slopes  $\tan(\gamma_\rho) \gg 1$  it reduces to

$$\omega_i = N \sqrt{1 - Ri(1 + Ro)} \quad (A13)$$

Thus, the maximum growing perturbations can grow practically in a few minutes, but only when the slope of the isopycnal surfaces significantly exceeds the angle of  $\pi/4$ .

### A3. Viscous non-adiabatic fluid in hydrostatic approximation, infinite depth layer

In this case we take  $\tan(\gamma_\rho) \approx \gamma_\rho \ll 1$ , and the growth rate equation is

$$\frac{A \cdot B}{N^2} + \frac{l}{m} \gamma_\rho \left( 1 + \frac{B}{A} \right) + \frac{f f^* B}{N^2 A} + \frac{l^2}{m^2} = 0 \quad (A14)$$

where  $A = \omega + PrKm^2$ , and  $B = \omega + Km^2$ . If  $Pr \neq 1$ , Eq. (A14) is reduced to a polynomial of the third degree:

$$\omega^3 + C_2 \omega^2 + C_1 \omega + C_0 = 0 \quad (A15)$$

It can be easily shown that the coefficients  $C_1$  and  $C_2$  in Eq. (A15) are nonnegative when  $Ri(1 + Ro) \geq 1$ . Therefore, for  $Ri(1 + Ro) \geq 1$  the polynomial Eq. (A15) has one and only one positive real root and only when  $C_0 < 0$ . To analyze the dissipation-related instability, let's consider the free term of Eq. (A15),

$$C_0 = Km^2 \left( Pr^2 K^2 m^4 + \gamma_\rho \frac{l}{m} (Pr + 1) N^2 + f f^* + Pr N^2 \frac{l^2}{m^2} \right) \quad (A16)$$

which can be re-written as

$$C_0 = Km^2 N^2 Pr \left( \frac{Pr K^2 m^4}{N^2} + \frac{f f^*}{Pr N^2} + \left( \frac{\gamma_\rho (Pr + 1)}{2Pr} + \frac{l}{m} \right)^2 - \frac{\gamma_\rho^2 (Pr + 1)^2}{4Pr^2} \right) \quad (A16a)$$

It follows from Eq. (A16a)' that the free term  $C_0$  can be negative only if

$$\frac{f f^*}{\gamma_\rho^2 N^2} = Ri(1 + Ro) < \frac{(Pr + 1)^2}{4Pr} \quad (A17)$$

which is a well-known condition for the McIntyre (1970) instability at  $Pr \neq 1$  (cf. Eq. (A17) and Eq. (8)). When the conditions  $1 \leq Ri(1 + Ro) < \frac{(Pr+1)^2}{4Pr}$  and  $Pr \neq 1$  are satisfied the slope of the maximum growing mode in accordance to (A16a)' is

$$\gamma_i = - \left( \frac{l}{m} \right)_i = \gamma_\rho \frac{Pr + 1}{2Pr} \quad (A18)$$

Equation (A18) says that for the McIntyre instability the slope of the maximum growing mode exceeds the isopycnal slope when  $Pr < 1$  and becomes less than it when  $Pr > 1$ . Note that at  $Pr = 1$  the instability criterion remains the same as in the case of ideal fluid (McIntyre, 1970).

### A4. Inviscid adiabatic fluid in hydrostatic approximation, finite depth layer

In contrast to the slope and growth rate of the maximum growing mode (Eq. (A9) and (A10)), the characteristic length scale of instability cannot be found from the inviscid adiabatic consideration in the infinite depth layer. To estimate the characteristic length scale of instability, let's consider, following Stone (1966), a finite depth layer with the barotropic shear additionally included and seek the solution of system of equations (A1)–(A5) with hydrostatic approximation in the form

$$\psi = \psi_0(z) \exp(\omega t + i l y) \quad (A19)$$

Substitution of Eq. (A19) into Eq. (A1)–(A5) reduces the latter to a second-order differential equation relative to the vertical velocity  $w$  with constant coefficients, which should be solved under the boundary conditions

$$w = 0 \text{ at } z = 0, H \quad (A20)$$

where  $H$  is the layer depth. Here, for the sake of brevity, we present only the equation for the growth rate, which is the result of solving the eigenvalue problem:

$$\left( \frac{\gamma_\rho l N^2}{\omega^2 + f f^*} \right)^2 = \frac{l^2 N^2}{\omega^2 + f f^*} + \frac{\pi^2 n^2}{H^2}, \quad (n = 1, 2, 3 \dots) \quad (A21)$$

The maximally growing mode is realized at  $n = 1$ .

It is easy to see from Eq. (A21) that, with the infinitely deep layer (that is, when the last term on the right-hand side of Eq. (A21) tends to zero), the formula for the growth rate fully corresponds to Eq. (A10). For a layer of finite depth, Eq. (A21) is reduced to a fourth-degree polynomial

$$\omega^4 + C_2 \omega^2 + C_0 = 0 \quad (A22)$$

Keeping in mind that in Eq. (A22)  $C_2 > 0$  if  $Ro > -1$ , the symmetric instability is possible only when  $C_0 < 0$ , i.e. when

$$l^2 N^2 f f^* - \gamma_\rho^2 l^2 N^4 + \frac{\pi^2 (f f^*)^2}{H^2} < 0 \quad (\text{A23})$$

It follows from Eq. (A23) that instability is possible when Eq. (A8) is satisfied, and the unstable wavenumber  $l$  lies in the range

$$l^2 > \frac{(\pi f(1 + Ro))^2}{U^2(1 - Ri(1 + Ro))} \quad (\text{A24})$$

where  $U$  is the maximum velocity of the basic geostrophic flow. The horizontal length scale of unstable disturbances should therefore satisfy the inequality

$$L = \frac{2\pi}{l} < \frac{2U(1 - Ri(1 + Ro))^{1/2}}{f(1 + Ro)} \quad (\text{A25})$$

Formula (A24) without barotropic shear included (at  $Ro = 0$ ) was first obtained by Stone (Stone, 1966). Note that in the considered problem it is impossible to find the growth rate of the maximum growing perturbation: the larger the wavenumber  $l$ , the greater the growth rate. This is a disadvantage of this problem, which should be further fixed by taking friction into account. However, one can assume that it would not result in a large error in some cases of observations in the ocean to estimate the maximum growth rate of disturbances in a layer of finite depth using Stone's (1966) formula Eq. (A10). Relation Eq. (A21) helps

to choose such cases. If the ratio  $\frac{IN}{f} \gg \frac{\pi}{H}$  is satisfied, then the estimate of the growth rate using formula Eq. (A10) is satisfactory.

## Appendix 2. Formation of striped texture by stirring of large scale inhomogeneities by the eddy field: an illustrating example

Let's consider an illustrating example of the formation of striped texture by stirring of large scale gradients in a 2D, periodically varying double-gyre velocity field described by the stream-function (Shadden et al., 2005)

$$\psi(x, y, t) = A \sin(\pi f(x, t)) \sin(\pi y) \quad (\text{A26})$$

where

$$f(x, t) = a(t)x^2 + b(t)x, \quad a(t) = \varepsilon \sin(\omega t), \quad b(t) = 1 - 2\varepsilon \sin(\omega t) \quad (\text{A27})$$

over the domain  $[0, 2] \times [0, 1]$ . The analytical forms (A26)–(A27) are chosen to produce a simple, time-dependent two-gyre flow with fixed boundaries, not to approach a solution of Navier–Stokes' equations. For  $\varepsilon \neq 0$  the flow consists of two gyres that conversely expand and contract periodically in the  $x$ -direction such that the rectangle enclosing the gyres remains invariant. The velocity field  $u = -\psi_y$ ,  $v = \psi_x$  and vorticity  $\zeta = -u_y + v_x$  generated

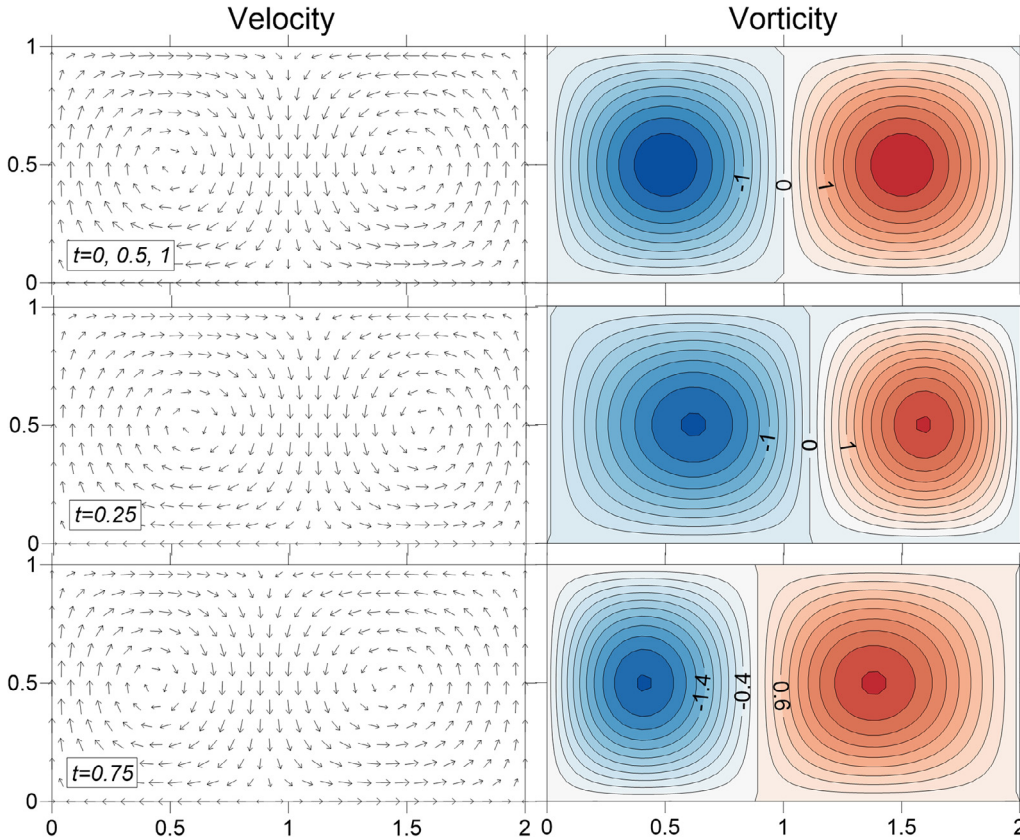


**Figure 13** Velocity and vorticity fields generated by the analytical forms Eqs. (A26)–(A27) for  $A = 0.1$ ,  $\varepsilon = 0.1$ ,  $\omega = 2\pi$  at the time moments  $t = 0, 0.25, 0.5, 0.75, 1$ .

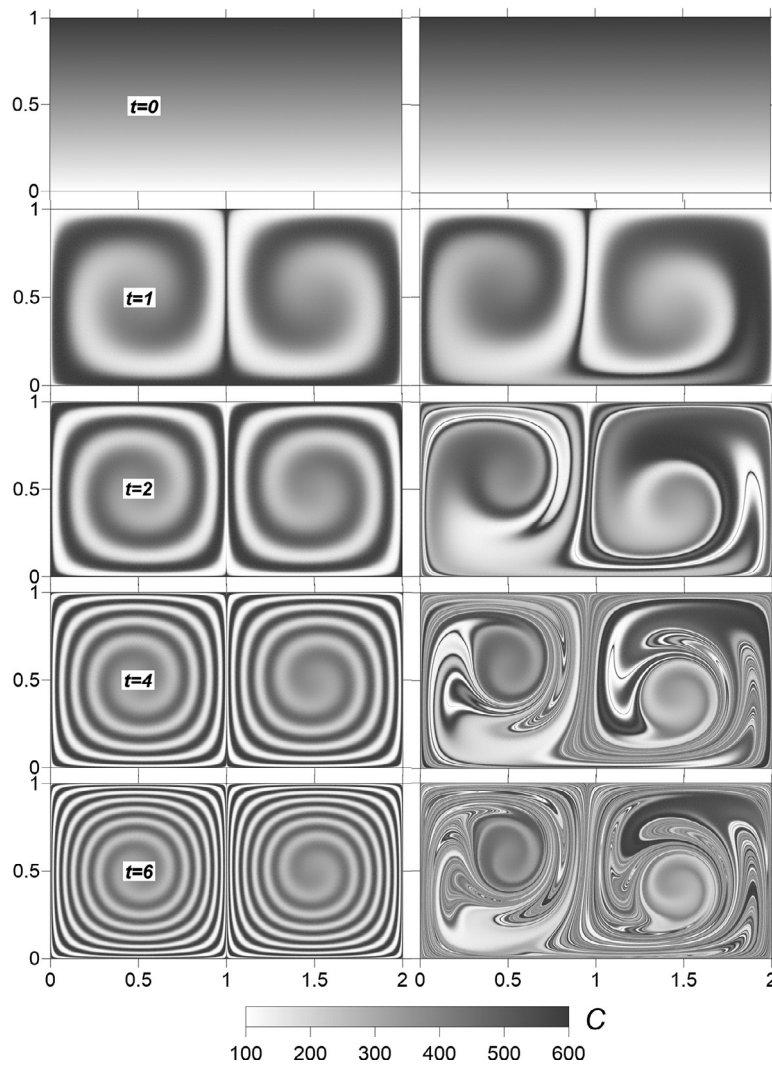


**Figure 14** Evolution of a constant  $y$ -gradient of tracer concentration in the two-gyre velocity field shown in Figure 13. The left panels correspond to the stationary case ( $\varepsilon = 0$ ), and the right panels to the non-stationary case at  $\varepsilon = 0.1$ .

by the analytical forms (A26)–(A27) for  $A = 0.1$ ,  $\varepsilon = 0.1$ ,  $\omega = 2\pi$  at different time moments are shown in Figure 13.

Advection of a passive tracer is described by the balance equation

$$C_t + (uC)_x + (vC)_y = \frac{dC}{dt} + C \operatorname{div}(\mathbf{u}) = 0 \quad (\text{A28})$$

where  $C(x, y, t)$  is the tracer concentration,  $\frac{dC}{dt} = C_t + uC_x + vC_y$  is the time derivative of concentration in the Lagrangian frame, and  $\operatorname{div}(\mathbf{u}) = u_x + v_y$  is the velocity divergence. Let's set the initial condition as a constant  $y$ -gradient of concentration

$$C(x, y, 0) = 100 + 500y, \quad x = [0, 2], \quad y = [0, 1] \quad (\text{A29})$$

and integrate Eq. (A28) numerically with the velocity field (A26)–(A27) for  $A = 0.1$ ,  $\omega = 2\pi$ , and  $\varepsilon = 0$  (stationary case) and  $\varepsilon = 0.1$  (non-stationary case), using a Lagrangian trajectories approach as described in Väli et al. (2018). The numerical solution presented in Figure 14 shows that in the stationary velocity field at  $t \gg 1$ , where  $t = 1$  corresponds to the period of eddy rotation, the initial constant gradient of concentration is found in a spiral-like

stripe of enhanced concentration, and the number of cycles in the stripe increases as  $t$ . In the non-stationary case, where  $t = 1$  corresponds to both the eddy rotation and eddy expansion-contraction periods, a complicated striped texture is formed at  $t \gg 1$ . The number of stripes per eddy is likely determined by superposition of two periodical processes and drastically increases with  $t$ .

## References

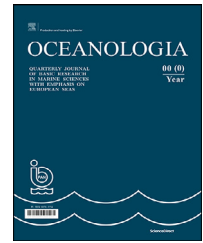
- Bachman, S.D., Fox-Kemper, B., Taylor, J.R., Thomas, L.N., 2017. Parameterization of frontal symmetric instabilities. I: Theory for resolved fronts. *Ocean Model.* 109, 72–95. <https://doi.org/10.1016/j.ocemod.2016.12.003>
- Barkan, R., Molemaker, M.J., Srinivasan, K., McWilliams, J.C., D'Asaro, E.A., 2019. The role of horizontal divergence in sub-mesoscale frontogenesis. *J. Phys. Oceanogr.* 49, 1593–1618. <https://doi.org/10.1175/JPO-D-18-0162.1>
- Brannigan, L., Marshall, D.P., Garabato, A.C.N., Nurser, A.J.G., 2017. Submesoscale instabilities in mesoscale eddies. *J. Phys. Oceanogr.* 47, 3061–3085. <https://doi.org/10.1175/JPO-D-16-0178.1>

- Burchard, H., Bolding, K., 2001. Comparative Analysis of Four Second-Moment Turbulence Closure Models for the Oceanic Mixed Layer. *J. Phys. Oceanogr.* 31, 1943–1968. [https://doi.org/10.1175/1520-0485\(2001\)031<1943:CAOFSM>2.0.CO;2](https://doi.org/10.1175/1520-0485(2001)031<1943:CAOFSM>2.0.CO;2)
- Burchard, H., Bolding, K., 2002. GETM – a general estuarine transport model. Scientific documentation, Technical report EUR 20253 en. In: Tech. rep., European Commission. Ispra, Italy.
- Canuto, V.M., Howard, A., Cheng, Y., Dubovikov, M.S., 2001. Ocean Turbulence. Part I: One-Point Closure Model—Momentum and Heat Vertical Diffusivities. *J. Phys. Oceanogr.* 31, 1413–1426. [https://doi.org/10.1175/1520-0485\(2001\)031<1413:OTPIOP>2.0.CO;2](https://doi.org/10.1175/1520-0485(2001)031<1413:OTPIOP>2.0.CO;2)
- Capet, X., McWilliams, J.C., Molemaker, M.J., Shchepetkin, A.F., 2008. Mesoscale to Submesoscale Transition in the California Current System. Part II: Frontal Processes. *J. Phys. Oceanogr.* 38 (1), 44–64. <https://doi.org/10.1175/2007JPO3672.1>
- Choi, J., Bracco, A., Barkan, R., Shchepetkin, A.F., McWilliams, J.C., Molemaker, J.M., 2017. Submesoscale dynamics in the Northern Gulf of Mexico. Part III: Lagrangian implications. *J. Phys. Oceanogr.* 47, 2361–2376. <https://doi.org/10.1175/JPO-D-17-0036.1>
- Chrysagi, E., Umlauf, L., Holtermann, P., Klingbeil, K., 2021. High-resolution simulations of submesoscale processes in the Baltic Sea. *J. Geophys. Res. Oceans* 126, e2020JC016411. <https://doi.org/10.1029/2020JC016411>
- D’Asaro, E.A., Shcherbina, A.Y., Klymak, J.M., Molemaker, J., Novelli, G., Guigand, C.M., Haza, A.C., Haus, B.K., Ryan, E.H., Jacobs, G.A., Huntley, H.S., Laxague, N.J.M., Chen, S., Judt, F., McWilliams, J.C., Barkan, R., Kirwan Jr., A.D., Poje, A.C., Özgökmen, T.M., 2018. Ocean convergence and the dispersion of flotsam. *Proc. Nat’l Acad. Sci. USA* 115, 1162–1167. <https://doi.org/10.1073/pnas.1802701115>
- Finni, T., Kononen, K., Olsonen, R., Wallström, K., 2001. The history of cyanobacteria blooms in the Baltic Sea. *Ambio* 30 (4–5), 172–178.
- Flather, R.A., 1994. A storm surge prediction model for the northern Bay of Bengal with application to the cyclone disaster in April 1991. *J. Phys. Oceanogr.* 24, 172–190. [https://doi.org/10.1175/1520-0485\(1994\)024<0172:ASSPMF>2.0.CO;2](https://doi.org/10.1175/1520-0485(1994)024<0172:ASSPMF>2.0.CO;2)
- Garrett, C., MacCready, P., Rhines, P., 1993. Arrested Ekman layers: Rotating stratified flow near a sloping boundary. *Annu. Rev. Fluid Mech.* 25, 291–323.
- Giudici, A., Suara, K.A., Soomere, T., Brown, R., 2021. Tracking areas with increased likelihood of surface particle aggregation in the Gulf of Finland: A first look at persistent Lagrangian Coherent Structures (LCS). *J. Mar. Syst.* 217, 103514. <https://doi.org/10.1016/j.jmarsys.2021.103514>
- Gräwe, U., Holtermann, P., Klingbeil, K., Burchard, H., 2015. Advantages of vertically adaptive coordinates in numerical models of stratified shelf seas. *Ocean Model.* 92, 56–68.
- Gula, J., Molemaker, M.J., McWilliams, J.C., 2014. Submesoscale cold filaments in the Gulf Stream. *J. Phys. Oceanogr.* 44, 2617–2643. <https://doi.org/10.1175/JPO-D-14-0029.1>
- Gula, J., Molemaker, M.J., McWilliams, J.C., 2016. Submesoscale dynamics of a Gulf Stream frontal eddy in the South Atlantic Bight. *J. Phys. Oceanogr.* 46, 305–325. <https://doi.org/10.1175/JPO-D-14-0258.1>
- Haine, T.W., Marshall, J., 1998. Gravitational, symmetric, and baroclinic instability of the ocean mixed layer. *J. Phys. Oceanogr.* 28 (4), 634–658. [https://doi.org/10.1175/1520-0485\(1998\)028<0634:GSABIO>2.0.CO;2](https://doi.org/10.1175/1520-0485(1998)028<0634:GSABIO>2.0.CO;2)
- Hofmeister, R., Burchard, H., Beckers, J.-M., 2010. Non-uniform adaptive vertical grids for 3D numerical ocean models. *Ocean Model.* 33 (1–2), 70–86. <https://doi.org/10.1016/j.ocemod.2009.12.003>
- Hoskins, B.J., 1974. The role of potential vorticity in symmetric stability and instability. *Q. J. R. Met. Soc.* 100, 480–482.
- Hoskins, B.J., 1982. The mathematical theory of frontogenesis. *Annu. Rev. Fluid Mech.* 82, 131–151. <https://doi.org/10.1146/annurev.fl.14.010182.001023>
- Hoskins, B.J., Bretherton, F.P., 1972. Atmospheric frontogenesis models: mathematical formulation and solution. *J. Atmos. Sci.* 29, 11–37. [https://doi.org/10.1175/1520-0469\(1972\)029<0011:AFMMA>2.0.CO;2](https://doi.org/10.1175/1520-0469(1972)029<0011:AFMMA>2.0.CO;2)
- Jing, Z., Fox-Kemper, B., Cao, H., Zheng, R., Du, Y., 2021. Submesoscale fronts and their dynamical processes associated with symmetric instability in the Northwest Pacific Subtropical Ocean. *J. Phys. Oceanogr.* 51, 83–100. <https://doi.org/10.1175/JPO-D-20-0076.1>
- Johansson, J., 2018. Total and regional runoff to the Baltic Sea, HELCOM Baltic Sea Environment Fact Sheets. Online. 20.12.2018. <http://www.helcom.fi/baltic-sea-trends/environment-fact-sheets/>
- Kalda, J., Soomere, T., Giudici, A., 2014. On the finite-time compressibility of the surface currents in the Gulf of Finland, the Baltic Sea. *J. Mar. Syst.* 129, 56–65. <https://doi.org/10.1016/j.jmarsys.2012.08.010>
- Karimova, S.S., Lavrova, O.Yu., Solov’ev, D.M., 2012. Observation of Eddy Structures in the Baltic Sea with the Use of Radiolocation and Radiometric Satellite Data. *Izvestiya, Atmos. Ocean. Phys.* 48 (9), 1006–1013. <https://doi.org/10.1134/S0001433812090071>
- Klingbeil, K., Mohammadi-Aragh, M., Gräwe, U., Burchard, H., 2014. Quantification of spurious dissipation and mixing – discrete variance decay in a finite-volume Framework. *Ocean Model.* 81, 49–64. <https://doi.org/10.1016/j.ocemod.2014.06.001>
- Klingbeil, K., Lemarié, F., Debreu, L., Burchard, H., 2018. The numerics of hydrostatic structured-grid coastal ocean models: State of the art and future perspectives. *Ocean Model.* 125, 80–105. <https://doi.org/10.1016/j.ocemod.2018.01.007>
- Krauss, W., Brüggge, B., 1991. Wind-produced water exchange between the deep basins of the Baltic Sea. *J. Phys. Oceanogr.* 21, 373–384. [https://doi.org/10.1175/1520-0485\(1991\)021<0373:WPWEBT>2.0.CO;2](https://doi.org/10.1175/1520-0485(1991)021<0373:WPWEBT>2.0.CO;2)
- Kuzmina, N.P., 1981. Non-linear numerical model of oceanic frontogenesis. *Izvestiya Akademii Nauk SSSR Fizika Atmosfery i Okeana* 17 (12), 1318–1325.
- Kuzmina, N.P., Rodionov, V.B., 1992. Influence of baroclinity on the formation of thermohaline intrusions in ocean frontal zones. *Izv. Akad. Sci. USSR, Atmos. Ocean. Phys.* 28, 804–810.
- Kuzmina, N.P., Rudels, B., Stipa, T., Zhurbas, V., 2005. The structure and driving mechanisms of the Baltic intrusions. *J. Phys. Oceanogr.* 35, 1120–1137. <https://doi.org/10.1175/JPO2749.1>
- Kuzmina, N.P., Zhurbas, V.M., 2000. Effects of double diffusion and turbulence on interleaving at baroclinic oceanic fronts. *J. Phys. Oceanogr.* 30 (12), 3025–3038. [https://doi.org/10.1175/1520-0485\(2000\)030<3025:EODDAT>2.0.CO;2](https://doi.org/10.1175/1520-0485(2000)030<3025:EODDAT>2.0.CO;2)
- Laanemets, J., Väli, G., Zhurbas, V., Elken, J., Lips, I., Lips, U., 2011. Simulation of mesoscale structures and nutrient transport during summer upwelling events in the Gulf of Finland in 2006. *Boreal Environ. Res.* 16 (A), 15–26.
- Lappe, C., Umlauf, L., 2016. Efficient boundary mixing due to near-inertial waves in a nontidal basin: Observations from the Baltic Sea. *J. Geophys. Res.- Oceans* 121 (11), 8287–8304. <https://doi.org/10.1002/2016JC011985>
- Liblik, T., Väli, G., Lips, I., Lilover, M.-J., Kikas, V., Laanemets, J., 2020. The winter stratification phenomenon and its consequences in the Gulf of Finland. *Baltic Sea, Ocean Sci.* 16, 1475–1490. <https://doi.org/10.5194/os-16-1475-2020>
- Lips, U., Zhurbas, V., Skudra, M., Väli, G., 2016. A numerical study of circulation in the Gulf of Riga, Baltic Sea. Part I: Whole-basin gyres and mean currents. *Cont. Shelf Res.* 112, 1–13. <https://doi.org/10.1016/j.csr.2015.11.008>

- Männik, A., Merilain, M., 2007. Verification of different precipitation forecasts during extended winter-season in Estonia. *HIRLAM Newsletter* 52, 65–70.
- MacVean, M.K., Woods, J.D., 1980. Redistribution of scalars during upper oceanfrontogenesis. *Quart. J. Roy. Met. Soc.* 106, 293–311.
- Martinsen, E.A., Engedahl, H., 1987. Implementation and testing of a lateral boundary scheme as an open boundary condition in a barotropic ocean model. *Coast. Eng.* 11, 603–627. [https://doi.org/10.1016/0378-3839\(87\)90028-7](https://doi.org/10.1016/0378-3839(87)90028-7)
- May, B.D., Kelley, D.E., 1997. Effect of baroclinicity on double-diffusive interleaving. *J. Phys. Oceanogr.* 27, 1997–2008. [https://doi.org/10.1175/1520-0485\(1997\)027<1997:EOBODD>2.0.CO;2](https://doi.org/10.1175/1520-0485(1997)027<1997:EOBODD>2.0.CO;2)
- McIntyre, E., 1970. Diffusive destabilization of the baroclinic circular vortex. *Geophys. Fluid Dynam.* 1, 19–57.
- McWilliams, J.C., 2016. Submesoscale currents in the ocean. *Proc. Royal Soc. A* 72, 20160117. <https://doi.org/10.1098/rspa.2016.0117>
- Munk, W., 2001. Spirals on the sea. *Scientia Mar* 65 (S2), 193–198. <https://doi.org/10.3989/scimar.2001.65s2193>
- Munk, W., Armi, L., Fischer, K., Zachariasen, F., 2000. Spirals on the sea. *Proc. R. Soc. Lond A* 456, 1217–1280.
- Onken, R., Baschek, B., Angel-Benavides, I.M., 2020. Very high-resolution modelling of submesoscale turbulent patterns and processes in the Baltic Sea. *Ocean Sci.* 16, 657–684. <https://doi.org/10.5194/os-16-657>
- Ooyama, K., 1966. On the stability of the baroclinic circular vortex: a sufficient criterion for instability. *J. Atmos. Sci.* 23, 43–53. [https://doi.org/10.1175/1520-0469\(1966\)023<0043:OTSOTB>2.0.CO;2](https://doi.org/10.1175/1520-0469(1966)023<0043:OTSOTB>2.0.CO;2)
- Ou, H.W., 1984. Geostrophic adjustment: a mechanism for frontogenesis. *J. Phys. Oceanogr.* 14, 994–1000. [https://doi.org/10.1175/1520-0485\(1984\)014<0994:GAAMFF>2.0.CO;2](https://doi.org/10.1175/1520-0485(1984)014<0994:GAAMFF>2.0.CO;2)
- Qiu, B., Chen, S., Klein, P., Sasaki, H., Sasai, Y., 2014. Seasonal mesoscale and submesoscale eddy variability along the North Pacific Subtropical Countercurrent. *J. Phys. Oceanogr.* 44, 3079–3098. <https://doi.org/10.1175/JPO-D-14-0071.1>
- Ruddick, B., 1992. Intrusive mixing in a Mediterranean salt lens - intrusion slopes and dynamical mechanisms. *J. Phys. Oceanogr.* 22 (11), 1274–1285. [https://doi.org/10.1175/1520-0485\(1992\)022<1274:IMIAM>2.0.CO;2](https://doi.org/10.1175/1520-0485(1992)022<1274:IMIAM>2.0.CO;2)
- Shadden, S.C., Lekien, F., Marsden, J.E., 2005. Definition and properties of Lagrangian coherent structures from finite-time Lyapunov exponents in two-dimensional aperiodic flows. *Physica D* 212, 271–304. <https://doi.org/10.1016/j.physd.2005.10.007>
- Schubert, R., Gula, J., Greatbatch, R.J., Baschek, B., Biastoch, A., 2020. The submesoscale kinetic energy cascade: Mesoscale absorption of submesoscale mixed layer eddies and frontal downscale fluxes. *J. Phys. Oceanogr.* 50, 2573–2589. <https://doi.org/10.1175/JPO-D-19-0311.1>
- Smith, K.S., Ferrari, R., 2009. The production and dissipation of compensated thermohaline variance by mesoscale stirring. *J. Phys. Oceanogr.* 39, 2477–2501. <https://doi.org/10.1175/2009JPO4103.1>
- Stern, M.E., 1967. Lateral mixing of water masses. *Deep-Sea Res.* 14, 747–753.
- Stone, P.H., 1966. On non-geostrophic baroclinic stability. *J. Atmos. Sci.* 23 (4), 390–400.
- Taylor, J.R., Ferrari, R., 2009. On the equilibration of a symmetrically unstable front via a secondary shear instability. *J. Fluid Mech.* 622, 103–113. <https://doi.org/10.1017/S0022112008005272>
- Thomas, L.N., 2005. Destruction of potential vorticity by winds. *J. Phys. Oceanogr.* 35, 2457–2466. <https://doi.org/10.1175/JPO2830.1>
- Thomas, L.N., Taylor, J.R., D’Asaro, E.A., Lee, C.M., Klymak, J.M., Shcherbina, A., 2016. Symmetric instability, inertial oscillations, and turbulence at the Gulf Stream front. *J. Phys. Oceanogr.* 46 (1), 197–217. <https://doi.org/10.1175/JPO-D-15-0008.1>
- Thomas, L.N., Taylor, J.R., Ferrari, R., Joyce, T.M., 2013. Symmetric instability in the Gulf Stream. *Deep-Sea Res. Part II* 91, 96–110. <https://doi.org/10.1016/j.dsr2.2013.02.025>
- Umlauf, L., Burchard, H., 2005. Second-order turbulence closure models for geophysical boundary layers. A review of recent work. *Cont. Shelf Res.* 25 (7–8), 795–827. <https://doi.org/10.1016/j.csr.2004.08.004>
- Umlauf, L., Arneborg, L., 2009. Dynamics of rotating shallow gravity currents passing through a channel. Part I: Observation of transverse structure. *J. Phys. Oceanogr.* 39, 2385–2401. <https://doi.org/10.1175/2009JPO4159.1>
- Väli, G., Zhurbas, V., 2021. Seasonality of submesoscale coherent vortices in the northern Baltic Proper: A model study. *Fundamentalnaya i Prikladnaya Gidrofizika* 14 (3) (in press).
- Väli, G., Zhurbas, V.M., Laanemets, J., Lips, U., 2018. Clustering of floating particles due to submesoscale dynamics: a simulation study for the Gulf of Finland, *Fundamentalnaya i prikladnaya gidrofizika* 11(2), 21–35. <https://doi.org/10.7868/S2073667318020028>
- Väli, G., Zhurbas, V., Lips, U., Laanemets, J., 2017. Submesoscale structures related to upwelling events in the Gulf of Finland, Baltic Sea (numerical experiments). *J. Mar. Syst.* 171 (SI), 31–42. <https://doi.org/10.1016/j.jmarsys.2016.06.010>
- Vankevich, R.E., Sofina, E.V., Eremina, T.E., Ryabchenko, V.A., Molchanov, M.S., Isaev, A.V., 2016. Effects of lateral processes on the seasonal water stratification of the Gulf of Finland: 3-D NEMO-based model study. *Ocean Sci.* 12, 987–1001. <https://doi.org/10.5194/os-12-987-2016>
- Villermaux, E., 2019. Mixing versus stirring. *Annu. Rev. Fluid Mech.* 51, 245–273. <https://doi.org/10.1146/annurev-fluid-010518-040306>
- Vortmeyer-Kley, R., Holtermann, P.L., Feudel, U., Gräwe, U., 2019. Comparing Eulerian and Lagrangian eddy census for a tide-less, semi-enclosed basin, the Baltic Sea, *Ocean Dyn.* 69, 701–717. <https://doi.org/10.1007/s10236-019-01269-z>
- Yu, X., Garabato, A.C.N., Martin, A.P., Buckingham, C.E., Brannigan, L., 2019. An annual cycle of submesoscale vertical flow and restratification in the upper ocean. *J. Phys. Oceanogr.* 49, 1439–1461. <https://doi.org/10.1175/JPO-D-18-0253.1>
- Zhurbas, V., Elken, J., Paka, V., Piechura, J., Väli, G., Chubarenko, I., Golenko, N., Shchuka, S., 2012. Structure of unsteady overflow in the Stupsk Furrow of the Baltic Sea. *J. Geophys. Res. Oceans* 117, C04027. <https://doi.org/10.1029/2011JC007284>
- Zhurbas, V., Laanemets, J., Vahtera, E., 2008. Modeling of the mesoscale structure of coupled upwelling/downwelling events and the related input of nutrients to the upper mixed layer in the Gulf of Finland, Baltic Sea. *J. Geophys. Res. Oceans* 113, C05004. <https://doi.org/10.1029/2007JC004280>
- Zhurbas, V., Väli, G., Golenko, M., Paka, V., 2018. Variability of bottom friction velocity along the inflow water pathway in the Baltic Sea. *J. Mar. Syst.* 184, 50–58. <https://doi.org/10.1016/j.jmarsys.2018.04.008>
- Zhurbas, V., Väli, G., Kostianoy, A., Lavrova, O., 2019a. Hindcast of the mesoscale eddy field in the Southeastern Baltic Sea: Model output vs satellite imagery. *Russian J. Earth Sci.* 19 (4), 1–17. <https://doi.org/10.2205/2019ES000672>
- Zhurbas, V., Väli, G., Kuzmina, N., 2019b. Rotation of floating particles in submesoscale cyclonic and anticyclonic eddies: a model study for the southeastern Baltic Sea. *Ocean Sci.* 15, 1691–1705. <https://doi.org/10.5194/os-15-1691-2019>

Available online at [www.sciencedirect.com](http://www.sciencedirect.com)

ScienceDirect

journal homepage: [www.journals.elsevier.com/oceanologia](http://www.journals.elsevier.com/oceanologia)

## ORIGINAL RESEARCH ARTICLE

# The process of modelling the elevation surface of a coastal area using the fusion of spatial data from different sensors

Marta Włodarczyk-Sielicka, Izabela Bodus-Olkowska\*, Małgorzata Łącka

*Maritime University of Szczecin, Szczecin, Poland*

Received 29 April 2021; accepted 17 August 2021

Available online 28 August 2021

## KEYWORDS

Digital elevation model;  
Seabed bottom model;  
Bathymetry;  
LiDAR data;  
GEBCO;  
ETOPO

**Abstract** Information regarding the depth distribution in a specific aquatic area is not also crucial for the safety of navigation, but also for modelling environmental processes, such as the quick establishment of marine-land boundaries or assessments of flood risk areas. Using elevation data from different available sources can be very convenient for individuals who wish to conduct quick analysis or need to obtain data covering a large area without the need for data collection and surveys. This study proposes a method of combining spatial data from different sources during surface modelling of a coastal area. The spatial data used for elevation surface modelling included hydrographic and topographic data, which are often collected separately for various purposes. Data are saved in different formats with various resolutions and accuracies; thus, a uniform surface model that will allow for easy and accurate analysis is currently lacking. The main aim of this study was to create a model of the surface of a coastal area using input data from various sources with the highest possible accuracy. This paper presents the available spatial data sources for coastal areas, along with the data pre-processing process. Furthermore, spatial data fusion is introduced, along with the results. The entire process of creating the

\* Corresponding author at: Maritime University of Szczecin, Wały Chrobrego 1–2, 70–500 Szczecin, Poland.

E-mail address: [i.olkowska@am.szczecin.pl](mailto:i.olkowska@am.szczecin.pl) (I. Bodus-Olkowska).

Peer review under the responsibility of the Institute of Oceanology of the Polish Academy of Sciences.



uniform surface model consisted of several steps that are described in detail and visualised. The obtained model was visualised using a three-dimensional map.

© 2021 Institute of Oceanology of the Polish Academy of Sciences. Production and hosting by Elsevier B.V. This is an open access article under the CC BY-NC-ND license (<http://creativecommons.org/licenses/by-nc-nd/4.0/>).

## 1. Introduction

Spatial data can be used for constructing complex three-dimensional (3D) models that can be useful in ensuring navigation safety. For example, they can be used in geographic information system (GIS) services operating in such areas, including the vessel traffic system (VTS), coastal zone monitoring by port services or border guards, or as an additional information layer for navigators of tourist vessels, such as sea yachts. An integrated altitude model of a given coastal zone can provide supplementary information for holders of a standardised electronic navigational chart (ENC). Additionally, such information is useful for creating flood risk and risk maps, aiding in obtaining information regarding the height of flood embankments, determining the dynamics of changes in the maritime coastal zone (Maune, 2007), determining the volume of landfills and heaps, monitoring land changes, and analysing falls and land exposure. They can also facilitate decision-making related to the design of new investments, road routing, and the minimisation of earthworks.

There are many different sources of data that can be used in coastal zone modelling, such as hydrographic surveying by multibeam (MBES) or single-beam (SBES) echosounders and other acoustic methods, including interferometric bathymetric systems (Fezzani et al., 2019; Grall et al., 2020); Light Detection and Ranging (LiDAR; Shan et al., 2017) for both for water areas and terrain; data gathered from open sources, including the General Bathymetric Chart of the Oceans (GEBCO), Earth Topography and Bathymetry (ETOPO1), Baltic Sea Bathymetry Database, Global Bathymetry Model DTU10, or Shuttle Radar Topography Mission (SRTM); or data that can be obtained from local institutions, who are obligated to share the data due to the INSPIRE directive.

Combined topographic and bathymetric model development has been reported. (Mandlbürger et al., 2020) conducted a single-device research experiment and presented the concept of a novel compact topobathymetric laser scanner that was suitable for capturing river bathymetry at a high spatial resolution. Quadros et al. (2008) focused on the integration of separately acquired topographic and bathymetric LiDAR data in Port Phillip Bay. Danielson et al. (2016) reported an updated methodology for developing coastal topobathymetric elevation models from multiple topographic data sources with adjacent intertidal topobathymetric and offshore bathymetric sources to generate seamlessly integrated topobathymetric elevation models (TBDEMs). Starek and Giessel (2017) presented a data acquisition and processing methodology based on unmanned aircraft system (UAS) consisting of a Sensefly eBee equipped with a Canon IXUS 127 HS digital camera and created a hybrid topo-bathy digital elevation model (DEM) us-

ing the data. Legleiter (2012) developed and evaluated a hybrid approach to the remote measurement of river morphology that combined LiDAR topography with spectral-based bathymetry. Gesch and Wilson (2001) created a seamless topobathymetric elevation model for the Tampa Bay region based on the integration of disparate USGS National Elevation Dataset and NOAA digital sounding data, while Freeman et al. (2003) presented a process for creating digital elevation models (DEMs) based on 3D surveys utilising real-time kinematic GPS and ultra-shallow water single-beam and multibeam technologies, and one difficulty was processing massive and oversampled datasets into accurate DEMs.

The research area of this study is a coastal zone, where the depths are variable and the harbour infrastructure is well-developed, providing excellent opportunities for surface modelling. The main goal of this work is to combine data from various sources into a uniform surface model. The data considered in the fusion process were collected by hydrographic sensors: multibeam and single-beam echosounders and LiDAR technology, and then supplemented by data gathered from open sources, such as GEBCO and ETOPO1. The data were obtained from different sensors with different resolutions, which translated directly into the model details. During the fusion procedure, a hierarchy closely related to the resolution of data was proposed. Multibeam echosounder and LiDAR data had the highest priority and are the main inputs of the model. The abovementioned data were obtained from direct surveying. Data from the ENC and SBES were then considered as secondary data with reliable accuracy. When data were lacking, the model could be supplemented by open-source data such as ETOPO1, GEBCO, or other sources. In the fusion procedure, open-source data were given the lowest priority stage due to their low resolution.

## 2. Material and methods

### 2.1. Data sources

The study area covers a square with a side-length of 1,300 m located in Świnoujście Port, Poland.

Depth points obtained using a multibeam echosounder were the main data source, which is the most frequently used method for obtaining high-resolution seabed data (Alberoni et al., 2019; Maleika and Forczmański, 2020; Maleika, 2020). The transducer sends many acoustic beams at different angles, forming a swath of acoustic beams. The depth of the water area can be measured by utilising the ability to reflect the acoustic signal from hard surfaces. Multibeam swath systems are widely used in almost every study requiring depth measurements with high resolution (Holland et al., 2021; Janowski et al., 2021; Somoza et al.,



2021). In this study, the data for the model were obtained from the Maritime Office in Szczecin (MOS), who collected the data using an EM3002D multi-beam echosounder during the depth control work of the Szczecin-Swinoujście fairway during September 2020. Grid data with a resolution of 1 m were generated from the depth point cloud.

The next data source was a single-beam echosounder system that generates a very narrow acoustic beam directed perpendicularly downwards. From the measurement, we obtained a narrow strip of data coverage, which was visualised as a single line of points in the hydrographic software. The data used for analysis were obtained from registration with the navigation echosounder during the implementation of the gravimetric and hydrographic tasks of the MOGRAV project on the trip of the Navigator XXI research vessel of the Maritime University of Szczecin. The data were obtained as a single line along the route of the ship. As there the data were insufficient to build a bottom model, they were used to compare the depth values with data from the multibeam echosounder.

An ENC was used as the next data source. Objects representing depth were generated based on actual measurement data obtained by hydrographic bathymetric systems, such as multibeam echosounders. The points representing the depths were pre-processed and generalised to obtain a clear overview of the information on the map. Additionally, the Hydrographic Office of the Polish Navy provided depth points with a resolution of 50 m.

The overall global ocean bathymetric map (GEBCO) is a joint project of the International Hydrographic Organization (IHO) and Intergovernmental Oceanographic Commission (IOC), bringing together an international group of experts dedicated to providing the most authoritative, publicly available bathymetry for scientific and educational use. The global bathymetric dataset is one of the GEBCO's products (IHO B-11, 2019). The data included depth (and land elevation) estimates on a grid of 15 arc seconds, which is a 1-km mesh near the equator. The depths were derived from actual ship soundings or interpolated using satellite estimates where no soundings were available. GEBCO data are widely used in many cases where global depth data are required (Jakobsson et al., 2020; Ramasamy et al., 2020; Ruan et al., 2020).

ETOPO1 (Amante and Eakins, 2009) is a global model of the Earth's surface that integrates land topography and bathymetry worldwide, and combines DEM data of land with digital bathymetric model (DBM) data for water-covered areas. The average resolution of the bathymetric data is 0.5 km, while that of the topographic data is 30 m.

The SRTM is an international research initiative that has acquired DEMs on a scale close to global. The SRTM data were provided by NASA JPL with a resolution of 1 arc-second (approximately 30 m). A raster with a cell size of 75 m was obtained for the research area.

The Baltic Sea Bathymetry Database (BSBD) service was developed by the state administrations of the Baltic countries and provides gridded bathymetric data of the Baltic Sea Basin. The resolution of the bathymetric data ranges from 500 m to 64 km.

The DTU10 bathymetry-radar satellite altimetry model is another data source derived from all available satellites and was mapped with a resolution of 1 min. Bathymetric

information can be obtained from traditional hydrographic systems, such as echosounders, while model depth data can be obtained via satellite altimetry in less explored waters, where vessel traffic is negligible.

LiDAR is the main source of topographic data. The point cloud from airborne laser scanning is a multibillion collection of points with X, Y, and Z coordinates, representing the surface and area coverage obtained from the airborne systems with a laser scanner.

A database of topographic objects corresponding to a topographic map (BDOT10k) can be used as an additional data source, which is a vector database containing the spatial locations of topographic objects along with their characteristics, and includes 10 main categories of objects, i.e., water networks, communication networks, land utility networks, land cover, protected areas, territorial division units, buildings, structures and devices, land use complexes, and other objects.

## 2.2. Spatial data pre-processing

Bathymetric data with depth points obtained from MOS and BHMW were provided in \*.txt format, in the form of a grid mesh. In the case of data from a multi-beam echosounder (UMS data source), a high-resolution grid with a cell size of 1 × 1 m was generated for multi-beam echosounder data (UMS data source). In the case of ENC depth points, a grid with a cell size of 50 × 50 m was obtained. The data provided by both institutions were previously filtered, corrected, and reduced (IHO C-13, 2013). As the hydrographic standard (IHO S-44, 2020) presents the depth data as positive values, the only necessary data preparation process in this study was to convert them into negative values. The MBES bathymetric point dataset included 511,749 points, covering an area of 1.5 × 1.5 km. The minimum and maximum depth in the study area were −2.25 and −18.15 m, respectively,

The collected by the single-beam echosounder included 378 measurement points with a minimum and maximum depth of −15.05 and −16.77 m, respectively.

Owing to the small mesh resolution, the preparation of data from the ENC was slightly longer and included the following steps:

- [1] building a raster model based on the ENC database;
- [2] increasing the spatial resolution of the raster and exporting the model to a raster with a cell size of 1 m as a regular grid of points (X, Y, Z);
- [3] the ENC model was used as a supplement to the base data; therefore, all points in the Odra area in the next step were clipped to the areas with no MBES data coverage. At this stage, the two different resolutions were merged.

The input data from the ENC included a total of 228 points with minimum and maximum depths of −0.4 and −16.8 m, respectively. The data were in the form of a regular grid. Figure 1 shows the distribution of points from the ENC (a) and the obtained raster model with a spatial resolution of 25 m (b).

The GEBCO model was downloaded from <https://download.gebco.net/> on 30/09/2020. To download the model, the area of interest and data format (ESRI ASCII,

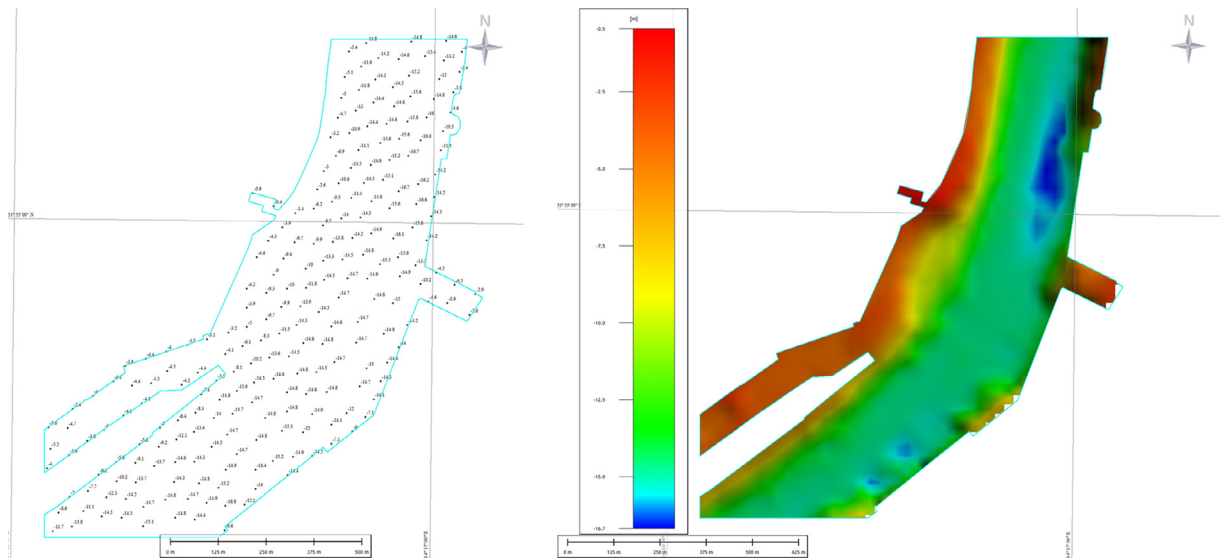


**Figure 1** ENC source dataset: a) bathymetric points, b) raster model with a spatial resolution of 25 m.

GeoTiff, or NetCDF) were indicated. The \*.asc format was used to build the model. The model was downloaded in the \*.asc format and was then clipped to the research area.

Owing to their low resolution (registration only on one profile), single-beam echosounder data were not considered further. Additionally, owing to their low resolution and lack of data in the research area, the models with DTU10, BSBD, and ETOPO1 data were not considered.

For the land area, data containing the classified point cloud were downloaded from the website of the National Geoportal of Poland ([www.geoportal.gov.pl](http://www.geoportal.gov.pl)). The scope of the data covered 12 modules (sections in the PUWG92 system and scale of 1:1250). From the classified point cloud, only class 2, i.e., the ground, was used for further elaboration. The situational and altitude accuracy of LiDAR data with the absolute georeferencing of the point cloud must be within the criteria specified in the Technical Guidelines, and the situational and altitude accuracies for Standard II were 0.40 and 0.10 m, respectively. The data were clipped to the scope of the study and then exported to the UTM 33N system. Class 2 data were visually inspected for a lack of data and the possibility of incorrect data in the water area.

Based on the BDOT10k data and orthophoto map, whether the lack of data on the LiDAR layer coincided with buildings or occurred in underwater areas was visually determined. The analysis results were positive, indicating the completeness of the LiDAR data for further processing. Therefore, it would not be necessary to use other supplementary materials, such as the SRTM model. Class 2 data (ground) may have been included in the area of water occurrence, which is typically due to misclassification (automatic or manual). Therefore, based on data from the layer covering the Odra River obtained from the BDOT10K database (PTWP02 – land cover, surface water, and 02 – flowing water), the ground-class points located inside this layer were removed. This procedure also avoids a situation in which layers from two different sources overlapped. The spatial data used in this study included 2,033,731 points with a minimum and maximum height of -0.75 and 17.51 m, respectively. [Figure 2](#) shows a visualisation of the points from

airborne laser scanning with a hypsometric scale based on the terrain height.

Points representing the ground are presented on the left, while a continuous raster surface created based on ground points is shown on the right.

### 2.3. Research methodology

A new model for integrating data from different sources is proposed here, with the main objective of combining data from the coastal area and creating and normalising a coherent model. The proposed process for the fusion of spatial data from coastal zones is schematically illustrated in [Figure 3](#).

The proposed approach consisted of the following steps:  
Step 1: Definition of the area and relevant coastal infrastructure.

Step 2: Fusion of MBES and LiDAR data.

Step 3: Filling the gaps with ENC and SBES data.

Step 4: Filling the gaps with GEBCO, ETOPO, and other data.

Step 5: Visualisation of the integrated surface model.

Step 6: Model validation.

Global Mapper with a LiDAR module was used for data modelling. This software was selected to optimise processing, enable working with different types of data acquired in different formats, and effectively visualise the data. The primary dataset consisted of dense LiDAR and high-resolution bathymetric data. The *Elevation Grid Creation* tool in the *Analysis* menu was then used to create a model based on these data. This tool allows spatial models to be created from point and vector data. The user can define parameters, such as the resolution of the final model, length of the side of the triangle in the network of triangles (TIN) and use of breaklines (hard and soft edge). When creating DEMs from LiDAR data, the user can select the interpolation type (in the basic version, triangulation is the only available option). When using LiDAR data, the program allows any user-defined filtering of data based on classes and/or return numbers ([Global Mapper – Knowledge Base, Elevation Grid](#)

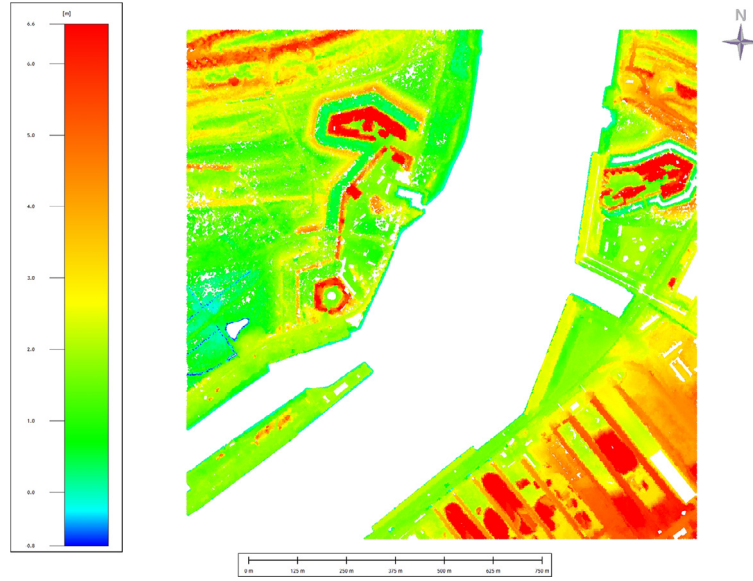


**Figure 2** Hypsometric-scale LiDAR source dataset based on the points of the height of the terrain.

Creation, 2021). Global Mapper also has tools to perform basic algebraic operations on rasters. The *Combine/Compare Terrain Layers* tool was used together with the *Subtraction Signed* option to create the differential model used for accuracy analysis.

The first step involved determining the scope of the future model of the coastal area and selecting relevant objects that will be required during the creation of the final model. Such objects may include quays, coastlines, and other objects that will aid in determining the boundary of the water area. Orthophoto maps from 2019 and 2017 were used for the visual assessment. The orthophoto map from 2019 had a better spatial resolution (10 cm) and better interpretative potential, while the orthophoto map from 2017, with a pixel size of 25 cm, was similar to the current acquisition from the layer representing the Odra River. Minor changes to the shoreline are visible on the left bank of the river, where natural coastal processes, accumulation, and erosion occur, and shown in Figure 4.

The study area in 2017 is presented on the left, and the same area in 2019 is presented on the right. The artificial, solid-faced berths did not change during the 2016–2019 period. Data from two basic measurement systems, i.e., MBES and LiDAR, are fused in the next step of the proposed process, in which the model with the best resolution was generated. For the study area, a resolution of 0.5 m was selected, which was optimal for both types of spatial data. The model was generated following the irregular triangle mesh method. As the input data for the model were characterised by high density, the binning minimum value (DTM) method was used for smoothing and denoising (Mills, 2020). The data were initially sorted and divided into parcels (buckets or bins). Smoothing is local as this method uses values in the vicinity of the points. Triangulation was then conducted.

Delaunay triangulation is the most common method, based on the construction of Voronoi diagrams. The set of points  $P$  can be described by Eq. (1):

$$P = \{p_1, p_2, \dots, p_n\} \text{ where } p_i \in R^2, n \in N \quad (1)$$

The Voronoi cell  $V_p$  for point  $p_i$  is as follows:

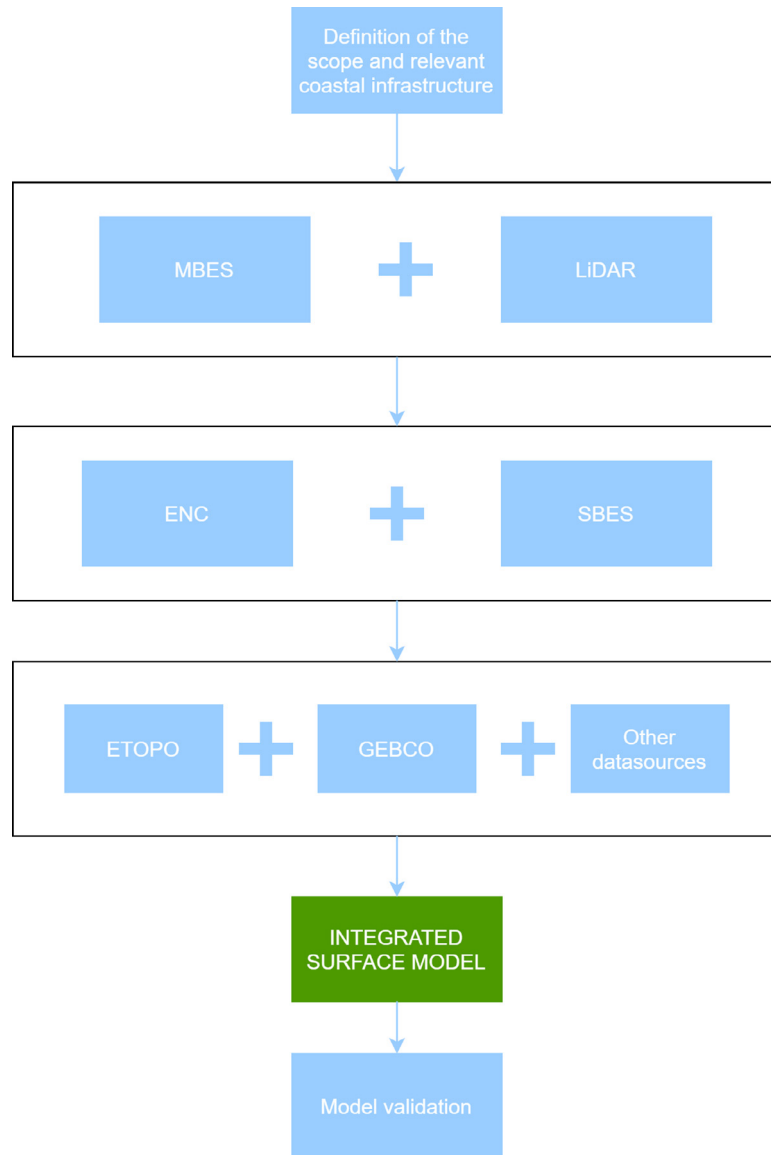
$$V_{p(p_i)} = \{x : \forall_{j \neq i} d(x, p_i) \leq d(x, p_j)\} \quad (2)$$

where  $d$  is the Euclidean norm. Therefore, the Voronoi cell  $V_{p(p_i)}$  is a set of points whose distance to  $p_i$  is smaller than that to any other vertex (Duan et al., 2017).

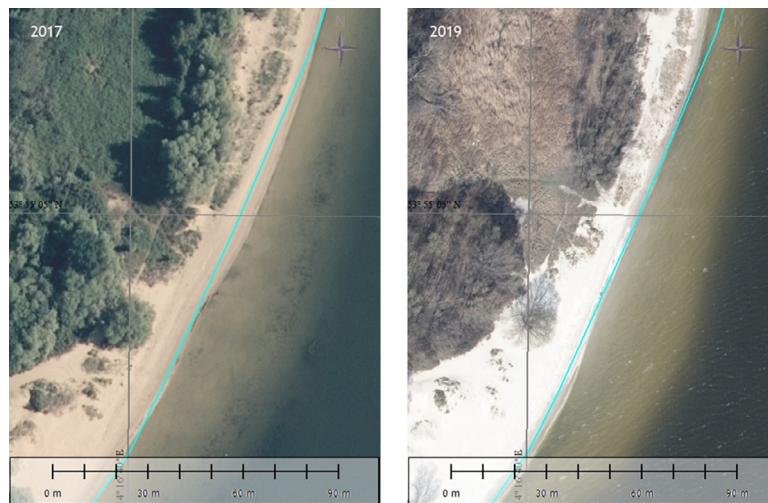
A parameterised size of triangles can form a network of triangulation to interpolate the model in areas where the density of the grid points is significantly lower or where there are data gaps. A high value for this parameter was used to avoid missing data points. At this stage, the problem of data redundancy should also be considered when the data overlap. The redundancy of data from different sources, presenting the depth and height in one area at the same time, will lead to a surface distortion, which is related to misinterpretation and incorrect surface mapping. An example of redundancy is shown in Figure 5.

Figure 5 presents the effects of data redundancy. The figure on the left shows the boundary between the water and land area. The depth data shown in purple were obtained from multibeam echosounder recordings. Terrestrial data were obtained from LiDAR and are shown in brown. Single points are shown in grey in the left and central panels of Figure 7, which provide information regarding the height values acquired from LiDAR data. As the LiDAR information does not contain the actual depth, only the value measured from the reflection from the water surface, disturbances in the overall terrain model appearing as a line from single peaks (spikes) are generated. The effect is visible on the boundary between water and land presented in the right panel of Figure 7. Such data should be removed from further analysis and should not be included in the data population to create the surface model.

The ranges of the data layers from LiDAR and MBES were checked to identify areas with a lack of data and redundancy. The data overlapped with the water area. Under the



**Figure 3** The process proposed for modelling the elevation surface.



**Figure 4** Visual assessment of the study area.

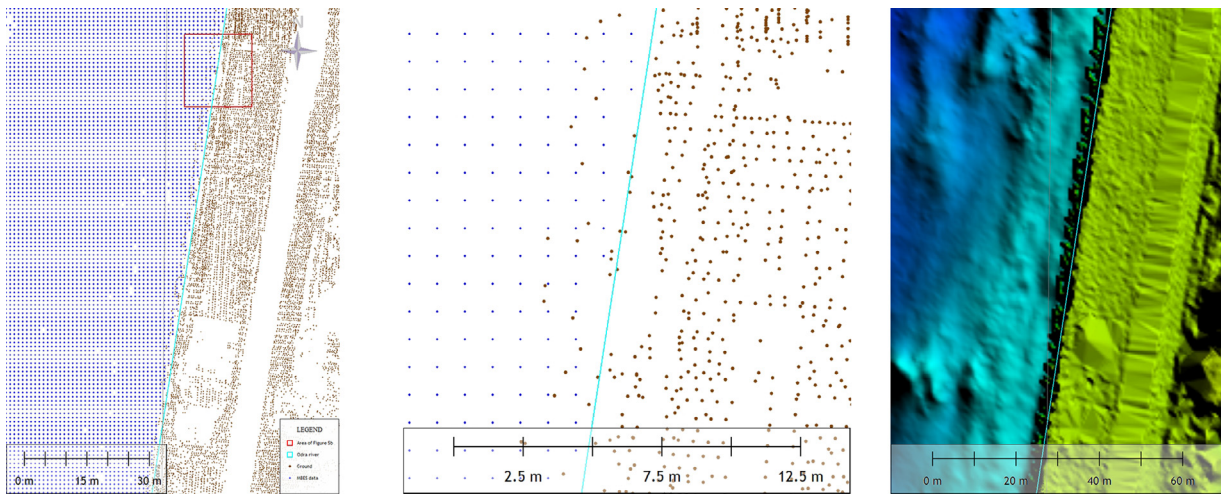


Figure 5 Redundancy problem of data obtained from various measurement systems.

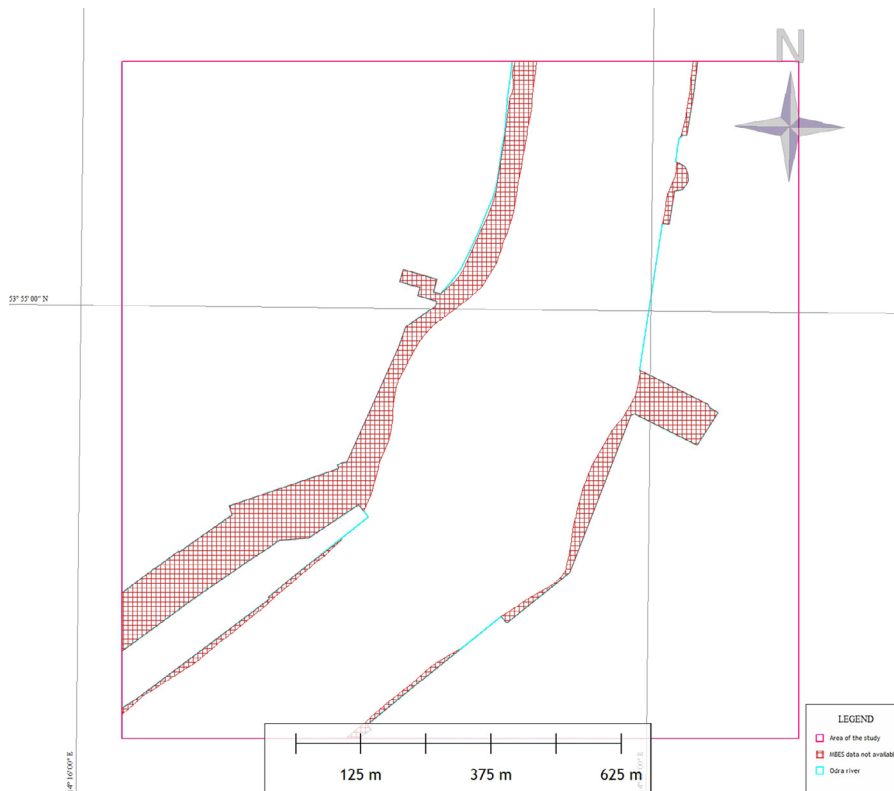


Figure 6 Areas without bathymetric data coverage.

assumptions of the proposed procedure, the LiDAR data representing depth values were deleted, as the depth information was not reliable in this case. Areas without bathymetric data were also identified, as shown in Figure 6.

Figure 7 presents the model created in the second stage, along with areas of missing data. The model was created based on 5,090,351 objects in the TIN, where the minimum and maximum height values were  $-18.14$  and  $17.48$  m, respectively.

During the third stage of the proposed approach, the areas with missing data were filled with points obtained

from the ENC. The main difficulty when using data from the ENC was the large difference in the resolution of the integrated data. We used the generated raster surface with automatic spatial resolution selection to optimise the model. The surface was created following the irregular TIN method. In the next step, the spatial resolution of the model was increased from that of the ENC data up to  $1$  m following the bicubic resampling method while simultaneously changing the format from raster to point. As a result, a regular grid mesh with a resolution of  $1$  m was obtained for the area of the Odra River. The data were then clipped to ar-

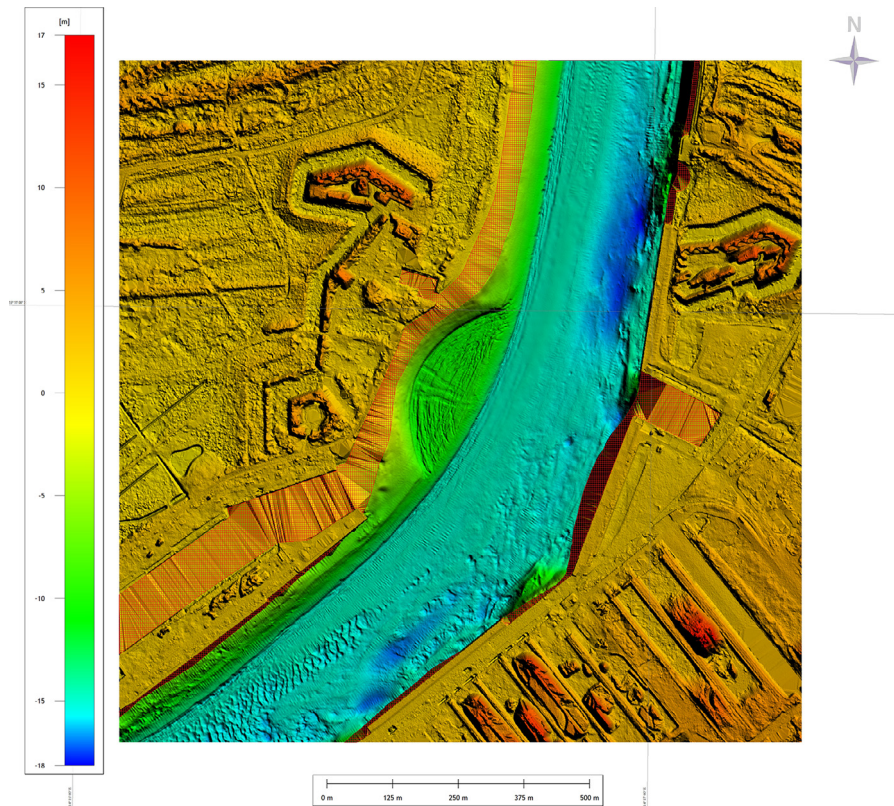


Figure 7 Surface model after MBES and LiDAR data fusion.

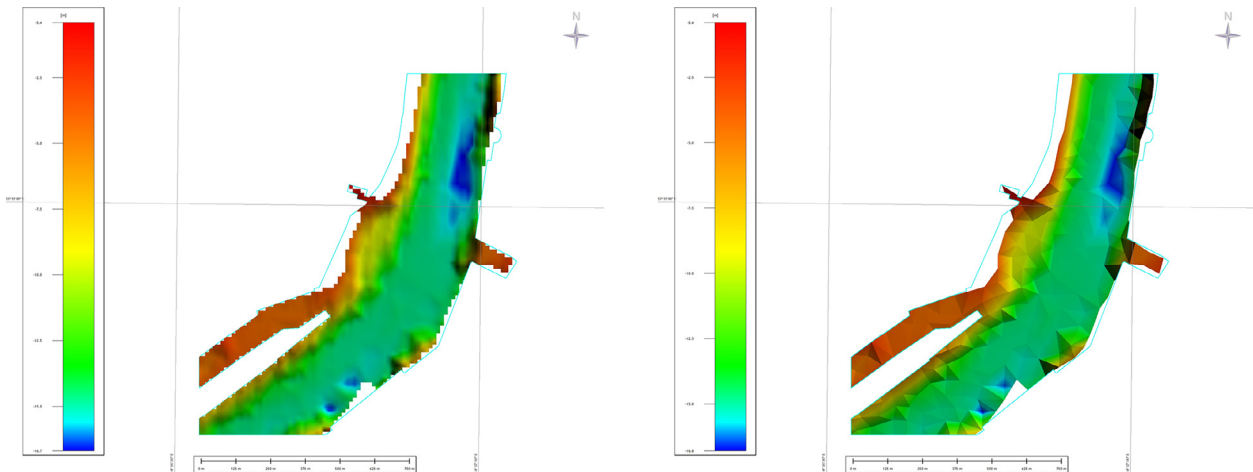


Figure 8 ENC data processing: a) raster model with the optimal spatial resolution, b) raster model with a spatial resolution of 1 m.

areas containing missing data from stage two of the proposed approach.

The results are presented in Figure 8. A raster model obtained based on ENC data with the optimal spatial resolution is presented on the left, while the same model with a spatial resolution of 1 m is shown on the right.

As a result, a new model was created based on three groups of data: LiDAR terrain data and hydrographic data (MBES and ENC; Figure 9).

Figure 9 shows the model developed during LiDAR, MBES, and ENC data integration. In areas where the information regarding the height of the terrain had high resolution, the

terrain mapping has a high level of detail. For example, in harbour channels, characteristic ripple marks on the bottom and changing depths at some quays (blue) are visible, and harbour infrastructure is easy to identify on land (green and brown). When the data resolution was low, the triangles were visible. This effect was observed for both port basins. Additionally, it was clear where the data resolution changed.

The next step is analysing whether or not the selected range of the remaining areas is covered by data. If so, they were covered with points from the free spatial data sources of GEBCO or ETOPO. This step was not necessary for the study area.

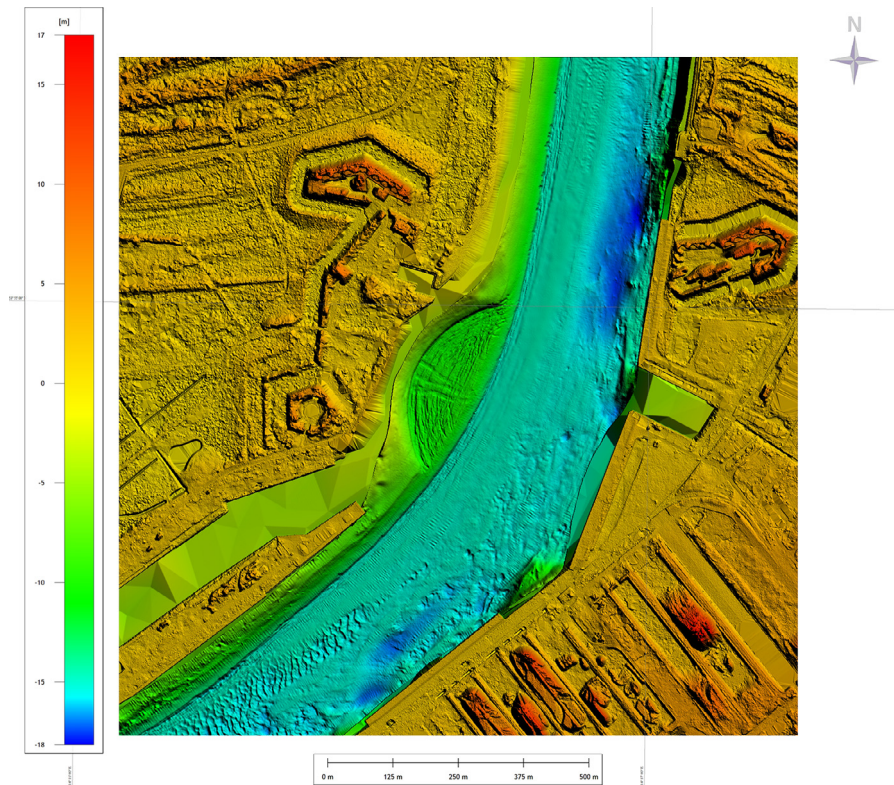


Figure 9 Surface model after fusing LiDAR, MBES, and ENC data.

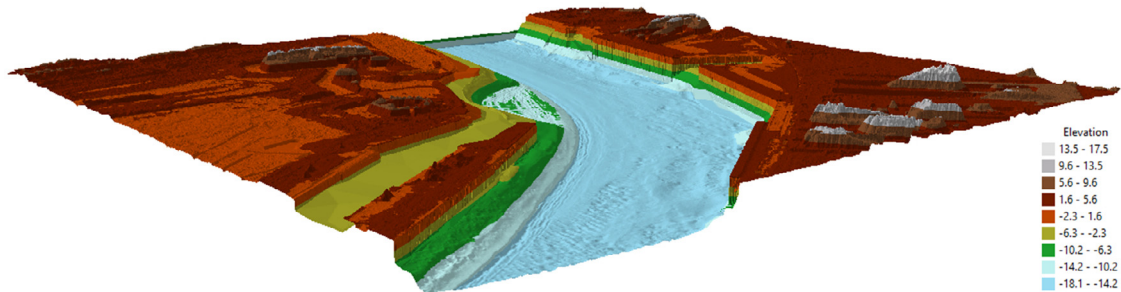


Figure 10 Visualisation of the integrated surface model.

The next stage of the method is the visualisation of the integrated surface model, as shown in Figure 10.

In the final stage, we propose assessing the accuracy and correctness of the constructed model by comparing it with the existing DTM combined with the multibeam echosounder data. The DTM model was obtained from resources provided by the Head Office of Geodesy and Cartography, and was downloaded in the GRID structure at a resolution of 1 m. An aerial point cloud used for constructing the integrated surface model was taken as the source data for the development of this model, which is shown in Figure 11.

### 3. Results

A raster showing the model differences was created using the subtraction tool to compare the height models, as shown in Figure 12. The new layer of height values was the differ-

ence between the first and second raster ([Global Mapper – Knowledge Base, Combine/Compare Terrain Layers 2021](#)).

The differences in the land part of the model reached 10 cm due to differences in data modelling. The data of the proposed model were scattered points, while those of the DTM were obtained as a 1-m grid mesh. The area covering the Odra River should be excluded from the analysis, as it contains a different set of data to the comparative model; therefore, the high values of the differential model in this area did not undergo further analysis.

The DTM model provided by technical standards was characterised by absolute accuracy verified by independent field measurements in the form of profiles and terrain mesh points.

Based on field measurements, deviations between the field points and heights obtained from the DTM were created, and the mean error was calculated based on all observations. The mean error must be  $m_h \leq 0.20$  m, and the maximum difference between the heights

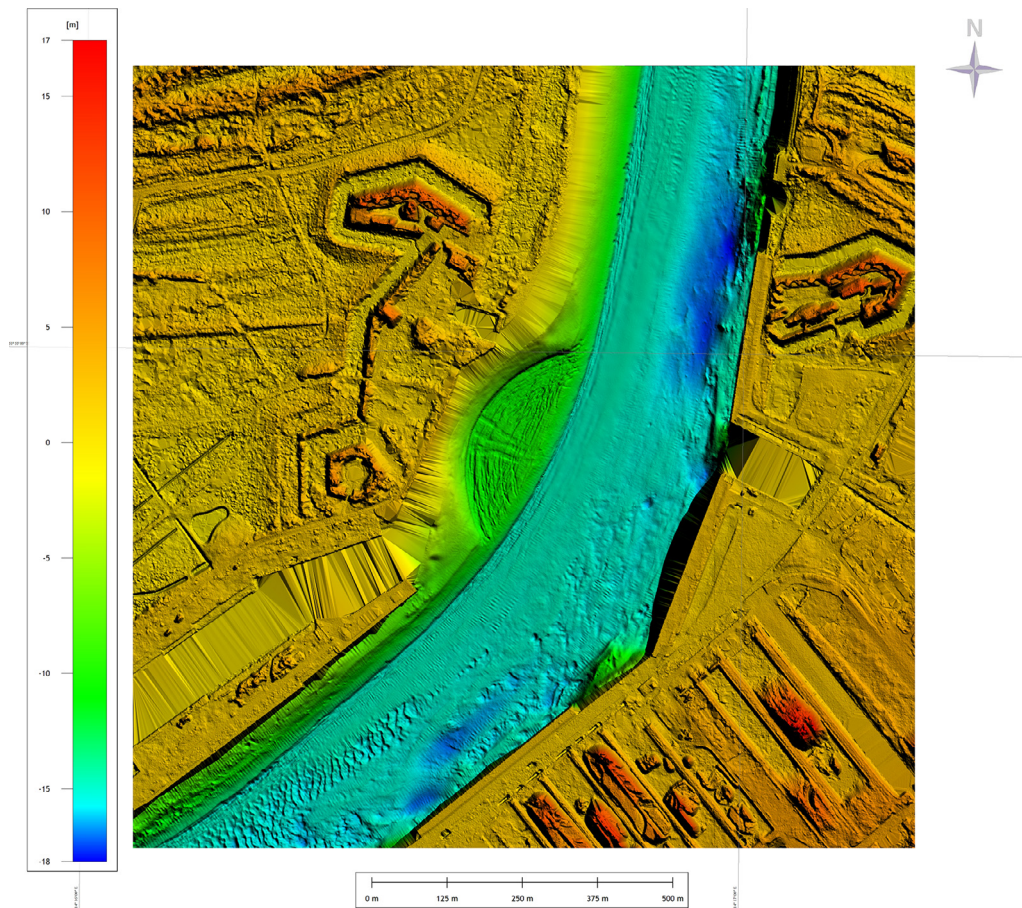
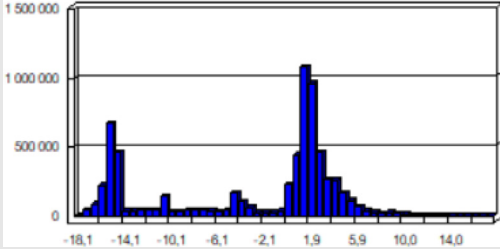
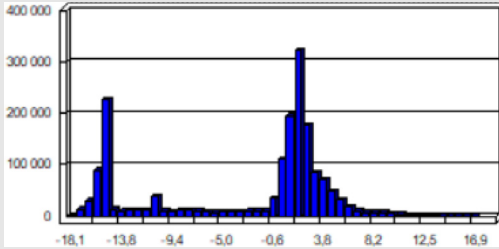


Figure 11 The surface model used for comparison.

Table 1 Statistics for the compared models.

	Integrated surface model	Model used for comparison
Number of points	6757399	1687685
Frequency Distribution		
Minimum Z (m)	-18.14	-18.13
Maximum Z (m)	17.48	17.39
Mean Z (m)	-2.82	-2.58

must not exceed 0.60 m, according to the technical standards.

In the next step, the basic statistical data of the compared models were analysed, and the results are shown in Table 1.

The number of points in the created model was 5069714 points higher than that in the model used for comparison, which is mainly due to the resolution of the model mesh. The main goal of this study was to obtain the best possi-

ble resolution, which was achieved. The number of height points was large; therefore, the model is highly resolving. The frequency distribution indicates that, in the case of the proposed integrated surface model, the highest number of points was observed within the range of -2.0 to 6 m. This range was -0.6 to 5 m for the existing model, which is much smaller. The frequency distribution parameter significantly influenced the resolution of the model and its level of detail. The difference between the models was because



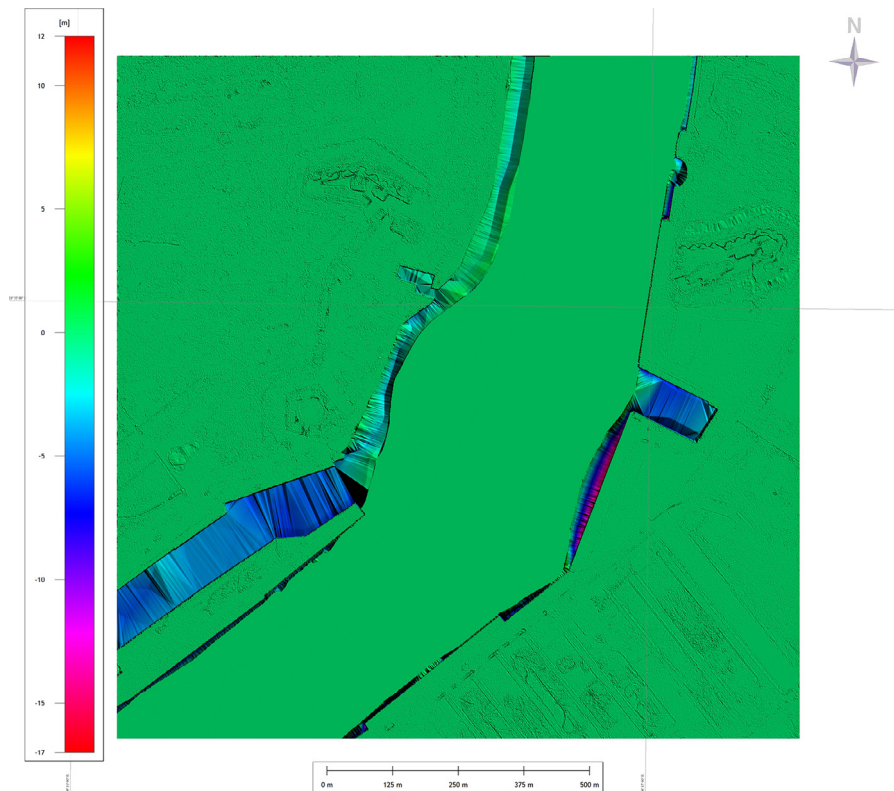


**Figure 12** Raster showing differences in height models based on a subtraction function.

the fused model covered more data sources. The minimum depth value, which is related to navigation safety in a given area, was also considered. The model created following the proposed approach had a smaller depth value and the difference was approximately 1 cm, which is not significant in the case of water areas. The maximum height in the compared models differed from each other by 10 cm, which was significant. In conclusion, the model proposed here was more accurate and had better detail; therefore, it can be used for future analysis and precise visualisation.

#### 4. Discussion

The process of creating a surface model for coastal areas proposed in this work involved spatial data from various available sources and consisted of six stages. The first was related to the definition of the scope of coastal areas. A further three were closely related to the fusion of the data and included information regarding the integration of different data densities. Stage five involves the visualisation of the designed model, and model validation was the final stage.

Some problems related to data availability were encountered, and the resolution of the resulting model depended on several factors. The density of the point clouds had the greatest impact on the terrain model, specifically the density of Class 2, representing the ground. In areas where data were lacking, such as underwater areas or those beneath buildings, interpolation was conducted based on neighbouring data. The mesh grid size limited the bathymetric data, which imposed a pixel with which the model could be cre-

ated. One of the main limitations of utilising open-source data is whether they are up to date. The integrated model was as valid as the source data from which the model was created and, their validity should be determined individually using several different datasets. The issues of data resolution and model accuracy can be considered in a similar manner. For high-resolution data, the details of the model, as well as the accuracy of the data, will be high; however, high-resolution data are lacking, and the model utilises  $n$  and is interpolated from lower-resolution data, resulting in a decrease in the horizontal and elevation accuracy in the "filled in" areas. Overlapping is another limitation in data processing, which can be of two types. Topographic and bathymetric data (such as at the land-water interface) or data of the same type (such as bathymetric data from different systems, including multibeam and single-beam echosounder) may overlap. In the first case, the data ranges should be adjusted based on the known position of the shoreline and overlaying bathymetric and LiDAR data with different heights can cause the situation shown in [Figure 5](#). In the case of overlapping data of the same type, the data should be explored in detail by comparative height analysis, and the accuracies of the systems from which the data originate should be compared. Such information will allow further action to be taken, such as merging the two data sets or selecting the more accurate set for further processing. Another limitation is the accuracy of the source data. we conducted a qualitative assessment of the data before the integration process, particularly of the LiDAR data, and analysed the correctness of the classification process, which affects the land class used in further studies. Models based

on such data will not correctly represent the terrain surface in the case of incorrect classification, such as that of the shoreline area.

The proposed integration of data from various available sources allows unsurveyed or inaccessible areas to be supplemented with data. In some cases, bathymetric data or terrain information is only complementary; hence, the measuring range can be significantly clipped or restricted. The proposed model for data source integration can then be used.

In the future, we intend to apply the proposed approach to other areas and modify it to obtain the best results.

## 5. Conclusions

The great added value of the method lies in its ability to create a uniform surface model consisting of data collected by various sensors with different resolutions. The model can be quickly and easily supplemented using open-source data, such as GEBCO or ETOPO1, whenever areas are unsurveyed. The created model can be used for projects requiring bathymetric and terrain data, without the need to devote time and resources to the direct acquisition and processing of measurement data. It also allows spatial analysis of models with other types of data, such as magnetometric, gravimetric, or sonar imaging. Moreover, the proposed fusion is relatively easy to implement and can be used in many cases where a coastal zone surface model is required, such as in geoinformatics systems that require an additional information and visualisation layer, other underwater exploration projects, or research of the underwater parts of hydrotechnical structures; however, this was not the main goal.

In future work, we plan to test the proposed approach in other research areas with different scopes and shapes. It is also assumed that the available data sources of future research areas will differ. We also plan to propose a modification process using optimal data reduction methods. Additionally, we plan to develop standardisation parameters for the integrated surface, along with the determination of the optimal parameters for alteration between data resolutions.

## Acknowledgments

This work was supported by Grants Nos. 2/S/KG/20 and 1/MB/KG/20, financed by a subsidy from the Ministry of Science and Higher Education for statutory activities.

## Supplementary materials

Supplementary material associated with this article can be found, in the online version, at <https://doi.org/10.1016/j.oceano.2021.08.002>.

## References

Alberoni, A.A.L., Jeck, I.K., Silva, C.G., Torres, L.C., 2019. The new Digital Terrain Model (DTM) of the Brazilian Continen-

tal Margin: detailed morphology and revised undersea feature names. *Geo-Mar. Lett.* 40 (6), 1–16. <https://doi.org/10.1007/s00367-019-00606-x>

Amante, C., Eakins, B.W., 2009. ETOPO1 Global Relief Model converted to PanMap layer format. NOAA-National Geophysical Data Center. PANGAEA. <https://doi.org/10.1594/PANGAEA.769615>

Danielson, J.J., Poppenga, S.K., Brock, J.C., Evans, G.A., Tyler, D.J., Gesch, D.B., Thatcher, C.A., Barras, J.A., 2016. Topobathymetric elevation model development using a new methodology: Coastal national elevation database. *J. Coastal Res.* 76 (Sp. Iss. 1), 75–89. <https://doi.org/10.2112/SI76-008>

Duan, X., Li, L., Zhu, H., Ying, S., 2017. A high-fidelity multiresolution digital elevation model for Earth systems. *Geosci. Model Devel.* 10, 239–253. <https://doi.org/10.5194/gmd-10-239-2017>

Fezzani, R., Zerr, B., Mansour, A., Legris, M., Vrignaud, C., 2019. Fusion of Swath Bathymetric Data: Application to AUV Rapid Environment Assessment. *IEEE J. Oceanic Eng.* 44 (1), 111–120. <https://doi.org/10.1109/JOE.2017.2773139>

Grall, P., Kochanska, I., Marszal, J., 2020. Direction-of-Arrival Estimation Methods in Interferometric Echo Sounding. *Sensors Sp. Iss.* 20 (12), 3556. <https://doi.org/10.3390/s20123556>

Gesch, D., Wilson, R., 2001. Development of a seamless multi-source topographic/bathymetric elevation model of Tampa Bay. *Mar. Technol. Soc. J.* 35 (4), 58–64. <https://doi.org/10.4031/002533201788058062>

Global Mapper – Knowledge Base, Combine/Compare Terrain Layers, accessed on 13 July 2021. [https://www.bluemarblegeo.com/knowledgebase/global-mapper-19/Create\\_Elevation\\_Grid\\_from\\_3D\\_Vector\\_Data.htm](https://www.bluemarblegeo.com/knowledgebase/global-mapper-19/Create_Elevation_Grid_from_3D_Vector_Data.htm)

Global Mapper – Knowledge Base, Elevation Grid Creation, accessed on 13 July 2021. [https://www.bluemarblegeo.com/knowledgebase/global-mapper-19/Create\\_Elevation\\_Grid\\_from\\_3D\\_Vector\\_Data.htm](https://www.bluemarblegeo.com/knowledgebase/global-mapper-19/Create_Elevation_Grid_from_3D_Vector_Data.htm)

Holland, M.M., Becker, A., Smith, J.A., Everett, J.D., Suthers, I.M., 2021. Characterizing the three-dimensional distribution of schooling reef fish with a portable multibeam echosounder. *Limnol. Oceanogr. Methods* 19 (5), 340–355. <https://doi.org/10.1002/lom3.10427>

IHO B-11, 2019. The IHO-IOC GEBCO Cook Book, IHO Publication B-11. [https://www.star.nesdis.noaa.gov/socd/lsa/GEBCO\\_Cookbook/](https://www.star.nesdis.noaa.gov/socd/lsa/GEBCO_Cookbook/)

IHO C-13. 2013. Manual on Hydrography.

IHO S-44. 2020. IHO S-44 Standards for Hydrographic Surveys. <https://iho.int/en/standards-and-specifications>

Jakobsson, M., Mayer, L., Bringensparr, C., Castro, C., Mohammad, R., Johnson, P., Ketter, T., Accetella, D., Amblas, D., An, L., Arndt, J.E., Canals, M., Casamor, J.L., Chauché, N., Coakley, B., Danielson, S., Demarte, M., Dickson, M.-L., Dorschel, B., Zinglensen, K., 2020. The International Bathymetric Chart of the Arctic Ocean Version 4.0. *Sci. Data* 7 (1), 176. <https://doi.org/10.1038/s41597-020-0520-9>

Janowski, Ł., Kubacka, M., Pydyn, A., Popek, M., Gajewski, Ł., 2021. From acoustics to underwater archaeology: Deep investigation of a shallow lake using high-resolution hydroacoustics—The case of Lake Lednica. *Poland. Archaeometry* 63 (5), 1059–1080. <https://doi.org/10.1111/arcm.12663>

Legleiter, C.J., 2012. Remote measurement of river morphology via fusion of LiDAR topography and spectrally based bathymetry. *Earth Surf. Proc. Land.* 37 (5), 499–518. <https://doi.org/10.1002/esp.2262>

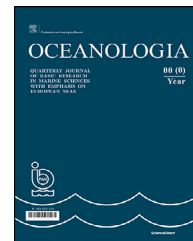
Maleika, W., Forczmański, P., 2020. Adaptive Modeling and Compression of Bathymetric Data With Variable Density. *IEEE J. Oceanic Eng.* 45 (4), 1353–1369. <https://doi.org/10.1109/JOE.2019.2941120>

Maleika, W., 2020. Inverse distance weighting method optimization in the process of digital terrain model creation based on data collected from a multibeam echosounder. *Appl. Geomat.* 12, 397–407. <https://doi.org/10.1007/s12518-020-00307-6>

- Mandlburger, G., Pfennigbauer, M., Schwarz, R., Flöry, S., Nussbaumer, L., 2020. Concept and performance evaluation of a Novel UAV-Borne Topo-Bathymetric LiDAR sensor. *Remote Sens.* 12 (6), 986. <https://doi.org/10.3390/rs12060986>
- Maune, D.F., 2007. *Digital Elevation Model Technologies and Applications: The DEM Users Manual*. 2nd Edn., ASPRS Publ., 655 pp.
- Mills, M., 2020. Elevation Grid Creation in Global Mapper: Creating a DTM. Blue Marble Geographics. <https://blog.bluemarblegeo.com/2020/06/23/elevation-grid-creation-in-global-mapper-creating-a-dtm/>
- Quadros, N., Collier, P., Fraser, C., 2008. Integration of bathymetric and topographic Lidar: a preliminary investigation. *The International Archives of the Photogrammetry Remote Sensing and Spatial Information Sciences Beijing XXXVII (B8)*, 1299–1304.
- Ramasamy, S.M., Saravanel, J., Kathiresan, P., Kumanan, C., Rajasekhar, D., 2020. Detection of submerged harbour using GEBCO and MBES data, in the offshore region of ancient port city Poompuhar, South India. *Curr. Sci.* 119, 526–534. <https://doi.org/10.18520/cs/v119/i3/526-534>
- Ruan, X., Cheng, L., Chu, S., Yan, Z., Zhou, X., Duan, Z., Li, M., 2020. A new digital bathymetric model of the South China Sea based on the subregional fusion of seven global seafloor topography products. *Geomorphology* 370, 107403. <https://doi.org/10.1016/j.geomorph.2020.107403>
- Shan, J., Toth, C.K. (Eds.), 2017. *Topographic Laser Ranging and Scanning: Principles and Processing*. CRC Press, 654 pp.
- Somoza, L., Medialdea, T., González, F.J., Machancoses, S., Cándón, J.A., Cid, C., Calado, A., Afonso, A., Pinto Ribeiro, L., Blasco, I., Albuquerque, M., Asensio-Ramos, M., Betten-court, R., De Ignacio, C., López-Pamo, E., Ramos, B., Rincón-Tomás, B., Santofimia, E., Souto, M., Madureira, P., 2021. High-resolution multibeam bathymetry of the northern Mid-Atlantic Ridge at 45–46° N: the Moytirra hydrothermal field. *J. Maps* 17 (2), 184–196. <https://doi.org/10.1080/17445647.2021.1898485>
- Starek, M.J., Giessel, J., 2017. Fusion of uas-based structure-from-motion and optical inversion for seamless topo-bathymetric mapping. *School of Engineering and Computing Sciences and Conrad Blucher Institute* 2999–3002. <https://doi.org/10.1109/IGARSS.2017.8127629>

Available online at [www.sciencedirect.com](http://www.sciencedirect.com)

ScienceDirect

journal homepage: [www.journals.elsevier.com/oceanologia](http://www.journals.elsevier.com/oceanologia)

## ORIGINAL RESEARCH ARTICLE

# A comparative study of biosynthesized marine natural-product nanoparticles as antifouling biocides

Khaled Mahmoud Abdelsalam<sup>a,\*</sup>, Nayrah Aly Shaltout<sup>b</sup>,  
Hassan Abdallah Ibrahim<sup>c</sup>, Hermine Ramzy Zaki Tadros<sup>b</sup>,  
Mohamed Abd-Elnaby Aly-Eldeen<sup>b</sup>, Ehab Aly Beltagy<sup>c</sup>

<sup>a</sup>Taxonomy & Biodiversity of Aquatic Biota Lab, National Institute of Oceanography and Fisheries, NIOF, Cairo, Egypt

<sup>b</sup>Marine Chemistry Lab, National Institute of Oceanography and Fisheries, NIOF, Cairo, Egypt

<sup>c</sup>Microbiology Lab, National Institute of Oceanography and Fisheries, NIOF, Cairo, Egypt

Received 15 December 2020; accepted 21 August 2021

Available online 10 September 2021

## KEYWORDS

Antifouling;  
Nanoparticles;  
Chitosan;  
*Ulva fasciata*;  
*Avicennia marina*  
leaves

**Abstract** In this study, biosynthesized nanoparticles using chitosan, *Ulva fasciata*, and *Avicennia marina* leaves extracts (A, B, and C, respectively), were evaluated as paint additives to control marine fouling on different substrates. These biocidal nanoparticle compounds were prepared using a green biosynthesis method. Their characterizations were conducted using Fourier-Transform Infrared spectroscopy and Transmission electron microscopy. Each nanoparticle compound was mixed with a prepared paint, resulting in three formulations for each (e.g. 1C, 2C, 3C), containing 20%, 40%, and 60% by weight. Painted PVC, wood, and steel with these nine paints, and the control were immersed in seawater for different periods. After two months of immersion, the least number of fouling species, (one species) was recorded on both the wood and steel panels that were coated with paint (1C). Meanwhile, after four months, the least numbers of fouling (four and six species) were recorded on wood and steel panels that were coated with paint (3C). After around seven months of immersion, the least numbers

\* Corresponding author at: National Institute of Oceanography and Fisheries, NIOF, Cairo, Egypt. Tel. +2 03 4801553; fax: +2 034801499.  
E-mail addresses: [kh.abdelsalam@gmail.com](mailto:kh.abdelsalam@gmail.com) (K.M. Abdelsalam), [nshaltout@gmail.com](mailto:nshaltout@gmail.com) (N.A. Shaltout), [drhassan1973@yahoo.com](mailto:drhassan1973@yahoo.com) (H.A. Ibrahim), [herminetadros@gmail.com](mailto:herminetadros@gmail.com) (H.R.Z. Tadros), [m\\_niof@yahoo.com](mailto:m_niof@yahoo.com) (M.A.-E. Aly-Eldeen), [ehab.beltagy@gmail.com](mailto:ehab.beltagy@gmail.com) (E.A. Beltagy).  
Peer review under the responsibility of the Institute of Oceanology of the Polish Academy of Sciences.



<https://doi.org/10.1016/j.oceano.2021.08.004>

0078-3234/© 2021 Institute of Oceanology of the Polish Academy of Sciences. Production and hosting by Elsevier B.V. This is an open access article under the CC BY-NC-ND license (<http://creativecommons.org/licenses/by-nc-nd/4.0/>).

of fouling species (five and ten) were recorded on wood and steel panels that were coated with paints (1C and 3C), respectively. The steel panel coated with (3C), harbored ~2% of the total number of barnacles found on the control, after 7 months of immersion. The superior antifouling agent efficiency of extract (C) nanoparticles can be attributed to its constituents of polyphenols, ammonium compounds, and high concentrations of alcohols, besides the presence of both aromatic and aliphatic amide and amide derivatives.

© 2021 Institute of Oceanology of the Polish Academy of Sciences. Production and hosting by Elsevier B.V. This is an open access article under the CC BY-NC-ND license (<http://creativecommons.org/licenses/by-nc-nd/4.0/>).

## 1. Introduction

In the marine environment, the surface of any submerged substratum is covered by the microbial colonizers which, form complex biofilms composed of bacteria, archaea, fungi, protozoa, and unicellular microalgae (Dobretsov and Rittschof, 2020). Biofilms could impact the larvae of marine invertebrates (macro-fouling) in their selection of suitable substrates on which to settle and metamorphose (Hadfield 2011; Peng et al., 2020).

Marine biofouling has spawned a billion-dollar industry, where biocides, cleaners, and antifouling materials are required globally to prevent their formation. On the other hand, green chemistry has been evolved as an alternative to the use of environmentally harmful processes and products due to the serious consequences that the world is facing (De Marco et al., 2019; Hurst, 2020), and the development of efficient and environmentally friendly antifouling compounds has become of pressing interest for marine coating businesses (Wang et al., 2017).

Marine macroalgae are widely perceived to be makers of a broad spectra of biogenic compounds, including polyunsaturated fatty acids, flavonoids, terpenoids, alkaloids, quinones, sterols, polyketides, phlorotannins, polysaccharides, glycerols, peptides, and lipids (Mohy El-Din and El-Ahwany, 2015) which have strong activities, for example, as antifouling (Bhadury and Wright, 2004), antimicrobial (Zbakh et al., 2012), and anticoagulant agents (Kolanjinathan et al., 2014; Shi et al., 2008).

Also, chitosan has been shown to be biocompatible, biodegradable, and non-toxic, making it suitable for a wide range of uses in the pharmaceutical industry (Puvvada et al., 2012; Tikhonov et al., 2006). Moreover, it has been widely used as an antimicrobial agent against fungi, viruses, and bacteria (Kong et al., 2010). Recently, metallic nanoparticles are the alternative in biological and scientific challenges in different fields of science (Patil and Kim, 2017, 2018; Shah et al., 2015). Nanoscale materials have emerged as novel antimicrobial agents owing to their high surface area-to-volume ratio, which increases their contact with microbes, hence increasing their ability to permeate cells (Lamsal et al., 2011).

Biological synthesis is a reliable production method of metal nanoparticles. For example, Silver nanoparticles (Ag-NPs), was one of the most widely used agent that have antifouling activity due to their size, shape, and applications (Krishnan et al., 2015). By using an aqueous extract of the green seaweed *Ulva (Enteromorpha) compressa* as a reductant and a stabilizing agent, (Ramkumar et al., 2017) synthesized biocompatible silver nanoparticles. They indicated

that metal nanoparticles synthesized by macroalgae could potentially be utilized in antifouling applications.

Given this background, the present study evaluates the effect of biosynthesized chitosan nanoparticles as well as biosynthesized iron nanoparticles capped with *Ulva fasciata* and mangrove leaf extracts, mixed in three different weight ratios with a prepared paint formulation and resulting in nine paints on biofilm formation on different surfaces for the control of marine fouling. Moreover, it targets to compare between different concentrations of the biosynthesized nanoparticles of various extracts, aiming to determine the most suitable extract concentration in the prepared paint formulation that will give the maximal antifouling activity.

## 2. Material and methods

### 2.1. Medium

A nutrient agar medium comprising 5 g peptone, 10 g yeast extract, and 15 g agar was prepared using 1-L seawater for the counting of marine viable heterotrophic bacteria and for detecting antibacterial activity.

### 2.2. Collection of mangrove plant samples

In April 2017, fresh mangrove leaves (*Avicennia marina*) were collected from the Safaga coastal area (26°35'42"N, 34°01'13"E) of the Red Sea, Egypt. The gathered sample leaves were washed using water from a faucet, and then with distilled water, to remove any adhering salt and other associated creatures. The leaves were dried in the shade, and then ground and powdered.

### 2.3. Collection of algal samples

In April 2017, fresh *U. fasciata* samples were collected from the Abu Qir Bay region (31°16'27"N, 30°07'16"E) of the Mediterranean Sea, Egypt. In the laboratory, the algae were washed using water from a faucet, to eliminate any remaining impurity and epiphyte. Microscopic identification of the investigated algae was carried out according to (Abdel Aleem, 1993).

### 2.4. Biosynthesis of iron nanoparticles

Around 10 g of finely cut *A. marina* leaves or *U. fasciata* were added to 100 mL of distilled water, and the mixture was boiled for 1 h. The resulting solution was filtered

through a Whatman no. 1 filter paper. A total of 10 mL of the collected filtrate was treated with 90 mL of an aqueous solution of iron chloride (0.001 M  $\text{FeCl}_3$ ), and then stirred for 2 h, resulting in the formation of a brownish solution, which indicated the formation of iron nanoparticles.

## 2.5. Preparation of chitosan nanoparticles

In the present study, a chitosan compound namely [Poly(beta-(1,4)-2-amino-2-deoxy-D-glucose) Poly(beta-(1,4)-D-glucosamine)] was used. The low molecular weight chitosan nanoparticles were prepared according to a method reported by (Tang et al., 2007). Briefly, 20 mg of chitosan was dissolved in 40 mL of 2.0% (v/v) acetic acid. Then, 20 mL of 0.75 mg/mL sodium tripolyphosphate was slowly dropped into the solution, with stirring. The chitosan nanoparticle suspension was collected and stored in deionized water. The supernatant was discarded and the chitosan nanoparticles were air-dried prior to further use and analysis.

## 2.6. Characterization of the biosynthesized nanoparticles

### 2.6.1. Fourier-transform infrared (FTIR) spectroscopy

Approximately 1 mL solution of the nanoparticles (diluted with 1:20 v/v Milli Q water) was centrifuged at 10 000 g for 10 min and their pellets were re-dispersed in sterile distilled water. This centrifugation and re-dispersion process was repeated three times to ensure the removal of any free biomass residue or compound that was not the capping ligand of the nanoparticles. Afterward, the purified suspension was freeze-dried to obtain a dry powdered sample. Finally, the dried purified nanoparticles as KBr pellets were analyzed using FTIR spectroscopy in the diffuse reflectance mode at a resolution of  $4\text{ cm}^{-1}$  in the range of 4000–375  $\text{cm}^{-1}$ , using a Thermo Nicolet AVATAR 300 FTIR spectrometer.

### 2.6.2. TEM analysis

The structure, size, and morphology measurements were conducted on the biosynthesized chitosan and iron nanoparticles using transmission electron microscopy (TEM, Jeol CX 100 – Eching b. München, Germany), in which a thin film of the sample placed on a gold-coated copper grid was used for capturing images of the nanoparticles.

## 2.7. Marine paint preparation

A marine paint formulation comprising 25 g of Linseed oil as a binder material, 10 g of iron oxide, 24 g of zinc oxide, 13 g of complementary pigment, and 38 g of xylene was prepared through careful blending of these paint ingredients using a ball mill. The three biosynthesized nanoparticles (chitosan, *U. fasciata*, and *A. marina*) were mixed with the paint composition in ratios of 20%, 40%, and 60%, (denoted as 1, 2, and 3, respectively), to produce nine marine paint formulations.

## 2.8. In situ experiments

In situ experiments were conducted in the Eastern Harbour of Alexandria, Egypt, to test the effectiveness of the paint

formulations as antifouling agents. Three iron frames (each measuring  $100 \times 70\text{ cm}$ , carrying test panels) were dangled under the jetty of the National Institute of Oceanography and Fisheries. These frames were exposed to the marine environment for different periods (around two, four, and seven months). The test panels ( $4 \times 10\text{ cm}$ ) made from three types of substrates, PVC, wood, and steel (Figure 1) were treated using the modified paints. Wood and steel are the main building components used for producing both small and large ships, while PVC is a neutral or inert substrate, similar to the material used in the manufacture of fiber glass boats. The panels were tightly fixed to each iron frame using thin silk ropes at both ends of the panel.

## 2.9. Preparation of the test panels prior to application of the paint

In this study, iron frames, holding 36 test panels, were used, of which 12 were made from PVC, 12 from wood, and 12 from steel. Each set of 12 panels comprised three control (untreated) panels and three sets of samples of modified paint with different active nanoparticles, with each sample containing three concentrations, 20%, 40%, and 60%, of each nanoparticle material in the paint composition. Before applying paint to the surfaces of the wood and steel panels, they were first polished using different grades of emery papers and cleaned using xylene.

## 2.10. Immersion of the panels

The three iron frames were immersed in seawater on the same starting date, 27/11/2017. After three, six, and ten days of immersion, microbiological samples from all test panels of the three iron frames were respectively collected to estimate the total bacterial count of the biofilms formed. Afterward, the level of marine fouling was monitored on different test panels of the three iron frames with different immersion durations, and photographed. The iron frames were collected in the following order: iron frame I (collected on 05/02/2018 after immersion for more than 2 months), iron frame II (collected on 12/04/2018 after immersion for more than 4 months), and iron frame III (collected on 25/06/2018 after immersion for around 7 months).

## 2.11. Physicochemical parameter measurements of the seawater

The physicochemical parameters (temperature, salinity, pH, dissolved oxygen (DO) content, and  $\text{PO}_4^{3-}$ ,  $\text{SiO}_3^-$ ,  $\text{NO}_2^-$ ,  $\text{NO}_3^-$ , and  $\text{NH}_3$  concentrations) of the water in the Eastern Harbour of Alexandria, Egypt, were measured each time the panels were inspected or collected. The pH values of the water samples were estimated in situ using a pH meter (Orion Research model 210 digital pH meter). The DO content was measured using the Winkler method, modified by FAO (Food and Agriculture Organization) in 1975. The  $\text{PO}_4^{3-}$ ,  $\text{SiO}_3^-$ ,  $\text{NO}_2^-$ ,  $\text{NO}_3^-$ , and  $\text{NH}_3$  concentrations in each sample were determined colorimetrically according to a previously proposed method (Parsons et al., 1984) using a double-beam spectrophotometer (Shimadzu UV-150-02), with the values

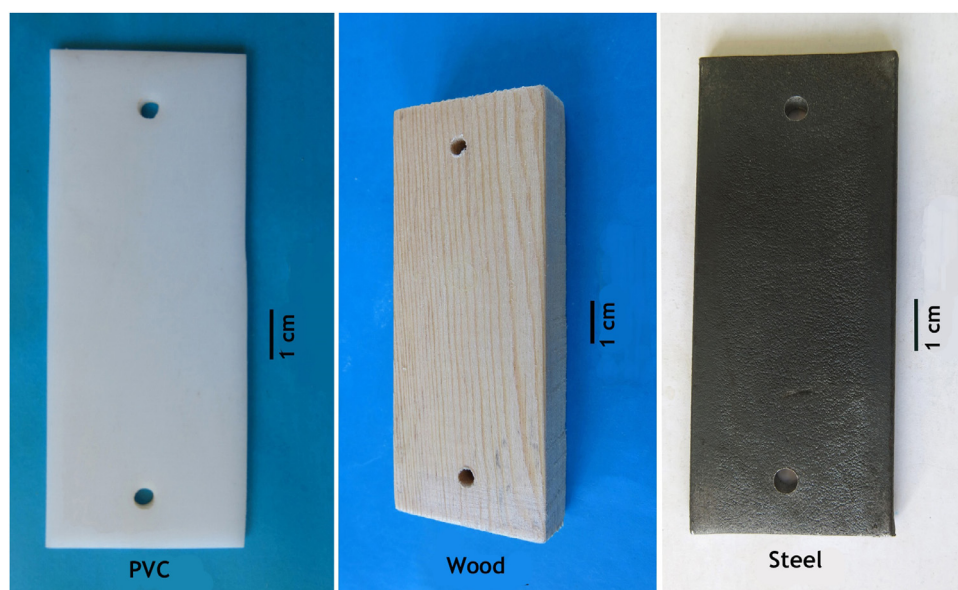


**Figure 1** The three types of substrates used in the study.

expressed in  $\mu\text{M}$ . The sulfate ( $\text{SO}_4^{2-}$ ) content of the samples was precipitated as barium sulfate, whose concentration was then measured turbidimetrically according to a previous method (Bather and Riley, 1954).

## 2.12. Microbiological investigation

### 2.12.1. Counting the bacteria that form the biofilms

Swabbing using sterile cotton toothpicks was carried out per  $\text{cm}^2$  of the panels in duplicate, to determine the viable bacterial counts on the different materials that had been submerged in seawater. Each swab was then added to 1 mL of sterilized seawater and shaken well. Next, a portion (100  $\mu\text{L}$ ) from each sample was transferred to nutrient agar plates prepared with seawater to count the bacteria. The plates were incubated at  $30^\circ\text{C}$  for 24–48 h, after which bacterial counts were estimated (Abou-Elela, 1994).

### 2.12.2. Antibacterial activity of the biosynthesized nanoparticles

A well-cut diffusion technique was used to test how the different crude extracts inhibit the growth of the indicator bacteria. The nutrient agar medium (50 mL) inoculated with the test bacteria were poured into the nutrient agar plates. After the medium had solidified, wells were punched out using a 0.5-cm cork-porer. The test extracts (50  $\mu\text{L}$ ) were then transferred into each well. All plates were incubated at an appropriate temperature for 24–48 h, after which the radius of the clear zone around each well (Y) and the radius of the well (X) were linearly measured in mm, where dividing  $Y^2$  by  $X^2$  allowed the determination of the absolute unit (AU) of the clear zone. Thus, the AU of the crude extract was calculated according to the following equation:  $\text{AU} = Y^2\pi / X^2\pi$  (Abdel-Latif et al., 2018).

## 2.13. Identification and estimation of the macro-fouling communities

In the laboratory, after the removal of the panels from the iron frames, each of them was photographed, and then preserved for careful inspection of the marine fouling species. Some relevant scientific publications were consulted for the identification of the species (Bellan-Santini et al., 1989; Campbell et al., 1982; Riedl, 1970; Zabala and Maluquer, 1988).

## 2.14. Statistical treatment

Data of marine fouling was treated with a two-way ANOVA test using SPSS software version (22). The number of recorded fouling species was used as a dependent variable meanwhile, durations and different concentrations of compounds as fixed factors. A  $P$ -value of  $<0.05$  is considered as a significant value. A post hoc test using (Tukey HSD) was used to test if there is a mean difference among durations or between control and different concentrations of the paint compounds.

## 3. Results

### 3.1. Physicochemical parameters

Some physicochemical parameters of the Eastern Harbour water, at the site of the panel immersion, were measured when the panels were inspected or collected (Supplementary Table 1). According to the data obtained, all measured physicochemical parameters are within the normal range of those expected for water from the Mediterranean Sea. Moreover, the chemical parameters of the water do not show any sudden variation, indicating that the paints do not pollute the environment.

### 3.2. FTIR spectral analysis

FTIR spectroscopy is a useful tool for studying the non-centrosymmetric (IR active) modes of vibrations, which enable the determination of the secondary structure in nanoparticle–biomolecule interactions. In the current study, the results of FTIR analysis of the used biosynthesized nanoparticles are as follows:

#### 3.2.1. Nano-chitosan

As shown in Figure 2a, the FTIR spectrum of nano-chitosan feature absorption bands closer to those of chitosan that have been reported previously by (Venkatesan et al., 2011), comprising carbonyl group (C=O, at  $1740\text{ cm}^{-1}$ ) and C–H stretching peaks at  $1411\text{ cm}^{-1}$ . The peaks observed at  $3190\text{ cm}^{-1}$  can be attributed to N–H and O–H stretching vibrations. The peak at  $1533\text{ cm}^{-1}$  can be assigned to the N–H bending vibration of amide II, while that at  $1379\text{ cm}^{-1}$  can be assigned to the  $-\text{CH}_3$  symmetrical deformation mode (scissoring) of the amide group. The bands assigned to the stretching vibrations of C–O–C linkages in the polysaccharide structure appear at  $1150$  and  $1063\text{ cm}^{-1}$ . The band at  $1150\text{ cm}^{-1}$  corresponds to the anti-symmetric stretching of the C–O–C bridge. The peak at  $2871.26\text{ cm}^{-1}$  corresponds to the methyl group ( $\text{CH}_3$ ), while that at  $2361.02\text{ cm}^{-1}$  represents the alkane group (CH). Two alkene (C=C) peaks can be observed at  $1631.91$  and  $647.69\text{ cm}^{-1}$ , while the ether group (C–O–C) exhibits a peak at  $1031.73\text{ cm}^{-1}$ .

These observed peaks represent the major functional groups of flavonoids, tri-terpenoids, and polyphenols. Hence, the terpenoids are proven to exhibit good activity in converting the aldehyde groups to carboxylic acids.

#### 3.2.2. Iron nanoparticles biosynthesized using a *U. fasciata* extract

The FTIR spectrum of the FeNPs synthesized using the *U. fasciata* extract was used to identify the functional groups of the active components in the sample, based on the peak values. The results of the FTIR analysis (Figure 2b) show different peaks at  $615.99$  and  $843.95\text{ cm}^{-1}$  for the functional group alkyl halides, while the peak at  $928.98\text{ cm}^{-1}$  corresponds to the carboxylic acid functional group. In addition, the peaks at  $1030.58\text{ cm}^{-1}$  represent aliphatic amines. The peak at  $1442.14\text{ cm}^{-1}$  represents aromatic amines, while the recorded peak at  $1631.71\text{ cm}^{-1}$  indicates amides. These strong peaks confirm the stretching vibrations of primary and secondary amines. Moreover, the peak at  $2324.05\text{ cm}^{-1}$  represents the nitrile functional group, while the identified peak at  $425.85\text{ cm}^{-1}$  corresponds to alcohols and phenols.

From the spectrum, hydroxyl, amino, and C–H group peaks can be observed in the region of  $3000\text{--}3600\text{ cm}^{-1}$ , corresponding to the OH group of the monomeric hydrogen bond and phenol rings. C=C ring stretching can be observed at  $2079.48\text{ cm}^{-1}$ . Overall, the peaks in this spectrum are characteristic of belonging to alginic acid, flavonoids, tannins, gallic acid, and other phenols. These soluble compounds act as reducing and stabilizing agents, preventing the aggregation of the nanoparticles in solution, explaining the high antibacterial activity of the material.

#### 3.2.3. Iron nanoparticles biosynthesized using an *A. marina* leaf extract

FTIR spectroscopy measurements were conducted to identify the biomolecules responsible for the reduction of  $\text{Fe}^{3+}$  and capping of the bio-reduced FeNPs synthesized using mangrove leaf extract (Figure 2c). The spectrum shows a broad band at  $3277\text{ cm}^{-1}$ , corresponding to the O–H stretching of a high concentration of alcohols or phenols. The band at  $2924.69\text{ cm}^{-1}$  is attributable to the O–H stretching of carboxylic acids, while the weak-to-strong band at  $1438.3\text{ cm}^{-1}$  corresponds to the C–C stretching of aromatic C=C.

Furthermore, the medium band at  $1220.36\text{ cm}^{-1}$  is attributable to the C–O stretching of carboxylic acids. In addition, the multiple broad peaks at  $2359.57\text{ cm}^{-1}$  correspond to the N–H stretching of ammonium ions, while the medium-intensity band at  $1628.10\text{ cm}^{-1}$  corresponds to C=N stretching. The band at  $1536\text{ cm}^{-1}$  can be assigned to the N–O stretching of nitro compounds. Moreover, the weaker band at  $1373.90\text{ cm}^{-1}$  corresponds to the N–O stretching of amides. The broad band at  $1023.87\text{ cm}^{-1}$  accounts for the C–X stretching of fluoroalkanes. The strong band at  $775.90\text{ cm}^{-1}$  can be assigned to the C–H stretching of aromatic benzene. The amide group peaks confirm the presence of the enzymes responsible for the reduction and stabilization of the metal ions. The recorded polyphenols of the mangrove leaf extract are proved to be a potential reducing agent in the synthesis of silver nanoparticles (Qi et al., 2004).

Notably, the FTIR spectra for the *U. fasciata* and *A. marina* nano-extracts with iron show the efficient binding of several functional groups (alcohols, carboxylic acids, esters, and ethers) with metal to form iron nanoparticles. These groups have been previously proven to act as potential reducing agents of major chemical classes (flavonoids, triterpenoids, and polyphenols) during the synthesis of iron nanoparticles. It was confirmed from the N–H stretching vibration of the primary amines and C–N stretching, besides the overlapping of the aliphatic amines, that the metal is strongly bound, so secondary metabolites from *U. fasciata* and the *A. marina* leaves form a capping of iron nanoparticles to prevent particle agglomeration and stabilize them in the medium. These results provide good evidence of their high efficiency as antibacterial and antifouling agents.

### 3.3. TEM analysis

The TEM image of the chitosan nanoparticles shown in Figure 3a revealed that the diameters of the nanoparticles were in the range of  $2.16\text{--}4.32\text{ nm}$  and that most of them were spherical, in accordance with the observations made by (Ali et al., 2011). The diameters of the iron nanoparticles biosynthesized using *U. fasciata* leaf and *A. marina* extracts were in the range  $1.44\text{--}18.5\text{ nm}$  (Figure 3b and c). The type of extract used determines the shapes and diameters of each type of biosynthesized nanoparticles, i.e., they are dependent on the reducing agent, which differs according to the extract used (see the FTIR spectra). The extracted compounds from the selected *U. fasciata* and *A. marina* leaves served as reducing agents and efficient stabilizers (Mahdavi et al., 2013).



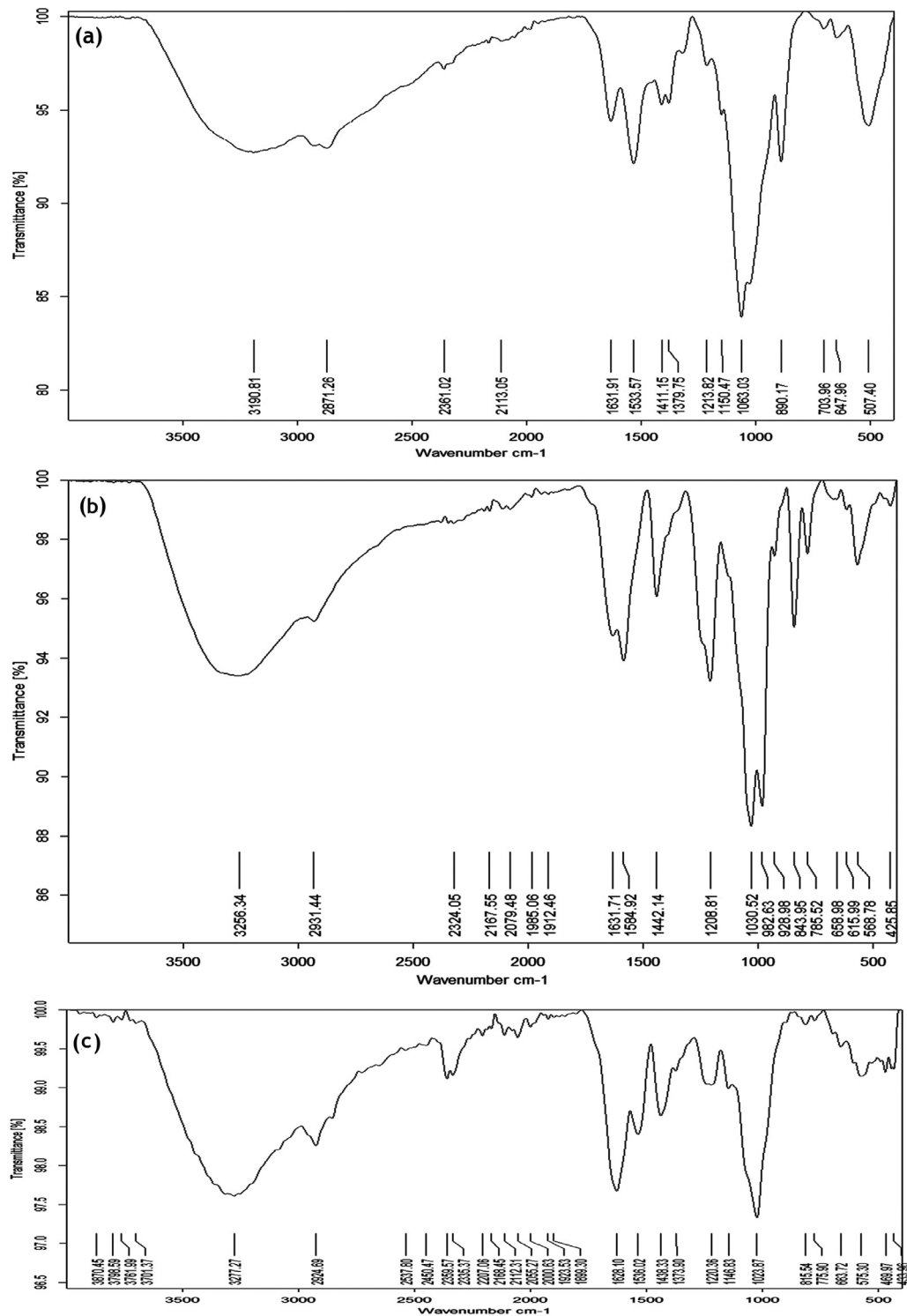


**Figure 2** FTIR spectra of the (a) chitosan nanoparticles, (b) iron nanoparticles biosynthesized using a *Ulva fasciata* extract, and (c) iron nanoparticles biosynthesized using an *Avicennia marina* leaf extract.

### 3.4. Antibacterial activity of the crude extracts

The antibacterial activities of several crude extracts (*U. fasciata* and *A. marina*) and nanoparticle composites (chitosan) were screened against the bacterial community in seawater taken from the Eastern Harbour of Alexandria,

Egypt, and then compared with the reference strains *Escherichia coli* ATCC 19404 and *Staphylococcus aureus* ATCC 6538. However, the data shown in [Table 1](#) indicate that the *A. marina* (leaf extract only) has no AUs against both bacterial community and *E. coli*, while, it shows low AU (1.8) against *S. aureus*. Also, the chitosan composite exhibits the

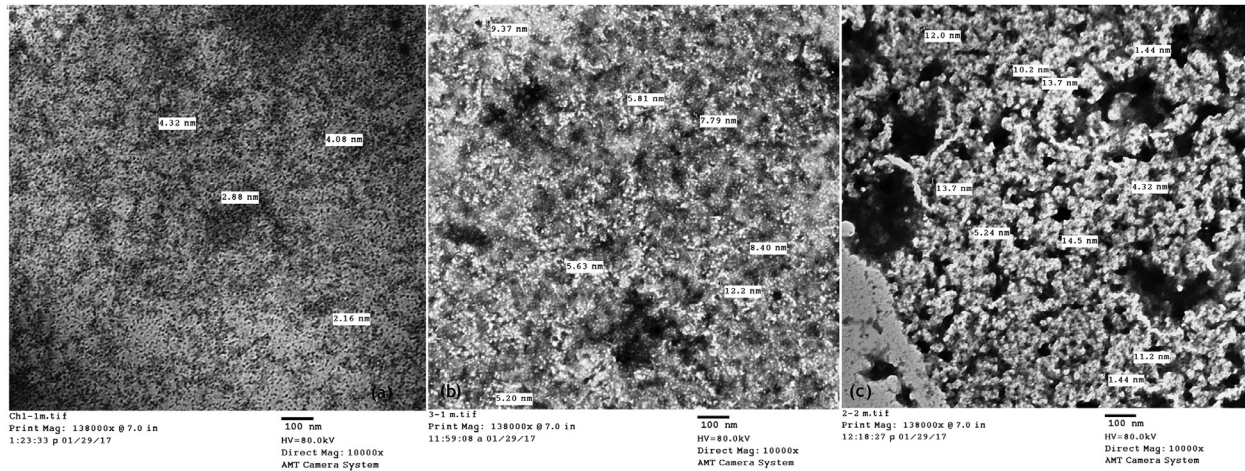


**Figure 3** TEM images of (a) nano-chitosan, (b) iron nanoparticles biosynthesized using a *Ulva fasciata* extract, and (c) iron nanoparticles biosynthesized using an *Avicennia marina* leaf extract.

**Table 1** AUs of the different extracts and nanoparticles.

Composite	Seawater community*	<i>Escherichia coli</i>	<i>Staphylococcus aureus</i>
<i>Ulva fasciata</i> extract only	1.8	—	—
<i>Avicennia marina</i> extract only	—	—	1.8
Iron nanoparticles + <i>Ulva fasciata</i> extract	2.3	4.0	4.0
Iron nanoparticles + <i>Avicennia marina</i> extract	3.4	2.3	3.4
Chitosan composite	1.8	—	1.8

\* This sample was collected from the Eastern Harbor of Alexandria, Egypt, for isolating the seawater community.

**Table 2** Numbers of recorded fouling species on the different test panels of the iron frames after being immersed for different periods in the water of the Eastern Harbor of Alexandria.

Frame	Iron frame I after more than 2 months			Iron frame II after more than 4 months			Iron frame III after around 7 months		
	PVC	Wood	Steel	PVC	Wood	Steel	PVC	Wood	Steel
Control	3	7	3	15	14	14	23	17	21
1A	1	2	4	10	8	6	17	14	15
1B	3	1	3	10	8	8	13	9	11
1C	3	1	1	9	9	8	11	5	14
2A	1	3	4	5	6	10	19	12	10
2B	3	1	4	10	7	9	12	12	12
2C	5	3	4	6	6	12	20	11	13
3A	5	7	4	7	6	12	13	8	11
3B	4	2	3	6	7	8	8	12	14
3C	3	4	4	8	4	6	7	14	10

same inhibition value against both the bacterial community of the water taken from the Eastern Harbour and *S. aureus* (AU = 1.8), but shows no activity against *E. coli*. Moreover, these data exhibit that high AUs are detected for the iron nanoparticles with either algal or mangrove extracts. In particular, the iron + *U. fasciata* composite shows the highest AUs against both *E. coli* and *S. aureus* (AU = 4.0), while the iron + *A. marina* composite exhibits high AUs of 3.4 against both the seawater community and *S. aureus*.

### 3.5. Bacterial counts on the different treated panels

The marine bacterial populations that adhere to the PVC, wood, and steel panels submerged in seawater were estimated over a period of 10 days. For the different control panels under investigation, the bacterial count increased regularly for up to six days and then started to decrease sharply until the 10th day. The bacterial counts on the PVC control panel were  $5 \times 10^2$ ,  $3 \times 10^3$ , and  $1.2 \times 10^3$

cfu/cm<sup>2</sup> after 3, 6, and 10 days, respectively. For wood control, these values were  $5 \times 10^2$ ,  $3.2 \times 10^3$ , and  $1.4 \times 10^3$  cfu/cm<sup>2</sup> after 3, 6, and 10 days, and for steel control, they were  $5 \times 10^2$ ,  $7.1 \times 10^3$ , and  $1.6 \times 10^3$  cfu/cm<sup>2</sup> after 3, 6, and 10 days, respectively. However, the observed bacterial counts on different treated panels were rather lower than their counts on the controls ( $p < 0.05$ ). There were variations in each treatment group and between different treatments. Generally, the bacterial count increased gradually until fouling appeared. So, the suppression percentages (%) detected by different biocides along the investigation period were calculated to express their antibacterial activity. The suppression % ranges from 64.3 to 100, but in most treatments, the values were ~97%, as shown in Figure 4.

### 3.6. Fouling community

After more than two months of immersion, the iron frame (I) was the first sample frame to be retrieved from the Eastern Harbour, upon which 15 marine fouling species were observed, including one Hydroid, four Bryozoa, three Polychaeta, two Barnacles, one Tanaidacea, and four Amphipoda species. Nine species were collected from the control panels. For the treated test panels, the number of recorded marine fouling varied according to the antifouling compounds used and their concentrations, as well as the type of substrate (Table 2, Figure 5).

It is evident that, for the control panels, the PVC panel was fouled by one Hydroid, one Polychaete, and one Barnacle species, the wood panel by three Bryozoa, one Polychaete, one Tanaidacea, and two Amphipoda species, and the steel panel by two Bryozoa and one Polychaete species. With respect to the treated test panels, only one species was recorded on PVC panels, which were coated with paints 1A and 2A. One species was observed on both the wood and steel panels coated with paint 1C.

Meanwhile, after more than four months of immersion, twenty marine fouling species were collected on iron frame II, including one Hydroid, eight Bryozoa, one Polychaete, four Barnacles, one Tanaidacea, and five Amphipoda species. Seventeen species were collected on the control test panels. The recorded marine fouling species were also diversified on the treated test panels (Table 2, Figure 6). With respect to the control panels; it was noticed that fifteen fouling species were settled on the control PVC panel, as well as fourteen species on both wood and steel panels, while the marine fouling species settled on the coated panels with different antifouling agents; only five species were recorded on PVC panel coated with paint 2A. Moreover, four species on wood, and six species on steel panels coated with paint 3C.

After around seven months of immersion, twenty-nine marine fouling species were collected on iron frame III, including two algae, five Bryozoa, five Polychaetes, four Barnacles, one Tanaidacea, three Isopoda, six Amphipoda, one Decapoda, and two Ascidia species. Meanwhile, twenty-six fouling species settled on the control test panels. On the other hand, the treated test panels also showed variable numbers of settled fouling species (Table 2, Figure 7).

The results of the iron frame (III) showed that for the control panels; the PVC test panel was fouled by 23 species, the wood by 17 species, and the steel by 21 species. While

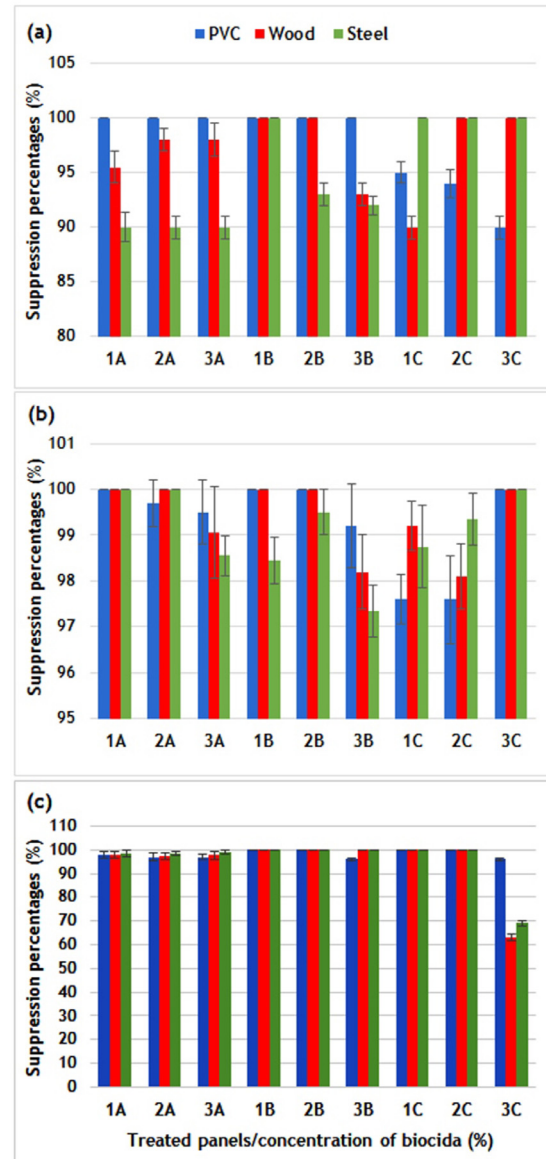


**Figure 4** Suppression percentages (%)  $\pm$  S.D. of the bacterial films by the different biocides after (a) 3 days, (b) 6 days, and (c) 10 days. 1A, 2A, and 3A contain 20%, 40%, and 60% nano-chitosan, respectively. 1B, 2B, and 3B contain 20%, 40%, and 60% *Ulva fasciata* extract. 1C, 2C, and 3C contain 20%, 40%, and 60% *Avicennia marina* extract; ( $n = 3$ ).

for the treated test panels; only five species were recorded on a wood panel coated with paint 1C, seven, and ten species were observed on PVC and steel panels coated with paint 3C, respectively.

However, the lists of all recorded fouling taxa on different test panels, during various immersion periods, are provided in the supplementary tables (2–4).

### 3.7. Statistical results

Based on the number of settled fouling species as a dependent variable, the two-way ANOVA test indicated that

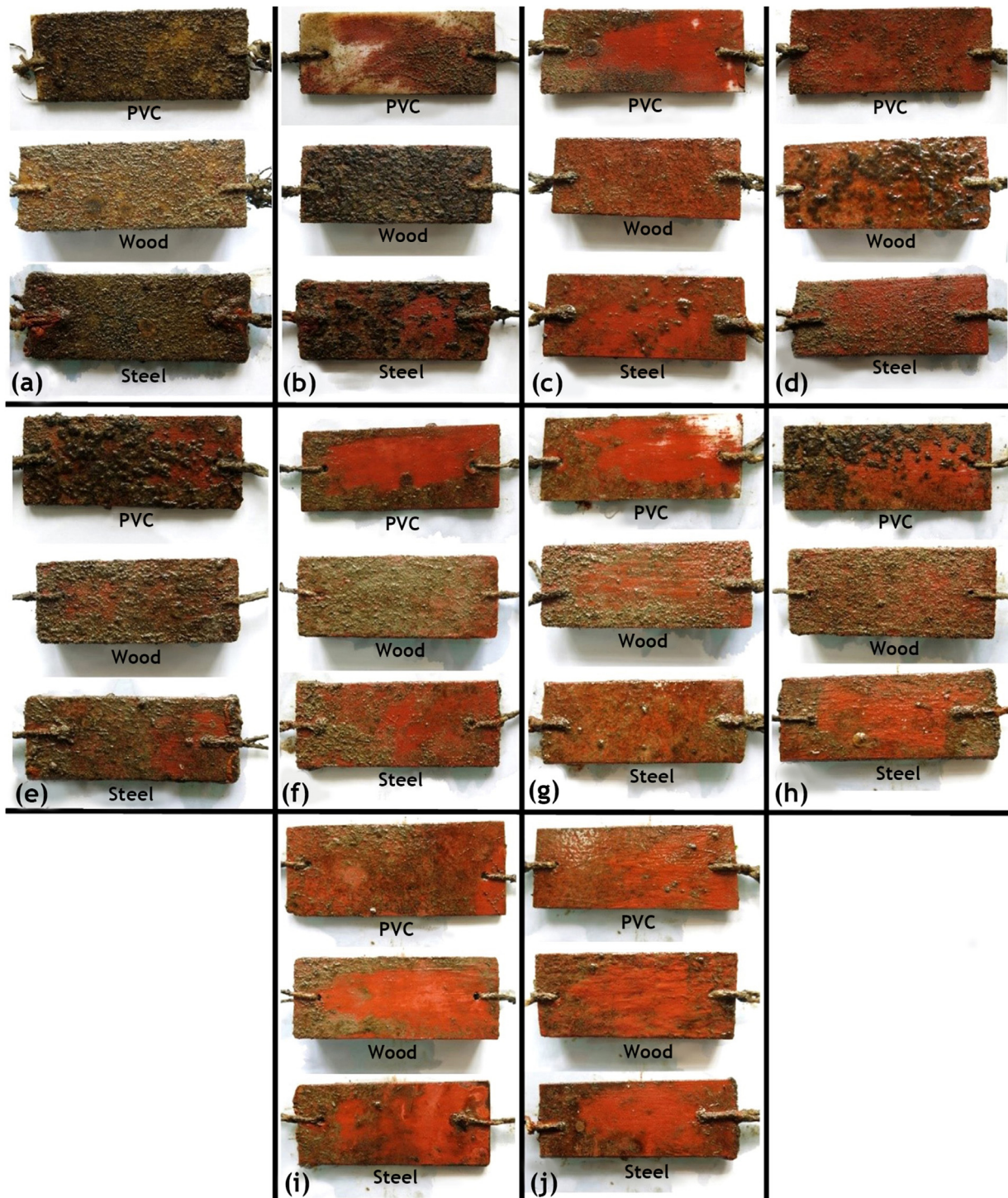


**Figure 5** Biofouling species collected on the control and treated test panels of frame I, (a) Control, (b) 1A, (c) 1B, (d) 1C, (e) 2A, (f) 2B, (g) 2C, (h) 3A, (i) 3B, and (j) 3C.

there is a significant difference between durations i.e. 2, 4, and 7 months (Table 3). Results of the Post hoc test (Tukey HSD) indicated a higher number of settled fouling species during longer periods of exposure whenever, the maximum number of species is recorded in 7 months' duration which was significantly higher than the 2 months ( $10.78^*$ ) and the 4 months ( $4.64^*$ ) durations (Table 4). In addition, there is

another significant difference between different compound concentrations and control. It is obvious from the estimated marginal means of the dependent variable (Figure 8) that the contrary effects of all compounds are more evident during longer periods (4 and 7-month durations) than the short one (2 months). Moreover, the extract of mangrove leaves *Avicennia marina* (compound C) was the most effec-

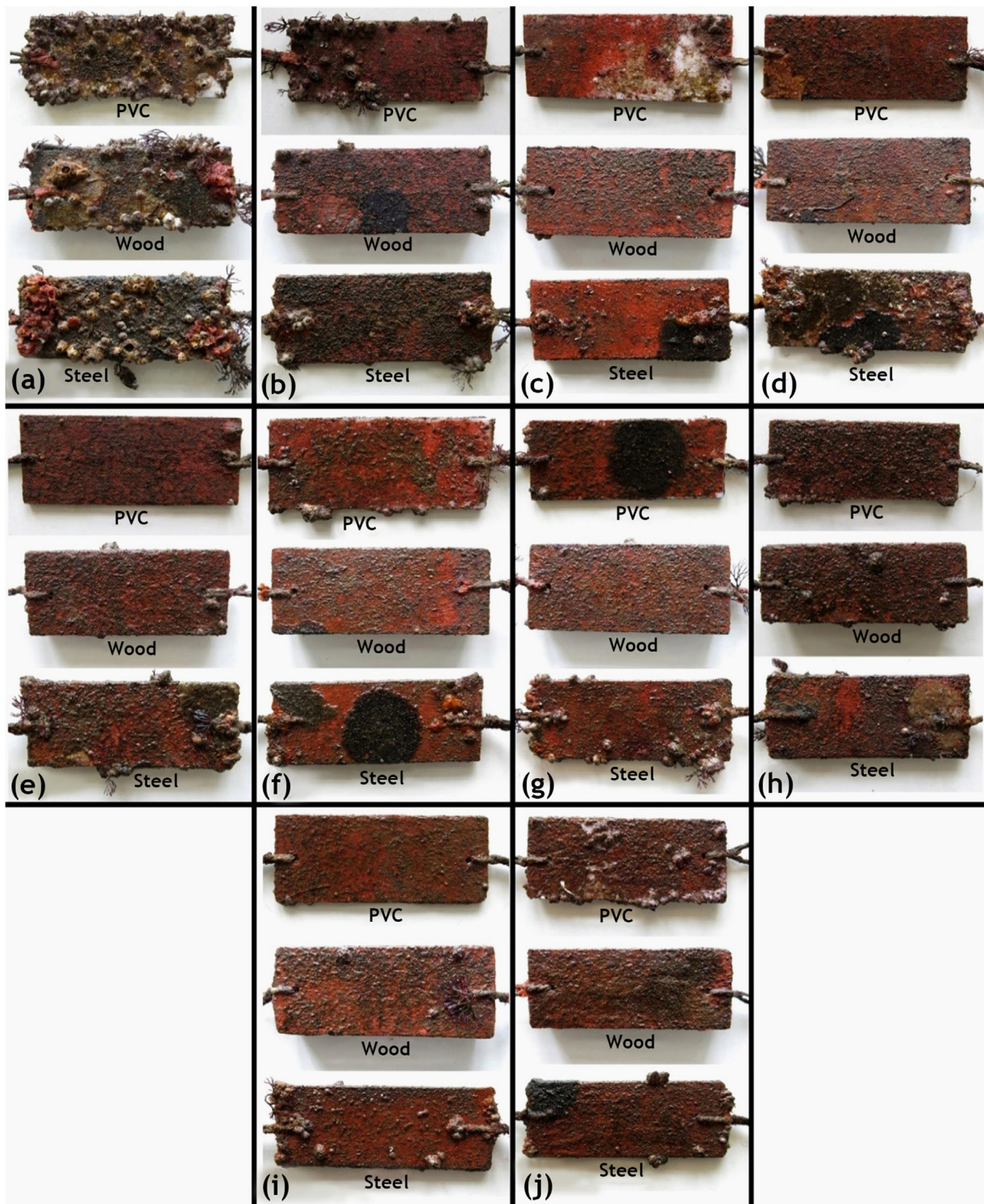


**Figure 6** Biofouling species collected on the control and treated test panels of frame II, (a) Control, (b) 1A, (c) 1B, (d) 1C, (e) 2A, (f) 2B, (g) 2C, (h) 3A, (i) 3B, and (j) 3C.

tive compound as an antifouling agent through different durations. Results of the Post hoc test (Tukey HSD) indicated that the maximum inhibitory effects were recorded with 3C ( $-6.44^*$ ) and 1C ( $-6.33^*$ ) which were significantly less than the control.

#### 4. Discussion

Marine biofouling is the term given to the accumulation of microorganisms, plants, algae, and small invertebrates on surfaces that are submerged in water. In the process of bio-

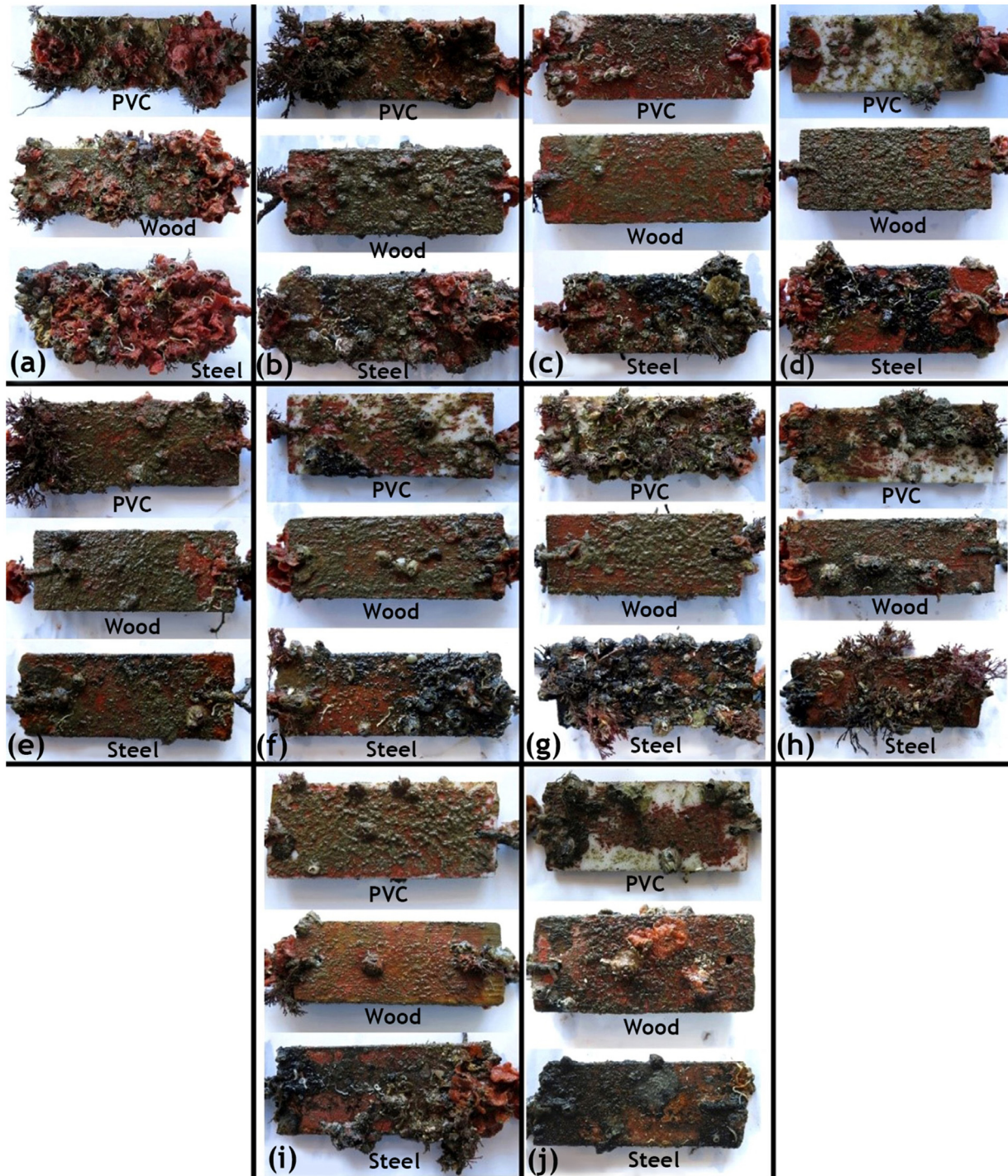


**Figure 7** Biofouling species collected on the control and treated test panels of frame III, (a) Control, (b) 1A, (c) 1B, (d) 1C, (e) 2A, (f) 2B, (g) 2C, (h) 3A, (i) 3B, and (j) 3C.

fouling, a biofilm first forms, where one of the critical factors that affect its development is the feedwater quality, in terms of temperature, pH, DO content, and the presence of organic and inorganic nutrients. Once a microorganism finds an environment to which it is suited, growth proceeds, unless the conditions in the system become too inhospitable (Qian et al., 2003). In temperate regions (such as in Egypt), marine fouling is a common phenomenon, where the rel-

atively high water temperature is the principal factor responsible for enhancing the breeding periods and increase the growth rates of fouling organisms (Rascio, 2000).

The hulls of ships are painted to keep fouling from 481 undesirable marine organisms under control (Chambers et al., 2006). However, there is evidence that some paints are poisonous and can undesirably affect non-target living organisms. Thus, the development of non-toxic

**Table 3** Results of the two-way ANOVA test.

Tests of Between-Subjects Effects					
Dependent Variable: Number of fouling species					
Source	Type III Sum of Squares	df	Mean Square	F	Sig.
Corrected Model	3031.583 <sup>a</sup>	29	104.537	20.216	.000
Intercept	6501.440	1	6501.440	1257.303	.000
Duration	1526.595	2	763.298	147.613	.000
Concentration	642.694	9	71.410	13.810	.000
Duration* Concentration	284.500	18	15.806	3.057	.000
Error	403.333	78	5.171		
Total	12237.000	108			
Corrected Total	3434.917	107			

<sup>a</sup> R Squared = .883 (Adjusted R Squared = .839).

**Table 4** Results of Post Hoc test (Tukey test) among durations.

Multiple Comparisons						
Dependent Variable: Number of fouling species						
Tukey HSD						
(I) Duration	(J) Duration	Mean Difference (I-J)	Std. Error	Sig.	95% Confidence Interval	
					Lower Bound	Upper Bound
2 months	4 months	-6.14*	.536	.000	-7.42	-4.86
	7 months	-10.78*	.536	.000	-12.06	-9.50
4 months	2 months	6.14*	.536	.000	4.86	7.42
	7 months	-4.64*	.536	.000	-5.92	-3.36
7 months	2 months	10.78*	.536	.000	9.50	12.06
	4 months	4.64*	.536	.000	3.36	5.92

Based on observed means.

The error term is Mean Square(Error) = 5.171.

\* The mean difference is significant at the .05 level.

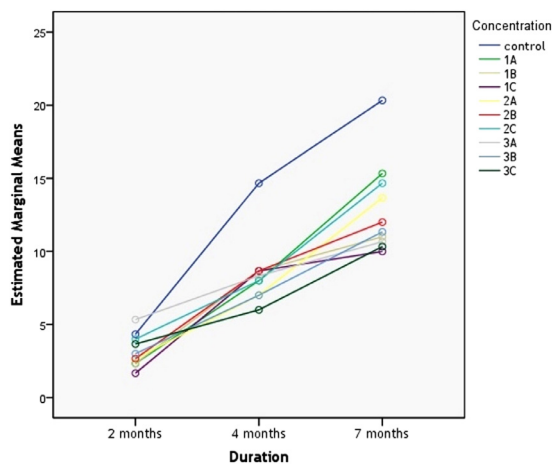


**Figure 8** Estimated marginal means of the number of settled fouling species on control and different concentration of various paints.

coatings that can successfully control biofouling is of high priority. Numerous natural plants and other organisms, such as coral, sponges, seaweed, and land plants, exhibit efficient antifouling behavior (Negm et al., 2018). Studies

are currently underway into the development of materials that can enable these to be combined with the polymeric matrices of antifouling paints, with the end goal of developing a product that does not leach out harmful compounds in water, and thus, does not pollute the environment (Almeida et al., 2007).

At the National Institute of Oceanography and Fisheries (NIOF, Egypt), several crude extracts have been prepared from marine organisms and resources, and their potentiality against microbial pathogens, especially *S. aureus*, has been tested. For instance, Botros Tadros et al. (2009) examined the free lipid *U. lactuca* on glass panels immersed in a medium inoculated with *S. aureus* ATCC 6538 as a model organism for biofilm formation. The results showed that 5% of the free lipid *U. lactuca* suppressed 82% of *S. aureus* (ATCC 6538) attached to the glass panels and 85% of free *S. aureus* in the medium. Recently, Negm et al. (2018) used an environmentally friendly method to synthesize silver nanoparticle (AgNP)-embedded biological marine extracts (BMEs) from four species of marine algae (*U. fasciata*, *Grateloupia* sp., *Pterocladia capillacea*, and *Corallina mediterranea*). They evaluated their antibacterial properties and anti-biofilm activity against indicator strains and 506 bacterial communities, and observed positive antibacterial activity in the range 2.4–23.6 AU. It was determined that

an aqueous extract of *Ulva fasciata* was the most efficient among the different algal species screened for use in the green synthesis of AgNPs/BMEs.

In the in situ experiments conducted in this study, attention has been focused on both wood and steel panels that representing the main materials used in various boats and vessels.

It should be noted that the number of marine fouling species settled on the panels was affected by both the duration of the panel immersion and the season in which the immersion was conducted (Brown and Swearingen, 1998). Generally, at temperate latitudes, heavy fouling might occur in the summer, but during the cold winter period, little growth occurs. In total, nine marine fouling species were collected on the control test panels of the iron frame (I), which was immersed for more than two months in seawater. This number increased to 17 on the iron frame (II), which was immersed in seawater for more than four months. Additionally, 26 marine fouling species were collected on the iron frame (III), which had been immersed in seawater for around seven months. The two-way ANOVA test confirmed that there is a significant difference between durations with more settled fouling species during longer periods of exposure ( $p < 0.05$ ).

The number of barnacles that settle on the tested steel panels is important in selecting the most favorable type of antifouling paint, as these creatures corrode metal surfaces (Shide, 1989). In this work, after four months of immersion, the steel panel coated with paint 3C contained only four barnacles, constituting ~5% of the total barnacles found on the control panel. In addition, the steel panel coated with paint formulation 3C showed only one barnacle attached to it, making up to ~2% of the total barnacles found on the control panel after around seven months of immersion. These results confirmed the great importance of using mangrove extract nanoparticles as an antifouling agent.

In accordance with our results, Pelletier et al. (2009) estimated the antifouling activity of chitosan in a marine environment, showing that a coating with 20% chitosan exhibited antibacterial activity after 14 days of immersion in an estuary, while that with 5% chitosan exhibited no antifouling activity. It is well-known that the cationic amine group in the chitosan molecule plays a major role in its antimicrobial activity, as it forms electrostatic interactions with anionic groups on the cell membrane of bacterial cells, which eventually lead to cell death (Alishahi and Aïder, 2012). This explains why chitosan antifouling efficiency increases by increasing its concentration in the paint.

In general, the promising results of the nanoparticle biosynthesized extracts from (chitosan, *U. fasciata*, and mangrove leaf *A. marina*), can be attributed to the antimicrobial activity of the bioactive compounds contained in the extracts, such as polyunsaturated fatty acids, phenols, alcohols, amines, amides, ammonium, flavonoids, terpenoids, alkaloids, quinones, sterols, polyketides, phlorotannins, polysaccharides, glycerols, peptides, and lipids. All these compounds prevent the formation of biofilm on immersed panels and hence inhibit or decrease the rate of fouling.

Traditionally, mangrove plant extracts are widely used as antimicrobial agents (Shamsuddin et al., 2013) and exhibit significant antifouling activity (Chen et al., 2008).

Many studies have shown their specific activity in inhibiting the growth of virulent strains of bacterial pathogens (Abou-Elela et al., 2009; Sahoo et al., 2012).

*Avicennia marina* contains a mixture of fatty acids such as alpha-linolenic, palmitic, stearic, lauric, myristic, and oleic acids, as well as their derivatives (Selvin et al., 2009). It has been confirmed that *A. marina* also contains terpenoids (Azuma et al., 2002), triterpenoids, and alkaloids (Abeyasinghe, 2010; Chen et al., 2008; Ravikumar et al., 2010). Moreover, Sahoo et al. (2012) revealed that mangrove plants contain saponins, glycosides, tannins, flavonoids, phenols, and volatile oils in their leaves. Therefore, these natural biocides are bioactive compounds and ideal for the development of biodegradable antifouling materials (Selvin et al., 2009).

The superior efficiency of the extract C nanoparticle additive as an antifouling agent, compared to extracts A and B, can be attributed to it containing polyphenols and ammonium compounds, very high concentrations of alcohol, and the presence of both aromatic and aliphatic amide and amide derivatives. Hydroxyl, carboxyl, and amino groups were found to exist in these compounds, as presented in its IR spectrum, showing that extract C has high antimicrobial activity. In addition, polyphenols act as a strong reducing agent of the metal (nano-iron), resulting in a remarkable increase in its antimicrobial activity (Cetin-Karaca, 2011). The presence of aliphatic, branched, and aromatic amides confirm the presence of enzymes that biologically control and prevent biofilm formation, hence reducing the development of fouling. Moreover, the presence of ammonium groups, identified in the IR spectrum, confirms the antimicrobial activity of the extract (Kabara et al., 1972).

The strong activity of extract C can also be explained by looking at the ionic state of the compounds, as it contains both anions (oxidizing compounds), such as fatty acids, amide derivatives, and N-methylated derivatives of amine compounds, and cationic compounds (non-oxidizing compounds), such as ammonium, aldehydes, alkaloids, terpenoids, and flavonoids, in amounts and greater variability than those in extracts A and B. The mechanism of action of anionic compounds in antifouling can be attributed to their efficiency as antimicrobial agents for a wide spectrum of gram-positive and negative bacteria. Only anionic compounds can completely diffuse through the cell membrane and cause lysis of the protoplast, and promote the complete dissolving of protein moieties, such as the lipoprotein of the membrane. The mode of action of cationic compounds in fouling prevention is limited to gram-positive bacteria, as they react with the phosphatidic, phosphatidic, and lipid components of the cytoplasmic membrane, disturbing its permeability (Alves et al., 2013; Farhadi et al., 2019).

In addition, most compounds in extract (C) are hydrophilic, such as alcohols, phenols, carboxylic compounds, ammonium, amides, branched amines, and alkyl halides. This means that the surface covered with paints mixed with extract C is less fouled than that coated with B (which contains both hydrophilic and hydrophobic compounds) and much less than those coated with extract A, in which most of its compounds are hydrophobic. The observed results reflect the constituents of each extract, as a hydrophobic surface may cause other non-polar or hydrophobic compounds to be adsorbed onto the surface, resulting in biofouling.



## 5. Conclusions

To develop active biocides that can control micro- and macrofouling, three natural resources (chitosan, *Ulva fasciata*, and *Avicennia marina* leaves) were immobilized with different nanoparticles, and then mixed with 20%, 40%, and 60% by weight of the prepared paint formulation, to produce nine paints. In situ experiments in the water of the Eastern Harbour of Alexandria, Egypt, were conducted to test the effectiveness of the coating as antifouling agents. The experimental results showed that no sample was completely resistant to fouling, but surfaces coated with compound C (containing the *A. marina* leaf extract) were the least fouled and could effectively resist both micro- and macro-fouling during different immersion intervals.

## Declaration of competing interest

This manuscript is original, not under consideration elsewhere and approved by all authors and institutions prior to submission.

The authors declare that they have no known competing financial interests or personal relationships that could have appeared to influence the work reported in this paper.

## Acknowledgements

This project was financially supported by the Marine Environment Division, National Institute of Oceanography and Fisheries, NIOF, Egypt [grant number MED 0004 – 2018]. Title of the project “Nanochitosan composites as anti-biofouling agents in vitro and in situ”.

## Supplementary materials

Supplementary material associated with this article can be found, in the online version, at <https://doi.org/10.1016/j.oceano.2021.08.004>.

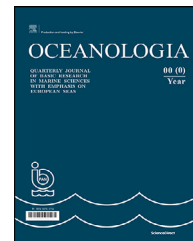
## References

- Abdel-Latif, H.H., Shams El-Din, N.G., Ibrahim, H.A.H., 2018. Antimicrobial activity of the newly recorded red alga *Gratelouppia doryphora* collected from the Eastern Harbor, Alexandria, Egypt. *J. Appl. Microbiol.* 125, 1321–1332. <https://doi.org/10.1111/jam.1405>
- Abdel Aleem, A., 1993. *The Marine Algae of Alexandria, Egypt*, 138 pp.
- Abeysinghe, P.D., 2010. Antibacterial activity of some medicinal mangroves against antibiotic resistant pathogenic bacteria. *Indian J. Pharm. Sci.* 72, 167–172. <https://doi.org/10.4103/0250-474X.65019>
- Abou-Elela, G.M., 1994. *Studies on the settlement of marine bacteria and its response to some coatings on artificial substrata in Alexandria Eastern Harbour*. M.Sc. thesis, Faculty of Science, Alexandria University, 156 pp.
- Abou-Elela, G.M., El-Sersy, N.A., El-Shenawy, M.A., Abd-Elnabi, H., Ibrahim, H.A.H., 2009. Bio-Control of *Vibrio fluvialis* in Aquaculture by Mangrove (*Avicennia marina*) Seeds Extracts. *Res. J. Microbiol.* 4, 38–48. <https://doi.org/10.3923/jm.2009.38.48>
- Ali, S.W., Rajendran, S., Joshi, M., 2011. Synthesis and characterization of chitosan and silver loaded chitosan nanoparticles for bioactive polyester. *Carbohydr. Polym.* 83, 438–446. <https://doi.org/10.1016/j.carbpol.2010.08.004>
- Alishahi, A., Aider, M., 2012. Applications of Chitosan in the Seafood Industry and Aquaculture: A Review. *Food Bioprocess Technol.* 5, 817–830. <https://doi.org/10.1007/s11947-011-0664-x>
- Almeida, E., Diamantino, T.C., de Sousa, O., 2007. Marine paints: The particular case of antifouling paints. *Prog. Org. Coatings* 59, 2–20. <https://doi.org/10.1016/j.porgcoat.2007.01.017>
- Alves, M.J., Ferreira, I.C.F.R., Froufe, H.J.C., Abreu, R.M.V, Martins, A., Pintado, M., 2013. Antimicrobial activity of phenolic compounds identified in wild mushrooms, SAR analysis and docking studies. *J. Appl. Microbiol.* 115, 346–357. <https://doi.org/10.1111/jam.12196>
- Azuma, H., Toyota, M., Asakawa, Y., Takaso, T., Tobe, H., 2002. Floral scent chemistry of mangrove plants. *J. Plant Res.* 115, 47–53. <https://doi.org/10.1007/s102650200007>
- Bather, J.M., Riley, J.P., 1954. The chemistry of the irish sea. Part I. The sulphate-chlorinity ratio. *ICES J. Mar. Sci.* 20, 145–152. <https://doi.org/10.1093/icesjms/20.2.145>
- Bellan-Santini, D., Diviacco, G., Krapp-Schickel, G., Ruffo, S., 1989. *The Amphipoda of the Mediterranean. Part 2. Gammaridea (Haustoriidae to Lysianassidae)*. Mémoires de l' Institut Océanographique, Monaco, 365–576.
- Bhadury, P., Wright, P.C., 2004. Exploitation of marine algae: Biogenic compounds for potential antifouling applications. *Planta* 219, 561–578. <https://doi.org/10.1007/s00425-004-1307-5>
- Botros Tadros, A., Abdalla Ibrahim, H., Ramzy Zaki, H., Mahmoud El-Naggar, M., Eid Abbas, A., 2009. Suppressive effect of coated surfaces contain *Ulva lactuca* free lipid on *Staphylococcus aureus* ATCC 6538. *Egypt. J. Aquat. Res.* 35, 405–412.
- Brown, K.M., Swearingen, D.C., 1998. Effects of seasonality, length of immersion, locality and predation on an intertidal fouling assemblage in the Northern Gulf of Mexico. *J. Exp. Mar. Bio. Ecol.* 225, 107–121. [https://doi.org/10.1016/S0022-0981\(97\)00217-7](https://doi.org/10.1016/S0022-0981(97)00217-7)
- Campbell, A.C., Gorringer, R., Nicholls, J., 1982. *The Hamlyn Guide to the Flora and Fauna of the Mediterranean Sea*. Hamlyn, London, New York, Sydney, Toronto, 321 pp.
- Cetin-Karaca, H., 2011. *Evaluation of Natural Antimicrobial Phenolic Compounds against Food borne Pathogens*. Faculty of Agriculture, University of Kentucky M.Sc. Thesis, 652 pp.
- Chambers, L.D., Stokes, K.R., Walsh, F.C., Wood, R.J.K., 2006. Modern approaches to marine antifouling coatings. *Surf. Coatings Technol.* 201, 3642–3652. <https://doi.org/10.1016/j.surfcoat.2006.08.129>
- Chen, J.J., Fei, D.Q., Chen, S.G., Gao, K., 2008. Antimicrobial triterpenoids from *Vladimiria muliensis*. *J. Nat. Prod.* 71, 547–550. <https://doi.org/10.1021/np070483l>
- De Marco, B.A., Rechelo, B.S., Tótolí, E.G., Kogawa, A.C., Salgado, H.R.N., 2019. Evolution of green chemistry and its multidimensional impacts: A review. *Saudi Pharm. J.* 27, 1–8. <https://doi.org/10.1016/j.jsps.2018.07.011>
- Dobretsov, S., Rittschof, D., 2020. Love at first taste: induction of larval settlement by marine microbes. *IJMS* 21, 731. <https://doi.org/10.3390/ijms21030731>
- Farhadi, F., Khameneh, B., Iranshahi, M., Iranshahy, M., 2019. Antibacterial activity of flavonoids and their structure–activity relationship: An update review. *Phyther. Res.* 33, 3–40. <https://doi.org/10.1002/ptr.6208>
- Hadfield, M.G., 2011. Biofilms and marine invertebrate larvae: what bacteria produce that larvae use to choose settlement sites. *Ann. Rev. Mar. Sci.* 3, 453–470. <https://doi.org/10.1146/annurev-marine-120709-142753>
- Hurst, G.A., 2020. Systems thinking approaches for international green chemistry education. *Curr. Opin. Green Sustain. Chem.* 21, 93–97. <https://doi.org/10.1016/j.cogsc.2020.02.004>

- Kabara, J.J., Conley, A.J., Truant, J.P., 1972. Relationship of chemical structure and antimicrobial activity of alkyl amides and amines. *Antimicrob. Agents Chemother.* 2, 492–498. <https://doi.org/10.1128/AAC.2.6.492>
- Kolanjinathan, K., Ganesh, P., Saranraj, P., 2014. Pharmacological Importance of Seaweeds: A Review. *World J. Fish Mar. Sci.* 6, 1–15. <https://doi.org/10.5829/idosi.wjfm.2014.06.01.76195>
- Kong, M., Chen, X.G., Xing, K., Park, H.J., 2010. Antimicrobial properties of chitosan and mode of action: A state of the art review. *Int. J. Food Microbiol.* 144, 51–63. <https://doi.org/10.1016/j.ijfoodmicro.2010.09.012>
- Krishnan, M., Sivanandham, V., Hans-Uwe, D., Murugaiah, S.G., Seeni, P., Gopalan, S., Rathinam, A.J., 2015. Antifouling assessments on biogenic nanoparticles: A field study from polluted offshore platform. *Mar. Pollut. Bull.* 101, 816–825. <https://doi.org/10.1016/j.marpolbul.2015.08.033>
- Lamsal, K., Kim, S.W., Jung, J.H., Kim, Y.S., Kim, K.S., Lee, Y.S., 2011. Application of silver nanoparticles for the control of *Colletotrichum* species in vitro and pepper anthracnose disease in field. *Mycobiology* 39, 194–199. <https://doi.org/10.5941/MYCO.2011.39.3.194>
- Mahdavi, M., Namvar, F., Ahmad, M., Bin, Mohamad, R., 2013. Green biosynthesis and characterization of magnetic iron oxide (Fe<sub>3</sub>O<sub>4</sub>) nanoparticles using seaweed (*Sargassum muticum*) aqueous extract. *Molecules* 18, 5954–5964. <https://doi.org/10.3390/molecules18055954>
- Mohy El-Din, S.M., El-Ahwany, A.M.D., 2015. Bioactivity and phytochemical constituents of marine red seaweeds (*Jania rubens*, *Corallina mediterranea* and *Pterocladia capillacea*). *J. Taibah Univ. Sci.* 10, 471–484. <https://doi.org/10.1016/j.jtusci.2015.06.004>
- Negm, M.A., Ibrahim, H.A.H., Shaltout, N.A., Shawky, H.A., Abdelmottaleb, M.S., Hamdona, S.K., 2018. Green Synthesis of Silver nanoparticles Using Marine Algae Extract and Their Antibacterial Activity. *Middle East J. Appl. Sci.* 8, 957–970.
- Parsons, T.R., Maita, Y., Lalli, C.M., 1984. *A Manual of Chemical & Biological Methods for Seawater Analysis*. Pergamon Press, Oxford and New York, 173 pp. <https://doi.org/10.1016/c2009-0-07774-5>
- Patil, M.P., Kim, G.-D., 2017. Eco-friendly approach for nanoparticles synthesis and mechanism behind antibacterial activity of silver and anticancer activity of gold nanoparticles. *Appl. Microbiol. Biotechnol.* 101, 79–92. <https://doi.org/10.1007/s00253-016-8012-8>
- Patil, M.P., Kim, G.-D., 2018. Marine microorganisms for synthesis of metallic nanoparticles and their biomedical applications. *Colloids and Surfaces B: Biointerfaces* 172, 487–495. <https://doi.org/10.1016/j.colsurfb.2018.09.007>
- Pelletier, É., Bonnet, C., Lemarchand, K., 2009. Biofouling growth in cold estuarine waters and evaluation of some chitosan and copper anti-fouling paints. *Int. J. Mol. Sci.* 10, 3209–3223. <https://doi.org/10.3390/ijms10073209>
- Peng, L.-H., Liang, X., Chang, R.-H., Mu, J.-Y., Chen, H.-E., Yoshida, A., Osatomi, K., Yang, J.-L., 2020. A bacterial polysaccharide biosynthesis-related gene inversely regulates larval settlement and metamorphosis of *Mytilus coruscus*. *Biofouling* 36 (7), 753–765. <https://doi.org/10.1080/08927014.2020.1807520>
- Puvvada, Y.S., Vankayalapati, S., Sukhvasi, S., 2012. Extraction of chitin from chitosan from exoskeleton of shrimp for application in the pharmaceutical industry. *Int. Curr. Pharm. J.* 1, 258–263. <https://doi.org/10.3329/icpj.v1i9.11616>
- Qi, L., Xu, Z., Jiang, X., Hu, C., Zou, X., 2004. Preparation and antibacterial activity of chitosan nanoparticles. *Carbohydr. Res.* 339, 2693–2700. <https://doi.org/10.1016/j.carres.2004.09.007>
- Qian, P.Y., Thiyagarajan, V., Lau, S.C.K., Cheung, S.C.K., 2003. Relationship between bacterial community profile in biofilm and attachment of the acorn barnacle *Balanus amphitrite*. *Aquat. Microb. Ecol.* 33, 225–237. <https://doi.org/10.3354/ame033225>
- Ramkumar, V.S., Pugazhendhi, A., Gopalakrishnan, K., Sivagurunathan, P., Saratale, G.D., Dung, T.N.B., Kannapiran, E., 2017. Biofabrication and characterization of silver nanoparticles using aqueous extract of seaweed *Enteromorpha compressa* and its biomedical properties. *Biotechnol. Reports* 14, 1–7. <https://doi.org/10.1016/j.btre.2017.02.001>
- Rascio, V.J.D., 2000. Antifouling coatings: Where do we go from here. *Corros. Rev.* 18, 133–154. <https://doi.org/10.1515/CORRREV.2000.18.2-3.133>
- Ravikumar, S., Gnanadesigan, M., Suganthi, P., Ramalakshmi, A., 2010. Antibacterial potential of chosen mangrove plants against isolated urinary tract infectious bacterial pathogens. *Int. J. Med. Med. Sci.* 2, 94–99.
- Riedl, R., 1970. *Fauna und Flora der Adria*. Verlag Paul Parey, Hamburg und Berlin, 702 pp. <https://doi.org/10.1007/BF02285734>
- Sahoo, G., Mulla, N.S.S., Ansari, Z.A., Mohandass, C., 2012. Antibacterial activity of mangrove leaf extracts against human pathogens. *Indian J. Pharm. Sci.* 74, 348–351. <https://doi.org/10.4103/0250-474X.107068>
- Selvin, J., Manilal, A., Sujith, S., Kiran, G.S., Shakir, C., 2009. Biopotentials of Mangroves Collected from the Southwest Coast of India. *Glob. J. Biotechnol. Biochem.* 4, 59–65.
- Shamsuddin, A.A., Najiah, M., Suvik, A., Azariyah, M.N., Kamaruzaman, B.Y., Effendy, A.W., Akbar John, B., 2013. Antibacterial properties of selected mangrove plants against vibrio species and its cytotoxicity against *Artemia salina*. *World Appl. Sci. J.* 25, 333–340. <https://doi.org/10.5829/idosi.wasj.2013.25.02.688>
- Shah, M., Fawcett, D., Sharma, S., Tripathy, S.K., Poinern, G.E.J., 2015. Green synthesis of metallic nanoparticles via biological entities. *Materials* 8, 7278–7308. <https://doi.org/10.3390/ma8115377>
- Shi, D., Li, J., Guo, S., Han, L., 2008. Antithrombotic effect of bromophenol, the alga-derived thrombin inhibitor. *J. Biotechnol.* 136, 577–588. <https://doi.org/10.1016/j.jbiotec.2008.07.1364>
- Shide, M., 1989. The corrosive effect of barnacles on low alloy steels. *Chinese J. Oceanol. Limnol.* 7, 271–273. <https://doi.org/10.1007/BF02842617>
- Tang, Z.X., Qian, J.Q., Shi, L.E., 2007. Preparation of chitosan nanoparticles as carrier for immobilized enzyme. *Appl. Biochem. Biotechnol.* 136, 77–96. <https://doi.org/10.1007/BF02685940>
- Tikhonov, V.E., Stepnova, E.A., Babak, V.G., Yamskov, I.A., Palma-Guerrero, J., Jansson, H.B., Lopez-Llorca, L.V., Salinas, J., Gerasimenko, D.V., Avdienko, I.D., Varlamov, V.P., 2006. Bactericidal and antifungal activities of a low molecular weight chitosan and its N-(2(3)-(dodec-2-enyl) succinoyl)-derivatives. *Carbohydr. Polym.* 64, 66–72. <https://doi.org/10.1016/j.carbpol.2005.10.021>
- Venkatesan, J., Qian, Z.J., Ryu, B., Ashok Kumar, N., Kim, S.K., 2011. Preparation and characterization of carbon nanotube-grafted-chitosan – Natural hydroxyapatite composite for bone tissue engineering. *Carbohydr. Polym.* 83, 569–577. <https://doi.org/10.1016/j.carbpol.2010.08.019>
- Wang, K.L., Wu, Z.H., Wang, Y., Wang, C.Y., Xu, Y., 2017. Mini-review: Antifouling natural products from marine microorganisms and their synthetic analogs. *Mar. Drugs* 15, 1–21. <https://doi.org/10.3390/md15090266>
- Zabala, M., Maluquer, P., 1988. Illustrated keys for the classification of Mediterranean Bryozoa. *Treballs – Mus. Zool.* 4, 1–294.
- Zbakh, H., Chiheb, H., Bouziane, H., Sánchez, V.M., Riadi, H., 2012. Antibacterial Activity of Benthic Marine Algae Extracts from the Mediterranean coast of Morocco. *J. Microbiol. Biotechnol. Food Sci.* 1, 219–228.

Available online at [www.sciencedirect.com](http://www.sciencedirect.com)

ScienceDirect

journal homepage: [www.journals.elsevier.com/oceanologia](http://www.journals.elsevier.com/oceanologia)

## ORIGINAL RESEARCH ARTICLE

# Steric and atmospheric contributions to interannual sea level variability in the eastern mediterranean sea over 1993–2019

Bayoumy Mohamed<sup>a,b,\*</sup>, Nikolaos Skliris<sup>c</sup>

<sup>a</sup>University of Alexandria, Faculty of Science, Department of Oceanography, Alexandria, Egypt

<sup>b</sup>Department of Arctic Geophysics, University Centre in Svalbard, Longyearbyen, Norway

<sup>c</sup>Ocean and Earth Science, University of Southampton, Southampton, United Kingdom

Received 21 April 2021; accepted 15 September 2021

Available online 1 October 2021

## KEYWORDS

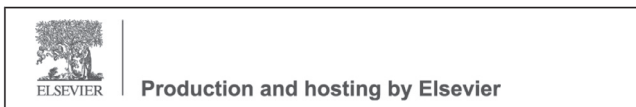
Sea level variability and trend;  
Thermosteric and halosteric effect;  
Atmospheric contribution;  
Eastern Mediterranean

**Abstract** Sea level trends and their forcing over the eastern Mediterranean basin are investigated by using 27 years (1993–2019) of gridded sea level anomalies (SLA) derived from satellite altimetry and 9 tide gauge stations, along with sea surface temperature (SST) and temperature and salinity profiles. The contributions of atmospheric (wind and pressure) and steric components to the interannual variability of total SLA were evaluated. The thermosteric component represents the major contributor to the linear trend and was positive over most of the eastern Mediterranean, with a spatially averaged trend of  $2.13 \pm 0.41$  mm/year, accounting for 69% of the total sea level trend ( $3.1 \pm 0.61$  mm/year). In contrast, the halosteric effect has a negative contribution to the steric SLA, with a mean trend of  $-0.75 \pm 0.19$  mm/year. The atmospheric component trend was much lower at  $0.32 \pm 0.24$  mm/year. The interannual variability of SLA accounts for about 36% of overall sea level variability. Steric and atmospheric contributions to the interannual variability of sea level in the eastern Mediterranean account for about 52% and 18%, respectively. The strongest interannual variability and trends in SLA were observed over the basin's main recurrent gyres, with the maximum positive trend obtained over the Mersa–Matruh and Cyprus gyres, as well as the North Shikmona eddy, and maximum negative trend over the Ierapetra gyre. Over the study period, all tide gauges showed a positive and statistically significant trend, ranging from  $1.47 \pm 0.77$  to  $5.79 \pm 1.32$  mm/year after applying glacial isostatic

\* Corresponding author at: University of Alexandria, Faculty of Science, Department of Oceanography, Alexandria, Egypt.

E-mail addresses: [m.bayoumy@alexu.edu.eg](mailto:m.bayoumy@alexu.edu.eg), [mohamedb@unis.no](mailto:mohamedb@unis.no) (B. Mohamed).

Peer review under the responsibility of the Institute of Oceanology of the Polish Academy of Sciences.



<https://doi.org/10.1016/j.oceano.2021.09.001>

0078-3234/© 2021 Institute of Oceanology of the Polish Academy of Sciences. Production and hosting by Elsevier B.V. This is an open access article under the CC BY-NC-ND license (<http://creativecommons.org/licenses/by-nc-nd/4.0/>).

adjustment and atmospheric correction, and were in good agreement with reconstructed steric sea level data.

© 2021 Institute of Oceanology of the Polish Academy of Sciences. Production and hosting by Elsevier B.V. This is an open access article under the CC BY-NC-ND license (<http://creativecommons.org/licenses/by-nc-nd/4.0/>).

## 1. Introduction

Quantifying sea level change and assessing its main forcing mechanisms have recently been at the forefront of challenges for the climate research community. The Mediterranean Sea has been identified as one of the most vulnerable regions to climate change (Giorgi, 2006). In particular sea level rise may have a strong impact in the Eastern Mediterranean (EM) Sea due to the many low-lying densely populated coastal areas such as the Nile River Delta in Egypt (Church et al., 2013). Sea level rise may strongly affect livelihoods in coastal populations and various essential economic activities of the countries surrounding the Eastern Mediterranean Sea including fishing, tourism, irrigation, transportation, and more recently, natural gas drilling projects.

Generally, the global mean sea level change depends on both mass addition (including glacier ice melting and changes in ground water storage) and redistribution, as well as on the steric effect, which is caused by changes in water-column density due to temperature and salinity variations (Ishii and Kimoto, 2009; Jordà and Gomis, 2013; Levitus et al., 2012). Since the rate of global sea-level rise is not uniform, and it is highly dependent on location (Stammer et al., 2013), studies of regional sea level variations and physical processes controlling them are required. Here, our study focuses on sea level change and its contributing mechanisms in the eastern Mediterranean Sea.

During the altimetry era, extensive work has been conducted to measure sea level variability and trends in the Mediterranean Sea. Mohamed et al. (2019a) revealed a strong positive sea level trend of  $2.7 \pm 0.41$  mm/year (after glacial isostatic adjustment correction), as well as a substantial warming of  $0.036 \pm 0.003^\circ\text{C}/\text{year}$  over the whole Mediterranean over 1993–2017. Bonaduce et al. (2016) reported that the Mediterranean Sea level has strongly risen with an average trend of  $2.44 \pm 0.5$  mm/year over 1993–2012. However, spatial variability of the trend was quite large with the eastern basin showing much higher trends as compared with the western basin, whereas even negative trends were observed in large parts of the Ionian Sea. The Mediterranean Sea upper-layer heat and salt contents are modulated at interannual/decadal timescales by the natural climate variability modes of the North Atlantic (Tsimplis and Josey, 2001), especially the North Atlantic Oscillation (NAO) (Hurrell, 1995), strongly affecting thermosteric sea level variability (Landerer and Volkov, 2013; Tsimplis et al., 2013). Previous studies have demonstrated that SST and SLA are highly correlated at seasonal and interannual scales, especially in the eastern Mediterranean basin (Cazenave et al., 2002; Fenoglio-

Marc, 2002). The strong correlation between the two parameters suggests that the thermosteric effect is a major factor controlling interannual variability of sea level in the eastern Mediterranean (Vigo et al., 2005). In general SLA interannual variability is more pronounced in the Eastern Mediterranean as compared with the western basin (Bonaduce et al., 2016; Cazenave et al., 2002). The eastern Mediterranean was strongly affected by the rapid rise in sea level over 1993–2001 with rates of 5–10 mm/year, which was partially attributed to accelerating sea surface warming (Cazenave et al., 2001; Vigo et al., 2005). Tsimplis et al. (2005) also associated the increasing sea level rise during that period to the Eastern Mediterranean Transient (Roether et al., 1996), a major climatic transient event during the 1990's affecting the EM thermohaline closed cell with the main source of deep water shifting from the Adriatic to the Aegean Sea. Roether et al. (1996) showed that an exceptionally dense Aegean Sea outflow had replaced 20% of the EM deep waters by the mid-nineties, lifting the older deep water of Adriatic origin and resulting in large changes of the EM overturning circulation and salt content distribution. More recently, Banaduce et al. (2016) found that the Mediterranean SLA trend over 1993–2012 was partially driven by strong positive SLA anomalies in 2010 and 2011 that mainly occurred in the eastern basin.

The role of atmospheric forcing in determining sea level variability and trends in the Mediterranean is well demonstrated by several studies (Gomis et al., 2008; Marcos and Tsimplis, 2008; Tsimplis et al., 2005). Considering dynamic atmospheric correction (DAC), Pascual et al. (2008) observed a sea level trend of about 0.6 mm/year over the period 1993–2001 due to the atmospheric forcing. The same authors observed minimum values in the western Mediterranean basin and maximum values in the Levantine basin up to 2 mm/year.

The main objective of this study is to investigate the interannual variability and trends of total SLA and its contributors in the eastern Mediterranean, based on altimetry and tide gauge sea level anomalies, as well as high resolution 3-D temperature and salinity observations from 1993 to 2019. In particular, we estimate the relative contributions of atmospheric, Glacial Isostatic Adjustment (GIA), thermosteric, halosteric, and total steric effects to SLA variability and trends.

## 2. Data and methodology

The contributions of the atmospheric and steric effects to the interannual sea level variability in the eastern Mediterranean Sea were analyzed using different data sources, as described in the following sub-sections.

**Table 1** Sea level trends (mm/year) for the observed tide gauges (TG), atmospheric, total steric and residual (observation minus atmospheric, GIA, and total steric) contributions to the sea level trend. R denotes the correlation coefficients between the atmospherically corrected TG and reconstructed steric sea level. All uncertainties are given at the 95% confidence interval. Not statistically significant trends are underlined in boldface.

Stations (Country)	Period	Trend (mm/year)						R
		TG	GIA	DAC	TG*	Steric	Residual	
Siros (Greece)	1993–2019	3.21±0.83	0.09	0.54±0.31	2.66±0.64	1.18±0.42	1.65±0.57	0.70
Khalkis north (Greece)	1993–2019	3.98±0.84	-0.05	0.58±0.36	3.46±0.61	1.83±0.41	1.61±0.63	0.64
Thessaloniki (Greece)	1993–2019	4.46±0.96	-0.17	0.60±0.38	3.78±0.70	1.17±0.28	2.84±0.63	0.73
Alexandroupolis (Greece)	1993–2019	1.95±1.03	-0.12	0.50±0.36	1.47±0.77	1.30±0.30	<b>0.23±0.67</b>	0.53
Khios (Greece)	1993–2013	3.02±1.37	-0.04	0.51±0.31	1.57±0.66	0.82±0.38	<b>0.11±1.02</b>	0.78
Leros (Greece)	1993–2019	2.00±0.80	0.03	0.40±0.27	2.00±0.80	1.27±0.37	2.00±0.80	0.47
Antalya II (Turkey)	1993–2009	6.48±1.48	-0.09	0.59±0.23	5.79±1.32	1.36±0.40	4.42±1.20	0.69
Hadera (Israel)	1993–2019	4.18±0.77	0.02	<b>0.17±0.17</b>	4.03±0.69	1.30±0.38	2.82±0.63	0.73
Alexandria (Egypt)	1993–2015	5.01±0.94	-0.01	<b>0.21±0.22</b>	4.65±0.88	2.00±0.41	1.85±0.92	0.73

\* Indicates that GIA, and DAC correction was applied to TG.

## 2.1. Altimetry and tide gauge mean sea level data

Monthly mean sea level data from 9 tide gauges (TG) stations (Table 1) obtained from the Permanent Service for Mean Sea Level (PSMSL) (Woodworth and Player, 2003) (<http://www.psmsl.org/>, accessed December 2020) were used in this study. The spatial distribution of these tide gauges stations over the eastern Mediterranean Sea is represented by black triangles, as shown in Figure 1. All stations have datum continuity and data exceeding 15 years. At the Alexandria station, a datum correction was applied as we extended the PSMSL record by 10 years of monthly data (2006 to 2015), which was quality controlled by Mohamed et al. (2019b).

Gridded daily mean sea level anomalies (SLA) at 1/8-degree spatial resolution for the period 1993–2019 were obtained from the Copernicus Marine Environment Monitoring Service (CMEMS; <http://marine.copernicus.eu/>, accessed December 2020). Monthly means were calculated from the daily values at each grid point. The data are produced by merging observations of T/P, ERS1/2, Jason 1/2/3, Sentinel-3A, HY-2A, Saral/AltiKa, Cryosat-2, ENVISAT, and GFO altimetry missions. This dataset is distributed under the name SEALEVEL\_MED\_PHY\_L4\_REP\_OBSERVATIONS\_008\_051 in the CMEMS catalogue. In which, all standard geophysical and environmental corrections have been applied, including atmospheric correction using the so-called dynamic atmospheric correction (DAC) (Landerer and Volkov, 2013; Pujol and Larnicol, 2005), which combines the low frequencies (>20 days) of the standard inverted barometer (IB) correction with the outputs of the barotropic MOG2D-G model (Carrère and Lyard, 2003). This procedure improves the representation of high-frequency (<20 day) atmospheric forcing considering both pressure and wind effects.

## 2.2. Atmospherically induced sea level variations

Dynamic atmospheric corrections were applied by AVISO processing algorithms to correct satellite altimetry data. Here, we analyze the DAC product to estimate the contribution of atmospheric forcing to the satellite altimetry and to correct TG data. This data is provided by AVISO website

(<ftp.avisio.altimetry.fr>, accessed December 2020) as an auxiliary dataset with a spatial grid resolution of  $0.25^\circ \times 0.25^\circ$  and a time resolution of 6 hours. The data were converted to monthly means to be consistent with altimetry and TG data used in this study.

## 2.3. Estimation of steric, thermosteric, and halosteric sea level anomalies

Steric SLA (SSLA) was calculated as the vertical integral of the density anomaly and then decomposed into thermosteric SLA (TSLA), and halosteric SLA (HSLA) by using the following equations (Jayne et al., 2003; Wang et al., 2017):

$$\begin{aligned} \text{SSLA} &= \text{TSLA} + \text{HSLA} = \frac{-1}{\rho_0} \int_{-H}^0 \Delta\rho \, dz \\ &= - \int_{-H}^0 (\alpha\Delta T - \beta\Delta S) dz \end{aligned}$$

Where  $\rho_0$  is the reference density ( $1025 \text{ kg/m}^3$ ),  $z$  denotes depth. And  $\Delta\rho$ ,  $\Delta T$ , and  $\Delta S$  are density, temperature, and salinity anomalies, respectively, referred to their climatic mean (1993–2019) at each layer, and  $\alpha$  and  $\beta$  are the thermal expansion and saline contraction coefficient, respectively, calculated from monthly temperature and salinity using the Thermodynamic Equation Of Seawater-2010 (TEOS-10) (Pawlowicz et al., 2012), and the Gibbs Sea Water (GSW) Oceanographic Toolbox (McDougall and Barker, 2011).  $H$  is the reference depth, which is set to 400 m or the bottom where the sea is shallower. The choice of 400 m for the lower level of integration was made here to be consistent with Tsimplis and Rixen, (2002). The steric effect in the Mediterranean Sea is limited to the upper 300 m of the water column, as shown by Tsimplis et al. (2013).

The steric height and its components were calculated using a high resolution monthly 3-D hydrographic gridded product provided by CMEMS (MULTIOBS\_GLO\_PHY\_TSUV\_3D\_MYNRT\_015\_012, <https://www.copernicus.eu/en>, accessed January 2021). This dataset is based on optimal interpolation of global quality-controlled ocean temperature and salinity profiles (Guinehut et al., 2012). It has a horizontal resolution of  $0.25^\circ \times 0.25^\circ$  and

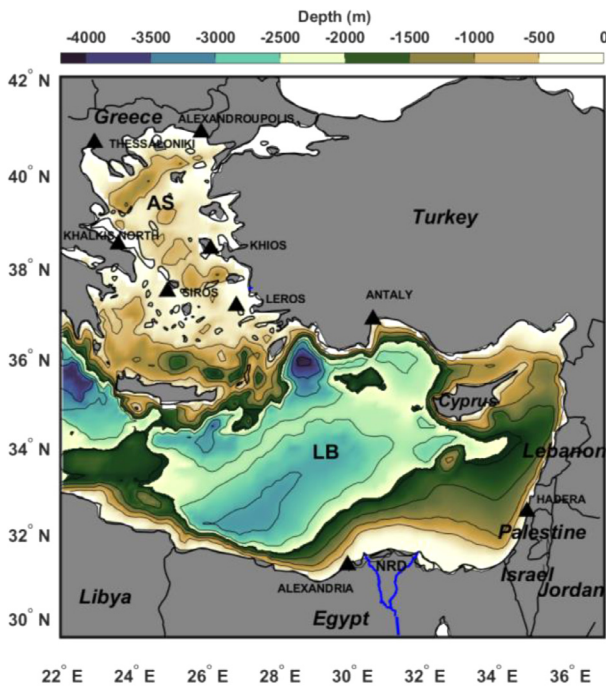


**Figure 1** Bathymetry of the study area and the location of the tide gauges used in our study (black triangles). Bathymetric data obtained from a global 30 arc-second interval grid (GEBCO, <https://www.gebco.net>) with 10 m as the minimum depth. The abbreviations stand for the Levantine Basin (LB), the Aegean Sea (AS), and the Nile River Delta (NRD).

a vertical resolution of 50 depth levels (standard depths) covering the period 1993–2019.

In addition, in order to investigate SST variations we use the NOAA Daily Optimum Interpolation Sea Surface Temperature dataset (version 2.1, NOAA\_DOISST\_V2.1, <https://www.ncei.noaa.gov/data/sea-surface-temperature-optimum-interpolation/v2.1/access/avhrr/>, accessed January 2021), with a spatial resolution of  $0.25^\circ \times 0.25^\circ$ , covering the period 1993–2019 (Huang et al., 2021). The ICE-6G\_C (VM5a) model provided by PSMSL (Peltier et al., 2015) is used for the GIA correction. The rate of relative sea level rise (dSea) and rate of change of geoid height (dGeoid) in this model (Peltier et al., 2015) are used to correct tide gauge and altimetry data used in our study, respectively.

#### 2.4. Linear trends of sea level and its components

Linear trends of the observed, atmospherically induced, steric, and residual (observation minus atmospheric, GIA, and total steric) sea level as well as SST over the period 1993–2019 are estimated by using the least squares method (Wilks, 2011). To properly estimate long-term trends and assess interannual and interdecadal variability of sea level it is important to remove the strong effect of seasonal variability. Thus, the mean and seasonal cycles were removed from the all-time series prior to the trend calculation. A 12-month climatology is built for each time series by averaging the monthly mean values for each calendar month at each grid point from 1993 to 2019. Then, the de-seasoned anomaly field is obtained by subtracting the

monthly climatology from each dataset. Since the Eastern Mediterranean is an eddy-rich area with eddies strongly affecting intra-annual variability, a 13-month running mean was used to highlight interannual variability. These trends were tested for statistical significance using the original two-tailed modified Mann-Kendall test at the 95% confidence interval (Hamed and Ramachandra Rao, 1998). MATLAB software R2020b, and Climate Data Toolbox (CDT) are used to estimate trends, remove seasonal cycles, and apply the Mann-Kendall test (Greene et al., 2019).

### 3. Results and discussion

In this section, the spatial and temporal variability of the total sea level from altimetry and tide gauges is analyzed in detail over the period 1993–2019. Then relative contributions of the atmospheric, GIA and steric effects to total change in sea level are explored.

#### 3.1. Observed mean sea level changes

A few TG stations are available in the eastern Mediterranean during the study period. Trends in sea level based on TG measurements and their estimated steric height are compared in Figure 2 and Table 1. The tide gauges time series show high coherence at all stations, suggesting that they are determined by large scale rather than local meteorological components. The total sea level trends are positive at all TG stations over the period 1993–2019, ranging from  $1.95 \pm 1.03$  mm/year at Alexandroupolis (Greece) to  $6.48 \pm 1.48$  mm/year at Antalya II (Turkey). The high trend at the Antalya II station is significantly affected by local land subsidence, which was about  $-3.2 \pm 0.5$  mm/year based on GPS data for the period 1994–2009 (Simav et al., 2012). Also, the vertical land motion was higher at Thessaloniki, Leros, and Hadera stations, as demonstrated by Fenoglio-Marc et al. (2004) and Mohamed and El-Din (2019).

Figure 3 depicts the spatial distribution of altimetry SLA trend and its components. The average spatial trend of the total atmospherically corrected SLA for the whole region is  $3.1 \pm 0.61$  mm/year. The GIA correction to altimetry data (dGeoid) is negative in the whole region, with values ranging from about  $-0.1$  to  $-0.18$  mm/year. Figure 3a shows the trends in altimetry after the GIA effect is removed. On average, these are about 0.13 mm/year larger due to the GIA effect on altimetry data. The average altimetry trend for the eastern Mediterranean after GIA correction is about  $3.23 \pm 0.61$  mm/year. The SLA trend is spatially coherent over most of the eastern Mediterranean where strong positive trends (up to 5.6 mm/year) were observed, while only the Ierapetra gyre (southeast of Crete) showed a significantly negative trend. The highest positive trend has been observed over the Mersa-Matruh and Cyprus gyres, as well as the North Shikmona eddy (Figure 3a). These gyres and eddies' positions are well defined by Menna et al. (2021). The general spatial pattern of SLA trend is in agreement with earlier studies (Bonaduce et al., 2016; Mohamed et al., 2019a; Taibi and Haddad, 2019). Relatively low (and not statistically significant at 95% confidence interval) trends were only found in the south-west part of the basin.

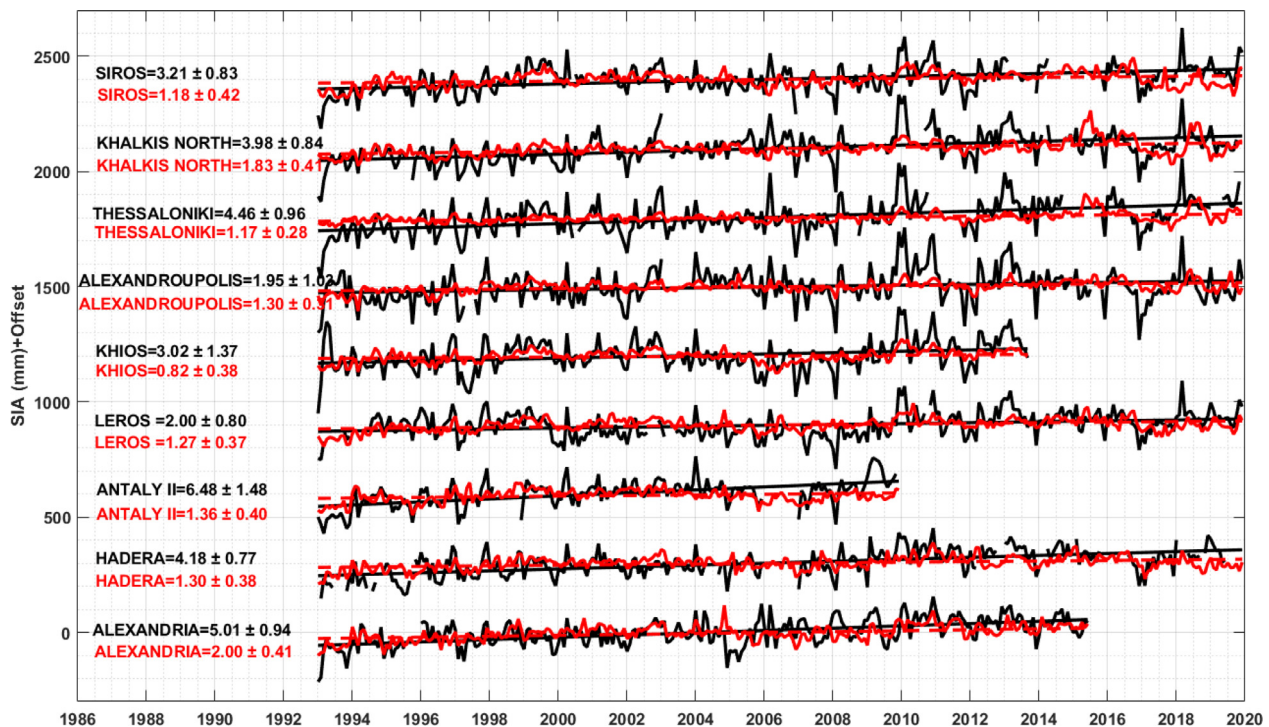


**Figure 2** Comparison between observed tide gauge (black) and steric sea level (red) at the available tide gauge stations in the eastern Mediterranean Sea, the mean and seasonal cycles have been removed from all-time series.

Figure 4 shows the time evaluation of the mean sea level anomaly and its components in the Eastern Mediterranean from 1993 to 2019. The total atmospherically corrected SLA shows a positive trend of  $3.05 \pm 0.25$  mm/year. The long-term trend has been found to be partially driven by the extreme positive anomaly occurred in 2010, which is mainly attributed to the strong negative phase of North Atlantic Oscillation (NAO) (Landerer and Volkov, 2013). Both the steric and mass (residual) component contribute positively to the total SLA trend. However, the mass component shows a higher variability and a stronger trend than the steric component (Figure 4a).

Separating the steric component into its thermosteric and halosteric contributions reveals that the rapid sea level rise is primarily due to the thermosteric component, while the halosteric contribution is negative, especially over the last 15 years (Figure 4b), indicating an increase in mean salinity over the entire domain (Figure 5d). The atmospheric contribution shows a slightly positive trend, as shown in Figure 4c. This result is consistent with (Gomis et al., 2008), who demonstrated that the atmospheric circulation pattern had changed dramatically in the Mediterranean Sea over the last decade, with a positive trend in the contribution of atmospheric pressure estimated from 1993 to 2001.

### 3.2. The atmospheric contribution

Over the analyzed period, the contribution of DAC at TG stations shows a positive trend (Table 1 column 5), with the highest trends found in the Aegean Basin, with a maximum value of about  $0.60 \pm 0.38$  mm/year at Thessaloniki (Greece). The atmospheric contribution to sea level trend in the Levantine Basin is negligible, as evidenced by low and not significant DAC trends at Alexandria (Egypt) and

Hadera (Israel) stations. Figure 3b depicts the spatial distribution of trends in atmospheric pressure and wind components (DAC) from 1993 to 2019. The average spatial trend is  $0.32 \pm 0.24$  mm/year, with values ranging from 0 to 0.72 mm/year. The eastern part of the EM shows the lowest (and not statistically significant) values, while the western part and the Aegean Sea shows the highest values. The DAC's average contribution accounted for about 10% of the overall sea level trend in EM.

### 3.3. SST, temperature, and salinity changes

The spatial distribution of the SST linear trends (Figure 5a) shows that significantly positive SST trends are observed throughout the entire basin. Stronger warming is obtained in the Levantine basin, with values up to  $0.06^\circ\text{C}/\text{year}$  in the Cretan Arc and west and south of Cyprus, while much weaker warming ( $\sim 0.01^\circ\text{C}/\text{year}$ ) is observed in the Ierapetra gyre, southeast of Crete. This spatial pattern is in good agreement with that reported by (Skliris et al., 2012) for the period 1992–2008 and with (Ibrahim et al., 2021) over the period 1982–2020. SST and sea level trend maps have similar spatial patterns, with strong sea surface warming coinciding with strong sea level rise and vice versa, except from the north part of the Aegean Sea. This correlation suggests that the thermosteric effect is the main factor controlling interannual sea level variability in the eastern Mediterranean.

Figures 5b and c show the averaged water-column (0–400 m depth) temperature and salinity trend maps, respectively. A strong positive and statistically significant trend in water-column averaged temperature was observed over most of the region following the accelerating surface warming of the Mediterranean Sea. An exception to this

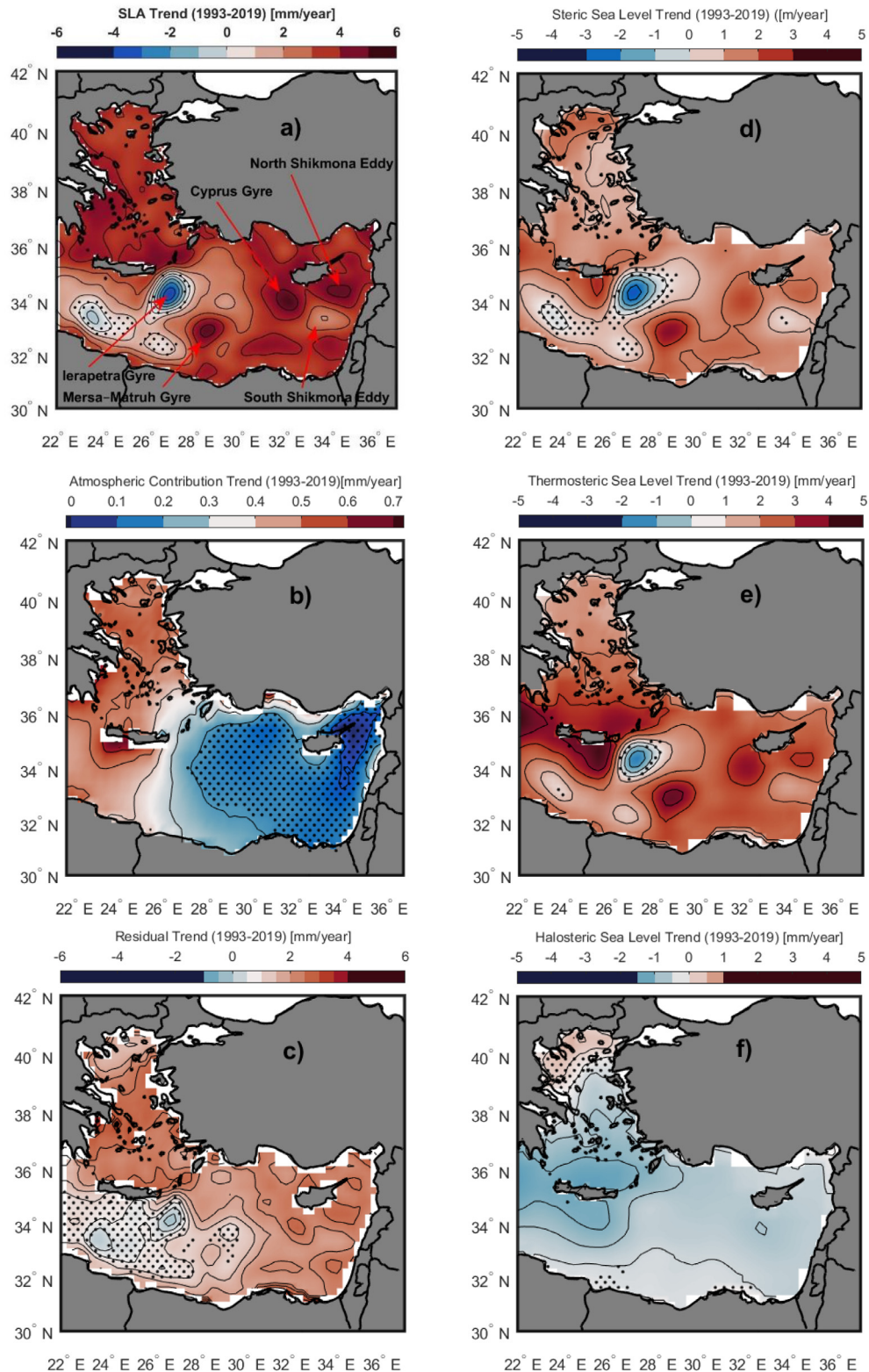


**Figure 3** Spatial patterns of trends (mm/year) over the period 1993–2019 for (a) the total atmospherically corrected SLA from altimetry after the application of the GIA correction, (b) atmospheric contribution to sea level from DAC, (c) altimetry after the steric component and the GIA correction are removed (residual), and (d, e, and f) steric, thermosteric and halosteric components, respectively. Mean and seasonal cycles were removed from all-time series at each grid points. Regions where the trends are not statistically significant at the 95% confidence interval are stippled. Major gyres mentioned in the text are also depicted in Figure 3a.



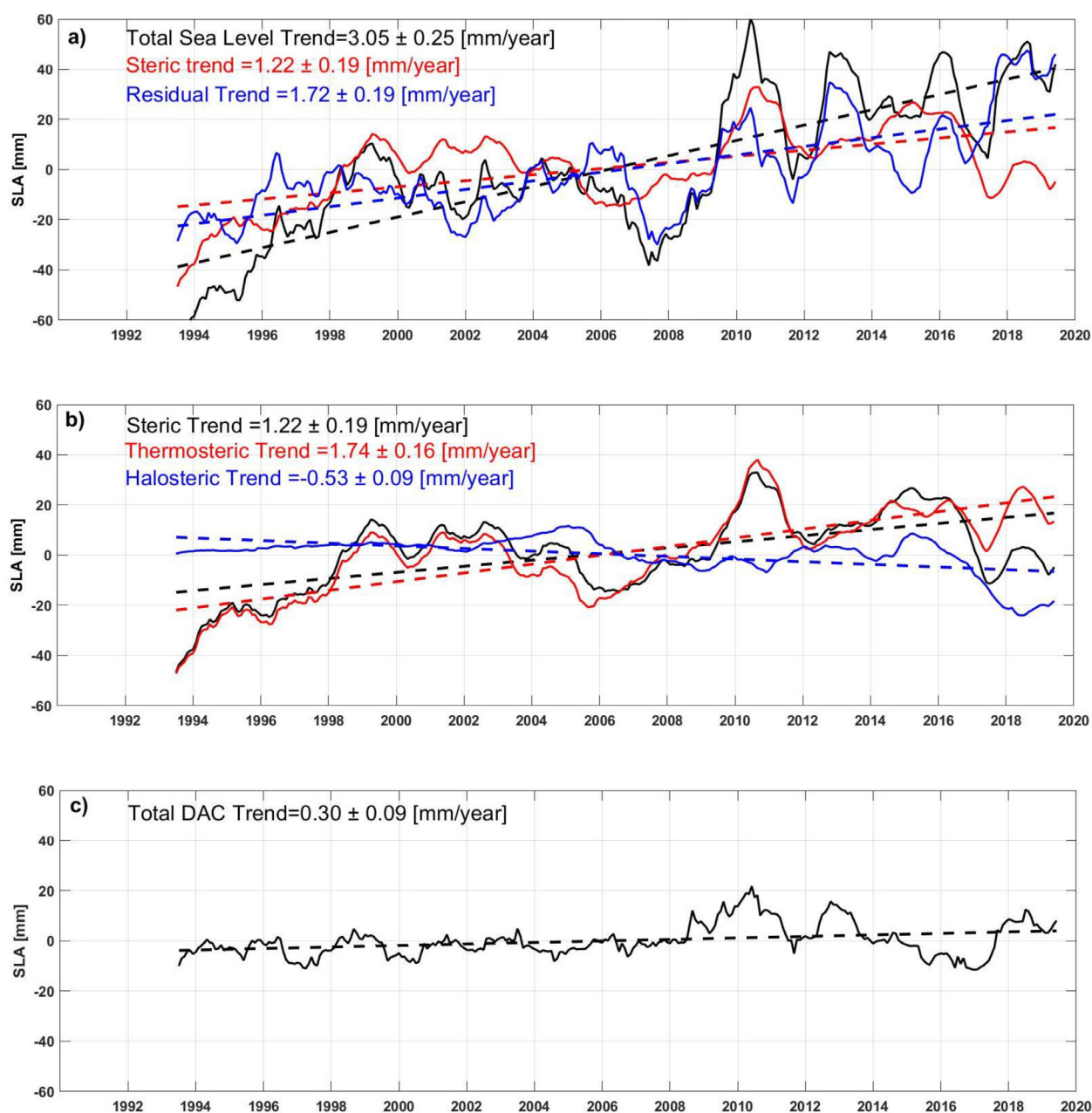


**Figure 4** Time evaluation of the mean sea level anomaly and its components in the Eastern Mediterranean over 1993–2019. a) Total atmospherically corrected altimetry SLA, steric component computed from the CEMES dataset, and residual component (the difference between the total atmospherically corrected sea level and steric effect). b) The contributions of the thermosteric and halosteric components to the total steric effect. c) Dynamic atmospheric contribution to the total sea level. The de-seasoned monthly time series have been low passed for improved visualization by using a 13-month running mean.

widespread upper-layer heat content increase is the Ierapetra gyre, where a negative trend was found. Salinity has been found to be increasing over most of the region during the same period, with the strongest trends obtained in the South Aegean and northwest part of the Levantine Basin. An acceleration of salt content increase of the Eastern Mediterranean has been observed over the last few decades linked with strong net evaporation increase, coincident with acceleration of surface warming and subsequent increase of latent heat loss over the Mediterranean surface (Skliris et al., 2018).

In contrast with the widespread strong increase in the upper layer salt content of EM a low negative (and mostly not statistically significant) trend was observed along the Egyptian coast and the north part of the Aegean Sea. Upper layer salinity in both these regions is controlled by freshwater inputs (Nagy et al., 2017; Skliris et al., 2018), under the influence of the Nile River and the Black Sea outflows, respectively.

The de-seasoned spatial mean of the SST and the averaged water-column (0–400 m depth) temperature and salinity timeseries in the eastern Mediterranean Sea for

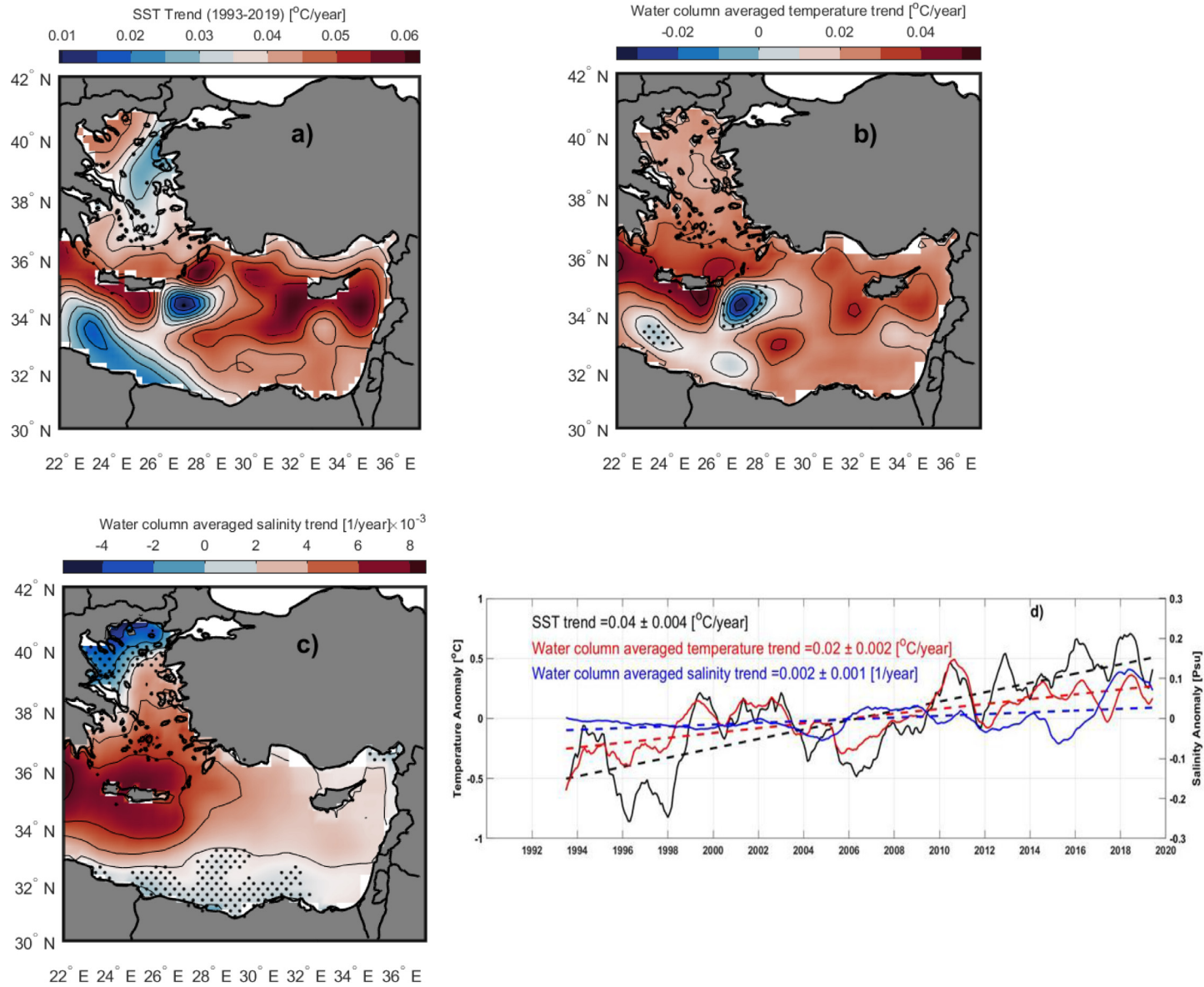


**Figure 5** Spatial distribution of trends (mm/year) over the period 1993–2019 for: (a) SST, (b and c) averaged water column (from 0 to 400 m) temperature and salinity, respectively. (d) The de-seasoned monthly mean time series and linear trends for the averaged of SST (black), 3-D spatially averaged temperature (red) and salinity (blue) over the eastern Mediterranean basin. To enhance the visualization and to emphasize inter-annual variability, the data was low passed using a 13-month moving average. Regions where the trends are not statistically significant at the 95% confidence interval are stippled.

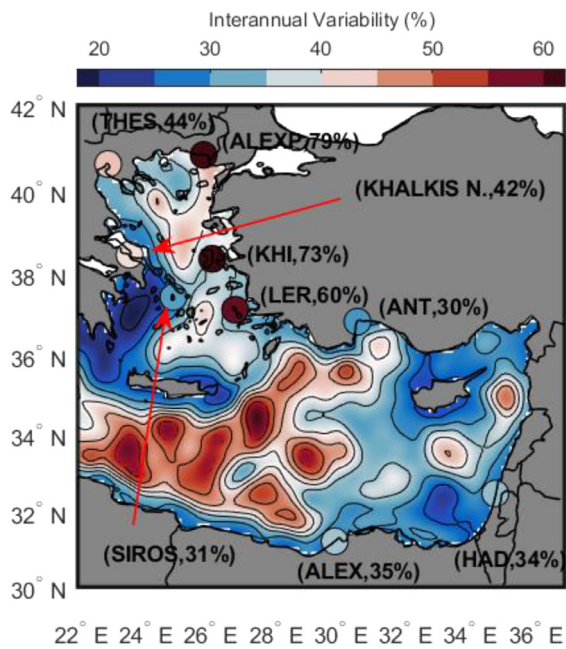


**Figure 6** Percentage of the variance explained by the inter-annual variability of SLA from Altimetry (contour map) and tide gauges (circles). For each tide gauge station, the value of variance explained is also provided between brackets next to the station name.

the period 1993–2019 are shown in Figure 5d. The SST shows a positive trend of  $0.04 \pm 0.004^\circ\text{C}/\text{year}$ , which is consistent with (Pastor et al., 2020) for the 1982–2019 period over the eastern Mediterranean Sea. The spatial mean 0–400 m water-column temperature and salinity show positive statistically significant trends of  $0.02 \pm 0.002^\circ\text{C}/\text{year}$ , and  $0.002 \pm 0.001 \text{ psu}/\text{year}$ , respectively, over 1993–2019. Although inter-annual variability is important there seems to be an accelerating trend for both parameters following the increasing surface warming rate of the basin over the last 15 years.

### 3.4. The steric contribution

The steric contribution to sea level trends is positive at all TG stations (Table 1, column 7), with values ranging between  $0.82 \pm 0.38 \text{ mm}/\text{year}$  at Khios station and  $2.00 \pm 0.41 \text{ mm}/\text{year}$  at Alexandria station. The de-seasoned monthly time series of steric contribution closely follow but show much lower inter-annual variability compared to observed total sea level at all TG stations (Figure 2). However, there are some deviations from the observations, especially in the Aegean Sea stations, induced by other processes that are not resolved in our study. The strong positive anomaly in 2010 is mainly caused by the strong negative NAO event, as indicated by (Landerer and Volkov, 2013; Tsimplis et al., 2013). In general, there is a good correlation between observed and reconstructed steric sea level, with correlations up to 0.7, as shown in Table 1.

Figure 3d shows the spatial distribution of the steric sea level trends. Steric sea level shows a positive significant trend over the whole Basin, except from the Ierape-

tra gyre, where a negative trend of up to  $-3.5 \text{ mm}/\text{year}$  was observed. The spatial distributions of the observed and estimated steric sea level trends are very similar (see, Figure 3a and d), which are largely explained by temperature variations with the difference being probably due to the mass contribution. The correlation coefficient between the observed SLA and steric height was 0.68 (statistically significant at the 95% confidence interval). The spatial average of steric trend over the entire basin was about  $1.38 \pm 0.42 \text{ mm}/\text{year}$ , which accounts for about 45% of the total sea level trend ( $\sim 3.1 \text{ mm}/\text{year}$ ).

Figures 3e and f show the thermosteric and halosteric sea level trends maps, respectively. The thermosteric sea level trend patterns are similar to the steric sea level trend patterns (see, Figure 3d and e), demonstrating that the steric sea level in the EM is dominated by temperature changes. The correlation coefficient between the observed SLA and thermosteric height was 0.73 (statistically significant at the 95% confidence interval). The thermosteric expansion, which has a basin average of about  $2.13 \pm 0.41 \text{ mm}/\text{year}$ , is responsible for most of the steric trend and accounts for 69% of the total sea level trend. Most of the eastern Mediterranean Sea has negative halosteric trends, with a basin average of  $-0.75 \pm 0.19 \text{ mm}/\text{year}$ , except in the north part of the Aegean Sea, where a positive trend of up to  $1 \text{ mm}/\text{year}$  was observed, possibly due to mixing with less saline water from the Black Sea (Stanev et al., 2000). The halosteric component contributes (negatively) by 24% to the total sea level trend.

### 3.5. Residuals contribution

The residual trends include the contribution of oceanic mass addition and local vertical land movement such as sediment load or compaction. Groundwater extraction and tectonics can also contribute to the residual trends of the tide gauge. The GIA values at all TG stations are very small, ranging from  $-0.17 \text{ mm}/\text{year}$  at Thessaloniki (Greece) to  $0.09 \text{ mm}/\text{year}$  at Siros (Greece). The residuals obtained after the GIA, atmospheric and total steric effects were removed from the observations, indicate positive trends which are statistically significant at all stations, except from Alexandroupolis and Khios stations in the North Aegean Sea.

The spatial distribution of the residual trend is shown in Figure 3c. The higher values were found in the Aegean Sea, while the lower values were observed in the Levantine basin, with an average value of  $1.6 \pm 0.51 \text{ mm}/\text{year}$  over the entire basin. Results suggest that the mass component is the dominant contributor to sea level trend in the Aegean Sea, while the steric component is the dominant contributor in the Levantine Sea.

### 3.6. Inter-annual variability

To quantify the interannual variability of sea level, we calculate the basin-averages of temporal variances at each grid point for both the observed datasets, which represent total variability, and the residual datasets, which represent the de-seasoned and detrended signal (Torres and Tsimplis, 2013). We found that, on average, the inter-annual variability of sea level accounts for 36% of the total

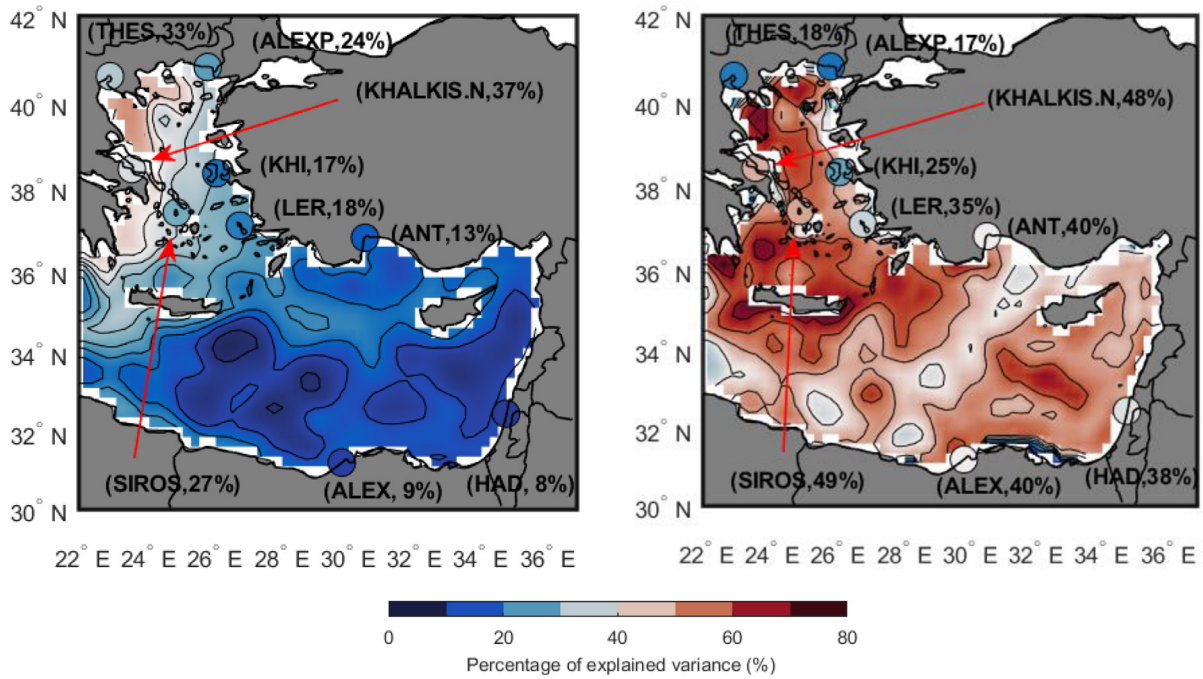


**Figure 7** Percentage of SLA inter-annual variability explained by a) atmospheric contribution, and b) total steric height above 400 m over 1993–2019.

variability in the entire basin, with a range of 18 to 62% (Figure 6). Higher interannual variability has been observed over the major circulation features and recurrent gyres of the basin, with the maximum percentage of the explained variance was found over the southwest part of the Aegean Sea, with less than 25% of sea level variability explained. The same results were obtained from tide gauges, except for three TG stations (Leros, Khios, and Alexandroupolis) on the Aegean Sea’s eastern coast, which show greater interannual variability, probably due to the small variance of observed sea level variability in that region.

We also evaluated the contribution of atmospheric and steric sea level to the inter-annual variability of total SLA at regional scale as shown in Figure 7. The atmospheric effect explains from 3% to 50% of the variability, with a basin average of 18%. The percentage of variance explained by the atmospheric contribution is much larger in the Aegean Sea, peaking in the northwestern part of the basin. The steric component of the sea level explains more than 40% of SLA variability in most regions. On average, the steric component accounted for 52% of the interannual sea level variability. Therefore, the changes in atmospheric and steric components account for 70% of the interannual sea level variability in the Eastern Mediterranean.

#### 4. Summary and conclusions

In this study, we have assessed the contribution of atmospheric, GIA, and steric components to the interannual variability and trend of sea level in the Eastern Mediter-

ranean Sea over the period 1993–2019, using altimetry and tide gauge SLA, together with hydrographic and atmospheric datasets.

After applying atmospheric and GIA correction, we found a spatially averaged SLA linear trend of  $3.23 \pm 0.61$  mm/year from 1993 to 2019, which is not statistically different from the global average trend of  $3.35 \pm 0.4$  mm/year estimated by Ablain et al. (2019) between 1993 and 2017. A widespread pattern of sea level rise was observed with strong positive and statistically significant trends over most of the region with maximum sea level rise obtained over the Mersa–Matruh and Cyprus gyres, as well as the North Shikmona eddy. In contrast a significant negative trend is observed over the Ierapetra gyre, whereas low and not statistically significant trends were only found in the southwestern part of the basin. The contributions of steric height and its components to total sea level rise in the EM were estimated for the period 1993–2019. The steric height of sea level rose at a rate of  $1.38 \pm 0.42$  mm/year, accounting for 45% of the total sea level rise. This result is consistent with a global steric trend of 1.1 mm/year, which accounts for 44% of the total sea level rise from 1993 to 2017 (Storto et al., 2019). Also, this result is in agreement with Criado-Aldeanueva et al. (2008), who found that the steric effect accounts for 55% of total sea level trend in the Mediterranean Sea.

Thermosteric and halosteric components have opposing contributions to the sea level trend. The thermosteric effect, following the accelerating surface warming, is by far the main driver of sea level rise in EM over this period. The thermosteric component trend was  $2.13 \pm 0.41$  mm/year, accounting for 69% of the total sea level trend. The halosteric trend was found to be negative in the largest part of the region, with a basin average of  $-0.75 \pm 0.19$  mm/year, con-

tributing (negatively) by 24% to the total sea level trend. These findings were in line with those obtained by [Storto et al. \(2019\)](#) for the North Atlantic Ocean. These authors demonstrated that the thermosteric effect dominates the steric sea level in the North Atlantic, while the halosteric component contributes negatively to the overall sea level trend. At the global scale, they found that about 25% of the temperature contribution to the total Steric SLA is compensated by salinity changes, in agreement with our result in the eastern Mediterranean.

The steric sea level in the eastern Mediterranean accounts for about 52% of total SLA interannual variability, which is consistent with [Storto et al. \(2019\)](#), who found that at the global scale, the steric sea level explains approximately 50%–70% of the sea level interannual variability. However, this is much higher than that observed by [Calafat et al. \(2012\)](#), who demonstrated that the steric effect explains less than 20% of the variance over the entire Mediterranean Sea and the eastern boundary of the North Atlantic northward of 45°N. They also found that the steric SLA in the eastern Mediterranean explains most of the sea level variation when compared to the western Mediterranean. The EM's dominance of the mass component is consistent with previous studies across the Mediterranean Sea ([Calafat et al., 2010](#)).

Over the study era, all tide gauges showed a positive and statistically significant trend. The most significant contributor to the SLA trend at the TG stations is again the thermosteric effect. However, at some stations, such as Thessaloniki, Leros, Antalya II, and Hadera the thermosteric contributions accounts for less than half of the observed trend, possibly due to the strong contribution of vertical land motion at these stations ([Fenoglio-Marc et al., 2004](#); [Mohamed and El-Din, 2019](#)), which is not addressed here. The interannual variability of SLA accounts for about 36% of overall sea level variability in the EM. On interannual time scales, atmospheric and steric effects contribute together ~70% to the total interannual variability of sea level from altimetry.

Our results demonstrate that increased warming is mainly responsible for the strong sea level rise in the Eastern Mediterranean Sea over the last two decades. Climate model projections indicate accelerating warming and sea level rise in the Mediterranean region during the twenty-first century ([Church et al. 2013](#)). Excessive sea level rise together with warming and drying of the Eastern Mediterranean basin are expected to have far-reaching environmental and societal impacts in this region.

## Declaration of competing interest

The authors declare that they have no known competing financial interests or personal relationships that could have appeared to influence the work reported in this paper.

## Acknowledgments

Authors would like to acknowledge the organizations that provided the sources of the data used in this work, including CMEMS Project for the altimetry and 3D temperature and

salinity products, the Permanent Service for Mean Sea Level (PSMSL) for tide gauge data, NOAA for the DOISST\_V2.1 data, and AVISO for providing a comprehensive access to DAC data. The authors are also grateful to the anonymous reviewers, who have greatly improved the quality of this work with their advice and helpful remarks.

## References

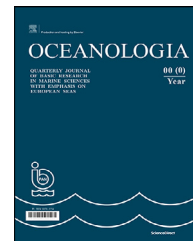
- Ablain, M., Meyssignac, B., Zawadzki, L., Jugier, R., Ribes, A., Spada, G., Benveniste, J., Cazenave, A., Picot, N., 2019. Uncertainty in satellite estimates of global mean sea-level changes, trend and acceleration. *Earth Syst. Sci. Data* 11, 1189–1202. <https://doi.org/10.5194/essd-11-1189-2019>
- Bonaduce, A., Pinaridi, N., Oddo, P., Spada, G., Larnicol, G., 2016. Sea-level variability in the Mediterranean Sea from altimetry and tide gauges. *Clim. Dyn.* 47, 2851–2866. <https://doi.org/10.1007/s00382-016-3001-2>
- Calafat, F.M., Chambers, D.P., Tsimplis, M.N., 2012. Mechanisms of decadal sea level variability in the eastern North Atlantic and the Mediterranean Sea. *J. Geophys. Res. Oceans* 117. <https://doi.org/10.1029/2012JC008285>
- Calafat, F.M., Marcos, M., Gomis, D., 2010. Mass contribution to Mediterranean Sea level variability for the period 1948–2000. *Glob. Planet. Change* 73, 193–201. <https://doi.org/10.1016/J.GLOPLACHA.2010.06.002>
- Carrère, L., Lyard, F., 2003. Modeling the barotropic response of the global ocean to atmospheric wind and pressure forcing – Comparisons with observations. *Geophys. Res. Lett.* 30. <https://doi.org/10.1029/2002GL016473>
- Cazenave, A., Bonnefond, P., Mercier, F., Dominh, K., Toumazou, V., 2002. Sea level variations in the Mediterranean Sea and Black Sea from satellite altimetry and tide gauges. *Glob. Planet. Change* 34, 59–86. [https://doi.org/10.1016/S0921-8181\(02\)00106-6](https://doi.org/10.1016/S0921-8181(02)00106-6)
- Cazenave, A., Cabanes, C., Dominh, K., Mangiarotti, S., 2001. Recent sea level change in the Mediterranean sea revealed by Topex/Poseidon satellite altimetry. *Geophys. Res. Lett.* 28, 1607–1610. <https://doi.org/10.1029/2000GL012628>
- Church, J., Clark, P., Cazenave, A., Gregory, J., Jevrejeva, S., Levermann, A., Merrifield, M., Milne, G., Nerem, R., Nunn, P., Payne, A., Pfeffer, W., Stammer, D., Unnikrishnan, A., 2013. Chapter 13: Sea Level Change. In: *Climate Change 2013: The Physical Science Basis: Contribution of Working Group I to the Fifth Assessment Report of the Intergovernmental Panel on Climate Change*. State Fed. Reports Publ.
- Criado-Aldeanueva, F., Del Río Vera, J., García-Lafuente, J., 2008. Steric and mass-induced Mediterranean sea level trends from 14 years of altimetry data. *Glob. Planet. Change* 60, 563–575. <https://doi.org/10.1016/J.GLOPLACHA.2007.07.003>
- Fenoglio-Marc, L., 2002. Long-term sea level change in the Mediterranean Sea from multi-satellite altimetry and tide gauges. *Phys. Chem. Earth* 27, 1419–1431. [https://doi.org/10.1016/S1474-7065\(02\)00084-0](https://doi.org/10.1016/S1474-7065(02)00084-0)
- Fenoglio-Marc, L., Dietz, C., Groten, E., 2004. Vertical land motion in the Mediterranean Sea from altimetry and tide gauge stations. *Mar. Geod.* 27, 683–701. <https://doi.org/10.1080/01490410490883441>
- Giorgi, F., 2006. Climate change hot-spots. *Geophys. Res. Lett.* 33. <https://doi.org/10.1029/2006GL025734>
- Gomis, D., Ruiz, S., Sotillo, M.G., Álvarez-Fanjul, E., Terradas, J., 2008. Low frequency Mediterranean sea level variability: The contribution of atmospheric pressure and wind. *Glob. Planet. Change* 63, 215–229. <https://doi.org/10.1016/j.gloplacha.2008.06.005>

- Greene, C.A., Thirumalai, K., Kearney, K.A., Delgado, J.M., Schwanghart, W., Wolfenbarger, N.S., Thyng, K.M., Gwyther, D.E., Gardner, A.S., Blankenship, D.D., 2019. The Climate Data Toolbox for MATLAB. *Geochem. Geophys. Geosy.* 20, 3774–3781. <https://doi.org/10.1029/2019GC008392>
- Guinehut, S., Dhomp, A.L., Larnicol, G., Le Traon, P.Y., 2012. High resolution 3-D temperature and salinity fields derived from in situ and satellite observations. *Ocean Sci.* 8, 845–857. <https://doi.org/10.5194/os-8-845-2012>
- Hamed, K.H., Ramachandra Rao, A., 1998. A modified Mann-Kendall trend test for autocorrelated data. *J. Hydrol.* 204, 182–196. [https://doi.org/10.1016/S0022-1694\(97\)00125-X](https://doi.org/10.1016/S0022-1694(97)00125-X)
- Huang, B., Liu, C., Banzon, V., Freeman, E., Graham, G., Hankins, B., Smith, T., Zhang, H.M., 2021. Improvements of the Daily Optimum Interpolation Sea Surface Temperature (DOISST) Version 2.1. *J. Clim.* 34, 2923–2939. <https://doi.org/10.1175/JCLI-D-20-0166.1>
- Hurrell, J.W., 1995. Decadal trends in the North Atlantic oscillation: Regional temperatures and precipitation. *Science* 269 (5224), 676–679. <https://doi.org/10.1126/SCIENCE.269.5224.676>
- Ibrahim, O., Mohamed, B., Nagy, H., 2021. Spatial Variability and Trends of Marine Heat Waves in the Eastern Mediterranean Sea over 39 Years. *J. Mar. Sci. Eng.* 9 (6), 643. <https://doi.org/10.3390/jmse9060643>
- Ishii, M., Kimoto, M., 2009. Reevaluation of historical ocean heat content variations with time-varying XBT and MBT depth bias corrections. *J. Oceanogr.* 65, 287–299. <https://doi.org/10.1007/s10872-009-0027-7>
- Jayne, S.R., Wahr, J.M., Bryan, F.O., 2003. Observing ocean heat content using satellite gravity and altimetry. *J. Geophys. Res. Ocean.* 108, 1–12. <https://doi.org/10.1029/2002jc001619>
- Jordà, G., Gomis, D., 2013. On the interpretation of the steric and mass components of sea level variability: The case of the Mediterranean basin. *J. Geophys. Res. Ocean.* 118, 953–963. <https://doi.org/10.1002/jgrc.20060>
- Landerer, F.W., Volkov, D.L., 2013. The anatomy of recent large sea level fluctuations in the Mediterranean Sea. *Geophys. Res. Lett.* 40, 553–557. <https://doi.org/10.1002/grl.50140>
- Levitus, S., Antonov, J.I., Boyer, T.P., Baranova, O.K., Garcia, H.E., Locarnini, R.A., Mishonov, A.V., Reagan, J.R., Seidov, D., Yarosh, E.S., Zweng, M.M., 2012. World ocean heat content and thermocline sea level change (0–2000m), 1955–2010. *Geophys. Res. Lett.* 39. <https://doi.org/10.1029/2012GL051106>
- Marcos, M., Tsimplis, M.N., 2008. Coastal sea level trends in Southern Europe. *Geophys. J. Int.* 175, 70–82. <https://doi.org/10.1111/j.1365-246X.2008.03892.x>
- McDougall, T.J., Barker, P.M., 2011. Getting started with TEOS-10 and the Gibbs Seawater (GSW) Oceanographic Toolbox. *Score/lapso Wg 127*, 28 pp.
- Menna, M., Gerin, R., Notarstefano, G., Mauri, E., Bussani, A., Paciaroni, M., Poulain, P.-M., 2021. On the Circulation and Thermohaline Properties of the Eastern Mediterranean Sea. *Front. Mar. Sci.* 8, art. 671469, 19 pp. <https://doi.org/10.3389/FMARS.2021.671469>
- Mohamed, B., Abdallah, A.M., Alam El-Din, K., Nagy, H., Shaltout, M., 2019a. Inter-Annual Variability and Trends of Sea Level and Sea Surface Temperature in the Mediterranean Sea over the Last 25 Years. *Pure Appl. Geophys.* 176, 3787–3810. <https://doi.org/10.1007/s00024-019-02156-w>
- Mohamed, B., El-Din, K.A., 2019. Sea level rise and vertical land motion in the eastern Mediterranean. In: *14th MEDCOAST Congress on Coastal and Marine Sciences, Engineering, Management and Conservation, MEDCOAST 2019*, 479–486.
- Mohamed, B., Mohamed, A., Alam El-Din, K., Nagy, H., Elsherbiny, A., 2019b. Sea level changes and vertical land motion from altimetry and tide gauges in the Southern Levantine Basin. *J. Geodyn.* 128, 1–10. <https://doi.org/10.1016/J.JOG.2019.05.007>
- Nagy, H., Elgindy, A., Pinardi, N., Zavatarelli, M., Oddo, P., 2017. A nested pre-operational model for the Egyptian shelf zone: Model configuration and validation/calibration. *Dyn. Atmos. Ocean.* 80, 75–96. <https://doi.org/10.1016/j.dynatmoce.2017.10.003>
- Pascual, A., Marcos, M., Gomis, D., 2008. Comparing the sea level response to pressure and wind forcing of two barotropic models: Validation with tide gauge and altimetry data. *J. Geophys. Res. Ocean.* 113. <https://doi.org/10.1029/2007JC004459>
- Pastor, F., Valiente, J.A., Khodayar, S., 2020. A Warming Mediterranean: 38 Years of Increasing Sea Surface Temperature. *Remote Sens.* 12, 2687. <https://doi.org/10.3390/rs12172687>
- Pawlowicz, R., McDougall, T., Feistel, R., Tailleux, R., 2012. An historical perspective on the development of the Thermodynamic Equation of Seawater-2010. *Ocean Sci.* <https://doi.org/10.5194/os-8-161-2012>
- Peltier, W.R., Argus, D.F., Drummond, R., 2015. Space geodesy constrains ice age terminal deglaciation: The global ICE-6G-C (VM5a) model. *J. Geophys. Res. Solid Earth* 120, 450–487. <https://doi.org/10.1002/2014JB011176>
- Pujol, M.I., Larnicol, G., 2005. Mediterranean sea eddy kinetic energy variability from 11 years of altimetric data. *J. Mar. Syst.* 58, 121–142. <https://doi.org/10.1016/j.jmarsys.2005.07.005>
- Roether, W., Manca, B.B., Klein, B., Bregant, D., Georgopoulos, D., Beitzel, V., Kovačević, V., Luchetta, A., 1996. Recent changes in eastern Mediterranean deep waters. *Science* 271 (5247), 333–335. <https://doi.org/10.1126/SCIENCE.271.5247.333>
- Simav, M., Yıldız, H., Türkez, A., Lenk, O., Özsoy, E., 2012. Sea level variability at Antalya and Menteş tide gauges in Turkey: Atmospheric, steric and land motion contributions. *Stud. Geophys. Geod.* 56, 215–230. <https://doi.org/10.1007/s11200-010-0067-x>
- Skliris, N., Sofianos, S., Gkanasos, A., Mantziafou, A., Vervatis, V., Axaopoulos, P., Lascaratos, A., 2012. Decadal scale variability of sea surface temperature in the Mediterranean Sea in relation to atmospheric variability. *Ocean Dyn.* 62, 13–30. <https://doi.org/10.1007/s10236-011-0493-5>
- Skliris, N., Zika, J.D., Herold, L., Josey, S.A., Marsh, R., 2018. Mediterranean sea water budget long-term trend inferred from salinity observations. *Clim. Dyn.* 51, 2857–2876. <https://doi.org/10.1007/S00382-017-4053-7>
- Stammer, D., Cazenave, A., Ponte, R.M., Tamisiea, M.E., 2013. Causes for Contemporary Regional Sea Level Changes. *Ann. Rev. Mar. Sci.* 5, 21–46. <https://doi.org/10.1146/annurev-marine-121211-172406>
- Stanev, E.V., Le Traon, P.Y., Peneva, E.L., 2000. Sea level variations and their dependency on meteorological and hydrological forcing: Analysis of altimeter and surface data for the Black Sea. *J. Geophys. Res. Ocean.* 105, 17203–17216. <https://doi.org/10.1029/1999jc900318>
- Storto, A., Bonaduce, A., Feng, X., Yang, C., 2019. Steric sea level changes from ocean reanalyses at global and regional scales. *Water (Switzerland)* 11, 1–31. <https://doi.org/10.3390/w11101987>
- Taibi, H., Haddad, M., 2019. Estimating trends of the Mediterranean Sea level changes from tide gauge and satellite altimetry data (1993–2015). *J. Oceanol. Limnol.* 37, 1176–1185. <https://doi.org/10.1007/s00343-019-8164-3>
- Torres, R.R., Tsimplis, M.N., 2013. Sea-level trends and interannual variability in the Caribbean Sea. *J. Geophys. Res. Ocean.* 118, 2934–2947. <https://doi.org/10.1002/jgrc.20229>
- Tsimplis, M.N., Álvarez-Fanjul, E., Gomis, D., Fenoglio-Marc, L., Pérez, B., 2005. Mediterranean Sea level trends: Atmospheric pressure and wind contribution. *Geophys. Res. Lett.* 32, 1–4. <https://doi.org/10.1029/2005GL023867>
- Tsimplis, M.N., Calafat, F.M., Marcos, M., Jordà, G., Gomis, D., Fenoglio-Marc, L., Struglia, M.V., Josey, S.A., Chambers, D.P.,

2013. The effect of the NAO on sea level and on mass changes in the Mediterranean Sea. *J. Geophys. Res. Ocean.* 118, 944–952. <https://doi.org/10.1002/jgrc.20078>
- Tsimplis, M.N., Josey, S.A., 2001. Forcing of the Mediterranean Sea by atmospheric oscillations over the North Atlantic. *Geophys. Res. Lett.* 28, 803–806. <https://doi.org/10.1029/2000GL012098>
- Tsimplis, M.N., Rixen, M., 2002. Sea level in the Mediterranean Sea: The contribution of temperature and salinity changes. *Geophys. Res. Lett.* 29. <https://doi.org/10.1029/2002GL015870>
- Vigo, I., Garcia, D., Chao, B.F., 2005. Change of sea level trend in the Mediterranean and Black seas. *J. Mar. Res.* 63, 1085–1100. <https://doi.org/10.1357/002224005775247607>
- Wang, G., Cheng, L., Boyer, T., Li, C., 2017. Halosteric sea level changes during the Argo era. *Water (Switzerland)* 9, 1–13. <https://doi.org/10.3390/w9070484>
- Wilks, D.S., 2011. *Statistical methods in the atmospheric sciences.* Academic Press.
- Woodworth, P.L., Player, R., 2003. The Permanent Service for Mean Sea Level: An Update to the 21st Century. *J. Coast. Res.* 19, 287–295.

Available online at [www.sciencedirect.com](http://www.sciencedirect.com)

ScienceDirect

journal homepage: [www.journals.elsevier.com/oceanologia](http://www.journals.elsevier.com/oceanologia)

## ORIGINAL RESEARCH ARTICLE

# Inhibitory effects of the brown macroalga *Turbinaria ornata* on cyst germination and progeny cells of five harmful dinoflagellate species

Zakaria Mohamed<sup>a,\*</sup>, Saad Alamri<sup>b</sup>, Mohamed Hashem<sup>b,c</sup><sup>a</sup>Department of Botany, Faculty of Science, Sohag University, Sohag, Egypt<sup>b</sup>Biological Science Department, Faculty of Science, King Khalid University, Abha, Saudi Arabia<sup>c</sup>Botany and Microbiology Department, Faculty of Science, Assiut University, Assiut, Egypt

Received 21 January 2021; accepted 16 September 2021

Available online 12 October 2021

## KEYWORDS

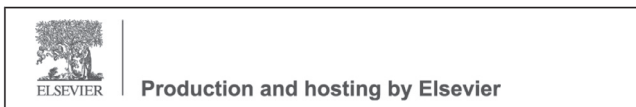
Cysts;  
Dinoflagellates;  
Harmful blooms;  
Macroalgal  
allelopathy

**Abstract** This study investigates the inhibitory effects of thalli and their extracts of the macroalga *Turbinaria ornata* on the germination of dinoflagellate cysts, previously isolated from Red Sea surface sediments. The experiments were conducted on cysts of five harmful dinoflagellate species including *Alexandrium catenella*, *Cochlodinium polykrikos*, *Dinophysis acuminata*, *Prorocentrum cordatum* and *Scrippsiella trochoidea*. The results showed neither macroalgal thalli nor their extracts had direct impact on the cyst germination of all species. Instead, these macroalgal materials remarkably affected the germling viability and culturability of progeny cells of these cysts. Dry macroalgal thalli exhibited stronger inhibitory effects on germling viability and cell culturability ( $IC_{50}$  = 0.235–0.543, 0.385–1.43 mg mL<sup>-1</sup>, respectively) than fresh thalli ( $IC_{50}$  = 2.201–4.716, 2.17–7.18 mg mL<sup>-1</sup>, respectively). The macroalgal ethanol extract was approximately 2–5 times more effective ( $IC_{50}$  = 0.012–0.047 and 0.024–0.089 mg mL<sup>-1</sup>, respectively) than aqueous extract ( $IC_{50}$  = 0.04–0.1 and 0.054–0.207 mg mL<sup>-1</sup>, respectively) against the germling viability and vegetative progeny cells of all cyst species. Among different species, *A. catenella* and *C. polykrikos* germlings were more sensitive to macroalgal thalli and their extracts than those of *S. trochoidea*, *P. cordatum* and *D. acuminata*.

\* Corresponding author at: Department of Botany, Faculty of Science, Sohag University, Sohag 82524, Egypt. Tel: 00201141705691.

E-mail addresses: [Zakaria.attia@science.sohag.edu.eg](mailto:Zakaria.attia@science.sohag.edu.eg), [mzakaria\\_99@yahoo.com](mailto:mzakaria_99@yahoo.com) (Z. Mohamed).

Peer review under the responsibility of the Institute of Oceanology of the Polish Academy of Sciences.



<https://doi.org/10.1016/j.oceano.2021.09.002>

0078-3234/© 2021 Institute of Oceanology of the Polish Academy of Sciences. Production and hosting by Elsevier B.V. This is an open access article under the CC BY-NC-ND license (<http://creativecommons.org/licenses/by-nc-nd/4.0/>).



Meanwhile, progeny cells of *A. catenella* exhibited the highest sensitivity to all macroalgal materials. Our results suggest that the use of *T. ornata* may be a promising strategy for inhibiting the division of progeny cells of dinoflagellate cysts and impairing the recurrence of HABs in confined coastal areas.

© 2021 Institute of Oceanology of the Polish Academy of Sciences. Production and hosting by Elsevier B.V. This is an open access article under the CC BY-NC-ND license (<http://creativecommons.org/licenses/by-nc-nd/4.0/>).

## 1. Introduction

Dinoflagellates are one of the phytoplankton groups that contribute to primary production in marine and freshwater environments (Bravo and Figueroa, 2014). However, many species can form harmful algal blooms (HABs) and produce toxins that represent a threat to aquaculture, fisheries and public health (Lewitus et al., 2012; Mohamed and Mosaad, 2007; Mohamed and Al-Shehri, 2012; Mohamed, 2018). The life cycle of many dinoflagellates encompasses an asexual vegetative phase, which reproduces by binary fission, and a sexual phase reproducing by fusion of haploid gametes (Pfiester and Anderson, 1987). The zygote may return to the vegetative stage or transform into a resting cyst, which sinks into sea bottom to sustain unfavorable conditions and remains viable in sediments for about 5–10 years (Anderson et al., 1995; Figueroa et al., 2007) or longer (up to 100 years) for cysts of some *Alexandrium* species (Miyazono et al., 2012). Upon the return of favorable conditions, these cysts can germinate and re-establish plankton cells that reproduce and form algal blooms in the sea water (Sun et al., 2007). Generally, cyst germination is regulated by external factors such as temperature, light, oxygen levels, and by physiological traits e.g., the dormancy period (Kremp et al., 2001). Dinoflagellate cysts thus constitute a seed source (i.e., initial inoculum) of plankton populations (Sun et al., 2007) and reflect the bloom location in subsequent seasons (Anderson et al., 2014). Climate change and warming would also enhance the germination of dinoflagellate cysts (Brosnahan et al., 2020). Therefore, the inhibition of cyst germination would restrict the development of extensive coastal blooms. Although several studies have reported the inhibitory properties of macroalgae on the growth of motile vegetative cells of HAB species through the release of algicidal allelochemicals (Ben Gharbia et al., 2017; Jin et al., 2003; Wang et al., 2007), no study has been made on the inhibitory effects of macroalgae on the cyst germination of dinoflagellate species. Therefore, the novelty of our study lies in the investigation of potential impact of macroalgae on early development stages (i.e., cyst germination, germling viability and culturability of progeny cells) of harmful dinoflagellates.

*Turbinaria ornata* is one of the most conspicuous macroalgal species that grows along the Red Sea coasts of Saudi Arabia. *T. ornata* has been reported to exhibit antifouling activities, particularly against microalgae (Salama et al., 2018). Therefore, our study aimed to assess the ability of this macroalga to inhibit the cyst germination and progeny cells of different dinoflagellate cysts collected from the same location, to be used as environmentally benign bioagent of controlling HABs formation.

## 2. Material and methods

### 2.1. Macroalgae and dinoflagellate cysts

*Turbinaria ornata* (Turner) J. Agardh used for this study was collected from Al-Shouyq region on the east coast of the Red Sea in Saudi Arabia (19°65'N, 42°18'E), and identified according to Guiry and Guiry (2011). The algal specimens were extensively rinsed with sterile filtered (0.2 μm) seawater and rubbed with a fine brush to remove debris and epiphytes. Thereafter, macroalgal thalli were treated with a mixture of 30% ethanol and 1% sodium hypochlorite for 10 min to kill and eliminate attached bacteria and microalgae without damaging algal cells (Kientz et al 2011). Cleaned macroalgal thalli were then dried in an oven at 37°C for 48 hours. Dried thalli were cut into small pieces, then ground into a fine powder, and stored in darkness until further use. Germination experiments were carried out on cysts in re-suspended slurries of natural sediments, that were previously collected from the Red Sea (Mohamed and Al-Sheri, 2011), and stored in 10 ml vials that were tightly sealed and wrapped with aluminum foil and kept at 4°C to prevent germination. The experiments were performed on cysts of five potentially toxic dinoflagellate species including *A. catenella*, *C. polykrikos*, *S. trochoidea*, *P. cordatum*, *D. acuminata* (Mohamed, 2018).

### 2.2. Inhibitory effects of fresh and dry thalli of *T. ornata* on cyst germination

Different amounts of washed fresh thalli of *T. ornata* (1.0, 2.5, 5, 10 and 20 mg mL<sup>-1</sup>) were added to glass culture tubes. Each tube was particularized for a single cyst species and contained 100 cyst individuals and 10 ml sterile filtered sea water. For the effect of dry thalli, the dry powder was added at 0.1, 0.5, 1, 5, and 10 mg mL<sup>-1</sup> to glass tubes each containing 100 cysts of each species and 10 ml sterile filtered sea water. Concentrations of fresh and dry thalli used in our experiments were chosen based on concentrations of other macroalgae used in previous studies (Fresh thalli: 1–16 mg mL<sup>-1</sup>; Dry thalli: 0.15–2.4 mg mL<sup>-1</sup>) and exhibited algicidal activity against harmful dinoflagellates (Sun et al. 2016). However, the concentrations 20 mg fresh thalli mL<sup>-1</sup> and 10 mg dry thalli mL<sup>-1</sup> were used to determine the inhibition effect at higher concentrations. The tubes were incubated at 15°C using a 12:12 h light: dark cycle provided by cool white illumination tubes at 80 μmol m<sup>-2</sup> s<sup>-1</sup>. These germination conditions were earlier reported as the optimum for the germination of our dinoflagellate cysts (Mohamed and Al-Shehri, 2011). Cysts were mon-

itored every 2 days for germination and growth for a maximum of one month. After the time-course of germination, the tubes were shaken gently to loosen cyst deposits on the bottom and distribute flagellate cells and cysts evenly. Three 1-mL subsamples were then taken from each tube and poured into a Sedgewick-Rafter chamber for counting ungerminated cysts by Zeiss light microscopy according to [Genovesi et al. \(2009\)](#). The percentage of cyst germination was calculated by dividing the number of germinated cysts (initial number of cysts – number of ungerminated cysts) by the initial number of cysts and then multiplying the product by 100. Meanwhile, each germling cell was isolated by pipetting immediately after germination and inoculated into a new 10 mL glass tube containing F/2 medium and the same concentration of macroalgal thalli or its extracts used in each treatment. Tubes were then incubated at the same conditions described above. After 7 days, the number of motile vegetative cells was determined in all tubes. The percentage of viable germlings was estimated as the number of cells observed alive after excystment divided by total germinated cysts  $\times$  100. The percentage of culturable cells was expressed as the number of tubes with living motile cells divided by total viable germlings, and then multiplying the product by 100.

### 2.3. Inhibitory effects of *T. ornata* aqueous and ethanolic extracts on cyst germination

Aqueous and ethanol extracts of *T. ornata* were prepared by grinding 5 g of dry thalli in sterile distilled water or 95% ethanol, respectively. The slurry was left on a shaker at room temperature for 24 hours, and then centrifuged at 6000 rpm at 15°C for 15 min. and the supernatant was filtered through 0.22  $\mu$ m polycarbonate filter. The supernatant of ethanol extract was evaporated to remove the organic solvent and the aqueous phase was adjusted to a final concentration of 10 mg mL<sup>-1</sup> with sterile distilled water. Aqueous and ethanol extracts of *T. ornata* were added at 0.01, 0.05, 0.1, 0.5, and 1 mg mL<sup>-1</sup> to glass culture tubes, each particularized for a single cyst species and containing 100 cysts and 10 ml sterile filtered sea water. These extract concentrations were selected based on concentrations of other macroalgae assessed in previous studies (0.01–0.96 mg mL<sup>-1</sup>) and showed strong inhibition against harmful microalgae ([Sun et al., 2016](#)). The tubes were incubated at the same conditions mentioned above in the experiments of effects of fresh and dry thalli. Inhibitory effects of aqueous and ethanol extracts on cyst germination, germling viability and progeny cells were assessed by the same methods described above. In all experiments, tubes containing 100 cysts and 10 ml sterile filtered sea water (i.e., without macroalgal thalli or extract) were used as control. Each experiment was run in triplicate.

### 2.4. GC-MS analysis of the macroalgal extract

The GC-MS analysis was carried out for the ethanol extract of *T. ornata*, as it showed the strongest inhibitory activity against germling and vegetative progeny cells of dinoflagellate cysts. The GC-MS analysis was done using GC-MS THERMO GC-TRACE ULTRA Version-5.0. The stan-

dard non-polar capillary column, with dimensions of 30 m  $\times$  25 mm  $\times$  0.25  $\mu$ m was used and the injection volume was one microliter. The extract was diluted in ethanol and injected in the split mode. Helium was used as a carrier gas with a flow rate of 1 ml min<sup>-1</sup>. The GC oven temperature was programmed from 80°C to 260°C at a rate of 5°C min<sup>-1</sup>. Chemical compounds were identified using spectrum database NIST 11 software installed in GC-MS instrument. The relative % amount was calculated by matching its peak area to the total areas.

### 2.5. Statistical analysis

All data were expressed as mean  $\pm$  standard deviation (SD). Data were analyzed using one-way analysis of variance (ANOVA) followed by Tukey's post-hoc test in order to assess the significant differences in cyst germination, germling and progeny cells viability between control and treatments, and as well as among different species using the software SPSS (version 16.0). Differences were considered to be significant at  $P < 0.05$ . Computations of median inhibitory concentration (IC<sub>50</sub>) of a data-set obtained from our study were performed using Finney's method of probit analysis with SPSS computer statistical software. The IC<sub>50</sub> value is derived by fitting a regression equation arithmetically.

## 3. Results

Results of the experiments of the inhibitory effects of the brown macroalga *T. ornata* on the percentages of cyst germination, germling viability and progeny cells of five dinoflagellate species are presented in [Figures 1–4](#). The first germinated cysts were observed on day 15 in both control and treatment groups. For all cyst species, the cyst germination percentage did not differ significantly between control and treatments ( $P > 0.05$ ). However, the addition of macroalgal materials to experimental tubes markedly influenced the germling viability (i.e., number of viable germling cells observed alive after germination) and their culturability (i.e., the ability of progeny cells to divide and give rise to motile vegetative cells). These effects varied significantly ( $P < 0.05$ ) between macroalgal materials (i.e., fresh thalli, dry thalli, aqueous extract and ethanol extract) for a single cyst species.

### 3.1. Effects of fresh and dry macroalgal thalli on cyst germination

Incubation of dinoflagellate cysts with different amounts of fresh macroalgal thalli suppressed the viability of germlings of all five cyst species used in this study. The percentage of viable germlings decreased (from 81% to 4%) with the increase of the amount of fresh algal thalli, and the viability of these germlings was completely lost at a concentration of 20 mg mL<sup>-1</sup> for all cyst species ([Figure 1A–E](#)). Results also showed that lower concentrations (1, 2.5, 5 and 10 mg mL<sup>-1</sup>) of fresh algal thalli exhibited marked mortality in progeny cells (i.e. culturability) of all cyst species, and all

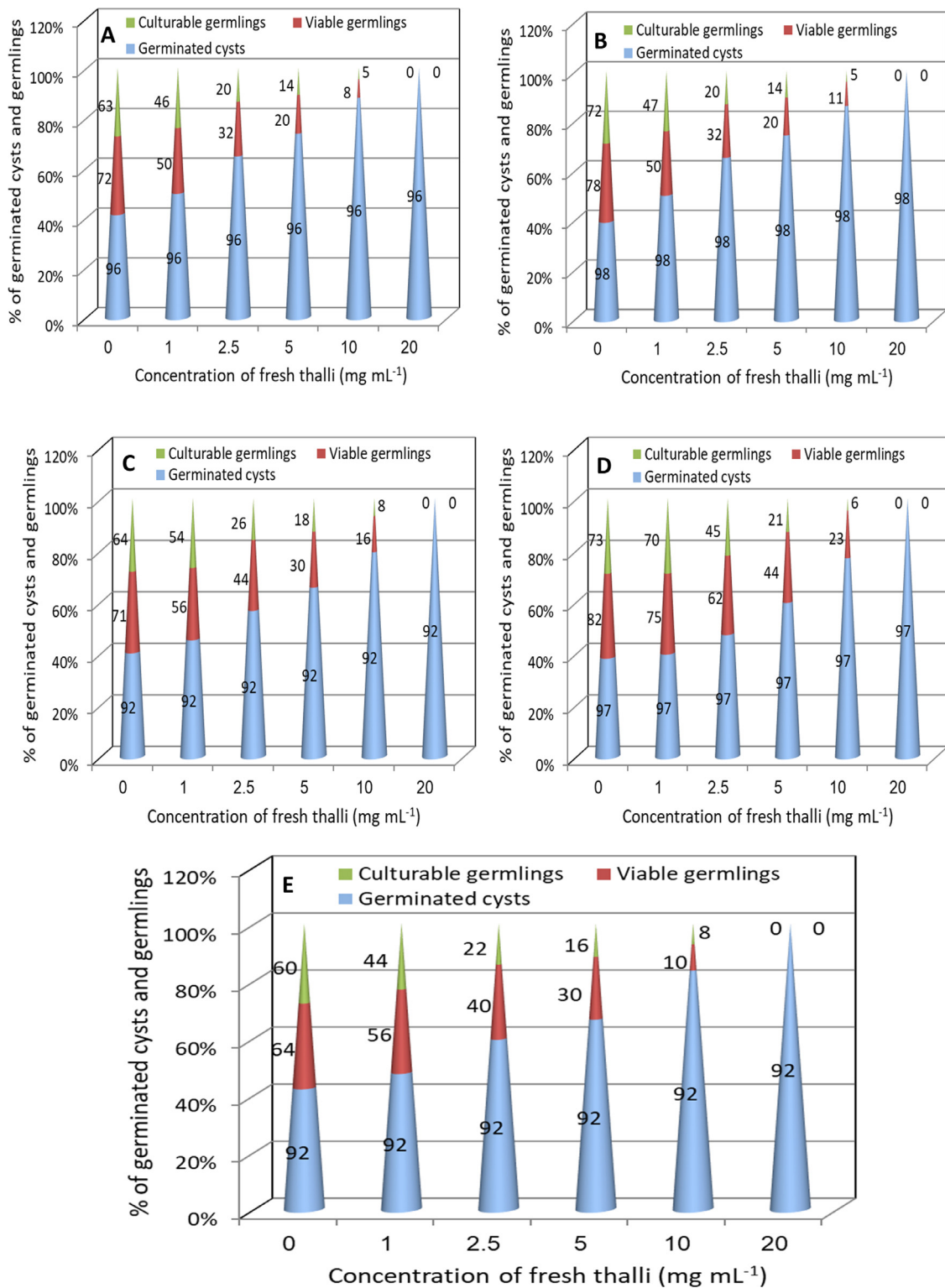


**Figure 1** Inhibitory effects of fresh thalli of *Turbinaria ornata* on cyst germination, and viability and culturability of germlings of HAB species cysts (A) *Alexandrium catenella*, (B) *Scrippsiella trochoidea*, (C) *Cochlodinium polykrikos*, (D) *Prorocentrum cordatum*, and (E) *Dinophysis acuminata*. Data points are means  $\pm$ SD (n = 3).

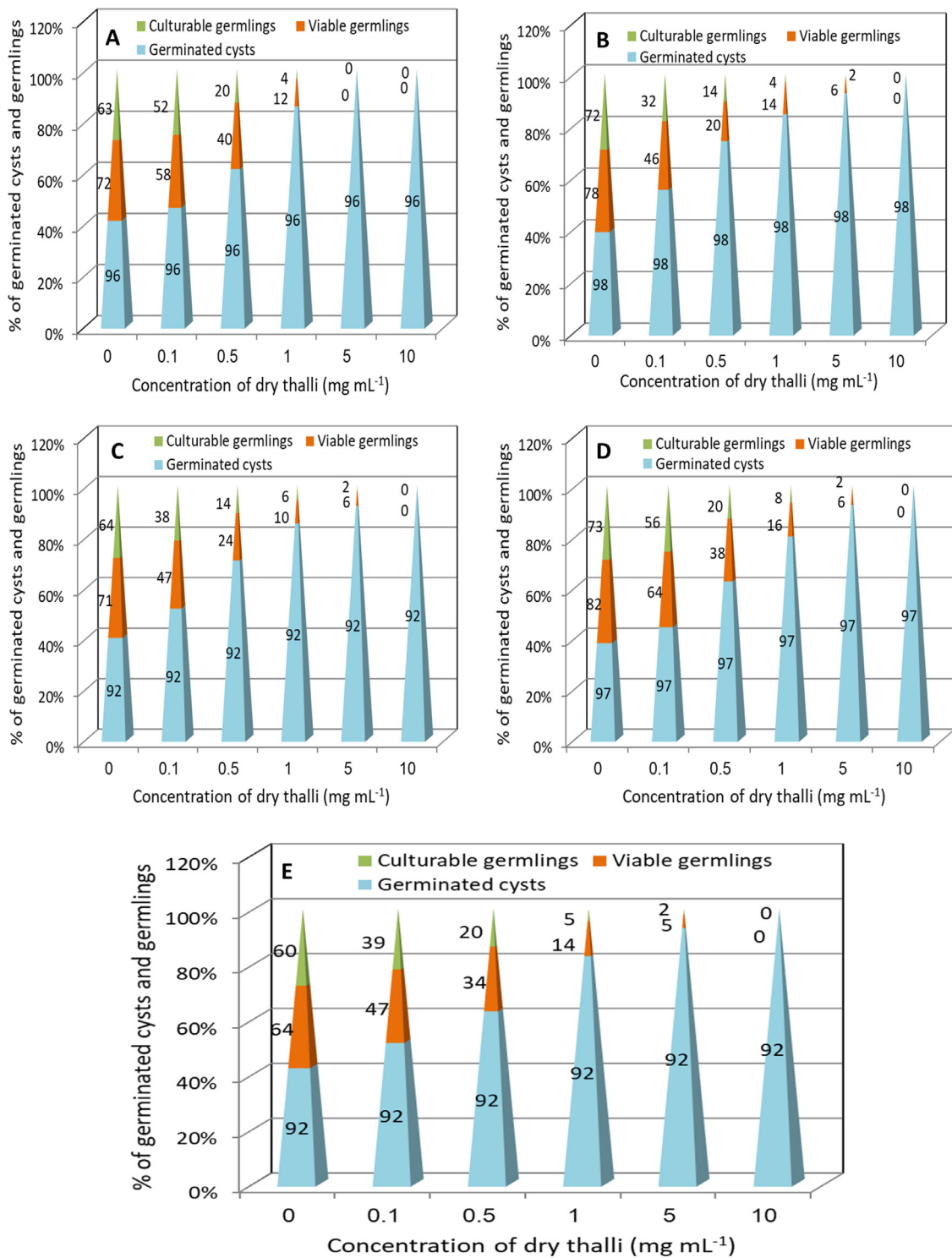


**Figure 2** Inhibitory effects of dry thalli of *Turbinaria ornata* on cyst germination, and viability and culturability of germlings of HAB species cysts (A) *Alexandrium catenella*, (B) *Scrippsiella trochoidea*, (C) *Cochlodinium polykrikos*, (D) *Prorocentrum cordatum*, and (E) *Dinophysis acuminata*. Data points are means  $\pm$ SD (n = 3).

progeny cells had died at the highest inoculation mass (20 mg mL<sup>-1</sup>) of fresh thalli (Figure 1A–E). The dried macroalgal thalli also had inhibitory effects on viable germlings of different cyst species, but with stronger inhibition (P < 0.05) than that of fresh thalli. The inhibitory effect of dry thalli on the viability of cyst germlings varied with the amount of

dry macroalga (P < 0.05). This viability was strongly suppressed by the highest two concentrations of dry thalli (5 and 10 mg mL<sup>-1</sup>), with no germlings survived (Figure 2A–E). On the other hand, lower concentrations of dry thalli (0.1, 0.5, and 1 mg mL<sup>-1</sup>) caused a remarkable reduction in the percentage of viable germlings of all cyst species, but with-

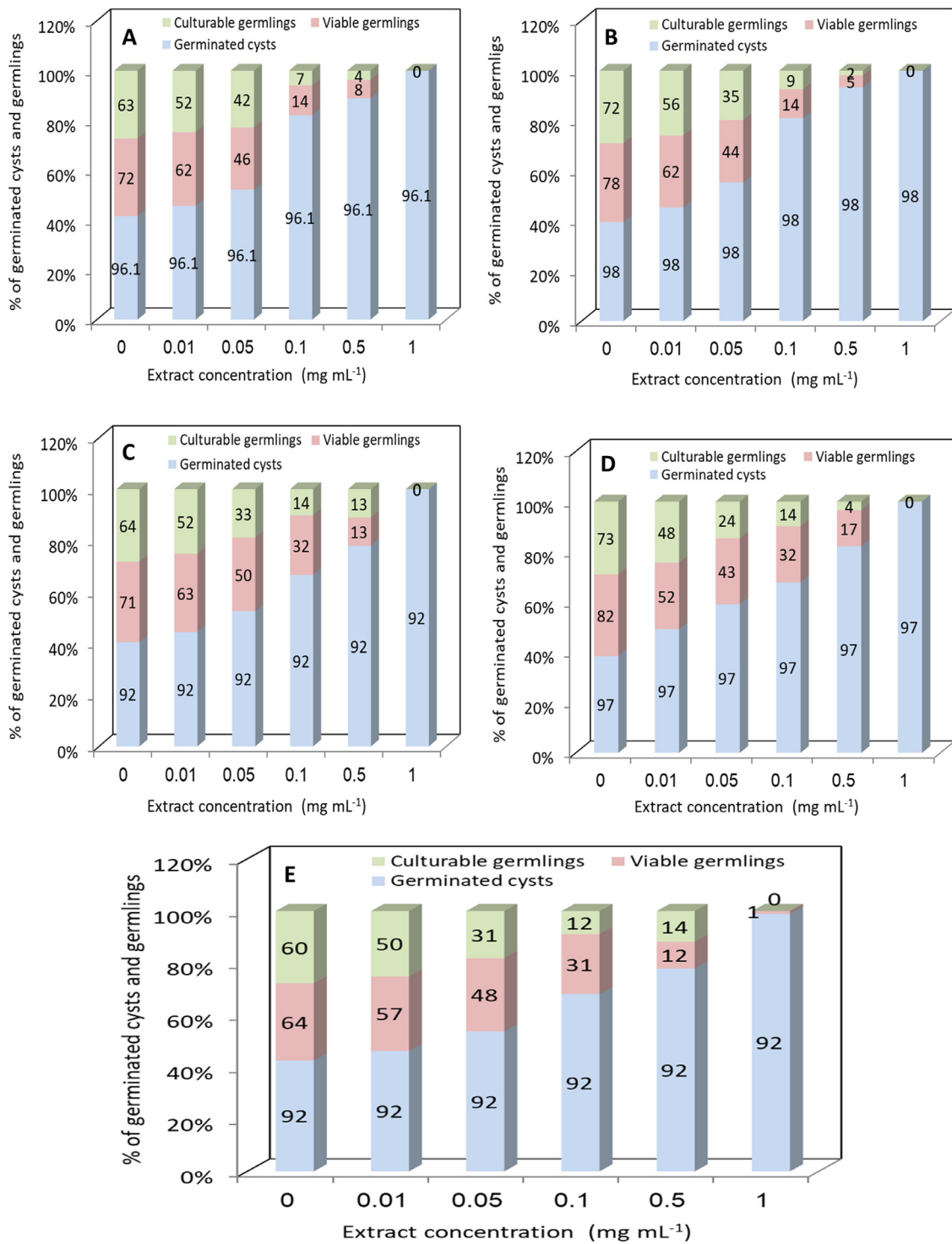


**Figure 3** Inhibitory effects of aqueous extract of *Turbinaria ornata* on cyst germination, and viability and culturability of germlings of HAB species cysts (A) *Alexandrium catenella*, (B) *Scrippsiella trochoidea*, (C) *Cochlodinium polykrikos*, (D) *Prorocentrum cordatum*, and (E) *Dinophysis acuminata*. Data points are means  $\pm$ SD (n = 3).

out complete death. The culturability of progeny cells of all cyst species was also influenced by dry macroalgal material, where it decreased gradually (from 73 to 1%) with the increase of dry macroalgal thalli and died at the two highest dosages (5 and 10 mg mL<sup>-1</sup>) (Figure 2A–E).

### 3.2. Effect of macroalgal extracts on cyst germination

The addition of aqueous or ethanol extract of *T. ornata* to cyst cultures caused a significant reduction in the percent-

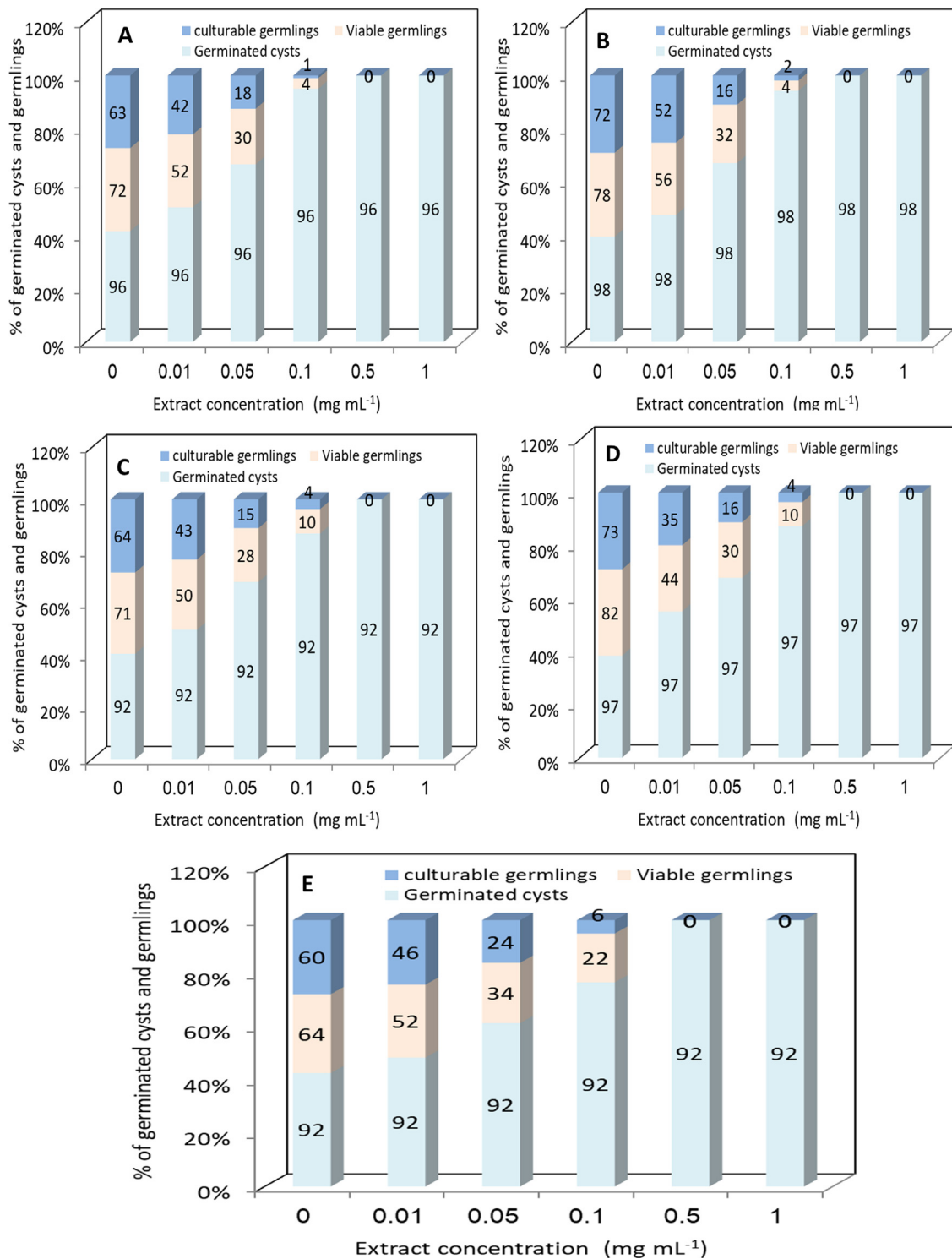


**Figure 4** Inhibitory effects of ethanol extract of *Turbinaria ornata* on cyst germination, and viability and culturability of germlings of HAB species cysts (A) *Alexandrium catenella*, (B) *Scrippsiella trochoidea*, (C) *Cochlodinium polykrikos*, (D) *Prorocentrum cordatum*, and (E) *Dinophysis acuminata*. Data points are means  $\pm$ SD (n = 3).

age of viable germlings of all cyst species. The germling viability percentage decreased markedly ( $P < 0.05$ ) with the concentration of aqueous or ethanol extract. Aqueous extract of a concentration of 1 mg mL<sup>-1</sup> resulted in the death of germlings of all cyst species (Figure 3A–E), while the

lethal effect of ethanol extract on germling viability was observed at a concentration of 0.5 mg mL<sup>-1</sup> (Figure 4A–E). Similarly, the culturability of progeny cells of different cyst species was suppressed by both aqueous and ethanol extracts. By increasing the concentration of either aqueous

**Table 1** Normalized IC<sub>50</sub> values (based on Probit analysis) of fresh and dry thalli, and aqueous and ethanolic extracts of *Turbinaria ornata* against germling viability.

Cyst species	IC <sub>50</sub> (mg mL <sup>-1</sup> )			
	Fresh thalli	Dry thalli	Aqueous extract	Ethanolic extract
<b>Gonyaulacales</b>				
<i>Alexandrium catenella</i>	2.237±0.4	0.403±0.1	0.05±0.004	0.028±0.003
<b>Gimnodinales</b>				
<i>Cochlodinium polykrikos</i>	2.201±0.5	0.083±0.02	0.042±0.001	0.026±0.002
<b>Peridinales</b>				
<i>Scrippsiella trochoidea</i>	2.936±0.8	0.235±0.05	0.1±0.02	0.022±0.004
<b>Prorocentrales</b>				
<i>Prorocentrum cordatum</i>	4.716±1	0.543±0.07	0.04±0.005	0.012±0.001
<b>Dinophysiales</b>				
<i>Dinophysis acuminata</i>	3.161±0.7	0.314±0.08	0.101±0.02	0.047±0.003

**Table 2** Normalized IC<sub>50</sub> values (based on Probit analysis) of fresh and dry thalli, and aqueous and ethanol extracts of *Turbinaria ornata* against culturability of germling cells.

Cyst species	IC <sub>50</sub> (mg mL <sup>-1</sup> )			
	Fresh thalli	Dry thalli	Aqueous extract	Ethanolic extract
<b>Gonyaulacales</b>				
<i>Alexandrium catenella</i>	2.17±0.7	0.385±0.8	0.054±0.001	0.024±0.003
<b>Gimnodinales</b>				
<i>Cochlodinium polykrikos</i>	7.18±1.5	1.07±0.2	0.107±0.003	0.076±0.004
<b>Peridinales</b>				
<i>Scrippsiella trochoidea</i>	7.17±1.7	1.11±0.3	0.144±0.02	0.086±0.003
<b>Prorocentrales</b>				
<i>Prorocentrum cordatum</i>	7.3±2	1.43±0.3	0.119±0.03	0.082±0.003
<b>Dinophysiales</b>				
<i>Dinophysis acuminata</i>	7.9±2.1	1.22±0.2	0.128±0.04	0.089±0.004

or ethanol extract, a concomitant decrease ( $P < 0.05$ ) was observed in the percentage of cell culturability (Figures 3A–E and 4A–E). Similar to germling viability, the cell culturability of all cyst species was completely lost at 1 mg mL<sup>-1</sup> aqueous extract (Figure 3A–E) compared to 0.5 mg mL<sup>-1</sup> ethanol extract (Figure 4A–E).

### 3.3. Comparison of inhibitory effects based on IC<sub>50</sub> values

IC<sub>50</sub> values of inhibitory effects of macroalgal thalli and its extracts against germlings and progeny cells of dinoflagellate cysts were compared in Tables 1, 2. The IC<sub>50</sub> values of dry macroalgal thalli (0.235–0.543 mg mL<sup>-1</sup>) for germling viability inhibition were significantly lower ( $P < 0.05$ ) than corresponding IC<sub>50</sub> values (2.201–4.716 mg mL<sup>-1</sup>) of fresh thalli (Table 1). Similarly, the IC<sub>50</sub> values of ethanol extract (IC<sub>50</sub> = 0.04–0.1 mg mL<sup>-1</sup>) towards germling viability were lower ( $P < 0.05$ ) than IC<sub>50</sub> values (0.04–0.1 mg mL<sup>-1</sup>) of aqueous extract (Table 1). Regarding the effect on progeny cells survival (i.e., culturability), the IC<sub>50</sub> values for dry thalli (0.385–1.43 mg mL<sup>-1</sup>) were about 4–5 folds greater ( $P < 0.05$ ) than that those of fresh thalli (2.17–7.18 mg mL<sup>-1</sup>) (Table 2). The IC<sub>50</sub> values of ethanol

extract (0.024–0.089 mg mL<sup>-1</sup>) against progeny cells of all cyst species were about 2 times lower ( $P < 0.05$ ) than those of aqueous extract (0.054–0.107 mg mL<sup>-1</sup>) (Table 2). At the level of cyst species, the ANOVA analysis showed that the IC<sub>50</sub> values of fresh and dry thalli, and aqueous and ethanol extracts towards germling viability (Table 1) and culturability of progeny cells (Table 2) varied significantly ( $P < 0.05$ ) among different species. However, Tukey's test revealed no significant differences in these IC<sub>50</sub> values between some cyst species. In this respect, no significant difference in IC<sub>50</sub> values of fresh thalli was found between *A. catenella* and *C. polykrikos* germlings ( $P=0.9$ ), nor between *S. trochoidea* and *D. acuminata* cysts ( $P=0.08$ ). The highest IC<sub>50</sub> value of fresh thalli (4.716 mg mL<sup>-1</sup>) was reported in *P. cordatum* germlings, and the lowest (2.201 mg mL<sup>-1</sup>) was in *C. polykrikos* germlings (Table 1). Also, the IC<sub>50</sub> values of dry macroalgal thalli, did not significantly vary between *A. catenella* and *P. cordatum* ( $P=0.2$ ) according to Tukey's test. The lowest IC<sub>50</sub> (0.083 mg mL<sup>-1</sup>) of dry thalli was incurred in *C. polykrikos* germlings, and the highest (0.543 mg mL<sup>-1</sup>) was in *P. cordatum* germlings (Table 1). For the inhibitory effect of macroalgal aqueous extract, Tukey's test revealed no significant variation in IC<sub>50</sub> values either among *A. catenella*, *C. polykrikos* and

**Table 3** GC-MS analysis of ethanol extract of *Turbinaria ornata*.

Peak No.	Retention time (min)	Compound	Chemical formula	Molecular mass	Peak area (%)
1	16.66	n-Hexadecanoic acid	C <sub>16</sub> H <sub>32</sub> O <sub>2</sub>	256.42	4.34
2	19.78	Benzo(k)fluoranthene	C <sub>20</sub> H <sub>12</sub>	252.30	4.74
3	23.25	Bufencarb-2	C <sub>13</sub> H <sub>19</sub> NO <sub>2</sub>	221.30	8.81
4	25.23	Heptachlor	C <sub>10</sub> H <sub>5</sub> Cl <sub>7</sub>	373.31	25.8
5	26.18	Kresoxim-Methyl	C <sub>18</sub> H <sub>19</sub> NO <sub>4</sub>	313.34	6.78
6	28.83	n-Tetradecane	C <sub>14</sub> H <sub>30</sub>	198.38	9.31
7	29.02	Isopropyl isothiocyanate	C <sub>4</sub> H <sub>7</sub> NS	101.17	9.16
8	29.38	Di-n-octylphthalate	C <sub>24</sub> H <sub>38</sub> O <sub>4</sub>	390.55	6.97
9	34.93	Vanillylmandelic acid	C <sub>9</sub> H <sub>10</sub> O <sub>5</sub>	198.17	1.87
10	36.91	Tetramethrin-1	C <sub>19</sub> H <sub>25</sub> NO <sub>4</sub>	331.40	2.46
11	37.92	Acetamidrid	C <sub>10</sub> H <sub>11</sub> ClN <sub>4</sub>	222.67	3.21
12	42.09	Eicosapentaenoic acid (EPA)	C <sub>20</sub> H <sub>30</sub> O <sub>2</sub>	302.45	3.77
13	44.19	Heptanal	C <sub>7</sub> H <sub>14</sub> O	114.18	6.78
14	45.12	Humulene epoxide III	C <sub>15</sub> H <sub>24</sub> O	220.35	6

*P. cordatum* germlings ( $P=0.4$ ), or between *S. trochoidea* and *D. acuminata* germlings ( $P=0.8$ ). The highest  $IC_{50}$  ( $0.1 \text{ mg mL}^{-1}$ ) was reported for *C. polykrikos* and *D. acuminata* germlings, while the lowest ( $0.04 \text{ mg mL}^{-1}$ ) was recorded for *P. cordatum* germlings. For ethanol extract, the  $IC_{50}$  values did not exhibit any significant difference ( $P=0.9$ ) among *A. catenella*, *C. polykrikos*, *S. trochoidea* germlings. The highest  $IC_{50}$  ( $0.047 \text{ mg mL}^{-1}$ ) was reported for *D. acuminata* germlings, and the lowest ( $0.012 \text{ mg mL}^{-1}$ ) was reported for *P. cordatum* germlings (Table 1). Regarding progeny cells culturability, the results revealed no significant differences in the  $IC_{50}$  values of all macroalgal materials ( $P=0.2-0.9$ ) among five cyst species (*A. catenella*, *C. polykrikos*, *S. trochoidea*, *P. cordatum* and *D. acuminata*) (Table 2). The lowest  $IC_{50}$  values of all algal materials against cell culturability were incurred in *A. catenella*, whereas the highest values were recorded in *D. acuminata* (Table 2).

### 3.4. GC-MS analysis of *T. ornata* extract

The GC-MS analysis of crude ethanol extract of *T. ornata* revealed the presence of 14 peaks of volatile compounds. The name of these compounds, their molecular mass, molecular formula and percentages were presented in Table 3. The extract contained potential algicidal substances including the halogenated aromatic compound-heptachlor (25.8%), the saturated fatty acid-n-hexadecanoic (4.34%), the unsaturated fatty acid-eicosapentaenoic acid (3.77%), the ester-di-n-octylphthalate (6.97%) and a monocyclic sesquiterpene-humulene epoxide-III (6%).

## 4. Discussion

This study clearly demonstrated that the macroalga *T. ornata* did not affect dinoflagellate cyst germination directly, but rather inhibited the viability of germling cells so that they became unable to produce motile vegetative cells (i.e. impaired the successful recurrence of new planktonic populations). Our results showed that all cysts of tested species could successfully germinate in both control and treatments

(93–99%), but not all germinated cysts could give rise to viable germlings even in control cultures (73%). This agrees with the concept that the cysts would be able to germinate but the germling cells would not be able to divide (Genovesi et al., 2009; Vahtera et al., 2014). Several studies showed that cyst germination and germling viability are largely associated with external environmental factors including temperature, light and oxygen availability (Brosnahan et al., 2020; Genovesi et al., 2009; Vahtera et al., 2014). Regarding the contribution of biotic factors to dinoflagellate cysts, our study is the first to explore the biological interaction between macroalgae and cyst germination. In this study, despite there was no significant effect on cyst germination, the percentages of viable germlings and progeny cells culturability of all cyst species were significantly reduced when exposed to *T. ornata* thalli or its extracts compared to control. This indicates that active substances of this macroalga could inhibit metabolic processes that govern the division and growth of germlings and progeny cells, with no effect on the enzymes involved in the cyst germination. Therefore, vegetative progeny cells survival after excystment is considered as a key factor in the process of dinoflagellate bloom initiation (Mardones et al., 2016), and hence the inhibition of germling cell viability and division of progeny cells of dinoflagellate cysts retards the recurrence of relevant species in the water column. Therefore, the viability of germling cells after excystment represents a bottleneck in the bloom initiation (Genovesi et al., 2009).

Based on  $IC_{50}$  values, dry thalli ( $IC_{50}=0.235-0.543 \text{ mg mL}^{-1}$ ) of *T. ornata* were more effective than fresh thalli ( $IC_{50}=2.201-4.716 \text{ mg mL}^{-1}$ ) against the germling viability and vegetative cell survival ( $IC_{50}=0.385-1.43, 2.17-7.18 \text{ mg mL}^{-1}$ , respectively) of all cyst species. This may be due to the addition of dry macroalgal material to experimental culture tubes as a large pulse so that initial concentrations of active substances were much higher than in fresh thalli. Additionally, the macroalgal ethanol extract was approximately 2–5 times more effective against the germling viability and vegetative motile cells of all cyst species ( $IC_{50}=0.012-0.047$  and  $0.024-0.089 \text{ mg mL}^{-1}$ , respectively) than aqueous extract ( $IC_{50}=0.04-0.1$  and



0.054–0.207 mg mL<sup>-1</sup>, respectively). These results confirmed the evidence that alcoholic solvents like ethanol are more suitable than water in extracting active substances from plants (Emad et al., 2009; Sultana et al., 2009). On the other hand, *T. ornata* extracts exhibited strong inhibitory effects on the germling viability and progeny cells survival compared to fresh and dry thalli. This could be attributed to the low amounts of active substances released from dry or fresh thalli into cyst cultures, compared to high amounts extracted and concentrated from the algal material. This also indicates that allelochemicals are congregated more in macroalgal cells than being released into the surrounding environment (Ye and Zhang, 2013).

The results of this study also showed that the IC<sub>50</sub> values required for the inhibition of germling viability are lower than those inhibiting the cell division and growth of motile vegetative cells (i.e. culturability). This indicates that germling cells are more sensitive towards the active substances of this macroalga than motile vegetative cells. Our experiments also demonstrated that *T. ornata* is a broad-spectrum macroalga, exerting an inhibitory effect on the germling viability and vegetative cells survival of different dinoflagellate cyst species. These results, therefore, support the findings of previous studies reporting the allelopathic inhibitory effects of marine macroalgae including green microalgae (*Ulva*) (Ben Gharbia et al., 2017), brown macroalgae (*Sargassum*) (Wang et al., 2007), and red macroalgae (*Gracilaria*, *Pyropia*) (Patil et al., 2020; Tang et al., 2015) against the growth of several HAB forming microalgae. However, in our study, the sensitivity of germling and vegetative progeny cells to macroalgal materials varied between some species. *A. catenella* and *C. polykrikos* germlings were more sensitive to macroalgal thalli and their extracts than *S. trochoidea*, *P. cordatum* and *D. acuminata* germlings. Whereas vegetative progeny cells of *A. catenella* were the most sensitive ones to all macroalgal materials tested. This indicates that *T. ornata* may affect germlings and progeny cells of dinoflagellate species at various extents. Previously, the brown alga *Ecklonia kurome* was found to inhibit the proliferation of several HAB microalgae, with higher susceptibility exhibited by *Karenia mikimotoi* and *C. polykrikoides* compared to lesser sensitivity reflected by *Chattonella antiqua* (Nagayama et al., 2003). Those authors attributed the inhibitory properties of *E. kurome* to the production of bioactive compounds, phlorotannins. In our study, the inhibitory properties of *T. ornata* against germling and vegetative progeny cells of dinoflagellate species may be due to the presence of a high percentage of heptachlor, which has been previously demonstrated to have anti-algal effects (Zeng et al., 2018). Other bioactive compounds, found with low percentages in *T. ornata* extract including n-hexadecanoic, eicosapentaenoic acid, di-n-octylphthalate and the sesquiterpene-humulene epoxide -III, could also be involved in the inhibitory effects of this macroalga. These compounds have been found in earlier studies to exhibit algicidal activity against red tide microalgae. The saturated fatty acid, n-hexadecanoic isolated from marine green alga *Ulva intestinalis* exerted potent algicidal activity against *Heterosigma akashiwo* and *Prorocentrum micans* (Sun et al., 2016). Eicosapentaenoic acid and di-n-octylphthalate isolated from the red alga *Corallina*

*pilulifera* showed strong algicidal activity against the toxic dinoflagellate, *C. polykrikoides* (Oh et al., 2010; Zerrifi et al., 2018). Sesquiterpenoids from the red alga, *Porphyra yezoensis* significantly inhibited two harmful red tide dinoflagellates, *K. mikimotoi* and *Prorocentrum donghaiense* (Sun et al., 2018). Nevertheless, isolation and identification of these active substances produced by *T. ornata*, and their inhibitory mechanisms on physiological processes of germlings and vegetative progeny cells certainly warrants further investigation for the purpose of controlling and mitigation of HABs.

## 5. Conclusions

Our results provide the first evidence that the brown macroalga *T. ornata* can suppress the germling viability and survival of vegetative progeny cells of dinoflagellate cysts after germination, and thereby could retard the recurrence of blooms of relevant species in the water column. The results revealed that the macroalgal dry powder and its ethanol extract were effectively strong against germling and vegetative progeny cells of dinoflagellate cysts. As macroalgae powders or extracts have been reported as environmentally benign means of potential HAB control (Jeong et al., 2000; Wang et al., 2007), these macroalgal materials of *T. ornata* could be applied to confined coastal areas to inhibit the growth and division of progeny cells after cyst excystment and restrict recurrence of HABs in these regions. In this respect, we pay attention that it is prudent to prevent the growth of harmful microalgae at early stages (i.e. germlings and progeny cells) rather than treatment of algal blooms with algicides that may exacerbate the problem through induction of the cell lysis and releasing tremendous amounts of algal toxins into the aquatic environment. However, prior to application, mesocosm experiments should be carried out to more accurately estimate the proportion of germlings and their progeny that reach the illuminated layers of the water column, in relation to the number of germinated cysts in the presence of macroalgal extracts or powders treatments under the natural environmental conditions. Further research is also required to test the negative effects of *T. ornata* on other organisms, particularly fish and bivalves. This assay could be carried out using oyster larvae as they have been found to be susceptible to pollutants and macroalgal extracts at low concentrations (His et al., 1999; Nelson and Gregg, 2013).

## Acknowledgement

The authors extend their appreciation to the Deanship of Scientific Research, King Khalid University for funding this work through research groups program under grant number R.G.P. 1/25/42. The authors have approved the final article.

## Supplementary materials

Supplementary material associated with this article can be found, in the online version, <https://doi.org/10.1016/j.oceano.2021.09.002>.

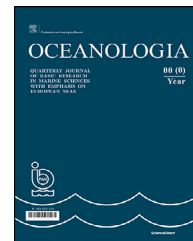
## References

- Anderson, D.M., Fukuyo, Y., Matsuoka, K., 1995. Cyst methodologies. In: Hallegraeff, G.M., Anderson, D.M., Cembella, A.D. (Eds.), *Manual on harmful marine microalgae*. IOC Manuals and Guides, no. 33. UNESCO, Paris, 229–245.
- Anderson, D.M., Keafer, B.A., Kleindinst, J.L., McGillicuddy, D.J., Martin, J.L., Norton, K., Pilskaln, C.H., Smith, J.L., Sherwood, C.R., Butman, B., 2014. *Alexandrium catenella* cysts in the Gulf of Maine: long-term time series of abundance and distribution, and linkages to past and future blooms. *Deep-Sea Res. Pt. II* 103, 6–26. <https://doi.org/10.1016/j.dsr2.2013.10.002>
- Ben Gharbia, H., Kéfi-Daly Yahia, O., Cecchi, P., Masseret, E., Amzil, Z., Herve, F., Rovillon, G., Nouri, H., M'Rabet, C., Couet, D., Triki, H.Z., Laabir, M., 2017. New insights on the species-specific allelopathic interactions between macrophytes and marine HAB dinoflagellates. *PLoS ONE* 12, e0187963. <https://doi.org/10.1371/journal.pone.0187963>
- Bravo, I., Figueroa, R.I., 2014. Towards an ecological understanding of dinoflagellate cyst functions. *Microorganisms* 2, 11–32. <https://doi.org/10.3390/microorganisms2010011>
- Brosnahana, M.L., Fischerb, A.D., Lopezc, C.B., Stephanie, K., Moored, S.K., Andersona, D.M., 2020. Cyst-forming dinoflagellates in a warming climate. *Harmful Algae* 91, 101728. <https://doi.org/10.1016/j.hal.2019.101728>
- Emad, M.A., Amna, S.K., Nazlina, I., 2009. Antibacterial activity of oleo-gum resins of *Commiphora molmol* and *Boswellia papyrifera* against methicillin resistant *Staphylococcus aureus* (MRSA). *Sci. Res. Essays* 4, 351–356.
- Figueroa, R.I., Garces, E., Bravo, I., 2007. Comparative study of the life cycles of *Alexandrium tamutum* and *Alexandrium minutum* (Gonyaulacales, Dinophyceae) in culture. *J. Phycol.* 43, 1039–1053. <https://doi.org/10.1111/j.1529-8817.2007.00393.x>
- Genovesi, B., Laabir, M., Masseret, E., Collos, Y., Vaquer, A., Grzebyk, D., 2009. Dormancy and germination features in resting cysts of *Alexandrium tamarense* species complex (Dinophyceae) can facilitate bloom formation in a shallow lagoon (Thau, southern France). *J. Plankton Res.* 31, 1209–1224. <https://doi.org/10.1093/plankt/fbp066>
- Guiry, M.D., Guiry, G.M., 2011. *AlgaeBase*. World-wide electronic publication. National University of Ireland, Galway. <http://www.algaebase.org>
- His, E., Beiras, R., Searman, M.N.L., 1999. The assessment of marine pollution: bioassays with bivalve embryos and larvae. *Adv. Mar. Biol.* 37, 1–178. [https://doi.org/10.1016/S0065-2881\(08\)60428-9](https://doi.org/10.1016/S0065-2881(08)60428-9)
- Jeong, J.H., Jin, H.J., Sohn, C.H., Suh, K.H., Hong, Y.K., 2000. Algicidal activity of the seaweed *Corallina pilulifera* against red tide microalgae. *J. Appl. Phycol.* 12, 37–43. <https://doi.org/10.1007/s10811-009-9478-x>
- Jin, Q., Dong, S., 2003. Comparative studies on the allelopathic effects of two different strains of *Ulva pertusa* on *Heterosigma akashiwo* and *Alexandrium tamarense*. *J. Exp. Mar. Bio. Ecol.* 293, 41–55. [https://doi.org/10.1016/S0022-0981\(03\)00214-4](https://doi.org/10.1016/S0022-0981(03)00214-4)
- Kientz, B., Thabard, M., Cragg, S.M., Pope, J., Hellio, C., 2011. A new method for removing microflora from macroalgal surfaces: an important step for natural product discovery. *Bot. Mar.* 54, 457–469. <https://doi.org/10.1515/BOT.2011.053>
- Kremp, A., 2001. Effects of cyst resuspension on germination and seeding of two bloom-forming dinoflagellates in the Baltic Sea. *Mar. Ecol. Prog. Ser.* 216, 57–66. <https://doi.org/10.3354/meps216057>
- Lewitus, A.J., Horner, R.A., Caron, D.A., Garcia-Mendoza, E., Hickey, B.M., Hunter, M., Huppert, D.D., Kudela, R.M., Langlois, G.W., Largier, J.L., Lessarde, J., Ralonde, R., Rensel, J.E.J., Strutton, P.G., Trainer, V.I., 2012. Harmful algal blooms along the North American west coast region: history, trends, causes, and impacts. *Harmful Algae* 19, 133–159. <https://doi.org/10.1016/j.hal.2012.06.009>
- Mardones, J.I., Bolch, C., Guzmán, L., Paredes, J., Varela, D., Hallegraeff, G.M., 2016. Role of resting cysts in Chilean *Alexandrium catenella* dinoflagellate blooms revisited. *Harmful Algae* 55, 238–249. <https://doi.org/10.1016/j.hal.2016.03.020>
- Miyazono, A., Nagai, S., Kudo, I., Tanizawa, K., 2012. Viability of *Alexandrium tamarense* cysts in the sediments of Funaka bay, Hokkaido, Japan: over a hundred year survival times for cysts. *Harmful Algae* 16, 81–88. <https://doi.org/10.1016/j.hal.2012.02.001>
- Mohamed, Z.A., 2018. Potentially harmful microalgae and algal blooms in the Red Sea: Current knowledge and research needs. *Mar. Environ. Res.* 140, 234–242. <https://doi.org/10.1016/j.marenvres.2018.06.019>
- Mohamed, Z.A., Al-Shehri, A.M., 2011. Occurrence and germination of dinoflagellate cysts in surface sediments from the Red Sea off the coasts of Saudi Arabia. *Oceanologia* 53 (1), 121–136. <https://doi.org/10.5697/oc.53-1.121>
- Mohamed, Z.A., Al-Shehri, A.M., 2012. The link between shrimp farm runoff and blooms of toxic *Heterosigma akashiwo* in the Red Sea coastal waters. *Oceanologia* 54 (2), 287–309. <https://doi.org/10.5697/oc.54-2.287>
- Mohamed, Z.A., Mesaad, I., 2007. First report on *Noctiluca scintillans* blooms in the Red Sea off the coasts of Saudi Arabia: consequences of eutrophication. *Oceanologia* 49 (3), 337–351.
- Nagayama, K., Shibata, T., Fujimoto, K., Honjo, T., Nakamura, T., 2003. Algicidal effect of phlorotannins from the brown alga *Ecklonia kurome* on red tide microalgae. *Aquaculture* 218, 601–611. [https://doi.org/10.1016/S0044-8486\(02\)00255-7](https://doi.org/10.1016/S0044-8486(02)00255-7)
- Nelson, T.A., Gregg, B.C., 2013. Determination of EC<sub>50</sub> for normal oyster larval development in extracts from bloom-forming green seaweeds. *Nautilus* 127, 156–159.
- Oh, M.Y., Lee, S.B., Jin, D.H., Hong, Y.K., Jin, H.J., 2010. Isolation of algicidal compounds from the red Alga *Corallina pilulifera* against red tide microalgae. *J. Appl. Phycol.* 22, 453–458. <https://doi.org/10.1007/s10811-009-9478-x>
- Patil, V., Abate, R., Wu, W., Zhang, J., Lin, H., Chen, C., Liang, J., Sun, L., Li, X., Li, Y., Gao, Y., 2020. Allelopathic inhibitory effect of the macroalga *Pyropia haitanensis* (Rhodophyta) on harmful bloom-forming *Pseudo-nitzschia* species. *Mar. Pollut. Bull.* 161, 111752. <https://doi.org/10.1016/j.marpolbul.2020.111752>
- Pfiester, L.A., Anderson, D.M., 1987. *Dinoflagellate life cycles and their environmental control*. In: Taylor, F.J.R. (Ed.), *The Biology of Dinoflagellates*. Blackwell Sci. Publ., 611–648.
- Salama, A.J., Satheesh, S., Balqadi, A.A., 2018. Antifouling activities of methanolic extracts of three macroalgal species from the Red Sea. *J. Appl. Phycol.* 30, 1943–1953. <https://doi.org/10.1007/s10811-017-1345-6>
- Sultana, B., Anwar, F., Ashraf, M., 2009. Effect of extraction solvent/technique on the antioxidant activity of selected medicinal plant extracts. *Molecules* 14, 2167–2180. <https://doi.org/10.3390/molecules14062167>
- Sun, A., Li, C., Lan, D., Zhu, Y., 2007. *Dinoflagellate Cysts Records from Core Samples of Modern Marine Sediment at the Luoyuan Bay Mouth*. *Mar. Sci. Bull.* 9, 36–45.
- Sun, X., Jin, H., Zhang, L., Hu, W., Li, Y., Xu, N., 2016. Screening and isolation of the algicidal compounds from marine green alga *Ulva intestinalis*. *Chin. J. Oceanol. Limnol.* 34, 781–788. <https://doi.org/10.1007/s00343-016-4383-z>
- Sun, Y.Y., Xing, J.Z., Zhang, J.S., Zhou, W.J., Pu, Y.F., 2018. Sesquiterpenoids with anti-algal activity against the common red tide microalgae from marine macroalga *Porphyra yezoensis*. *Environ. Sci. Pollut. Res.* 25, 7844–7859. <https://doi.org/10.1007/s11356-017-0958-2>
- Tang, Y.Z., Kang, Y., Berry, D., Gobler, C.J., 2015. The ability of the red macroalga, *Porphyra purpurea* (Rhodophyceae) to

- inhibit the proliferation of seven common harmful microalgae. *J. Appl. Phycol.* 27, 531–544. <https://doi.org/10.1007/s10811-014-0338-y>
- Vahtera, E., Crespo, B.G., McGillicuddy Jr, D.J., Olli, K., Anderson, D.M., 2014. *Alexandrium fundyense* cyst viability and germling survival in light vs. dark at a constant low temperature. *Deep-Sea Res. Pt. II.* 103, 112–119. <https://doi.org/10.1016/j.dsr2.2013.05.010>
- Ye, C., Zhang, M., 2013. Allelopathic effect of macroalga *Gracilaria tenuistipitata* (Rhodophyta) on the photosynthetic apparatus of red-tide causing microalga *Prorocentrum micans*. *IERI Procedia* 5, 209–215. <https://doi.org/10.1016/j.ieri.2013.11.094>
- Wang, Z.-H., Qi, Y.Z., Yang, Y.F., 2007. Cyst formation: an important mechanism for the termination of *Scrippsiella trochoidea* (Dinophyceae) Bloom. *J. Plankton Res.* 29, 209–218. <https://doi.org/10.1093/plankt/fbm008>
- Zeng, H., Fu, X., Liang, Y., Qin, L., Mo, L., 2018. Risk assessment of an organochlorine pesticide mixture in the surface waters of Qingshitan Reservoir in Southwest China. *RSC Adv.* 8, 17797–17805. <https://doi.org/10.1039/c8ra01881b>
- Zerrifi, S.E.A., El Khalloufi, F., Oudra, B., Vasconcelos, V., 2018. Seaweed bioactive compounds against pathogens and microalgae: Potential uses on pharmacology and harmful algae bloom control. *Mar. Drugs* 16, 55. <https://doi.org/10.3390/md16020055>

Available online at [www.sciencedirect.com](http://www.sciencedirect.com)

ScienceDirect

journal homepage: [www.journals.elsevier.com/oceanologia](http://www.journals.elsevier.com/oceanologia)

## ORIGINAL RESEARCH ARTICLE

# Spatial variability of summer hydrography in the central Arabian Gulf

Elnaiem Ali Elobaid\*, Ebrahim M.A.S. Al-Ansari, Oguz Yigiterhan,  
Valliyl Mohammed Aboobacker, Ponnumony Vethamony

*Environmental Science Center (ESC), Qatar University, Doha, Qatar*

Received 27 April 2021; accepted 16 September 2021

Available online 12 October 2021

**KEYWORDS**

Arabian Gulf;  
Exclusive Economic  
Zone (EEZ) of Qatar;  
Physicochemical  
parameters;  
Water masses;  
Stratification

**Abstract** The Arabian Gulf is a very significant ocean body, which hosts more than 55% of the oil reserves of the world and produces about 30% of the total production, and thus, it is likely to face high risk and adverse problems by the intensified environmental stressors and severe climatic changes. Therefore, understanding the hydrography of the Gulf is very essential to identify various marine environmental issues and subsequently, developing marine protection and management plans. In this study, hydrography data collected at 11 stations along 3 linear transects in the early summer of 2016 were analyzed. The physicochemical parameters exhibited apparent variations along each transect, both laterally and vertically, connected to stratification, formation of different water masses and excessive heating. The temperature and salinity decreased laterally from nearshore to offshore, while layered density structures were identified in the offshore regions. The pH, dissolved oxygen (DO) and chlorophyll fluorescence (Fo) exhibited distinct horizontal and vertical variations. The observed pH is within the normal ranges, indicating that seawater acidification may not be a threat. The highest DO (6.13–8.37

\* Corresponding author at: Environmental Science Center (ESC), Qatar University, P.O. Box 2713, Doha, Qatar.

E-mail addresses: [elnaiemali123@gmail.com](mailto:elnaiemali123@gmail.com), [elnaiem@qu.edu.qa](mailto:elnaiem@qu.edu.qa) (E.A. Elobaid).

Peer review under the responsibility of the Institute of Oceanology of the Polish Academy of Sciences.



mg/l) was observed in a layer of 24–36 m water depth in the deeper regions of the central transect.

© 2021 Institute of Oceanology of the Polish Academy of Sciences. Production and hosting by Elsevier B.V. This is an open access article under the CC BY-NC-ND license (<http://creativecommons.org/licenses/by-nc-nd/4.0/>).

## 1. Introduction

The Arabian/Persian Gulf (hereafter “Gulf”) is a significant pathway from regional and international perspectives, hosting more than 55% of the oil reserves of the world and producing about 30% of the total world oil production (BP, 2011; Soliman et al., 2019). Thus, the Gulf is likely to face high risk and adverse environmental problems due to intensified natural and anthropogenic stressors in addition to climate change effects. The semi-enclosed Gulf is a western arm of the Indian Ocean, covering an area of  $\approx 233,100 \text{ km}^2$ , length of  $\approx 1,000 \text{ km}$ , the maximum width of  $\approx 338 \text{ km}$ , with an average depth of about 36 m (Kampf and Sadrinasab, 2006). This unique physical setting extends within the most saline hyper-arid climate zone of the Arabian Peninsula desert belt, situated within the photic zone, as one of the most saline and hottest water bodies (Sheppard, 1993). In general, the Gulf is characterized by a tidal range of more than 1 m everywhere, with diurnal and semi-diurnal oscillations. The central Gulf waters are characterized by high salinity, which varies between 40 and 50 (Hunter, 1986). This is attributed to the high evaporation rate, which ranges from 144 to 500 cm/y (Brewer and Dyrssen, 1985). These combined factors make the system a reverse estuary and create an anticlockwise Mediterranean-like flow (Al-Majed et al., 2000; Reynolds, 1993; Yoshida et al., 1998).

The Gulf is subject to harsh natural and anthropogenic environmental stressors such as high salinity and extreme temperature during summer. The anthropogenic influence on salinity along the Arabian coast of the central part of the Gulf is mainly due to brine discharge from the desalination plants, resulting in adverse impacts on the marine ecosystem, particularly in the spatial distribution, diversity, existence and abundance of living organisms in this environment (Jones et al., 2002; Prasad et al., 2001; Privett, 1959; Soliman et al., 2019). Despite these harsh conditions, the Gulf hosts distinctive assemblage and habitats (Sheppard et al., 2010), but the natural environmental stressors have been reflected and witnessed by a decrease in the species richness levels (Price, 2002). The hypersalinity has adverse issues on the living organisms of the ecosystem (Joydas et al., 2015). For example, unhealthy benthic communities living in the hypersaline (salinity up to 63) region like the Gulf of Salwa are under high risk of radical natural stressors in comparison with the healthiest benthic communities living in relatively lower salinity regions of the Gulf (such as the east coast of Qatar and the coast of UAE). Moreover, the key physicochemical parameters of the water column, namely, temperature and salinity, influence the dissolution processes, affinity adsorption and mobility of pollutants in the marine environment (Ma et al., 2016; Soliman et al., 2019).

The small and limited freshwater input and high evaporation rate have influence and control on the circula-

tion and water masses of the Gulf (Campos et al., 2020; John et al., 1990; Prasad et al., 2001; Reynolds, 1993), and hence the information on physical oceanographic parameters such as temperature, salinity and density is vital to analyze the horizontal and vertical distribution of the water masses and to assess the diffusive and advection transports within the water column (Al Azhar et al., 2016; Kampf and Sadrinasab, 2006; Pous et al., 2015). The circulation characteristics are important to determine the distribution of sediments, dynamics of nutrients and fate of pollutants (Soliman et al., 2019). Beltagy (1983) reported that the main controlling factors of vertical and horizontal salinity distribution in the Gulf are higher rates of evaporation, seepage of fresh water, brine discharges and evaporitic deposits. The spatial distribution pattern of salinity and temperature have been investigated previously by several researchers (Beltagy, 1983; Emery, 1956; Kampf and Sadrinasab, 2006; Reynolds, 2002; Shepherd, 1993). They reported that the salinity decreases towards the offshore areas, and increases within the coastal areas and ports, whereas temperature decreases from the coastline towards the offshore and also decreases as depth increases.

A detailed understanding of spatial variability of physicochemical parameters is important to analyze the physical and biogeochemical interactions and their impact on the marine ecosystem of the central Gulf. There are very few studies in this part of the Gulf on the spatial variability of physical and biogeochemical parameters. The present study aims at understanding the spatial variability in the physicochemical parameters of the central Gulf by analyzing the measured hydrographic data during summer. The role of different water masses and seasonal stratification in the biogeochemical processes of Qatar’s Exclusive Economic Zone (QEEZ) have been addressed. The study also explores the statistical relationship between various physicochemical key parameters.

The paper is organized as follows: Section 2 describes the area of study, Section 3 explains the data and methodology used, Section 4 explains the important results and their discussions, and Section 5 summarizes the major inferences.

## 2. Area of study

The Qatar Peninsula is situated in the central Gulf with an area of  $11,437 \text{ km}^2$ , centered at  $25^\circ\text{N}$  and  $51^\circ\text{E}$ . The EEZ of Qatar is located between the longitudes  $51^\circ00'\text{E}$  and  $52^\circ30'\text{E}$  and latitudes  $24^\circ50'\text{N}$  and  $26^\circ58'\text{N}$  (Figure 1), with an area of  $35,000 \text{ km}^2$  (Al-Ansari, 2006). The winds are predominantly from the NW-N directional sector, where the highest wind speeds of the order of 22 m/s are due to shamal winds (Aboobacker et al., 2021a). The surface currents within the QEEZ are mainly wind-driven; however, the deeper regions are influenced by thermohaline circulation

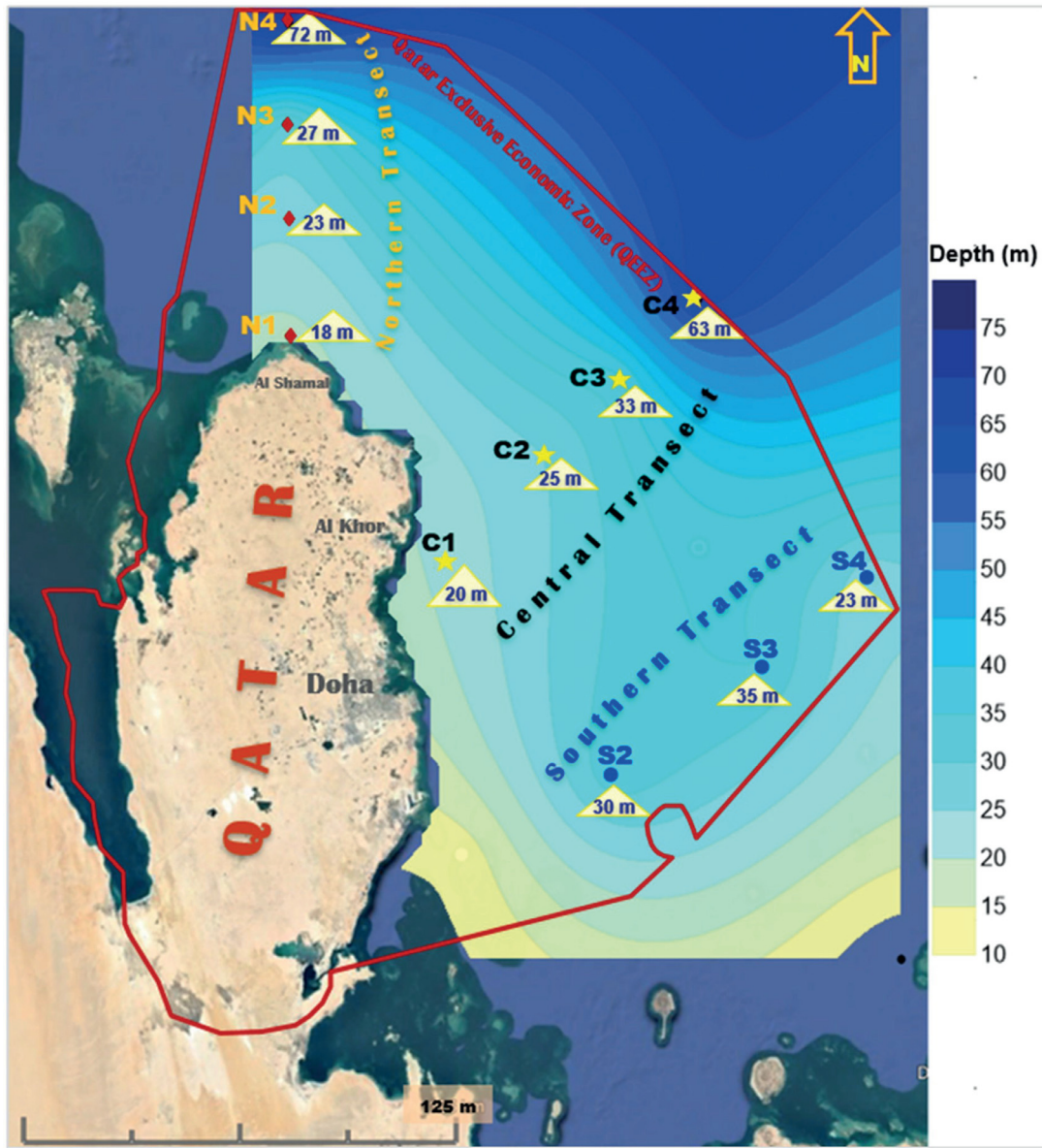


**Figure 1** Area of study with sampling stations along the three transects together with generalized bathymetry (bathymetry data is retrieved from Ocean Data View). The water depth of each station, measured using echo-sounder onboard r/v *Janan*, is given inside the yellow triangle. Bathymetry contours are generated using Surfer software.

(Chao et al., 1992; Thoppil and Hogan, 2010). The physical processes such as circulation, eddy formation and sedimentation in the QEEZ are largely influenced by the geographical setting of the Qatar peninsula, which in turn influence the development/survival of the ecosystem (Al-Ansari, 2006).

In this study, we considered 3 major transects with a total of 11 stations. The transects are directed from the coastline towards the deep sea, more or less perpendicular to the coast as shown in Figure 1. The southern transect is about 110 km long, occupying three stations S2, S3 and S4; the central transect is about 100 km long with four stations C1, C2, C3 and C4; the northern transect is about 90 km long with four stations N1, N2, N3 and N4.

### 3. Data and methodology

The physicochemical parameters such as temperature (T), salinity (S), density (D), pH, dissolved oxygen (DO), chlorophyll fluorescence and the water column depth were measured using Seabird-911plus CTD and auxiliary sensors, manufactured by Seabird Scientific Company and used onboard R.V *Janan*. Seasoft software was integrated to the CTD system for the simultaneous processing of the data. The vertical sampling frequency of the CTD was set to 1.0 m. The bin size was 1.0 m and the raw data was averaged over each bin. The accuracies of conductivity, temperature and pressure are  $\pm 0.0003$  S/m,  $\pm 0.001^\circ$  and 0.015% of full-scale range, respectively. The potential density ( $\sigma_t$ ), calculated us-

ing the formula described in Fofonoff and Millard (1983), was obtained from the CTD records.

The processed physicochemical parameters have been analyzed to derive their spatial variabilities. Ocean Data Viewer (ODV) software version 5.03 was used to create the 2D profiles of temperature, salinity, density, pH, dissolved oxygen (DO), and fluorescence (Schlitzer, 2020). The Pearson correlation matrix method was performed using SPSS version 25 to evaluate the statistical relationship between the physicochemical key parameters.

## 4. Results and discussion

### 4.1. Distribution of temperature, salinity and density

The distribution of physicochemical parameters in the Gulf is primarily controlled by the geographical settings, air-sea interactions and ocean processes (Figure S1). For instance, higher salinity is observed along the Arabian coast of the Gulf, where the evaporation is much higher (144 cm/y) and the freshwater influx is very low (1,456 m<sup>3</sup>/s) (Reynolds, 1993). As a result, higher salinity water masses are formed in the southern coast of the Gulf (Al-Ansari, 2006 and Rivers et al., 2019). In addition to natural processes, anthropogenic forcing in the form of brine discharges from the desalination plants operated along the Arabian coasts may also add an accountable amount of salinity to the nearshore waters, although their impact in the deeper waters is not that significant (Ibrahim et al., 2020; Ibrahim and Eltahir, 2019; Rakib et al., 2021). Our analysis shows that higher salinity in each transect is found in the nearshore stations, and the salinity gradually decreases towards offshore as shown in the generalized spatial contour map (Figure 2).

A wedge-like intrusion of low saline water is visible in the offshore, deeper regions of the central transect, which is quite unique compared to the other two transects. This is in agreement with the pattern of low salinity intrusion identified from the Arabian Sea to the Gulf by Ghaemi et al. (2021). This is linked with the exchanges between the Gulf of Oman and the Arabian Gulf, which are driven by the differences in sea surface heights of the two regions (Swift and Bower, 2003) and also due to baroclinic forcing developed by the density gradients (Chao et al. 1992; Yao and Johns, 2010). The exchanges are intensified following an enhanced two-layer flow during late winter through early summer, whilst the flow diminishes during mid-summer to mid-winter (Vasou et al., 2020). Among the three transects, the highest salinity is found in the northern transect, and it could be attributed to the following reasons: (i) higher evaporation due to relatively stronger winds in the offshore region (deeper) compared to the nearshore region (shallower) (Aboobacker et al., 2021b), (ii) considerable heating because of very shallow depths, (iii) advection of hypersaline Gulf of Salwa Water (GSW) (Al-Ansari et al., 2015) and (iv) dispersion of brine discharged from the desalination plants situated along the northeast coast of Qatar. The higher evaporation along with dense water flow from the northern Gulf has got prime importance in higher salinity in the northern tran-

sect (Smith et al., 2007). Recent studies point out that the hypersalinity in the southwestern Gulf at specific locations can also be attributed to the presence of desalination plants (Ibrahim and Eltahir, 2019), though the general surface circulation of the Gulf does not permit building-up of salinity.

In the nearshore regions of the northern transect, temperature, salinity and density are relatively higher compared to the surface layer of other stations (Figure 3a1, a2, a3). The temperature and salinity in the nearshore regions are vertically homogeneous due to limited depths of the water column, whereas they decrease from nearshore to offshore. In the offshore, there is a distinct vertical variability in temperature and salinity, especially with substantially low saline water in the surface layer and low temperature in the bottom layer both leading to vertical stratification. These differences are reflected in the density distribution with distinct patterns, indicating the presence of two water masses. Earlier studies indicate that the low salinity water mass, Indian Ocean Surface Water (IOSW) intrudes up to the central Gulf during summer (Kampf and Sadrinasab, 2006). Although similar features (salinity and density variations) are found in the central transect, more investigations are needed to establish the intrusion of IOSW up to the east coast of Qatar as the salinity differences obtained in this study are relatively small. In addition, the sea surface temperature (SST) has shown little variation from nearshore to offshore (Figure 3b1, b2, b3), which is due to the excessive surface heating distributed equally in the central Gulf during summer compared to the other regions (Van Lavieren et al., 2011). Interestingly, there is a sublayer of intermediate density, indicating the role of eddies in the central Gulf (Reynolds, 1993). The low salinity surface water of the order of 38.5–40.0 and 38.2–39.5 in the northern and central transects, respectively, point to the exchange of low salinity water from the Sea of Oman to the offshore regions of QEEZ. The region of influence of this low salinity surface water and the dense bottom water is small in the southern transect as identified by their minimal vertical variations (Figure 3c2, c3). The vertical variation in temperature is also not significant in this transect (Figure 3c1).

The vertical variation in temperature, salinity and density is significant only in the deepest stations among all the transects (Figures 4a, b, c). The temperature variations in the northern, central and southern transects during early summer are in the range of 19.9°–30.2°C, 20.2°–28.4°C and 26.8°–28.7°C, respectively (Table S1). The salinity variations in the above transects are 38.7–42.2, 38.5–40.9 and 39.6–40.1, respectively. Previous studies identified a significantly higher salinity (above 44) along the nearshore regions of Doha and Mesaieed, the central east coast of Qatar during the summer of 2000 (Abdel-Moati and Al-Ansari, 2000; Rakib et al., 2021). However, our present analysis does not represent these coastal stations as they are far from the transects under consideration. It is worthy to note that the central east coast of Qatar is housing several desalination plants, which are discharging a high amount of brine into the sea. In the GCC countries, for every 1 m<sup>3</sup> fresh water produced, 2 m<sup>3</sup> brine is generated and discharged into the Gulf (Sezer et al., 2017). Brine can drop the level of DO in seawater near desalination plants with "profound impacts" on benthic biota such as shellfish and crabs on the seabed. The ambient salinity in the vicinity of the outfalls might have in-

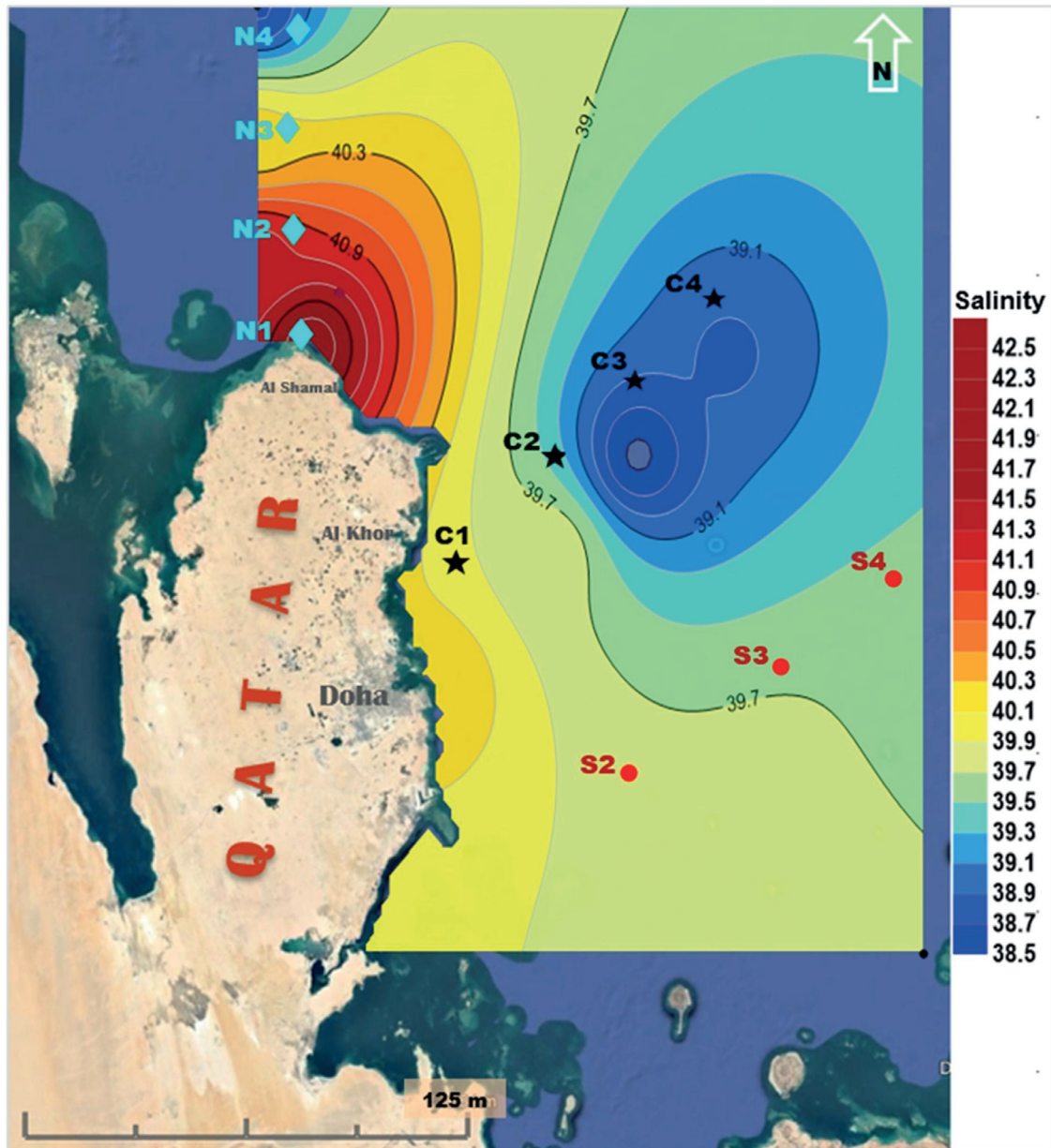


**Figure 2** Generalized spatial contours of sea surface salinity (SSS) at 5 m depth derived from the CTD measurements along the three transects.

creased due to the hypersaline influx. A detailed investigation on the cumulative impact of the discharged brine over a longer period of time in the QEEZ is yet to be conducted to quantify the anthropogenic influence on the hyper salinification of the nearshore waters of the central east coast of Qatar. The changes in salinities within the water mass is likely to affect the growth of some of the marine organisms (Joydas et al., 2015). Consequently, brine discharges lead to negative ecological impacts observable throughout the food chain in the Gulf.

#### 4.2. Water masses in the QEEZ

The water masses in the QEEZ have been determined by analyzing the T-S diagram of each transect (Figure 5). The

Qatar Shallow Water (QSW) with the density between 24.98 and 27.55 kg/m<sup>3</sup> has been identified at all the transects, which is characterized by high temperature, low salinity and low density (Figure 5a). The Qatar Deep Water (QDW) with the density between 27.87 and 29.32 kg/m<sup>3</sup> has been identified in the northern and central transects, which is characterized by low temperature, high salinity and high density (Figure 5b). Recently, Rakib et al. (2021) identified these two water masses during the late summer (September 2014) in a deep-water location, adjacent to the deepest station in the central transect, but with an increased SST due to seasonal transformation from early summer to late summer. The Qatar Intermediate Water (QIW) with distinct values of temperature, salinity and density has been observed in between QSW and QDW in the central transect (Figure 5c). This



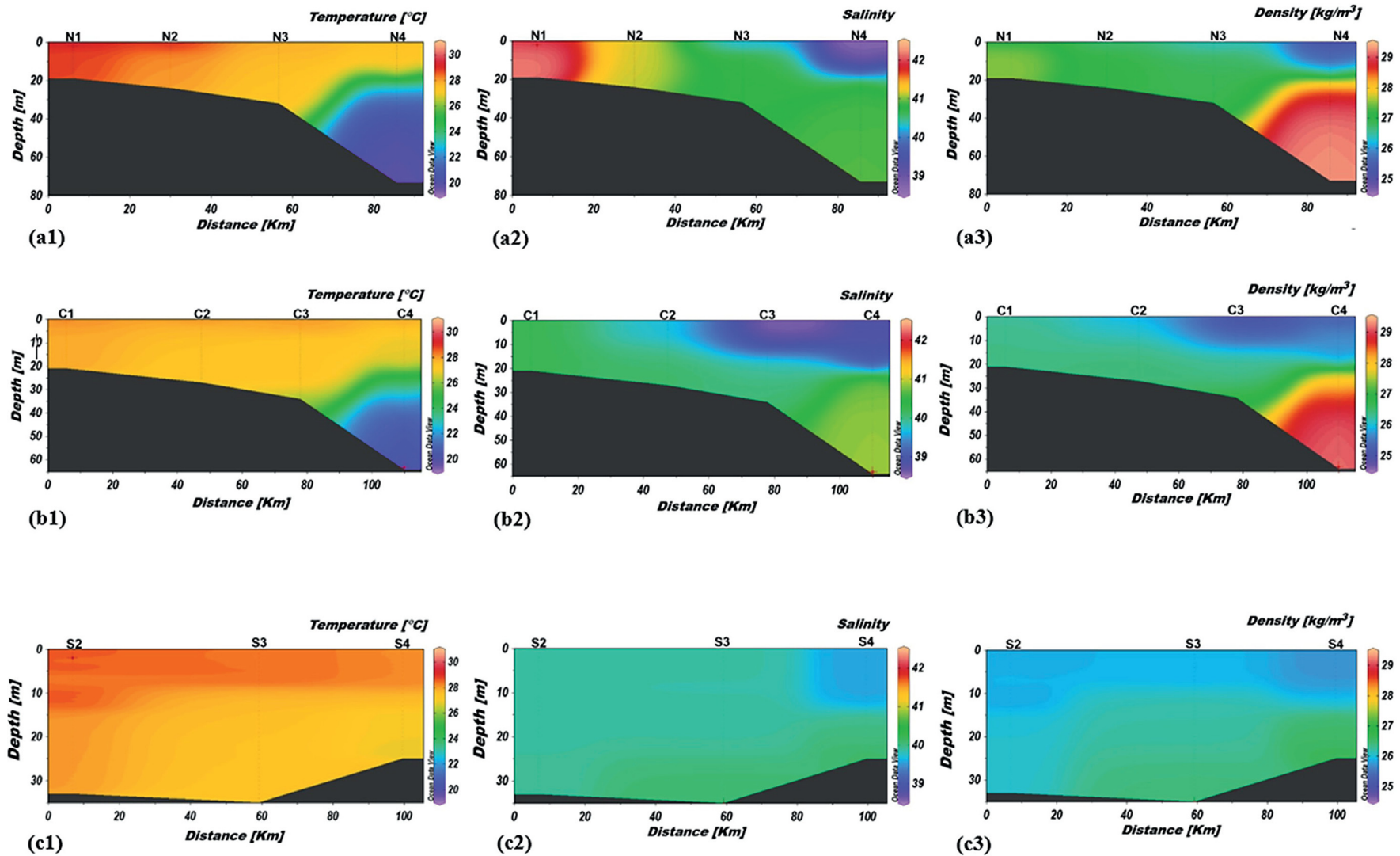
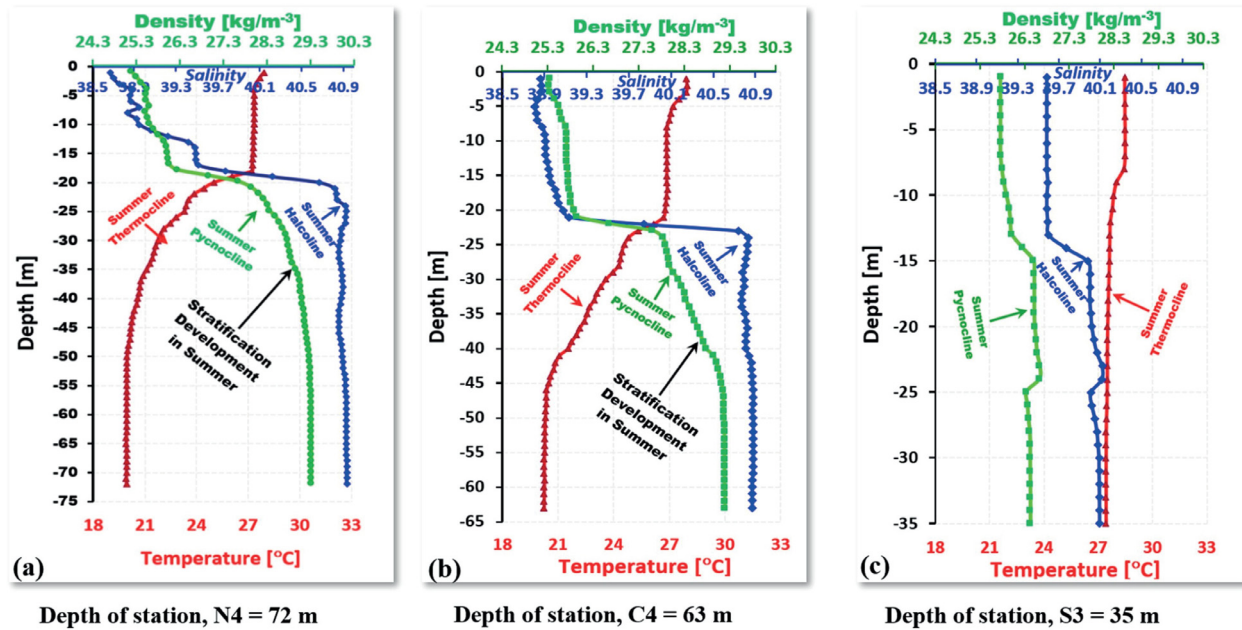
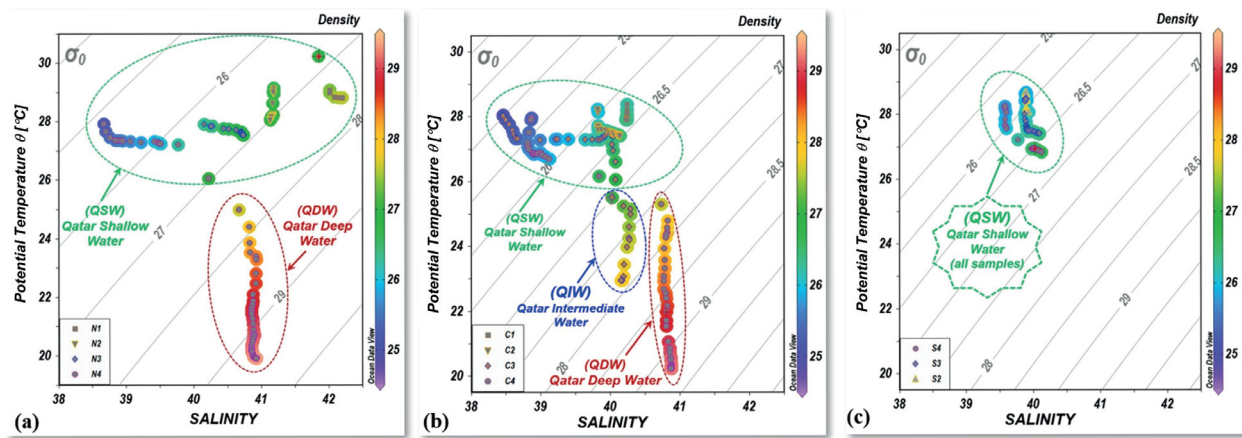


Figure 3 2D profiles of the measured temperature (a1, b1 and c1), salinity (a2, b2, c2) and density (a3, b3, c3) along the northern (a), central (b) and southern (c) transects. The plots are made using Ocean Data View Software, Version 5.03, (Schlitzer, 2020).



**Figure 4** Vertical profiles of temperature, salinity and density at the deepest stations in the northern (a), central (b) and southern (c) transects. The plots are made using Microsoft Excel Data Analysis Tool.



**Figure 5** (a)  $\theta/S$  diagram derived from the measurements during May 28–30, 2017: (a) Qatar Shallow Water (QSW) and Qatar Deep Water (QDW) identified at the deepest station (N4=72m) in northern transect, (b) Qatar Shallow Water (QSW), Qatar Intermediate Water (QIW) and Qatar Deep Water (QDW) identified at the deepest station (C4=67m) in central transect and (c) Qatar Shallow Water (QSW) identified in the southern transect. The plots are made using Ocean Data View Software, Version 5.03, (Schlitzer, 2020).

is consistent with that identified from the measurements of July 2000.

The physicochemical properties of the water masses in the QEEZ, namely, Qatar Central Arabian Gulf Water (QCAGW) during summer is quite different from those derived for the water masses (listed in Table 1) at different regions in the Gulf (Al-Said et al., 2018). Though the distinct variation in temperature is observed among all the water masses, only in the QCAGW, wider variation is found. The salinity difference in the Indian Ocean Surface Water (IOSW) and Central Arabian Coastal Water (CACW) is relatively small, while that in the QCAGW is relatively higher. DO ranges widely in QCAGW compared to other water masses, and pH has no significant variations among the water masses in the Gulf.

### 4.3. Distribution of pH, dissolved oxygen and fluorescence

The pH in each transect shows distinct variations horizontally and vertically (Figure 6a1, b1, c1). Although small, the variations in pH are consistent with the water mass distributions, especially in the deep-water regions of northern and central transects. In the central transect, the highest pH (~8.2) is in the subsurface layer, which clearly depicts the presence of QIW. The variations in pH among all the transects (8.01–8.21) are well within the acceptable limits of the oceanic waters, where the average pH of seawater could be around 8.1 (Fallatah et al., 2018).

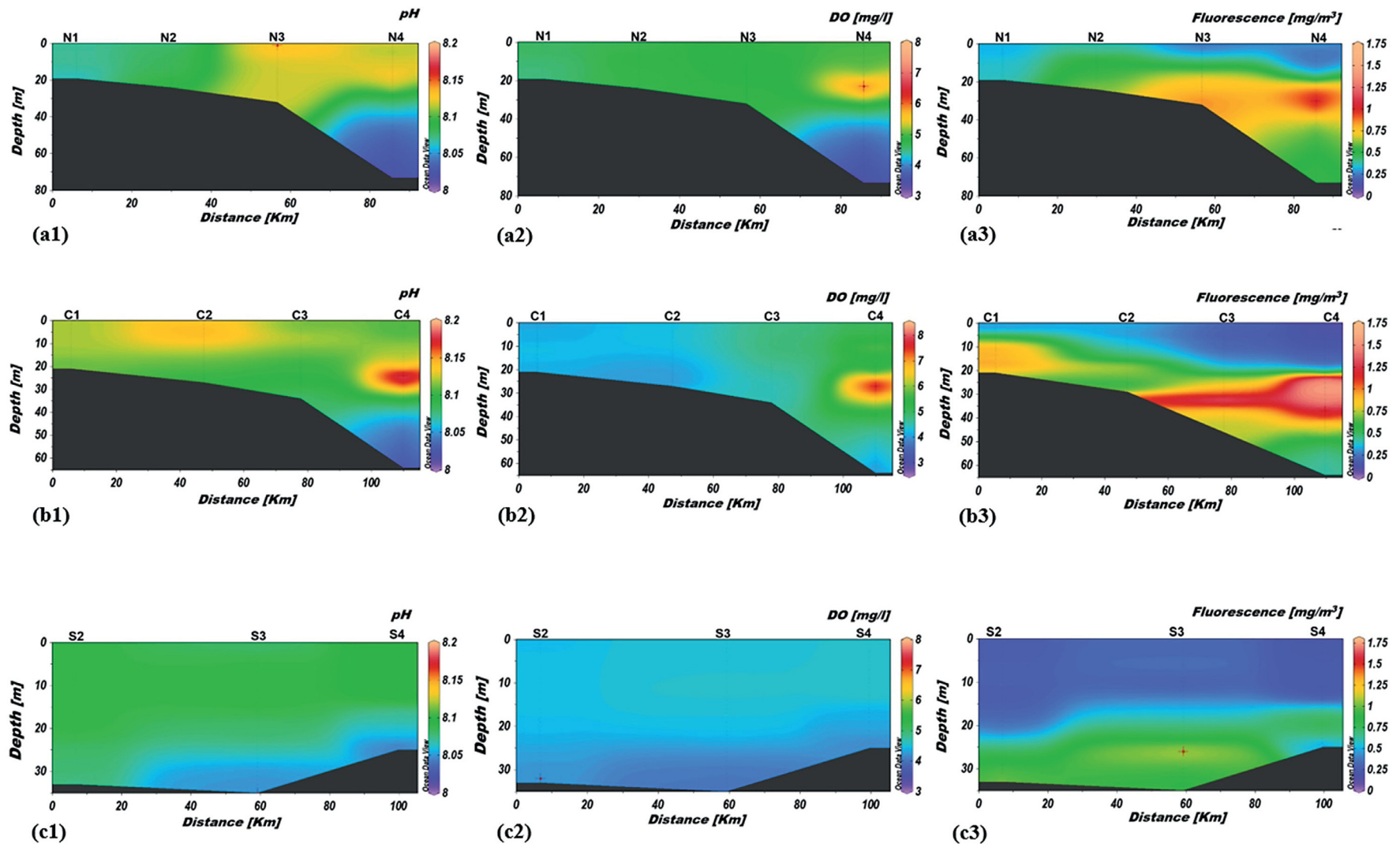


Figure 6 2D profiles of the measured pH (a1, b1, c1), DO (a2, b2, c2) and fluorescence ( $\text{mg/m}^3$ ) (a3, b3, c3) along the northern central and southern transects. The plots are made using Ocean Data View Software, Version 5.03 (Schlitzer, 2020).

**Table 1** The physicochemical parameters in the composite water masses in the study area: Qatar Central Arabian Gulf Water (QCAGW) and their comparison with those in the Kuwait Coastal Waters (KCW), Northern Gulf Waters (NGW), Central Arabian Coastal Waters (CACW) and Indian Ocean Surface Water (IOSW) (after Al-Said et al., 2018).

Parameters	KCW*	NGW*	CACW*	IOSW*	QCAGW (present study)
Temperature (°C)	32.4–32.8	32.8–34.0	33.9–34.6	32.7–35.4	19.9–30.23
Salinity	40.8–41.1	39.2–40.7	38.1–39.9	38.8–40.2	38.46–42.20
DO (ml/l)	4.8–5.1	4.7–5.3	4.0–5.8	4.5–5.3	3.43–8.37
pH	7.9–7.9	7.7–8.0	8.0–8.2	7.7–8.1	4.3–8.21

**Table 2** Correlation matrix derived for the physicochemical parameters of northern, central and southern transects; <sup>a</sup>positive correlation significant at  $p=0.01$ , <sup>b</sup>positive correlation significant at  $p=0.05$ , <sup>c</sup>negative correlation significant at  $p=0.01$  and <sup>d</sup>negative correlation significant at  $p=0.05$  (only significant correlations are given).

Transects	Parameters	Temperature (°C)	Salinity	Density (kg/m <sup>3</sup> )	pH	DO (mg/l)	Fluorescence (mg/m <sup>3</sup> )
<b>Northern</b>	Depth (m)	-0.91 <sup>c</sup>		0.86 <sup>a</sup>	-0.70 <sup>c</sup>	-0.59 <sup>c</sup>	0.28 <sup>a</sup>
	Temperature (°C)			-0.87 <sup>c</sup>	0.58 <sup>a</sup>	0.38 <sup>a</sup>	-0.36 <sup>c</sup>
	Salinity			0.47 <sup>a</sup>	-0.46 <sup>c</sup>	-0.20 <sup>d</sup>	0.17 <sup>b</sup>
	Density (kg/m <sup>3</sup> )				-0.74 <sup>c</sup>	-0.43 <sup>c</sup>	0.41 <sup>a</sup>
	pH					0.81 <sup>a</sup>	
	DO (mg/l)						
<b>Central</b>	Depth (m)	-0.92 <sup>c</sup>	0.72 <sup>a</sup>	0.91 <sup>a</sup>	-0.70 <sup>c</sup>		0.37 <sup>a</sup>
	Temperature (°C)		-0.67 <sup>c</sup>	-0.95 <sup>c</sup>	0.63 <sup>a</sup>	0.17 <sup>b</sup>	-0.31 <sup>c</sup>
	Salinity			0.87 <sup>a</sup>	-0.30 <sup>c</sup>		0.66 <sup>b</sup>
	Density (kg/m <sup>3</sup> )				-0.53 <sup>c</sup>		0.50 <sup>a</sup>
	pH					0.52 <sup>a</sup>	
	DO (mg/l)						0.50 <sup>a</sup>
<b>Southern</b>	Depth (m)	-0.58 <sup>c</sup>	0.63 <sup>a</sup>	0.70 <sup>a</sup>	-0.74 <sup>c</sup>	-0.83 <sup>c</sup>	0.86 <sup>a</sup>
	Temperature (°C)		-0.43 <sup>c</sup>	-0.91 <sup>c</sup>	0.65 <sup>a</sup>	0.43 <sup>a</sup>	-0.56 <sup>c</sup>
	Salinity			0.76 <sup>a</sup>	-0.83 <sup>c</sup>	-0.73 <sup>c</sup>	0.65 <sup>a</sup>
	Density (kg/m <sup>3</sup> )				-0.84 <sup>c</sup>	-0.64 <sup>c</sup>	0.70 <sup>a</sup>
	pH					0.90 <sup>a</sup>	-0.77 <sup>c</sup>
	DO (mg/l)						-0.81 <sup>c</sup>
	Fluorescence (mg/m <sup>3</sup> )						

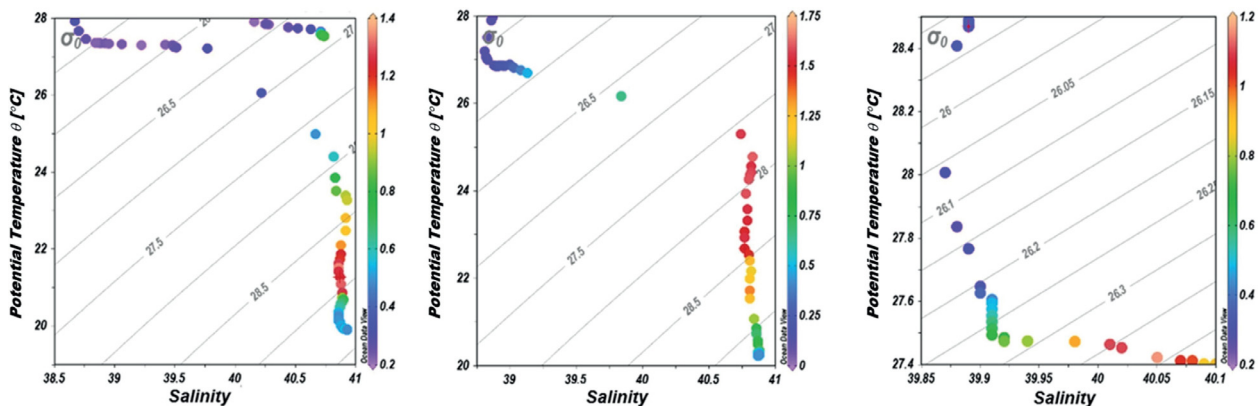


**Figure 7** Fluorescence profiles along the northern (a), central (b) and southern (c) transects, indicating the most productive zone associated with high values of fluorescence (mg/m<sup>3</sup>). In the potential temperature-salinity-fluorescence plots, high values are shown in yellow and red colors.

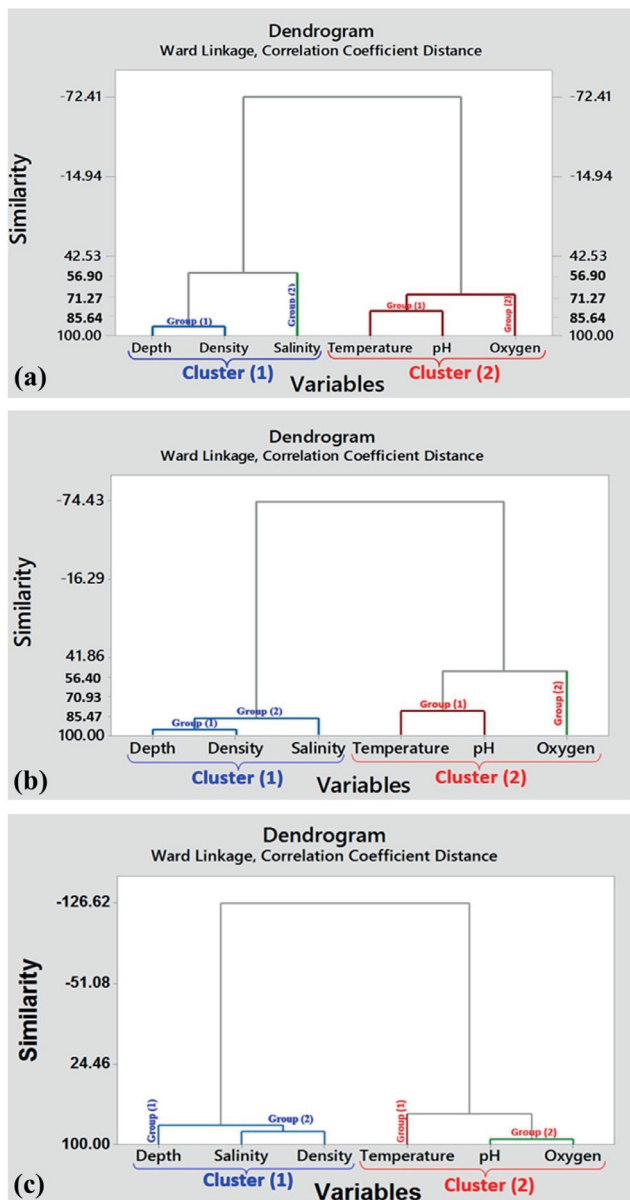


**Figure 8** Hierarchical cluster analysis (HCA) of the physicochemical parameters in the: (a) northern transect, (b) central transect and (c) southern transect. (Dendrograms are made using Minitab Software Version 17).

DO varies between 3 and 7 mg/l in the northern transect and between 3.5 and 8.5 mg/l in the central transect, while the southern transect has no significant variation, which is between 4.0 and 4.6 mg/l (Figure 6a2, b2, c2). The highest DO is found in the subsurface layer (20–30 m) in the deep-water locations of the northern and central transects. This indicates that the subsurface layer in the QEEZ is well oxygenated during early summer. Earlier studies reported hypoxia at a depth of 60 m in the central Gulf in the mid/late summer developed by summer stratification (Al-Ansari et al., 2015; Rakib et al., 2021). However, the minimum recorded DO in early summer in the present study is 3.43 mg/l, quite a comfortable situation compared to hypoxic conditions in the later stage. This shows that the Gulf

is still relatively healthy, despite several coastal development activities in the last few decades.

The Chlorophyll Fluorescence parameter (Fo) is used as a tracer in biological studies to estimate the primary productivity (Chen et al., 2017). Distinct variation in fluorescence is identified in all the transects (Figure 6a3, b3, c3). The surface layer of the deep-water locations has the lowest fluorescence (0–0.2 mg/m<sup>3</sup>), while the subsurface layer (20–40 m) produces the highest fluorescence (1.0–1.6 mg/m<sup>3</sup>). Overall, the central transect is characterized by high fluorescence and thus high primary productivity. The northern transect also has a wide range of primary productive zone with reasonably high fluorescence, but relatively low compared to the central transect.

The higher fluorescence values are associated with a potential density of 28.100–29.020 and 27.590–29.000 kg/m<sup>3</sup>, respectively, as shown in the northern and central transects, while Fo is associated with a lower potential density of 26.320–26.427 kg/m<sup>3</sup> in the southern transect (Figure 7a, b, c). The salinity associated with the higher fluorescence is around 40.8 in the northern and central transects, while that is around 40.0 in the southern transect. The temperature associated with higher fluorescence is 20.5–22.5°C, 21.0–25.5°C and 27.4–27.5°C, respectively, in the northern, central and southern transects. The central transect has a wider range of temperature variations in the productive zone compared to the other two transects.

#### 4.4. Correlation matrix between the physicochemical parameters

The statistical relationship between the physicochemical key parameters has been analyzed using the correlation matrix (Table 2) as well as the dendrograms (Figure 8). A higher positive correlation is found between density and depth in all the transects, which is quite common in oceanic waters. The depth versus salinity as well as density versus salinity has a strong positive correlation in the central and southern transects. This may be because of the sinking of high salinity water and the formation of dense bottom water; however, more in situ observations are needed to substantiate this feature. High negative correlations are found between the depth and temperature as well as density versus temperature in all transects. Although it is normal in oceanic waters, such a high correlation within the shallower depths of the Gulf is notable. The pH versus DO in the northern and southern transects, and pH versus temperature in the central and southern transects have high positive correlations. The pH has negative correlations with depth and density in all the transects, but within the shorter and normal range of pH (8.01–8.21), the shallow QEEZ does not yield any harmful impacts. The DO versus salinity has a strong negative correlation in the southern transect, within the limited data points. In the southern transect, the fluorescence has a strong positive correlation with depth, salinity and density. It suggests that although the salinity and density increase with depth, the reasonable amount of fluorescence (above 1.0 mg/m<sup>3</sup>) present in this region supports the primary productivity.

The hierarchical cluster analysis (HCA) produces the similarity percentage between the physicochemical parameters

ters at each transect, which is represented by dendrograms (Figure 8). In the northern transect, the cluster (1) consists of depth, density and salinity, in which depth and density have high similarity (85%), whereas the cluster (2) consists of temperature, pH and DO, in which the temperature and DO have high similarity (75%) (Figure 8a). However, clusters (1) and (2) mutually exhibit a high negative similarity (–70%) in the northern transect. In the central and southern transects, the cluster components remain the same but differ in their similarity index compared to that in the northern transect. In the central transect, the depth and density in the cluster (1) have very high similarity (around 95%), indicating that density increases with depth, as reflected in the profiles, while both together show high similarity with salinity (around 85%) (Figure 8b). In the cluster (2), the temperature and pH show high similarity (around 80%). Similar to the northern transect, the clusters (1) and (2) in the central transect produce a high negative similarity (around –70%). In the southern transect, the density and salinity in the cluster (1) and pH and temperature in cluster (2) show high similarities (80% and 90%, respectively) (Figure 8c). The clusters (1) and (2) are mutually in a moderate negative similarity (–65%). These similarities suggest that salinity and density in the QEEZ are directly proportional to each other and have strong link between them, while both are inversely proportional to temperature and pH. Furthermore, density is more or less independent of temperature and pH, and salinity determines the water column density and stability.

## 5. Summary and conclusions

This study investigated the spatial variability of key physicochemical parameters – temperature, salinity, density, pH, DO and fluorescence, in the Qatar's Exclusive Economic Zone (QEEZ) during early summer. There were 11 sampling stations across 3 transects – northern, central and southern. The results indicate that physicochemical parameters show distinct spatial variability, which is connected to the stratification and formation of different water masses in the QEEZ. The variations in temperature, salinity and potential density are in the range 19.9°–30.2°C, 38.46–42.20, 24.98–29.32 kg/m<sup>3</sup>, respectively. The minimum recorded salinity was in the intermediate region of the central transect, while the maximum recorded salinity was in the nearshore region of the northern transect. The higher salinity in the northern transect is primarily attributed to the higher evaporation rates along with dense water flow from the northern Gulf. A detailed investigation is required to evaluate the relative contribution of desalination plants in the hypersalinity of this region.

The pH in all the transects shows a little spatial variation (in the range of 8.01–8.21). Although small, the variations in pH are consistent with the water mass distributions, especially in the deep-water regions of northern and central transects. The DO was minimum (3.43 mg/l) in the deepest region of the northern transect, and maximum (8.37 mg/l) in the deepest region of the central transect. The summer stratification often leads to hypoxia in the central Gulf as literature reports, however, that is not quite evident in early summer based on the present study. The maximum recorded fluorescence was 1.61 mg/m<sup>3</sup> in the deepest re-

gion of the northern transect. The high fluorescence in the QEEZ was confined to a depth of 20–40 m, where the primary productivity was relatively higher.

The northern and the central transects are situated in the deep-water zone and exhibited similar vertical and horizontal distribution patterns and layering of physicochemical key parameters, whereas the southern transect is situated in a relatively shallow water zone, exhibiting a weak stratification. The correlation matrix and hierarchical cluster analysis indicate that depth, salinity and density are in cluster 1 and pH, DO and Temperature are in cluster 2, and both are inversely correlated to each other. The inferences derived in this study are preliminary in nature due to a limited number of datasets available in the QEEZ. A detailed investigation is planned by executing further measurements in the QEEZ, not only in summer but also in other seasons with the aim of studying the temporal variability of physicochemical parameters.

## Acknowledgments

This research was carried out as a part of the mission of the Environmental Science Center (ESC), Qatar University. The multipurpose research vessel, *r/v Janan* was utilized for data collection and sampling. The authors thank Prof. Hamad A. Al Saad, Director, ESC for his encouragement, keenness and continuous support. We thank Dr. Ahmed Saif Ibrahim for providing useful suggestions. We thank the sediment-focused research group and Mr. Mehmet Demirel for their assistance in data collection and analyses. Part of this work has been completed under the IRCC project (No. IRCC-2019-002).

## Declaration of competing interest

The authors of this study would like to declare that they have no conflict of interest.

## Disclaimer

The manuscript contents are solely the responsibility of the authors, and do not necessarily represent the official views of the Qatar University and the Environmental Science Center (ESC).

## CRedit Authorship contribution statements

Elnaiem Ali Elobaid: Conceptualization, research methodology, project administration, collection of samples, investigation, formal analysis, visualization, resources, writing the original draft of the manuscript, reviewing and editing.

Ebrahim S. Al Ansari: Conceptualization, methodology, project administration, resources, visualization, writing up, reviewing, and editing.

Oguz Yigiterhan: Conceptualization, research methodology, collection of samples methodology, resources, visualization, writing, reviewing, and editing.

V.M. Aboobacker: Conceptualization, research methodology, writing, reviewing, and editing.  
P. Vethamony: reviewing and editing.

## Supplementary materials

Supplementary material associated with this article can be found, in the online version, at <https://doi.org/10.1016/j.oceano.2021.09.003>.

## References

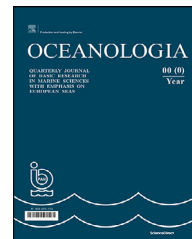
- Abdel-Moati, M.A.R., Al-Ansari, I.S., 2000. Impact of the Expansion in Fertilizer Industry on the Levels of Ammonia and Urea of Mes-saieed Marine Area (Qatar), Arabian Gulf. *Fresenius Envir. Bull.* 9, 040–046. <https://doi.org/10.1029/92JC00841>
- Aboobacker, V.M., Shanas, P.R., Veerasingam, S., Ibrahim M.A.S. Al-Ansari, Fadhil N Sadooni, Vethamony, P., 2021a. Long-term assessment of onshore and offshore wind energy potentials of Qatar, *Energies* 14, 1178. <https://doi.org/10.3390/en14041178>
- Aboobacker, V.M., Shanas, P.R., Al-Ansari, E.M.A.S., Sanil Kumar, V., Vethamony, P., 2021b. The maxima in northerly wind speeds and wave heights over the Arabian Sea, the Arabian/Persian Gulf and the Red Sea derived from 40 years of ERA5 data. *Clim. Dyn.* 56, 1037–1052. <https://doi.org/10.1007/s00382-020-05518-6>
- Al-Ansari, E.M.A.S., Rowe, G., Abdel-Moati, M.A.R., Yigiterhan, O., Al-Maslmani, I., Al-Yafei, M.A., Al-Shaikh, I., Upstill-Goddard, R., 2015. Hypoxia in the central Arabian Gulf Exclusive Economic Zone (EEZ) of Qatar during summer season. *Estuar. Coast. Shelf Sci.* 159, 60–68. <https://doi.org/10.1016/j.ecss.2015.03.022>
- Al-Ansari, I.M.A.S., 2006. A hydrographic and biogeochemical study of waters and sediment of the exclusive economic zone (EEZ) of Qatar (Arabian Gulf) Ph.D. thesis. the University of Newcastle upon Tyne, UK.
- Al Azhar, M., Temimi, M., Zhao, J., Ghedira, H., 2016. Modeling of circulation in the Arabian Gulf and the Sea of Oman: Skill assessment and seasonal thermohaline structure. *J. Geophys. Res. Oceans* 121, 1700–1720. <https://doi.org/10.1002/2015JC011038>
- Al-Majed, N., Mohammadi, H., Al-Ghadban, A., 2000. Regional Report of the State of the Marine Environment. ROPME/GX-10/001/1. Revised by Al-Awadi A., Regional Organization for the Protection of the Marine Environment. Available at [http://www.ropme.org/Uploads/SOMER/SOMER\\_2000.pdf](http://www.ropme.org/Uploads/SOMER/SOMER_2000.pdf)
- Al-Said, T., Yamamoto, Madhusoodhanan, R., Al-Yamani, F., Pokavanich, T., 2018. Summer hydrographic characteristics in the northern ROPME Sea Area: Role of ocean circulation and water masses. *Estuar. Coast. Shelf Sci.* 213, 18–27. <https://doi.org/10.1016/j.ecss.2018.07.026>
- Beltagy, A.I., 1983. Some oceanographic measurements in the Gulf waters around Qatar Peninsula. *Qatar Univ. Sci. Bull.* 3, 329–341.
- BP, 2011. Statistical Review of World Energy, June 2011. London SW1 Y 4PD, UK [sr@bp.com](mailto:sr@bp.com)
- Brewer, P.G., Dyrssen, D., 1985. Chemical oceanography of the Persian Gulf. *Prog. Oceanogr.* 14, 41–55. [https://doi.org/10.1016/0079-6611\(85\)90004-7](https://doi.org/10.1016/0079-6611(85)90004-7)
- Campos, E.J.D., Gordon, A.L., Kjerfve, B., Vieira, F., Cavalcante, G., 2020. Freshwater budget in the Persian (Arabian) Gulf and exchanges at the Strait of Hormuz. *PLoS ONE* 15 (5), e0233090. <https://doi.org/10.1371/journal.pone.0233090>
- Chao, S.Y., Kao, T.W., Al-Hajri, K.R., 1992. A numerical investigation of circulation in the Arabian Gulf. *J. Geophys. Res.* 97 (C7), 11219–11236. <https://doi.org/10.1029/92JC00841>
- Chen, H., Zhou, W., Chen, W., Xie, W., Jiang, L., Liang, Q., Huang, M., Wu, Z., Wang, Q., 2017. Simplified, rapid, and inexpensive estimation of water primary productivity based on chlorophyll fluorescence parameter *Fo*. *J. Plant Physiol.* 211, 128–135. <https://doi.org/10.1016/j.jplph.2016.12.015>
- Emery, K.O., 1956. Sediments and Water of the Persian Gulf. *AAPG Bull.* 40, 2354–2383. <https://doi.org/10.1306/5CEAE595-16BB-11D7-8645000102C1865D>
- Fallatah, M.M., Kamil, Y.N., Ibrahim, A.S.A., Orif, M.I., Shaban, Y.A., Al Farawati, R., 2018. Hydrographic parameters and distribution of dissolved Cu, Ni, Zn and nutrients near Jeddah desalination plant. *Open Chem.* 16, 245–257. <https://doi.org/10.1515/chem-2018-0029>
- Fofonoff, N.P., Millard, R.C., 1983. Algorithms for the computation of fundamental properties of seawater. UNESCO Tech. Papers Marine Sci. 44, 53. <http://hdl.handle.net/11329/109>.
- Ghaemi, M., Abtahi, B., Gholamipour, S., 2021. Spatial distribution of nutrients and chlorophyll *a* across the Persian Gulf and the Gulf of Oman. *Ocean Coast. Manage.* 201, 105476. <https://doi.org/10.1016/j.ocecoaman.2020.105476>
- Hunter, J.R., 1986. The physical oceanography of the Arabian Gulf: a review and theoretical interpretation of previous observations. In: Halwagy, R., Clyton, D., Behbehani, M. (Eds.), *First Arabian Gulf Conference on Environment and Pollution*, Kuwait, February 7–9, 1982. University of Kuwait, 1–23.
- Ibrahim, H.D., Xue, P., Eltahir, E.A., 2020. Multiple Salinity Equilibria and Resilience of Persian/Arabian Gulf Basin Salinity to Brine Discharge. *Front. Marine Sci.* 7, 573. <https://doi.org/10.3389/fmars.2020.00573>
- Ibrahim, H.D., Eltahir, E.A., 2019. Impact of brine discharge from seawater desalination plants on persian/arabian gulf salinity. *J. Environ. Eng.* 145, 04019084. [https://doi.org/10.1061/\(ASCE\)EE.1943-7870.0001604](https://doi.org/10.1061/(ASCE)EE.1943-7870.0001604)
- John, V.C., Coles, S.L., Abozed, A.I., 1990. Seasonal cycles of temperature, salinity and water masses of the western Arabian Gulf. *Oceanologica Acta* 13, 273–282.
- Jones, D.A., Price, A.R.G., Al-Yamani, F., Al-Zaidan, A., 2002. Coastal and marine ecology. In: Khan, N.Y., Munawar, M., Price, A.R.G. (Eds.), *The Gulf Ecosystem: Health and Sustainability*. Backhuys Publishers, Leiden, 65–103. <https://doi.org/10.14321/J.CTT1TM7JKG.12>
- Joydas, T.V., Qurban, M.A., Manikandan, K.P., Ashraf, T.T.M., Ali, S.M., Al-Abdulkader, K., Qasem, A., Krishnakumar, P.K., 2015. Status of macrobenthic communities in the hypersaline waters of the Gulf of Salwa, Arabian Gulf. *J. Sea Res.* 99, 34–46. <https://doi.org/10.1016/j.seares.2015.01.006>
- Kampf, J., Sadrinasab, M., 2006. The circulation of the Persian Gulf: a numerical study. *Ocean Sci.* 2, 27–41. <https://doi.org/10.5194/os-2-27>
- Ma, X., Zuo, H., Tian, M., Zhang, L., Meng, J., Zhou, X., Min, N., Chang, X., Liu, Y., 2016. Assessment of heavy metals contamination in sediments from three adjacent regions of the Yellow River using metal chemical fractions and multivariate analysis techniques. *Chemosphere* 144, 264–272. <https://doi.org/10.1016/j.chemosphere.2015.08.026>
- Pous, S., Pascal, L., Xavier, C., 2015. A model of the general circulation in the Persian Gulf and in the Strait of Hormuz: Intra-seasonal to interannual variability. *Cont. Shelf Res.* 94, 55–70. <https://doi.org/10.1016/j.csr.2014.12.008>
- Prasad, T.G., Ikeda, M., Prasanna Kumar, S., 2001. Seasonal spreading of the Persian Gulf Water mass in the Arabian Sea. *J. Geophys. Res.* 106 (C8), 17059–17071. <https://doi.org/10.1029/2000JC000480>

- Price, A., 2002. Simultaneous hotspots and coldspots of the marine biodiversity and the implications for global conservation. *Mar. Ecol. Prog. Ser.* 241, 23–27. <https://doi.org/10.3354/meps241023>
- Privett, D.W., 1959. Monthly charts of evaporation from the N. Indian Ocean (including the Red Sea and the Persian Gulf). *Q. J. Roy. Meteor. Soc.* 85, 424–428. <https://doi.org/10.1002/qj.49708536614>
- Rakib, F., Al-Ansari, E.M.A.S., Husrevoglu, Y.S., Yigiterhan, O., Al-Maslamani, I., Aboobacker, V.M., Vethamony, P., 2021. Observed variability in physical and biogeochemical parameters in the central Arabian Gulf. *Oceanologia* 63 (2), 227–237. <https://doi.org/10.1016/j.oceano.2020.12.003>
- Reynolds, M., 1993. Physical oceanography of the Gulf, Strait of Hormuz and Gulf of Oman: results from the Mt. Mitchell expedition. *Mar. Pollut. Bull.* 27, 35–59. [https://doi.org/10.1016/0025-326X\(93\)90007-7](https://doi.org/10.1016/0025-326X(93)90007-7)
- Reynolds, R.M., 2002. *Oceanography*. In: Khan, N.Y., Munawar, M., Price, A.R.G. (Eds.), *The Gulf Ecosystem: Health and Sustainability*. Backhuys Publishers, Leiden, 53–64.
- Rivers, J.M., Varghese, L., Yousif, R., Whitaker, F.F., Skeat, S.L., Al-Shaikh, I., 2019. The geochemistry of Qatar coastal waters and its impact on carbonate sediment chemistry and early marine diagenesis. *J. Sediment. Res.* 89, 293–309. <https://doi.org/10.2110/jsr.2019.17>
- Schlitzer, R., 2020. Ocean Data View Latest ODV Version: ODV 5.3.0 (June 03 2020). <https://odv.awi.de>
- Sezer, N., Evis, Z., Koc, M., 2017. Management of Desalination Brine in Qatar and the GCC Countries. 10th International Conference on Sustainable Energy and Environmental protection (June 27th–30th, 2017, Bled, Slovenia). University of Maribor Press. <https://doi.org/10.18690/978-961-286-053-0.11>
- Sheppard, C.R.C., 1993. Physical environment of the Gulf relevant to marine pollution: An overview. *Mar. Pollut. Bull.* 27, 3–8. [https://doi.org/10.1016/0025-326X\(93\)90003-3](https://doi.org/10.1016/0025-326X(93)90003-3)
- Sheppard, C., Al-Husiani, M., Al-Jamali, F., Al-Yamani, F., Baldwin, R., Bishop, J., Benzoni, F., Dutrieux, E., Dulvy, N.K., Durvasula, S.R.V., Jones, D.A., Loughland, R., Medio, D., Nithyanandan, M., Pilling, G.M., Polikarpov, I., Price, A.R.G., Purkis, S., Riegl, B., Saburova, M., Namin, K.S., Taylor, O., Wilson, S., Zainal, K., 2010. The Gulf: A young sea in decline. *Mar. Pollut. Bull.* 60, 13–38. <https://doi.org/10.1016/j.marpolbul.2009.10.017>
- Smith, R., Purnama, A., Al-Barwani, H.H., 2007. Sensitivity of hypersaline Arabian Gulf to seawater desalination plants. *Appl. Math. Model.* 31, 2347–2354. <https://doi.org/10.1016/j.apm.2006.09.010>
- Soliman, Y.S., Alansari, E.M.A., Sericano, J.L., Wade, T.L., 2019. Spatio-temporal distribution and sources identifications of polycyclic aromatic hydrocarbons and their alkyl homolog in surface sediments in the central Arabian Gulf. *Sci. Total Environ.* 658, 787–797. <https://doi.org/10.1016/j.scitotenv.2018.12.093>
- Swift, S.A., Bower, A.S., 2003. Formation and circulation of dense water in the Persian/Arabian Gulf. *J. Geophys. Res.* 108, 4-1–4-21. <https://doi.org/10.1029/2002jc001360>
- Thoppil, P.G., Hogan, P.J., 2010. Persian Gulf response to a wintertime shamal wind event. *Deep Sea Res. Pt. I* 57, 946–955. <https://doi.org/10.1016/j.dsr.2010.03.002>
- Van Lavieren, H., Burt, J., Feary, D.A., Cavalcante, G., Marquis, E., Benedetti, L., Trick, C., Kjerfve, B., Sale, P.F., 2011. *Managing the growing impacts of development on fragile coastal and marine ecosystems*. Policy Report. UNU-INWEH, Hamilton, ON, Canada, 100 pp.
- Vasou, P., Vervatis, V., Krokos, G., Hoteit, I., Sofianos, S., 2020. Variability of water exchanges through the Strait of Hormuz. *Ocean Dynam.* 70, 1053–1065. <https://doi.org/10.1007/s10236-020-01384-2>
- Yao, F., Johns, W.E., 2010. A HYCOM modeling study of the Persian Gulf: 1. Model configurations and surface circulation. *J. Geophys. Res.* 115, C11017. <https://doi.org/10.1029/2009JC005781>
- Yoshida, J., Matsuyama, M., Senjyu, T., Ishimaru, T., Mopingaga, T., Arakwa, H., Kamatani, A., Maeda, M., Otsuki, A., Hashimoto, S., Kasuga, I., Koike, Y., Mine, Y., Kurita, Y., Kitazawa, A., Noda, A., Hayashi, T., Miyazaki, T., Takahashi, K., 1998. Hydrography in the RSA during the RT/V Umitaka-Maruk cruises. In: Otsuki, A., Abdeulraheem, M., Reynolds, M. (Eds.), *Offshore Environment of the ROPME Sea Area after the War-Related Oil Spill – Results of the 1993–94 Umitaka-Maruk Cruise*. Terra Sci. Publ. Company, Tokyo, 1–22.



Available online at [www.sciencedirect.com](http://www.sciencedirect.com)

ScienceDirect

journal homepage: [www.journals.elsevier.com/oceanologia](http://www.journals.elsevier.com/oceanologia)

## ORIGINAL RESEARCH ARTICLE

# Assessment of Sentinel-2 to monitor highly dynamic small water bodies: The case of Louro lagoon (Galicia, NW Spain)

Gema Casal\*

National Centre for Geocomputation, Maynooth University, Maynooth, Co. Kildare, Ireland

Received 8 April 2021; accepted 17 September 2021

Available online 6 October 2021

**KEYWORDS**

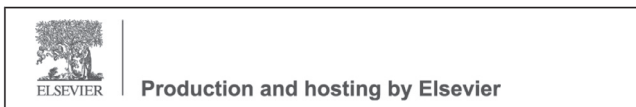
Coastal lagoons;  
Intermittent inlet;  
Water bodies;  
Coastal monitoring;  
Multiband water  
indices

**Abstract** Coastal lagoons have been providing ecological, economic and cultural benefits for many centuries. Despite their importance, the monitoring of coastal lagoons poses numerous challenges related to their complex environmental processes, their large variability in size and their remote location, inhibiting effective management programmes. This study demonstrates the effectiveness of Sentinel-2 satellites to map highly dynamic morphological and hydrological changes in the Louro lagoon, a small choked lagoon located on the Galician coast (NW Spain). For this purpose, a simple methodology using the Normalised Difference Water Index (NDWI) has been evaluated, which allows to monitor the sand barrier changes and the inlet formation. The results show that the sand barrier's opening and closing might take only a very short period, and the recovery of the lagoon to its full water level can happen in less than a month. Sentinel-2 images also reveal drastic changes in the water level once the sand barrier is broken. A water surface area of 0.24 km<sup>2</sup> was estimated on 04/11/2019, while this surface was reduced to 0.10 km<sup>2</sup> on 04/12/2019. Monitoring these changes is critical to understand the different processes

\* Corresponding author at: National Centre for Geocomputation, Maynooth University, Maynooth, Co. Kildare, Ireland.

E-mail address: [gema.casal@mu.ie](mailto:gema.casal@mu.ie)

Peer review under the responsibility of the Institute of Oceanology of the Polish Academy of Sciences.



ongoing in these valuable environments and making informed decisions for their management and protection.

© 2021 Institute of Oceanology of the Polish Academy of Sciences. Production and hosting by Elsevier B.V. This is an open access article under the CC BY-NC-ND license (<http://creativecommons.org/licenses/by-nc-nd/4.0/>).

## 1. Introduction

Coastal lagoons occupy 13% of the global coastline (Barnes, 1980; Kjerfve, 1994) and represent essential ecosystems that provide many ecological, economic, social and cultural benefits. Several definitions for coastal lagoons have been proposed (Tagliapietra et al., 2009). The most widely used is the one suggested by Kjerfve (1994) that define coastal lagoons as “a shallow coastal water body separated from the ocean by a barrier, connected at least intermittently by one or more restricted inlets and usually oriented shore-parallel”. Bird et al. (1994) added to this definition some aspects regarding the enclosing barrier whose nature is responsible for lagoon formation (Duck and Figueiredo da Silva, 2012). These authors define coastal lagoons as “areas of relatively shallow water that have been partly or wholly sealed off from the sea by the deposition of spits or barriers, usually of sand or shingle, build up above high tide level by wave action”. Considering their geomorphology and degree of isolation coastal lagoons can be sub-divided into: “choked”, “restricted” and “leaky” (Kjerfve, 1994). Following Kjerfve (1994) “choked” lagoons are connected to the sea by a single long narrow entrance channel and usually located along a stretch of coast with high wave energy and significant littoral drift; “restricted” lagoons consist of a large and wide water body, usually oriented parallel to the coast, with two or more entrance channels, while “leaky” lagoons are elongated water bodies parallel to the coast but with many ocean entrance channels.

Coastal lagoons are highly variable systems influenced both by global aspects such as climate change or sea-level rise and by local aspects such as the nature of the basement, coastal orientation, topography or sediment sources (Costas et al., 2009). The local aspects have particular relevance on the NW Iberian coast, which has an abrupt topography with incised river valleys, producing shallow and small coastal lagoons (<1 km<sup>2</sup> in size) (González-Villanueva et al., 2015). In Galicia (NW Spain), these small coastal lagoons are relevant environments that provide many ecosystem services and that are protected by the “Habitat Directive of the European Union” (92/43/EEC) (EC, 1992). A large number of these lagoons holds protected taxa, some of which are listed in the “Galician Catalogue of Endangered Species” (González-Villanueva et al., 2015).

Despite the current environmental protection of Galician coastal lagoons, these systems are progressing towards their collapse (Fraga-Santiago et al., 2019). The principal observed cause is clogging (accumulation of sediment particles), which leads the free water body to disappear, implying a progressive loss of diversity, mainly of aquatic birds (Bao et al., 2007). This effect is of particular relevance in the Louro lagoon. As a choked lagoon, the Louro lagoon has shallow waters periodically connected with the open ocean

by a narrow channel (called an inlet). The temporary connection between the lagoon and the open sea causes significant hydrodynamic variations. This change is probably the most critical factor governing the structure and functioning of the resident biotic communities (Smakhtin, 2004). In many choked lagoons, the occasional break of the sand barrier might be produced in an artisanal manner associated with cultural traditions, generally related to fisheries (Bertotti-Crippa et al., 2013) or agricultural purposes (Fortunato et al., 2014). In the case of the Louro lagoon, due to the abandonment of traditional agriculture practises, the sand barrier’s opening mainly depends now on meteorological and oceanographic conditions.

In choked lagoons, the opening of the sand barrier has a direct effect on their morphology and biogeochemical flows by promoting the exchange of water, sediments, nutrients, and pollutants between the lagoon and the sea (Moreno et al., 2010). After the rupture, the sand barrier can remain open or close after a variable period of time, depending on the hydraulic efficiency related to the rainfall regime, the tide cycle and the sediment transport at the local level (Green et al., 2013). These openings can occur regularly throughout the year (seasonal cycles) or irregularly due to anthropogenic interventions. For example, seasonal openings can be caused by high waves produced by storms, intense river discharges, or elevated rain levels (Gale et al., 2006; Weidman and Ebert, 2013). The unpredictable nature of natural closures and openings hampers their monitoring and, in many cases, they have not been explicitly evaluated (Yáñez-Arancibia et al., 2014). Information about the evolution of coastal lagoons and their monitoring is crucial for their management and sustainable protection (Newton et al., 2018). However, the environmental and morphological variability, together with their isolation and dispersion, makes it challenging to acquire robust and continuous data of coastal lagoons, and thus to establish a holistic management approach. On the other hand, there is a growing need to expand the coverage and frequency of coastal monitoring for regulation purposes, which derive from legislation such as the European Union Water Framework Directive (WFD) (2000/60/EC) (EC, 2000). The WFD considers coastal lagoons as both “transition waters” and “coastal waters” that need specific monitoring instruments to assess their ecological status and derive possible actions.

Data obtained by remote sensors, combined with in situ monitoring programmes, are crucial to provide new knowledge of the diverse processes taking place in coastal lagoons. The use of satellite data is well established in different applications related to coastal water bodies such as flood monitoring (DeVries et al., 2020), water quality assessment (Gholizadeh et al., 2016) or the extraction of surface water area (Sun et al., 2012). In light of increasing new satellite data, the present moment is particularly impor-

tant to provide new knowledge in this field. As part of the Copernicus programme, the European Space Agency (ESA) together with the European Commission has launched the Sentinel missions to increase existing Earth observation capabilities. Of particular relevance for the study and monitoring of coastal areas is the Sentinel-2 mission. This mission includes the twin satellites Sentinel-2A, launched in 2015, and Sentinel-2B, launched in 2017. The Multispectral Imager (MSI) sensor on board Sentinel-2 provides 13 spectral bands covering from visible and near-infrared (VNIR) to shortwave infrared (SWIR) wavelengths, with four of these bands (B2, B3, B4 and B8) offering a spatial resolution of 10 m. This relatively high spatial resolution combined with a short revisit time (5 days at the equator and 2–3 days at mid-latitudes) is an advantage for monitoring highly dynamic small water bodies. Sentinel-2 data will have a temporal continuity with the launch of Sentinel-2C and Sentinel-2D in the future.

Although the Sentinel-2 satellites were primarily designed for terrestrial environments, numerous studies have shown their usefulness for different coastal applications (e.g. [Ansper and Alikas, 2019](#); [Casal et al., 2020](#); [Hedley et al., 2018](#)), including coastal lagoons ([Brisset et al., 2021](#); [Sebastiá-Frasquet et al., 2019](#)) and water bodies delimitation ([Zhou et al., 2017](#)). Sentinel-2 provides continuity regarding medium resolution missions such as Satellite Pour l'Observation de la Terre (SPOT) or Landsat, which have provided successful results in the mapping of diverse water bodies ([Casal et al., 2011](#); [Lavery et al., 1993](#); [Luis et al., 2019](#)). The Landsat mission had been used extensively due to its open data access and long-term data series (the first Landsat satellite was launched in the 70s). However, the revisit time of Landsat satellites (16 days) limits their use for monitoring highly dynamic events.

Regarding coastal lagoons, the number of studies using Sentinel-2 data is still scarce. A search in the Web of Science using the words “Sentinel-2” and “lagoon” as topic reported only 17 records between 2017 and 2020, including articles and proceeding papers. The Sentinel-2 applications in coastal lagoons mainly include monitoring water quality parameters ([Braga et al., 2020](#); [Sebastiá-Frasquet et al., 2019](#); [Sòria-Perpinyà et al., 2020](#)) and only a few applications were found related to water body changes ([Karim et al., 2019](#)) and waterline detection ([Salameh et al., 2020](#)). None of the records reported by Web of Science included highly dynamic changes.

The objective of this study is the evaluation of Sentinel-2 data to monitor highly dynamic morphological and hydrological changes in a small choked lagoon. The detection of the breaking and closing of the sand barrier, the inlet formation and the water level variations are assessed using existing water extraction indices. Establishing the barrier break frequency and its closure is crucial for evaluating the barrier vulnerability and preventing damage to infrastructures and ecosystem services.

## 2. Material and methods

### 2.1. Study area

The Louro lagoon is located on the Atlantic coast of Galicia (NW Spain) at the northern end of the Ría de Muros

([Figure 1](#)). This area, catalogued as a “Site of Community Importance” (Natura 2000 Network, Directive 92/43/EEC) under the European Union Habitats Directive, is an essential habitat for many species of fauna and flora ([González-Villanueva et al., 2017](#)). The lagoon ecosystem hosts amphibians, reptiles and small mammals and has become a relevant place for ornithological observation.

The Louro lagoon is separated from the open sea by a sand barrier of 300–600 m wide and 1500 m long, fixed to a rocky substrate on both sides ([González-Villanueva et al., 2017](#)). The sand barrier hosts vegetated dunes fragmented by corridors produced by wind action. The lagoon is mainly shallow, with depths ranging between 2 m in winter and 0.5 m in summer ([Pérez-Arlucea et al., 2011](#)). It presents an inner permanent flood area and a peripheral area subject to occasional flood periods ([Pérez-Arlucea et al., 2011](#)). Precipitation in the study area is highly variable, with oscillations between monthly averages of 300 mm in autumn-winter to less than 50 mm in summer. Communication between the lagoon and the open sea is temporary and occurs under certain circumstances related to spring tides, intense rain periods and storms with south-southwesterly winds. The sand barrier break causes a water exchange between the open sea and the lagoon through the formation of an inlet. In general, the inlet can be described as a channel 2 m deep and an average of 15 m wide that cuts the barrier perpendicular to the coast ([González-Villanueva et al., 2013](#); [Pérez-Arlucea et al., 2011](#)). The Louro lagoon system is classified as mesotidal ([Davies, 1964](#)), with an average tidal range of around 3 m.

Recent studies have demonstrated that the Louro lagoon is experiencing a progressive siltation and eutrophication process, which alters its natural evolution and could eventually affect its inherent environmental value ([González-Villanueva et al., 2015](#); [Fraga-Santiago et al., 2019](#)). Several factors have been identified affecting these processes, the most relevant of which is the abandonment of traditional agriculture practices ([Fraga-Santiago et al., 2019](#)) that lead to changes in the land use around the lagoon. Since the last decades of the 20<sup>th</sup> century, crop cultivation has been progressively abandoned, leading to riparian forest growth ([Fraga-Santiago et al., 2019](#)). This expansion in tree-covered areas around the lagoon implied a decrease in water availability. Moreover, frequent forest fires have also contributed to transporting nutrients and sediments into the lagoon, thus incrementing the siltation and eutrophication processes.

### 2.2. Satellite imagery

The intense storms in winter 2019/2020 severely impacted the Louro lagoon by producing several breaks of the sand barrier with the subsequent formation of an inlet. Prior information about morphological and environmental changes in the Louro lagoon during this period motivate this study to evaluate the suitability of Sentinel-2 images to monitor these processes. Sentinel-2 images were downloaded from the Copernicus Scientific Data Hub between 1<sup>st</sup> November 2019 and 29<sup>th</sup> February 2020 at level 1C, Top-of-Atmosphere reflectance (TOA) and projection UTM/WGS84.

Although a total number of 24 Sentinel-2 images were registered during this period, only seven had no clouds or

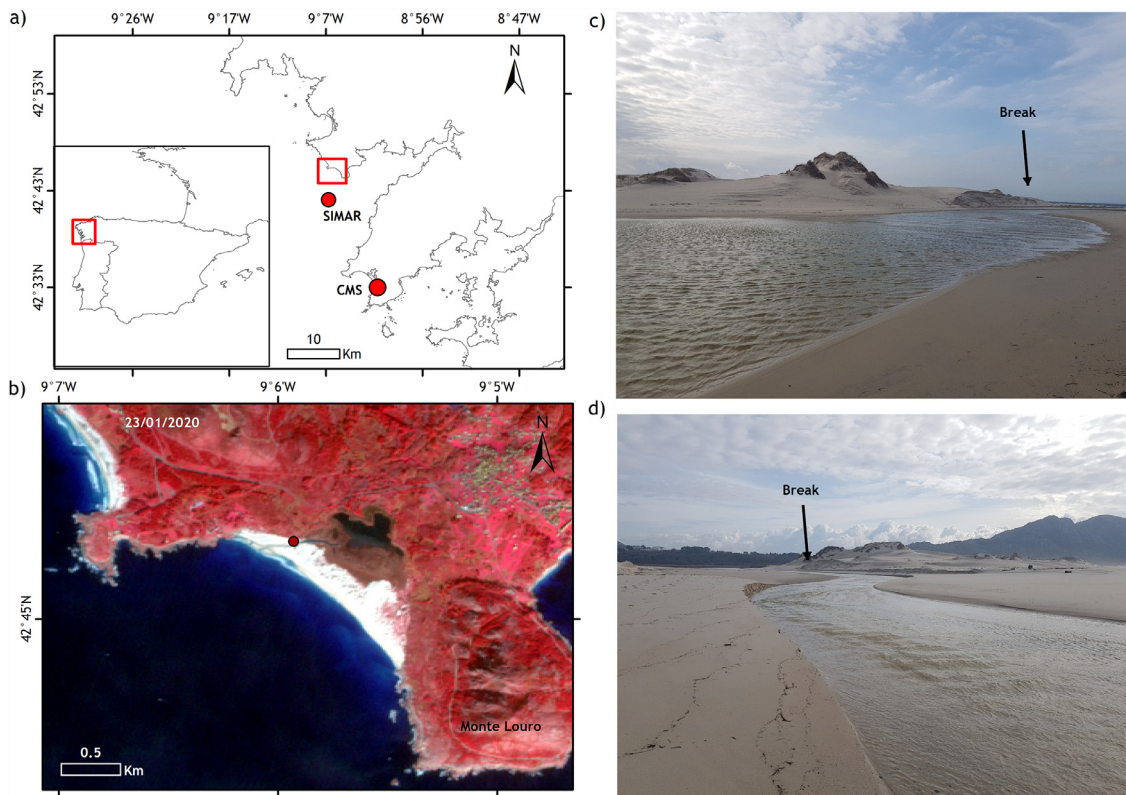


**Figure 1** a) Map of the study area showing the locations of the SIMAR node and the Corrubedo Meteorological Station (CMS). b) Sentinel-2 image in false infrared colour (NIR, R, G), taken on 23/01/2020. This image also shows the sand barrier break. The red dot in b) indicates the place where the photographs in panels c) and d) were taken on 26/01/2020.

**Table 1** Detail of the Sentinel-2 images included in the study. The tidal coefficient was registered in Muros Port and indicates the tidal amplitude (difference between low and high tide).

Date	Sensor	S2-granule	Acquisition time (UTM)	Tidal coefficient	Observations
04/11/2019	S2A	T29THM	11:33:21	34 (very low)	Strong swell
29/11/2019	S2B	T29THM	11:33:29	75 (high)	Clouds partially covering the lagoon
04/12/2019	S2A	T29THM	11:34:41	39 (low)	Strong swell
29/12/2019	S2B	T29THM	11:33:59	70 (high)	Strong swell
03/01/2020	S2A	T29THM	11:34:51	42 (low)	Clouds partially covering the lagoon
23/01/2020	S2A	T29THM	11:33:51	77 (high)	No swell. Low clouds over the open sea but not over the actual lagoon
22/02/2020	S2A	T29THM	11:33:11	44 (low)	Strong swell. Clouds over the open sea but not over the lagoon

a low cloud coverage (Table 1). Cloud coverage is a critical limiting factor in the NW of Iberian Peninsula; however, the revisit time of Sentinel-2 constellation allowed for at least two suitable images almost every month during the study period. Most of the images showed a strong swell with waves breaking in the shore producing white caps. No sun glint conditions were visually appreciated in any of the images. The images were resized to the area of the Louro lagoon.

### 2.3. Meteorological and oceanographic data

Because the break of the sand barrier in winter is mainly related to meteorological and oceanographic conditions, information about rainfall, wind and significant wave height was consulted for the period of this study (Figure 2). Rainfall data (L/m<sup>2</sup>) and wind speed (km/h) were downloaded from the Corrubedo Meteorological Station (CMS) through the Meteogalicia website (<https://www.meteogalicia.gal>).

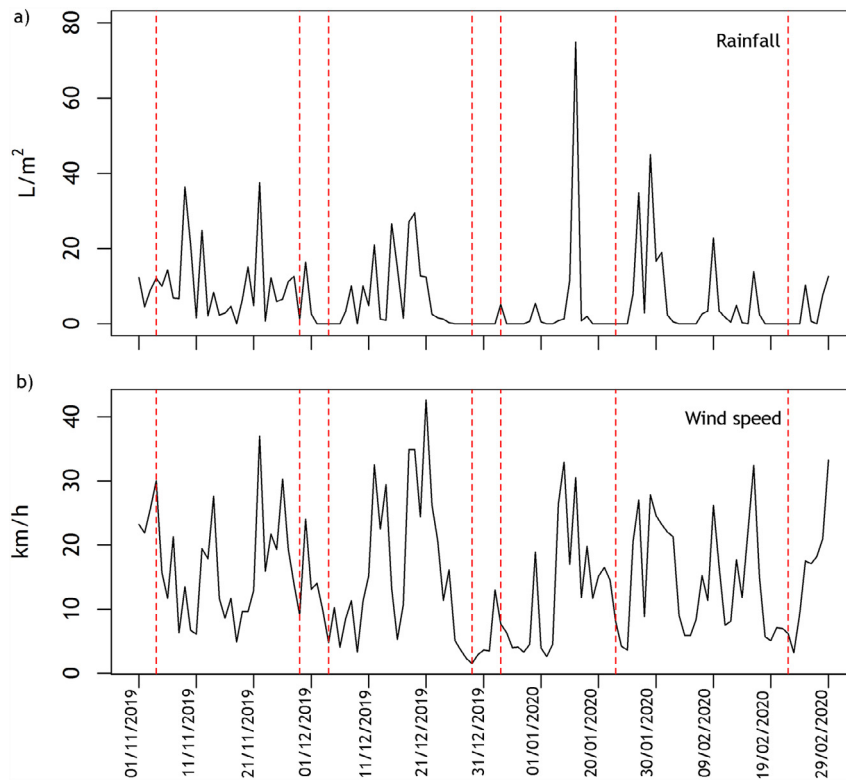


**Figure 2** a) Daily rainfall data ( $L/m^2$ ) and (b) wind speed (km/h) registered by the Corrubedo Meteorological Station. Red dashed lines indicate the dates on which the Sentinel-2 images analysed in this study were taken (Table 1).

The wave height was taken from the node of 3009017 of the SIMAR dataset provided by Puertos del Estado (<http://www.puertos.es>) (not shown here as the data are not downloadable). Numbers in the SIMAR database are obtained through a wave reanalysis model. The location of CMS and SIMAR node is shown in Figure 1.

#### 2.4. Surface water delimitation

The extraction of water bodies from optical images uses the difference between the low reflectance levels of water surfaces and the high reflectance levels of terrestrial substrates in the infrared channels. Several algorithms for surface water delimitation have been proposed. Examples are the digitalisation of water bodies through visual interpretation (Yang et al., 2017), object-based image analysis (Zhang et al., 2013), spectral mixture analysis (Guo et al., 2015; Liu et al., 2017), single-band thresholding (Bryant and Rainey, 2002; Frazier and Page, 2000) or spectral water indices (Feyisa et al., 2014; McFeeters, 1996; Xu, 2006). The spectral water indices commonly take two different bands to distinguish the water surfaces, having the advantage of both simplicity and high precision (Xie et al., 2014). For this reason, these indices are among the most widely used.

One of the most popular multiband spectral water indices is the so-called Normalised Difference Water Index (NDWI) which uses the green and the near-infrared bands (McFeeters, 1996). The NDWI had first been developed us-

ing Landsat Multispectral Scanner images in digital numbers and a zero threshold value. Positive NDWI values were identified as water, while negative values were classified as non-water. Some years later, Xu (2006) proposed a different index, the Modified Normalized Difference Water Index (MNDWI), in which the green and shortwave infrared bands were used. Although the MNDWI is widely used in applications such as the delimitation of surface water bodies, land-use changes and ecology (Duan and Bastiaanssen, 2013; Xu, 2006), it has limitations in urban and shaded mountainous areas (Acharya et al., 2018). Some years later, Feyisa et al. (2014) proposed the Automated Water Extraction Index (AWEI) using Landsat Thematic Mapper. In this case, Feyisa et al. developed two variants: the AWEIsh designed to identify water bodies by eliminating shadow pixels and the AWEInsh designed to delimit water bodies in urban areas. Because the Louro lagoon area is a rural area without large urban settlements, the AWEInsh index was not considered here. The Normalised Difference Vegetation Index (NDVI) was also evaluated since several studies have demonstrated that vegetation indices can also be effective in delimiting water bodies (Rokni et al., 2014).

Most of the indices considered here were initially developed for satellites other than Sentinel-2. For this reason, their equations were adapted to Sentinel-2 bands as detailed in Table 2. This band adaptation approach is not novel and has already been described in other studies (Du et al., 2016; Wang et al., 2018; Yang et al., 2017). The selected Sentinel-2 bands were: band 2 (490 nm) as a blue band, band 3 (560 nm) as a green band, band 4 (665 nm) as

**Table 2** Water surface extraction indices were considered in this study.  $\rho$  represents the top of atmosphere reflectance (TOA) at different Sentinel-2 bands.

Multiband Index	Equation	Water value	Reference
Normalised Difference Vegetation Index	$NDVI = (\rho_{B8} - \rho_{B4}) / (\rho_{B8} + \rho_{B4})$	Negative	Rouse et al. (1973)
Normalised Difference Water Index	$NDWI = (\rho_{B3} - \rho_{B8}) / (\rho_{B3} + \rho_{B8})$	Positive	McFeeters et al. (1996)
Modified Normalised Difference Water Index	$MNDWI = (\rho_{B3} - \rho_{B11}) / (\rho_{B3} + \rho_{B11})$	Positive	Xu et al. (2006)
Automated Water Extraction Index	$AWEIsh = \rho_{B2} + 2.5 * \rho_{B3} - 1.5 * (\rho_{B8} + \rho_{B11}) - 0.25 * \rho_{B12}$	Positive	Feyisa et al. (2014)

a red band and band 8 (842 nm) as NIR band. Band 11 (1614 nm) and band 12 (2190 nm) were chosen for SWIR1 and SWIR2, respectively. All selected bands have a spatial resolution of 10 m except for SWIR1 and SWIR2 for which the resolution is 20 m per pixel. Image sharpening processes to convert 20 m bands into 10 m bands were not performed since this study aimed to develop a methodology as simple as possible so that potential users can implement it quickly. The SNAP 8.0 software was used to resample the bands with 20 m of spatial resolution into 10 m. The same software was also used for the generation of the indices.

All the water indices described above allow water pixels to be classified by applying a simple threshold (T), which can be adjusted to different images or different classification priorities. The determination of the optimal threshold value is of great importance for the accurate delimitation of water bodies, and it can be done manually (Meng et al., 2013; Xu et al., 2005) or using automated methods (Ji et al., 2009; Zhang et al., 2018). In this study, the threshold values (T) were initially set to zero but generally, threshold adjustments to individual situations can achieve a more accurate delineation of water bodies (Du et al., 2012; Sekertekin, 2019). The extracted water bodies were converted to polygons and water level changes were evaluated using ArcGIS 10.3.1.

### 3. Results

#### 3.1. Selection of the optimal multiband indices

The performance of the different indices mentioned in Table 2 was first interpreted visually and compared with the near-infrared (NIR) band at 842 nm. NIR wavelengths are strongly absorbed by water and reflected by terrestrial vegetation and dry soil (Sun et al., 2012). Even though NIR bands can also be used to extract water bodies using a threshold, this process requires an individual evaluation in each image. Changes in the image conditions (e.g. illumination) can modify the optimal threshold value. These changes are minimised using band ratios; for this reason, the NIR bands were only used to support the interpretation results.

All the evaluated indices have a spatial resolution of 10 m; however, some bands used for the MNDWI and AWEIsh indices were resampled from 20 m to 10 m. It is also important to remind here that the Louro lagoon is located in a rural environment with small and isolated settlements in the surrounding areas. The terrain elevations of nearby Monte Louro (~241 m) produces shadows, but they do not affect the lagoon area. Taking into account these aspects, some differences were found between the indices in the visual analysis.

As expected, the lagoon’s delimitation and its inlet were less defined when the indices with the 20 m bands, MNDWI and AWEIsh, were used (see Figure 3). The AWEIsh index results were more affected by the swell, and showed the highest values close to the shore where the waves were breaking. This issue was not evident in MNDWI, but this index seems to be more sensitive to the shade produced by terrain elevations (Figure 3). In this case, the shade does not affect the lagoon, but the 20 m bands lead to a lower definition at which the water surface and inlet were mapped. The MNDWI and the AWEIsh indices were excluded from the analysis to avoid adding a sharpening step to the processing chain.

The visual analysis of the NDVI and NDWI indices showed a clear differentiation between land and water and a better delimitation of the inlet because of the higher spatial resolution (10 m) (Figure 3). NDVI was initially developed for separating green vegetation from other surfaces. However, some studies reported that the NDVI performs well for water detection (Rokni et al., 2014), giving water features negative values. On the other hand, the NDWI enhances information about water bodies by including the green band while reducing vegetation and soil features (Li et al., 2013). The NDWI index classifies water features with positive values, while vegetation and soil are classified with negative values (McFeeters et al., 1996).

To evaluate the results obtained with NDVI and NDWI indices in more detail, the frequency density histograms were analysed. The differentiation between land and water pixels was confirmed by the density distributions (Figure 4). The histogram of both indices showed a clear bimodal distribution with a higher peak representing water pixels and a lower peak representing land pixels. In the NDWI the land and water peaks were further apart, indicating a better differentiation between both substrates. This behaviour was

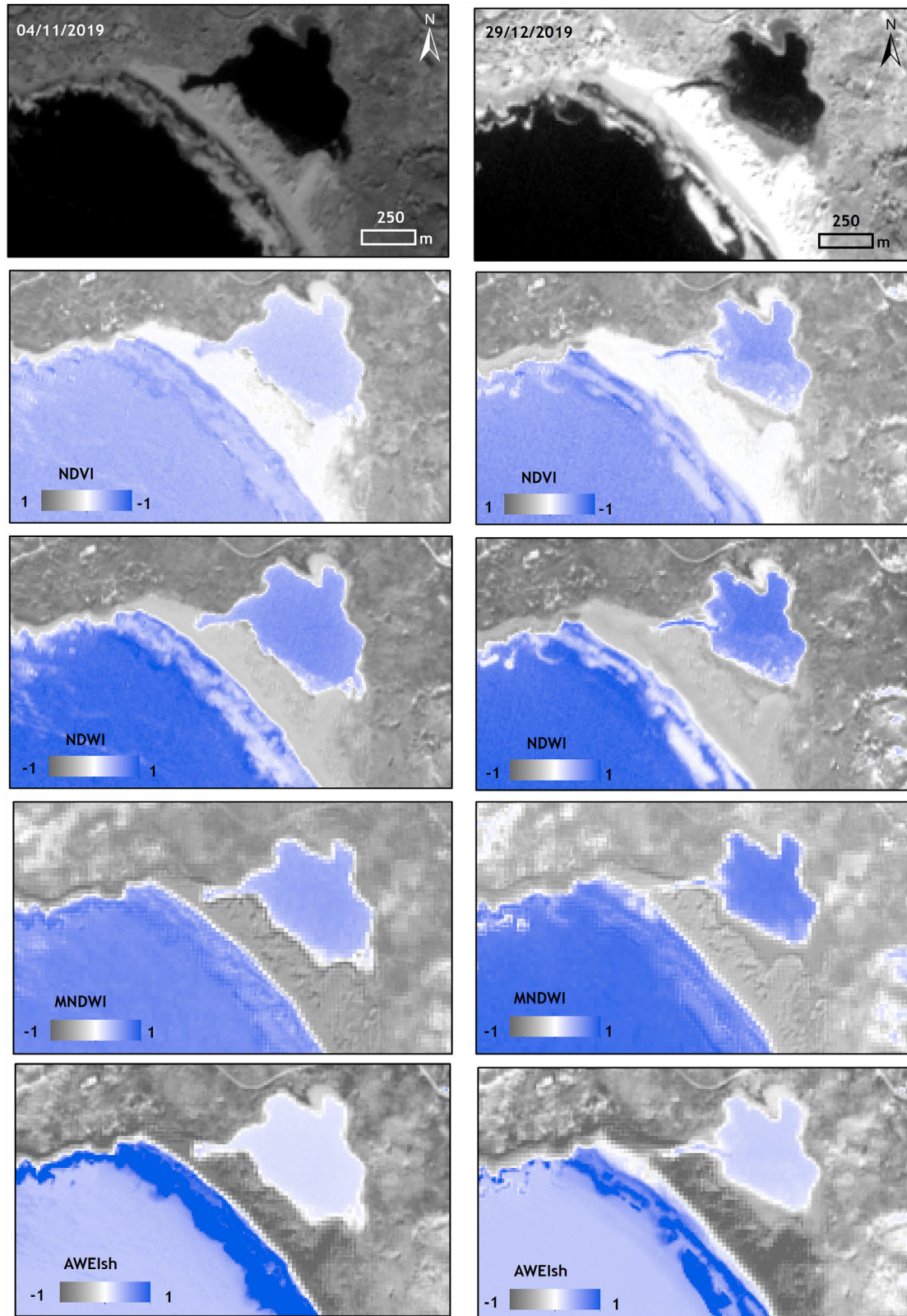


**Figure 3** Example of the water surface extraction indices evaluated in this study applied to two different Sentinel-2 images (04/11/2019 and 29/12/2019). The first image on the left and right corresponds to band 8 (842 nm). The AWEIsh index values were rescaled to values between  $-1$  and  $1$  for comparison with the other indices.

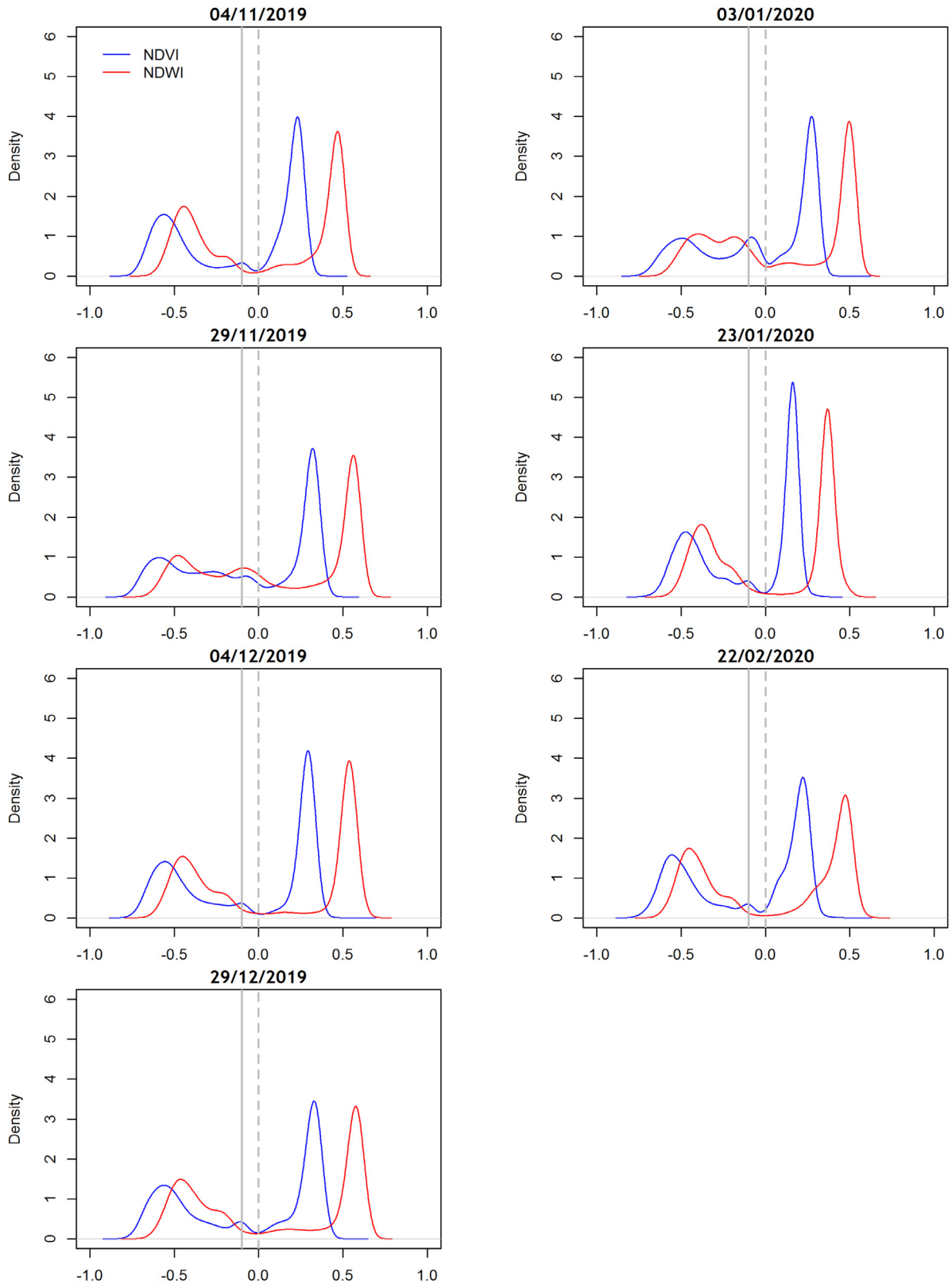


**Figure 4** Density distributions of the NDVI and NDWI. The grey dashed line indicates the threshold value  $T \geq 0$ , while the solid line indicates a threshold of  $T \geq -0.1$ . NDVI values were inverted for a better comparison.



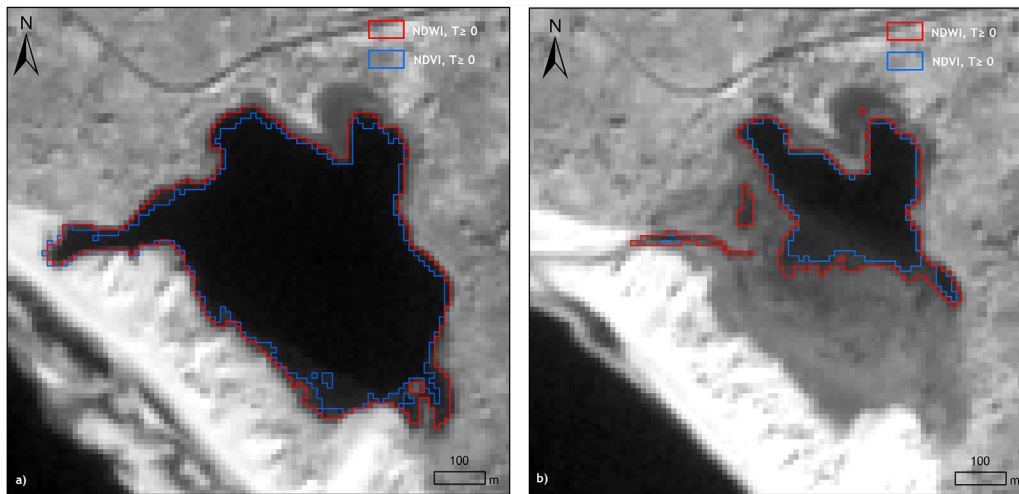


**Figure 5** Comparison of the water surface extension using the NDVI and NDWI and a threshold value of  $T \geq 0$ . a) Delimitation of the water body on 04/11/2019. b) Delimitation of the water body on 23/01/2020. The NDVI shows more conservative results missing water pixels located at the edge of the lagoon.

confirmed by comparing the extracted water surface obtained by the two indices using the default threshold value of  $T \geq 0$  (Figure 5). In all the cases, the NDVI showed more conservative results missing water pixels located on the water body's edge. This fact was especially evident when the lagoon showed a low water level, as was the case on 23/01/2020 (Figure 5b). For this reason, the NDWI was selected as the optimal index.

### 3.2. Delimitation of water surface

The histograms of the NDWI index showed a well-defined region between water and land peaks that could be interpreted as mixed pixels (Figure 4). Mixed pixels are caused by two or more land-cover classes in a surface area smaller than the spatial resolution of the image (Ji et al., 2009), and their amount will depend on the heterogeneity of the substrates. These mixed pixels can be identified in the histograms as a flat area between water and land peaks. Except for the images affected by clouds (29/11/2019 and 03/01/2020) the histograms revealed that mixed pixels could reach thresholds of  $-0.1$  (Figure 4). Each image was individually evaluated in order to identify those pixels with a value lower than zero and higher than  $-0.1$ . All those pixels were located in well-defined areas at the lagoon's border. Further analysis is required since these pixels could be interpreted as pixels with a high water content but not submerged and pixels located in very shallow areas. When the lagoon had a high water level, both threshold values showed very similar results (Figure 6a); however, the largest differences were found when the water level started to decrease. In this case, a threshold value of  $T \geq 0$  seems to be more conservative. This issue affects the inlet's delimitation since during the process of the sand barrier closing the water flow might be only a few centimetres deep (e.g. Figure 1b and 1c), and in this case, its delimitation using a threshold of  $T \geq 0$  can be more challenging. Considering the objective of this study, the threshold value of  $T \geq 0$  was selected. This value led to a good delimitation of the surface water

level and allowed the inlet's detection and monitoring. For a more detailed delimitation of the inlet, further research would be required exploring other threshold values with the support of specific field campaigns.

Using a value of  $T \geq 0$ , the NDWI index was evaluated for the detection of the sand barrier break and its associated water level variations (Figure 7). The analysis of these Sentinel-2 images revealed that the Louro lagoon suffers significant morphological and hydrological variations. Between November 2011 and February 2020, the sand barrier broke and closed several times, allowing the water inside the lagoon to flow into the sea. The image acquired on 04/11/2019 showed the lagoon to have a high water level with the water about to flow over the dune crest. This situation presents a critical moment and indicates an imminent break of the sand barrier if the trigger conditions appear (e.g. heavy rains, southwesterly winds or high tides). During the storms, waves driven in the SW direction generate dissipative morphologies in the sand barrier and modify currents and sediment transport (Amécija et al., 2009). The current convergence promotes a rip current formation and the breaking of the sand barrier. However, the formation of the inlet and the consequent water outflow also needs the water elevation in the lagoon to be higher than the high tide water level by about 1 m, which requires prolonged periods of high rainfall levels (Pérez-Arlucea et al., 2011). This high water level generates enough pressure and potential energy to break the sand barrier, thus forming the inlet.

Between 04/11/2019 and 29/11/2019 meteorological data registered at the CMS weather station reported winds close to 30 km/h (Figure 2) while the SIMAR node showed significant wave heights ( $\sim 6$  m). Moreover, between 09/11/2019 and 15/11/2019, the tide reached high coefficient values between 74 and 87. Meteorological factors, together with tides, could be the main triggers for breaking the sand barrier and forming the inlet detected on 29/11/2019. This Sentinel-2 image reveals that the inlet formation could have been produced some days before the image acquisition. This is suggested by the fact that the inlet shows a narrow part (Figure 7b), indicating that sand

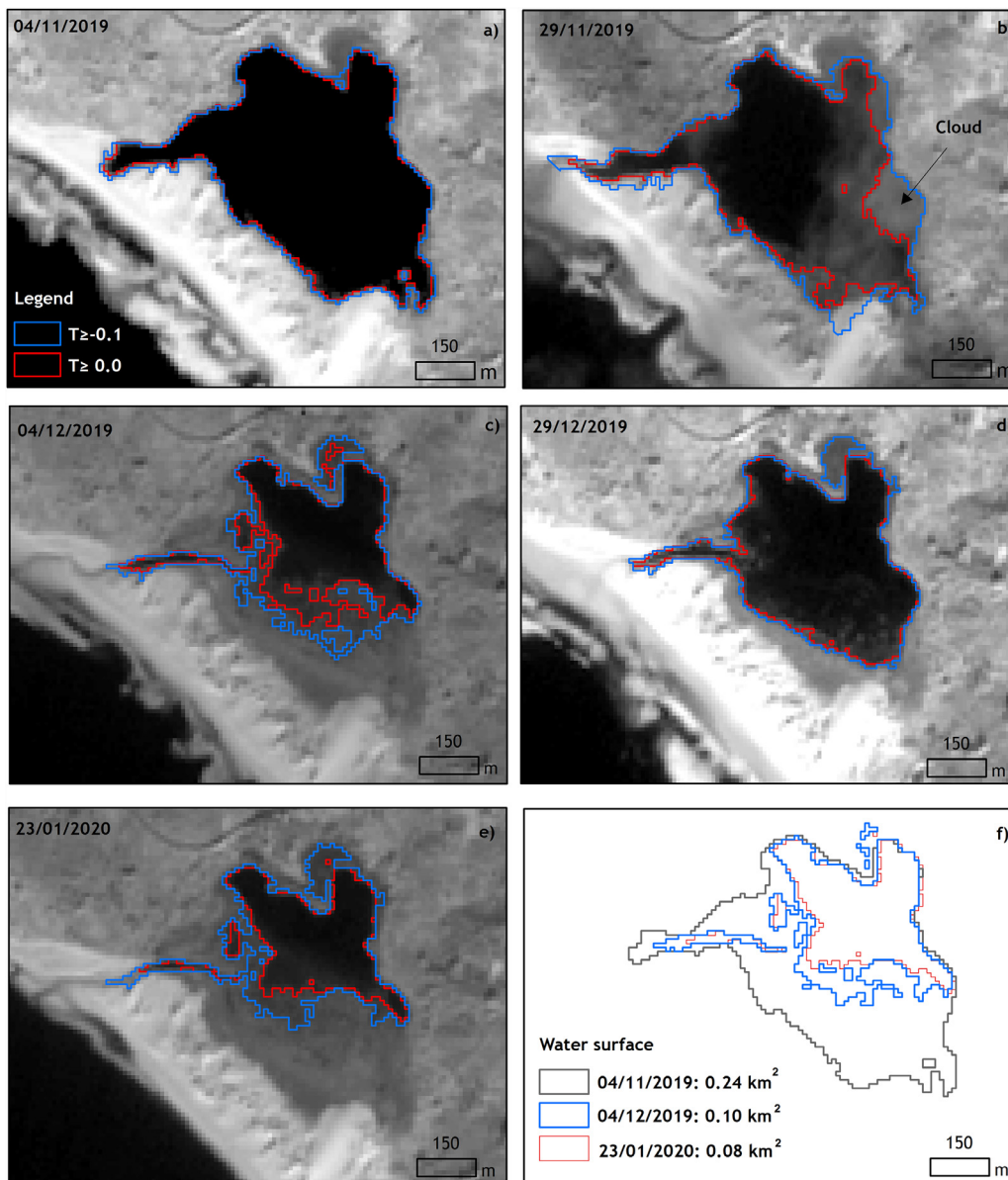


**Figure 6** a–e) Example of extracted water body surfaces in different images using threshold values of  $T \geq 0$  (red) and  $T \geq -0.1$  (blue); f) variation of water levels using the NDWI and  $T \geq 0$ .

movements have already occurred and the communication with the open sea has started to reduce. The next available Sentinel-2 image, registered one month later (29/12/2019), showed the sand barrier sealed and the water level almost fully recovered. The Sentinel-2 image registered on 23/01/2020 revealed a lower water level again, indicating that a new break of the sand barrier had happened prior to the acquisition of the image. A heavy rain period ( $>70 \text{ L/m}^2$ ) in mid-January, together with moderate winds ( $\sim 30 \text{ km/h}$ ) and high tide coefficients (74–92), could have triggered the inlet formation after 03/01/2013 since on this date the lagoon showed a high water level. The image registered on 22/02/2020 indicates a recovery of the sand barrier and the lagoon water level.

These observations confirm that the Sentinel-2 images showed the sand barrier to break and close several times

during the four-month period. These changes were associated with meteorological and oceanographic conditions that produced drastic water level changes. During the timescale of only one month, the water surface can be reduced from  $0.24 \text{ km}^2$  to  $0.10 \text{ km}^2$  or even lower (Figure 6f). However, in wintertime and in the absence of breaks, the lagoon’s water level can be fully recovered within less than a month.

#### 4. Discussion

The results obtained in this study demonstrate that Sentinel-2 data can provide valuable information to detect and monitor highly dynamic morphological and hydrological changes in small coastal lagoons using a simple processing chain. This information can be essential to complement

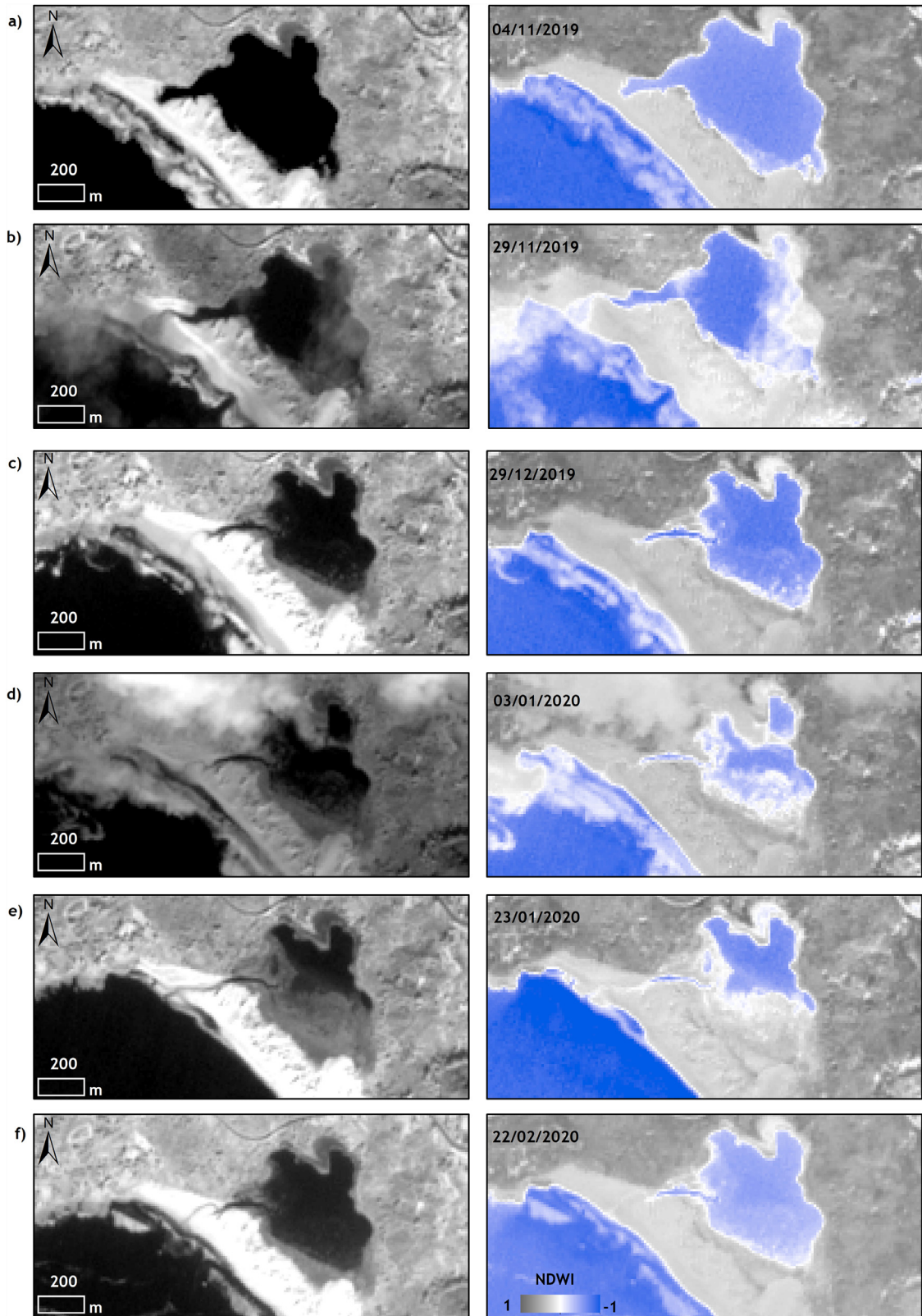


**Figure 7** Example of the NDWI ( $T \geq 0$ ) results compared to the NIR band (842 nm). Note that the Sentinel-2 images registered on 29/11/2019 and 03/01/2020 were both affected by clouds.

conventional in situ monitoring programmes providing continuous data in space and time. Although the breaking and closing of the sand barrier is a quick process that might happen within a timescale of a few days (Pérez-Arlucea et al., 2011), the number of available images (around two per month) was enough to reveal interesting information about these processes in combination with ancillary data. The availability of good quality images without cloud coverage affecting the lagoon determines the success of the methodology described in this study. Even though it was possible to have at least two images per month in the winter period, it is expected that summertime conditions increase the chance of having a higher number of good quality images that could allow a more detailed study.

Processing remote sensing images from digital levels (DN) or TOA values to surface reflectance is generally complicated. An accurate atmospheric correction needs input from many atmospheric variables such as aerosol concentration, optical depth or air pressure at sea level, as well as information about optically active constituents present in the water surface. Having data about all these parameters at the time of image acquisition is challenging (Du et al., 2002). Several studies have used DN or TOA, instead of surface reflectance to build water indices (Danaher et al., 2006; Donchyts et al., 2016; Ko et al., 2015), and obtained very similar results than when using surface reflectance (Fisher et al., 2016). In this study, TOA Sentinel-2 images provided a good delimitation of the lagoon water surface, and the results allowed the detection of the sand barrier break and the inlet. Two factors could explain why such a good delimitation from the data is possible. First, resizing the image to the Louro lagoon area remarkably reduces the pixel variability. Second, the arithmetic operation of the multiband water indices cancels out a large portion of noise (i.e. sensor calibration and changing radiation conditions caused by the illumination, soil, topography or atmospheric conditions) (Ji et al., 2009).

Although various comparative studies on multiband indices have been performed, no index was found to be effective in all scenarios (Boschetti et al., 2014). The Louro lagoon is located in a rural area with no significant terrain elevations around the lagoon. Both issues facilitate the delimitation of water bodies without interferences produced by urban areas or topographic shades. As expected, the spatial resolution of Sentinel-2 bands influenced the water surface delimitation, especially at the edges of the lagoon and the inlet. The NDVI and NDWI indices showed the best results regarding the water surface and inlet detection due to their higher spatial resolution bands (10 m). These results coincided with other studies where both indices were more efficient in extracting water bodies while removing most classification errors for shadow and other non-water surfaces (Acharya et al., 2018). The frequency density histograms analysis showed that the NDWI produced a better differentiation between water and terrestrial substrates (Figure 4). Thus, the NDWI was selected as the optimal index to monitor morphological and hydrological changes in the Louro lagoon. The discharge of water from the lagoon makes other substrates such as vegetation and sand appear (Fraga-Santiago et al., 2019). High reflection of vegetation and soil in NIR bands causes the NDWI to be less affected by this interaction at the lagoon edge and hence giving more accurate results. The lack of built-up classes

adjacent to the water mass increases the accuracy of the NDWI, which generally cannot sufficiently suppress the reflectance from built-up areas. The selection of the NDWI as the optimal index was coincident with the results provided by Zhou et al. (2017). These authors (Zhou et al., 2017) compared several indices to map open surface water in the Poyang Lake Basin (China). Other studies also reported that the NDWI performs better in small lakes due to less interaction with classes adjacent to the water body (Özelkan, 2020).

One of the critical aspects of applying multiband water indices is the determination of an optimal threshold value. The optimal value can depend on the characteristics of each particular site and on the threshold method employed (Sekertekin, 2019). Due to the reflectance characteristics, the NDWI values for water are usually higher than zero. Therefore, a zero ( $T \geq 0$ ) threshold is often applied to extract water from satellite images using this index. In the Louro lagoon, this threshold value showed a good delimitation of the water surface, including the inlet detection (Figure 7), except for the images registered on 29/11/2019 and 03/01/2020, due to the presence of clouds.

Employing the frequency histograms, populations of water, land and mixed pixels were identified. The number of mixed pixels is significant for coarse resolution satellite images (e.g. AVHRR (1 km), Sentinel-3 OLCI (300), MODIS (250 m)) where large pixels usually contain multiple types of substrates. Compared to these optical satellites, the spatial resolution of Sentinel-2 (10 m) reduces mixed pixels and their associated omission errors. For the purpose of this study, good results were obtained using a threshold value of  $T \geq 0$ . This threshold value ( $T \geq 0$ ) accurately delimited submerged areas and was well suited to detect the sand barrier break and the inlet. The threshold value of  $T \geq -0.1$  included mixed pixels that were interpreted as very shallow areas. It also showed a better delimitation of the inlet when the water flow is very low (e.g. Figure 1). However, new analyses of Sentinel-2 images, supported by field campaigns, will be necessary to better understand how the lagoon's water surface variations affect the selection of the optimal threshold value.

This study revealed that the lagoon suffers drastic water level variations during the opening and closing of the sand barrier. Even though field campaigns were not performed, the results related to the estimation of water surface coverage were very similar to those reported by other authors using different methodologies in the same study area (e.g. González-Villanueva et al., 2015). The results showed that the breaking and closing of the sand barrier could be a rapid process supporting the results obtained by Pérez-Arlucea et al. (2011). However, the water level can be recovered within less than one month. The sand barrier-breaking frequency and duration can drive different and complex effects on ecological, chemical and physical processes (Conde et al., 2015) and in many cases, these processes have not been explicitly evaluated yet (Yáñez-Aranciabía et al., 2014).

Sentinel-2 data could provide valuable information for establishing the sand barrier vulnerability frequency and preventing damage in these ecosystem services such as fisheries. For example, the breaking and closing of the sand bar-

rier of the Baldaio lagoon, a similar lagoon located on the Galician coast, has a direct impact on shellfish harvesting areas. The methodology proposed here could be transferred to similar sites for supporting coastal management.

Although the number of satellite applications in coastal lagoons has increased, the number of studies that include Sentinel-2 data is still small. Most of the Sentinel-2 applications are related to the assessment and monitoring of water quality parameters (e.g. Vaičiūtė et al., 2021), but the number of applications related to water body extraction is still scarce (e.g. Kaplan et al., 2017; Salameh et al., 2020). Due to the relatively short lifespan of Sentinel-2 mission (up to now 6 years), it is also common to find a combination of Sentinel-2 and Landsat data to study long term changes (e.g. Karim et al., 2019; Vaičiūtė et al., 2021). The series of Sentinel-2 data will increase in the future with the launch of Sentinel-2C and Sentinel-2D.

The vulnerability of the Louro lagoon and other similar lagoons will be enhanced in the coming decades due to climate change effects. Sea-level rise, intensification of storms, alteration in the tidal regimes, or changes in the freshwater inputs will have a substantial impact on the functioning of these areas. To prevent ecological losses and degradation due to climate change effects, continuous spatial and temporal information will be required. This study demonstrates the importance of Sentinel-2 data to monitor highly dynamic coastal areas such as coastal lagoons. The combination of Sentinel-2 data with in situ monitoring programmes will provide valuable information for coastal management that could contribute to face climate change effects and protect ecosystem services.

## Declaration of competing interest

The authors declare that they have no known competing financial interests or personal relationships that could have appeared to influence the work reported in this paper.

## Acknowledgements

The Copernicus programme, European Space Agency and European Commission are thanked for providing Sentinel-2 data. The author also thank Gloria Portilla for her assistance in the access to tide data and the two anonymous reviewers that, with their comments, helped to improve the initial version of this manuscript.

## References

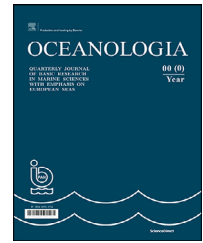
- Acharya, T.D., Subedi, A., Lee, D.H., 2018. Evaluation of water indices for Surface Water Extraction in a Landsat 8 Scene of Nepal. *Sensors* 18, 2580. <https://doi.org/10.3390/s18082580>
- Amécija, C., Villaceros-Robineau, N., Alejo, I., Pérez-Arlucea, M., et al., 2009. Morphodynamic conceptual model of an exposed beach: the case of Louro Beach (Galicia, NW Iberia). *J. Coast Res.* S156 1711–1715.
- Anspér, A., Alikas, K., 2019. Retrieval of chlorophyll a from Sentinel-2 MSI data for the European Union Water Framework Directive Reporting Purposes. *Remote Sens* 11 (1), 64. <https://doi.org/10.3390/rs11010064>
- Bao, R., Alonso, A., Delgado, C., Pagés, J.L., 2007. Identification of the main driving mechanisms in the evolution of a small coastal wetland (Traba, Galicia, NW Spain) since its origin 5700 cal yr BP. *Palaeogeogr. Palaeoclimatol. Palaeoecol.* 247, 296–312. <https://doi.org/10.1016/j.palaeo.2006.10.019>
- Barnes, R.S.K., 1980. *Coastal Lagoons*. Cambridge University Press, Cambridge, 106 pp.
- Bertotti-Crippa, L., Stenert, C., Maltchik, L., 2013. Does the management of sandbar openings influence the macroinvertebrate communities in southern Brazil wetlands? A case study at Lagoa do Peixe National Park Ramsar site. *Ocean Coastal Manage.* 71, 26–32. <https://doi.org/10.1016/j.ocecoaman.2012.10.009>
- Bird, E.C.F., 1994. Physical setting and geomorphology of coastal lagoons. In: Kjerfve, B. (Ed.), *Coastal Lagoon Processes*. Elsevier, Amsterdam, 9e39.
- Boschetti, M., Nutini, F., Manfron, G., Brivio, P.A., Nelson, A., 2014. Comparative analysis of Normalised Difference Spectral Indices derived from MODIS for detecting surface water in flooded rice cropping systems. *PLoS ONE* 9 (2), e88741. <https://doi.org/10.1371/journal.pone.0088741>
- Braga, F., Scarpa, G.M., Branco, V., Manfé, G., Zaggia, L., 2020. COVID-19 lockdown measures reveal human impact on water quality transparency in the Venice Lagoon. *Sci. Total Environ.* 736, 139612. <https://doi.org/10.1016/j.scitotenv.2020.139612>
- Brisset, M., Van Wynsberge, S., Andréfouët, S., Payri, C., Soulard, B., Bourassin, E., Gendre, R.L., Coutures, E., 2021. Hindcast and Near Real-Time Monitoring of Green Macroalgae Blooms in Shallow Coral Reef Lagoons Using Sentinel-2: A New-Caledonia Case Study. *Remote Sens.* 13, 211. <https://doi.org/10.3390/rs13020211>
- Bryant, R.G., Rainey, M.P., 2002. Investigation of flood inundation on playas within the Zone of Chotts, using a time-series of AVHRR. *Remote Sens. Environ.* 82, 360–375. [https://doi.org/10.1016/S0034-4257\(02\)00053-6](https://doi.org/10.1016/S0034-4257(02)00053-6)
- Casal, G., Hedley, J.D., Monteys, X., Harris, P., Cahalane, C., McCarthy, T., 2020. Satellite-derived bathymetry in optically complex waters using a model inversion approach and Sentinel-2 data. *Estuar. Coast. Shelf Sci.* 241, 106814. <https://doi.org/10.1016/j.ecss.2020.106814>
- Casal, G., Sánchez-Carnero, N., Sánchez-Rodríguez, E., Freire, J., 2011. Remote sensing with SPOT-4 for mapping kelp forest in turbid waters on the south European Atlantic shelf. *Estuar. Coast. Shelf Sci.* 91 (3), 371–378. <https://doi.org/10.1016/j.ecss.2010.10.024>
- Conde, D., Vitancurt, J., Rodríguez-Gallego, L., de Álava, D., Verrastro, N., Chreties, C., Solari, S., Teixeira, L., Lagos, X., Piñeiro, G., Seijo, L., Caymaris, H., Panario, D., 2015. Solutions for Sustainable Coastal Lagoon Management: From Conflict to the Implementation of a Consensual Decision Tree for Artificial Opening. In: Baztan, J., Chouinard, O., Jorgensen, B., Tett, P., Vanderlinden, J.P., Vasseur, L. (Eds.), *Coastal Zones. Solutions for the 21st Century*. Elsevier, Amsterdam, The Netherlands, 217–250.
- Costas, S., Muñoz-Sobrino, C., Alejo, I., Pérez-Arlucea, M., 2009. Holocene evolution of a rock-bounded barrier-lagoon system. Cies Islands, northwest Iberia, *Earth Surf. Proc. Land* 34, 1575–1586. <https://doi.org/10.1002/esp.1849>
- Danaher, T., Collett, L., 2006. Development, optimisation and multi-temporal application of a simple Landsat based water index. Paper presented at 13th Australasian Remote Sensing and Photogrammetry Conference, Canberra, Australia, 21–22 November 2006.
- Davies, J.L., 1964. A morphogenetic approach to world shorelines. *Zeitschrift für Geomorphologie* 8, 127–142.
- DeVries, B., Huang, C., Armston, J., Huang, W., Jones, J.W., Lang, M.W., 2020. Rapid and robust monitoring of flood events

- using Sentinel-1 and Landsat data on the Google Earth Engine. *Remote Sens. Environ.* 240, 111664. <https://doi.org/10.1016/j.rse.2020.111664>
- Donchyts, G., Schellekens, J., Winsemius, H., Eisemann, E., van de Giesen, N., 2016. A 30 m resolution surface water mask including estimation of positional and thematic differences using Landsat 8, SRTM and OpenStreetMap: A case study in the Murray-Darling Basin, Australia. *Remote Sens.* 8 (5), 386. <https://doi.org/10.3390/rs8050386>
- Du, Y., Teillet, P.M., Cihlar, J., 2002. Radiometric normalisation of multitemporal high-resolution satellite images with quality control for land cover change detection. *Remote Sens. Environ.* 82 (1), 123–134. [https://doi.org/10.1016/S0034-4257\(02\)00029-9](https://doi.org/10.1016/S0034-4257(02)00029-9)
- Du, Y., Zhan, Y., Ling, F., Wang, Q., Li, W., Li, X., 2016. Water bodies' mapping from Sentinel-2 imagery with Modified Normalized Difference Water Index at 10-m spatial resolution produced by sharpening the SWIR band. *Remote Sens.* 8 (4), 354. <https://doi.org/10.3390/rs8040354>
- Du, Z., Linghu, B., Ling, F., Li, W., Tian, W., Wang, H., Gui, Y., Sun, B., Zhang, X., 2012. Estimating surface water area changes using time-series Landsat data in the Qingjiang River Basin, China. *J. Appl. Remote Sens.* 6, 063609. <https://doi.org/10.1117/1.JRS.6.063609>
- Duan, Z., Bastiaanssen, W.G.M., 2013. Estimating water volume variations in lakes and reservoirs from four operational satellite altimetry databases and satellite imagery data. *Remote Sens. Environ.* 134, 403–416. <https://doi.org/10.1016/j.rse.2013.03.010>
- Duck, R.W., Figueiredo da Silva, J., 2012. Coastal lagoons and their evolution: A hydromorphological perspective. *Estuar. Coast. Shelf.* 110, 2–14. <https://doi.org/10.1016/j.ecss.2012.03.007>
- EC, 1992. Council Directive 92/43/EEC of 21 May 1992 on the conservation of natural habitats and of wild fauna and flora. *Official Journal L* 206, 7–50. <https://eur-lex.europa.eu/LexUriServ/LexUriServ.do?uri=CELEX:31992L0043:EN:HTML>
- EC, 2000. Directive 2000/60/EC of the European Parliament and of the Council of 23 October 2000 establishing a framework for Community action in the field of water policy. *Official Journal L* 327, 0001–0073, 22/12/2000 P. <https://eur-lex.europa.eu/eli/dir/2000/60/oj>
- Feyisa, G.L., Meilby, H., Fensholt, R., Proud, S.R., 2014. Automated water extraction index: A new technique for surface water mapping using Landsat imagery. *Remote Sens. Environ.* 140, 23–35. <https://doi.org/10.1016/j.rse.2013.08.029>
- Fisher, A., Flood, N., Danaher, T., 2016. Comparing Landsat water index methods for automated water classification in eastern Australia. *Remote Sens. Environ.* 175, 167–182. <https://doi.org/10.1016/j.rse.2015.12.055>
- Fortunato, A.B., Nahon, A., Dodet, G., Pires, A.R., Freitas, M.C., Bruneau, N., Azevedo, A., Bertin, X., Benevides, P., Andrade, C., Oliveira, A., 2014. Morphological evolution of an ephemeral tidal inlet from opening to closure: the Albufeira inlet, Portugal. *Cont. Shelf Res.* 73 (1), 49–63. <https://doi.org/10.1016/j.csr.2013.11.005>
- Fraga-Santiago, P., Gómez-Pazo, A., Pérez-Alberti, A., Montero, P., Otero-Pérez, A., 2019. Trends in the recent evolution of coastal lagoons and lakes in Galicia (NW Iberian Peninsula). *J. Mar. Sci. Eng.* 7, 272. <https://doi.org/10.3390/jmse7080272>
- Frazier, P.S., Page, K.J., 2000. Water body detection and delineation with Landsat TM data. *Photogramm. Eng. Remote Sens.* 66 (12), 1461–1467.
- Gale, E., Pattiaratchi, C., Ranasinghe, R., 2006. Vertical mixing processes in intermittently closed and open lakes and lagoons, and the dissolved oxygen response. *Estuar. Coast. Shelf Sci.* 69 (1–2), 205–216. <https://doi.org/10.1016/j.ecss.2006.04.013>
- Gholizadeh, M.H., Melesse, A.M., Reddi, L., 2016. A comprehensive review on water quality parameters estimation using remote sensing techniques. *Sensors* 16 (8), 1298. <https://doi.org/10.3390/s16081298>
- González-Villanueva, R., Costas, S., Pérez-Arlucea, M., Jerez, S., Trigo, R.M., 2013. Impact of atmospheric circulation patterns on coastal dune dynamics, NW Spain. *Geomorphology* 185, 96–109. <https://doi.org/10.1016/j.geomorph.2012.12.019>
- González-Villanueva, R., Pérez-Arlucea, M., Costas, S., 2017. Lagoon water-level oscillations driven by rainfall and wave climate. *Coast. Eng.* 130, 34–45. <https://doi.org/10.1016/j.coastaleng.2017.09.013>
- González-Villanueva, R., Pérez-Arlucea, M., Costas, S., Bao, R., Otero, X.L., Goble, R., 2015. 8000 years of environmental evolution of barrier–lagoon systems emplaced in coastal embayments (NW Iberia). *The Holocene* 25 (11), 1786–1801. <https://doi.org/10.1177/0959683615591351>
- Green, A., Cooper, J.A.G., LeVieux, A., 2013. Unusual barrier/inlet behaviour associated with active coastal progradation and river-dominated estuaries. *J. Coast. Res.* 35–45. [https://doi.org/10.2112/SI\\_69\\_4](https://doi.org/10.2112/SI_69_4)
- Guo, Y.L., Li, Y.M., Zhu, L., Liu, G., Wang, S., Du, C.G., 2015. An Improved Unmixing-Based Fusion Method: Potential application to remote monitoring of inland waters. *Remote Sens.* 7, 1640–1666. <https://doi.org/10.3390/rs70201640>
- Hedley, J.D., Roelfsema, C., Brando, V., Giardino, C., Kutser, T., Phinn, S., Mumby, P.J., Barrilero, O., Laporte, J., Koetz, B., 2018. Coral reef applications of Sentinel-2: Coverage, characteristics, bathymetry and benthic mapping with comparison to Landsat 8. *Remote Sens. Environ.* 216, 598–614. <https://doi.org/10.1016/j.rse.2018.074>
- Ji, L., Zhang, L., Wylie, B., 2009. Analysis of dynamic thresholds for the normalised difference water index. *Photogramm. Eng. Remote Sens.* 75 (11), 1307. <https://doi.org/10.14358/PERS.75.11.1307>
- Kaplan, G., Avdan, U., 2017. Object-based water body extraction model using Sentinel-2 satellite imagery. *Int. J. Remote Sens.* 50 (1), 1297540. <https://doi.org/10.1080/22797254.2017.1297540>
- Karim, M., Maanan, M., Maanan, M., Rhinane, H., Rueff, H., Baidder, L., 2019. Assessment of water body change and sedimentation rate in Moulay Bouselham wetland, Morocco, using geospatial technologies. *Int. J. Sediment Res.* 34, 65–72. <https://doi.org/10.1016/j.ijsrc.2018.08.007>
- Kjerfve, B., 1994. In: Kjerfve, B. (Ed.). *Coastal Lagoon Processes, Amsterdam*, 1–8.
- Ko, B., Kim, H., Nam, J., 2015. Classification of potential water bodies using Landsat 8 OLI and a combination of two boosted Random Forest classifiers. *Sensors* 15 (6), 13763. <https://doi.org/10.3390/s150613763>
- Lavery, P., Pattiaratchi, C., Wyllie, A., Hick, P., 1993. Water quality monitoring in estuarine waters using the Landsat thematic mapper. *Remote Sens. Environ.* 46 (3), 268–280. [https://doi.org/10.1016/0034-4257\(93\)90047-2](https://doi.org/10.1016/0034-4257(93)90047-2)
- Li, W., Du, Z., Ling, F., Zhou, D., Wang, H., Gui, Y., Sun, B., Zhang, X.A., 2013. A comparison of land surface water mapping using the normalised difference water index from TM, ETM+ and ALI. *Remote Sens.* 5 (11), 5530–5549. <https://doi.org/10.3390/rs5115530>
- Liu, X., Deng, R., Xu, J., Zhang, F., 2017. Coupling the modified linear spectral mixture analysis and pixel-swapping methods for improving subpixel water mapping: application to the Pearl River Delta, China. *Water* 9 (9), 658. <https://doi.org/10.3390/w9090658>
- Luis, K.M.A., Rheuban, J.E., Kavanaugh, M.T., Glover, D.M., Wei, J., Lee, Z., Doney, S.C., 2019. Capturing coastal water clarity variability with Landsat 8. *Mar. Pollut. Bull.* 145, 96–104.
- McFeeters, S.K., 1996. The use of the Normalised Difference Water Index (NDWI) in the delineation of open water features. *Int. J. Remote Sens.* 17, 1425–1432. <https://doi.org/10.1080/01431160600589179>

- Meng, W., Zhu, S., Cao, W., Su, X., Cao, B., 2013. Establishment of synthetic water index. *Science of Surveying and Mapping* 38 (4), 130–133.
- Moreno, I.M., Avila, A., Losada, M.A., 2010. Morphodynamics of intermittent coastal lagoons in southern Spain: Zahara de los atunes. *Geomorphology* 121 (3–4), 305–316. <https://doi.org/10.1016/j.geomorph.2010.04.028>
- Newton, A., Brito, A.C., Icely, J.D., Derolez, V., Clara, I., Angus, S., Schernewski, G., Inácio, M., Lillebø, A.I., Sousa, A.I., Béjaoui, B., Solidoro, C., Tosic, M., Cañedo-Argüelles, M., Yamamuro, M., Reizopoulou, S., Tseng, H.C., Canu, D., Roselli, L., Maanan, M., Cristina, S., Ruiz-Fernández, A.C., Lima, R.F.D., Kjerfve, B., Rubio-Cisneros, N., Pérez-Ruzafa, A., Marcos, C., Pastres, R., Pranovi, F., Snoussi, M., Turpie, J., Tuchkovenko, Y., Dyack, B., Brookes, J., Povilanskas, J.R., Khokhlov, V., 2018. Assessing, quantifying and valuing the ecosystem services of coastal lagoons. *J. Nat. Conserv.* 44, 50–65. <https://doi.org/10.1016/j.jnc.2018.02.009>
- Özelkan, E., 2020. Water body detection analysis using NDWI indices derived from Landsat-8 OLI. *Pol. J. Environ. Stud.* 29 (2), 1759–1769. <https://doi.org/10.15244/pjoes/110447>
- Pérez-Arlucea, M., Almecija, C., González-Villanueva, R., Alejo, I., 2011. Water dynamics in a barrier-lagoon system: controlling factors. *J. Coast. Res. SI* 64, 15–19.
- Rokni, K., Ahmad, A., Selamat, A., Hazini, S., 2014. Water feature extraction and change detection using multitemporal Landsat Imagery. *Remote Sens.* 6, 4173–4189. <https://doi.org/10.3390/rs6054173>
- Rouse, J.W., Haas, R.H., Schell, J.A., Deering, D.W., 1973. Monitoring vegetation systems in the Great Plains with ERTS (Earth Resources Technology Satellite). In: *Proceedings of the Third Earth Resources Technology Satellite Symposium, Greenbelt, ON, Canada, 10–14 December*, 309–317.
- Salameh, E., Frappart, F., Turki, I., Laignen, B., 2020. Intertidal topography using the waterline method from Sentinel-1 and Sentinel-2 images: the examples of Arcachon and Veys Bays in France. *ISPRS J. Photogramm. Remote Sens.* 163, 98–120. <https://doi.org/10.1016/j.isprsjprs.2020.03.003>
- Sebastiá-Frasquet, M.T., Aguilar-Maldonado, J.A., Santamaría-del-Ángel, E., Estornell, J., 2019. Sentinel 2 analysis of turbidity patterns in a coastal lagoon. *Remote Sens.* 11 (24), 2926. <https://doi.org/10.3390/rs11242926>
- Sekertekin, A., 2019. Potential of global thresholding methods for the identification of surface water resources using Sentinel-2 satellite imagery and normalised difference water index. *J. Appl. Remote Sens.* 13 (4), 044507. <https://doi.org/10.1117/1.JRS.13.044507>
- Smakhtin, V., 2004. Simulating the hydrology and mouth conditions of small, temporarily closed/open estuaries. *Wetlands* 24, 123–132. [https://doi.org/10.1672/0277-5212\(2004\)024\[0123:STHAMC\]2.0.CO;2](https://doi.org/10.1672/0277-5212(2004)024[0123:STHAMC]2.0.CO;2)
- Sòria-Perpinyà, X., Vicente, E., Urrego, P., Pereira-Sandoval, M., Ruiz-Verdú, A., Delegido, J., Soria, J.M., Moreno, J., 2020. Remote sensing of cyanobacterial blooms in a hypertrophic lagoon (Albufera of Valencia, Eastern Iberian Peninsula) using multitemporal Sentinel-2 images. *Sci. Total Environ.* 698, 123305. <https://doi.org/10.1016/j.scitotenv.2019.134305>
- Sun, F., Sun, F., Chen, J., Gong, P., 2012. Comparison and improvement of methods for identifying waterbodies in remotely sensed imagery. *Int. J. Remote Sens.* 33, 6854–6875. <https://doi.org/10.1080/01431161.2012.692829>
- Tagliapietra, D., Sigovini, M., Ghirardini, A.V., 2009. A review of terms and definitions to categorise estuaries, lagoons and associated environments. *Mar. Freshw. Res.* 60, 497e509. <https://doi.org/10.1071/MF08088>
- Vaičiūtė, D., Bučas, M., Bresciani, M., Dabulevičienė, T., Gintauskas, J., Mėžinė, J., Tiškus, E., Umgiesser, G., Morkūnas, J., De Santi, F., Bartoli, M., 2021. Hot moments and Hotspots of cyanobacteria hyperblooms in the Curonian Lagoon (SE Baltic Sea) revealed via remote sensing-based retrospective analysis. *Sci. Total Environ.* 769, 145053. <https://doi.org/10.1016/j.scitotenv.2021.145053>
- Wang, Z., Liu, J., Li, J., Zhang, D.V., 2018. Multi-Spectral Water Index (MuWI): A native 10-m multi-spectral water index for accurate water mapping on Sentinel-2. *Remote Sens.* 10 (10), 1643. <https://doi.org/10.3390/rs10101643>
- Weidman, C.R., Ebert, J.R., 2013. In: *Aubrey, D.G., Giese, G.S. (Eds.), Cyclic Spit Morphology in a Developing Inlet System*, 44. American Geophysical Union, Washington DC, 186–212.
- Xie, H., Luo, X., Xu, X., Tong, X., Jin, Y., Pan, H., Tong, X., 2014. New hyperspectral difference water index for the extraction of urban water bodies by the use of airborne hyperspectral images. *J. Appl. Remote Sens.* 8, 5230–5237. <https://doi.org/10.1117/1.JRS.8.085098>
- Xu, H., 2005. A study on information extraction of water body with the modified normalised difference water index (MNDWI). *Int. J. Remote Sens.* 9 (5), 589–595. <https://doi.org/10.1080/01431160600589179>
- Xu, H., 2006. Modification of normalised difference water index (NDWI) to enhance open water features in remotely sensed imagery. *Int. J. Remote Sens.* 27, 3025–3033. <https://doi.org/10.1080/01431160600589179>
- Yang, X., Zhao, S., Qin, X., Zhao, N., Liang, L., 2017. Mapping of urban surface water bodies from Sentinel-2 MSI imagery at 10 m resolution via NDWI-based image sharpening. *Remote Sens.* 9 (6), 596. <https://doi.org/10.3390/rs9060596>
- Yáñez-Aranciabía, A., Day, J.W., Sánchez-Gil, P., Day, J.N., Lane, R.R., Zárate-Lomelíc, D., Alafita-Vásquez, H., Rojas-Galaviz, J.L., Ramírez-Gordillo, J., 2014. Ecosystems functioning: the basis for restoration and management of a tropical coastal lagoon, Pacific coast of Mexico. *Ecol. Eng.* 65, 88–100. <https://doi.org/10.1016/j.ecoleng.2013.03.007>
- Zhang, F., Li, J., Zhang, B., Shen, Q., Ye, H., Wang, S., Lu, Z., 2018. A simple automated dynamic threshold extraction method for the classification of large water bodies from Landsat-8 OLI water index images. *Int. J. Remote Sens.* 39 (11), 3429–3451. <https://doi.org/10.1080/01431161.2018.1444292>
- Zhang, T., Yang, X., Hu, S., Su, F., 2013. Extraction of coastline in aquaculture coast from multispectral remote sensing images: object-based region growing integrating edge detection. *Remote Sens.* 5 (9), 4470–4487. <https://doi.org/10.3390/rs5094470>
- Zhou, Y., Dong, J., Xiao, X., Xiao, T., Yang, Z., Zhao, G., Zou, Z., Qin, Y., 2017. Open surface water mapping algorithms: a comparison of water-related spectral indices and sensors. *Water* 9 (4), 256. <https://doi.org/10.3390/w9040256>

Available online at [www.sciencedirect.com](http://www.sciencedirect.com)

ScienceDirect

journal homepage: [www.journals.elsevier.com/oceanologia](http://www.journals.elsevier.com/oceanologia)

## ORIGINAL RESEARCH ARTICLE

# Combining multivariate statistical analysis to shed light on distribution and interaction of halogens in two economic ports along Red Sea Coast in Egypt

Gehan M. El Zokm, Ghada F. El-Said\*, Abeer A.M. El Sayed

National Institute of Oceanography and Fisheries, NIOF, Egypt

Received 14 February 2021; accepted 29 September 2021

Available online 14 October 2021

## KEYWORDS

Halogens;  
Seawater;  
Sediment;  
Multivariate analysis;  
Mabahiss and Safaga  
bays;  
Red Sea

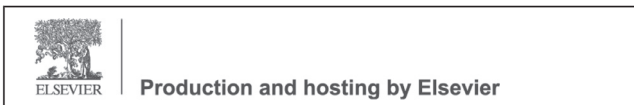
**Abstract** Mabahiss Bay and Safaga Bay are two important ports along the Red Sea coast of Egypt. The present study is the first to monitor halogen concentrations in these two ports. Certain halogens (F, Cl, Br and I) in coastal waters and sediments exhibited different behaviors. Fluoride (1.92–8.31 mg/L and 0.34–1.24 mg/g), chloride (20.76–22.68 g/L and 0.38–8.31 mg/g), bromide (95.90–151.84 mg/l and 6.66–50.61 mg/g), and iodide (2.77–39.19  $\mu$ g/L and 1.71–3.76  $\mu$ g/g) appeared in the seawater and sediments of Mabahiss Bay, respectively. In Safaga Bay, F, Cl, Br and I yielded ranges of (1.80–10.15 mg/L and 0.14–0.74 mg/g), (21.47–22.57 g/L and 0.68–1.42 mg/g), (15.98–146.51 mg/L and 6.13–74.59 mg/g) in seawater and sediments, respectively. In Mabashis Bay exclusively, the bromide and iodide levels in seawater increased significantly, and the sediments were vice versa. The average fluoride value in the two ports' seawater was higher than that in the unpolluted Mediterranean Sea. In contrast, the average bromide content in Mabahiss Bay seawater exceeded the Mediterranean Sea level. The seawater chloride content of the two ports was within the Mediterranean seawater's value, but the iodide concentration was lower than that of the unpolluted seawater. The application of different multivariate statistical techniques showed that halogen's distribution and halogen's geochemical characteristics control interaction in each region, ground flux, and proximity to human sources.

© 2021 Institute of Oceanology of the Polish Academy of Sciences. Production and hosting by Elsevier B.V. This is an open access article under the CC BY-NC-ND license (<http://creativecommons.org/licenses/by-nc-nd/4.0/>).

\* Corresponding author at: National Institute of Oceanography and Fisheries, NIOF, Egypt.

E-mail addresses: [gehanelzokm@yahoo.com](mailto:gehanelzokm@yahoo.com) (G.M. El Zokm), [ghadafarouk25@yahoo.com](mailto:ghadafarouk25@yahoo.com), [ghadafarouk25@gmail.com](mailto:ghadafarouk25@gmail.com) (G.F. El-Said), [perry201277@hotmail.com](mailto:perry201277@hotmail.com) (A.A.M. El Sayed).

Peer review under the responsibility of the Institute of Oceanology of the Polish Academy of Sciences.



<https://doi.org/10.1016/j.oceano.2021.09.007>

0078-3234/© 2021 Institute of Oceanology of the Polish Academy of Sciences. Production and hosting by Elsevier B.V. This is an open access article under the CC BY-NC-ND license (<http://creativecommons.org/licenses/by-nc-nd/4.0/>).



## 1. Introduction

Seawater is the main source of iodine (I), and the iodine concentration in seawater ranges from 40 to 60  $\mu\text{g/L}$ . Approximately 70% of the iodine in the earth's crust is bound to ocean sediments (Muramatsu and Wedepohl, 1998). Fluorine (F) was mobilized during marine carbonate diagenesis. However, it is fixed in newly formed carbonate, apatite, or clay minerals. Bromide and chloride are traceable chemicals in hydrology because they do not absorb negatively charged ions in the solid phase; thus, they are widely used to study the movement of water in marine sediments. Like iodine, bromine may volatilize from the marine environment and be carried to the land's surface. An increase in the I/Cl and Br/Cl ratios indicates an increase in iodine and bromine content, which is caused by prohibited substances flowing from external outlets to the surface of the marine environment. Limited information on halogens' geochemistry in the soil indicates that the adjacent sea influences the concentrations of chlorine, bromine, and iodine in the soil. In contrast, the content of fluorine in the soil depends on its content in the parent material. In some areas, the source of halogen pollutants significantly participates in its environmental concentration. The high electronegativity of fluorine makes it the most reactive element and enables it to form compounds with almost all elements except inert gases. However, the electronegativity (eV) of halogen decreases in the order of  $F (3.9) > Cl (3.0) > Br (2.8) > I (2.5)$ . Fluoride in seawater exists in the form of  $\text{MgF}^+$  (46%),  $\text{F}^-$  (51%), and  $\text{CaF}^+$  (2%) (Liteplo et al., 2002). Fluorine replaces any other halide ions in its compound (Brescia et al., 1975). Fluoride is found in nature as fluorite, fluorapatite, cryolite, fluorite and sellaite and carbonate-fluorapatite (El-Said et al., 2015, 2020, 2021; Masoud and El-Said, 2011), while human fluoride sources are such as coal combustion, oil refining, steel manufacturing, aluminum smelting, textile by-products, brick production, and phosphate fertilizer plants (Masoud and El-Said, 2011). Many fluoride compounds such as beryllium fluoride and aluminum fluoride are used industrially as phosphatase inhibitors (Masoud and El-Said, 2011). In environment, the anthropogenic sources of fluoride have been considered a major source among them. Bromine is produced as a by-product of many industries including pesticides, disinfectants, dyes, textiles, cosmetics (El-Said et al., 2020). Iodine and chloride are also produced from burning of coal or fuel oil for power generation and iodine is used in the pharmaceutical industry (Harlove and Aranovich, 2018).

The four halogens commonly occur as the X ion (Harlove and Aranovich, 2018). Iodine also exists in the form of the iodate anion ( $\text{IO}_3^-$ ) in oxidizing alkaline media (such as seawater). Iodine's low electron affinity results in the occurrence of  $\text{I}_2$  in the environment. Fluorine, chlorine, and a small amount of bromine are lithophilic due to their accumulation in silicate minerals. However, iodine is chalcophilic rather than lithophilic in character (Harlove and Aranovich, 2018). Chlorine is the most abundant halogen in sedimentary formation waters with concentrations ranging from  $<100$  to  $>250000$   $\text{mg/L}$  (Worden, 1996), followed by bromine with a range of ( $1 < Br > 6000$   $\text{mg/l}$ ). Chlorine and bromine exhibit strong systemic covariation, suggesting that they are subject to the same control mechanisms

(Worden, 1996). Fluorine only shows relatively high concentration at higher chlorine and bromine concentrations, indicating that the same processes can control fluorine, chlorine, and bromine. Iodine is not related to any other halogen, indicating that a unique process controls iodine. The key processes affecting halogen concentration are seawater evaporation and dilution, water-salt interaction, and organic sources' input.

The Red Sea is a semi-enclosed basin representing one of the marginal seas of the Indian Ocean. The Red Sea is a unique, large marine ecosystem with coral reef systems spreading across its coastline. In addition to its unique, attractive environment, the Red Sea is a significant trading navigational route (Attia and Ghrefat, 2013). Hurghada and Safaga are important ports along the Egyptian Red Sea coast serving industrial activities, petroleum activities, marine sports, and fishers societies (El-Geziry et al., 2020; Nour et al., 2018; Nour and Nouh, 2020). Hurghada is considered the largest Egyptian resort city in the Red Sea.

This study provides a framework to understand halogen distribution in two Red Sea ports in Egypt. It examines the concentrations of F, Br, Cl and I in seawater and marine sediments relative to environmental parameters. This study also aimed to demonstrate the utility of multivariate analysis for evaluating and interpreting large data sets for environmental parameters, identifying pollution sources, and obtaining better concepts of halogen interactions at the two ports.

## 2. Material and methods

### 2.1. Sampling area

Fourteen sampling sites (M1–M14) were selected in the northern part of Mabahiss Bay (Figure 1). The sampling area extends from latitude  $27.29^\circ$  to  $27.32^\circ$  and longitude  $33.73^\circ$  to  $33.77^\circ$  (Figure 1). Mabahiss Bay occupies an area of approximately 35  $\text{km}^2$  near the southern end of the Suez Gulf north of Hurghada, and granitic mountains in the Eastern Desert bound its coast. The coastal area contains several dry valleys and is covered by Pleistocene reefal limestone, gravels, and sands (Attia and Ghrefat, 2013). The wide range of depths in the study area reflects the irregularity in this area's bottom topography (Attia et al., 2012). The offshore islands and the submerged coral system serve to dissipate wave energy during stormy conditions. Fishing is the main impact in this area, especially fishing with nets on reef flats and lagoons (Selim, 2007). Many *Parupeneus* (goatfish), polychaetes, sponges, gastropod shells (*Strombus* and *Lambus*), seagrass, and seaweed inhabit this reef flat. There are some activities in Hurghada area, especially, the export of Egyptian phosphate, packed of cement and alchortz ore (Abouhend and El-Moselhy, 2015). Besides, the construction of major shipyards to build fishing vessels and brine discharge for mega desalination plants has affected this region.

Fifteen sampling locations (S1–S15) represent the northern and central parts of Safaga Bay. The study ranged from the Ras Abu Soma Peninsula to the fortress area north of Safaga Island (Figure 1). Safaga Bay is on the Red Sea west side with a maximum depth of 70 m (Abd EL Wahab et al., 2011). The bay is bordered by a narrow dry coastal plain

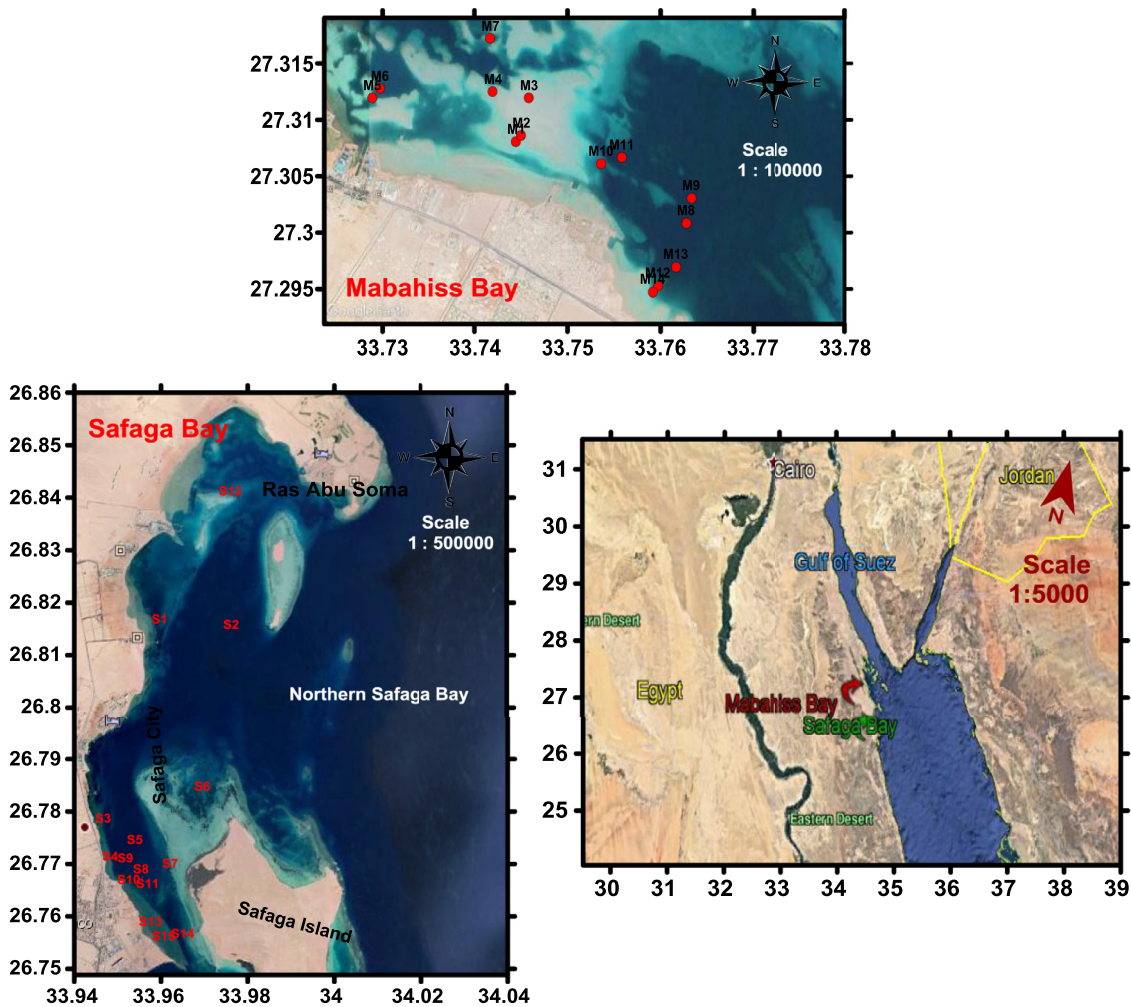


Figure 1 Sampling sites in Mabahiss and Safaga bays along the studied area.

on the west, while the eastern and southern areas are bordered by steep slopes, and the northern area borders the well-known Ras Abu Soma Peninsular. Safaga Bay can be subdivided into the northern and western sides. The sampling area extends from latitude 26.75° to 26.84° and longitude 33.94° to 33.98° (Figure 1). Additionally, this area plays an important role in Egyptian international trade, characterized by transport volumes with frequent loading and unloading. The port includes passenger and freight terminals for bauxite, coal, grain, quartz, and orthoclase (El-Metwally et al., 2017; Mansour et al., 2011). Safaga area is also affected by heavy oil spills due to crude oil extraction and shipping activities (Abouhend and El-Moselhy, 2015).

## 2.2. Sampling and preparation of seawater and sediment samples

Twenty-nine triplicate inshore surface seawater (w) and sediment (s) samples were collected from various sites in Mabahiss Bay (14 sites, M1–M14) and Safaga Bay (15 sites, S1–S15) during 2018 (Figure 1). Duplicate seawater samples were collected using Niskin bottle from a depth range 10–24 m and preserved in 1-liter stoppered, dark polyethylene bottles, which were transferred in iceboxes to the National

Institute of Oceanography and Fisheries lab. The other 29 bottles were immediately used to analyze  $CO_{3w}$ ,  $HCO_{3w}$ ,  $Ca_w$ ,  $Mg_w$ ,  $B_w$ , and  $SO_{4w}$ . Sediment samples from each sampling site at different depths were collected using a Van Veen grab sampler and were kept in colorless polyethylene bags at  $-20^{\circ}C$  until they were air-dried in the lab. Sediment samples were spread on a clean plastic plate and then air-dried at room temperature. The particle size of the air-dried sediment sample was estimated (Folk, 1974).

The sediment samples were crushed to a fine powder and then digested with an acid mixture (3 mL  $HNO_3$ , 2 mL  $HClO_4$ , and 1 mL HF) at  $70^{\circ}C$  in closed Teflon containers. The filtered digested sediment samples were preserved in colorless well-closed plastic bottles for  $Ca_s$ ,  $Mg_s$ ,  $B_s$ , and  $SO_{4s}$  determination. The extracted halogen solutions were obtained from the fusion of  $Na_2CO_3$  with fine sediment powder (Jeffery, 1975; Mohamed, 1999; Saenger, 1972).

## 2.3. Analysis of water and sediment samples

The values of temperature ( $T_w$ ;  $^{\circ}C$ ), pH, salinity ( $S_{\text{‰}}$ ), and total dissolved salts (TDS; g/L) in seawater samples were measured in the field using portable equipment (CTD YSI: 566). Fluoride content in seawater and extracted sediment

solution was measured using the established zirconium-Alizarin Red S method (El-Said and El-Sikaily, 2013). The chloride content in seawater was calculated from the salinity value (Strickland and Parsons, 1972). The bromide content in seawater and extracted sediment solution was determined using the titrimetric method (Grasshoff, 1976). The catalytic reduction method using the Ce(IV)-As(III) reaction was applied to determine the iodine concentration in seawater and extracted sediment solution (APHA-AWWA-WPCF, 1999). The calcium and magnesium content in seawater and digested sediment samples, the carbonate and bicarbonate content in water and sediment samples were determined using the titrimetric method (APHA-AWWA-WPCF, 1999; Balázs et al., 2005; Strickland and Parsons, 1972). Reactive phosphorus in seawater was determined (APHA-AWWA-WPCF, 1999). Silicate was measured in seawater using the calorimetric method (Strickland and Parsons, 1972). The turbidimetric method was applied to estimate  $\text{SO}_4$  in seawater and digested sediment samples (APHA-AWWA-WPCF, 1999). The curcumin colorimetric method was used to determine the amount of boron in seawater and digested sediment samples (APHA-AWWA-WPCF, 1999). Mohr's method determined the chloride contents in sediments (APHA-AWWA-WPCF, 1999; Manual of Methods of Analysis of Foods, 2005). The total phosphorus (TP) content in sediment samples was determined (Aspila et al., 1976). Total carbonates (%  $\text{CO}_3$ ) and total silicate (%  $\text{SiO}_4$ ) in sediment samples were estimated (Molnia, 1974).

#### 2.4. Quality control and quality assurance

The used glassware was cleaned with detergent and steeped in 10%  $\text{HNO}_3$ . For each determined parameter, a calibration procedure was examined for five external standards. An external standard must be close to but above the method detection limit. The detection limit and limit of quantification values for fluoride, iodide, phosphorus, silicate, and sulfate were 0.1 and 0.3 mg/L, 9.0 and 24.0  $\mu\text{g/L}$ , 0.04 and 0.13  $\mu\text{g/L}$ , 0.01 and 0.035  $\mu\text{g/L}$  and 1.0 and 3.0 mg/L, respectively. Other concentrations should correspond to the range of parameter concentrations expected in the environmental samples. The work calibration curve was verified in each work shift by measuring one or more calibration standards. Each standard has a recovery rate of approximately 90%. The precision of the data was set as the coefficient variation (CV). CV determined to be at a value of 10% was through three duplicate analyses of one sample.

#### 2.5. Statistical analysis

Multivariate analyses are recommended for monitoring and environmental studies (Abdel Ghani et al., 2013; El-Said, 2013; El Zokm et al., 2020a, 2020b; Soliman et al., 2018; Tokatli et al., 2014). They can help ecologists discover the structure of many data properties and predict a relatively prior objective. These discoveries make it easier to understand the structure and function of very complex theoretical studies. IBM-SPSS Statistics version 22 and STATISTICA version 12.0 software were used. In this study, data structures were explained using four multivariate statistical

techniques: correlation matrix with a correlation coefficient ( $r$ ), multiple regressions with a multiple regression coefficient ( $R$ ), principal component analysis (PCA), and cluster analysis (CA) at a  $p \leq 0.05$  significance level. These techniques were applied to quantitatively analyze a sample of 27 variables distributed in seawater and sediment samples in each area.

### 3. Results and discussion

#### 3.1. Hydrographical and chemical parameter's distribution in surface seawater

The specific hydrographic parameters in Mabahiss Bay and Safaga Bay ranges of temperature ( $T_w$ ), salinity ( $S_{\text{‰}}$ ), TDS and pH are 20.7–23.0°C, 37.50–40.96‰, 33.22–36.28 g/L and 7.78–7.98, and 23.2–26.7°C, 38.78–40.77‰, 37.35–36.11 g/L and 8.13–8.23, respectively. The average values of  $S_{\text{‰}}$  in Mabahiss Bay and Safaga Bay are lower than those reported for the Egyptian Red Sea Coast (39.63–40.22‰; Fahmy, 2003). The decrease in the detected pH values from those of the unpolluted Egyptian Red Sea Coast (8.06–8.22; Fahmy, 2003) is also due to the discharge from tourist resorts and desalination plants, in addition to the agricultural and industrial wastes. The TDS of Mabahiss Bay and Safaga Bay (Supplementary Table 1) are relatively similar and smaller than the TDS recorded for the open sea (39.420 g/L; Jones et al., 1999); however, Mabahiss Bay's  $\text{pH}_w$  tends to be neutral. The pH values are influenced by the water temperature ( $\text{pH} \& T_w$ :  $r = -0.6673$ ,  $p < 0.007$ ) in Safaga Bay.

The distribution of certain chemical parameters ( $\text{Ca}_w$ ,  $\text{Mg}_w$ ,  $\text{P}_w$ ,  $\text{HCO}_{3w}$ ,  $\text{CO}_{3w}$ ,  $\text{SO}_{4w}$ ,  $\text{B}_w$  and  $\text{Si}_w$ ) in Mabahiss and Safaga Bay's seawater are also determined (Supplementary Table 1). The chemical parameters take the order of  $\text{TDS} > \text{SO}_{4w} > \text{Mg}_w > \text{Ca}_w > \text{HCO}_{3w} > \text{CO}_{3w} > \text{B}_w > \text{Si}_w > \text{P}_w$  in the two bays. The calcium contents in the surface waters of Mabahiss Bay and Safaga Bay range from 256.5–432.9 and 256.5–625.2 mg/L, with an average of 333.1 and 397.6 mg/L, respectively, which are lower than the content reported in the Mediterranean Sea (459 mg/L; Jones et al., 1999). Whereas magnesium levels give ranges 1770.0–2470.2 and 1215.6–2324.3 mg/L and average levels 2124.2 and 1831.8 mg/L in Mabahiss Bay and Safaga Bay, respectively, are higher than those reported for open seawater and the Mediterranean Sea (Millero et al., 2008; Shapiro et al., 2018). The magnesium content of these two ports is higher than the specified value in the Mediterranean Sea (1211 mg/L; Jones et al., 1999), which may be due to human activity in the area. The abundance of magnesium in the seawater of Mabahiss Bay and Safaga Bay is closely related to the decomposition of minerals such as *sabkhas* in Safaga Bay ( $\text{Mg}_w \& \text{CO}_{3w}$ ,  $r = 0.7402$ ,  $p < 0.002$ ; and  $\text{Mg}_w \& \text{SO}_{4w}$ ,  $r = 0.6757$ ,  $p < 0.006$ ) and the salinity of the flow of freshwaters.

The  $\text{mMg}/\text{Ca}$  values of both Mabahiss and Safaga Bays are 7.9–14.21 and 4.16–11.01, respectively, which are higher than two of the records of non-biological, carbonate deposition in seawater in the form of aragonite + high-magnesium calcite (El-Said et al., 2016a; Ries, 2010).

In Safaga Bay, the strong correlation between  $Mg_w$  and  $CO_{3w}$  ( $r = 0.7402$ ,  $p < 0.002$ ) and  $SO_{4w}$  ( $r = 0.6757$ ,  $p < 0.006$ ) may reflect the formations of  $MgCO_3$  and  $MgSO_4$  compounds. The average values of active phosphorus in Mabahiss (0.04–20.81  $\mu\text{g/L}$ ) and Safaga (2.97–10.41  $\mu\text{g/L}$ ) bays are 7.19 and 6.78  $\mu\text{g/L}$ , respectively. These two ports seem to be somewhere between moderate eutrophic (4.65  $\mu\text{g P/L}$ ) and high eutrophic (9.30  $\mu\text{g P/L}$ ) coastal waters (Fahmy, 2003; Fahmy et al., 2016). The calculated ecological risk assessment of phosphorus ( $RQ_p$ ; El Nemr and El-Said, 2017) indicated that phosphorylation distress occurred in both ecological regions.

The  $HCO_{3w}$  average content of the surface water of Mabahiss Bay (29.67–180.56 mg/L) and Safaga Bay (78.08–146.40 mg/L) is lower than the publicly reported value of 169 mg/L; Jones et al., 1999) and above the specified level in the Mediterranean Sea coast in Egypt (97.88 mg/L; El-Said et al., 2016a). The presented data's correlation matrix concluded that the amount of boron in the seawater of Mabahiss Bay is related to the outflow's water quantity ( $S_{\%} \& B_w$ ;  $r = -0.6421$ ,  $p < 0.024$ ), the ion pair formation of borate complexes with the abundant Mg, and its deposition and adsorption or use in this area's sediment texture ( $Mg_w \& B_w = -0.6769$ ,  $p < 0.016$ ; Kot, 2009). Sulfate shows dramatic changes in Mabahiss (5535.7–9862.2 mg/L) and Safaga (4775.5–10913.3 mg/L) bays. The sulfate content along these two ports is higher than the sulfate content in the open Mediterranean Sea area (2700 mg/L; Jones et al., 1999). The high sulfate in Mabahiss Bay and Safaga Bay might be associated with disintegrated sabkhas minerals, landfill operations and terrigenous fluxes (Mansour et al., 2013). The high correlation coefficient between silicon and  $B_s$  in the seawater of Mabahiss Bay ( $r = 0.7914$ ,  $p < 0.002$ ) might be related to the biological activity of boron in cyanobacteria and diatoms (Kot, 2009). The average  $Si_w$  contents of Mabahiss Bay (65.73–244.38  $\mu\text{g/L}$ ) and Safaga Bay (55.21–326.97  $\mu\text{g/L}$ ) are 149.88 and 180.31  $\mu\text{g/L}$ , respectively.

### 3.2. Halogens' distribution in surface seawater

The distribution of halogens in seawater (w) gives the same order of  $Cl_w > Br_w > F_w > I_w$  in both Mabahiss Bay and Safaga Bay (Supplementary Table 1). Fluoride in Mabahiss Bay (1.92–8.31 mg/L) and Safaga Bay (1.80–10.15 mg/L) give average values of 4.18 and 5.30 mg/L, respectively, which is higher than those established in unpolluted seawater (1.3 mg/L; El-Sarraf et al., 2003). The current fluoride concentrations in Mabahiss Bay and Safaga Bay are within the range previously determined in the Red Sea (4.7±0.3 mg/L; El-Said, 2005). The chloride in Mabahiss Bay's seawater (21.90±0.65 g/L) and Safaga Bay (21.94±0.37 g/L) show relatively similar contents. The chloride concentrations in both bays are also relatively similar to those established in the open Mediterranean Sea (21.94 g/L; Jones et al., 1999) and lower than those recorded in the Egyptian Red Sea coast (22.2–22.7 g/L) due to its anion abundance in seawater. The bromide content in Mabahiss Bay (95.90–151.84 mg/L) is higher than that recorded in Safaga Bay (15.98–146.51 mg/L) with average values of 114.56 and 61.57 mg/L, respectively. The increased Br in Mabahiss Bay may be associated with water-soluble release and leached Br from

sediment to seawater-sediment interface (Harlov and Aronovich, 2018). However, in the earth's crust, rocks containing more than 70–80% Br are present in non-sediment rocks. The Br in Mabahiss Bay (114.56±17.24 mg/L) is also higher than that reported in the Mediterranean Sea and Lake Mariout (74.1 and 18.91 mg/L; Jones et al., 1999; El-Said et al., 2020). The variation of chloride is also related to seawater's evaporation in semi-enclosed areas and tropical regions (Jones et al., 1999). The iodide values show variable higher contents in Mabahiss Bay (2.77–39.19  $\mu\text{g/L}$ ) than those recorded in Safaga Bay (2.50–12.96  $\mu\text{g/L}$ ) with average values of 17.33 and 5.05  $\mu\text{g/L}$ , respectively. Iodide contents in the two bays are lower than that reported in seawater (50  $\mu\text{g/L}$ ; Jones et al., 1999).  $I^-$  plays an important role in the oxidation or reduction reactions in geochemical systems and strongly adsorb to mineral surfaces. The average levels of chloride, bromide, and iodide in seawater in Mabahiss Bay are higher than those recorded in Safaga Bay.

A correlation analysis revealed the relationship between halogens and studied environmental parameters in seawater and sediments of the two ports.

In Mabahiss Bay, there are high interactions relating to  $F_w \& Cl_s$  ( $r = 0.9071$ ,  $p < 0.00$ ),  $Cl_w \& F_s$  ( $r = -0.6382$ ,  $p < 0.026$ ), and  $Br_w \& Cl_s$  ( $r = -0.7107$ ,  $p < 0.010$ ). Halogens are incorporated into the earth's crust, bio-organic matter, and minerals presented; however, Cl is abundant in the oceanic crust as an amphibole mineral with 0.5 mg/g (Jones et al., 1999). The high correlation of  $Cl_w \& Mg_w$  ( $r = 0.681$ ,  $p < 0.015$ ) may accompany the mobilization of Cl and Mg in amphiboles containing iron or magnesium ions (Jones et al., 1999). The release of chloride, magnesium, bromide ( $Br_w \& Ca_w$ ;  $r = -0.6747$ ,  $p < 0.016$ ) and iodide ( $I_w \& CO_{3w}$ ;  $r = 0.815$ ,  $p < 0.001$ ) probably refer to the decomposition of sabkhas minerals and organisms fragments along with landfills and land flows. Iodine is present in the anionic  $I^-$  form and oxyanionic species such as iodate ( $IO_3^-$ ) depending on pH, oxidation potential and biological activities in seawater (Jones et al., 1999). The moderate negative correlation of  $F_s \& Mg_w$  ( $r = -0.6013$ ,  $p < 0.039$ ) may be referred to the precipitation of the  $MgF^+$  ion pair and the sparingly soluble magnesium complex (El-Said et al., 2015). The high correlations of  $B_w \& Cl_w$  ( $r = -0.6421$ ,  $p < 0.024$ ) and  $F_s \& B_w$  ( $r = 0.8112$ ,  $p < 0.001$ ) may be related to anthropogenic sources and boron's geological cycle (Kot, 2009). The release of Cl from minerals such as sabkhas and feldspar during the hydration process and the deposition of fluoroboron compounds such as (ferrucite ( $NaBF_6$ ) and avogadrite ( $(K,Cs)BF_4$ ), along with the adsorption of boron on minerals such as Al and Fe oxide, and calcareous and clay minerals in marine sediments may also be associated with high relationships between  $B_w \& Cl_w$  and  $F_s \& B_w$  (Kot, 2009).

In Safaga Bay, the relationship between the parameters defined in the correlation matrix reflects that the chlorine content in the seawater is related to the water chemistry process, landfill discharge and human activities. The relationship of  $Cl_w \& B_w$  ( $r = 0.6067$ ,  $p < 0.016$ ),  $Cl_w \& Cl_s$  ( $r = 0.6151$ ,  $p < 0.015$ ),  $Cl_w \& CO_{3w}$  ( $r = 0.6034$ ,  $p < 0.017$ ),  $I_w \& SO_{4w}$  ( $r = 0.7196$ ,  $p < 0.002$ ),  $Br_s \& I_s$  ( $r = 0.6553$ ,  $p < 0.008$ ), and  $I_w \& Si_w$  ( $r = -0.7727$ ,  $p < 0.001$ ) may indicate dissolution and/or deposition of boron, chloride, bromide, and iodide in certain marine minerals, as well as the incorporation of these elements into organic compounds,

organic matter in sediments and organic-rich sediments. (Harlove and Aranovich, 2018; Kot, 2009). Bromine and chlorine are mixed with organic matter of coal, kerogen, and petroleum (Harlove and Aranovich, 2018). The high correlations of  $B_w \& S_{\%}$  ( $r = 0.6089$ ,  $p < 0.016$ ),  $B_w \& Cl_w$  ( $r = 0.6067$ ,  $p < 0.016$ ), and  $B_w \& CO_{3w}$  ( $r = -0.6168$ ,  $p < 0.014$ ) also possibly refer to the anthropogenic and geologic origin of boron in Safaga Bay.

The horizontal distribution of halogens in Mabahiss and Safaga Bay's seawater and sediments shows different trends (Figures 2 and 3). In Mabahiss Bay, the fluoride in the seawater and sediments gradually decreases towards the sea. The contents of chloride, bromide, and iodide show the same distribution. The halogen's content in seawater decreases in seawater's direction and increases in the opposite direction in sediments. In Safaga Bay, the distribution of halogen contents declines from the shore toward the seawater and in the opposite direction of the sediments.

### 3.3. Chemical parameters' distribution in sediment

The chemical parameters determined in Mabahiss and Safaga Bay are listed in descending order:  $CO_{3s} > Mg_s > Ca_s > SiO_{4s} > SO_{4s} > B_s > P_s$  and  $CO_{3s} > Ca_s > Mg_s > SiO_{4s} > SO_{4s} > B_s > P_s$ , respectively (Supplementary Table 2). Mabahiss Bay has higher average  $Ca_s$ ,  $Mg_s$ ,  $CO_{3s}$  and  $B_s$  levels than those in Safaga Bay. These high recorded values in Mabahiss Bay may be due to the presence of sabkhas minerals containing soluble sulfate and chloride salts and carbonate minerals (Bahafzullah et al., 1993). The average boron content in Mabahiss Bay is relatively similar to the average content recorded in clay sediments (2.30 mg/g; Kot, 2009), while the boron content in Safaga Bay is lower than the average. In contrast, the  $SiO_{4s}$ ,  $SO_{4s}$  and  $P_s$  contents in the sediment subarea of Safaga Bay are higher than that of Mabahiss Bay. The weak correlation between  $SO_{4s}$  and  $HCO_{3w}$  ( $r = 0.5274$ ,  $p < 0.043$ ) and  $SO_{4s} \& T_w$  ( $r = 0.5348$ ,  $p < 0.040$ ) may be related to the influence of temperature and sulfate content on the microbial activity in Safaga Bay sediments (Sawicka et al., 2012). The moderate correlations of  $Ca_s \& T_w$  ( $r = 0.6371$ ,  $p < 0.026$ ) and  $P_s \& pH$  ( $r = 0.7226$ ,  $p < 0.008$ ) may reflect the influence of water temperature on calcium carbonate dissolution and the release of phosphorus during calcite formation in Mabahiss Bay sediment (El-Said et al., 2016b).

### 3.4. Halogens' distribution in sediment

The halogen distribution in sediments (s) give the same order of  $Br_s > Cl_s > F_s > I_s$  in the two bays (Supplementary Table 2 and Figures 2 and 3). Mabahiss Bay shows a slightly higher average fluoride content (0.63 mg/g) than that established for the earth's crust (0.55 mg/g; Harlove and Aranovich, 2018), while Safaga Bay exhibits lower content (0.38 mg/g; Harlove and Aranovich, 2018). The halogen current results of  $Cl_s$ ,  $Br_s$ , and  $I_s$  in Mabahiss Bay and Safaga Bay are higher than those reported for the earth's crust (0.24 mg/g, 0.88  $\mu g/g$ , and  $I = 0.7 \mu g/g$ ; Harlove and Aranovich, 2018). The moderate negative association of  $F_s \& Mg_w$  ( $r = -0.6013$ ,  $p < 0.039$ ) slightly reflects

the precipitation of the  $MgF^+$  ion pair and the soluble Mg complex (El-Said et al., 2015). The high correlations of  $B_w \& Cl_w$  ( $r = -0.6421$ ,  $p < 0.024$ ) and  $F_s \& B_w$  ( $r = 0.8112$ ,  $p < 0.001$ ) may be related to the anthropogenic source and geological cycle of boron (Kot, 2009). The release of Cl could result from minerals such as: sabkhas, and feldspar during the hydration process and the deposition of fluoride-boron compounds like ferrucite ( $NaBF_6$ ) and avogadrite ( $(K,Cs)BF_4$ ) and the adsorption of boron on minerals such as aluminum oxide, iron oxide, calcareous and clay minerals in marine sediments (Kot, 2009). The fluoride content in Safaga Bay gives high relationships of  $F_s \& CO_{3s}$  ( $r = -0.6474$ ,  $p < 0.009$ ),  $F_s \& B_s$  ( $r = 0.6477$ ,  $p < 0.009$ ), and  $F_s \& Si_s$  ( $r = 0.6474$ ,  $p < 0.009$ ). These relationships may release fluoride from fluorite minerals and form calcium carbonate in alkaline media, in addition to decomposing carbonate and crystalline rock fragments (Dehbandi et al., 2017; El-Said et al., 2016a).

## 4. Multivariate analysis

### 4.1. Box and whisker plot

Figures 4 and 5, present the box and whisker plots of the studied parameters between the two ports. Figure 4 represents the plot for  $SO_{4w}$  (mg/L),  $HCO_{3w}$  (mg/L),  $CO_{3w}$  (mg/L),  $Ca_w$  (mg/L),  $Mg_w$  (mg/L),  $B_w$  (mg/L),  $Si_w$  ( $\mu g/L$ ), and  $P_w$  ( $\mu g/l$ ) in seawater of Mabahiss (M) and Safaga Bays (S) by the box and whisker method. The boxes show the 25<sup>th</sup> percentile (first quartile) and the 75<sup>th</sup> percentile (third quartile), and the whiskers represent the lowest and the highest coefficients. In contrast, the line inside the boxes expresses the median (second quartile). Figure 5 is the plot of  $Ca_s$  (mg/g),  $Mg_s$  (mg/g),  $SO_{4s}$  (mg/g),  $CO_{3s}$  (%),  $SiO_{4s}$  (%),  $B_s$  (mg/g), and  $P_s$  ( $\mu g/g$ ) in marine sediments of Mabahiss (M) and Safaga Bays (S) drawn using the box and whisker method, where the first, second and third quartile are illustrated.

### 4.2. Multiple regression analysis

The multiple regression equation for halogen is listed as the dependent parameter. At the same time, other variables are defined as independent parameters in the surface seawater and sediments of the Mabahiss and Safaga bays (Table 1). The seven equations of Mabahiss Bay and the eight equations of Safaga Bay were constructed. Based on these equations, halogen's chemistry and other features in the two ports can be deduced.

A striking feature is that there is no regression equation for chloride in Mabahiss Bay, even between chloride and salinity, which indicates the stability of the chloride content in this region (Harlove and Aranovich, 2018). The dissolved chloride salts seems to mainly influence the chloride in seawater of the shallow Mabahiss Bay in sabkhas minerals. The multiple regression equations for the variable distribution of halogens in Mabahiss Bay may relate to marine organisms biological activities, decomposition of organic matter, formation/dissolution of carbonate minerals, and the partial dissolution of quartz particles transported to the sea from the surrounding desert during sandstorms. In Safaga Bay, the type of pollutants in this region's wastewaters play an important role in the chemistry of specific

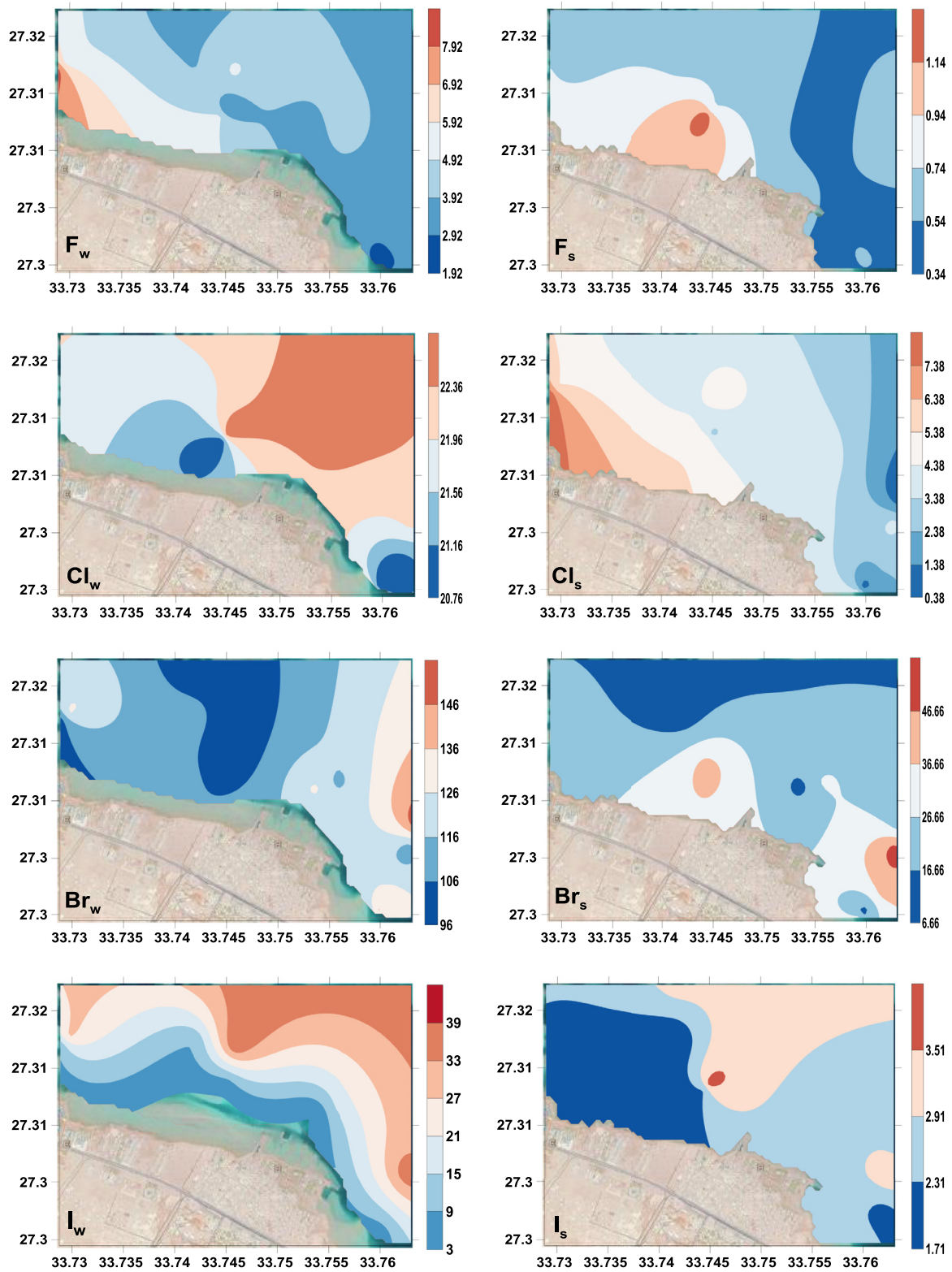
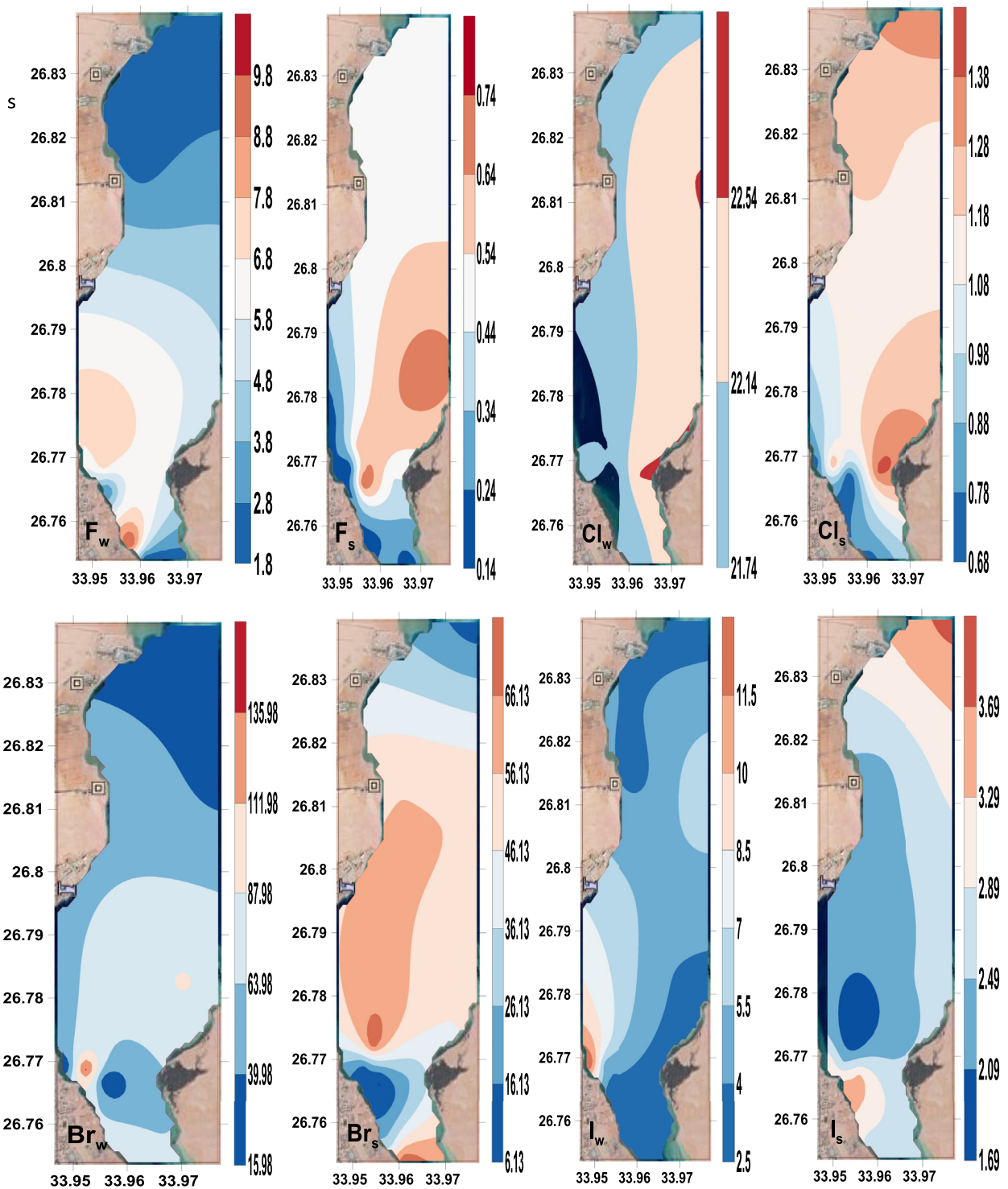


Figure 2 Distribution of F, Cl, Br, and Cl in seawater and sediment (mg/L and mg/g, respectively) and I ( $\mu/L$  and  $\mu/g$ , respectively) in Mabahiss Bay.



**Figure 3** Distribution of F, Cl, Br, and Cl in seawater and sediment (mg/L and mg/g, respectively) and I ( $\mu$ /L and  $\mu$ g/g, respectively) in Safaga Bay.

halogen contents (Attia and Ghrefat, 2013; Nour and El-Sorogy, 2018; Nour and Nouh, 2020). In the four equations describing the halogen reaction in Safaga Bay, the high pollution state and high phosphorus content indicate that the study area suffers from high phosphorus pollution (Abou El-Anwar et al., 2019). Fluoride in the two bay's sediments is usually affected by calcium, controlled by the adsorption

balance on the sediments and the solubility or precipitation of fluorite ( $CaF_2$ ) and carbonate minerals (El-Said et al., 2015). In most of the bay's equations, each halogen's unique interaction with other halogens reveals similar chemical properties between them, especially F, Cl, and Br. Halogens form a class of compounds called inter-halogen compounds, in which halogen atoms are covalently bonded to

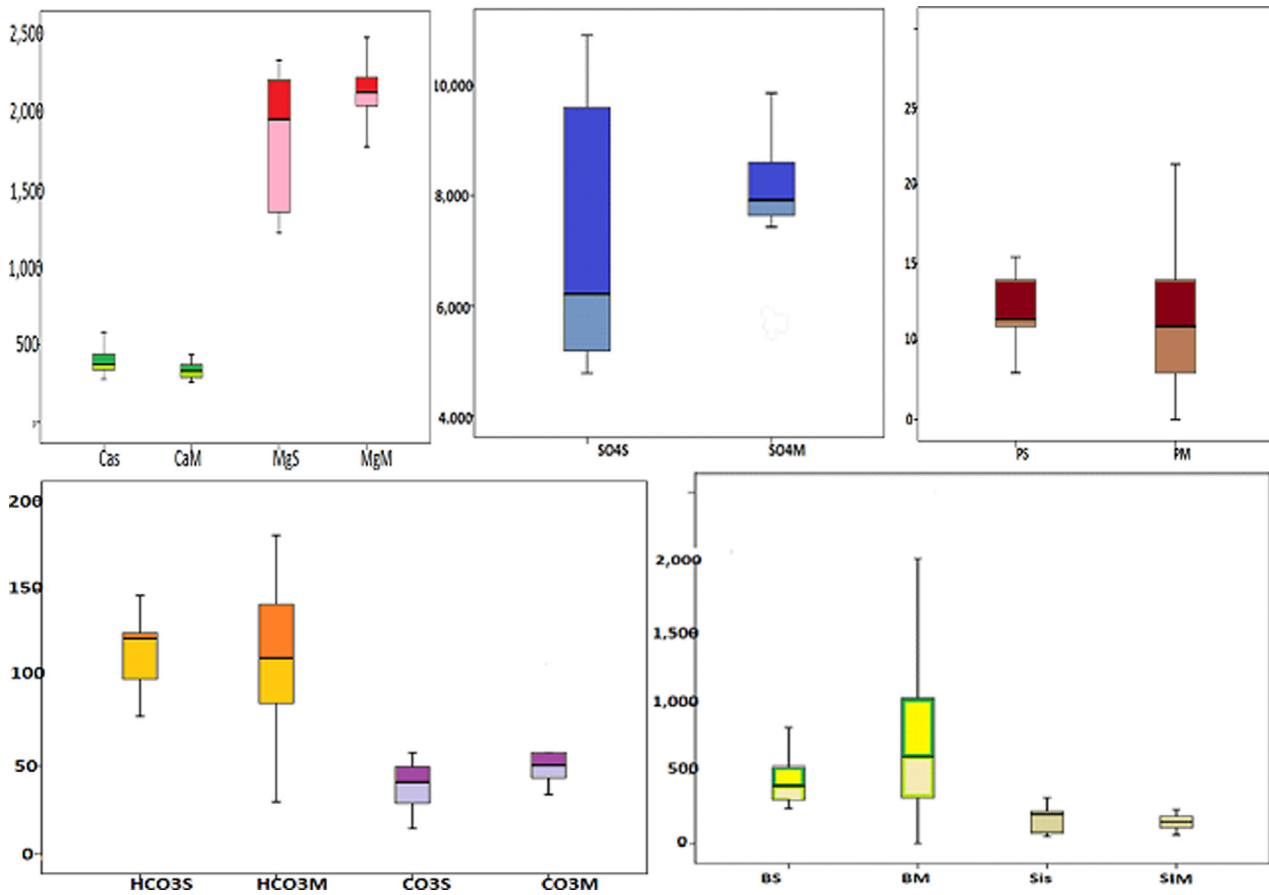


Figure 4 Box and whisker plot for chemical parameters in seawater of Mabahiss (M) and Safaga (S) bays.

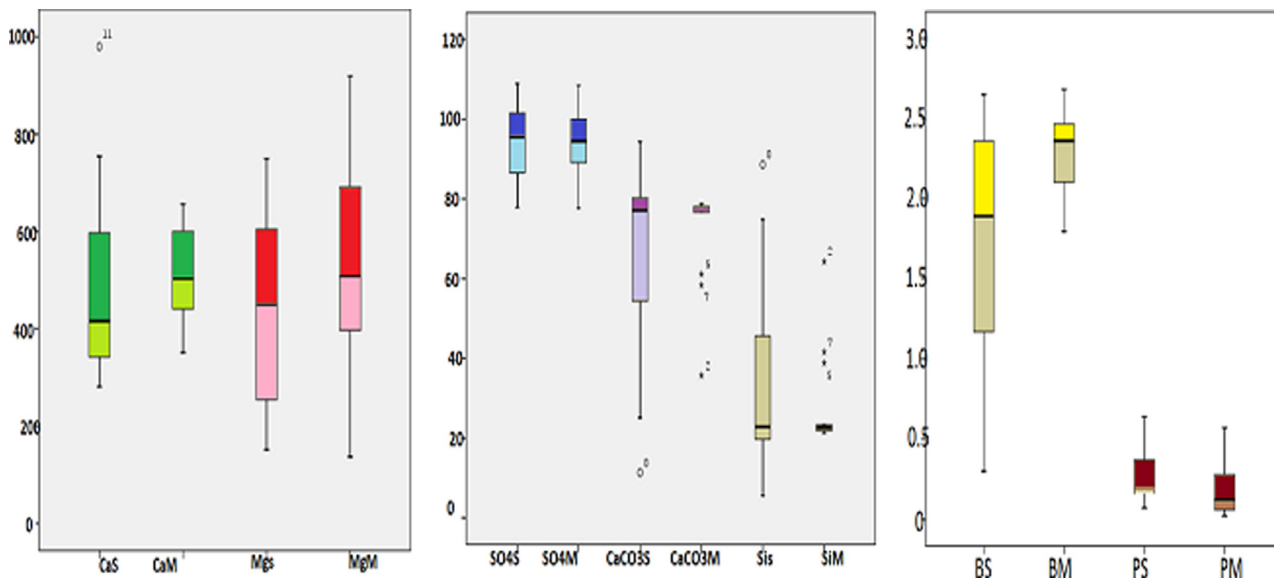


Figure 5 Box and whisker plot for chemical parameters in sediments of Mabahiss (M) and Safaga (S) bays.

each other to form Lewis bases, such as  $\text{BrCl}$  and  $\text{ICl}_4$ . Interestingly, most of the two port's halogens have important interactions with coastal water and sediment's environmental parameters.

### 4.3. Cluster analysis (CA)

In recent years, CA has had efficacious applications in assessing spatiotemporal changes in coastal seawater and



**Table 1** The multiple regression analyses of halogens as dependent variables and other parameters in seawater and sediment in Mabahiss and Safagaa Bays.

Dependent variable		Multiple regression equation	R <sup>2</sup>
Fluoride	Seawater	Mabahiss Bay $F_w = -13.2 + 0.84 Cl_s + 0.42 Br_w + 0.42 SO_{4w} - 0.37 Ca_s - 0.31 I_s - 0.02 Depth - 0.22 SO_{4s} + 0.11 T_w + 0.16 F_s$	0.9999
	Sediment	$F_s = -0.1 + 0.69 B_w - 0.48 Depth + 0.51 SO_{4s} - 0.07 B_s + 0.16 HCO_3 + 0.24 I_w - 0.14 Ca_w + -0.01 pH + 0.38 Si_w + 0.16 F_w$	0.9999
Chloride	Seawater	No regression	0.0000
	Sediment	$Cl_s = 35.8 + 0.93 F_w - 0.36 Br_w - 0.18 SO_{4w} + 0.17 Ca_s - 0.12 pH_w + 0.30 Br_s + 0.21 Si_w + 0.10 Depth + 0.09 P_w + 0.05 Mg_w$	0.9999
Bromide	Seawater	$Br_w = 99.2 - 1.56 Cl_s - 0.17 Ca_w - 0.44 Si_s + 0.90 F_w + 0.42 B_s + 0.10 Br_s - 0.22 Mg_s + 0.08 B_w$	0.9999
	Sediment	$Br_s = -0.09 - 1.54 Si_w + 1.36 I_s + 0.18 B_w + 0.71 Cl_s - 0.67 SO_{4w} + 0.75 B_s + 0.34 Ca_s - 0.21 I_w - 0.15 S\%$	0.9999
Iodide	Seawater	$I_w = -76.7 + 0.80 CO_{3w} + 0.46 P_w - 0.33 SO_{4s} - 0.09 B_s - 0.15 \%CO_{3s} + 0.28 T_w - 0.15 Br_w$	0.9999
	Sediment	$I_s = 6.1 + 0.64 Si_s + 1.09 I_w - 0.42 F_w + 1.10 Br_s + 0.70 Si_w + 0.85 Depth - 0.74 S\% + 0.41 Mg_w + 0.33 B_s + 0.05 pH_w$	0.9999
Fluoride	Seawater	Safag Bay $F_w = 510 - 0.55 B_w + 0.86 HCO_{3w} + 0.36 Br_w + 0.44 B_s + 0.75 P_w + 0.59 Ca_w + 0.38 Ca_s - 0.82 pH_w - 0.48 T_w - 0.23 Mg_s + 0.17 SO_{4s} - 0.09 Si_s - 0.03 F_s$	0.9999
	Sediment	$F_s = 2.75 - 0.83 B_s + 1.64 Si_s + 0.59 Ca_s + 0.18 P_s - 0.46 SO_{4s} - 1.19 Si_w - 1.03 I_s - 0.49 Br_w - 0.84 SO_{4w} - 0.30 Mg_s - 0.13 Cl_s + 0.13 Depth + 0.22 I_w$	0.9999
Chloride	Seawater	$Cl_w = -0.19 + 1.01 S\%$	0.9999
	Sediment	$Cl_s = 15.13 + 0.69 Cl_w + 0.97 CO_{3w} - 0.53 Mg_s + 0.37 P_w - 0.06 F_s - 0.40 pH_w + 0.21 Ca_s + 0.09 B_s - 0.20 HCO_{3w} - 0.39 Br_w + 0.19 SO_{4s} - 0.34 Mg_w$	0.9999
Bromide	Seawater	$Br_w = -1139.77 + 2.42 CO_{3w} - 0.05 pH - 1.55 Mg_w + 0.66 SO_{4s} - 0.44 Mg_s - 0.27 B_s + 0.81 S\% - 0.59 Cl_s + 0.33 HCO_{3w} - 0.07 I_w + 0.04 I_s - 0.02 F_w$	0.9999
	Sediment	$Br_s = -1682.1 - 0.95 I_s + 0.91 B_w - 0.19 T_w - 0.47 S\% + 0.05 Si_s - 0.43 Ca_w - 0.16 Mg_s + 0.33 SO_{4w} + 0.43 pH - 0.28 B_s - 0.19 F_s - 0.14 SO_{4s}$	0.9998
Iodide	Seawater	$I_w = -135.7 - 0.55 Si_w - 0.55 Br_w - 0.14 F_s + 0.80 SO_{4w} - 0.65 Mg_w - 0.32 B_s - 0.15 B_w + 0.20 pH_w - 0.12 Ca_s + 0.17 T_w - 0.03 Depth - 0.02 HCO_{3w} + 0.01 Ca_w$	0.9999
	Sediment	$I_s = -33.77 - 0.27 Br_s - 0.31 Br_w - 0.28 F_w - 0.80 F_s - 0.66 \%CO_{3s} - 0.306 Cl_s + 0.356 Ca_s - 0.72 Si_w + 0.285 pH_w - 0.24 Depth - 0.57 SO_{4w} - 0.197 P_w$	0.9999

identifying pollution sources (El-Said, 2013). In this study, cluster analysis is performed using hydrological methods, and the chemical parameters are represented in a dendrogram (Figure 6). However, the dendrograms aM and aS and bM and bS recombine the 16 and 15 parameters in Mabahiss and Safaga Bay's seawater and sediments, respectively. On the other hand, cM and cS represent the station's assembly in the bays of Mabahiss and Safaga, respectively.

In Mabahiss Bay, the presence of fluoride in seawater is mainly affected by pH and boron content (Figure 6aM and bM). This observation may indicate that precipitation of fluoroboron compounds such as  $NaBF_6$  and  $(K,Cs)BF_4$  (Kot, 2009). In this bay, fluoride contains the minerals from fluorapatite, phosphate, and sabkhas in marine sediments. In Mabahiss Bay, the bromide content is affected by the content of bicarbonate in seawater. The release of bromide and/or its deposition in sabkhas minerals may influence the content of marine sediments.

In the seawater of Safaga Bay, marine organisms can absorb fluoride and iodide or release them from sediments rich in organic matter, landfills, and land flows (Figure 6aS). The halogen content in the Safaga Bay sediments can be covalently

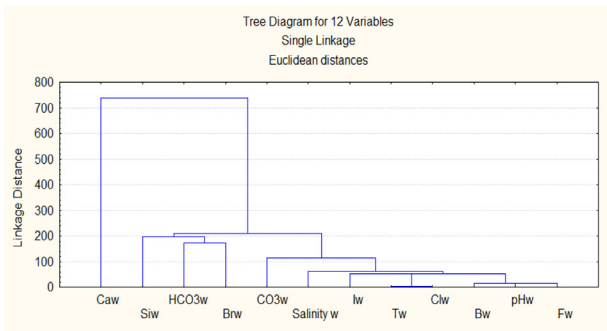
bonded to each other to form Lewis bases, such as  $BrCl$  and  $ICl_4$  (Schmidt et al. 2020). Fluoride can also replace other halogens in its minerals (Figure 6bS). Water-soluble halogens may be released and leached during the process of mineralization and weathering, resulting in their local abundance (Harlove and Aranovich, 2018).

The cM and cS tree diagram show the combined station assembly due to the distribution of various parameters in seawater and sediments and human activities, landfills, and land flows in Mabahiss and Safaga bays, respectively.

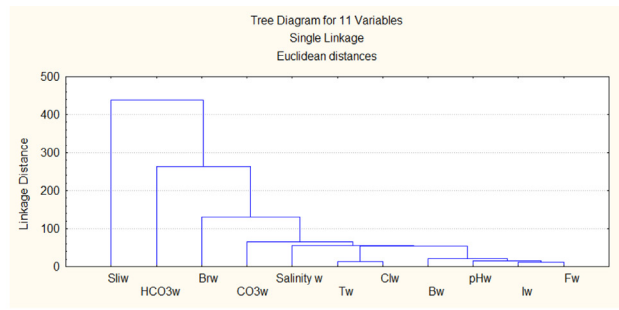
#### 4.4. Principal component analysis (PCA)

PCA/FA is applied to parameter to classify seawater and sediments (14 and 15 stations in Mabahiss and Safaga ports, respectively) (Supplementary Table 3). The six PCs explain 83.17% and 78.65% of Mabahiss and Safaga Bays' total variance, respectively. The calculated data shows that the loading parameter sets are different in the two regions, so each region is discussed separately.

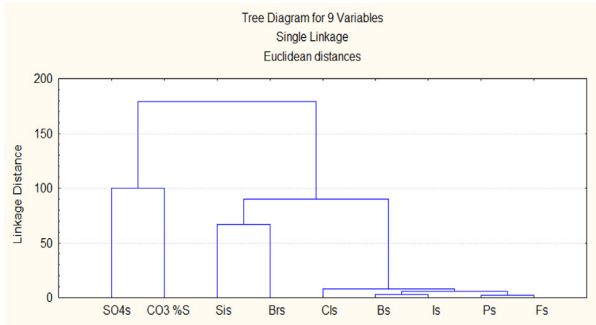
For Mabahiss Bay, PC1 accounts for 18.81% of the total variance. It has a higher positive load on  $Cl_w$  (0.919),



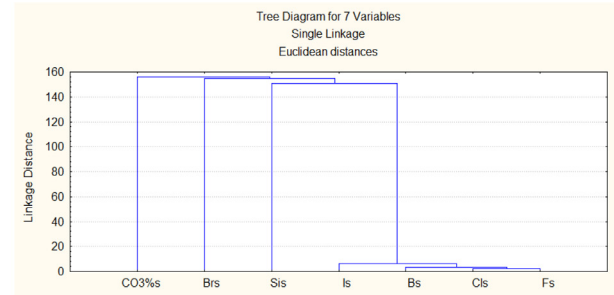
(aM)



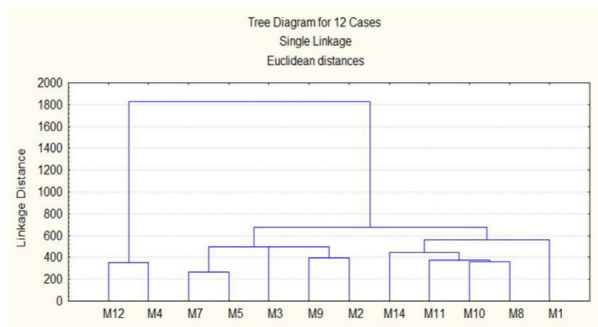
(aS)



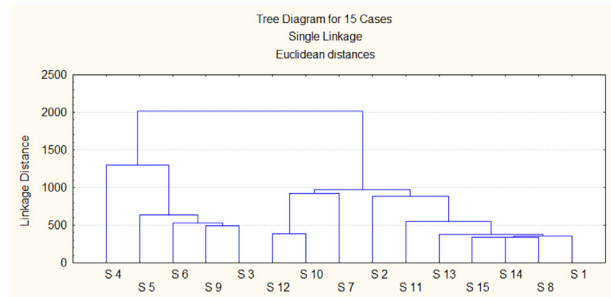
(bM)



(bS)



(cM)



(cS)

**Figure 6** Cluster analysis of Mabahiss and Safaga bays: variables in water samples (aM and aS; the cluster grouping of  $SO_{4w}$  is missed), variables in sediment samples (bM and bS) and stations grouping (cM and cS).

$S\%_o$  (0.919), and  $Mg_w$  (0.793), and a negative load on  $B_w$  ( $-0.815$ ).  $F_s$  ( $-0.831$ ) and  $Mg_s$  ( $-0.667$ ). This factor can be referred to as the salinity factor and mineral deposition factor because the hydrolysis of  $MgCl_2$  causes Mg to be fixed in hydrous silicate minerals, including chlorite. The chloride content influences the boron concentration in seawater, and B/Cl is its geochemical distribution (Moneer et al., 2012). PC2 contributes to 17.59% of the total variance with high positive loads on  $Si_s$  (0.848) and moderate positive loads on pH (0.668) and  $Br_s$  (0.672), however high negative loads may be associated with B ( $-0.848$ ),  $HCO_{3w}$  ( $-0.739$ ) and  $Si_w$  ( $-0.887$ ). Therefore, this factor is mainly due to diagenetic systems, such as dissolved silica content and feldspar diagenesis (Worden, 1996). PC3 is articulated by  $Ca_w$  (0.832),  $Ca_s$  ( $-0.597$ ),  $P_w$  (0.831), and  $T_w$  ( $-0.768$ ) at 14.16%, and

this factor may be combined with Ca as a special geochemical reaction element, especially in the formation of Ca-Hydroxyapatite ( $Ca(PO_4)(OH)$ ). PC4 contributes 12.72% of the  $F_w$  (0.951),  $SO_{4w}$  (0.635), and  $Cl_s$  (0.884) of the positive load. This factor may be due to the Lewis acid-base reaction and the degradation of the sabkhas minerals. PC5 shows 10.03%, where  $I_s$  ( $-0.792$ ) and  $\%CO_{3s}$  (0.700) are loaded. PC6 contributes 9.86% to  $I_w$  (0.833) and  $CO_{3w}$  (0.754) and  $SO_{4s}$  ( $-0.772$ ). This factor may relate to the degradation of sabkhas minerals and seawater's biological activity (Jones et al., 1999).

For Safaga Bay, PC1 shares 15.57% of the total variance with  $HCO_{3w}$  (0.625),  $Mg_s$  (0.650),  $Br_w$  ( $-0.637$ ),  $Ca_w$  ( $-0.629$ ),  $Mg_w$  ( $-0.620$ ) and  $CO_{3w}$  ( $-0.897$ ). Bromide in seawater mainly exists as  $CaBr_2$  and  $NaBr$  (Harlove and Ara-

novich, 2018). This factor can be considered the carbonate and bicarbonate balance. The evaporation of seawater causes halite to recrystallize and form dissolved bromides, such as NaBr (a better dissolved salt than NaCl) (Worden, 1996). The share of PC2 in  $P_w$  ( $-0.776$ ), pH ( $-0.778$ ),  $T_w$  (0.880), and  $SO_{4s}$  (0.651) is 13.85%. This factor involves human made sources. PC3 contributes to 13.15% of the total variance of  $F_s$  (0.822),  $CO_{3w}$  ( $-0.857$ ),  $B_s$  (0.806) and  $Si_s$  (0.857). This factor may contribute to the sediment's nature as fluorine is the most reactive halogen (Ichikuni, 1979). PC4 accounts for 13.12%, which is related to  $I_w$  (0.928),  $SO_{4w}$  (0.856) and  $Si_w$  ( $-0.901$ ). PC5 clarifies 11.97% of the data, where  $Cl_w$  (0.938),  $S_{‰}$  (0.938), and  $Cl_s$  (0.728) are loaded, and the chloride content controls this factor. PC6 has 10.98% which takes part with depth (0.658),  $Br_s$  (0.844), and  $I_s$  ( $-0.807$ ), dealing with the biological activities of marine organisms, and decomposition of organic materials, as well as human activities. This factor may be related to the Br compound in leaded gasoline.

## 5. Conclusion

The horizontal distribution profile of the halogens in seawater and sediment showed the same order of  $Cl_w > Br_w > F_w > I_w$  and  $Br_s > Cl_s > F_s > I_s$ , respectively, in both Mabahiss Bay and Safaga Bay. Interestingly, this study presented the difference in the origin of halogens in the examined bays due to the diverse geochemical distribution of sediments, landfills, land flows and sources of human activities. However, fluoride in seawater in Safaga Bay showed higher mean content than that in Mabahiss Bay and vice versa for bromide and iodide. Specific high levels of fluoride and bromide may indicate anthropogenic sources such as tourism activities, fishing, urbanization, plastic waste, shipyards, anti-corrosion and anti-fouling coatings, surface water and landfills.

On the other hand, multivariate statistical analyses reflected the different distribution of halogens in the bays. From the application of these analyses in the present study, the following conclusions were drawn, in particular. The results of these five statistical methods were complementary. The box plot and whisker method described the different distribution of halogens and specific parameters in seawater and sediments in the Bays of Mabahiss and Safaga. The correlation matrix, CA, and PCA identified the two bays' parameters sources, while multiple regression analyses mainly discussed the interaction between variables. Depending on the configuration, the cluster analysis evaluated nearby stations, and these stations may have the same source of supply. The multivariate statistical analyses in this study also revealed the geological origin of the halogens in the Mabahiss Bay sediments. In contrast, the halogens in Safaga Bay appeared to be controlled by terrestrial flows and anthropogenic sources. The Safaga Bay contains a passenger terminal and a terminal for loading and unloading bauxite, coal, grain, quartz, and feldspar. Accordingly, the statistical analyses used in the current study confirmed the relationship of human activity sources of and geochemical characteristics to the origin of the halogen changes in the study area. This conclusion forces us to use more than one statis-

tical method in the future in predicting the levels of pollutants in the environment as well as their sources.

## Acknowledgments

The authors are grateful to Prof. dr. Mahmoud Ismail, Marine Geology Laboratory, National Institute of Oceanography and Fisheries, NIOF for providing the samples used in this study.

## Supplementary materials

Supplementary material associated with this article can be found, in the online version, at <https://doi.org/10.1016/j.oceano.2021.09.007>.

## References

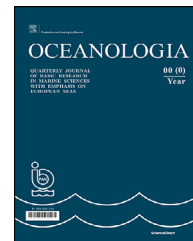
- Abd El Wahab, M., Melegy, A., Hela, S., 2011. Distribution and enrichment of heavy metals in recent sediments of Safaga Bay. *Egypt. Mar. Georesources Geotechnol.* 29, 364–375. <https://doi.org/10.1080/1064119X.2011.586014>
- Abdel Ghani, S.A., El Zokm, G., Shobier, A., Othman, T., Shreadah, M., 2013. Metal pollution in surface sediments of Abu-Qir Bay and Eastern Harbour of Alexandria. *Egypt. J. Aquat. Res.* 39 (1), 1–12. <https://doi.org/10.1016/j.ejar.2013.03.001>
- Abou El-Anwar, E.A., Mekky, H.S., Abdel Wahab, W., 2019.  $P_2O_5$ –F–U Characterization and Depositional Environment of Phosphatic Rocks for the Duwi Formation, Qussier – Safaga Region, Red Sea Coast. *Egypt. J. Chem.* 62 (12), 2213–2228. <https://doi.org/10.21608/ejchem.2019.11366.1728>
- APHA-AWWA-WPCF (American Public Health Association), 1999. *Standard Methods for the Examination of Water and Waste Water*, 20th edn., American Publ. Health Assoc., Washington, DC, USA.
- Abouhend, A.S., El-Moselhy, Kh.M., 2015. Spatial and seasonal variations of heavy metals in water and sediments at the Northern Red Sea Coast. *Am. J. Water Resour.* 3 (3), 73–85. <https://doi.org/10.12691/ajwr-3-3-2>
- Aspila, K.I., Agemian, H., Chau, A.S.Y., 1976. A semi-automated method for the determination of inorganic, organic and total phosphate in sediments. *Analyst* 101, 187–197. <https://doi.org/10.1039/AN9760100187>
- Attia, O.E.A., Abu Khadra, A.M., Nawwar, A.H., Radwan, G.E., 2012. Impacts of human activities on the sedimentological and geochemical characteristics of Mabahiss Bay, North Hurghada, Red Sea. *Egypt. Arab. J. Geosci.* 5, 481–499. <https://doi.org/10.1007/s12517-010-0193-3>
- Attia, O.E.A., Ghrefat, H., 2013. Assessing heavy metal pollution in the recent bottom sediments of Mabahiss Bay, North Hurghada, Red Sea. *Egypt. Environ. Monit. Assess.* 185, 9925–9934. <https://doi.org/10.1007/s10661-013-3302-4>
- Bahafzullah, A., Fayetf, L.A., Kazi, A., Al-Saify, M., 1993. Classification and distribution of the Red Sea coastal Sabkhas near Jeddah-Saudi Arabia. *Carbonates Evaporites* 8 (1), 23–38. <https://doi.org/10.1007/BF03175160>
- Balázs, H., Opara-Nadib, O., Beesea, F., 2005. A simple method for measuring the carbonate content of soil. *Soil. Sci. Soc. Am. J.* 69, 1066–1068. <https://doi.org/10.2136/sssaj2004.0010>
- Brescia, F., Arents, J., Meislich, H., Amos, T., 1975. *Fundamental of Chemistry: A Modern Introduction*, 3rd edn. Academic Press, Inc., New York.

- Dehbandi, R., Moore, F., Keshavarzi, B., 2017. Provenance and geochemical behavior of fluorine in the soils of an endemic fluorosis belt, central Iran. *J. African Earth Sci.* 129, 56–71. <https://doi.org/10.1016/j.jafrearsci.2016.12.016>
- El-Geziry, T.M., Dabbous, A.S., Abdallah, A.M., 2020. General pattern of sea level in Safaga and Qusseir Harbours on the Egyptian Red Sea coast. *Arab. J. Geosci.* 13, 436. <https://doi.org/10.1007/s12517-020-05447-y>
- El-Metwally, M.E.A., Madkour, A.G., Fouad, R.R., Mohamedein, L.I., Nour Eldine, H.A., Dar, M.A., El-Moselhy, Kh.M., 2017. Assessment the leachable heavy metals and ecological risk in the surface sediments inside the Red Sea ports of Egypt. *Int. J. Mar. Sci.* 7 (23), 214–228. <https://doi.org/10.5376/IJMS.2017.07.0023>
- El Nemr, A., El-Said, G.F., 2017. Assessment and ecological risk of heavy metals in sediment and molluscs from the Mediterranean Coast. *Water Environ. Res.* 89 (3), 195–210. <https://doi.org/10.2175/106143016x14798353399458>
- El-Said, G.F., 2005. Distribution of Fluoride Content in Some Localities of Egyptian Coastal Water Ph.D. Thesis. Chemistry Department, Faculty of Science, University of Alexandria, Alexandria, Egypt.
- El-Said, G.F., El-Sikaily, A., 2013. Chemical composition of some seaweed from Mediterranean Sea coast. *Egypt. Environ. Monit. Assess.* 185, 6089–6099. <https://doi.org/10.1007/s10661-012-3009-y>
- El-Said, G.F., 2013. Bioaccumulation of key metals and other contaminants by seaweeds from the Egyptian Mediterranean Sea Coast in relation to human health risk. *Hum. Ecol. Risk Assess.* 19, 1285–1305. <https://doi.org/10.1080/10807039.2012.708253>
- El-Said, G.F., El-Sadaawy, M.M., Moneer, A.A., Shaltout, N.A., 2015. The effect of fluoride on the distribution of some minerals in the surface water of an Egyptian lagoon at the Mediterranean Sea. *Egypt. J. Aquat. Res.* 41 (1), 31–39. <https://doi.org/10.1016/j.ejar.2015.02.004>
- El-Said, G.F., Shaltout, N.A., Moneer, A.A., El-Sadaawy, M.M., Morsy, A.M.H., 2016a. The precipitation of fluoride, calcium and magnesium minerals from Egyptian Mediterranean Sea coast in relation to discharged waters. *Desalin. Water Treat.* 57, 2113–2124. <https://doi.org/10.1080/19443994.2014.979243>
- El-Said, G.F., Khalil, M.Kh., Draz, S.E.O., 2016b. Anomalous distribution of fluoride and phosphorus forms in surface sediments along eastern Egyptian Mediterranean Sea coast. *Environ. Sci. Pollut. Res.* 23, 14240–14253. <https://doi.org/10.1007/s11356-016-6552-1>
- El-Said, G.F., El Zokm, G.M., El Sayed, A.A., El Ashmawy, A.A., Shreadah, M.A., 2020. Anomalous fluctuation of halogens in relation to the pollution status along Lake Mariout. *Egypt. J. Chem.* Article ID 8102081, 1–20. <https://doi.org/10.1155/2020/8102081>
- El-Said, G.F., El-Sadaawy, M.M., Shaltout, N.A., Moneer, A.A., 2021. Spatiotemporal distribution of some dissolved salts and minerals in Lake Edku connected to Mediterranean Sea: in relation to different pollutant inputs. *Environ. Monit. Assess.* 193, 155. <https://doi.org/10.1007/s10661-021-08935-0>
- El-Sarraf, W.M., Masoud, M.S., Harfoush, A.A., El-Said, G.F., 2003. Fluoride distribution and the effect of some ions along Alexandria coastal Mediterranean seawater of Egypt. *J. Environ. Sci.* 15 (5), 639–646.
- El Zokm, G.M., Ibrahim, M.I.A., Mohamed, L.A., El-Mamoney, M., 2020a. Critical geochemical insight into Alexandria coast with special reference to diagnostic ratios (TOC/TN & Sr/Ca) and heavy metals ecotoxicological hazards. *Egypt. J. Aquat. Res.* 46 (1), 27–33. <https://doi.org/10.1016/j.ejar.2019.12.006>
- El Zokm, G.M., Ismail, M.M., El-Said, G.F., 2020b. Halogen content relative to the chemical and biochemical composition of fifteen marine macro and micro algae: nutritional value, energy supply, antioxidant potency, and health risk assessment. *Environ. Sci. Pollut. Res.* <https://doi.org/10.1007/s11356-020-11596-0>
- Fahmy, M.A., 2003. Water quality in Red Sea coastal waters (Egypt): Analysis of spatial and temporal variability. *Chem. Ecol.* 19 (1), 67–77. <https://doi.org/10.1080/0275754031000087074>
- Fahmy, M.A., Abdel Fattah, L.M., Abdel-Halim, A.M., Aly-Eldeen, M.A., Abo-El-Khair, E.M., Ahdy, H.H., Hemeilly, A., Abu El-Soud, A., Shreadah, M.A., 2016. Evaluation of the quality for the Egyptian Red Sea Coastal waters during 2011-2013. *J. Environ. Prot.* 7, 1810–1834. <https://doi.org/10.4236/jep.2016.712145>
- Folk, R.L., 1974. *Petrology of Sedimentary Rocks*. University of Texas, Austin, TX, USA.
- Grasshoff, K., 1976. *Methods of Seawater Analysis*. Verlag Chemie, Weinheim and New York, 317 pp.
- Harlove, D.E., Aranovich, L., 2018. The Role of Halogens in Terrestrial and Extraterrestrial. In: *Geochemical Processes, Surface, Crust, and Mantle*. Springer Geochemistry, Springer International Publishing AG, Switzerland, 1030 pp.
- Ichikuni, M., 1979. Uptake of fluoride by aragonite. *Chem. Geol.* 27 (3), 207–214. [https://doi.org/10.1016/0009-2541\(79\)90039-1](https://doi.org/10.1016/0009-2541(79)90039-1)
- Jeffery, P.G., 1975. *Chemical Methods of Rock Analysis*, second edn., Pergamon Press, New York, NY, USA.
- Jones, B.F., Vengosh, A., Rosenthal, E., Yechieli, Y., 1999. Chapter 3: Geochemical Investigations. In: Bear, J., Cheng, A.H.-D., Sorek, S., Ouaza, D., Herrera, I. (Eds.), *Seawater Intrusion in Coastal Aquifers-Concepts, Methods and Practices, Theory and Applications of Transport in Porous Media*, Volume 14. Springer Science+Business Media, Dordrecht, The Netherlands, 625 pp.
- Kot, F.S., 2009. Boron sources, speciation and its potential impact on health. *Rev. Environ. Sci. Biotechnol.* 8, 3–28. <https://doi.org/10.1007/s11157-008-9140-0>
- Liteplo, R., Gomes, R., Howe, P., Malcom, H., 2002. *Environmental Health Criteria 227*. World Health Organization (WHO), Geneva.
- Mansour, A.M., Askalany, M.S., Madkour, H.A., Assran, B.B., 2013. Assessment and comparison of heavy-metal concentrations in marine sediments in view of tourism activities in Hurghada area, northern Red Sea. *Egypt. J. Aquat. Res.* 39, 91–103. <https://doi.org/10.1016/j.ejar.2013.07.004>
- Mansour, A.M., Nawar, A.H., Madkour, H.A., 2011. Metal pollution in marine sediments of selected harbours and industrial areas along the Red Sea coast of Egypt. *Ann. Naturhist. Mus. Wien Ser. A113*, 225–244.
- Manual of Methods of Analysis of Foods*, 2005. Fruit and Vegetable Products: Directorate General of Health Services. Ministry of Health and Family Welfare, Government of India, New Delhi, 57 pp.
- Masoud, M.S., El-Said, G.F., 2011. Behavior of some chloride, carbonate, phosphate, sulphate and borate additive salt–NaCl aqueous solution systems in the absence and presence of NaF. *Desalin. Water Treat.* 29, 1–9. <https://doi.org/10.5004/dwt.2011.1169>
- Millero, F.J., Feistel, R., Wright, D.G., McDougal, T.J., 2008. The composition of standard seawater and the definition of the reference-composition salinity scale. *Deep-Sea Res. Pt. I* 55, 50–72. <https://doi.org/10.1016/j.dsr.2007.10.001>
- Mohamed, A.A., 1999. *Natural Pigments and Iodine Contents in Certain Marine Macroalgae*. Helwan University, Egypt, 202 pp.
- Molnia, B.F., 1974. A rapid and accurate method for the analysis of calcium carbonate in small samples. *J. Sed. Petrol.* 44 (2), 589–590.
- Moneer, A.A., El-Sadawy, M.M., El-Said, G.F., Radwan, A.A., 2012. Boron human health risk assessment relative to the environmental pollution of Lake Edku. *Egypt. J. King Saud Univ. (JKAU): Mar. Sci.* 23 (2), 41–55. <https://doi.org/10.4197/Mar.23-2.3>
- Muramatsu, Y., Wedepohl, K.H., 1998. The distribution of iodine in the earth's crust. *Chem. Geol.* 147 (3–4), 201–216. [https://doi.org/10.1016/S0009-2541\(98\)00013-8](https://doi.org/10.1016/S0009-2541(98)00013-8)

- Nour, H.E., El-Sorogy, A., Abdel-Wahab, M., Almadani, S., Al-faifi, H., Youssef, M., 2018. Assessment of sediment quality using different pollution indicators and statistical analyses, Hurghada area, Red Sea coast, Egypt. *Mar. Pollut. Bull.* 133, 808–813. <https://doi.org/10.1016/j.marpolbul.2018.06.046>
- Nour, H.E., Nouh, E., 2020. Comprehensive pollution monitoring of the Egyptian Red Sea coast by using the environmental indicators. *Environ. Sci. Pollut. Res.* <https://doi.org/10.1007/s11356-020-09079-3>
- Ries, J.B., 2010. Review: Geological and experimental evidence for secular variation in seawater Mg/Ca (calcite-aragonite seas) and its effects on marine biological calcification. *Biogeosciences* 7, 2795–2849. <https://doi.org/10.5194/bg-7-2795-2010>
- Saenger, P., 1972. A rapid spectrophotometric method for the determination of bromine in seawater and in the ash of marine algae. *Helgoländer wissenschaftliche Meeresuntersuchungen* 23 (1), 32–37. <https://doi.org/10.1007/BF01616309>
- Sawicka, J.E., Jørgensen, B.B., Bruchert, V., 2012. Temperature characteristics of bacterial sulfate reduction in continental shelf and slope sediments. *Biogeosciences* 9, 3425–3435. <https://doi.org/10.5194/bg-9-3425-2012>
- Schmidt, B., Ponath, S., Hannemann, J., Voßnacker, P., Sonnenberg, K., Christmann, M., Riedel, S., 2020. In situ synthesis and applications for polyinterhalides based on BrCl. *Chem. Eur. J.* 26, 15183–15189. <https://doi.org/10.1002/chem.202001267>
- Selim, A.E.M., 2007. *Sedimentation Threats to Red Sea Corals : An Ecological Study of Reefs in the Hurghada region.* Egypt, Ph.D. Thesis. Hull University, England, 207 pp.
- Shapiro, O.H., Kartvelishvily, E., Kramarsky-Winter, E., Vardi, A., 2018. Magnesium-rich nanometric layer in the skeleton of *Pocillopora damicornis* with possible involvement in fibrous aragonite deposition. *Front. Mar. Sci.* 5, Article 246. <https://doi.org/10.3389/fmars.2018.00246>
- Soliman, N.F., El Zokm, G.M., Okbah, M.A., 2018. Risk assessment and chemical fractionation of selected elements in surface sediments from Lake Qarun, Egypt using modified BCR technique. *Chemosphere* 191, 262–271. <https://doi.org/10.1016/j.chemosphere.2017.10.049>
- Strickland, J.D.H., Parsons, T.R., 1972. *A Practical Handbook of Seawater Analysis*, second ed., Fisheries Research Board of Canada. *Bulletin 167*, Ottawa, Canada, 311 pp.
- Tokatli, C., Çiçek, A., Emiroğlu, Ö., Arslan, N., Köse, E., Dayoğlu, H., 2014. Statistical approaches to evaluate the aquatic ecosystem qualities of a significant mining area: Emet stream basin (Turkey). *Environ. Earth Sci.* 71, 2185–2197. <https://doi.org/10.1007/s12665-013-2624-4>
- Worden, R.H., 1996. Controls on halogen concentrations in sedimentary formation waters. *Mineral. Mag.* 60 (399), 259–274. <https://doi.org/10.1180/minmag.1996.060.399.02>

Available online at [www.sciencedirect.com](http://www.sciencedirect.com)

ScienceDirect

journal homepage: [www.journals.elsevier.com/oceanologia](http://www.journals.elsevier.com/oceanologia)

## ORIGINAL RESEARCH ARTICLE

# Chemical characterization and biochemical activity of polysaccharides isolated from Egyptian *Ulva fasciata* Delile

Madelyn N. Moawad<sup>a</sup>, Abeer A.M. El-Sayed<sup>a</sup>, Hala H. Abd El Latif<sup>a</sup>, Naglaa A. El-Naggar<sup>a,b</sup>, Nihal G. Shams El-Din<sup>a</sup>, Hermine R.Z. Tadros<sup>a,\*</sup>

<sup>a</sup>National Institute of Oceanography and Fisheries, NIOF, Egypt

<sup>b</sup>Department of Chemistry, College of Science, University of Hafr Al Batin, Hafr Al Batin, Saudi Arabia

Received 30 January 2021; accepted 30 September 2021

Available online 14 October 2021

## KEYWORDS

Ulvan;  
Chemical composition;  
Biological activities;  
FT-IR, <sup>1</sup>H NMR

**Abstract** This study gives updated information on the isolation of ulvan from green alga *Ulva fasciata* Delile in Egypt through isolation and chemical characterization of sulfate polysaccharides by two sequential extraction steps using different solvents; distilled water, HCl and Na<sub>2</sub>EDTA forming fraction I (F-I). Fraction II (F-II) was obtained from remaining seaweeds using NaOH to give F<sub>DW</sub>NaOH, F<sub>HCl</sub>NaOH, and F<sub>EDTA</sub>NaOH. All products obtained were tested for their biological activities. The highest polysaccharides total extraction yield was 11.8% for water extract (F-I and F-II). The highest protein content was found in F<sub>EDTA</sub>NaOH (2.44%). The highest sulfate content was recorded for F-I (HCl) (21.38%). Total carbohydrates range was 11.99–63.90% for F-I and 15.06–76.65% for F-II. Monosaccharides; galactose, rhamnose, and uronic acid were detected at all fractions, with concentrations varying from 0.11 to 1.34%, from 0.61 to 1.81% and from 11.06 to 19.30%, respectively. <sup>1</sup>H NMR of F-II demonstrated the signals of ring and methyl protons of polysaccharide. The appearance of the stretching bands of the sulfate ester (C-O-S) and sulfate groups (S=O) in the FT-IR spectrum of F<sub>HCl</sub>NaOH confirmed the presence of sulfated polysaccharides, typical of ulvan. The microbial species *Vibrio damsela* was the most susceptible to F<sub>DW</sub>NaOH, followed by *Aeromonas hydrophila* and *Vibrio fluvialis* with inhibition zones of 30, 22, 22 mm at 150 mg/ml, respectively. F<sub>DW</sub>NaOH was the most ef-

\* Corresponding author at: National Institute of Oceanography and Fisheries, NIOF, Egypt. Tel: +203-480155.

E-mail address: [herminetadros@gmail.com](mailto:herminetadros@gmail.com) (H.R.Z. Tadros).

Peer review under the responsibility of the Institute of Oceanology of the Polish Academy of Sciences.



fective fraction having antifouling property. The highest antioxidant activity was observed for F-HCl followed by F<sub>DW</sub>NaOH. At concentrations 25 and 50 mg/l, F<sub>EDTA</sub>NaOH displayed the highest anti-inflammatory activity (94.0 and 91.40%, respectively).

© 2021 Institute of Oceanology of the Polish Academy of Sciences. Production and hosting by Elsevier B.V. This is an open access article under the CC BY-NC-ND license (<http://creativecommons.org/licenses/by-nc-nd/4.0/>).

## 1. Introduction

Macroalgae or seaweeds are highly diversified marine organisms, providing a great variety of metabolites and natural bioactive compounds with potential therapeutic agents (Smit, 2004). Marine algae are characterized by the presence of large amounts of polysaccharides (Murata and Nakazoe, 2001) which are natural compounds, some of them associated with several biological activities and potential health benefits, making them interesting potent for the application in pharmaceuticals, therapeutics, and regenerative medicine (De Jesus Raposo et al., 2015). They protect the human against tissue damage by reactive oxygen species (ROS) (Wijesekara et al., 2011). Furthermore, they include anticoagulant and/or antithrombotic properties, and are also good antidyslipidaemic and hypoglycaemic agents, and can be powerful antibiotics (De Jesus Raposo et al., 2015).

Ulvan molecule has been designated as being a sulfated polysaccharide composed of  $\alpha$ - and  $\beta$ -(1,4)- linked monosaccharides (rhamnose, xylose, glucuronic acid and iduronic acid) with characteristic repeating disaccharide units (Lahaye, 1998; Lahaye and Robic, 2007; Paradossi et al., 1999). Ulvan contributes from 9 to 36% dry weight of the biomass of *Ulva* spp. (Lahaye and Robic, 2007) with three other cell wall polysaccharides (cellulose, xyloglucan, and glucuronan) account for up to 45% of the dry weight biomass (Lahaye et al., 1997).

The structure of sulfated polysaccharide is responsible for its distinguishing properties (El-Baky et al., 2009). It can be successfully used in many applications such as antibacterial (Boisvert et al., 2015), antiviral (Jiao et al., 2012), anti-oxidant (Courtois, 2009), anti-cancer (El-Baky et al., 2009), anti-inflammatory (Faury et al., 2011) and immunostimulating agent (Leiro et al., 2007). All these activities increased the awareness of sulfated polysaccharide importance in different domains over the world (Hernández-Garibay et al., 2010; Lahaye et al., 1999; Robic et al., 2009a; Tako et al., 2015) and applicability, in order to understand the full range of its capabilities and boost the industrial interest in green algae (Alves et al., 2013; Kidgell et al., 2019).

In Egypt, Matloub et al. (2013) carried out a study on the physico-chemical characterizations of water-soluble polysaccharides isolated from *Ulva fasciata* as a natural anti-hyperlipidemic agent, whereas Hussein et al. (2015) investigated the biological activity of ulvan extracted from *Ulva fasciata* and *Ulva lactuca* affecting growth and metabolism of the microalga *Chlorella vulgaris*. Furthermore, Abou El Azm et al. (2019) carried out a study to obtain bioactive compounds from the aqueous high molecular weight sulfated polysaccharides isolated from *Ulva lactuca*.

The aim of the current study is to isolate and chemically characterize sulfated polysaccharide from *Ulva fasci-*

*ata* Delile by two steps sequential extraction using distilled water (DW), HCl, and Na<sub>2</sub> EDTA to form fraction I (F-I), then preparing fraction II (F-II) from remaining seaweeds. Evaluation of these different extracts through testing their biological activities (antimicrobial, antifouling, antioxidant, and anti-inflammatory) is also a main goal for this study.

## 2. Material and methods

### 2.1. Sample collection

Samples of the green alga *U. fasciata* were collected during summer (2018) from the sub-littoral zone (0.5–1 m depth) in front of Scout club located in the Eastern Harbor, Alexandria, Egypt at 29°53.10'E longitude and 31°13.3'N latitude. The samples were washed with seawater *in situ* to remove the adhered sediments and impurities, separated in polyethylene bags and stored in an ice box, at temperature 4°C. At the laboratory, the alga was rinsed immediately with tap water to get rid of the remaining impurities and epiphytes. The species of *U. fasciata* Delile was identified according to Aleem (1993). It belongs to class Chlorophyceae, order Ulvales, family Ulvaceae.

### 2.2. Extraction of polysaccharides from *U. fasciata*

Before polysaccharides extraction, the algal samples were air-dried at room temperature of 25°C and homogenized with a grinder to a particle size from 0.3–0.5 mm. The powder was stored in plastic bags at 4°C for further analysis. A weight of 20 g seaweed powder was treated with 200 ml ethanol (80%) under constant stirring overnight at ambient temperature (20°C) to remove lipids, pigments and low molecular weight compounds (Tabarsa et al., 2018). The mixture was centrifuged at 10°C and 8000 rpm for 10 min and the supernatant was discarded. The residual was rinsed with acetone and dried at room temperature.

The de-pigmented powder was extracted with 200 ml (1:10w/v) of DW, or 0.2 N HCl or 0.1 M Na<sub>2</sub>EDTA by stirring in a water bath for 2 h at 60°C. The mixture was centrifuged and the residues were re-extracted twice with additional 200 ml of the same media for 60 min. and centrifuged again. The different extracts were filtered and concentrated by evaporation under reduced pressure at 60°C. The extracts were precipitated by adding three volumes of ethanol then centrifuged to recover the precipitates. The precipitates were desalted two times for 30 min, each with 15 ml 70% ethanol and two times with full concentrated ethanol. The precipitate was dried at 60°C in the oven until constant weight and grounded into fine powder to ob-

tain fraction I, F-I<sub>DW</sub>, F-I<sub>HCl</sub>, and F-I<sub>EDTA</sub> from DW, HCl, and Na<sub>2</sub> EDTA, respectively, according to the simple method described by [Hernández-Garibay et al. \(2010\)](#). The fraction II (F<sub>DW</sub>NaOH, F<sub>HCl</sub>NaOH, and F<sub>EDTA</sub>NaOH) was obtained sequentially from the remaining seaweeds of each of the above treatments by extraction with 200 ml 0.1 M NaOH at 60°C for 2 h ([Hernández-Garibay et al., 2010](#)). The polysaccharides in solution were recovered, as described above.

### 2.3. Chemical characterization of algal polysaccharides

A weight of 100 mg fine powder of F-I and F-II was suspended in a volume of 3 ml DW to prepare different concentrations of each fraction. All measurements of biochemical contents were conducted in duplicates.

#### 2.3.1. Determination of protein content

The protein content was analyzed spectrophotometrically at 650 nm according to the method described by [Lowry et al. \(1951\)](#), using standard salt-free bovine serum albumin.

#### 2.3.2. Determination of carbohydrates content

Total carbohydrates content was assayed by phenol-sulfuric acid method ([Dubois et al., 1956](#)).

#### 2.3.3. Determination of sulfate content

Sulfate content was determined turbidimetrically after acid hydrolysis with 0.5 M HCl by barium chloride-gelation method using K<sub>2</sub>SO<sub>4</sub> as a standard ([Dodgson and Price, 1962](#)).

#### 2.3.4. Monosaccharides composition of isolated polysaccharides

Polysaccharides fractions (0.1 g) were hydrolyzed with 50 ml trifluoro-acetic acid (10 M) at 80°C for 12 h. After filtration, neutral sugars in hydrolyzed samples were analyzed by Agilent 1260 infinity HPLC Series (Agilent, USA), equipped with Phenomenex® Rezex RCM-Monosaccharide column (300 mm × 7.8 mm) operated at 80°C with Refractive Index detector operated at 40°C. The uronic acids were quantified by using HPLC (Knauer, Germany) with Rezex® column for organic acids analysis (300 mm × 7.8 mm). At 214 nm, UV detector was set. Reference sugars (glucosamine, sucrose, glucose, galactose, mannose, rhamnose, fructose, galacturonic acid, glucuronic acid) were used to identify the chromatographic peaks.

### 2.4. Structural analysis

#### 2.4.1. Determination of <sup>1</sup>H NMR spectra

For <sup>1</sup>H NMR spectra, approximately 5 mg of each of the F<sub>DW</sub>NaOH, F<sub>HCl</sub>NaOH, and F<sub>EDTA</sub>NaOH fractions were dissolved solely in deuterated water (D<sub>2</sub>O), and the spectrum was acquired at ambient temperature (198.1 K) using FT-NMR spectrometer at 300 MHz using Bruker NMR spectroscopy.

#### 2.4.2. Fourier transform infrared (FT-IR)

Fourier transform infrared (FT-IR) spectra of obtained fractions were acquired in transmission mode at wave numbers ranging from 400 cm<sup>-1</sup> to 4000 cm<sup>-1</sup> using FT-IR Spectrometer (Bruker Platinum ATR Vertex 70).

### 2.5. Bioactivity of polysaccharides fractions

#### 2.5.1. Antimicrobial bioassay

Three gram-negative bacterial strains were examined as pathogens, namely *Aeromonas hydrophila*, *Vibrio damsela*, and *Vibrio fluvialis* from National Institute of Oceanography and Fisheries, Alexandria, Egypt (Microbiology Lab.).

A volume of 15 ml of the sterilized media (nutrient agar CM 3 Oxoid) for bacteria was poured into sterile capped test tubes and were allowed to cool in a water bath. A 0.5 ml of inocula (10<sup>8</sup> CFU for bacteria) was added, and finally poured onto a sterile Petri dish for solidification ([Mtolera and Semesi, 1996](#)).

The well-cut diffusion technique was used to evaluate the antimicrobial activity ([El-Masry et al., 2000](#)). In nutrient agar plates inoculated with the tested microorganisms, wells have been done using a sterile 0.7 cm cork borer. Different concentrations (35, 50, 65, 75, 112 and 150 mg/ml) of the extracted polysaccharides were transferred into each well. The experiments were performed in triplicate. All plates were subjected to 4°C incubation for 2 h. The plates were incubated latterly at 37°C for 24 h. The results were obtained by measuring the inhibition zone diameter for each well and expressed in millimeters.

#### 2.5.2. Antifouling activity

A volume of 100 ml sterilized seawater (filtered and then autoclaved) was mixed separately with each fraction of F<sub>DW</sub>NaOH, F<sub>HCl</sub>NaOH, and F<sub>EDTA</sub>NaOH (50, 100, and 150 mg/l) in a conical flask containing cover glass and then was supplied with the fouling bacteria *Escherichia coli*. The mixture was incubated overnight at 30°C. Afterwards, the cover glasses were dyed with crystal violet solution (0.4%) for 10 minutes, then washed with water, and dried at room temperature and checked under the microscope. One flask was prepared without any fractions and was kept as a control ([Kumaran et al. 2011](#)).

#### 2.5.3. Total antioxidant capacity

The determination of total antioxidant capacity was also conducted spectrophotometrically on various fractions at 695 nm using phosphomolybdenum reagent according to the method described by [Prieto et al. \(1999\)](#). The antioxidant activity was expressed as L-ascorbic acid equivalents (μM AAE/g).

#### 2.5.4. Anti-inflammatory activity

The anti-inflammatory activity was studied using the inhibition of albumin denaturation technique ([Mizushima and Kobayashi, 1968](#); [Sakat et al., 2010](#)) with minor modifications. Two concentrations of each fraction of the extracted polysaccharides were prepared (25 and 50 mg/l). A volume of 2.25 ml of bovine serum albumin (BSA) (5%, w/v aqueous solution) was added to 0.25 ml of each fraction, control (without extract), and standards. Samples, control and standard solutions (Diclofenac sodium Voltaren® ampoule Novartis Pharma 1000 μg/ml) were adjusted to pH 5.5 using a small amount of 0.1 M HCl or 0.1 M NaOH. The solutions were incubated at 37°C for 30 min and then transferred to 70°C water bath for 10 min. Following incubation, the solutions were left to cool down at room temperature (25°C)



then 5 ml of phosphate buffer was added to the above solutions. The turbidity of the above solutions was measured by using a UV-Visible spectrophotometer at 660 nm (UNICO-UV Visible Spectrophotometer Model UV-2000 USA). The inhibition % was determined for protein denaturation as follows:

$$\text{Inhibition\%} = \left[ \frac{\text{Abs}_{\text{control}} - \text{Abs}_{\text{sample/standard}}}{\text{Abs}_{\text{control}}} \right] \times 100 \quad (1)$$

The activity of each fraction was compared with three concentrations (100, 250 and 500 µg/ml) of the standard commercial anti-inflammatory agent 'Diclofenac sodium'.

### 2.5.5. Statistical analysis

Three microbial species (*A. hydrophila*, *V. damsela* and *V. fluvialis*) were randomly distributed as main plots according to the split-split plot design. Six concentrations (35, 50, 65, 75, 112, and 150 mg/ml) occupied sub-plots and six fractions (F-I<sub>DW</sub>, F-I<sub>HCl</sub>, and F-I<sub>EDTA</sub>, F<sub>DW</sub>NaOH, F<sub>HCl</sub>NaOH, and F<sub>EDTA</sub>NaOH) were assigned in the sub-sub plots. Statistical analyses of the experimental data were performed according to Gomez and Gomez (1984) by using the Statistical Analysis System (SAS, 2007) version 9.1.3. Comparison between treatment means was carried out by using the least significant differences at the 0.05 level of probability (LSD<sub>0.05</sub>).

## 3. Results and discussion

### 3.1. Biochemical composition of different algal fraction

The yield and the chemical composition of crude polysaccharides fractions obtained from *U. fasciata* varied according to the extraction media (Table 1). The total extraction yield for polysaccharides (F-I+F-II) was found to be 11.81% (w/w of algae dry weight) for water extract which was higher than that of EDTA and HCl fractions being 10.03 and 9.72%, respectively. The yield of F-I<sub>HCl</sub> and F-I<sub>EDTA</sub> (2.38 and 3.29%) was lower than F<sub>HCl</sub>NaOH and F<sub>EDTA</sub>NaOH (7.34 and 6.74%), respectively, whereas the DW fractions showed the inverse pattern (Table 1). Polysaccharides extraction at pH < pKa decreases its solubility (Kidgell et al., 2019). This explains the decrease in F-I<sub>HCl</sub> yield % (2.38%). F<sub>HCl</sub>NaOH and F<sub>EDTA</sub>NaOH demonstrated high yield % (Table 1). This is attributed to an increase in solution solubility at pH levels greater than pka (Kidgell et al., 2019; Robic et al., 2009b). In this study, the total extraction yield (%) ranged from 9.72 to 11.81%, which was within the ranges reported by Lahaye and Robic (2007), Hernández-Garibay et al. (2010), and Wahlström et al. (2020). This variation in extraction yield may be due to environmental variation (Kidgell et al., 2019), seaweed species, and extraction procedures (Costa et al., 2010; Kaeffer et al., 1999).

The highest sulfate content was recorded for F-I<sub>HCl</sub> (21.38%) followed by F-I<sub>EDTA</sub> (17.13%), and F-I<sub>DW</sub> (14.92%), with respect to F-II; F<sub>DW</sub>NaOH showed the highest sulfate content (15.03%) followed by F<sub>HCl</sub>NaOH (12.73%), and F<sub>EDTA</sub>NaOH (7.76%). The present study showed higher sulfate content in polysaccharides of F-I<sub>HCl</sub> than that of other

Table 1 Biochemical composition of different algal fractions of *Ulva fasciata*.

Fractions	Yield %	Soluble carbohydrates	Total carbohydrates	Proteins	Sulfate	Monosaccharides composition				
						Glucose	Galactose	Rhamnose	Glucosamine	Uronic acid
F-I	Water	6.02	63.90	1.20	14.92	ND	0.11	0.76	51.79	11.23
	HCl	2.38	12.62	1.89	21.38	0.14	0.17	0.61	ND	11.70
	EDTA	3.29	11.99	0.33	17.13	ND	0.25	0.68	ND	11.06
F-II	Water	5.79	15.06	1.68	15.03	ND	0.59	1.81	ND	12.67
	HCl	7.34	21.91	1.30	12.73	0.76	0.65	1.20	ND	19.30
	EDTA	6.74	76.65	2.44	7.76	ND	1.34	1.77	58.30	15.23

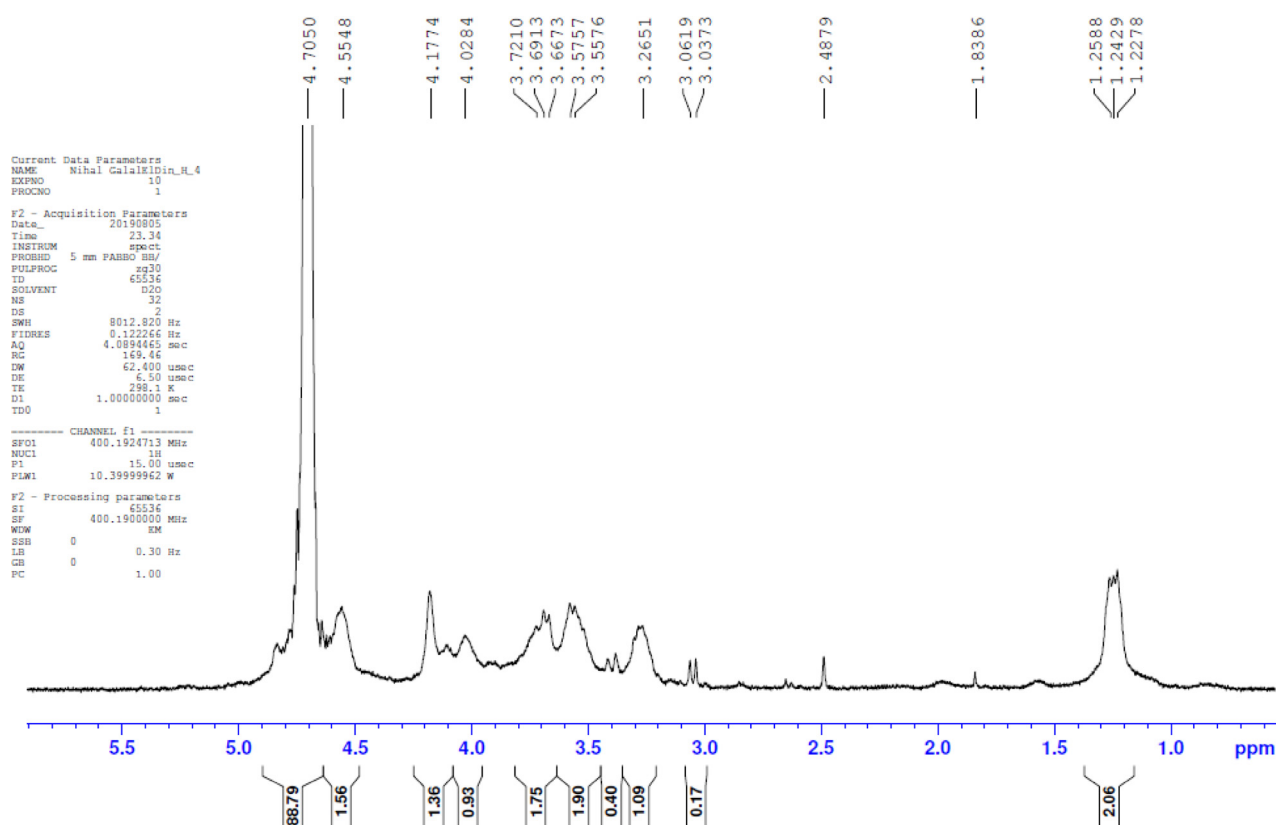


Figure 1  $^1\text{H}$  NMR spectrum of  $F_{\text{DWNaOH}}$  extract.

fractions while Wahlström et al. (2020) found that the extraction of polysaccharides using HCl resulted in low sulfate content. This variation may be caused by extraction conditions such as the acid concentration, temperature, and solid/liquid ratio.

The protein content did not differ significantly between F-I and F-II for water (1.20 and 1.68%) and HCl (1.89 and 1.30%) extracts, respectively while in case of  $F_{\text{EDTA NaOH}}$  contained a higher amount of protein content (2.44%) than F-I (0.33%). Since proteins were released by the breaking of hydrogen bridges in the alkaline solution,  $F_{\text{EDTA NaOH}}$  had higher protein content than the corresponding  $F_{\text{I EDTA}}$  (Robic et al., 2008). Proteins, in general, are an impurity that may occur in the extracts (Glasson et al., 2017).

The total carbohydrates range was 11.99–63.90% for F-I and 15.06–76.65% for F-II. F-II exhibited higher values of total carbohydrates than F-I, except for  $F_{\text{I DW}}$ . The total carbohydrates content in  $F_{\text{EDTA NaOH}}$  was 76.65% followed by  $F_{\text{I DW}}$  (63.90%). In case of  $F_{\text{I DW}}$ , extraction media resulted in a low salt content of algal biomass, which decreased polysaccharide aggregation properties, in addition to the exposure of cell wall components through osmotic shock, resulting in a high yield percent and total carbohydrates content (Kidgell et al., 2019).

In addition, monosaccharides; galactose, rhamnose, and uronic acids were detected at all fractions, with concentrations varying from 0.11 to 1.34%, from 0.61 to 1.81% and from 11.06 to 19.30%, respectively. Cell wall rigidity can be increased by the presence of large quantities of rhamnose-containing polysaccharides (Rashidi and Trindade, 2018). The presence of glucose and glucosamine

below the detection limit was noticed in most fractions. The recorded concentrations for glucose were 0.14 and 0.76% in  $F_{\text{I HCl}}$  and  $F_{\text{HCl NaOH}}$ , respectively. According to Wahlström et al. (2020), polysaccharides extracted in acid media had higher glucose content. Glucosamine concentrations of 51.79 and 58.30% were indicated for  $F_{\text{I DW}}$  and  $F_{\text{EDTA NaOH}}$ , respectively. Glucosamine (an amino sugar) was reported by Rashidi and Trindade (2018) as a component of cell wall polysaccharides from Chlorophyta. In general, sequential extracts (F-II) using alkaline media showed higher monosaccharides content than F-I.

### 3.2. $^1\text{H}$ NMR spectra of $F_{\text{DWNaOH}}$ , $F_{\text{HClNaOH}}$ , and $F_{\text{EDTA NaOH}}$ extracts

$^1\text{H}$  NMR spectra of  $F_{\text{DWNaOH}}$ ,  $F_{\text{HClNaOH}}$ , and  $F_{\text{EDTA NaOH}}$  are shown in Figures 1, 2, 3. The methyl proton of the  $\alpha$ -L-rhamnosyl residues was observed in the range of 1.23–1.26 ppm. The signals of the ring protons appeared at the range of 3.28–4.18 ppm. O-acetyl group was detected in fractions  $F_{\text{DWNaOH}}$  and  $F_{\text{EDTA NaOH}}$  at 2.49 and 2.49 ppm, respectively.

The overlapping signals in the spectra of  $^1\text{H}$  NMR gave an indication for the complex form of polysaccharide. The signals of ring and methyl protons in the current study have been mentioned for polysaccharide from *Ulva* sp. by Hernández-Garibay et al. (2010) and Lahaye and Robic (2007). The observed O-acetyl group found in  $F_{\text{DWNaOH}}$  and  $F_{\text{EDTA NaOH}}$  may be considered as a part of the structure of polysaccharide or as an impurity (Monsur et al., 2017).

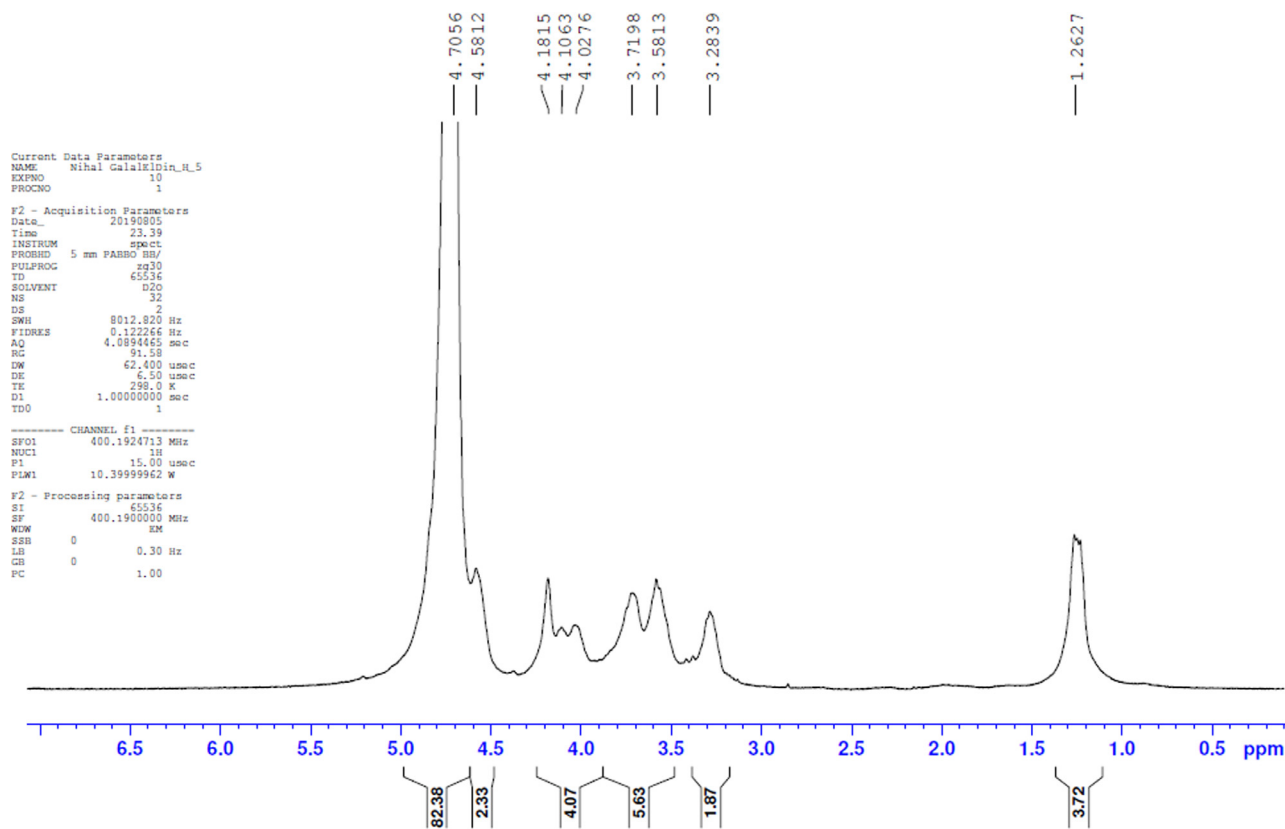


Figure 2  $^1\text{H}$  NMR spectrum of  $\text{F}_{\text{HClNaOH}}$  extract.

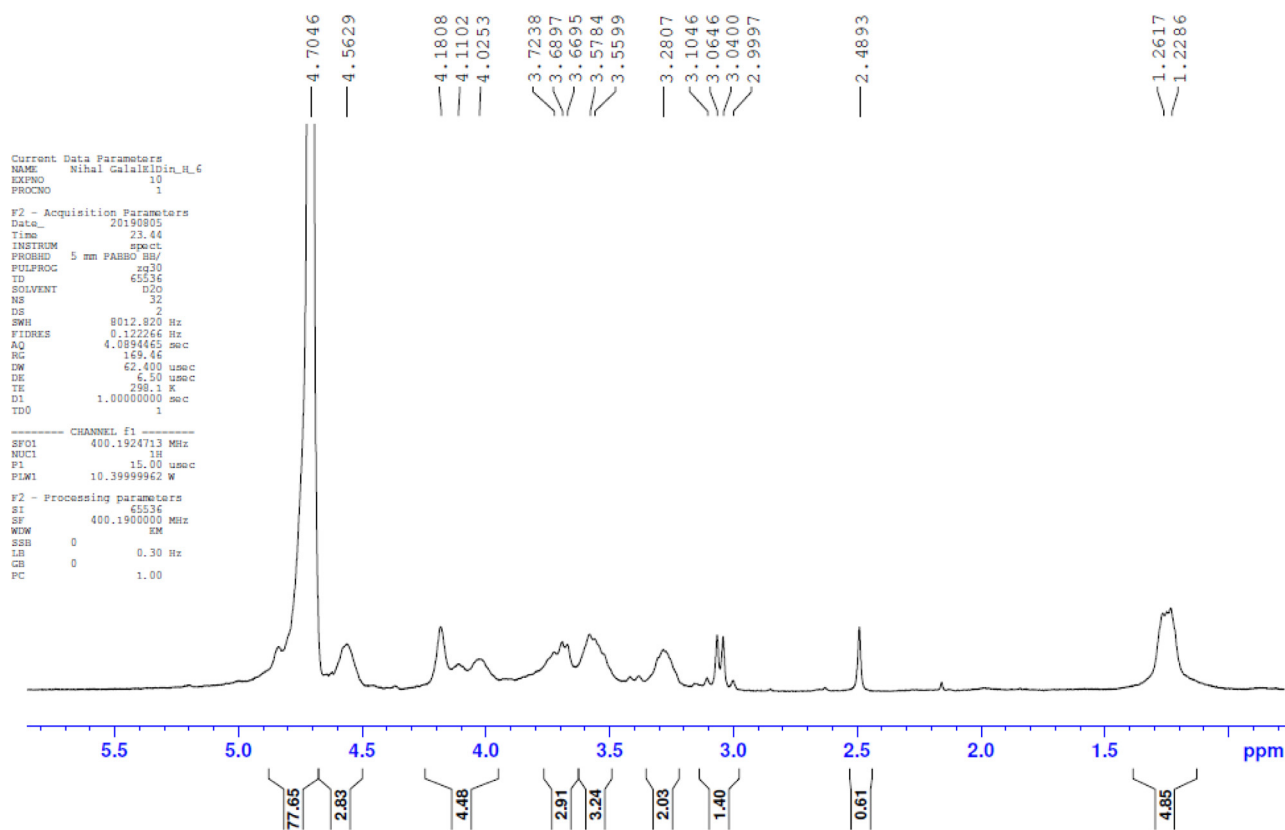
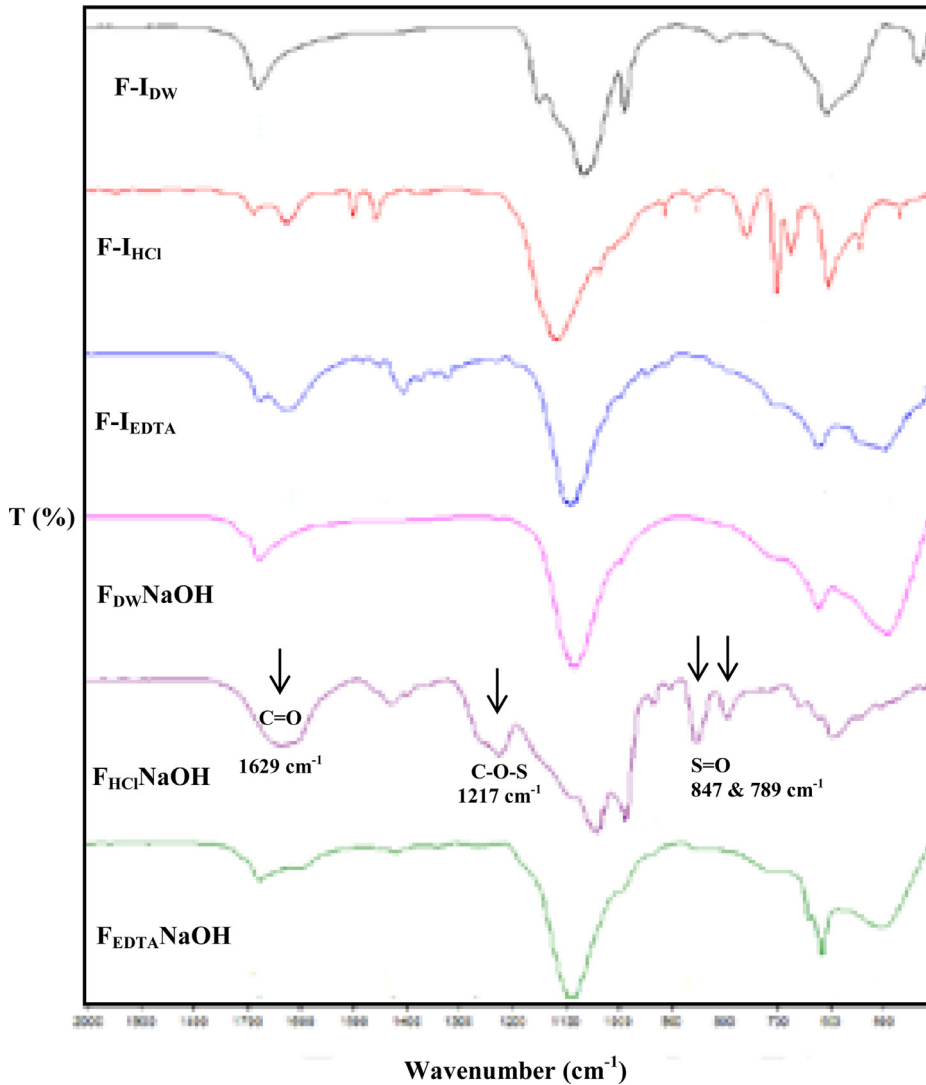


Figure 3  $^1\text{H}$  NMR spectrum of  $\text{F}_{\text{EDTANaOH}}$  extract.

**Table 2** Assignments of infrared bands to the corresponding functional groups in different fractions of *Ulva fasciata*.

Fractions		Functional groups						
		cm <sup>-1</sup>						
		O-H	C=O	C=O	C-O-S	C-O-C	Pyranose Ring & S=O	C-H
F-I	Water	3197	1672	-	-	1054	981	603-427
	HCl	3399-3526	1620	1493-1451	-	1109	752	696-668-598
	EDTA	3335	1617	1397	-	1081	-	614-492
F-II	Water	3331	1669	-	-	1075	-	616-488
	HCl	3351	1629	1421	1217	1033	847-789	592
	EDTA	3347	1668	-	-	1080	-	634-611-497



**Figure 4** FTIR spectra in different fractions (F-I and F-II) using different extraction media.

### 3.3. FT-IR spectra for fractions I and II

The infrared spectra for F-I and F-II showed nearly similar signals, except for F-I<sub>HCl</sub> and F-II<sub>HClNaOH</sub> which were more complex (Table 2 and Figure 4). The broad signals in the range of 3526 to 3197 cm<sup>-1</sup> were attributed to the stretching vibrations of OH groups. The stretching bands that appeared at 1672 to 1617 cm<sup>-1</sup> were as-

signed to the carboxylate group (C=O). The other weak stretching bands of carboxylate group (C=O) appeared for F-I<sub>HCl</sub> (1493–1451 cm<sup>-1</sup>), F-I<sub>EDTA</sub> (1397 cm<sup>-1</sup>), and F-II<sub>HClNaOH</sub> (1421 cm<sup>-1</sup>) (Robic et al., 2009a; Yaich et al., 2017). The signal band shown at 1217 cm<sup>-1</sup> was attributed to the stretching band of the sulfate ester (C-O-S) in F-II<sub>HClNaOH</sub> (Wahlström et al. 2020). Two additional signals at 849 and 789 cm<sup>-1</sup> were pointed to sulfates (S=O) in the polysaccha-

ride (Hernández-Garibay et al., 2010; Pengzhan et al., 2003; Ray and Lahaye, 1995; Robic et al., 2009a).

The spectra showed strong signal bands at 1054, 1109, 1081, 1075, 1033, and 1080  $\text{cm}^{-1}$  in F-1<sub>DW</sub>, F-1<sub>HCl</sub>, F-1<sub>EDTA</sub>, F<sub>DW</sub>NaOH, F<sub>HCl</sub>NaOH, and F<sub>EDTA</sub>NaOH, respectively, this may be due to the overlapping of C-OH side group and C-O-C glycosidic bond as well as the sugar ring.

The other bands in the range of 1000–750  $\text{cm}^{-1}$  related to sugar cycles (pyranose ring). The stretching bands (700–400  $\text{cm}^{-1}$ ) were assigned to C-H group in all fractions.

F<sub>HCl</sub>NaOH showed better defined spectrum than those of other fractions (Figure 4). This may be due to the stretching bands of the sulfate ester (C-O-S) and sulfate groups (S=O) in the polysaccharide (Hernández-Garibay et al., 2010; Robic et al., 2009a) which indicates the presence of sulfated polysaccharides, typical for ulvan in this fraction (Li et al., 2018). Extraction at pH less than pKa plays a significant role in the selectivity of ulvan over other macromolecules. Moreover, the addition of HCl solution (0.1N) to the *U. fasciata* promotes ulvan release in the sequential extraction using NaOH. Similar observation was recorded by Hernández-Garibay et al. (2010).

In our study, sulfated polysaccharides consist mainly of rhamnose, sulfate groups, and uronic acid in F<sub>HCl</sub>NaOH. Method of extraction, geographical distribution, maturity, environmental condition, and seasonality, may affect the amount of each monosaccharide residue or the arrangement of the polysaccharide, resulting in different ulvan structures (Alves et al., 2013; Lahaye and Robic, 2007).

### 3.4. Antimicrobial activity of polysaccharides

The results of the antimicrobial activity of polysaccharides showed significant differences based on the media of extraction (F-1<sub>DW</sub>, F-1<sub>HCl</sub>, F-1<sub>EDTA</sub>, F<sub>DW</sub>NaOH, F<sub>HCl</sub>NaOH, and F<sub>EDTA</sub>NaOH) (Table 3 and 4). Currently, the microbial species *V. damsela* was the most susceptible to F<sub>DW</sub>NaOH, with inhibition zone (30 mm) at a concentration of 112 and 150 mg/ml, followed by *A. hydrophila* and *V. fluvialis* both with inhibition zone (22 mm) at 150 mg/ml (Table 3). This was supported by the results of statistical analysis, where the effect of F<sub>DW</sub>NaOH on *V. damsela*, *A. hydrophila*, and *V. fluvialis* showed the mean of 14.83, 14.61 and 7.83, respectively (Table 5). The efficiency of F<sub>DW</sub>NaOH as solvent was supported by the mean of 12.42, whereas the mean of the ascending concentrations for all fractions (35, 50, 65, 75, 112 and 150 mg/ml) showed ascending increase mean from 1.72 to 2.88, 4.50, 10.33, 13.0 and 15.64, respectively (Table 5). The antibacterial activity of polysaccharides was promising, where all the fractions inhibited the three tested bacteria with a different degree. The fraction of F<sub>DW</sub>NaOH was the most effective one for *V. damsela* followed by *A. hydrophila* and *V. fluvialis*. In contrast, Paulert et al. (2007) reported that polysaccharides extracted from *U. fasciata* did not show any antibacterial activity against different bacterial strains (*Escherichia coli*, *Staphylococcus aureus*, *Pseudomonas aeruginosa*, *Bacillus cerus*, *Micrococcus luteus*, *Xanthomonas campestris*, and *Erwinia carotovora*). This difference may be attributed to the different method for polysaccharides extraction as well as different bacterial strain. Despite of the same macroalgae species *U. fasciata*, the discrepancies between the results may be explained on

**Table 3** Inhibition zone (mm) of microbial growth by different concentrations of algal extracts from *Ulva fasciata*.

Fractions	Aeromonas hydrophila						Vibrio fluvialis						Vibrio damsela						
	Fraction concentration (mg/ml)						Fraction concentration (mg/ml)						Fraction concentration (mg/ml)						
	35	50	65	75	112	150	35	50	65	75	112	150	35	50	65	75	112	150	
F-I	Water	10	10	11	12	13	13	0	0	0	15	17	18	0	0	0	10	12	13
	HCl	0	10	10	12	13	14	0	0	12	9	9	12	0	0	0	14	15	15
	EDTA	0	0	0	13	15	20	0	0	0	13	14	15	0	0	12	13	14	15
F-II	Water	12	13	14	15	15	22	0	0	0	12	13	22	0	9	10	10	30	30
	HCl	9	10	12	13	13	14	0	0	0	13	15	17	0	0	0	0	14	15
	EDTA	0	0	0	12	12	12	0	0	0	0	9	9	0	0	0	0	0	9

**Table 4** Mean squares of antimicrobial activity of the extracted Ulvan in different media as affected by type of fraction, concentration, microbial species, and their interactions.

Source of variations	Degrees of freedom (df)	Mean squares
Replica	2	110.206
Microbial species (A)	2	434.410**
Error of A	4	3.095
Concentration (B)	5	1800.588**
Interaction between A and B	10	60.254**
Error of B	30	3.910**
Fraction (C)	5	484.943**
Interaction between A and C	10	80.610**
Interaction between B and C	25	40.761**
Interaction between A, B, and C	50	52.361**
Interaction between E and C	180	1.236

\*\* The value is highly significant at 0.01 probability level.

**Table 5** Means of antimicrobial activity of the extracted Ulvan in different media as affected by type of fraction, concentration, microbial species, and their interactions.

Microbial species	Conc.	Fractions						Microbial *Conc.	Microbial	Conc.
		F-I DW	F-I HCl	F-I EDTA	F-II DW	F-II HCl	F-II EDTA			
<i>Aeromonas hydrophila</i>	35	10	0	0	12	9	0	5.16 <sup>e</sup>		
	50	10	10	0	13	10	0	7.16 <sup>d</sup>		
	65	11	10	0	14	12	0	7.83 <sup>d</sup>		
	75	12	12	13	15	13	12	12.83 <sup>b</sup>		
	112	13	13	15	15	13	12	13.50 <sup>b</sup>		
	150	13	14	20	22 <sup>b</sup>	14	12	15.27 <sup>ab</sup>		
<i>Aeromonas</i> * fraction		11.50 <sup>b</sup>	9.83 <sup>c</sup>	8.0 <sup>ef</sup>	14.61 <sup>a</sup>	11.83 <sup>b</sup>	6.0 <sup>h</sup>		10.29 <sup>a</sup>	
<i>Vibrio fluvialis</i>	35	0	0	0	0	0	0	0 <sup>h</sup>		
	50	0	0	0	0	0	0	0 <sup>h</sup>		
	65	0	12	0	0	0	0	2.0 <sup>g</sup>		
	75	15	9	13	12	13	0	10.33 <sup>c</sup>		
	112	17	9	14	13	15	0	11.33 <sup>c</sup>		
	150	18	12	15	22 <sup>b</sup>	17	9	15.5		
<i>Vibrio</i> * fraction		8.33 <sup>e</sup>	7.0 <sup>g</sup>	7.0 <sup>g</sup>	7.83 <sup>f</sup>	7.50 <sup>fg</sup>	1.50 <sup>j</sup>		6.52 <sup>c</sup>	
<i>Vibrio damsela</i>	35	0	0	0	0	0	0	0 <sup>h</sup>		
	50	0	0	0	9	0	0	1.50 <sup>g</sup>		
	65	0	0	12	10	0	0	3.66 <sup>f</sup>		
	75	10	14	13	10	0	0	7.83 <sup>d</sup>		
	112	12	15	14	30 <sup>a</sup>	14	0	14.16 <sup>b</sup>		
	150	13	15	15	30 <sup>a</sup>	15	9	16.16 <sup>a</sup>		
<i>Vibrio</i> * fraction		5.83 <sup>h</sup>	7.33 <sup>g</sup>	9.0 <sup>d</sup>	14.83 <sup>a</sup>	4.83 <sup>i</sup>	1.50 <sup>j</sup>		7.22 <sup>b</sup>	
Con* fraction										
35		3.33 <sup>j</sup>	0 <sup>k</sup>	0 <sup>k</sup>	4.0 <sup>j</sup>	3.0 <sup>j</sup>	0 <sup>k</sup>			1.72 <sup>f</sup>
50		3.33 <sup>j</sup>	3.33 <sup>j</sup>	0 <sup>k</sup>	7.33 <sup>i</sup>	3.33 <sup>j</sup>	0 <sup>k</sup>			2.88 <sup>e</sup>
65		3.66 <sup>j</sup>	7.33 <sup>i</sup>	4.0 <sup>j</sup>	8.0 <sup>h</sup>	4.0 <sup>j</sup>	0 <sup>k</sup>			4.50 <sup>d</sup>
75		12.33 <sup>f</sup>	11.66 <sup>f</sup>	13.0 <sup>ef</sup>	12.33 <sup>f</sup>	8.66 <sup>h</sup>	4.0 <sup>j</sup>			10.33 <sup>c</sup>
112		14.0 <sup>e</sup>	12.33 <sup>f</sup>	14.33 <sup>de</sup>	19.33 <sup>b</sup>	14.0 <sup>e</sup>	4.0 <sup>j</sup>			13.0 <sup>b</sup>
150		14.66 <sup>de</sup>	13.66 <sup>e</sup>	16.66 <sup>c</sup>	23.55 <sup>a</sup>	15.33 <sup>d</sup>	10.0 <sup>g</sup>			15.64 <sup>a</sup>
Fraction		8.55 <sup>b</sup>	8.05 <sup>c</sup>	8.0 <sup>c</sup>	12.42 <sup>a</sup>	8.05 <sup>c</sup>	3.0 <sup>d</sup>			

**Note:** LSD<sub>0.05</sub>: between microbial spp. = 0.66; between fractions = 0.42; between concentrations = 0.77; between microbial spp. × fraction = 0.46; between microbial spp. × concentration = 1.34; between concentration × fraction = 1.03; between microbial spp. × fraction × concentration = 1.79

Means followed by the same letter (s) are statistically equal according to LSD<sub>0.05</sub> values.

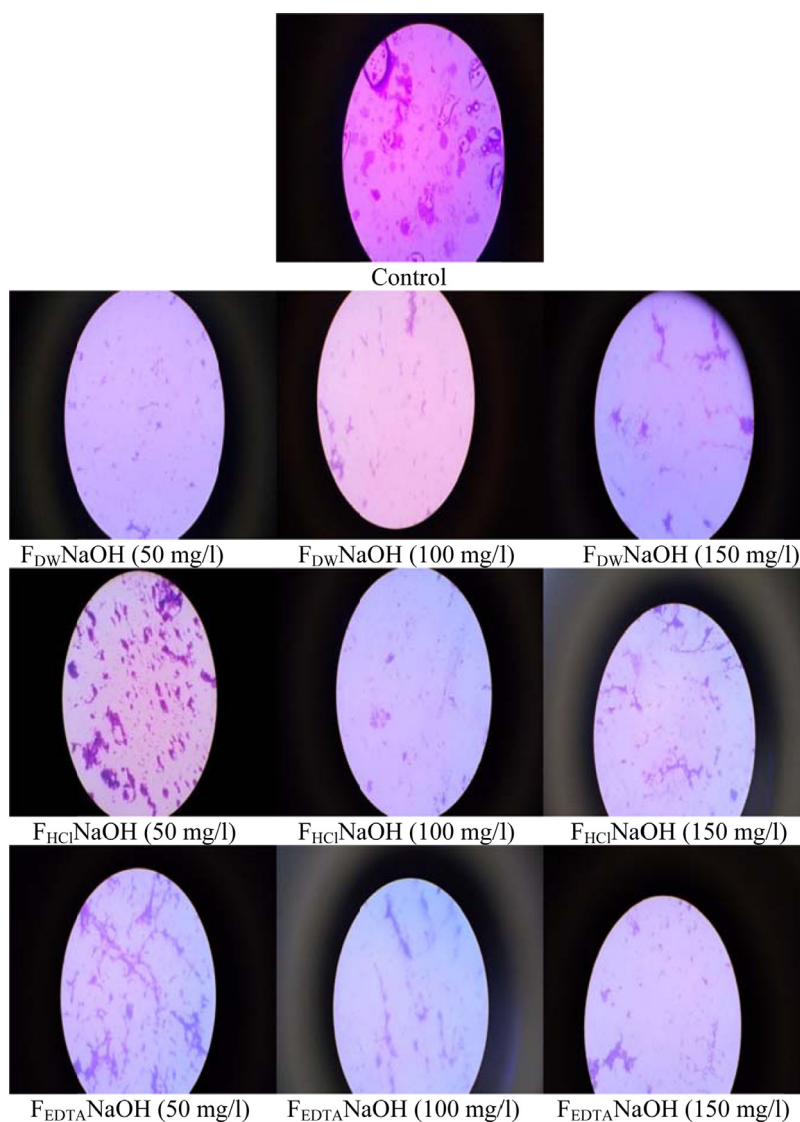


**Figure 5** Antifouling activity at different concentrations of polysaccharides for  $F_{Dw}NaOH$ ,  $F_{HCl}NaOH$ , and  $F_{EDTA}NaOH$  extracts using *Escherichia coli* as fouling microorganism.

the basis of the strong influence of environmental factors on different metabolites produced by algae (Selvin and Lip-ton, 2004). Species of *Vibrios* are pathogenic to human and marine organisms (micro flora, fish, shellfish, and penaeid shrimp). *Vibrios* also cause food borne diseases as well as the death of farmed fish species, leading to significant economic losses (Damsgard et al., 2004; FDA, 1992). Moreover, *A. hydrophila* is beta-haemolytic bacteria and produced cytotoxins (Scoglio et al., 2001).

### 3.5. Antifouling activity of polysaccharides

The results of polysaccharides as an antifouling agent showed that  $F_{Dw}NaOH$  in descending concentration order (150, 100, 50 mg/l) was the most effective fraction in inhibiting the formation of a bacterial film on the cover glass, which is the first step of the biofouling process compared with the control. On the other hand, the other two fractions ( $F_{HCl}NaOH$ , and  $F_{EDTA}NaOH$ ) showed negligible antifoul-

ing activity (Figure 5). Marine macroalgae could be an interesting antifouling agent, since they are an untapped source of bioactive compounds (Plouguerné et al., 2014), particularly polysaccharides (Arciola et al., 2003; Capo et al., 2009; Morra, 2005).

Gadenne et al. (2013) performed an adhesion assay by applying sulfated polysaccharides, ulvan against *Pseudomonas aeruginosa* which showed that immobilized polysaccharides on titanium surface strongly decreased by about 90% the adhesion of this microorganism. Furthermore, Gadenne et al. (2013) tested three pre-treated polysaccharides against *Staphylococcus aureus*. The better antifouling surface was that of a desulfated ulvan, showing that the absence of the sulfate group discouraged the bacterial adhesion. The current results agreed with these findings, since the  $F_{Dw}NaOH$  was the most effective fraction in inhibiting the formation of a bacterial film which confirmed the previous mentioned antimicrobial activity. In general, the molecular weight, charge density, degree of sulfate content, properties of structure and conformation affect the antimicro-

**Table 6** Antioxidant capacity and anti-inflammatory activity of different algal extracts from *Ulva fasciata*.

Fractions		Antioxidant capacity ( $\mu\text{M AAE/g}$ )	Anti-inflammatory activity (%)	
			25 mg/ml	50 mg/ml
F-I	Water	24.8	38.4	53.2
	HCl	63.3	71.4	86.3
	EDTA	34.4	66.3	*
F-II	Water	48.6	62.9	38.8
	HCl	27.5	85.4	88.5
	EDTA	26.5	94.0	91.4

bial activity of polysaccharides from seaweed (Silva et al., 2020).

### 3.6. Antioxidant activity of polysaccharides

The investigation of the antioxidant capacity of polysaccharide fractions showed that F-I<sub>HCl</sub> was the best one (63.3  $\mu\text{mole AAE/g}$ ), followed by F<sub>DW</sub>NaOH being 48.6  $\mu\text{mole AAE/g}$ , while F-I<sub>DW</sub> was the lowest one (24.8  $\mu\text{mole AAE/g}$ ) (Table 6). Previous studies have reported that the strong antioxidant activity of sulfated polysaccharides correlated to the degree substitution of sulfate groups along the polymeric backbone (Massironi et al., 2019). The antioxidant activity results agreed with those obtained by Huimin et al. (2005), who found that the high sulfate content of polysaccharides had a better antioxidant effect. F-I<sub>HCl</sub> and F<sub>DW</sub>NaOH showed the best results which had the highest sulfate contents (21.38 and 15.03% for F-I and F-II, respectively) (Table 1). The least antioxidant capacity was noticed in F-I<sub>DW</sub> with respect to F-I as it had the least sulfate content (14.92%) (Table 1). Several studies concluded that the antioxidant activity was directly proportional to the reduction potential of polysaccharides that depends on the molecular weight, the type of sugar, the glycoside bond, the degree of sulfation and site of acetylation (Del Olmo et al., 2018; Guedes et al., 2013; Kellogg and Lila, 2013; Kosanić et al., 2015; Raja et al., 2016; Wang et al., 2008).

### 3.7. Anti-inflammatory activity of polysaccharides

The anti-inflammatory activity of the polysaccharides fractions showed great variations. The increase in the anti-inflammatory activity with the higher concentration was the general trend. The F<sub>EDTA</sub>NaOH demonstrated the highest activity at both concentrations 25 and 50 mg/l being 94.0 and 91.40%, followed by F<sub>HCl</sub>NaOH being 85.4 and 88.5%, respectively (Table 6). Null activity was observed in F-I<sub>EDTA</sub> at 50 mg/ml. The concentration of standard anti-inflammatory agent diclofenac sodium at 100  $\mu\text{g/ml}$  was not effective, whereas anti-inflammatory activity at 250 and 500  $\mu\text{g/ml}$  were equivalent to 75.71% and 88.97%, respectively. Inflammation is caused by the release of chemicals from tissues and cells that migrate throughout the organism (Faradila et al., 2020). Polysaccharides from macroalgae possess anti-inflammatory properties as reported by De Jesus Raposo et al. (2014). F<sub>EDTA</sub>NaOH recorded the highest anti-inflammatory activities followed by F<sub>HCl</sub>NaOH. The

highest anti-inflammatory activity of F<sub>EDTA</sub>NaOH may be due to the high content of protein, total carbohydrates, galactose, and glucosamine (Table 1).

## 4. Conclusion

This study is considered as updated information in Egypt on the isolation of sulfate polysaccharides from green alga *U. fasciata*. The spectrum of <sup>1</sup>H NMR of (F-II) demonstrated the ring and methyl protons signals of polysaccharides. F<sub>HCl</sub>NaOH showed well-defined spectrum than those of other fractions due to the stretching bands of the sulfate ester (C-O-S) and sulfate groups (S=O) which indicates the presence of sulfated polysaccharides, typical for ulvan. In our study, sulfated polysaccharides consist mainly of rhamnose, sulfate groups, and uronic acid in F<sub>HCl</sub>NaOH. The microbial species *Vibrio damsela* was the most susceptible to F<sub>DW</sub>NaOH, followed by *Aeromonas hydrophila* and *Vibrio fluvialis* with inhibition zones of 30, 22, 22 mm at 150 mg/ml, respectively. In addition, F<sub>DW</sub>NaOH was the most effective fraction possessing antifouling activity. F-I<sub>HCl</sub> and F<sub>DW</sub>NaOH showed the best results for antioxidant activity which had the highest sulfate contents (21.38 and 15.03% for F-I and F-II, respectively). The F<sub>EDTA</sub>NaOH demonstrated the highest anti-inflammatory activity at both concentrations 25 and 50 mg/l being 94.0 and 91.40%, respectively.

## Acknowledgement

The authors are grateful to the Marine Environment Division and the National Institute of Oceanography and Fisheries for the support.

## References

- Abou El Azm, N., Fleita, D., Dalia, R.D., Mpingirika, E.Z., Amleh, A., Mayyada, El-S., MM, H., 2019. Production of bioactive compounds from the sulfated polysaccharides extracts of *Ulva lactuca*: post-extraction enzymatic hydrolysis followed by ion-exchange chromatographic fractionation. *Molecules* 24 (11), 2132. <https://doi.org/10.3390/molecules24112132>
- Aleem, A.A., 1993. The marine algae of Alexandria, Egypt. *Priv. Publ., Alexandria*, 139 pp.
- Alves, A., Sousa, R.A., Reis, R.L., 2013. A practical perspective on ulvan extracted from green algae. *J. Appl. Phycol.* 25, 407–424. <https://doi.org/10.1007/s10811-012-9875-4>



- Arciola, C.R., Bustanji, Y., Conti, M., Campoccia, D., Baldassarri, L., Samori, B., Montanaro, L., 2003. *Staphylococcus epidermidis* – fibronectin binding and its inhibition by heparin. *Biomaterials* 24, 3013–3019. [https://doi.org/10.1016/S0142-9612\(03\)00133-9](https://doi.org/10.1016/S0142-9612(03)00133-9)
- Boisvert, C., Beaulieu, L., Bonnet, C., Pelletier, É., 2015. Assessment of the antioxidant and antibacterial activities of three species of edible seaweeds. *J. Food Biochem.* 39, 377–387. <https://doi.org/10.1111/jfbc.12146>
- Capo, X., Pettit, M.E., Conlan, S.L., Wagner, W., Ho, A.D., Clare, A.S., Callow, J.A., Callow, M.E., Grunze, M., Rosenhahn, A., 2009. Resistance of polysaccharide coatings to proteins, hematopoietic cells, and marine organisms. *Biomacromolecules* 10, 907–916. <https://doi.org/10.1021/bm8014208>
- Costa, L.S., Fidelis, G.P., Cordeiro, S.L., Oliveira, R.M., Sabry, D.A., Câmara, R.B.G., Nobre, L.T.D.B., Costa, M.S.S.P., Almeida-Lima, J., Farias, E.H.C., Leite, E.L., Rocha, H.A.O., 2010. Biological activities of sulfated polysaccharides from tropical seaweeds. *Biomed. Pharmacother.* 64, 21–28.
- Courtois, J., 2009. Oligosaccharides from land plants and algae: production and applications in therapeutics and biotechnology. *Curr. Opin. Microbiol.* 12, 261–273. <https://doi.org/10.1016/j.mib.2009.04.007>
- Damsgard, B., Sorum, U., Ugelstad, I., Eliassen, R.A., Mortensen, A., 2004. Effects of feeding regime on susceptibility of Atlantic salmon (*Salmosalar*) to cold water vibriosis. *Aquaculture* 239, 37–46.
- De Jesus Raposo, M.F., de Morais, A.M.B., de Morais, R.M.S.C., 2015. Marine polysaccharides from algae with potential biomedical applications. *Mar. Drugs* 13, 2967–3028. <https://doi.org/10.3390/md13052967>
- De Jesus Raposo, M.F., de Morais, A.M.B., de Morais, R.M.S.C., 2014. Bioactivity and Applications of polysaccharides from marine microalgae. In: Merillon, J.-M., Ramawat, K.G. (Eds.), *Polysaccharides: Bioactivity and Biotechnology*. Springer, Cham. [https://doi.org/10.1007/978-3-319-03751-6\\_47-1](https://doi.org/10.1007/978-3-319-03751-6_47-1)
- Del Olmo, A., Picon, A., Nuñez, M., 2018. The microbiota of eight species of dehydrated edible seaweeds from North West Spain. *Food Microbiol.* 70, 224–231. <https://doi.org/10.1016/j.fm.2017.10.009>
- Dodgson, K.S., Price, R.C., 1962. A Note on the Determination of the Ester Sulfate Content of Sulfated Polysaccharides. *Biochem. J.* 84, 106–110. <https://doi.org/10.1042/bj0840106>
- Dubois, M., Gilles, K.A., Hamilton, J.K., Rebers, P.A., Smith, F., 1956. Colorimetric method for the determination of sugars and related substances. *Anal. Chem.* 18, 350–356. <https://doi.org/10.1021/ac60111a017>
- El-Baky, H.H.A., Baz, F.K.E., Baroty, G.S.E., 2009. Potential biological properties of sulphated polysaccharides extracted from the macroalgae *Ulva lactuca* L. *Acad. J. Cancer Res.* 2 (1), 1–11.
- El-Masry, H.A., Fahmy, H.H., Abdelwahed, A.S.H., 2000. Synthesis and antimicrobial activity of some new benzimidazole derivatives. *Molecules* 5 (12), 1429–1438. <https://doi.org/10.3390/51201429>
- Faradila, R.C.M., Gofarana, W., Hari, P.D., Nasrul, W., 2020. Ulvan, a polysaccharide from macroalgae *Ulva* sp.: a review of chemistry, biological activities and potential for food and biomedical applications. *Appl. Sci.* 10 (16), 5488. <https://doi.org/10.3390/app10165488>
- Faury, G., Molinari, J., Rusova, E., Mariko, B., Raveaud, S., Huber, P., Velebny, V., Robert, A.M., Robert, L., 2011. Receptors and aging: structural selectivity of the rhamnose-receptor on fibroblasts as shown by Ca<sup>2+</sup> – mobilization and gene-expression profiles. *Arch. Gerontol. Geriat.* 53, 106–112. <https://doi.org/10.1016/j.archger.2010.05.017>
- FDA, 1992. *Bacteriological Analytical Manual*, 7 edn., Food and Drug Administration (FDA), USA, 111–140.
- Gadanne, V., Lebrun, L., Jouenne, T., Thebault, P., 2013. Anti-adhesive activity of ulvan polysaccharides covalently immobilized onto titanium surface. *Colloids Surf. B* 112, 229–236. <https://doi.org/10.1016/j.colsurfb.2013.07.061>
- Glasson, C.R.K., Sims, I.M., Carnachan, S.M., de Nys, R., Magnusson, M., 2017. A cascading biorefinery process targeting sulfated polysaccharides (ulvan) from *Ulva ohnoi*. *Algal Res.* 27, 383–391. <https://doi.org/10.1016/j.algal.2017.07.001>
- Gomez, K.A., Gomez, A.A., 1984. *Statistical procedures for agricultural research*, 2nd. Edition John Wiley & Sons, New York, USA. ISBN: 978-0-471-87092-0
- Guedes, É.A.C., da Silva, T.G., Aguiar, J.S., de Barros, L.D., Pinotti, L.M., Sant’Ana, A.E.G., 2013. Cytotoxic activity of marine algae against cancerous cells. *Braz. J. Pharmacogn.* 23, 668–673. <https://doi.org/10.1590/S0102-695X2013005000060>
- Hernández-Garibay, E., Zertuche-González, J.A., Pacheco-Ruiz, I., 2010. Isolation and chemical characterization of algal polysaccharides from the green seaweed *Ulva clathrata* (Roth) C. Agardh. *J. Appl. Phycol.* 23, 537–542. <https://doi.org/10.1007/s10811-010-9629-0>
- Huimin, Q., Quanbin, Z., Tingting, Z., Rong, C.H., Hong, Z., Xizhen, N., Zhien, L., 2005. Antioxidant activity of different sulfate derivatives of polysaccharide extracted from *Ulva pertusa* (Chlorophyta) *in vitro*. *Int. J. Biol. Macromol.* 37 (4), 195–199. <https://doi.org/10.1016/j.ijbiomac.2005.10.008>
- Hussein, M.H., Hamouda, R.A., El-Naggar, N.El., Karim-Eldeen, M.A., 2015. Characterization, antioxidant, potentiality, and biological activities of the polysaccharide ulvan extracted from the marine macroalgae *Ulva* spp. *J. Agric. Chem. Biotechn. Mansoura Univ.* 6 (9), 373–392. <https://doi.org/10.21608/jacb.2015.48435>
- Jiao, G., Yu, G., Wang, W., Zhao, X., Zhang, J., Ewart, S.H., 2012. Properties of polysaccharides in several seaweeds from Atlantic Canada and their potential anti-influenza viral activities. *J. Ocean. Univ. China* 11 (2), 205–212. <https://doi.org/10.1007/s11802-012-1906-x>
- Kaeffer, B., Benard, C., Lahaye, M., Blottiere, H.M., Cherbut, C., 1999. Biological properties of ulvan, a new source of green seaweed sulfated polysaccharides, on cultured normal and cancerous colonic epithelial cells. *Planta Med.* 65, 527–531. <https://doi.org/10.1055/s-1999-14009>
- Kellogg, J., Lila, M.A., 2013. Chemical and *in vitro* assessment of Alaskan coastal vegetation antioxidant capacity. *J. Agric. Food Chem.* 61 (46), 11025–11032. <https://doi.org/10.1021/jf403697z>
- Kidgell, J.T., Magnusson, M., de Nys, R., Glasson, C.R.K., 2019. Ulvan: A systematic review of extraction, composition and function. *Algal Res.* 39, 101422. <https://doi.org/10.1016/j.algal.2019.101422>
- Kosanić, M., Ranković, B., Stanojković, T., 2015. Biological activities of two macroalgae from Adriatic coast of Montenegro. *Saudi J. Biol. Sci.* 22, 390–397. <https://doi.org/10.1016/j.sjbs.2014.11.004>
- Kumaran, S., Radhakrishnan, M., Balagurunathan, R., 2011. Biofouling inhibitory substances from marine actinomycetes isolated from Palk Strait, India. *Adv. Biotech.* 12, 22–26.
- Lahaye, M., 1998. NMR spectroscopic characterization of oligosaccharides from two *Ulva rigidula* samples (Ulvales, Chlorophyta) degraded by a lyase. *Carbohydr. Res.* 314, 1–12. [https://doi.org/10.1016/S0008-6215\(98\)00293-6](https://doi.org/10.1016/S0008-6215(98)00293-6)
- Lahaye, M., Alvarez-Cabal Cimadevilla, E., Kuhlenskamp, R., Quemener, B., Lognone, V., Dion, P., 1999. Chemical composition and <sup>13</sup>C NMR spectroscopic characterization of ulvans from *Ulva* (Ulvales, Chlorophyta). *J. Appl. Phycol.* 11, 1–7. <https://doi.org/10.1023/A:1008063600071>
- Lahaye, M., Brunel, M., Bonnin, E., 1997. Fine chemical structure analysis of oligosaccharides produced by an ulvan-lyase degradation of the water-soluble cell wall polysaccharides from *Ulva* sp. (Ulvales, Chlorophyta). *Carbohydr. Res.* 304, 325–333. [https://doi.org/10.1016/S0008-6215\(97\)00270-x](https://doi.org/10.1016/S0008-6215(97)00270-x)

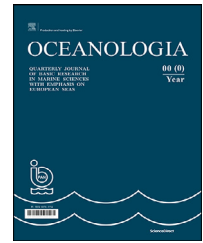
- Lahaye, M., Robic, A., 2007. Structure and functional properties of ulvan, a polysaccharide from green seaweeds. *Biomacromolecules* 8, 1765–1774.
- Leiro, J.M., Castro, R., Arranz, J.A., Lamas, J., 2007. Immunomodulating activities of acidic sulphated polysaccharides obtained from the seaweed *Ulva rigida* C. Agardh. *Int. Immunopharmacol.* 7, 879–888. <https://doi.org/10.1016/j.intimp.2007.02.007>
- Li, Q., Luo, J., Wang, C., Tai, W., Wang, H., Zhang, X., Liu, K., Jia, Y., Lv, X., Wang, L., He, H., 2018. Ulvan extracted from green seaweeds as new natural additives in diets for laying hens. *J. Appl. Phycol.* 30. <https://doi.org/10.1007/s10811-017-1365-2>
- Lowry, O.H., Rosebrough, N.J., Farr, A.L., Randall, R.J., 1951. Protein measurement with folin phenol reagent. *J. Biol. Chem.* 193, 265–275. [https://doi.org/10.1016/S0021-9258\(19\)52451-6](https://doi.org/10.1016/S0021-9258(19)52451-6)
- Massironi, A., Morelli, A., Grassi, L., Puppi, D., Braccini, S., Maisetta, G., Esin, S., Batoni, G., Della Pina, C., Chiellini, F., 2019. Ulvan as novel reducing and stabilizing agent from renewable algal biomass: application to green synthesis of silver nanoparticles. *Carbohydr. Polym.* 203, 310–321. <https://doi.org/10.1016/j.carbpol.2018.09.066>
- Matloub, A.A., El-Sherbini, M., Borai, I.H., Ezz, M.K., Rizk, M.Z., Aly, H.F., Fouad, G.I., 2013. Assessment of anti-hyperlipidemic effect and physico-chemical characterization of water soluble polysaccharides from *Ulva fasciata* Delile. *J. Appl. Sci. Res.* 9 (4), 2983–2999.
- Mizushima, Y., Kobayashi, M., 1968. Interaction of anti-inflammatory drugs with serum proteins, especially with some biologically active proteins. *J. Pharm. Pharmacol.* 20 (3), 169–173. <https://doi.org/10.1111/j.2042-7158.1968.tb09718.x>
- Monsur, H.A., Jaswir, J., Simsek, S., Amid, A., Alam, Z., 2017. Chemical structure of sulfated polysaccharides from brown seaweed (*Turbinariaturbinata*). *Int. J. Food Prop.* 20 (7), 1457–1469.
- Morra, M., 2005. Engineering of biomaterials surfaces by hyaluronan. *Biomacromolecules* 6, 1205–1223. <https://doi.org/10.1021/bm049346i>
- Mtolera, M.S.P., Semesi, A.K., 1996. Antimicrobial activity of extracts from six green algae from Tanzania. *Curr. Trends Mar. Bot. Res. East Afr. Regul.* 211–217. <http://hdl.handle.net/1834/469>
- Murata, M., Nakazoe, J.I., 2001. Production and Use of Marine Algae in Japan. *JARQ-Jpn. Agr. Res. Q.* 35 (4), 281–290.
- Paradossi, G., Cavalieri, F., Pizzoferrato, L., Liguori, A.M., 1999. A physico-chemical study on the polysaccharide ulvan from hot water extraction of the macroalga *Ulva*. *Int. J. Biol. Macromol.* 25, 309–315. [https://doi.org/10.1016/s0141-8130\(99\)00049-5](https://doi.org/10.1016/s0141-8130(99)00049-5)
- Paulert, R., Junior, A.S., Stadnik, M.J., Pizzolatti, M.G., 2007. Antimicrobial properties of extracts from the green seaweed *Ulva fasciata* Delile against pathogenic bacteria and fungi. *J. Algol. Stud.* 123, 123–130. <https://doi.org/10.1127/1864-1318/2007/0123-0123>
- Pengzhan, Y., Quanbin, Z., Ning, L., Zuhong, X., Yanmei, W., Zhi, L., 2003. Polysaccharides from *Ulva pertusa* (Chlorophyta) and preliminary studies on their antihyperlipidemia activity. *J. Appl. Phycol.* 15, 21–27. <https://doi.org/10.1023/A:1022997622334>
- Plouguerné, E., da Gama, B.A.P., Pereira, R.C., Barreto-Bergter, E., 2014. Glycolipids from seaweeds and their potential biotechnological applications. *Front. Cell. Infect. Microbiol.* 4, 1–5. <https://doi.org/10.3389/fcimb.2014.00174>
- Prieto, P., Pineda, M., Miguel Aguilar, M., 1999. Spectrophotometric quantitation of antioxidant capacity through the formation of a phosphomolybdenum complex: specific application to the determination of vitamin E. *J. Anal. Biochem.* 269 (2), 337–341. <https://doi.org/10.1006/abio.1999.4019>
- Raja, R., Hemaiswarya, S., Arunkumar, K., Carvalho, I.S., 2016. Antioxidant activity and lipid profile of three seaweeds of Faro, Portugal. *A Review, Bras. Bot.* 39, 9–17. <https://doi.org/10.1007/s40415-015-0200-8>
- Rashidi, B., Trindade, L.M., 2018. Detailed biochemical and morphologic characteristics of the green microalga *Neochloris oleoabundans* cell wall. *Algal Res.* 35, 152–159. <https://doi.org/10.1016/j.algal.2018.08.033>
- Ray, B., Lahaye, M., 1995. Cell-wall polysaccharides from the marine green alga *Ulva* “rigida” (Ulvales, Chlorophyta). Chemical structure of ulvan, *Carbohydr. Res.* 274, 313–318. [https://doi.org/10.1016/0008-6215\(95\)00059-3](https://doi.org/10.1016/0008-6215(95)00059-3)
- Robic, A., Bertrand, D., Sassi, J.F., Lerat, Y., Lahaye, M., 2009a. Determination of the chemical composition of ulvan, a cell wall polysaccharide from *Ulva* spp. (Ulvales, Chlorophyta) by FT-IR and chemometrics. *J. Appl. Phycol.* 21, 451–456. <https://doi.org/10.1007/s10811-008-9390-9>
- Robic, A., Gaillard, C., Sassi, J.F., Lerat, Y., Lahaye, M., 2009b. Ultrastructure of ulvan: a polysaccharides from green seaweed. *Biopolymers* 91, 652–664. <https://doi.org/10.1002/bip.21195>
- Robic, A., Sassi, J.F., Lahaye, M., 2008. Impact of stabilization treatments of the green seaweed *Ulva rotundata* (Chlorophyta) on the extraction yield, the physico-chemical and rheological properties of ulvan. *Carbohydr. Polym.* 74, 344–352. <https://doi.org/10.1016/j.carbpol.2008.02.020>
- Sakat, S., Juvekar, A.R., Gambhire, M.N., 2010. In vitro antioxidant and anti-inflammatory activity of methanol extract of *Oxalis corniculata* Linn. *Inter. J. Pharm. Pharm. Sci.* 2 (1), 146–155.
- SAS, 2007. SAS Technical Report SAS/STAT software: Changes and Enhancements. Users’ Guide. Vol. 2, version 9.1.3, 4th edn., SAS Institute, Inc., Cary, NC. <http://support.sas.com/thirdpartylicenses>
- Scoglio, M.E., Di Pietro, A., Picerno, I., Delia, S., Mauro, A., Laganà, P., 2001. Virulence factors in *Vibrios* and *Aeromonads* isolated from seafood. *New Microbiolgy* 24 (3), 273–280.
- Selvin, J., Lipton, A.P., 2004. Biopotentials of *Ulva fasciata* and *Hypnea musciformis* collected from the peninsular coast of India. *J. Mar. Sci. Technol.* 12, 1–6. <https://www.researchgate.net/publication/228766271>
- Silva, A., Silva, S.A., Carpena, M., Garcia-Oliveira, P., Gullón, P., FátimaBarroso, M., Prieto, M.A., Simal-Gandara, J., 2020. Macroalgae as a source of valuable antimicrobial compounds: extraction and applications. *Antibiotics* 9, 642. <https://doi.org/10.3390/antibiotics9100642>
- Smit, A.J., 2004. Medicinal and pharmaceutical uses of seaweed natural products: a review. *J. Appl. Phycol.* 16, 245–262. <https://doi.org/10.1023/B:JAPH.0000047783.36600.ef>
- Tabarsa, M., You, S.G., Dabaghian, E.H., Surayot, U., 2018. Water-soluble polysaccharides from *Ulva intestinalis*, Molecular properties, structural elucidation and immunomodulatory activities. *J. Food Drug Anal.* 26, 599–608. <https://doi.org/10.1016/j.jfda.2017.07.016>
- Tako, M., Tamanaha, M., Tamashiro, Y., Uechi, S., 2015. Structure of Ulvan isolated from the edible green seaweed, *Ulva pertusa*. *Adv. Biosci. Biotechnol.* 6 (10), 645–655. <https://doi.org/10.4236/abb.2015.610068>
- Wahlström, N., Nylander, F., Malmhäll-Bah, E., Sjövoid, K., Edlund, U., Westman, G., Albers, E., 2020. Composition and structure of cell wall ulvans recovered from *Ulva* spp. along the Swedish west coast. *Carbohydr. Polym.* 233, 115852. <https://doi.org/10.1016/j.carbpol.2020.115852>
- Wang, J., Zhang, Q., Zhang, Z., Li, Z., 2008. Antioxidant activity of sulfated polysaccharide fractions extracted from *Laminaria japonica*. *Int. J. Biol. Macromol.* 42 (2), 127–132. <https://doi.org/10.1016/j.ijbiomac.2007.10.003>
- Wijesekara, I., Pangestuti, R., Kim, S.K., 2011. Biological activities and potential health benefits of sulfated polysaccharides derived from marine algae. *Carbohydr. Polym.* 84 (1), 14–21. <https://doi.org/10.1016/j.carbpol.2010.10.062>

Yaich, H., Amira, A.B., Abbas, F., Bouaziz, M., Besbes, S., Richel, A., Blecker, C., Attia, H., Garna, H., 2017. Effect of extraction procedures on structural, thermal and antioxidant

properties of ulvan from *Ulva lactuca* collected in Monastir coast. *Int. J. Biol. Macromol.* 105 (2), 1430–1439. <https://doi.org/10.1016/j.ijbiomac.2017.07.141>

Available online at [www.sciencedirect.com](http://www.sciencedirect.com)

ScienceDirect

journal homepage: [www.journals.elsevier.com/oceanologia](http://www.journals.elsevier.com/oceanologia)

## ORIGINAL RESEARCH ARTICLE

# Response of the Bay of Bengal to super cyclone Amphan examined using synergistic satellite and in-situ observations

Neethu Chacko\*, Chiranjivi Jayaram

Regional Remote Sensing Centre – East National Remote Sensing Centre, ISRO, Kolkata, India

Received 9 February 2021; accepted 30 September 2021

Available online 14 October 2021

**KEYWORDS**

Amphan;  
Tropical cyclone;  
Bay of Bengal;  
Sea Surface  
Temperature;  
Salinity;  
Upper ocean  
response;  
Mixed layer budget

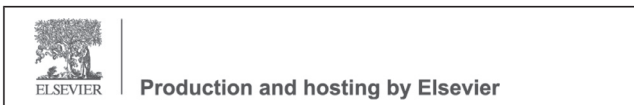
**Abstract** Tropical cyclone Amphan is the first super cyclone that happened in the north Indian Ocean in the last 20 years. In this work, multi-platform datasets were used to investigate the responses of the upper ocean to cyclone Amphan. The most striking response was the cold wake left by the cyclone spanning the entire Bay of Bengal with an amplitude up to  $\sim 4^{\circ}\text{C}$ . Satellite salinity observations revealed that the maximum increase in surface salinity was  $\sim 1.5$  PSU on the right side of the track of Amphan. Surface circulation was also observed to be modulated with the passage of a cyclone with a rightward bias in the change in its speed and direction. The currents observed from a moored buoy showed strong inertial oscillations. Argo observations showed that changes induced by the cyclone occurred up to 150 m depth of the cyclone and ocean heat content in the upper 150 m depth decreased due to the passage of the cyclone. There was an enhancement of surface chlorophyll concentration ( $\sim 1.5$  mg/m<sup>3</sup>) after the passage of the cyclone, which was centred along the track of the cyclone where the winds were the highest. Mixed layer heat and salinity budget analysis showed that the sea surface cooling and increase in salinity was primarily driven by vertical mixing processes, though horizontal advection contributed meagrely. This study also brings forward the fact that regional differences exist in the responses of the ocean to the forcing of cyclones.

© 2021 Institute of Oceanology of the Polish Academy of Sciences. Production and hosting by Elsevier B.V. This is an open access article under the CC BY-NC-ND license (<http://creativecommons.org/licenses/by-nc-nd/4.0/>).

\* Corresponding author at: Regional Remote Sensing Centre – East National Remote Sensing Centre, ISRO, BG2, Action Area 1B, Kolkata, India.

E-mail address: [neethuchacko@gmail.com](mailto:neethuchacko@gmail.com) (N. Chacko).

Peer review under the responsibility of the Institute of Oceanology of the Polish Academy of Sciences.



<https://doi.org/10.1016/j.oceano.2021.09.006>

0078-3234/© 2021 Institute of Oceanology of the Polish Academy of Sciences. Production and hosting by Elsevier B.V. This is an open access article under the CC BY-NC-ND license (<http://creativecommons.org/licenses/by-nc-nd/4.0/>).

## 1. Introduction

Tropical cyclones are among the most devastating natural disasters that pose a significant threat to the property and lives of coastal regions around the world. The Bay of Bengal (BoB) experiences a greater number of cyclones annually compared to the Arabian Sea (Singh et al., 2000; Singh and Koll, 2020). BoB is prone to cyclones during pre-monsoon (March, April and May) and post-monsoon (October and November) seasons. A recent addition was the tropical cyclone Amphan, which happened in May 2020. Amphan was the first super-cyclone in the north Indian Ocean that happened after the super cyclone which occurred in the year 1999.

During the passage of a cyclone, the strong wind stress imposed by the cyclone produces various responses in the upper ocean. Cyclones induce intense mixing of ocean waters that results in entrainment and upwelling (Price, 1981). The upper ocean responds to strong cyclone forcing in many ways depending upon the strength, translation speed and the oceanic preconditions. The implications of these responses could be manifested in various physical and biological parameters such as sea surface temperature, salinity, chlorophyll concentration, and ocean currents. The most striking aspect of the oceanic response to cyclones is the modulation of the sea surface temperature (Cione and Uhlhorn, 2003; D'Asaro et al., 2007; Dare and McBride, 2011; Price et al., 1994; Schade and Emanuel, 1999) and upper ocean temperature structure (Maneesha et al., 2012). Stronger winds of the cyclones produce intense oceanic entrainment and upwelling, thereby deepening the mixed layer.

Sea surface salinity also undergoes variations under cyclones, which are also dependant on the underlying oceanic conditions (Lin et al., 2003; Sun et al., 2010; Sing and Koll, 2020). In addition to the cyclone induced vertical mixing of the near surface waters, precipitation due to cyclones also will have a profound impact on the ocean salinity. Cyclones also influence upper ocean biological processes, which result in phytoplankton blooms in the wake of the cyclone (Babin et al., 2004; Chacko, 2017; Chacko 2019; Chen et al., 2003; Jayaram et al., 2019; Walker et al., 2005). The strong cyclonic winds induce Ekman transport and subsequently initiate strong upwelling which brings cold nutrient-rich water towards the surface (Subrahmanyam et al., 2002). The interaction between the cyclone and the ocean is very complex and the response of the ocean is manifested in each parameter differently. For example, sea surface temperature cooling after a cyclone could vary from 1–9 degrees (Black and Dickey, 2008; Lin et al., 2003; Shang et al., 2001; Sun et al., 2010; Song et al., 2020). The changes induced by each cyclone are different and it is worthwhile to study the interactions and responses of the ocean to cyclones. It is also important to understand the variations of oceanic parameters and the environment itself with the cyclone locally.

Each tropical cyclone is unique in its genesis and the subsequent impact it leaves on the ocean that is also equally singular in nature. Ocean observations enable a detailed examination of the air-sea interaction processes associated with a cyclone. A synergistic utilization of satellite as well as in-situ data sets is thus imperative in understanding the

changes induced by cyclones. In this study, satellite and in-situ observations were used to characterize the upper ocean response to super cyclone Amphan. The present study investigates the impact of super cyclone Amphan on the comprehensive response of the BoB in terms of sea surface winds, surface and subsurface variability of the temperature, salinity, currents, mixed layer depth, the heat and salt budgets, and chlorophyll concentration. We focus on the detailed processes and underlying dynamics for the rapid upper ocean response due to Amphan.

## 2. Material and methods

The six hourly cyclone track data and wind speeds used in this study were obtained from Regional Specialized Meteorological Centre (RSMC), India Meteorological Department (<http://www.rsmcnewdelhi.imd.gov.in>). To provide a basin-scale view of the upper ocean response to Amphan, we have analyzed gridded satellite data products. Daily Advanced Microwave Scanning Radiometer (AMSR-2) sea surface temperature and rainfall data used in this study were obtained from <http://apdrc.soest.hawaii.edu/index.php>. The product has a spatial resolution of 25 km x 25 km. Sea surface height anomalies (SSHA) are used to observe the signatures of mesoscale eddies. Daily SSHA data from Archiving, Validation, and Interpretation of Satellite Oceanographic (AVISO) data with a spatial resolution of 25 km x 25 km were used. The altimeter products were produced and distributed by AVISO (<http://www.aviso.altimetry.fr/en/data/products/sea-surface-heightproducts/global/msla-h.html>), as part of the Ssalto ground processing segment. Observations from a few in-situ platforms were analyzed to provide insights into the upper-ocean response to Amphan. The temperature and salinity observations from an Argo float (WMO ID: 2902230) located at the central Bay of Bengal were assessed. The Argo float was sampled at an interval of 5 days. The daily surface meteorological and oceanographic observations from a RAMA buoy (McPhaden et al., 2009) located at 90°E, 15°N were also used in this study. Observations from a moored buoy BD8 located at 89°E longitude and 18°N latitude was used in this study to characterize the variability of surface and subsurface temperature, salinity and currents. The moored buoy measures various parameters at 3 hourly intervals at various depths. The daily Soil Moisture Active Passive (SMAP) level 3, sea surface salinity data with a resolution of 0.33° x 0.33° were used to explore Amphan induced surface salinity variations. The daily wind data from Scatsat-1 with a spatial resolution of 0.25 degrees (Mandal et al., 2018) was used to assess the wind speeds during Amphan. The Visible Infrared Imaging Radiometer Suite (VIIRS) chlorophyll-*a* concentration at 4 km x 4 km at 8-day temporal scale was used in this study. VIIRS is one of the key instruments onboard the Suomi National Polar-Orbiting Partnership (Suomi NPP) spacecraft. The daily NCEP Climate Forecast System Version 2 (CFSV2) flux data products from Asia-Pacific Data Research Centre (APDRC) with a spatial resolution of 0.25 degrees were used in this study for the evaluation of mixed layer heat budget.

Mixed layer depth is defined as the depth at which the density increases by the amount which is equivalent to the decrease in temperature by 0.8°C from the surface

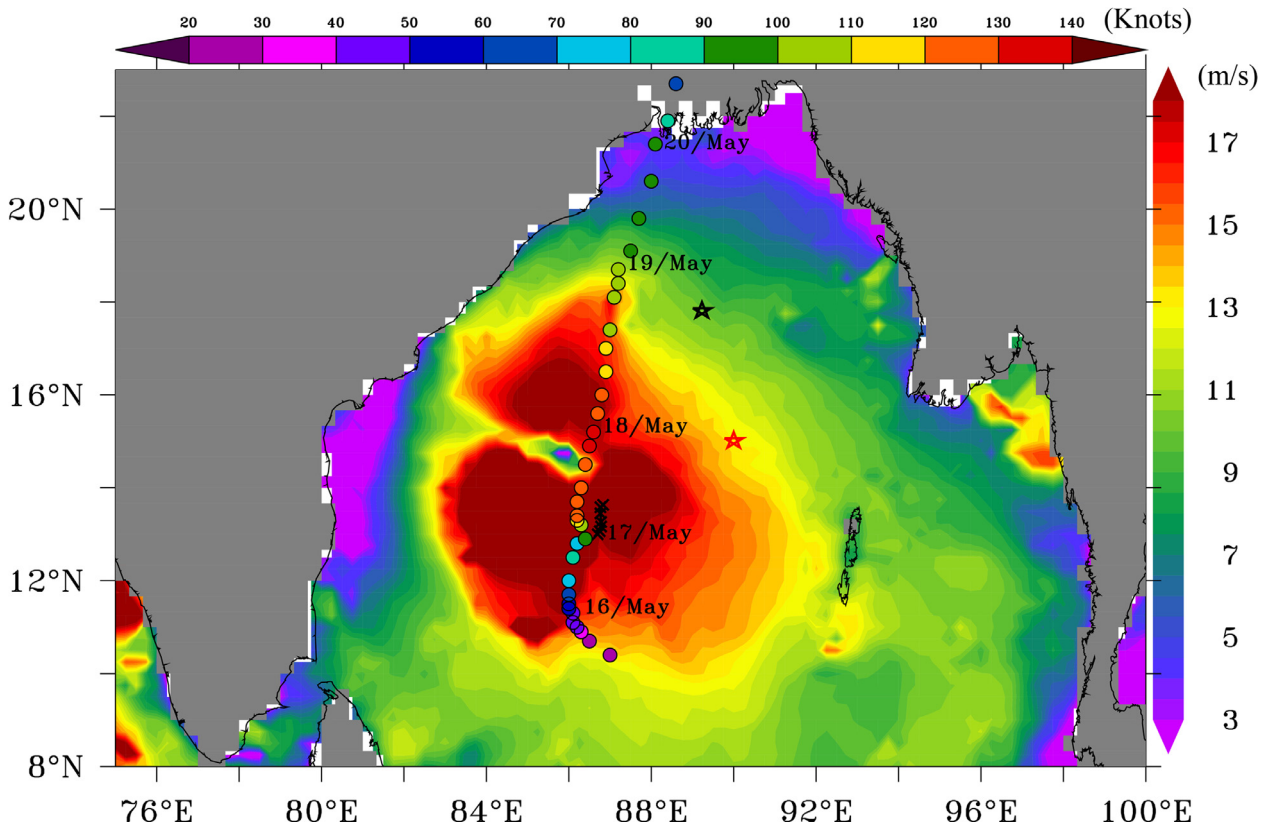


**Figure 1** The study area and the track of cyclone Amphan overlaid over the wind distribution (m/s) on 18 May 2020 on which cyclone Amphan experienced the peak intensity. The location of the cyclone on each day at 21:00 UTC is indicated by the corresponding dates. The colours on the cyclone track indicate the maximum surface wind speed of the cyclone (knots). The black and red stars denote the locations of the moored buoy BD8 and Rama mooring respectively. The black cross signs denote the position of the Argo float (2902230) during May 2020.

(Kara et al., 2000). The Ekman pumping velocity (WE) is calculated as

$$WE = \frac{1}{\rho f} \text{Curl}(\tau) \quad (1)$$

where  $\rho$  is the density of the sea water set to  $1025 \text{ kg/m}^3$ ,  $\tau$  is the wind stress,  $f$  is the Coriolis parameter. The vertically integrated ocean heat content (OHC) is computed with the equation,

$$\text{OHC} = \rho C_p \int T dz \quad (2)$$

where  $\rho$  and  $C_p$  are the density and heat capacity of sea water for which the values used in this study are  $1025 \text{ kg/m}^3$  and  $4000 \text{ J/kg/K}$  respectively and  $z$  is the water depth. In order to examine the response to Amphan, 7 days before the Amphan (9–15 May) was considered as the pre-cyclone period and 7 days after Amphan (21–27 May) was considered as the post-cyclone period. The difference between these two periods was chosen to evaluate the response of the parameters considered.

To examine the relative roles of the various processes that contributed to the changes in mixed layer temperature and salinity, mixed layer heat and salinity budgets were evaluated following Rao and Sivakumar (2000) and

Chacko et al. (2012) using the following set of equations:

$$\frac{\partial T}{\partial t} = \frac{Q_{net} - Q_{pen}}{h\rho C_p} - \left[ u \frac{\partial T}{\partial x} + v \frac{\partial T}{\partial y} \right] - H \left[ w_h + \frac{dh}{dt} \right] \times \frac{(T - T_h)}{h} \quad (3)$$

The terms in the equations represent from left to right, the mixed layer temperature tendency, surface net heat flux term, horizontal advection term and vertical processes term.

$$\frac{\partial S}{\partial t} = \frac{(E - P)S}{h} - \left[ u \frac{\partial S}{\partial x} + v \frac{\partial S}{\partial y} \right] - H \left[ w_h + \frac{dh}{dt} \right] \times \frac{(S - S_h)}{h} \quad (4)$$

The terms in the mixed layer salinity budget equation represent from left to right, the mixed layer salinity tendency, Evaporation minus Precipitation (E-P) term, the horizontal advection term, and the vertical processes term. The vertical processes are due to a combination of entrainment at the base of the mixed layer and upwelling. In Eqs. (3) and (4),  $\rho$  is the density of seawater,  $C_p$  is the specific capacity of sea water ( $4000 \text{ J/K/kg}$ );  $T$  and  $T_h$  are mixed layer temperature and temperature at a depth 5 m below the mixed layer ( $h$ );  $S$  and  $S_h$  are mixed layer salinity and salinity at a depth 5 m below the mixed layer ( $h$ );  $u$  and  $v$  are the

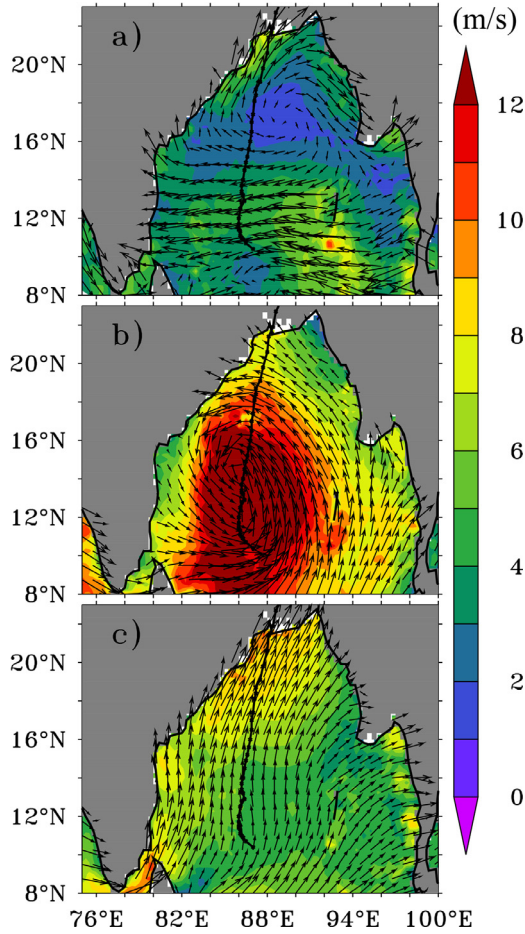


**Figure 2** Daily sea surface wind speeds from Scatsat-1 a) before (10–15, May 2020), b) during (16–20, May 2020) and c) the difference for (b) minus (a) of cyclone Amphan. The colour contours show the wind speeds, and the arrows show the direction of the winds at that location.

zonal and meridional currents;  $w_h$  is the vertical velocity at the thermocline below the mixed layer;  $\frac{dh}{dt}$  is the variability of the mixed layer depth. Here  $H$  is a scale factor which is taken as 1 if  $[w_h + \frac{dh}{dt}]$  is positive and 0 if  $[w_h + \frac{dh}{dt}]$  is negative. The net heat flux at the surface ( $Q_{net}$ ) is given by  $Q_{swf} - Q_{lwf} - Q_{sen} - Q_{lat}$ , where,  $Q_{swf}$  is shortwave flux,  $Q_{lwf}$  is longwave radiation,  $Q_{sen}$  is sensible heat flux, and  $Q_{lat}$  is latent heat flux. Penetrative solar radiation  $Q_{pen}$  is the solar radiation at the base of the mixed layer and it is estimated as  $Q_{pen} = Q_{swf}(1-R) e(-h/\zeta)$ , where  $R = 0.58$ , the radiation lost by getting absorbed in the upper layers (Paulson and Simpson, 1977),  $h$  the mixed layer depth, and  $\zeta$  the attenuation depth. For computing horizontal advection, sea surface temperature and sea surface salinity gradients are calculated using AMSR-2 sea surface temperature and SMAP sea surface salinity as centered differences over a distance of  $0.25^\circ$  from the moored buoy BD8 location.

### 3. Results

#### 3.1. Tropical cyclone Amphan

Tropical cyclone Amphan originated from a low-pressure region over east of Sri Lanka in the southeast BoB on 16 May

2020. It moved north-eastward and intensified into a cyclonic storm on 16 May. Afterwards, it moved northwards and further intensified into a severe cyclonic storm on 17 May. It underwent rapid intensification within a few hours and became a super cyclone on 18 May. It maintained the intensity of the super cyclone over west central BoB before weakening into an extremely severe cyclonic storm on 19 May. Amphan made landfall across the Sunderbans and crossed West-Bengal and Bangladesh coasts on 20 May with maximum sustained wind speeds of 155–165 kmph. Figure 1 shows the study area as well as track of the super cyclone along with wind speeds over the BoB. The locations of the Argo float, moored buoy (BD8) and the RAMA buoy during cyclone Amphan are also shown in the figure.

The surface wind fields that were prevalent before and during Amphan are shown in Figure 2. The background wind speeds before the cyclone (Figure 2a) were predominantly easterly in the central BoB. In the northern BoB (north of  $15^\circ N$  latitudes), the wind speeds were slightly weaker (1–4 m/s) than in the southern BoB. Figure 2b shows the wind speeds during cyclone Amphan wherein, the wind speeds were significantly higher, reaching  $> 12$  m/s all along the west-central BoB. The magnitude of wind speed was stronger on the right side of the track of the cyclone. The anticlockwise circulation of the cyclonic wind fields was clearly visible in the figure. Post-cyclone, the wind fields were observed to be reduced to  $< 8$  m/s in the entire BoB and the direction of the wind vectors were aligned south westerly in accordance with the prevailing monsoonal wind systems during that period.

#### 3.2. Upper ocean response to Amphan

The temporal evolution of major atmospheric and oceanic surface variables obtained from the RAMA buoy are shown in Figure 3. The sea level pressure before the cyclone was around 1009 hPa accompanied by moderate winds of 2 to 4 m/s (Figure 3a,b). Before the cyclone, there was no rainfall event (Figure 3e) and the air temperature was in the range  $30$  to  $30.5^\circ C$  (Figure 3c). The sea surface temperature was greater than  $31^\circ C$  and the sea surface salinity was  $\sim 33$  PSU (Figure 3d,f). The effect of the super cyclone could be clearly inferred from the observations of the buoy during 16–20 May. During the passage of Amphan, the sea level pressure rapidly dropped to 994 hPa on 18 May. The surface winds before Amphan were  $\sim 4$  m/s which is consistent with the satellite observations in (Figure 2) that increased significantly to 15 m/s (Figure 3b). In response to the cyclone, the air temperature dropped from  $30^\circ C$  to a minimum of  $27^\circ C$ , sea surface temperature decreased from the pre-cyclone value of  $31.5^\circ C$  to  $29^\circ C$ , and the sea surface salinity increased from 33.17 PSU (15 May) to 33.34 PSU (21 May). The sea surface cooling was essentially very high  $\sim 2^\circ C$  compared to the pre-Amphan values.

#### 3.3. Sea Surface Temperature

To explore the spatial and temporal features of the surface ocean response to Amphan, multiple satellite observations were employed. First, we assessed the response of sea surface temperature using satellite observations. Figure 4 il-

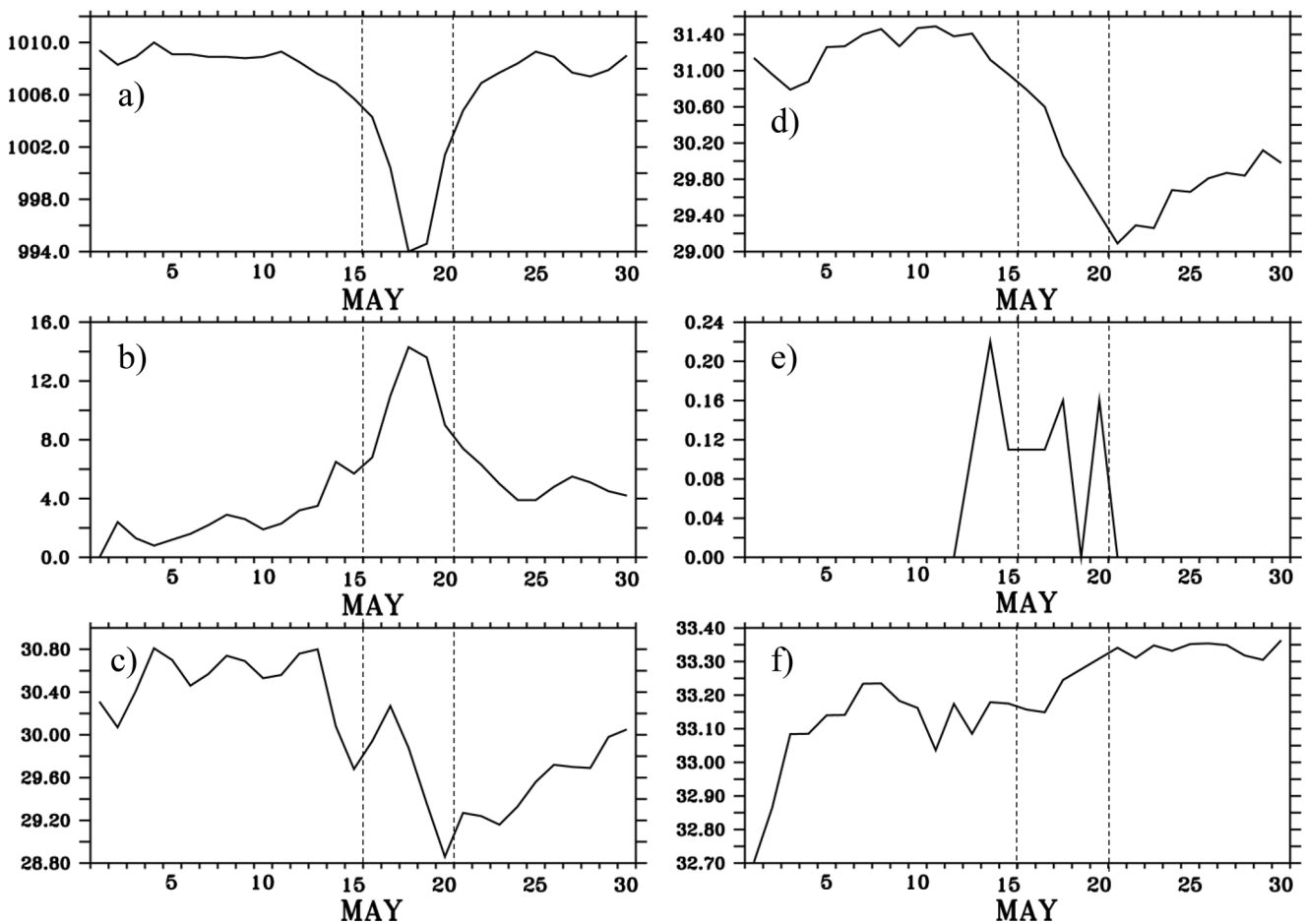


**Figure 3** Meteorological and oceanographic parameters observed from a RAMA buoy located at 90°E longitude, 12°N latitude from 01–31 May 2020. a) Sea level pressure (hPa), b) surface wind speed (m), c) air temperature (°C), d) Sea surface temperature (°C), e) rainfall (mm/hr) and f) sea surface salinity (PSU). The period of activity of Amphan was 16–20 May 2020 which is indicated by vertical lines on each plot.

illustrates the sea surface temperature response due to Amphan in the BoB that was evident from AMSR-2 data. Before the arrival of Amphan, the entire BoB was capped by warm surface waters, with sea surface temperatures greater than 31°C (Figure 4a). It was observed that Amphan originated in the southern BoB, over warmer waters. The passage of Amphan cooled the ocean surface substantially (Figure 4b) compared to the pre-Amphan sea surface temperature with distinct magnitudes across the basin. The difference between the post-cyclone and pre-cyclone sea surface temperature clearly depicted the extent of the cold wake left by Amphan (Figure 4c). There were many studies which reported on the strong sea surface cooling by cyclones (Navaneeth et al., 2019; Qiu et al., 2019), but a cold wake extending over the entire BoB is a rarity. A strong sea surface temperature cooling spread over a large area with a slight rightward bias to the track of Amphan could be seen in Figure 4c. The rightward bias shown in the sea surface temperature cooling was consistent with the previous studies (Black and Dickey, 2008; Chu et al., 2000; Yue et al., 2018). It was mainly due to the fact that the cyclone induced wind stress vector turns clockwise on the right side of the cyclone track and resonate with the mixed layer cur-

rent (Cheung, et al., 2013; Price, 1981). Though cooling was spread over the entire BoB, strong decrease in the sea surface temperature (~4°C) was observed along the central BoB, where the cyclone exhibited its strongest wind speeds during its lifetime (see Figure 1).

### 3.4. Sea Surface Salinity

The sea surface salinity maps before and after Amphan are shown in Figure 5a and b. Before cyclone (Figure 5a), there was an east-west salinity gradient in the BoB with higher salinity (>33.5 PSU) in the western Bay and lower salinity (Value) in the eastern BoB. The northern BoB showed very low salinity values (< 30 psu) owing to the high freshwater influx into the region from the rivers. After Amphan, the sea surface salinity was observed to have increased (1 PSU) (Figure 5b). Figure 5c illustrates the Amphan induced salinity changes and it could be observed that sea surface salinity in the regions right of the track of the cyclone had increased compared to the left side of the track. The maximum salinity increase was ~1.5 PSU to the right side of the Amphan track along the central Bay. This is consistent with the observation of Chacko (2018) which reported that



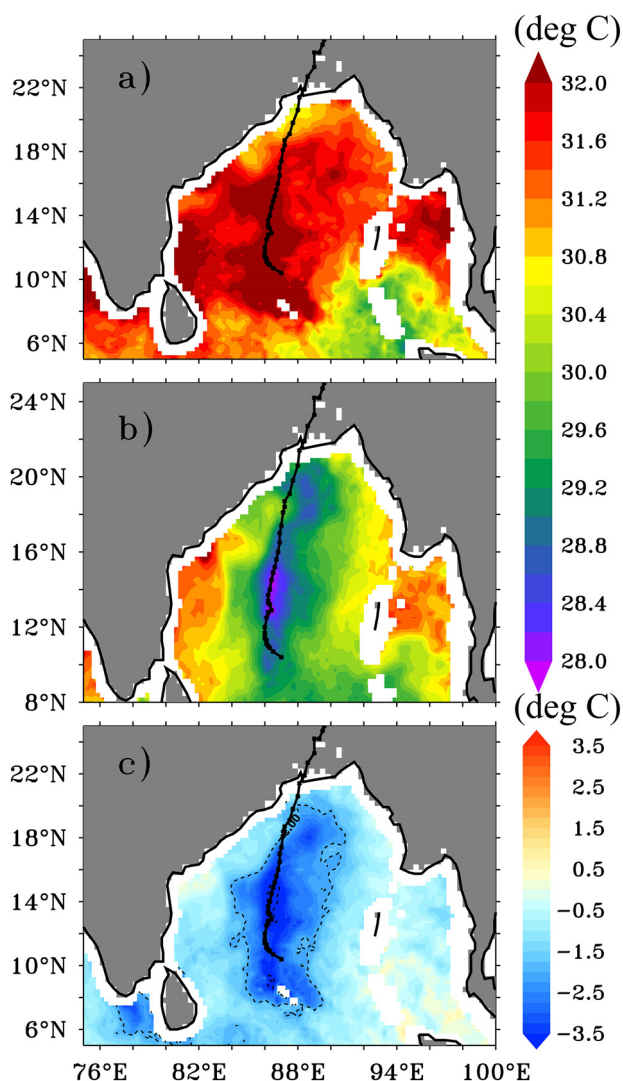


**Figure 4** AMSR-2 sea surface temperature ( $^{\circ}\text{C}$ ) averaged for the periods: a) Pre-Amphan (10–15 May), b) post-Amphan (21–28 May), c) the difference for (b) minus (a). The track of Amphan is overlaid on each plot. The dashed lines overlaying on (c) indicate  $2^{\circ}\text{C}$  isothermal contours.

cyclone Vardah (2016) induced a significant increase of surface salinity on the right side of the storm using SMAP salinity data. In contrast, only a weak drop in salinity ( $\sim 0.7$  PSU) was found over most regions to the left of the track of Amphan. The rainfall rate measured by AMSR-2 (Figure 6) indicates high rainfall along the left of the track of Amphan (3–6 mm/hr) than the right side of the track. Previous studies had reported on this asymmetric rainfall distribution during cyclones is due to the vertical wind shear, topography and water vapor flux (Burpee and Black, 1989; Chacko, 2018; Chen et al., 2010; Corbosiero and Molinari, 2003; Yue et al., 2018). The influx of fresh water from the intense precipitation was responsible for freshening on the left side of the track.

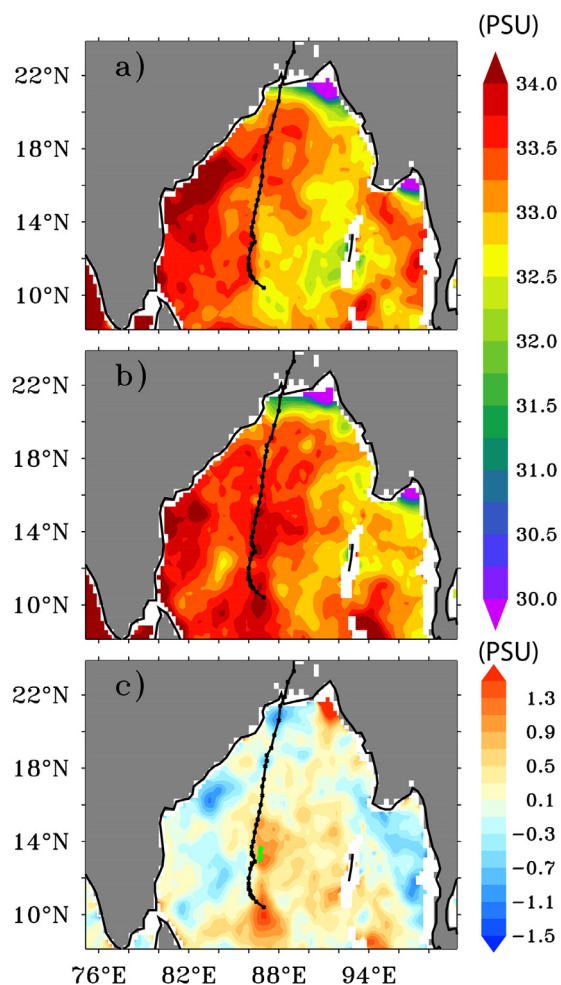


**Figure 5** SMAP level-3 8-day running mean sea surface salinity (PSU) showing the a) pre-cyclone b) post-cyclone and c) post-cyclone minus pre-cyclone salinity. The location of the Argo float is overlaid on (c) as green dots (Qiu et al., 2019).

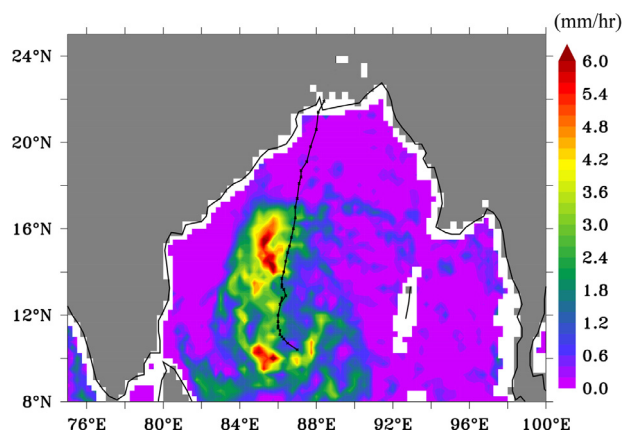


**Figure 6** AMSR-2 measured rainfall rate during the period of Amphan (16–20 May 2020).

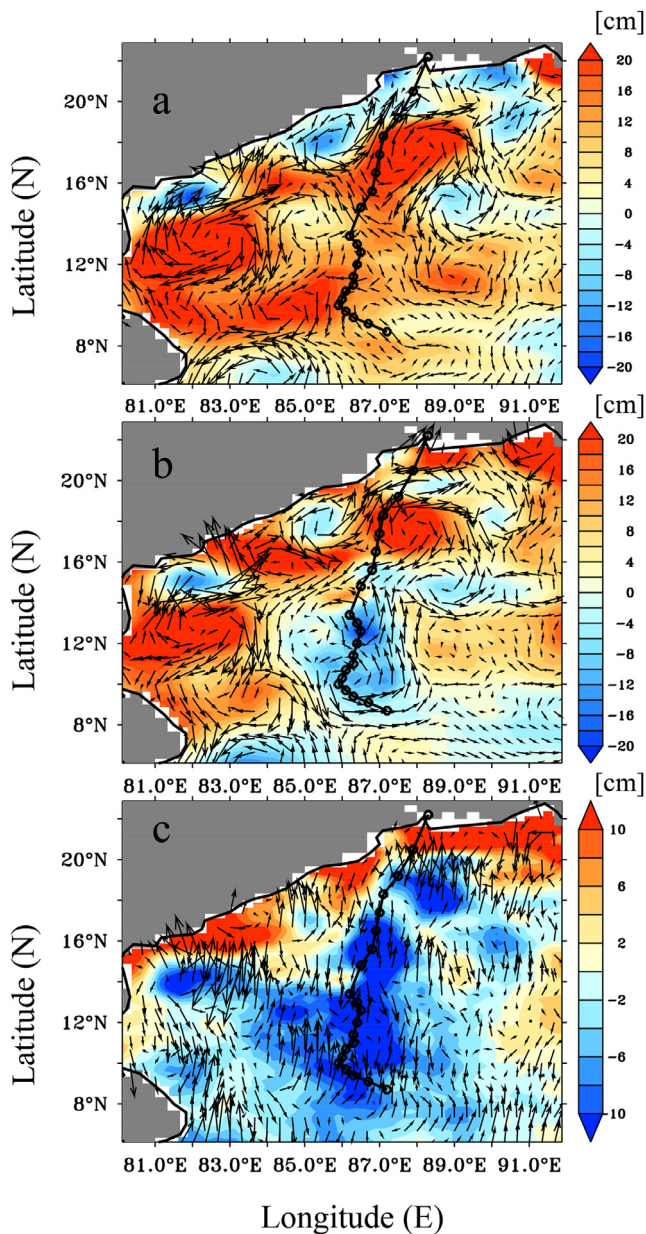


**Figure 7** OSCAR surface currents (cm/s) overlaid on mean sea level anomalies (coloured fields, cm) during a) pre-Amphan, b) post-Amphan, and c) pre-Amphan minus post-Amphan.

### 3.5. Sea Surface Currents

Upper ocean current response to Amphan is characterized using OSCAR currents. Figure 7 shows the surface current speeds overlaid on the mean sea level anomaly during the periods before and after the cyclone. It could be seen that the pre-Amphan periods were characterised by strong positive sea level anomalies that depicted warm core regions. This also implied the presence of warmer subsurface waters before the cyclone. The sea surface currents were distributed along the warm core regions with speeds greater than 50 cm/s. The strong surface winds of the cyclone could modulate the near surface ocean currents. Figure 7b shows the surface currents during the post-Amphan period. Note

that the increase (decrease) of the surface winds always depends on the direction of the wind vector. If the current and wind vectors are in the same direction, the current increases and vice versa. This is illustrated in Figures 7a and b, wherein the southward strong surface currents that prevailed during the pre-Amphan period in the central BoB were observed to be reduced in their magnitude. This was because the surface currents were in the opposite direction (southwards) to that of the cyclonic winds (northwards). The surface currents in the southern BoB however, have increased in magnitude compared to the pre-Amphan conditions. The maximum enhancement of the surface currents due to Amphan happened on the right side of its track. This was because, in the right-hand side of the cyclone track, the inertial forces turn the ocean currents in the same (opposite) direction as the wind stress in the right (left) side of the track (Zhang et al., 2020). This illustrates that the surface currents also exhibited rightward bias under the cyclonic forcing, similar to the other analysed parameters.

The variability of subsurface currents due to Amphan was also studied using the moored buoy (BD8) data (location of the buoy is provided in Figure 1). During the passage of Amphan, the current speed at all depths was observed to rise in response to the increase in wind speed (Figure 8a,b). Amphan increased the subsurface current speed to ~130 cm/s from the pre-cyclone values of ~25 cm/s. The surface and subsurface currents are observed to be restored to the pre-cyclone values by 26 May, 6 days after the cyclone passed over the buoy. The pattern of variability of the surface and subsurface currents induced by Amphan is similar. The maximum current speed of 130 cm/s was recorded at the buoy location on 20 May. A lag of 2 days can be noted between the maximum increase in wind and current speeds as evident from the observations. Figure 8c shows the direction of surface current measured by the buoy. South-southwestward current with an average speed of 20 cm/s is observed at the buoy location before Amphan (Figure 8b and c). The current direction plotted in Figure 8c shows the clockwise rotation of the currents during the period 19–26 May. The existence of near inertial oscillations is reported after the passage of cyclones (Joseph et al., 2007). The near inertial period at the buoy location is 15.9 hours given by  $2\pi/f$  where  $f$  is the Coriolis parameter. The periodicity of the surface currents computed using Fast Fourier Transform method given in Figure 8d shows 13 hours closely matching with the theoretical values. In the northern hemisphere, the inertial oscillations are clockwise. The inertial oscillations that are forced by Amphan disappeared on 26 May, lasting for ~9 inertial periods after its passage.

### 3.6. Chlorophyll concentration

Satellite derived ocean colour chlorophyll will have limited coverage due to cloud cover. During cyclone time, the coverage will be much hampered. To assess the biological changes induced by Amphan, surface chlorophyll concentration from VIIRS was used (Figure 9). From the 8-day chlorophyll-*a* data, it could be seen that during the pre-cyclone period, the chlorophyll values were in the range of 0–0.2 mg m<sup>-3</sup> (Figure 9a), very less values which was typical of the oligotrophic BoB. Post-cyclone, while the data

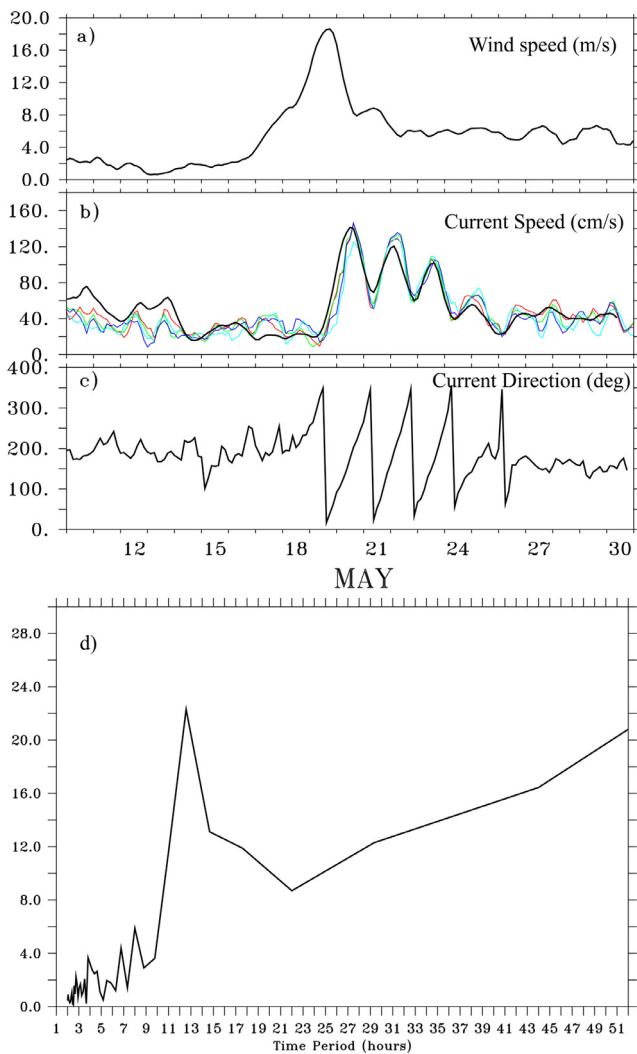


**Figure 8** Observed time series of a) wind speed (m/s); b) current speed at different depths (cm/s) at the surface (black), 15 m (red), 25 m (green), 35 m (cyan); c) current direction (degrees) at the surface measured by moored buoy BD8; d) Fast Fourier Transform of the surface current during Amphan observed from the moored buoy BD8.

coverage over most of the regions over the BoB were hampered by cloud cover, in the central Bay, the signatures of a strong bloom could be observed. Chlorophyll concentration increased markedly after the passage of the cyclone from an average value of  $\sim 0.1 \text{ mg/m}^3$  to  $\sim 1.5 \text{ mg/m}^3$  (Figure 9b,c). A visual comparison of Figure 4c and Figure 8c shows that regions of higher chlorophyll were collocated with that of regions where cooling was maximum. The region of chlorophyll enhancement was also collocated with the region where the cyclone exhibited its highest maximum sustainable wind speed of 245 km/h (18 May). Thus, tight coupling exists between changes in sea surface temperature, chlorophyll and the wind forcing. This substantiates the impact of wind induced vertical mixing and upwelling in elevating higher chlorophyll concentration and reducing sea surface temperature. This also shows that the positive surface chlorophyll concentration observed after passage of

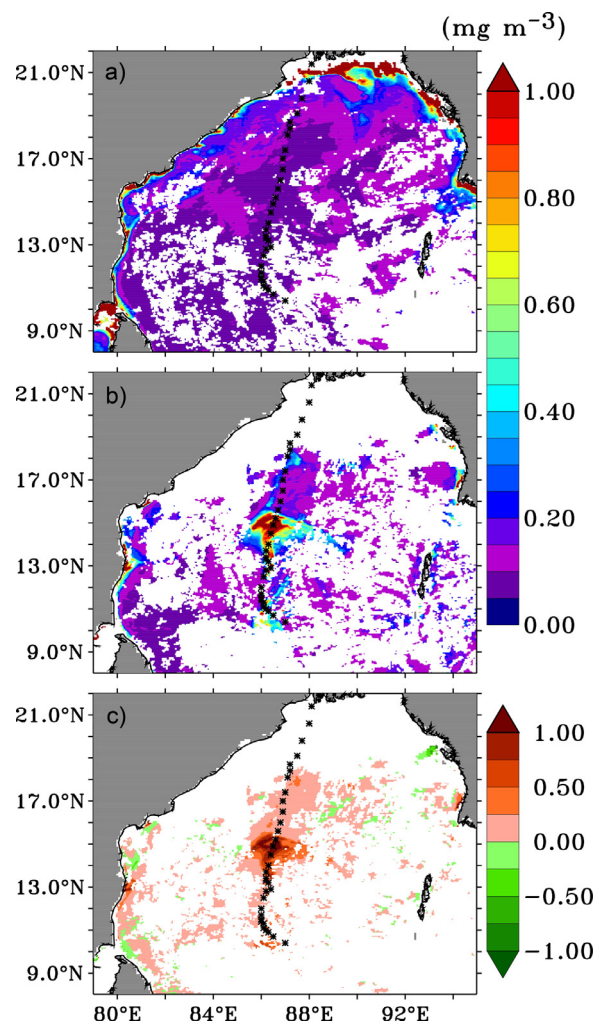


**Figure 9** VIIRS chlorophyll concentration ( $\text{mg/m}^3$ ) averaged over a) pre-Amphan (7–15 May), b) post-Amphan (24–31 May) and c) the difference post-Amphan minus pre-Amphan.

Amphan was dominated by vertical processes such as entrainment and upwelling.

### 3.7. Subsurface response

In order to examine the subsurface temperature and salinity response to Amphan, observations from an Argo float and a moored buoy were employed. The Argo float was located very near to the track, within 50 km from the eye of the cyclone and the moored buoy was located  $\sim 3$  degrees away from the track. So, this provided a unique opportunity to assess the difference in oceanic response induced by Amphan at different locations away from the track. The temporal evolution of temperature and salinity profiles from Argo float are shown in Figures 10a and b. The mixed layer depth before Amphan was relatively shallow, in the range of  $\sim 15$  m depth. Below the mixed layer, relatively colder and saltier waters prevailed before the passage of Amphan (Figures 10a and b). A decrease in the temperature in the upper 100 metre depth is shown in Figure 10a after 16 May which was attributed to the cyclone forcing. The depth of the mixed

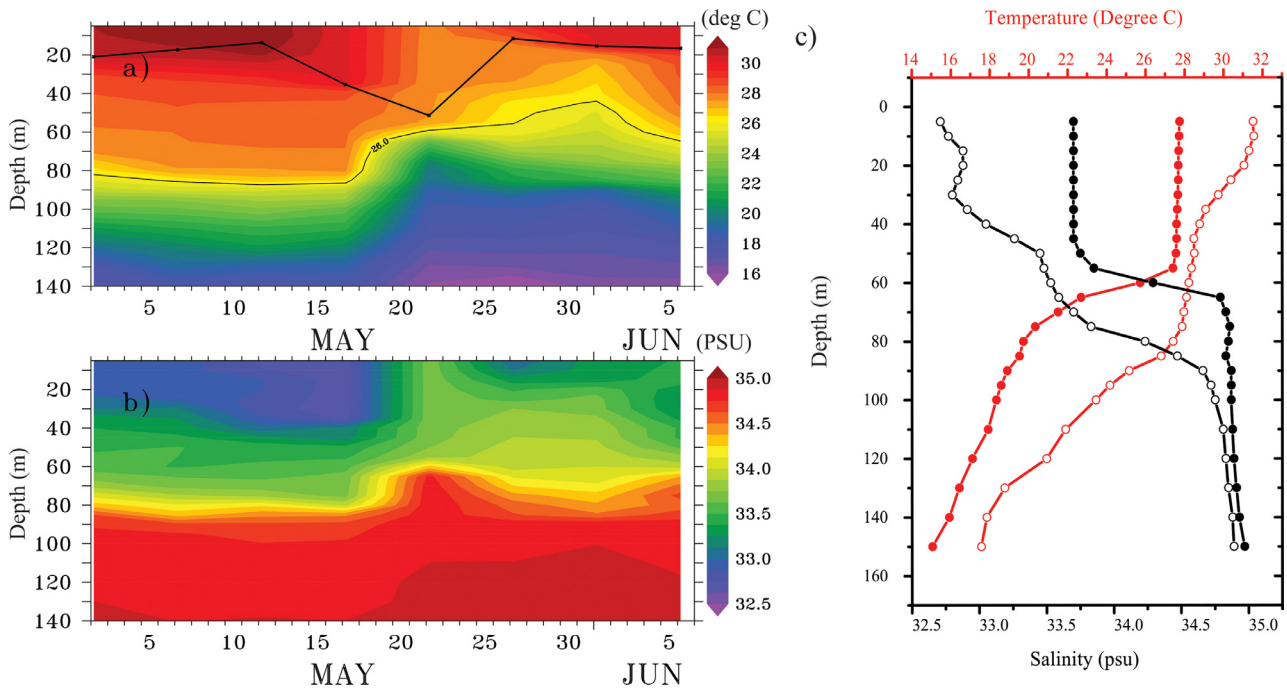


**Figure 10** Subsurface a) temperature (°C) and b) salinity (PSU) from Argo float (WMO id 2902230). The thick and thin black lines in a) are mixed layer depth (m) and depth of 26°C (m) isotherm respectively. c) Temperature (red) and salinity profiles (black) observed by Argo float. Open and closed circles represent pre-cyclone and post-cyclone periods respectively.

layer was observed to have increased from 20 m to 55 m by 20 May. Deepening of the mixed layer is the manifestation of the entrainment and mixing that is induced by the current shear due to the cyclone forcing. Depth of the 23°C isotherm is considered as a proxy for the thermocline depth, and had shoaled from 80 m (pre-Amphan) to 60 m (post-Amphan) (Figure 10a). This deepening of the mixed layer and the rising of thermocline was due to strong vertical mixing induced by the super cyclone. The upper ocean temperature decreases with the cyclone forcing as the mixed layer deepened. While it could be seen that after the cyclone passage, the surface temperatures started to warm more rapidly than subsurface waters, eventually the sub-surface water column also appeared to restore to their pre-cyclone values within 2 weeks after the passage of Amphan. The impact of Amphan was clearly visible throughout the upper 150 m depth of the ocean in the Argo observations.

Unlike the reduction in the ocean temperature, ocean salinity was observed to increase after the passage of Amphan (Figure 10b). The Argo float was located on the right side of the track of Amphan and the observed response of salinity was consistent with the increase in surface salinity observed from the satellite data. The vertical mixing causes the saline sub-surface water to advocate to the surface, causing the upper ocean salinity to increase from the pre-cyclone values of 33 PSU to 34 PSU that are consistent with the satellite observations of surface salinity change. After the cyclone, the near surface salinity was observed to have reduced to 33.5 PSU. This could be due to the advection of fresh surface water resulted from the cyclone induced precipitation. The increase in surface salinity lasted for a week and was restored to pre-cyclone values by 27 May. However, the subsurface salinity was not restored until the first week

of June. Recovery time of salinity is reported to take weeks after the passage of cyclone (Du and Park, 2019; Sun et al., 2021). The variations of temperature and salinity profiles before and after the cyclone observed from the Argo float are shown in Figure 10c. The pre-cyclone salinity profile showed the salt-stratified barrier layer in the near surface below the thin mixed layer. The vertical mixing induced by Amphan brought the higher saline waters from the barrier layer to the surface that resulted in intense post-cyclone surface salinity enhancement. The mixed layer increased to 50 m depth after the cyclone (Figure 10c). Figure 5c depicts saltier waters along the location of the Argo float. This significant salinity increase at this region could be attributed to the intrusion of saltier water present just below the surface layer. Increase in the magnitude of salt wake in the regions with higher vertical salinity gradient below the mixed layer was reported by Reul et al., (2021) and Sun et al., (2021).

The temperature and salinity observed by the moored buoy BD8 is shown in Figure 11a. The buoy was farther to the cyclone track, yet the influence of the cyclone was evident in the temperature and salinity fields. The warmer near surface water layer was cooled under the influence of Amphan. The initial mixed layer depth before Amphan was shallower over this region (15 m), which deepened to a depth of 60 m under the cyclone forcing. The deepened mixed layer depth suggested strong vertical mixing induced by Amphan. Prior to Amphan, salinity in the near surface layer was low (32.9 PSU). The salinity rapidly increased to 33.6 PSU by 18 May which suggested that subsurface salty waters were mixed or uplifted to the surface (Figure 11b). Increase in salinity and decrease in temperature was observed at the buoy location, concurrent to the observations from Argo.

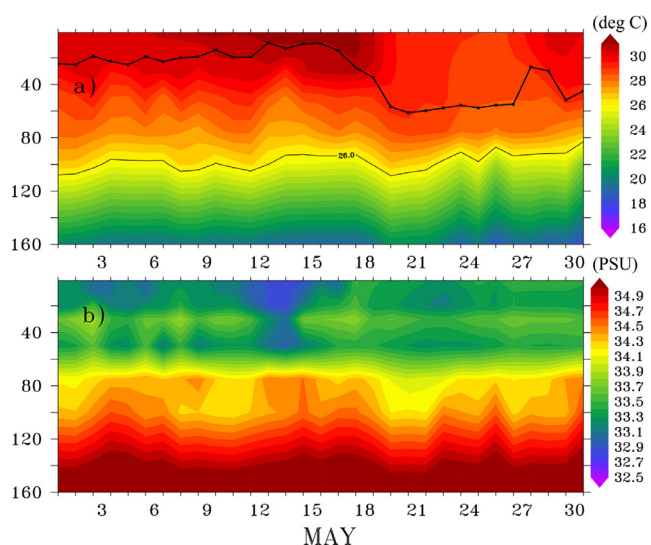


**Figure 11** Observations of a) temperature ( $^{\circ}\text{C}$ ) and b) salinity (PSU) from moored buoy BD8. The thick and thin overlaying lines on a) represent mixed layer depth and the depth of  $26^{\circ}\text{C}$  isotherm respectively.

However, the thermocline depth variability depicted by the depth of the  $26^{\circ}\text{C}$  isotherm showed slight deepening during the cyclone period, contrasting the observations from Argo wherein, the thermocline shoaled during the cyclone (Figure 10a). The thermocline displacement is a manifestation of the upwelling process which brings subsurface waters to the surface under strong wind forcing. The thermocline displacements due to Amphan at the location of Argo was computed from the wind stress using the relation  $\eta = \tau / (\rho f T_s)$  (Price, 1981), where  $\eta$  is the thermocline displacement,  $\tau$  is the wind stress,  $\rho$  is the sea water density,  $f$  is the Coriolis parameter, and  $T_s$  is the translation speed of the cyclone. The thermocline displacement estimated at the Argo location was 14 m. This was consistent with the observed thermocline displacement of  $\sim 16$  m (Figure 10a).

The rising (deepening) contours of the thermocline depicts upwelling (downwelling) induced by the cyclone. The strength of the upwelling can be understood from the Ekman pumping velocity, the positive (negative) Ekman pumping velocity indicates upwelling (downwelling). Figure 12 shows the Ekman pumping velocity during the Amphan cyclone which was computed from Scatsat-1 wind data. Positive Ekman pumping velocity along the track of Amphan inferred the upwelling induced by the cyclone. Considerable difference in the Ekman pumping velocity was seen at the locations of Argo and BD8. At the location of Argo float, strong Ekman pumping velocity and at the location of moored buoy negative Ekman pumping velocity prevailed during Amphan. This corroborated the fact that at the location of BD8, Amphan did not induce upwelling. Thus, it appears that at the location of Argo both entrainment and upwelling processes contributed to the observed near surface cooling and increase in salinity. Also, it is evident from Figure 1 and Figure 2 that the wind speeds at the locations of Argo float and BD8 were different. Argo float was located where the cyclone had its maximum wind speeds and BD8 was located at the region where the cyclone had relatively

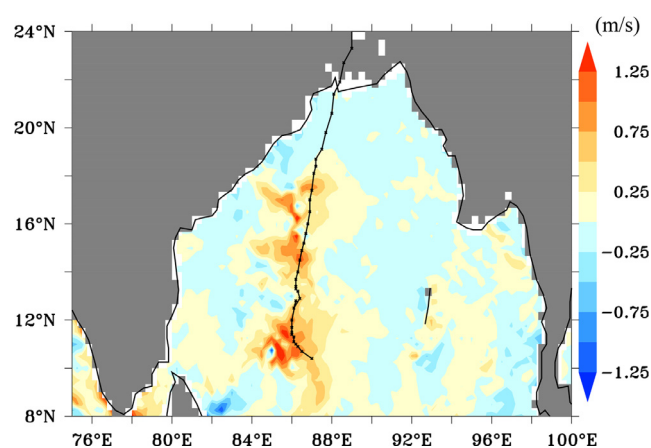


**Figure 12** Ekman pumping velocity (m/s) during Amphan (16–20, May 2020) computed from SCATSAT winds.

lower wind speeds. It is also worth to note that the translation speed of Amphan was significantly different in its later course than during its initial course. Figure 1 clearly depicts the same. Above (below)  $16^{\circ}\text{N}$  latitudes, Amphan traveled faster (slowly). The translation speed of Amphan was higher at the location of the moored buoy, and slower at the Argo. It is reported that upwelling has negligible role in reducing the sea surface temperature for fast moving cyclones, whereas for slow moving cyclones it plays important role (Behera et al., 1998; Bender et al., 1993; Black, 1983; Lin, 2012; Price, 1981). The strong winds and slower translation speeds could be presumed as the reason for inducing strong vertical entrainment and upwelling at the Argo location and similarly, weaker winds and faster translation speeds the reason for failing to induce upwelling at the moored buoy location.

Strong winds induced by the super cyclone pumped cold and salty, deeper waters to the near surface layers, which resulted in the cooling of sea surface temperature and increased surface salinity at the Argo location. The subsurface cooling was also evident in the OHC computed from the Argo measured subsurface temperature. The depth of the vertical mixing induced by Amphan was approximated as 150 m based on Figure 9 and the OHC was computed over 150 m depth of the water column. The Argo measured OHC decreased from  $1.6 \times 10^{10} \text{ J/m}^2$  to  $1.4 \times 10^{10} \text{ J/m}^2$  (Figure 13). This shows that the subsurface lost heat during the cyclone. As heat from the ocean provides energy to cyclones, it is expected to have loss of ocean heat content after the cyclone.

#### 4. Discussion

To explore the causes for the variations in the mixed layer temperature and salinity during the cyclone forcing, heat and salinity budget estimations are conducted using the observations at BD8 owing to its high temporal resolution compared to Argo. The impact and relative roles of the major processes on the mixed layer temperature and salinity changes can be deciphered from the budget estimations. Post-cyclone sea surface temperature cooling is a very complex process, involving hydrodynamic (entrainment and up-

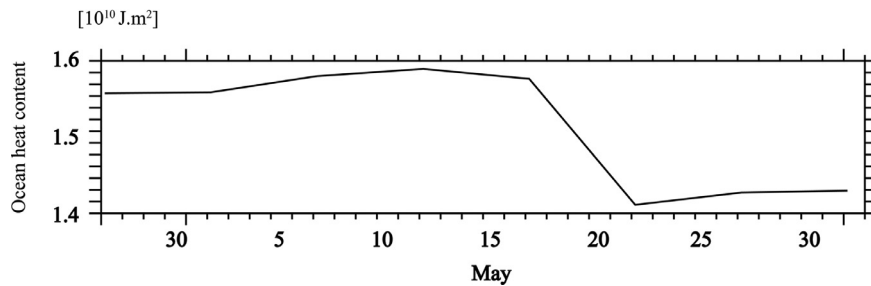


**Figure 13** Ocean heat content ( $\text{J/m}^2$ ) up to 150 m depth of the vertical water column estimated from Argo temperature fields.

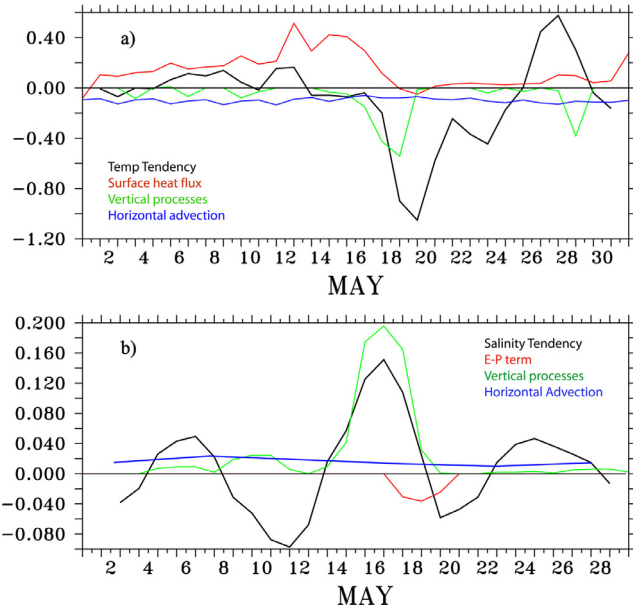


**Figure 14** a) Mixed layer heat budget and b) mixed salinity budget terms computed from observations from moored buoy BD8.

welling) and thermodynamic processes (surface heat flux). The time series of each term from the heat budget estimation is presented in Figure 14a. The various terms of the heat budget equations: temperature tendency, net heat flux term, vertical processes and horizontal advection are plotted in the figure. Before the passage of Amphan, slight warming ( $\sim 0.18^\circ\text{C}/\text{day}$ ) was observed in the mixed layer temperature consistent with the pre-cyclone warmer surface waters as presented in Figure 14a. With the advent of Amphan, the mixed layer temperature tendency showed strong cooling ( $-1.1^\circ\text{C}/\text{day}$ ) from 16–20 May. The cooling continued varying in magnitude in the following days and by 26 May the mixed layer temperature tendency appears to reverse the sign, implying recovering to the pre-storm conditions. The surface net heat flux term is observed as having strong influence in warming the mixed layer temperature before the period of Amphan. However, a considerable reduction in the surface net heat flux occurred during the cyclone and it remained low until 26 May. The contribution of horizontal advection term on the heat budget was observed to be having far smaller contributions ( $-0.1^\circ\text{C}/\text{day}$ ) but indicative of cooling the mixed layer temperature. In contrast, a far stronger cooling was seen from the ver-

tical processes ( $-0.6^\circ\text{C}/\text{day}$ ) during Amphan. Entrainment and upwelling contributed to the vertical processes term in the heat budget equation. The combined effect of these two processes induced mixed layer temperature tendency in general. As shown in the Section 3.7, at the location of BD8, the depth of the  $26^\circ\text{C}$  did not shoal and the Ekman pumping velocity was weakly negative. This indicates that Amphan did not induce upwelling at this location and hence the contribution of entrainment cooling was much stronger at this location. The observed strong mixed layer cooling ceases by 26 May. Therefore, the mixed layer heat budget estimations showed that the strong cooling induced by Amphan at this region was due to the combined contributions of vertical processes and horizontal advection. As shown in Section 3.7, at the location of the moored buoy, cyclone could not induce upwelling. The major contributor of the cooling can be attributed to the vertical entrainment from below the mixed layer.

A mixed layer salinity budget estimation was carried out to examine the roles of processes, which determine the salinity variability. The processes considered are Evaporation minus Precipitation ( $E - P$ ), vertical processes, and horizontal advection. These terms along with mixed layer salinity tendency are illustrated in Figure 14 b. The mixed layer salinity tendency oscillates between increase and decrease during the month of May. The amplitude of oscillation is significantly positive during Amphan (16–20 May) reaching  $0.160 \text{ PSU}/\text{d}$ . The  $E - P$  term showed negative tendency during Amphan attempting to reduce the mixed layer salinity. The precipitation induced by the cyclone tries to freshen the salinity. Horizontal advection term is slightly positive trying to increase salinity through the month of May. The term due to vertical processes appears to have a significant contribution during the cyclone period ( $0.19 \text{ PSU}/\text{d}$ ). The significant increase in salinity during Amphan was observed due to the vertical processes. While  $E - P$  term tries to freshen the mixed layer salinity, combined contribution from vertical processes and horizontal advection results in a net increase in the mixed layer salinity. The two mixed layer budget analysis at the location of BD8 indicates that the vertical entrainment was the major contributor in inducing an increase in salinity and decrease in temperature.

Very few studies examined the mixed layer heat and salinity budget equations during cyclones in the Indian Ocean. Girishkumar et al. (2014) observed that vertical mixing was the dominant factor which controlled the sea surface cooling in the case of cyclone Jal which occurred in the year 2010. Prakash and Pant (2017) showed using numerical modelling that the sea surface temperature cooling

during cyclone Phailin was due to the combined effect of horizontal advection and vertical mixing with stronger contribution from horizontal advection. Our results showed that vertical processes are the significant contributor in decreasing the mixed layer temperature and increasing the mixed layer salinity. This result is contradicting the previous study by Prakash and Pant (2017), and agrees well with the study of Girishkumar et al. (2014).

The post-Amphan surface chlorophyll bloom is observed along the regions where the Amphan had highest wind speeds. This anomaly (Figure 9c) of higher chlorophyll concentration is consistent with the studies of Chacko (2017); Gierach and Subrahmanyam (2008) and Walker et al. (2005) which reported on surface chlorophyll blooms near the trajectory of the cyclones. The areas of strong cooling and higher chlorophyll concentration are spatially collocated, which can be seen in the spatial plots in Figure 4 and Figure 9c. This is due to the fact that the physical mechanism which results in the variability of these two parameters are the same. i.e., vertical mixing due to the strong cyclone winds. The vertical mixing induced by the cyclone winds brings cooler subsurface waters which are also rich in nutrients and chlorophyll content into the surface waters. Thus, the sea surface cooled and the chlorophyll concentration increased after Amphan. However, the surface salinity variability after the cyclone was different compared to the sea surface temperature and chlorophyll concentration. This is because in addition to the vertical processes, strong rainfall induced by the cyclone also played a key role in the salinity variability. The net result in the salinity will be the resultant between these two opposing processes. Hence the areas of cooling and increase in salinity does not match unlike areas of cooling and chlorophyll bloom.

Satellite observations revealed that the wake of the super-cyclone Amphan was apparent in the sea surface temperature, sea surface salinity, chlorophyll concentration, and on the surface currents. It is also evident from the spatial picture of the parameters assessed that the pronounced variability was observed in the central Bay of Bengal where Amphan was at its best intensity. This indicates the fact that intensity of the cyclone drives dominant oceanic response (Lin, 2012). This study also brings forward the regional differences in the responses of the ocean to the forcing of cyclone. For example, observations from Argo suggested that both entrainment and upwelling contributed to the surface cooling at that location. At the location of the moored buoy in the northern BoB, however, upwelling was observed as absent and wind induced mixing results in entrainment alone. At this location the vertical entrainment can be considered as driver of ocean cooling, whereas in the central Bay at the location of Argo, vertical entrainment and upwelling can be considered as the drivers of ocean cooling. This shows that the relative position of the oceanic features to the cyclone track determines the response of the ocean to the cyclone.

One of the key findings of this study is the intense cooling ( $\sim 4^\circ\text{C}$ ) in the cold wake which spanned all over the BoB. Vertical entrainment and upwelling contributed to the strong cooling observed, but in different regions of the BoB the contributions from these were different. Many previous researchers conducted experiments to assess the impact of cyclones on the oceans. Though significant progress has been made in understanding the oceanic processes under

cyclones, there is a continuous need to identify the processes and mechanisms which induce the oceanic response due to cyclones. It should be noted that each cyclone is different and as it passes over oceanic regions of different conditions, the resulting responses of the ocean also will be different.

## 5. Conclusions

This study used synergistic observations from satellite and in-situ to understand the oceanic responses to super-cyclone Amphan during 16–20 May in the year 2020. Various parameters such as sea surface temperature, sea surface salinity, surface currents, surface chlorophyll concentration, subsurface temperature, salinity and currents are assessed. Spatial analysis using AMSR-2 data show significant sea surface temperature cooling in the wake of Amphan with a cooling amplitude reaching up to of  $\sim 4^\circ\text{C}$ . Not only a rightward bias in sea surface temperature cooling, but a large spatial extent of the cooling spanning entire BoB is observed. Surface salinity increased to the right of the track ( $> 1.5$  PSU) and slightly decreased along the left of the track. The strong asymmetric rain rate towards the left side of the cyclone track of amplitude  $\sim 6$  mm/hr is attributed to the suppressed salinity wake along the left side of the cyclone track. While the intense freshwater influx due to the cyclone rains freshened the water on the left, strong vertical mixing induced by the winds of the cyclone resulted in the influx of saltier water and increase in the salinity on the right of the track. Similarly, there is an enhancement of  $\sim 1.5$   $\text{mg m}^{-3}$  of surface chlorophyll concentration after the passage of the cyclone, which is centred along the track of the cyclone where the cyclone winds were the highest. The surface chlorophyll and sea surface temperature variability are observed as collocated and tightly coupled to each other suggesting the common causal factors are the same. Surface and subsurface currents observed revealed that currents are strongly modulated by the passage of Amphan. It is observed that spatially, the sea surface temperature, salinity and surface currents exhibited rightward biases which is due to the rotation of the wind vector with the wind-driven inertial currents.

The vertical structure of the ocean is also clearly affected by the passage of cyclone in addition to the changes in the surface layer. Subsurface observations showed that Amphan induced strong subsurface mixing occurred vertically in the upper 150 m of the water column. The OHC estimated from the Argo observations revealed heat lost during the cyclone in the upper 150 m depth. Mixed layer heat and salinity budget estimations showed that the vertical mixing was the dominant process driving the mixed layer salinity and temperature response during Amphan. Vertical mixing induced by the super-cyclone brought cooler and saltier waters from below which resulted in the cooling and increase of salinity in the near surface layers. Observations from Argo revealed that the mixed layer depth was deepened, and the thermocline depth shoaled, both were the manifestations of the entrainment and upwelling induced by the cyclone. However, at the moored buoy location, upwelling was absent and entrainment was the major factor driving the variability of salinity and temperature. It is seen that regional

differences in the response of ocean were observed due to Amphan. More details into the spatially distinct oceanic response can be deciphered with the availability of more in-situ datasets. This study also reports the recovery time of all the parameters considered. Studies on the recovery of the parameters after passage of cyclones are limited. It is observed that upper ocean recovered in approximate 2 weeks after the passage of Amphan.

It is concluded that the synergistic use of in-situ and satellite observations are required to understand the complete picture of the upper ocean response to tropical cyclones. Understanding the response of the oceans to cyclones is important in the recent times when the frequency and intensity of tropical cyclones are observed to have increased. As the tropical cyclone activity increases, an increase in the oceanic response also could be expected. The present study points that while in-situ observations are relatively sparse, an extended network of the same is vital for better understanding the variability of the ocean during cyclones.

## Declaration of competing interest

The authors declare that they have no known competing financial interests or personal relationships that could have appeared to influence the work reported in this paper.

## Acknowledgement

Argo data (DOI: <https://doi.org/10.25921/q97e-d719>) were collected and made freely available by the International Argo Program and the national programs that contribute to it (<http://www.argo.ucsd.edu>, <http://argo.jcommops.org>). The Argo Program is part of the Global Ocean Observing System. GSFC – NASA are sincerely acknowledged for making available the level-3 chlorophyll data pertaining to VIIRS. We express our sincere gratitude to all concerned who has directly or indirectly contributed for the successful execution of this project. This research did not receive any specific grant from funding agencies in the public, commercial, or not-for-profit sectors. We greatly acknowledge Indian National Centre for Ocean Information Services (ESSO-INCOIS) for providing the moored buoy data. We thank the two anonymous reviewers for their valuable comments and suggestions which helped in improving this manuscript immensely.

## References

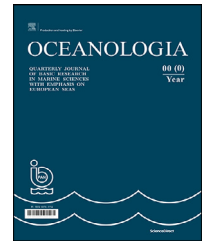
- Babin, S.M., Carton, J.A., Dickey, T.D., Wiggert, J.D., 2004. Satellite evidence of hurricane-induced phytoplankton blooms in an oceanic desert. *J. Geophys. Res.* 109, C03043. <https://doi.org/10.1029/2003JC001938>
- Behera, S.K., Deo, A.A., Salvekar, P.S., 1998. Investigation of mixed layer response to Bay of Bengal cyclone using a simple ocean model. *Meteorol. Atmos. Phys.* 65, 77–91. <https://doi.org/10.1007/BF01030270>
- Bender, M.A., Ginis, I., Kurihara, Y., 1993. Numerical simulations of tropical cyclone–ocean interaction with a high-resolution coupled model. *J. Geophys. Res.* 98, 23245. <https://doi.org/10.1029/93JD02370>
- Black, P.G., 1983. Ocean temperature changes induced by tropical cyclones. *The Pennsylvania State University*, 278 pp.
- Black, W.J., Dickey, T.D., 2008. Observations and analyses of upper ocean responses to tropical storms and hurricanes in the vicinity of Bermuda. *J. Geophys. Res. Oceans*. 113, C08009. <https://doi.org/10.1029/2007JC004358>
- Burpee, R.W., Black, M.L., 1989. Temporal and spatial variations of rainfall near the centers of two tropical cyclones. *Mon. Weather Rev.* 117, 2204–2218.
- Chacko, N., Ravichandran, M., Rao, R.R., Shenoi, S.S.C., 2012. An anomalous cooling event observed in the Bay of Bengal during June 2009. *Ocean Dynam.* 62, 671–681. <https://doi.org/10.1007/s10236-012-0525-9>
- Chacko, N., 2017. Chlorophyll bloom in response to tropical cyclone Hudhud in the BoB: Bio-Argo subsurface observations. *Deep Sea Res. Pt. I*. 124, 66–72. <https://doi.org/10.1016/j.dsr.2017.04.010>
- Chacko, N., 2018. Insights into the haline variability induced by cyclone Vardah in the BoB using SMAP salinity observations. *Remote Sens. Lett.* 9 (12), 1205–1213. <https://doi.org/10.1080/2150704X.2018.1519271>
- Chacko, N., 2019. Differential chlorophyll blooms induced by tropical cyclones and their relation to cyclone characteristics and ocean pre-conditions in the Indian Ocean. *J. Earth Syst. Sci.* 128, 177. <https://doi.org/10.1007/s12040-019-1207-5>
- Chen, C.T.A., Liu, C.T., Chuang, W.S., Yang, Y.J., Shiah, F.K., Tang, T.Y., Chung, S.W., 2003. Enhanced buoyancy and hence upwelling of subsurface Kuroshio waters after a typhoon in the southern East China Sea. *J. Marine Syst.* 42, 65–79.
- Chen, L.S., Li, Y., Cheng, Z.Q., 2010. An overview of research and forecasting on rainfall associated with landfalling tropical cyclones. *Adv. Atmos. Sci.* 27, 967–976.
- Cheung, H.F., Pan, J., Gu, Y., Wang, Z., 2013. Remote sensing observation of ocean responses to Typhoon Lupit in the northwest Pacific. *Int. J. Remote Sens.* 34, 1478–1491.
- Chu, P.C., Veneziano, J.M., Fan, C., 2000. Response of the South China Sea to tropical cyclone Ernie 1996. *J. Geophys. Res.* 105 (C6), 3991–14009.
- Cione, J.J., Uhlhorn, E.W., 2003. Sea surface temperature variability in hurricanes: Implications with respect to intensity change. *Mon. Weather Rev.* 131, 1783–1796.
- Corbosiero, K.L., Molinari, J., 2003. The relationship between storm motion, vertical wind shear, and convective asymmetries in tropical cyclones. *J. Atmos. Sci.* 60, 366–376.
- Dare, R.A., McBrie, A., 2011. Sea Surface Temperature Response to Tropical Cyclones. *Mon. Weather Rev.* 139 (12), 3798–3808. <https://doi.org/10.1175/MWR-D-10-05019.1>
- D’Asaro, E.A., Sanford, T.B., Niiler, P.P., Terrill, E.J., 2007. Cold wake of Hurricane Frances. *Geophys. Res. Lett.* 34, L15609. <https://doi.org/10.1029/2007GL030160>
- Du, J., Park, K., 2019. Estuarine salinity recovery from an extreme precipitation event: Hurricane Harvey in Galveston Bay. *Sci. Total Environ.* 670, 1049–1059. <https://doi.org/10.1016/j.scitotenv.2019.03.265>
- Gierach, M.M., Subrahmanyam, B., 2008. Biophysical responses of the upper ocean to major Gulf of Mexico hurricanes in 2005. *J. Geophys. Res.* 113, C04029. <https://doi.org/10.1029/2007JC004419>
- Girishkumar, M.S., Suprit, K., Jayaram, C., Udaya Bhaskar, T.V.S., Ravichandran, M., Shesu, V., Rama Rao, E.P., 2014. Observed oceanic response to tropical cyclone Jal from a moored buoy in the south-western Bay of Bengal. *Ocean Dynam.* 64, 325–335. <https://doi.org/10.1007/s10236-014-0689-6>
- Jayaram, C., Udaya Bhaskar, T.V.S., Kumar, J.P., Swain, D., 2019. Cyclone enhanced chlorophyll in the BoB as evidenced from satellite and BGC-Argo float observations. *J. Indian*



- Soc. Remote Sens. 47, 1875–1882. <https://doi.org/10.1007/s12524-019-01034-1>
- Joseph, J.K., Balchand, A.N., Hareeshkumar, P.V., Rajish, G., 2007. Inertial oscillation forced by the September 1997 cyclone in the Bay of Bengal. *Current Sci.* 92 (2007), 790–794.
- Kara, A.B., Rochford, P.A., Hurlbutt, H.E., 2000. Mixed layer depth variability and barrier layer formation over the North Pacific Ocean. *J. Geophys. Res.* 105 (C7), 16783–16801.
- Lin, I.-I., Liu, W.T., Wu, C.-C., Wong, G.T.F., Hu, C., Chen, Z., Liang, W.-D., Yang, Y., Liu, K.-K., 2003. New evidence for enhanced ocean primary production triggered by tropical cyclone. *Geophys. Res. Lett.* 30, 1718.
- Lin, I.I., 2012. Typhoon induced phytoplankton blooms and primary productivity increase in the western North Pacific subtropical ocean. *J. Geophys. Res.* 117, C03039. <https://doi.org/10.1029/2011JC007626>
- Mandal, S., Sil, S., Shee, A., Swain, D., Pandey, P.C., 2018. Comparative analysis of SCATSAT-1 gridded winds with Buoys, ASCAT, and ECMWF winds in the Bay of Bengal. *IEEE J. Sel. Top. Appl.* 11 (3), 845–851. <https://doi.org/10.1109/JSTARS.2018.2798621>
- Maneasha, K., Murty, V.S.N., Ravichandran, M., Lee, T., Yu, W., McPhaden, M.J., 2012. Upper Ocean Variability in the BoB during the Tropical Cyclones Nargis and Laila. *Prog. Oceanogr.* 106, 49–61. <https://doi.org/10.1016/j.pocean.2012.06.006>
- McPhaden, M.J., Meyers, G., Ando, K., Masumoto, Y., Murty, V.S.N., Ravichandran, M., Syamsudin, F., Vialard, J., Yu, L., Yu, W., 2009. RAMA: The Research Moored Array for African–Asian–Australian Monsoon Analysis and Prediction. *B. Am. Meteorol. Soc.* 459–480. <https://doi.org/10.1175/2008BAMS2608.1>
- Navaneeth, K.N., Martin, M.V., Joseph, K.J., Venkatesan, R., 2019. Contrasting the upper ocean response to two intense cyclones in the Bay of Bengal. *Deep-Sea Res. Pt. I.* <https://doi.org/10.1016/j.dsr.2019.03.010>
- Paulson, C.A., Simpson, J.J., 1977. Irradiance measurements in the upper ocean. *J. Phys. Oceanogr.* 7, 952–956.
- Prakash, K.R., Panth, V., 2017. Upper oceanic response to tropical cyclone Phailin in the Bay of Bengal using a coupled atmospheric-ocean model. *Ocean Dyn.* 67, 51–64. <https://doi.org/10.1007/s10236-016-1020-5>
- Price, J.F., 1981. Upper ocean response to a hurricane. *J. Phys. Oceanogr.* 11, 153–175. [https://doi.org/10.1175/1520-0485\(1981\)011<0153:UORTAH>2.0.CO;2](https://doi.org/10.1175/1520-0485(1981)011<0153:UORTAH>2.0.CO;2)
- Price, J.F., Sanford, T.B., Forristall, G.Z., 1994. Forced stage response to a moving hurricane. *J. Phys. Oceanogr.* 24, 233–260.
- Qiu, W., Ren, F., Wu, L., Chen, L., Ding, C., 2019. Characteristics of tropical cyclone extreme precipitation and its preliminary causes in Southeast China. *Meteorol. Atmos. Phys.* 131, 613–626. <https://doi.org/10.1007/s00703-018-0594-5>
- Rao, R.R., Sivakumar, R., 2000. Seasonal variability of the near-surface thermal structure and heat budget of the mixed layer of the tropical Indian Ocean from a new global ocean temperature climatology. *J. Geophys. Res.* 105, 995–1015. <https://doi.org/10.1029/1999JC900220>.
- Reul, N., Chapron, B., Grodsky, S.A., Guimbard, S., Kudryavtsev, V., Foltz, G.R., Balaguru, K., 2021. Satellite observations of the sea surface salinity response to tropical cyclones. *Geophys. Res. Lett.* 48, e2020GL091478. <https://doi.org/10.1029/2020GL091478>
- Schade, L.R., Emanuel, K.A., 1999. The ocean's effect on the intensity of tropical cyclones: Results from a simple coupled atmosphere–ocean model. *J. Atmos. Sci.* 56, 642–651.
- Shang, S.L., Li, L., Sun, F.Q., Wu, J.Y., Hu, C.M., Chen, D.W., Ning, X.R., Qiu, Y., Zhang, C.Y., Shang, S.P., 2001. Changes of temperature and bio-optical properties in the South China Sea in response to Typhoon Lingling. *Geophys. Res. Lett.* 35, L10602.
- Singh, O.P., Khan, T.A., Rahman, M.S., 2000. Changes in the frequency of tropical cyclones over the North Indian Ocean. *Meteorol. Atmos. Phys.* 75 (1–2), 11–20.
- Singh, V.K., Koll, R.M. 2020. A review of the ocean-atmosphere interactions during tropical cyclones in the north Indian Ocean. <https://arxiv.org/abs/2012.04384>
- Song, D., Xiang, L., Guo, L., Li, B., 2020. Estimating Typhoon-Induced Sea Surface Cooling Based upon Satellite Observations. *Water* 12, 3060. <https://doi.org/10.3390/w12113060>
- Subrahmanyam, B., Rao, K.H., Rao, N.S., Murty, V.S.N., Sharp, R.J., 2002. Influence of a tropical cyclone on Chlorophyll-a Concentration in the Arabian Sea. *Geophys. Res. Lett.* 29 (22), 2065. <https://doi.org/10.1029/2002GL015892>
- Sun, L., Yang, Y., Xian, T., Lu, Z., Fu, Y., 2010. Strong enhancement of chlorophyll a concentration by a weak typhoon. *Mar. Ecol. Prog. Ser.* 404, 39–50. <https://doi.org/10.3354/meps08477>
- Sun, J., Vecchi, G., Soden, B., 2021. Sea Surface Salinity Response to Tropical Cyclones Based on Satellite Observations. *Remote Sens.* 13 (3), 420. <https://doi.org/10.3390/rs13030420>
- Walker, N.D., Leben, R.R., Balasubramanian, S., 2005. Hurricane-forced upwelling and chlorophyll a enhancement within cold-core cyclones in the Gulf of Mexico. *Geophys. Res. Lett.* 32, L18610. <https://doi.org/10.1029/2005GL023716>
- Yue, X., Zhang, B., Liu, G., Li, X., Zhang, H., He, Y., 2018. Upper Ocean Response to Typhoon Kalmaegi and Sarika in the South China Sea from Multiple-Satellite Observations and Numerical Simulations. *Remote Sens.* 10, 348. <https://doi.org/10.3390/rs10020348>
- Zhang, H., Xiaohui, L., Renhao, W., Chen, D., Dongna, Z., Xiaodong, S., Yuan, W., Xunshu, S., Weifang, J., Linghui, Y., Yongfeng, Q., Di, T., Wenyan, Z., 2020. Sea Surface current response patterns to tropical cyclones. *J. Marine Syst.* 208, 103345. <https://doi.org/10.1016/j.jmarsys.2020.103345>

Available online at [www.sciencedirect.com](http://www.sciencedirect.com)

ScienceDirect

journal homepage: [www.journals.elsevier.com/oceanologia](http://www.journals.elsevier.com/oceanologia)

## ORIGINAL RESEARCH ARTICLE

# *Asterionellopsis glacialis* (Family: Fragilariaceae, Class: Bacillariophyceae, Phylum: Ochrophyta) bloom and its impact on plankton dynamics at Kalpakkam (Bay of Bengal, Southeast coast of India)

Gouri Sahu<sup>a</sup>, Ajit Kumar Mohanty<sup>a,\*</sup>, Ranjit Kumar Sarangi<sup>b</sup>, Kamala Kanta Satpathy<sup>c</sup>

<sup>a</sup> Radiological and Environmental Safety Division, Indira Gandhi Centre for Atomic Research, Kalpakkam, India

<sup>b</sup> Planetary Sciences & Marine Biology Division, Space Applications Centre (ISRO), Ahmedabad, India

<sup>c</sup> Department of Environmental Science, Central University of Rajasthan, India

Received 24 September 2020; accepted 28 April 2021

Available online 21 May 2021

## KEYWORDS

*Asterionellopsis* bloom;  
Phytoplankton;  
Zooplankton;  
Plankton dynamics;  
Coastal waters;  
Southeast coast of India

**Abstract** An intense bloom of *Asterionellopsis glacialis* (Family: Flagellariaceae; Class: Bacillariophyceae; Phylum: Ochrophyta) was observed in the near-shore waters at Kalpakkam, Tamil Nadu. Proliferation was supported by the favorable temperature, salinity, and nutrient levels in the coastal waters prevailing in the post-northeast monsoon period. BIOENV analysis and PCA confirmed salinity and nitrate as the key environmental factors responsible for the *A. glacialis* abundance. Cluster analysis further supported the distinct state of coastal water during the bloom with respect to physicochemical properties. The bloom period was floristically and faunistically richer than the pre- and post-bloom periods. The cluster and nMDS analysis confirmed the effects of bloom on plankton dynamics in the near-shore waters at Kalpakkam. The dominance of meroplankters especially, Cirripedia nauplii and Bivalvia larvae over Copepoda during the peak bloom period, was a significant result of the study. PCA ordination plot for the quantitative aspects of phytoplankton and zooplankton groups further supported the above observation. Among Copepoda, Cyclopoida and Poecilostomatoida (mostly carnivorous) exceeded the Calanoida (mostly herbivorous) during the peak bloom period unlike the reverse trend observed during other periods. Fish eggs and larvae were available in substantial numbers

\* Corresponding author at: Radiological and Environmental Safety Division, Indira Gandhi Centre for Atomic Research, Kalpakkam - 603102, India.

E-mail address: [ajit@igcar.gov.in](mailto:ajit@igcar.gov.in) (A.K. Mohanty).

Peer review under the responsibility of the Institute of Oceanology of the Polish Academy of Sciences.



<https://doi.org/10.1016/j.oceano.2021.04.005>

0078-3234/© 2021 Institute of Oceanology of the Polish Academy of Sciences. Production and hosting by Elsevier B.V. This is an open access article under the CC BY-NC-ND license (<http://creativecommons.org/licenses/by-nc-nd/4.0/>).

during the bloom which indicated their proliferation in the presence of the blooming diatom standing stock as the food material.

© 2021 Institute of Oceanology of the Polish Academy of Sciences. Production and hosting by Elsevier B.V. This is an open access article under the CC BY-NC-ND license (<http://creativecommons.org/licenses/by-nc-nd/4.0/>).

## 1. Introduction

Phytoplankton blooms have become regular phenomena in the coastal marine environment due to the eutrophication caused by anthropogenic impacts and natural events such as upwelling and water currents (Jocelyn et al., 2000; Rao, 1969). Margalef (1978) also recognized that the most important features governing bloom are turbulence and advection, as they decide the plankton mass how long to stay at the photic zone and in favorable environmental conditions. Phytoplankton blooms generally take place in coastal waters in a nutrient-enriched environment in the presence of light. The bloom is usually of a variety of colors, i.e., from green to red. *Trichodesmium erythraeum*, blue-green algae, is a very common bloom-forming species along the Indian coasts. However, diatom blooms are very meager along this coast. Among diatoms, blooms of *Asterionellopsis glacialis* have been reported from different parts of Indian coasts. Rao (1969) reported the bloom of *A. glacialis* in the coastal waters of Visakhapatnam for the first time. Subsequently, *A. glacialis* bloom was reported from the Vellar river estuary, Tamil Nadu coast (Mani et al., 1986), from coastal waters of Orissa (Choudhury and Panigrahy, 1989; Mishra and Panigrahy, 1995; Panigrahy and Gouda, 1990). The occurrence of *A. glacialis* bloom was also reported from Kalpakkam coast, Tamil Nadu by Satpathy and Nair (1996). The bloom of marine phytoplankton is becoming a cosmopolitan phenomenon and has spread across all the latitudes (Bhat et al., 2006). The increased appearance of phytoplankton blooms in the coastal and offshore waters of India, as reported by various studies during recent times (D'Silva et al., 2012; Latha et al., 2014; Mohanty et al., 2010; Sahu et al., 2016) has threatened the marine ecosystems. Impacts of bloom on marine fishing activities have long been reported from Indian waters (Nagabhushanam, 1967; Prabhu et al., 1971). Human health hazards arisen from bloom-infested waters have also been reported (Karunasagar et al., 1984, 1998) from India. During our regular coastal water monitoring program, *Asterionellopsis glacialis* bloom was encountered (January 2015) in the coastal near-shore zone of Kalpakkam (12°33'N Lat.; 80°11'E Long.). The bloom patches were brownish colored and were observed in the surf zone. The bloom was observed to be extended to ~10 km along the coastline. Besides, blooms of Dinophyta *Noctiluca scintillans* (Sargunam et al., 1989) and Cyanobacteria *Trichodesmium erythraeum* (Mohanty et al., 2010; Satpathy et al., 2007) have also been reported from coastal waters of Kalpakkam. Interestingly, though *Asterionella* bloom has been reported about six times from the Indian coastal waters, all the bloom events for this species occurred in the Bay of Bengal (BOB) coast. Most of the diatom blooms have no direct harmful impact on the economy but generally alter the physicochemical and biological properties of water and

consequently affect flora and fauna (Campbell, 1996). The present investigation focused on describing the phyto- and zoo-plankton community structure along with the abiotic factors measured during the *A. glacialis* bloom encountered at Kalpakkam coast, BOB. Recent observations on phytoplankton blooms from Indian coastal waters (Jyothibabu et al., 2017; Roy et al., 2016; Sarma et al., 2020; Shanmugam et al., 2017; Sridevi et al., 2019) have mainly concentrated on physicochemical aspects and remote sensing data. Apart from the reports from the 1990s to 2000s, some of which dealt with phytoplankton and rarely included zooplankton, recent studies in this regard are very scarce (Baliarsingh et al., 2016; Srichandan et al., 2019). Moreover, although phytoplankton blooms have been reported earlier from this coast, those investigations only emphasized physicochemical aspects. Hence, there is a paucity of information regarding plankton, particularly zooplankton community organization during such blooms. Besides, an effort has been made to determine the spatial extent and dynamics of the bloom by satellite sensor-derived Chl-*a* images, which provide quick and effective means to detect and monitor bloom formation.

## 2. Material and methods

### 2.1. Study area

Kalpakkam (12°33'N Lat. and 80°11'E Long.) is situated about 70 km south of Chennai metro city, southeast coast of India. It is an emerging hub of nuclear installations. It harbors Madras Atomic Power Station (MAPS), Prototype First Breeder Reactor (PFBR), First Breeder Fuel Cycle Facility (FRFCF – under construction), Indira Gandhi Centre for Atomic Research (IGCAR), and desalination plant (Nuclear Demonstration & Desalination Plant, NDDP). The bloom was encountered during the regular coastal water monitoring program (December 2014–January 2015) near the seawater intake of MAPS, which is ~500 m away from the shore (Figure 1). Water column depth near the sampling location is about 8 m, and tides are small (0.3–1.5 m; micro-tidal). The surf zone is ~100 m at this location. In this part of the southeastern Indian peninsula, three seasons are observed annually according to the wind regime (i) pre-monsoon (PRM) or southwest monsoon (SWM) (June–Sept.), (ii) Northeast monsoon (NEM) (October to January) and (iii) post-monsoon (POM)/summer (February–May) (Sahu et al., 2015). The coastal current at Kalpakkam is bidirectional, northerly from February to October (speed of 0.2–1.8 km/h) and southerly from October to February (speed 0.1–1.3 km/h). Southerly (~0.5 million m<sup>3</sup>/y) and northerly littoral drift (~1 million m<sup>3</sup>/y) takes place at this location due to monsoon winds (10–40 km/h). The surface seawater temperature (SST) shows bimodal oscillation with two annual peaks

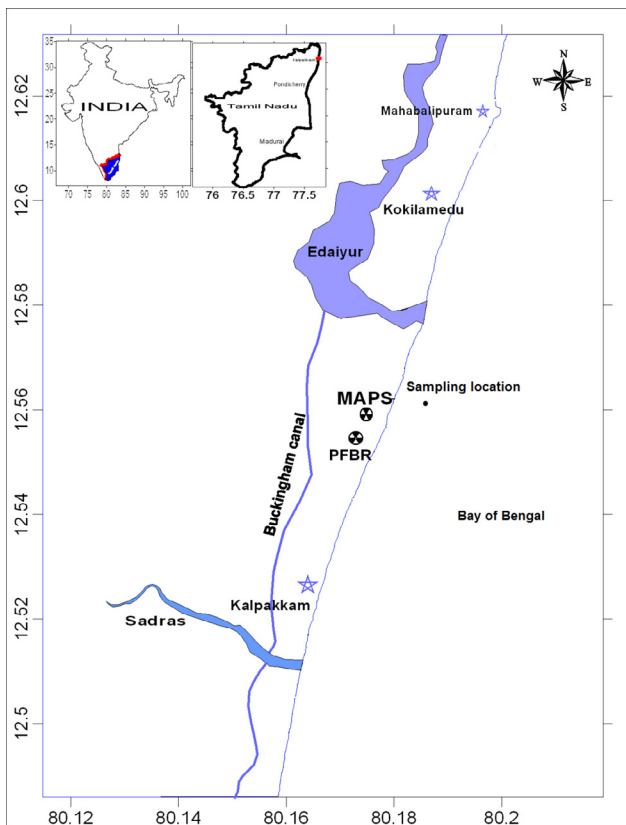


**Figure 1** Study area showing the sampling location, Kalpakkam coast, east coast of India.

(April/May, August/September) and two minima during December/January and June/July (Satpathy and Nair, 1990). This region receives about 65% of total rainfall (~1250 mm) during the dominant NEM period. Monsoonal rain and the monsoon-dependent wind and current reversals drastically affect the coastal water ecology (Satpathy et al., 2009, 2010). Also, the Sadras and the Edaiyur backwater systems present at this location play an important role in the coastal ecology by discharging a large amount of freshwater mainly during the NEM period.

## 2.2. Methods

Surface water was collected daily during the bloom (14<sup>th</sup> to 19<sup>th</sup> January 2015), and post-bloom (20, 21 and 23 January 2015) periods, whereas weekly samples were collected before bloom during regular monitoring program (24 December 2014; 12 January 2015) and those were considered as pre-bloom samples. Samples were analyzed for physicochemical parameters. Dissolved Oxygen (DO) was measured using Winkler's titrimetric method (Parsons et al., 1984). Salinity was estimated by Knudsen's argentometric titration (Grasshoff et al., 1983) and CyberScan PCD 5500 multi-parameter probe was used for measurement of pH (accuracy of ±0.01). Micro-nutrients such as nitrate, ammonia, silicate, phosphate, total Nitrogen (TN), and total phosphorus (TP) were estimated following standard methods of Grasshoff et al. (1983) and Parsons et al. (1984). Chl-*a* and phaeopigments were estimated by the spec-

trophotometric method of Parsons et al. (1984). Chemito Spectrascan UV 2600 spectrophotometer was used for all the spectrophotometric analyses. Utermohl's sedimentation technique (Vollenweider, 1974) was used for phytoplankton abundance estimation. The settled phytoplankton was counted using Sedgwick Rafter cell under an inverted research microscope (Zeiss Axiovert 40) using magnification up to 1000×. Phytoplankton was identified up to species level using taxonomic literature (Desikachary, 1987; Fristch, 1935; Subramanian, 1968, 1971; Tomas, 1996). The horizontal hauling method of zooplankton sample collection was adopted in the study using a conical zooplankton net (200 μm mesh size) fitted with the Hydro-Bios flow meter. 5% neutralized formaldehyde was used to preserve the zooplankton samples and then examined for quantitative and qualitative aspects using a zooplankton counting chamber at a magnification of 200× under an inverted microscope. Zooplankton identification (up to species level) was carried out using standard literature (Bradford-Grieve, 1994; Conway et al., 2003; Kasturirangan, 1963; Newell and Newell, 1967). The bigger individuals were counted separately after sorting them out from the sample. The zooplankton abundance was presented in terms of organisms 10 m<sup>-3</sup>. Zooplankton biomass, dry weight (g. dry wt. 10 m<sup>-3</sup>), was estimated after filtering through the plankton net (200 μm mesh size). The residuals were oven-dried for 24 h at 80°C, then stored for 2 hours in a desiccator at room temperature and weighted with a Sartorius analytical microbalance (±0.01 g accuracy).

Species diversity indices such as species diversity (D), species richness (R), and evenness (J) were estimated using the formulae of Gleason (1922), Shannon and Weaver (1963), and Pielou (1966), respectively. To get an insight into the interrelation between bloom and various physicochemical parameters, principal component analysis (PCA) and Pearson's correlation matrix analysis was performed by using XLSTAT Pro. Hierarchical cluster analysis (HCA) and non-metric multidimensional scaling (nMDS) were performed using PRIMER v6.0 (Plymouth Routines in Multivariate Ecological Research) to establish the relations between the phyto- and zooplankton species during different bloom phases. The potential relationships between the bloom and other biotic and abiotic parameters were assessed using BEST submodule BIOENV (biota-environment correlation analysis) of PRIMER v6.0 to explore (Clarke and Gorley, 2006). Pre-treatment of all data was carried out as required for the above analyses (Xu et al., 2008). To determine the spatial distribution of the *A. glacialis* bloom, satellite Chl-*a* and sea surface temperature (SST) images retrieved from NASA Moderate Resolution Imaging Sensor (Modis/Terra) were analyzed for the study period.

## 3. Results and discussion

### 3.1. Environmental variables

Relatively low water temperature was observed during the bloom period (26.1–27.4°C) as compared to pre-bloom (27.5–27.8°C) and post-bloom (27.6–28.2°C) periods (Table 1). To get a broader picture, the in situ temperature was compared with the satellite data. The near-shore

**Table 1** Summary of environmental variables observed during the *Asterionellopsis glacialis sensu lato* bloom in the coastal waters of Kalpakkam (Temperature – °C, Salinity – PSU, dissolved oxygen – mg l<sup>-1</sup>, nutrients (nitrate, ammonia, total nitrogen, phosphate, total phosphorus, silicate – μ mol l<sup>-1</sup>).

	Temp	pH	Salinity	DO	Nitrate	Phosphate	Ammonia	Silicate	TN	TP
<b>Pre-bloom period</b>										
24th Dec.	27.8	8.0	32.4	5.8	0.86	0.08	0.24	4.56	8.56	0.52
12th Jan. M	27.5	8.1	32.7	6.2	1.12	0.12	0.05	3.42	6.89	0.48
<b>Bloom period</b>										
14th Jan. M	27.2	7.9	32.6	7.1	1.18	0.07	0	3.90	7.06	1.64
17th Jan. M	26.2	7.7	32.8	7.2	1.32	0.75	0	3.45	40.26	7.03
17th Jan. AN	27.6	7.7	33.4	7.4	1.05	0.50	0	6.60	2.49	1.10
18th Jan. M	26.1	8.0	31.9	8.0	1.18	0.55	0	3.90	13.28	0.68
19th Jan. M	27.4	7.8	32.6	7.6	1.68	0.05	0	3.23	8.09	0.05
<b>Post-bloom period</b>										
20th Jan. M	28.2	8.0	32.8	6.1	1.53	0.21	0.12	3.75	9.52	0.72
21st Jan. M	27.9	8.1	33.7	5.7	1.24	0.18	0.05	3.59	8.67	0.42
23rd Jan. M	27.6	8.1	33.1	5.4	1.42	0.24	0.08	3.87	9.23	0.57

**Table 2** Correlation matrix (Pearson).

Variables	Temp	pH	DO	Phosphate	Silicate	TN	TP	<i>A. glacialis</i> density	Phyto density	Zoopl. density	Chl <i>a</i>
Temp.	<b>1</b>										
pH	0.378	<b>1</b>									
Salinity	0.530	-0.014									
DO	<b>-0.690</b>	<b>-0.687</b>	<b>1</b>								
Nitrate	0.046	-0.095	0.104								
Phosphate	<b>-0.697</b>	-0.506	0.456	<b>1</b>							
Ammonia	<b>0.550</b>	0.457	<b>-0.691</b>	-0.416							
Silicate	0.178	-0.395	0.151	0.251	<b>1</b>						
TN	<b>-0.658</b>	-0.391	0.202	<b>0.685</b>	-0.362	<b>1</b>					
TP	<b>-0.598</b>	<b>-0.575</b>	0.251	<b>0.708</b>	-0.114	<b>0.928</b>	<b>1</b>				
<i>A. glacialis</i> density	<b>-0.670</b>	<b>-0.618</b>	0.411	<b>0.599</b>	-0.123	<b>0.822</b>	<b>0.939</b>	<b>1</b>			
Phyto density	<b>-0.745</b>	<b>-0.664</b>	<b>0.542</b>	<b>0.618</b>	-0.103	<b>0.786</b>	<b>0.895</b>	<b>0.987</b>	<b>1</b>		
Zoopl. density	-0.159	<b>-0.675</b>	<b>0.558</b>	<b>0.552</b>	<b>0.776</b>	-0.066	0.119	0.130	0.198	<b>1</b>	
Chl- <i>a</i>	<b>-0.570</b>	<b>-0.592</b>	0.258	<b>0.627</b>	-0.131	<b>0.892</b>	<b>0.990</b>	<b>0.963</b>	<b>0.919</b>	0.098	<b>1</b>
Phaeopigments	<b>-0.583</b>	-0.603	0.275	<b>0.670</b>	-0.074	<b>0.883</b>	<b>0.989</b>	<b>0.963</b>	<b>0.922</b>	0.156	<b>0.997</b>

Values in bold are significantly different from 0 with a significance level alpha=0.1 (variables which developed significant correlations only are given in the table).

waters of the north Tamil Nadu coast showed a relatively low SST, about 0.8 to 1.2°C lower than that of the offshore regions (Figure 2a–b), indicating the upwelling process is taking place in the coastal zone during this season. Many workers have reported coastal upwelling during pre-SWM and SWM along the east coast of India (La Fond, 1957, 1958; Murty and Varadachari, 1968). The cooling of water along the south Andhra coast and north Tamil Nadu coast was suggested as the factor responsible for algal bloom formation in this region (Mishra et al., 2006). The 3-day composite image of SST during January 14–16<sup>th</sup>, 2015, showed lower values (range: 25–26°C) in the coastal waters than in the non-blooming offshore water mass (≥26.5–28°C). Moreover, a negative correlation ( $r = -0.670$ ;  $p = 0.03$ ) in between *A. glacialis* abundance and temperature (Table 2) indicated the association of the bloom with upwelling. The concentration of DO was also relatively high during the bloom

period, and it showed a positive correlation ( $r = 0.542$ ;  $p = 0.09$ ) with phytoplankton abundance. Similarly, the DO contents increased during the blooms of *Noctiluca* (Sargunam et al., 1989) and *Asterionella* (Choudhury and Panigrahy, 1989; Gouda and Panigrahy, 1990; Mishra et al., 2006; Misra and Panigrahy, 1995; Sasmal et al., 2005), although severe Oxygen depletion has also been recorded (1.25 ml l<sup>-1</sup>) during *Noctiluca* bloom reported from southwestern India coast (Naqvi et al., 1998). Nitrogen and Phosphorus released from the algal biomass during bloom lead to the observation of relatively high values of these nutrients during the peak bloom phase (Table 1). The above observation was supported by strong positive correlations of TN and TP with the abundance of phytoplankton and pigment concentrations ( $p = 0.0001$ ). Similar observations of an increase in phosphate concentration have been reported during phytoplankton blooms from various Indian

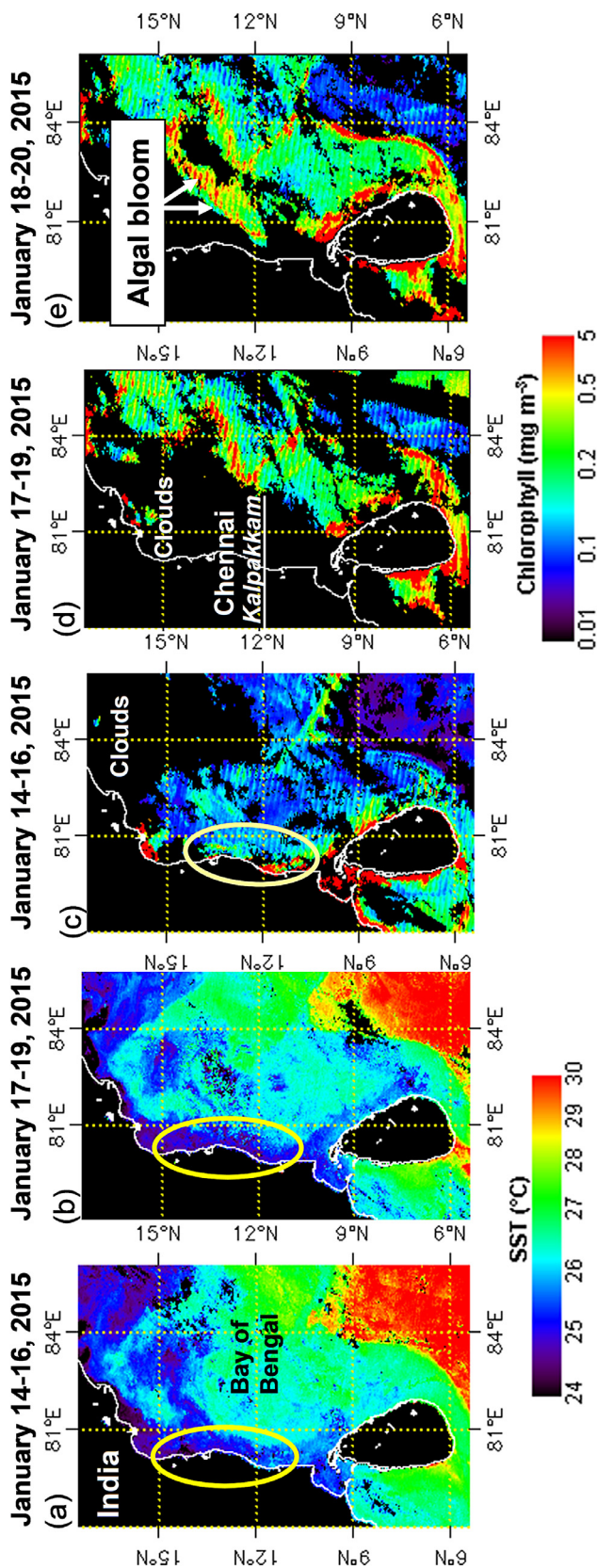


Figure 2 NASA MODIS-Terra satellite sensors derived 3-day composite images of SST (a–b) indicate the cooling zones and chlorophyll images (c–e) reflect the phytoplankton bloom water along southwest Bay of Bengal.

coastal waters (Dharani et al., 2004; Raghuprasad and Jayaraman, 1954; Sahayak et al., 2005; Satpathy and Nair, 1996). Though silicate is used by diatoms to synthesize the siliceous frustules, visible variation in concentrations of silicate during this study was not observed. Silicate, being one of the most important nutrients, regulates the growth of diatoms and ultimately phytoplankton blooms, as it gets depleted during the bloom occurrence (Choudhury and Panigrahy, 1989; Gouda and Panigrahy, 1990; Mishra et al., 2006; Mishra and Panigrahy, 1995; Rao, 1969; Sasmal et al., 2005). In contrast, silicate increased during dinoflagellate and cyanobacteria blooms reported from BOB (Dharani et al., 2004; Raghuprasad and Jayaraman, 1954; Sargunam, 1989; Satpathy et al., 2007).

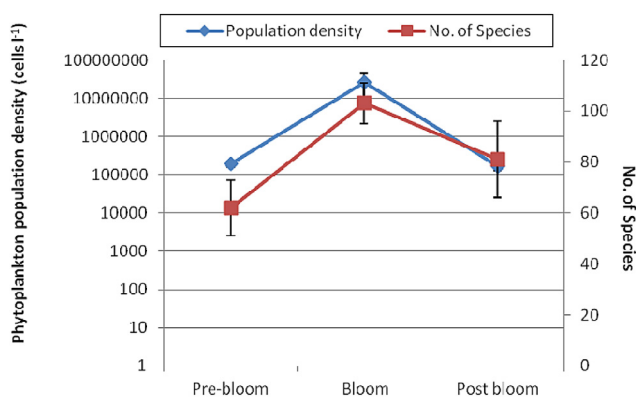
The highest Chl-*a* content ( $15.99 \text{ mg m}^{-3}$ ) was recorded on 17<sup>th</sup> January (Table 3), coinciding with the highest phytoplankton abundance. However, on 18<sup>th</sup> and 19<sup>th</sup> January the abundance was still high, although the Chl-*a* concentration decreased significantly. It suggested that the exponential growth phase of the bloom had already passed during its observation and it was in the waning phase. Further, relatively high phaeopigment concentrations observed during the bloom period depicted that bloom biomass was declining. Similar observations of the rapid disappearance of blooms from the coastal water of India have also been reported (Mishra et al., 2006; Mohanty et al., 2010; Satpathy et al., 2007). Chl-*a*, as well as phaeopigments, showed strong positive correlations ( $p=0.0001$ ) with the phytoplankton abundance during the study. The satellite Chl-*a* images indicated three types of water mass (Figure 2c–e): (i) patches with red and yellow color, where the concentration of Chl-*a* was  $0.30\text{--}5.0 \text{ mg m}^{-3}$  indicated the presence of a highly eutrophic/bloom water mass, (ii) green patches with Chl-*a* concentration of  $0.1\text{--}0.3 \text{ mg m}^{-3}$  indicated the presence of non-bloom but eutrophic/productive water mass and (iii) cyan and blue color patches with Chl-*a* concentration:  $0.01\text{--}0.10 \text{ mg m}^{-3}$  characterized a low productive/oligotrophic water mass. Composite satellite images for Chl-*a* for 14–16<sup>th</sup> January 2015 showed that its concentration was relatively high along the southern Andhra Pradesh coast and northern Tamil Nadu waters. It indicated that the bloom was extended to a broad region (Figure 2c). In situ values of chlorophyll measured in the study corroborated with values obtained from satellite images. During the post-bloom period, the absence of the bloom in the coastal waters and distribution of irregular stripes of bloom biomass in the off-shore regions of the study area was noticed from the combined images of 17–20<sup>th</sup> January (Figure 2d–e).

### 3.2. Phytoplankton composition

Based on the concentration of *A. glacialis* (Table 3), the period of observation was divided into 3 phases, pre-bloom (December 2014–early January 2015), bloom (14<sup>th</sup> January–21<sup>st</sup> January 2015), and post-bloom (January end–early February 2015). A total of 120 species consisting of: 105 diatoms (Phylum: Ochrophyta, Class: Bacillariophyceae) – 38 Pennate diatoms (Order: Pennales) and 67 Centric diatoms, (Order: Centrales), 12 dinoflagellates (Phylum: Dinoflagellata), two cyanobacteria (Phylum: Cyanobacteria; Class: Cyanophyceae) and one chlorophyta (Phylum: Chlorophyta) were observed, with the remarkable difference be-

**Table 3** Summary of plankton dynamics observed during the *Asterionellopsis glacialis* bloom in the coastal waters of Kalpakkam.

	<i>A. glacialis</i> cells L <sup>-1</sup>	Phytoplankton cells L <sup>-1</sup>	Zooplankton cells L <sup>-1</sup>	Chl <i>a</i> mg m <sup>-3</sup>	Phaeopigments mg m <sup>-3</sup>
<b>Pre-bloom period</b>					
4th Dec	15600	215000	46890	1.98	2.64
12th Jan M	21566	168500	42055	2.15	2.42
<b>Bloom period</b>					
14th Jan M	29513333	33926667	52604	5.87	7.83
17th Jan M	56284000	57956000	59198	15.99	21.59
17th Jan AN	7386667	11406667	90180	3.21	5.2
18 Jan M	8006667	16633333	62792	1.54	2.67
19th Jan M	2153333	8479999	57475	1.54	1.29
<b>Post-bloom period</b>					
20th Jan M	24400	154533	53406	1.89	2.35
21st Jan M	18444	137460	56410	2.25	3.46
23rd Jan M	21040	204500	48950	1.68	1.97

**Figure 3** Population density and number of species of phytoplankton during different phases of bloom.

tween the three phases. The bloom phytoplankton assemblage was floristically richer (103 species) compared to the pre-bloom (62 species) and post-bloom period (81 species) (Figure 3). HCA and nMDS analysis for the phytoplankton community structure during the three phases of bloom developed seven phytoplankton groups (Figure 4–5). These groups were characterized by the presence of phytoplankton species exclusively during pre-bloom (4 species), bloom (5 species), post-bloom (9 species), pre-bloom+bloom (31 species), pre-bloom+post-bloom (5 species), bloom+post-bloom (45 species) and pre-bloom+bloom+post-bloom (22 species). These combinations showed that most of the species which thrived during the bloom period survived the impact of the bloom. Interestingly, the highest number of exclusive phytoplankton species were observed to be present during post-bloom observations (9 species). The above observations showed that the bloom had influenced the phytoplankton dynamics at the Kalpakkam coast. Out of the 22 species of phytoplankton found throughout the study, *Bacteriastrium delicatulum*, *Biddulphia heteroceros*, *B. iddulphia mobilensis*, *B. iddulphia sinensis*, *Chaetoceros curvisetus*, *Chaetoceros lorenzianus*, *Chaetoceros socialis*, *Nitzschia panduriformis*, *Pleurosigma formosum* and *Skele-*

*tonema costatum* contributed significantly to the abundance during all three periods. The above species are common in tropical coastal waters and are available throughout the year (Achary et al., 2014; Sahu et al., 2013). Scrutiny of data showed that the number of both Pennales (pre-bloom – 17; post-bloom – 26) and Centrales (pre-bloom – 36; post-bloom – 45) increased from pre-bloom to post-bloom period. Others gave similar increased species numbers during *A. glacialis* bloom (Mishra et al., 2006; Mishra and Panigrahy, 1995) and bloom of other phytoplankton species (Mohanty et al., 2010; Satpathy et al., 2007). Similarly, the number of Dinoflagellata species increased from 5 during the pre-bloom period to 9 during bloom, and subsequently, it decreased to 7. It indicated that Dinoflagellata, which are generally abundant in oligotrophic oceanic waters, could have been transported to the coastal waters by current and circulation patterns (Sahu et al., 2014).

The abundance of *A. glacialis* with respect to total phytoplankton is depicted in Figure 6. The total phytoplankton abundance (cells L<sup>-1</sup>) showed a sharp increase from  $1.6 \times 10^5$  to  $5.7 \times 10^7$  during different bloom phases. The numerical abundance of phytoplankton was found to be the highest when the *A. glacialis* reached the bloom phase, with 97.1% contribution to the total phytoplankton population. The lowest abundance was observed in December 2014, when the *A. glacialis* population was only about 10% of the phytoplankton cells. The abundance grew rapidly during the bloom period and declined from January end onwards. A vigorous multiplication of *A. glacialis* was noticed from 14<sup>th</sup> January to 21<sup>st</sup> January 2015 and during this period, its contribution to total abundance was about 64.5%. The abundance of other phytoplankters was found sporadically. Such a monospecific bloom of *A. glacialis* has been already reported along the Visakhapatnam coast (Rao, 1969), off Gopalpur (Choudhury and Panigrahy 1989; Mishra et al. 2006). The relative abundance of other species during the pre-bloom period was about 90%, which declined to 2.9% during the peak bloom. The contribution of other species increased from the end of January 2015 and was found to be ~86.8%.

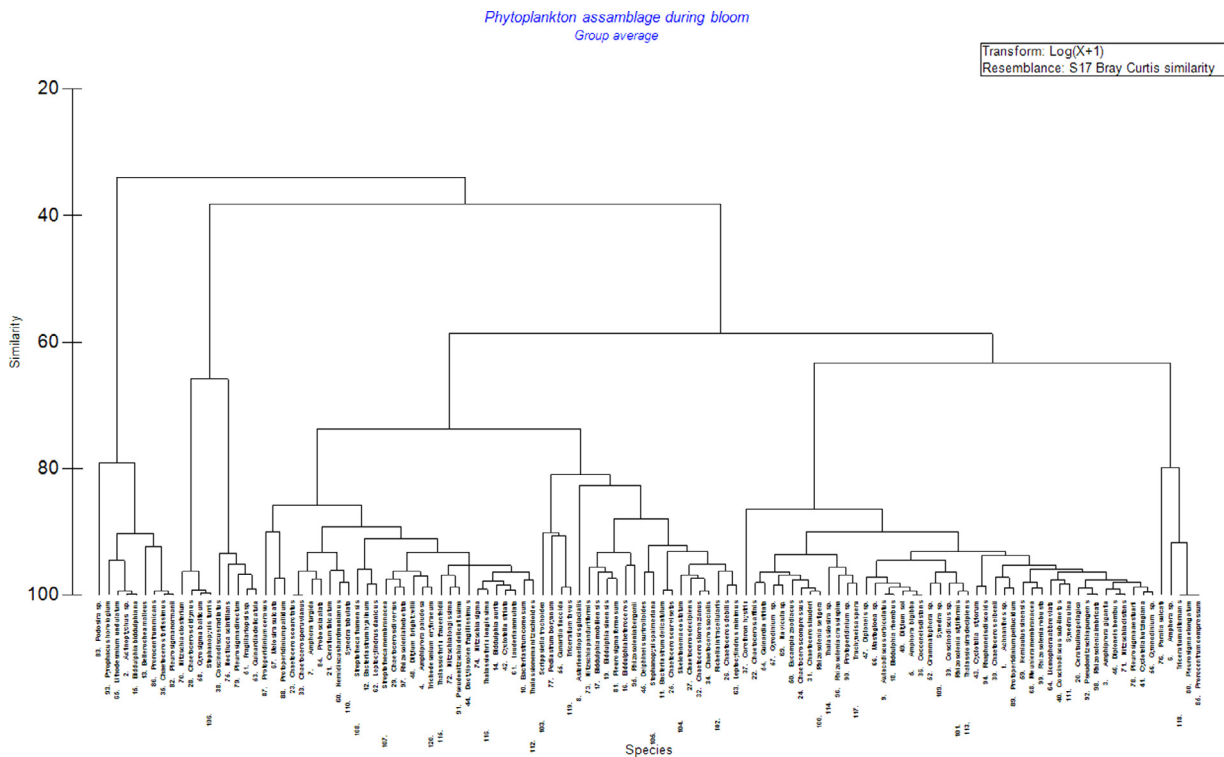


**Figure 4** Hierarchical cluster analysis of phytoplankton species abundance during the study period (numerical digit given against each species is serial number of the species).

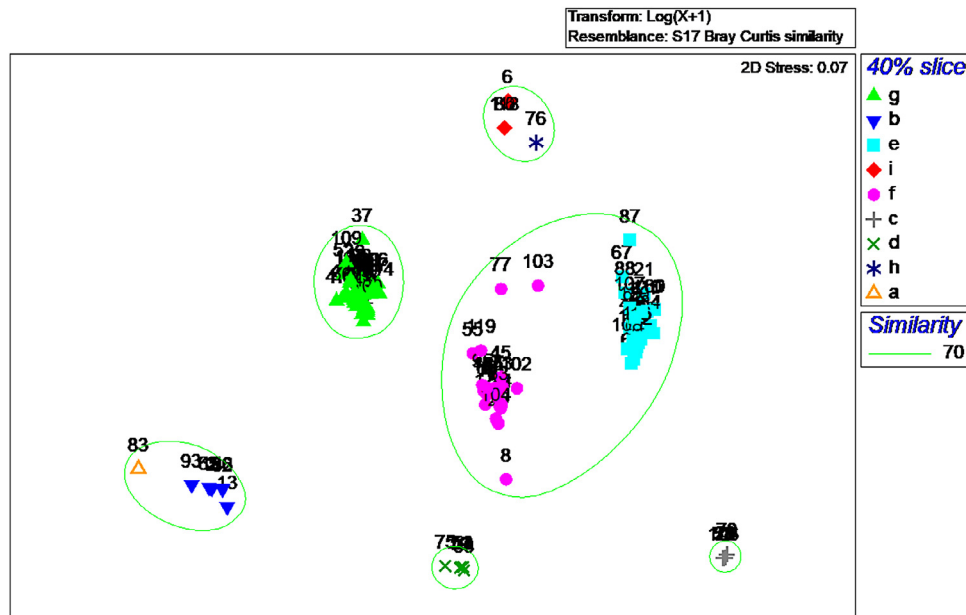


**Figure 5** Non-metric multidimensional scaling (nMDS) of phytoplankton species showing the species associations (numerical digits represent the species serial numbers as given in Figure 4).

### 3.3. Zooplankton composition

Phytoplankton bloom has long been known to change the aquatic ecosystem drastically with respect to physicochemical and biological properties (Landsberg, 2002; Shumway, 1990; Smayda, 1989). It has been reported that

nutrients enrichment in the coastal water takes place in this region due to monsoon precipitation, which leads to spring outbursts of phytoplankton that subsequently affects the zooplankton composition and distribution (Padmavati and Goswami, 1996; Satpathy and Nair, 1996). Zooplankton community in this study comprised of 67 taxa out of which 57



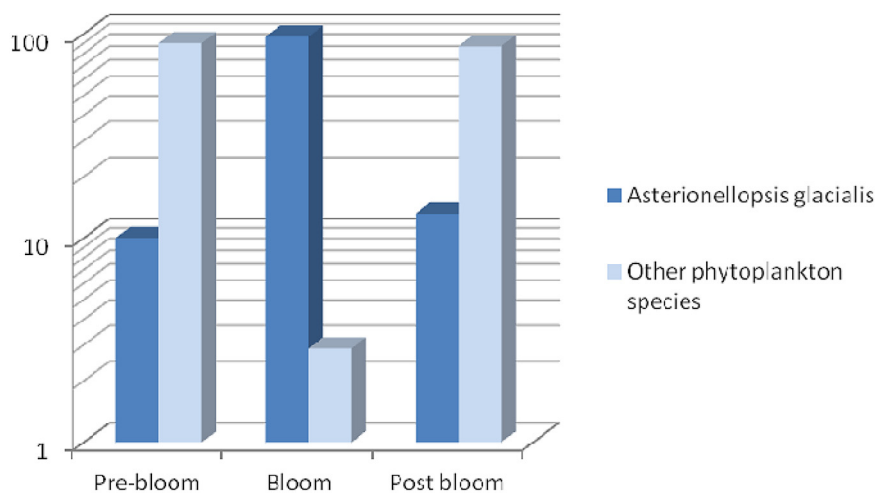


**Figure 6** Relative abundance of *Asterionellopsis glacialis* and other phytoplankters in coastal waters of Kalpakkam during different phases of bloom.

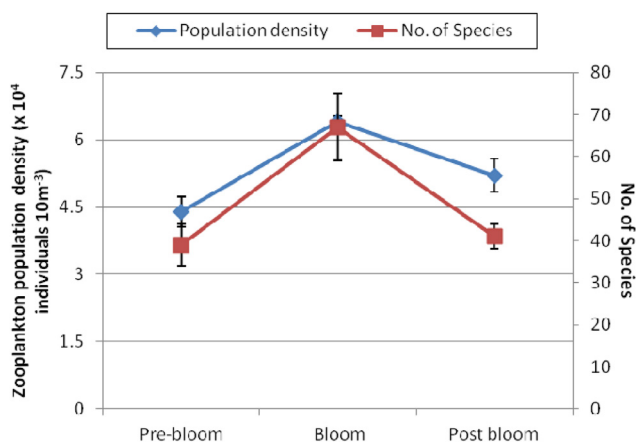


**Figure 7** Population density and number of species of zooplankton during different period of bloom.

were identified (39 holoplankters, 13 meroplankters, five benthopelagic forms), with Copepoda the dominant component including 24 species, followed by 15 non-copepod holoplankton (NCH). The highest number of Copepoda species (24) coincided with the peak bloom followed by pre-bloom (13) and post-bloom (10) observations. In general, a relatively high number of zooplankters species was observed during the bloom phase (Figure 7), as it was already observed during a *Trichodesmium erythraeum* bloom at Kalpakkam coastal waters (Sahu et al., 2015). Copepod nauplii and Copepodites, i.e., juveniles of various copepod groups (Calanoida, Cyclopoida, and Harpacticoida) were recorded during all three periods, and ovigerous females of *Oithona rigida*, *Oithona similis*, *Pseudodiaptomus serri-caudatus*, and *Euterpina acutifrons* were commonly found. Zooplankton of pre-bloom and post-bloom periods was represented mainly by *Bestiolina similis*, *Paracalanus parvus*, *Oithona rigida*, *Centropages tenuiremis*, among Copepoda, and Gastropoda and Polychaeta larvae and fish eggs among meroplankton. During the peak bloom period, meroplankters (Cirripedia nauplii, Bivalvia larvae), Copepoda (*Besti-*

*olina similis*, *Oithona* spp.) and the Appendicularia *Oikopleura dioeca* were the most common forms. The HCA and nMDS analyses showed zooplankton assemblage was different in terms of species richness than the phytoplankton assemblage. Zooplankton taxa were organized into four groups (Figure 8–9) viz., common taxa occurred during all three phases of bloom (23), bloom and post-bloom (15), bloom and pre-bloom (12) and exclusively in the bloom period (12). No species were found to be present exclusively during the pre-bloom, post-bloom and pre-bloom+post-bloom period. The above analysis indicated that the zooplankton species present during the pre-bloom thrived well in addition to a few more species, especially the meroplankton, added during the bloom period. On the other hand, it also indicated no drastic change in zooplankton species succession in the post-bloom phase, as there were no new species found in the post-bloom period.

Zooplankton abundance increased during the bloom period ( $6.4 \times 10^4$  individuals  $10\text{m}^{-3}$ ) compared to the pre-bloom ( $4.4 \times 10^4$  individuals  $10\text{m}^{-3}$ ) and post-bloom ( $5.2 \times 10^4$  individuals  $10\text{m}^{-3}$ ) periods (Figure 7). However, the contribution of Copepoda was the lowest during the bloom (~31%) and relatively high during pre-bloom (~68.5%) and post-bloom (~48.9%) periods (Figure 10). Among Copepoda, Calanoida were dominant (avg. 20% of the total zooplankton population), especially with species of the families Paracalanidae and Acrocalanidae, contributing respectively with ~7% and ~9% to the zooplankton assemblage during the peak bloom period, when Cyclopoida and Poecilostomatoida (~19.5%) exceeded the Calanoida (~17%). Calanoida are the most abundant Copepoda in the world Ocean, and the observed decrease in their abundance could be due to predation by Cyclopoida and Poecilostomatoida. The highest zooplankton abundance during the bloom period was associated with meroplankters, especially Cirripedia nauplii and Bivalvia larvae. Among meroplanktonic components, Cirripedia nauplius, Bivalvia larva, and Gastropoda larva contributed 25%, 14.5%, and 6% of meroplankton density respectively during the bloom period. A subsequent decrease in their abundance was observed during the post-bloom period (Cirripedia nauplius – 17%, Bivalvia larva

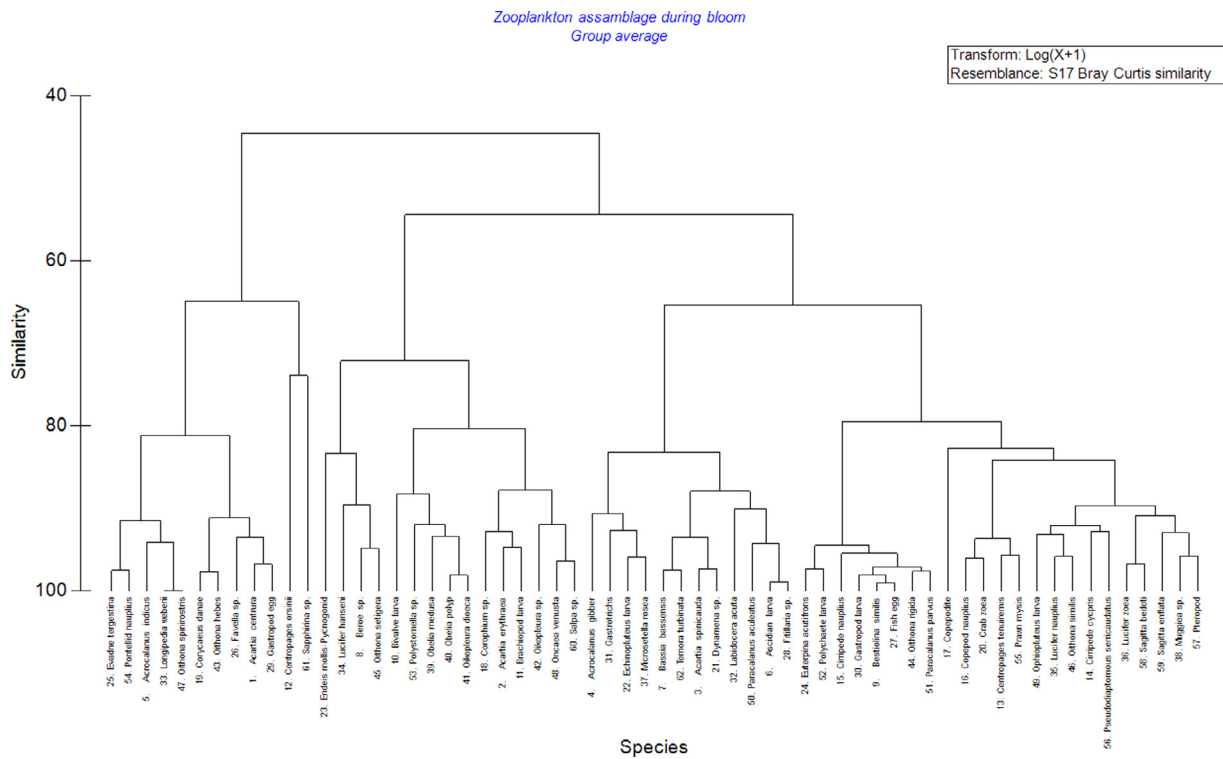


**Figure 8** Hierarchical cluster analysis of zooplankton species abundance during the study period (numerical digit given against each species is serial number of the species).

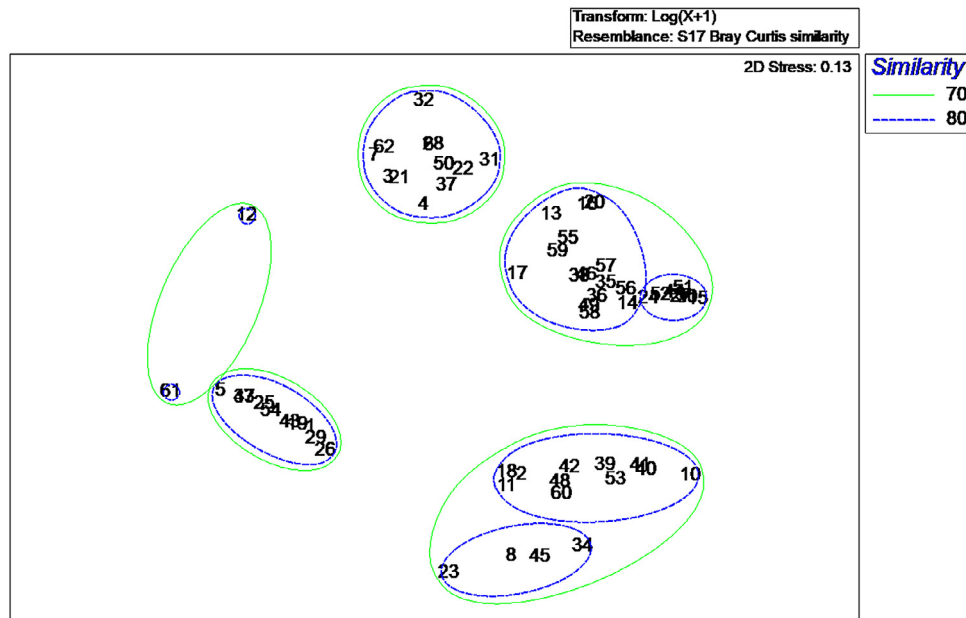


**Figure 9** Non-metric multidimensional scaling (nMDS) of zooplankton species showing the species associations (numerical digits represent the species serial numbers as given in Figure 8).

– 10.5%, and Gastropoda larva – 4%). The present study area, with sporadic reefs and power plant-related marine structures, harbors a sizable population of barnacles (sessile Cirripedia) and Bivalvia. The larvae of the localized population of barnacles and bivalves thrived well during the above period as the blooming species *A. glacialis* could have served as the principal food source. Moreover, the in-

creased reproductive capacity of adults during the availability of plenty of food could be another probable cause for the observed increased density of cirripede nauplii during the bloom and post-bloom periods. Naupliar release in barnacles coinciding with phytoplankton blooms have been reported by Barnes (1962) and Starr et al. (1991), and a similar reproduction behavior for urchins and mussels has also

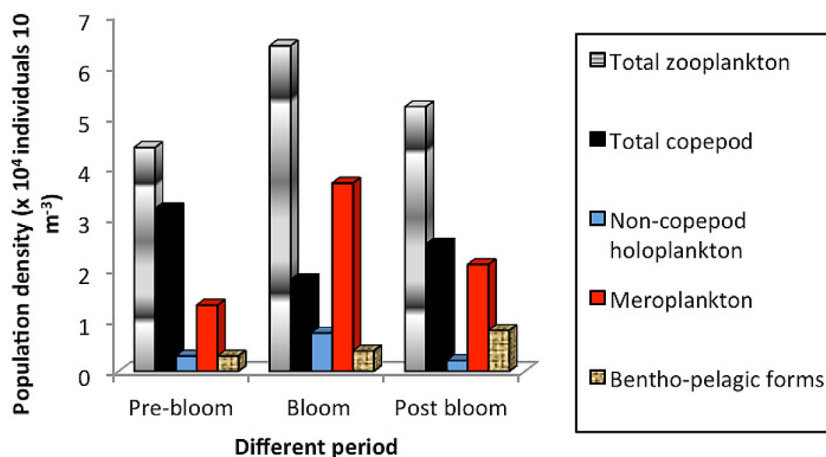


Figure 10 Population density of different groups of zooplankton during the study period.

been observed. Meroplankton showed its highest dominance during the peak bloom period. Fish eggs and larvae were available in substantial numbers during the bloom which indicated their proliferation in diatom standing stock as the food material (Padmakumar et al., 2010). Among NCH, major forms were *Oikopleura dioeca*, *Lucifer hansenii*, and *Sagitta bedoti*, etc. which all together contributed ~9–10% of the zooplankton assemblage.

The present study was compared with an event of *Trichodesmium* bloom from the same coastal area to find out any similarities or dissimilarities with respect to zooplankton community structure during the blooms. Although *Asterionellopsis glacialis* (Phylum: Ochrophyta; Class: Bacillariophyceae) and *Trichodesmium* (Phylum: Cyanobacteria) are not in the same group of phytoplankton, their blooming creates almost similar kind of environment in the coastal milieu, where qualitative aspects (number of species) of zooplankton showed relatively comparable trends. In the present study, during the peak bloom period, *Bestiolina similis* and *Oithona* spp. were very commonly found in the Copepoda community, whereas, during *Trichodesmium erythraeum* bloom (Sahu et al., 2015), *Canthocalanus pauper*, *Parvocalanus crassirostris*, *Pseudodiaptomus serricaudatus*, *Temora turbinata*, *Labidocera pavo*, *Pontellopsis scotti*, *Pontella securifer*, *Oithona hebes* were the common forms in Copepoda. Meroplankton population showed Cirripedia nauplii, Gastropoda larvae and Bivalvia larvae were the commonly occurring forms during *A. glacialis* bloom, which is comparable with Sahu et al. (2015), where a unique grouping of various crustacean meroplankters (nauplius, protozoa, post-zoea, mysis, etc.), Bivalvia veliger larvae, Polychaeta larvae and Cirripedia nauplii was reported. However, Echinodermata larva was the meroplankton form that appeared exclusively during the peak bloom period of *T. erythraeum* and neither in pre-bloom nor in the post-bloom period the same has appeared. In non-Copepoda holoplanktonic group, *Oikopleura dioeca* was frequently observed form during the bloom phase in the present study, which is the dominant form during *Trichodesmium* bloom (Sahu et al., 2015) also along with *Sagitta* sp. and two Cladocera species i.e., *Penilia avirostris* and *Evadne tergestina*. These above-

mentioned comparisons between two bloom periods from the same location signify the prevalence of similar coastal water quality caused due to such bloom events.

Zooplankton ( $\text{g } 10 \text{ m}^{-3}$  dry weights) biomass, which ranged from 0.35–0.62, exhibited almost the same variation trend as population density. The observed lowest value during the pre-bloom period coincided with the lowest abundance of zooplankton and the highest biomass during the bloom period could be ascribed to the overwhelming abundance of cirripede nauplii and bivalve larvae. Previous literature, on the contrary, showed phytoplankton proliferation during the post-monsoon period leading to the observation of higher zooplankton biomass in the near-shore region of SW-BOB (Sahu et al., 2013).

#### 4. Diversity indices

Measurement of the relationship between qualitative and quantitative numbers of a community is known as species diversity. It is known to be low in a physically controlled system (Odum, 1971). Variations in species diversity indices in the present study indicated the change in phytoplankton and zooplankton community structure during different bloom phases. The phytoplankton diversity presented maximum values during the bloom period (4.87) and the lowest (1.05) during the pre-bloom period. The values of species richness and evenness were in tune with phytoplankton species diversity: the lowest (0.07) and highest (3.21) species richness was observed respectively during the pre-bloom and bloom period; evenness values remained low (0.08) during the pre-bloom period, and maximum (0.9) during the bloom period. Similarly, zooplankton diversity (3.1) and richness (2.8) were highest during the peak bloom period and lowest (2.1 and 1.4, respectively) during the post-bloom period. A steady trend was observed for Evenness values throughout the study, and it ranged from 0.3–0.6. This was in tandem with the number of species and population abundance, i.e., essentially due to the abundance of Copepoda such as, Cyclopoida and Poecilostomatoida and meroplankton such as Bivalvia larva and Cirripedia nauplius.

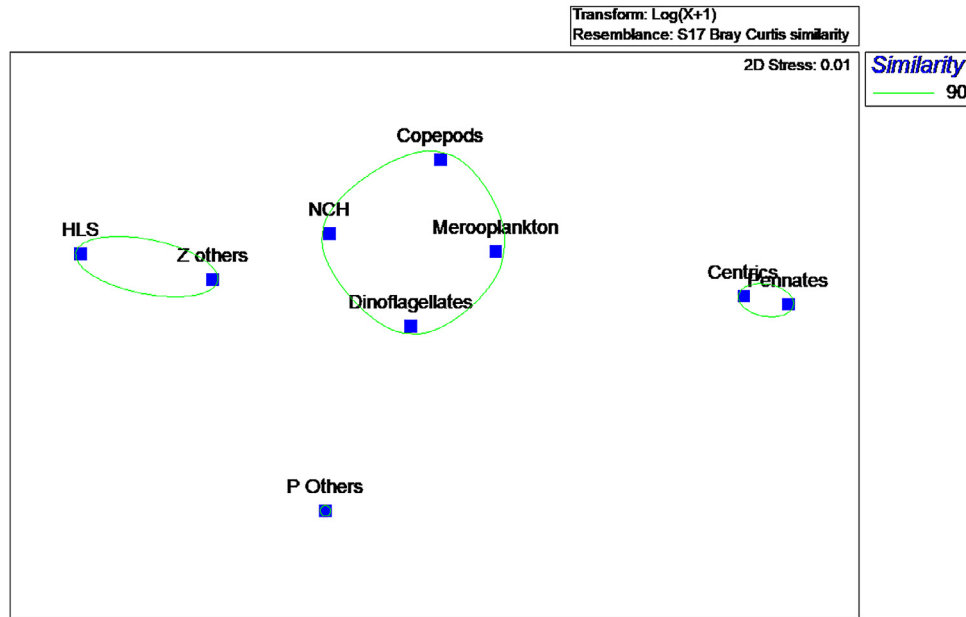


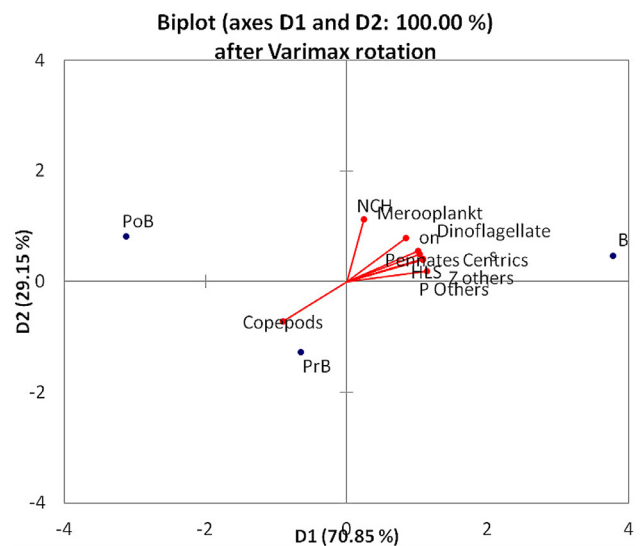
**Figure 11** Non-metric multidimensional scaling (nMDS) showing the interrelation between phytoplankton and zooplankton groups during the study.

### 5. Interrelations between phyto- and zooplankton groups

For assessing the interrelation between phytoplankton and zooplankton during the study, both were segregated into groups. Phytoplankton species were grouped into centric diatoms (Order: Centrales), pennate diatoms (Order: Pennales), Dinoflagellata, others (Cyanobacteria, Chlorophyta, etc.). Similarly, zooplankton species were grouped as Copepoda, meroplankton, non-copepod holoplankton (NCH), holoplankton larval stages (HLS), and others (Gastrotricha, Polystomella – Phylum: Protozoa, Class: Rhizopoda; Obelia – Phylum: Cnidaria, Class: Hydrozoa, etc.). The nMDS analysis with cluster overlay (Figure 11) showed a distinct pattern. Centric (Order: Centrales) and Pennate (Order: Pennales) diatoms were clubbed together indicating their co-occurrence during the study period. Copepoda, meroplankton, Dinoflagellata, and NCH which were encountered with relatively high diversity during the bloom, formed a separate group. HLS and other zooplankton formed a separate group which was commonly observed throughout the study period. With respect to quantitative aspects, the factor plane distribution of plankton groups in the PCA with Varimax rotation showed the overall impact of the bloom on the plankton community. It was observed that Copepoda that contributed significantly (~68.5%) to the zooplankton abundance during the pre-bloom period were negatively loaded on PC1 as well as PC2 (Figure 12). All the other groups of phyto- and zooplankton were positively loaded on both the PCs, which indicated the general increase in abundances of all these groups during the bloom period.

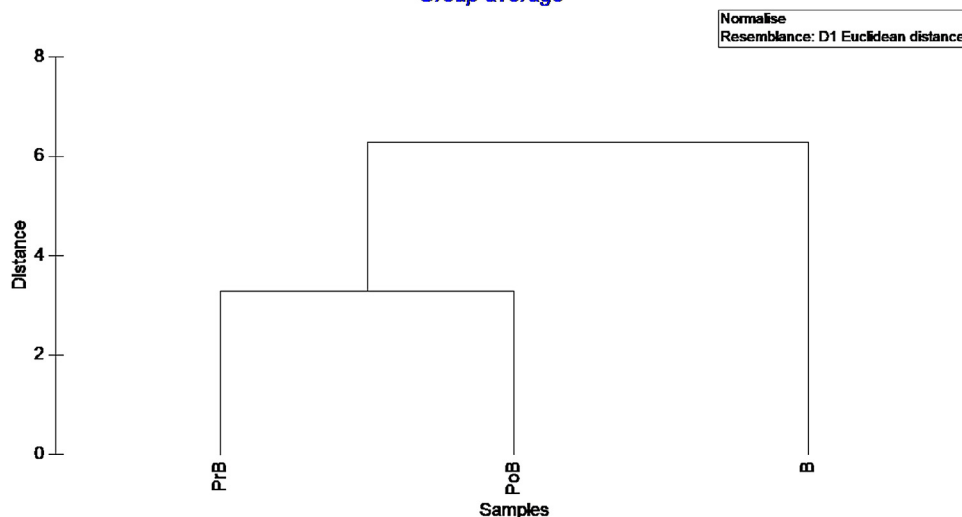
#### 5.1. Classification of bloom periods

Cluster analysis carried out for water quality characteristics supported the observation of temporary change in coastal

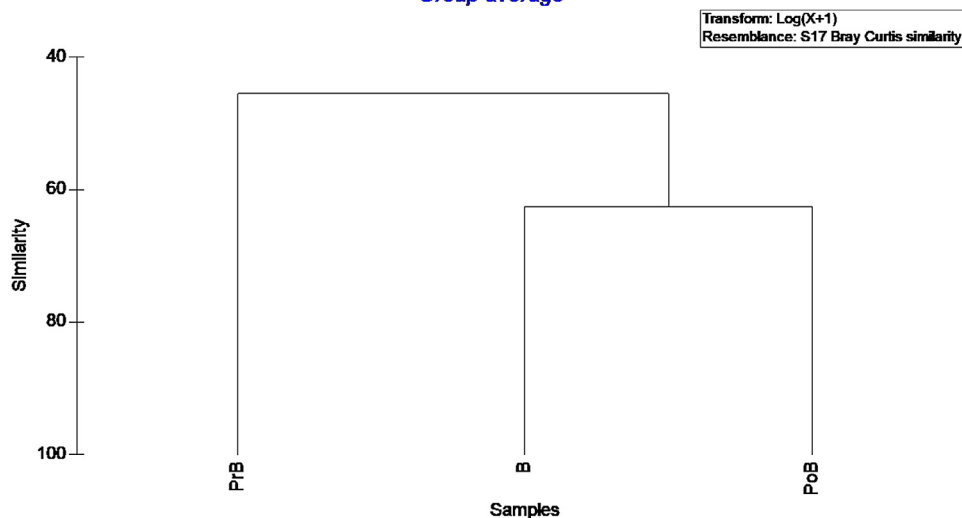


**Figure 12** PCA ordination with Varimax rotation, showing the overall impact of the bloom on the plankton community (phyto- and zooplankton are given in groups).

water characteristics during the bloom period (Figure 13). It showed that the bloom period alone formed a separate cluster whereas; pre- and post-bloom periods formed the other cluster. It can be inferred from the above that either the bloom had altered the physicochemical properties of coastal water or the entire coastal water mass carrying the bloom was drifting along the coast during the observation. The sharp changes in water quality and plankton community structure during the bloom phase indicated the second hypothesis. Similar observations of sudden appearance and disappearance of blooms have been attributed to the drifting water mass that carried the bloom along with it (Mohanty et al., 2010; Satpathy et al., 2007).

**Classification of bloom periods with respect to physico-chemical parameters***Group average*

**Figure 13** Classification of bloom periods with respect to physico-chemical parameters showing the changes in coastal water characteristics during the bloom.

**Classification of bloom periods with respect to Phyto- and Zoo-plankton dynamics***Group average*

**Figure 14** Classification of bloom periods with respect to phyto- and zooplankton dynamics observed during the bloom.

Cluster analysis with respect to phyto- and zooplankton dynamics during the three phases of bloom developed two clusters. Unlike the classification of bloom phases concerning physicochemical parameters, where the bloom period was observed to be a separate entity, the pre-bloom period was found to be different from the other two periods in this case (Figure 14). The bloom and post-bloom periods were more similar to each other with respect to the commonness in species between these two periods. The above observation attributed to the fact that 45 phytoplankton species and 15 species of zooplankton were common between bloom and post-bloom period (Figures 4 and 8), which are the highest among all the combinations possible among the three phases of bloom, except common species found during all the phases.

## 5.2. Interrelations between bloom and other parameters

Multivariate statistical analyses are considered to be more useful for detecting the variations in complicated data containing biotic and abiotic variables. The usefulness of multivariate analyses to analyze spatiotemporal variations between communities and their variations with changing ecological and climatic conditions has been depicted by various authors (Hourston et al., 2009; Jiang et al., 2011a,b, 2012; Kim et al., 2007; Xu et al., 2011a,b,c). Biota-environment (BIOENV) analysis was carried out to find the correlations between phytoplankton abundances and environmental variables observed during the bloom period (Table 4). The BIOENV analysis aims to select a set of abiotic param-

**Table 4** The best results.

No.	Vars	Corr. Selections
1	1.000	Nitrate
2	1.000	Salinity, Phosphate
2	1.000	Salinity, Ammonia
2	1.000	Salinity, Zooplankton
3	1.000	Salinity, nitrate, Phosphate
3	1.000	Salinity, Nitrate, Ammonia
3	1.000	Salinity, Nitrate, TN
3	1.000	Salinity, Nitrate, Zooplankton
4	1.000	Temperature, Salinity, Nitrate, Phosphate
4	1.000	Temperature, Salinity, Nitrate, Ammonia

eters that significantly impact the distribution patterns of phytoplankton groups in the community. The BIOENV test was carried out by maximizing the Spearman rank correlation between the resemblance matrices of environmental and biotic variables (Euclidean distance) and community abundances (Bray-Curtis distance) (Izquierdo and Guerra-García, 2010). Results of BIOENV analysis (with maximum ten variable combinations) confirmed that a set of variables, such as salinity, nitrate, phosphate, ammonia, zooplankton, TN, and temperature, is related to the *A. glacialis* abundance. Even though ten variable combinations were chosen for BEST analysis, the results were truncated at a maximum of four parameters combination, indicating that all the studied parameters were not important with respect to the bloom formation. Salinity and/or nitrate seems to have played important roles in the proliferation of *A. glacialis* or the bloom formation as these were the only two parameters found in all the combinations of BEST results which has also been reported by others (Baliarsingh et al., 2016; Srichandan et al., 2019) as the controlling factor of blooms.

Principal component analysis for both planktonic and environmental variables yielded two PCs. These two PCs contributed to 100% of the variance and indicated that the state of the coastal environment during the study could be divided broadly into two periods. The PC1, which contributed 81.77% of the variance, represented the bloom and post-bloom period with significant positive/negative factor loadings of all the variables except salinity and nitrate (Figure 15). The second PC was positively loaded with salinity and nitrate, representing the pre-bloom period. Thus, PCA results indicated a change in salinity and nitrate that mainly influenced the bloom formation in the coastal waters. The above observations corroborated the results of BIOENV results.

## 6. Conclusion

Optimum temperature, salinity, and nutrient levels prevailed during the post-northeast monsoon period, led to the appearance of *A. glacialis* bloom in the coastal waters of Kalpakkam. Results of BIOENV analysis and PCA confirmed that salinity and/or nitrate played important roles in the proliferation of *A. glacialis* or the bloom formation. Cluster analysis further supported the distinct state of coastal wa-

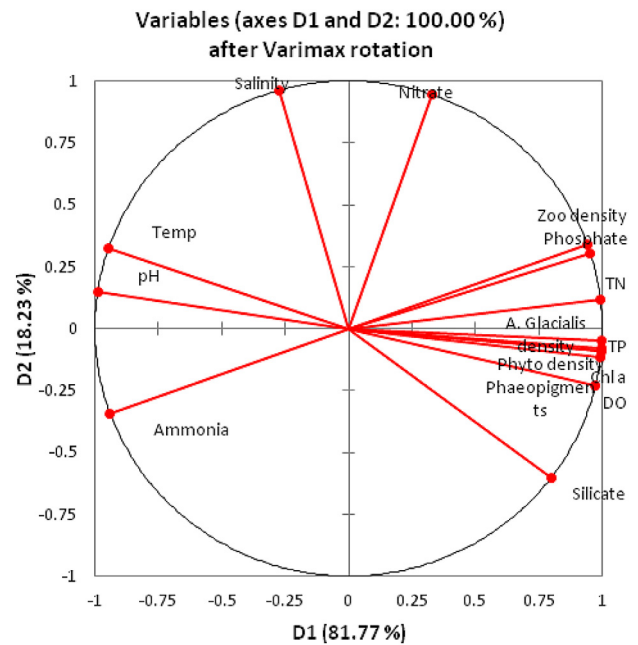


**Figure 15** PCA ordination with vectors for both planktonic and environmental variables indicating the probable cause of bloom in the coastal waters.

ter during the bloom pertaining to physicochemical properties. The cluster and nMDS analysis confirmed a considerable impact of the bloom on the plankton dynamics in the coastal waters of Kalpakkam. The peak bloom period was characterized by the dominance of meroplankters especially, Cirripedia nauplii and Bivalvia larvae over Copepoda. Among Copepoda, Cyclopoida and Poecilostomatoida (mostly carnivorous) exceeded the Calanoida population (mostly herbivorous) during the peak bloom period. The observations were supported by the PCA ordination plot for the quantitative aspects of phytoplankton and zooplankton groups. Such alterations in the plankton community structure could be attributed to the intra- and inter-community interactions of plankton assemblages in the ambiance. Coastal waters thus demand continuous monitoring to find out the impact of such phenomenon and its relation to alteration in the ecosystem either due to natural processes or anthropogenic activities.

## Declaration of competing interest

The authors declare that there is no conflict of interest in this manuscript.

## References

Achary, M.S., Panigrahi, S., Satpathy, K.K., Sahu, G., Mohanty, A.K., Panigrahy, R.C., 2014. Nutrient dynamics and seasonal variation of phytoplankton assemblages in the coastal waters of south-west Bay of Bengal. *Environ. Monit. Assess.* 186, 5681–5695.  
 Baliarsingh, S.K., Lotliker, A.A., Trainer, V.L., Wells, M.L., Parida, C., Sahu, B.K., Srichandan, S., Sahoo, S., Sahu, K.C., Ku-

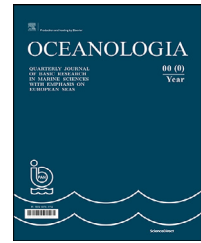
- mar, T.S., 2016. Environmental dynamics of red *Noctiluca scintillans* bloom in tropical coastal waters. *Mar. Pollut. Bull.* 111 (1–2), 277–286.
- Barnes, H., 1962. Note on variations in the release of nauplii of *Semibalanus balanoides* with special reference to the spring diatom outburst. *Crustaceana* 4, 118–122.
- Bhat, S.R., De Souza, P., Devi, L., Verlecar, X.N., Naik, C.G., 2006. Multiple dimensions of global environmental change. TERI Press, India, 419–431.
- Bradford-Grieve, J.M., 1994. The marine fauna of New Zealand: Pelagic Calanoid Copepod: Megacalanidae, Calanidae, Paracalanidae, Mecynoceridae, Eucalanidae, Spinocalanidae, Clausocalanidae. New Zealand Oceanographic Institute memoir, National Institute of Water and Atmospheric Research (NIWA), Wellington, New Zealand, 157 pp.
- Campbell, E.E., 1996. The global distribution of surf diatom accumulations. *Rev. Chil. Hist. Nat.* 69, 450–495.
- Choudhury, S.B., Panigrahy, R.C., 1989. Occurrence of bloom of diatom *Asterionella glacialis* in nearshore waters of Gopalpur, Bay of Bengal. *Indian J. Mar. Sci.* 18, 204–206.
- Clarke, K.R., Gorley, R.N., 2006. User Manual/Tutorial. PRIMER-E Ltd, Plymouth.
- Conway, D.V.P., White, R.G., Hugues-Dit-Ciles, J., Gallienne, C.P., Robins, D.B., 2003. Guide to the coastal and surface zooplankton of the south-western Indian Ocean. *Mar. Biol. Assoc. UK* (15) 354.
- D’Silva, M.S., Anil, A.C., Naik, R.K., D’Costa, P.M., 2012. Algal blooms: A perspective from the coasts of India. *Nat. Hazards* 63, 1225–1253.
- Deshikachary, T.V., 1987. Atlas of diatoms. Fascicle (Marine diatoms of Indian ocean region). Madras Science Foundation, Madras.
- Dharani, G., Abdul Nazar, A.K., Kanagu, L., Venkateshwaran, P., Kumar, T.S., Ratnam, K., Venkatesan, R., Ravindran, M., 2004. On the reoccurrence of *Noctiluca scintillans* bloom in Minnie Bay, Port Blair: Impact on water quality and bioactivity of extracts. *Curr. Sci.* 87, 990–994.
- Fritch, F.E., 1935. The Structure and Reproduction of Algae, II. Cambridge Univ. Press, London.
- Gleason, H.A., 1922. On the relation between species and area. *Ecology* 156–162.
- Gouda, R., Panigrahy, R.C., 1990. Occurrence of bloom of the diatom *Asterionella glacialis* (Castracane) in the Rushikulya estuary. East Coast of India. *Mahasagar: Bull. Natl. Inst. Oceanogr.* 23, 179–182.
- Grasshoff, K., Ehrhardt, M., Kremling, K., 1983. Methods of seawater analysis. Wiley-VCH, New York.
- Hourston, M., Potter, I.C., Warwick, R.M., Valesini, F.J., Clarke, K.R., 2009. Spatial and seasonal variations in the ecological characteristics of the free-living nematode assemblages in a large microtidal estuary. *Estuar. Coast. Shelf Sci.* 82, 309–322.
- Izquierdo, D., Guerra-García, J.M., 2010. Distribution patterns of the peracarid crustaceans associated with the alga along the intertidal rocky shores of the Iberian Peninsula. *Helgol. Mar. Res.* 65 (2), 233–243.
- Jiang, Y., Xu, H., Al-Rasheid, K.A.S., Warren, A., Hu, X., Song, W., 2011b. Planktonic ciliate communities in a semi-enclosed bay of Yellow Sea, northern China: annual cycle. *J. Mar. Biol. Assoc. UK.* 91, 97–105.
- Jiang, Y., Xu, H., Hu, X., Zhu, M., Al-Rasheid, K.A.S., Warren, A., 2011a. An approach to analyzing spatial patterns of planktonic ciliate communities for monitoring water quality in Jiaozhou Bay, northern China. *Mar. Pollut. Bull.* 62, 227–235.
- Jiang, Y., Xu, H., Zhang, W., Zhu, M., Al-Rasheid, K.A.S., 2012. Can body-size patterns of ciliated zooplankton be used for assessing marine water quality? A case study on bioassessment in Jiaozhou Bay, northern Yellow Sea. *Environ. Sci. Pollut. Res.* 19, 1747–1754.
- Jocelyn, D.C., Penelope, A., Randall, L., Suthers, I., 2000. *Noctiluca scintillans* – An indicator of coastal eutrophication. HAB ninth conference Tasmania. [www.utas.edu.au/docs/plant-science/HAB2000/abstracts/docs](http://www.utas.edu.au/docs/plant-science/HAB2000/abstracts/docs)
- Jyothibabu, R., Karnan, C., Jagadeesan, L., Arunpandi, N., Pandiarajan, R.S., Muraleedharan, K.R., Balachandran, K.K., 2017. *Trichodesmium* blooms and warm-core ocean surface features in the Arabian Sea and the Bay of Bengal. *Mar. Pollut. Bull.* 121 (1–2), 201–215.
- Karunasagar, I., Gowda, H.S.V., Subburaj, M., Venugopal, M.N., Karunasagar, I., 1984. Outbreak of paralytic shellfish poisoning in Mangalore west coast of India. *Curr. Sci.* 53, 247–249.
- Karunasagar, I., Joseph, B., Philipose, K.K., Karunasagar, I., 1998. Another outbreak of PSP in India. *Harmful Algae News* 17, 1.
- Kasturirangan, L.R., 1963. A Key to the identification of the more common planktonic copepoda of India coastal waters. In: Indian National Committee on Oceanic Research, Council of Scientific and Industrial Research, New Delhi, 87.
- Kim, Y.O., Chae, J., Hong, J.S., Jang, P.G., 2007. Comparing the distribution of ciliate plankton in inner and outer areas of a harbor divided by an artificial breakwater. *Mar. Environ. Res.* 64, 38–53.
- La Fond, E.C., 1957. Oceanographic studies in Bay of Bengal. *Proc. Indian Natl. Sci. Acad.* 46 (3), 1–46.
- La Fond, E.C., 1958. In: On the circulation of surface layers off the east coast of India, 2. Andhra University Memoirs of Oceanography, 1–11.
- Landsberg, J.H., 2002. The effects of harmful algal blooms on aquatic organisms. *Rev. Fish. Sci.* 10, 113–390.
- Latha, T.P., Rao, K.H., Amminedu, A., Nagamani, P.V., Choudhury, S.B., Lakshmi, E., Sridhar, P.N., Dutt, C.B.S., Dhadwal, V.K., 2014. Seasonal variability of phytoplankton blooms in the coastal waters along the east coast of India. The International Archives of the Photogrammetry, Remote Sensing and Spatial Information Sciences XL-8, 1065–1071.
- Mani, P., Krishnamurthy, K., Palaniappan, R., 1986. Ecology of phytoplankton blooms in the Vellar estuary, east coast of India. *Indian J. Mar. Sci.* V 15, 24–28.
- Margalef, R., 1978. Life-forms of phytoplankton as survival alternatives in an unstable environment. *Oceanol. Acta* 1, 193–509.
- Mishra, S., Panigrahy, R.C., 1995. Occurrence of diatom blooms in Bahuda estuary, east coast of India. *Indian J. Mar. Sci.* 24, 99–101.
- Mishra, S., Sahu, G., Mohanty, A.K., Singh, S.K., Panigrahy, R.C., 2006. Impact of the diatom *Asterionella glacialis* (Castracane) bloom on the water quality and phytoplankton community structure in coastal waters of Gopalpur Sea. Bay of Bengal. *Asian J. Water, Environ. Pollut.* 3, 71–77.
- Mohanty, A.K., Satpathy, K.K., Sahu, Gouri, Hussain, K.J., Prasad, M.V.R., Sarkar, S.K., 2010. Bloom of *Trichodesmium erythraeum* (Ehr.) and its impact on water quality and plankton community structure in the coastal waters of southeast coast of India. *Indian J. Mar. Sci.* 39 (3), 323–333.
- Murty, C.S., Varadachari, V.V.R., 1968. Upwelling along the east coast of India. *Bull. Nat. Inst. Sci. India.* 36, 80–86.
- Nagabhushanam, A.K., 1967. On an unusually dense Phytoplankton bloom around Minicoy Island (Arabian Sea) and its effect on the local Tuna fisheries. *Curr. Sci.* 36, 611–612.
- Naqvi, S.W.A., George, M.D., Narvekar, P.V., Jayakumar, D.A., Shailaja, M.S., Sardesai, S., Sarma, V.S., Shenoy, D.M., Naik, H., Maheswaran, P.A., KrishnaKumari, L., Rajesh, G., Sudhir, A.K., Binu, M.S., 1998. Severe fish mortality associated with ‘red tide’ observed in the sea off Cochin. *Curr. Sci.* 75, 543–544.
- Newell, G.E., Newell, R.C., 1967. *Marine Plankton, A Practical Guide.* Hutchinson Educational, London, 221 pp.
- Odum, E.P., 1971. *Fundamentals of Ecology.* W.B. Saunders, Philadelphia, PA.
- Padmakumar, N.R., Smitha, B.R., Thomas, L.C., Fanimol, C.L., SreeRenjima, G., Menon, N.R., Sanjeevan, V.N., 2010. Blooms

- of *Trichodesmium erythraeum* in the South Eastern Arabian Sea during the onset of 2009 Summer Monsoon. *Ocean Sci.* 45 (3), 151–157.
- Padmavati, G., Goswami, S.C., 1996. Zooplankton ecology in the Mandovi-Zuari estuarine system of Goa. West coast of India. *Indian J. Mar. Sci.* 25, 268–273.
- Panigrahy, R.C., Gouda, R., 1990. Occurrence of bloom of the diatom *Asterionella glacialis* (Castracane) in the Rushikulya estuary. East Coast of India. *Mahasagar: Bull. Natl. Inst. Oceanogr.* 23, 179–182.
- Parsons, T.R., Matia, Y., Lalli, C.M., 1984. A manual of chemical and biological methods for sea water analysis. Pergamon Press, Maxwell, New York, 14–17.
- Pielou, E.C., 1966. The measurement of diversity in different types of biological collections. *J. Theor. Biol.* 13, 131–144.
- Prabhu, M.S., Ramamurthy, S., Dhulkhed, M.H., Radhakrishnan, N.S., 1971. *Trichodesmium* bloom and the failure of Oil sardine fishery. *Mahasagar* 4, 62–64.
- Raghuprasad, R., Jayaraman, R., 1954. Preliminary studies on certain changes in the plankton and hydrological conditions associated with the swarming of *Noctiluca*. *Proc. Indian Acad. Sci.* 40, 49–57.
- Rao, S.D.V., 1969. *Asterionella japonica* bloom and discolouration off Waltair, Bay of Bengal. *Limnol. Oceanogr.* 14, 632–634.
- Roy, R., Rao, K.H., Preethi Latha, T., Dadhwal, V.K., Sarma, V.V.S.S., Nagamani, P.V., Choudhury, S.B., Pondala, S., 2016. Satellite and In Situ Observations of a Phytoplankton Bloom from Coastal Bay of Bengal: Role in pCO<sub>2</sub> Modulation. *J. Indian Soc. Remote.* 45, 3. <https://doi.org/10.1007/s12524-016-0604-3>
- Sahayak, S., Jyothibabu, R., Jayalakshmi, K.J., Habeebrehman, H., Sabu, P., Prabhakaran, M.P., Jasmine, P., Shaiju, P., Rejomon, G., Thresiamma, J., Nair, K.K.C., 2005. Red tide of *Noctiluca miliaris* off south of Thiruvananthapuram subsequent to be “stench event” at the south Kerala coast. *Curr. Sci.* 89, 1472–1473.
- Sahu, G., Mohanty, A.K., Achary, M.S., Sarkar, S.K., Satpathy, K.K., 2015. Changes in mesozooplankton community structure during *Trichodesmium erythraeum* bloom in the coastal waters of southwestern Bay of Bengal. *Indian J. Mar. Sci.* 44 (9), 1282–1293.
- Sahu, G., Mohanty, A.K., Samantara, M.K., Satpathy, K.K., 2014. Seasonality in the distribution of dinoflagellates with special reference to harmful algal species in tropical coastal environment, Bay of Bengal. *Environ. Monit. Assess.* 186, 6627–6644.
- Sahu, G., Mohanty, A.K., Sarangi, R.K., Bramha, S.N., Satpathy, K.K., 2016. Upwelling initiated algal bloom event in the coastal waters of Bay of Bengal during post northeast monsoon period. *Curr. Sci.* 10, 979–981.
- Sahu, G., Satpathy, K.K., Mohanty, A.K., Biswas, S., Achary, M.S., Sarkar, S.K., 2013. Larval abundance and its relation to macrofouling settlement pattern in the coastal waters of Kalpakkam, south-eastern part of India. *Environ. Monit. Assess.* 185, 1951–1967.
- Sargunam, C.A., Rao, V.N.R., Nair, K.V.K., 1989. Occurrence of *Noctiluca* bloom in Kalpakkam coastal waters, east coast of India. *Indian J. Mar. Sci.* 18, 289–290.
- Sarma, V.V.S.S., Rajula, G.R., Durgadevi, D.S.L., Sampath Kumar, G., Loganathan, J., 2020. Influence of eddies on phytoplankton composition in the Bay of Bengal. *Cont. Shelf Res.* 208, 104241. <https://doi.org/10.1016/j.csr.2020.104241>
- Sasmal, S.K., Panigrahy, R.C., Misra, S., 2005. *Asterionella* bloom in the north-western Bay of Bengal during 2004. *Int. J. Remote Sens.* 26, 3853–3858.
- Satpathy, K.K., Mohanty, A.K., Sahu, G., Prasad, M.V.R., Venkatesan, R., Natesan, U., Rajan, M., 2007. On the occurrence of *Trichodesmium erythraeum* (Ehr.) bloom in the coastal waters of Kalpakkam, east coast of India. *Indian J. Sci. Technol.* 1, 1–11.
- Satpathy, K.K., Mohanty, A.K., Sahu, G., Sarkar, S.K., Natesan, U., Venkatesan, R., Prasad, M.V.R., 2010. Variations of physico-chemical properties in Kalpakkam coastal waters, east coast of India, during southwest to northeast monsoon transition period. *Environ. Monit. Assess.* 171, 411–424.
- Satpathy, K.K., Nair, K.V.K., 1996. Occurrence of phytoplankton bloom and its effect on coastal water quality. *Indian J. Mar. Sci.* 25, 145–147.
- Satpathy, K.K., Nair, K.V.K., 1990. Impact of power plant discharge on the physico-chemical characteristics of Kalpakkam coastal waters. *Mahasagar* 23, 117–125.
- Satpathy, K.K., Sahu, G., Mohanty, A.K., Prasad, M.V.R., Panigrahy, R.C., 2009. Phytoplankton community structure and its variability during southwest to northeast monsoon transition in the coastal waters of Kalpakkam, east coast of India. *Int. J. Oceans Oceanogr.* 3 (1), 43–74.
- Shannon, C.E., Weaver, W., 1963. The mathematical theory of communication. Univ. Illinois Press, Urbana.
- Shumway, S., 1990. A review of the effects of algal blooms on shellfish and aquaculture. *J. World Aquac. Soc.* 21, 65–104.
- Shunmugam, S., Gayathri, M., Prasannabalaji, N., Thajuddin, N., Muralitharan, G., 2017. Unraveling the presence of multi-class toxins from *Trichodesmium* bloom in the Gulf of Mannar region of the Bay of Bengal. *Toxicon* 135, 43–50.
- Smayda, T.J., 1989. Primary production and the global epidemic of phytoplankton blooms in the sea: a linkage? In: Cosper, E.M., Bricelj, V.M., Carpenter, E.J. (Eds.) *Novel Phytoplankton Blooms. Coastal and Estuarine Studies* No. 35. Springer-Verlag, New York, 449–484.
- Srichandan, S., Baliarsingh, S.K., Prakash, S., Lotliker, A.A., Parida, C., Sahu, K.C., 2019. Seasonal dynamics of phytoplankton in response to environmental variables in contrasting coastal ecosystems. *Environ. Sci. Pollut. Res.* 26 (12), 12025–12041.
- Sridevi, B., Srinivasu, K., Bhavani, T.S.D., Prasad, K.V.S.R., 2019. Extreme events enhance phytoplankton bloom in the south-western Bay of Bengal. *Indian J. Geo. Mar. Sci.* 48 (02), 253–258.
- Starr, M., Himmelman, J.H., Therriault, J.C., 1991. Coupling of nauplii release in barnacles with phytoplankton blooms: a parallel strategy to that of spawning in urchins and mussels. *J. Plankton Res.* 13 (3), 561–571.
- Subramanian, R., 1971. The Dinophyceae of Indian Seas Part-II. Peridiniaceae. *Mar. Biol. Assoc. India*, 134 pp.
- Subramanyan, R., 1968. The Dinophyceae of the Indian Sea. *J. Mar. Biol. Assoc. India*. 3, 118–133.
- Tomas, C.R., 1996. *Identifying Marine Diatoms and Dinoflagellates*. Acad. Press Inc., New York, 598.
- Vollenweider, R.A., 1974. A manual on methods for measuring primary production in aquatic environments. In: *IBP handbook* No 12. Blackwell Sci. Publ., London, 225 pp.
- Xu, H., Jiang, Y., Al-Rasheid, K.A.S., Al-Farraj, S.A., Song, W., 2011a. Application of an indicator based on taxonomic relatedness of ciliated protozoan assemblages for monitoring water quality of periphytic ciliate communities for monitoring water quality of coastal waters. *Ecol. Indic.* 11, 1228–1234.
- Xu, H., Song, W., Warren, A., Al-Rasheid, K.A.S., Al-Farraj, S.A., Gong, J., Hu, X., 2008. Planktonic protist communities in a semi-enclosed mariculture pond: structural variation and correlation with environmental conditions. *J. Mar. Biol. Assoc. UK.* 88, 1353–1362.
- Xu, H., Zhang, W., Jiang, Y., Min, G.S., Choi, J.K., 2011b. An approach to identifying potential environmental assessment. *Environ. Sci. Pollut. Res.* 18, 1213–1221.
- Xu, H., Zhang, W., Jiang, Y., Zhu, M., Al-Rasheid, K.A., Warren, A., Song, W., 2011c. An approach to determining the sampling effort for analyzing biofilm-dwelling ciliate colonization using an artificial substratum in coastal waters. *Biofouling* 27, 357–366.



Available online at [www.sciencedirect.com](http://www.sciencedirect.com)

ScienceDirect

journal homepage: [www.journals.elsevier.com/oceanologia](http://www.journals.elsevier.com/oceanologia)

## ORIGINAL RESEARCH ARTICLE

# Defining a single set of calibration parameters and prestorm bathymetry in the modeling of volumetric changes on the southern Baltic Sea dune coast

Natalia Bugajny\*, Kazimierz Furmańczyk

University of Szczecin, Institute of Marine and Environmental Sciences, Szczecin, Poland

Received 24 April 2021; accepted 15 October 2021

Available online 5 November 2021

## KEYWORDS

XBeach;  
Model calibration;  
Coastal erosion;  
Volume errors

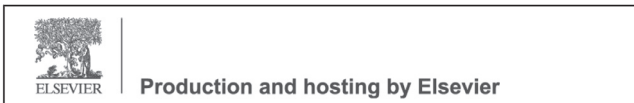
**Abstract** The studies described herein aimed to estimate the accuracy of determination of the volumetric changes on the dune coast of the southern Baltic Sea through the application of the XBeach numerical model, which is crucial for coastal engineering. In the first phase of the study, the profile (1D) mode of the model was adapted to 19 cross-shore profiles located along the Dziwnów Spit.

The model was calibrated with a storm event in 2009 that caused significant changes to dunes and beaches. Cross-shore profiles were measured approximately one and a half months before and after the storm. An evaluation of model performance was made based on the Brier skill score (BSS), the visual match of the profile shape (VMS), the absolute volumetric change error ( $\text{m}^3/\text{m}$ ) and the relative volumetric change error (%). In this study, parameters related to the asymmetry transport (*facua*) and the dune erosion algorithm (*wetslp*) were taken into account. The best results for model calibration on all 19 cross-shore profiles were obtained with *facua* values ranging from 0.16 to 0.40 and *wetslp* values from 0.35 to 0.60. The calibration of individual profiles yielded good results, with an average absolute error of approximately  $4 \text{ m}^3/\text{m}$  and an average relative error of ca. 20%. The poorest results were collected for the profiles situated near coastal engineering structures, where the average absolute error was  $10 \text{ m}^3/\text{m}$  and the relative error was 60%. The possibility of accepting one set of parameter values for all the profiles at once was also investigated. These studies revealed that the application of one

\* Corresponding author at: University of Szczecin, Institute of Marine and Environmental Sciences, Adama Mickiewicza 16, 70–383 Szczecin, Poland.

E-mail addresses: [natalia.bugajny@usz.edu.pl](mailto:natalia.bugajny@usz.edu.pl) (N. Bugajny), [kazimierz.furmanczyk@usz.edu.pl](mailto:kazimierz.furmanczyk@usz.edu.pl) (K. Furmańczyk).

Peer review under the responsibility of the Institute of Oceanology of the Polish Academy of Sciences.



<https://doi.org/10.1016/j.oceano.2021.10.004>

0078-3234/© 2021 Institute of Oceanology of the Polish Academy of Sciences. Production and hosting by Elsevier B.V. This is an open access article under the CC BY-NC-ND license (<http://creativecommons.org/licenses/by-nc-nd/4.0/>).

set of *facua* and *wetslp* values for all profiles simultaneously resulted in a relative volumetric change error of ca. 25% on average, with the maximum of about 40%.

Due to the difficulty of collecting data just before and after the storm event, complex studies using all available bathymetric data were performed. Using a joint dataset composed of prestorm topography recorded before that storm and bathymetry from different years, a simulation of the 2009 storm event was carried out. The studies revealed that the prestorm bathymetry and the randomness of the selection of calibration parameters have similar effects on the accuracy of volumetric changes.

Moreover, the impact of the nearshore bathymetry (to a depth of 2 m) on modeling the volumetric changes in the terrestrial part of the shore is evident. A change in the sea bottom inclination and a successive change in the nearshore sediment volume can increase the difference between modeled and actual volumetric changes.

© 2021 Institute of Oceanology of the Polish Academy of Sciences. Production and hosting by Elsevier B.V. This is an open access article under the CC BY-NC-ND license (<http://creativecommons.org/licenses/by-nc-nd/4.0/>).

## 1. Introduction

Sea level rise and the increasing frequency of storm events, which are two phenomena that have been observed recently in some regions, have become real hazards in coastal areas, especially those with low dune berms as their first line of defense. If coastal parameters are insufficient to resist these phenomena, the continuous dune berm may be breached, leading to inland flooding. Therefore, to mitigate the adverse effects of coastal hazards, it is necessary to develop a tool that would allow emergency units to be ready to launch specific procedures to mitigate these hazards.

Coastal zone studies are increasingly supported by numerical models that determine shoreline displacement and volumetric changes. These models are used for both early warning systems and for coastal zone modeling systems that are convenient tools for coastal zone management (Barnard et al., 2014; Furmańczyk et al., 2014; Haerens et al., 2012). However, it should always be kept in mind that models have limitations in reflecting the natural processes that occur in coastal zones. These limitations result from simplified assumptions or equations that describe coastal processes and from the insufficient availability of up-to-date datasets; hence, these models may generate errors.

A vast number of models, both analytical (Bruun, 1954; Dean and Maurmeyer, 1983; Edelman, 1972; Kriebel et al., 1991) and numerical (Larson and Kraus, 1989; Seetzel, 1993), that concern coastal erosion have been developed so far. XBeach (Roelvink et al., 2009), which is a process-based model, is the most widely used. It was created to simulate the processes that occur in the coastal zone during storm events in line with storm impact regimes (Sallenger, 2000). It has been adapted and tested all around the world to simulate wave runup (Palmsten and Splinter, 2016) as well as morphological changes in profiles (1D mode) (Dissanayake et al., 2014; Harley et al., 2011; Pender and Karunaratna, 2013; Vousdoukas et al., 2011) and domains (2D mode) (McCall et al., 2010; Williams et al., 2015). XBeach has become a tool for the long-term simulation of volumetric changes (Pender and Karunaratna, 2013)

and for simulations of storm groups rather than single storm events only (Karunaratna et al., 2014).

The XBeach model (*XBeach Quatorze\_Juillet, revision 1241*) was applied on the southern Baltic coast for the first time by Bugajny et al. (2013). Further studies to widen the applicability of the model were performed in Bugajny et al. (2015). The results of these studies confirmed that XBeach is a relevant model for predicting beach and dune changes on the dune coast of a tideless sea and proved the usefulness of that model in creating an efficient tool to predict hazards in the Baltic Sea coastal zone.

Despite being quite versatile, XBeach requires site-specific calibration (Splinter and Palmsten, 2012), since the good calibration of process-based models improves their efficiency, making them optimal tools for simulating storm events that end in dune erosion (Armaroli et al., 2013; Harley et al., 2011). One of the most common calibration methods is ‘trial and error’. Having over 100 ‘free’ parameters to tune, this process may become time-consuming, yet it is crucial for the proper application of the model. Studies performed for the Baltic coast have so far revealed that the most significant influence on volumetric change simulations have *facua* and *wetslp* parameters.

In technical terms, the application of the model should cover the largest area possible. However, the application of the model is limited to case studies due to the time-consuming calibration process. Model calibration in 1D mode raises the following questions: What is the variety of calibration parameters along the coast? How would the one set of parameters work if used for other profiles along a given section of the coast? Is there a set of parameters that would be optimal for a given case study? To answer these questions, the model was calibrated focusing on selected parameters and then the influence of calibration parameter sets on the modeled volumetric changes was analyzed based on the selected measures.

Furthermore, the availability of data, both pre- and post-storm, is another point of concern. Is it possible to predict the recorded volumetric changes on the coast using the model without a valid prestorm bathymetry? To answer that question, storm simulations were carried out by changing

the prestorm bathymetry recorded in different years on the selected profiles used in the research and the errors of modeled volumetric changes were calculated. Therefore, the goals of this study were:

- to study the influence of a set of calibration parameters on modeling volumetric changes on a dune coast and on the accuracy of the model predictions;
- to study the influence of prestorm bathymetry on the accuracy of modeling volumetric changes in a dune coast.

These studies took place on a several-kilometer-long section of the dune coast of the southern Baltic Sea. As a result, two issues were discussed: the selection of a set of calibration parameters and their impact on the accuracy of the model results and the influence of the underwater morphology of the nearshore on the subaerial volumetric changes of the coast that was modeled.

## 2. Study area and materials

### 2.1. Dziwnów Spit

The Dziwnów Spit is a barrier that separates Kamieński Lagoon from the Baltic Sea (Figure 1). It includes a 12 km-long section of the Baltic dune coast that is pushed into a Pleistocene cliff high plain between km 385 and 397 of chainage as set out by the Maritime Office. The spit is divided at its central point by a manmade channel dug at the turn of the 19th and 20th centuries (Racinowski and Seul, 1999) that flows southwards into a natural part of the Dziwna inlet. The Dziwnów Spit may thus be split into two parts: eastern and western. The eastern part is narrow. It is not wider than 0.5 km at its narrowest segment. The dune berm height there ranges from 3 to 4 m. In turn, the western part is wider and reaches approximately 2 km in width. The dune berm system is well developed, with dunes reaching 12 m. The entire spit is gently inclined toward the northwest and has the shore with a wide (30–50 m) sandy beach. In the nearshore region, a system of 2–3 underwater bars can be observed (Dobrcki and Zachowicz, 2005; Musielak et al., 2007).

The new channel that replaced the natural Dziwna inlet and the construction of jetties on both sides disrupted alongshore sediment transport, causing intensified erosion that led to the construction of the coastal defense system. Currently, the spit is well protected by diverse coastal engineering structures such as groynes, seawalls and beach nourishment that modify the course of natural processes (Dudzińska-Nowak, 2015). Despite these efforts, alternating accumulative and erosive systems tend to appear here, with dominating erosion (Dudzińska-Nowak, 2006a,b; Zawadzka-Kahlau, 1999). The greatest loss of the dune berm due to storm events is observed at km 388 (seawalls), km 391 (jetties) and km 394 (the area adjacent to groynes) (Furmańczyk and Dudzińska-Nowak, 2009; Furmańczyk et al., 2011). The comparison of volumetric changes caused by weak storms (that do not cause dune erosion) along protected and natural sections has shown that, in such weak wave conditions, groynes do not increase the volumetric change dynamics on the protected coast, while their protective function leads to both seaward shoreline displacement and positive values of volumetric changes.

As the wave action intensifies, groynes lose their protective function, causing the protected coast to behave like a natural coast, showing landward shoreline displacement and negative values of volumetric changes (Bugajny and Furmańczyk, 2017).

Due to its size and geographical location, as well as the limited water exchange between the Danish Straits and the North Sea, the tides in the Baltic Sea are weak, limited to a few centimeters (Sztobryn et al., 2005). Hence, the Baltic Sea is considered a nontidal sea. Because of the negligible impact of tides, it seems that the most important hydrodynamic factor influencing morphological changes on the coast is wave action (Zeidler et al., 1995) accompanied by a storm surge.

The western coast of the southern Baltic Sea, where the study area is located, is classified in the range 1.96–2.22 m above AMSL due to maximum storm surges in the period 1811–2006 (Musielak et al., 2017), while the monthly maximal deep-water significant wave height in the years 1998–99 for the Pomeranian Bay ranged between 2.89–4.22 m (Paplińska and Reda, 2001).

### 2.2. Morphological and hydrodynamic data

As a part of the annual monitoring of the coastal zone, the morphology of the coastal zone was recorded in the form of bathymetric-topographic profiles that are shared by the Maritime Office in Szczecin. The profiles are taken perpendicular to the coast at intervals of 500 m and reach no further than 2000 m toward the sea from base points located on land. The numbering of profiles increases every 1 km from east to west and receives a number according to the chainage along the coast. Topographic measurements of the profiles (the subaerial part and to a depth of –1 m) were made using geodetic methods with a vertical precision of  $\pm 5$  cm. Bathymetric measurements were made from a depth of –1 m to approximately –15 m using an echo sounder with vertical precision of  $\pm 8$  cm and a horizontal precision of  $\pm 20$  cm (Bugajny et al., 2013). In these studies, profiles measured in late August of 2009 were used to calibrate the model, as a prestorm registration, while profiles from 2004, 2006, 2008, 2010 and 2012 for the study area, i.e., 395.5–386.5 km (Figure 1), were used to study the influence of bathymetry on the volumetric changes on the coast.

In addition, data from an airborne laser scanner (red LIDAR – topographic), acquired on November 30, 2009, by a TopEye scanner were used. The dataset is characterized by a density of 8 pt/m<sup>2</sup> and horizontal and vertical accuracy x, y, z of  $\pm 20$  cm and was made as part of the annual monitoring of the coastal zone by the Maritime Office in Szczecin (Bugajny et al., 2013, 2015; Dudzińska-Nowak and Wężyk, 2014). The data were used as the poststorm morphological data.

Water level data from 2009 (12–16.10) were registered every 4 hours by a tide gauge located in the port of Dziwnów and provided by the Maritime Office in Szczecin.

Basic wave parameters were derived from the WAM model (WAMDI Group, 1988), shared by the Interdisciplinary Centre for Mathematical and Computational Modeling, University of Warsaw (ICM UW). Due to a very good correspondence between the modeled and measured wave parameters for the Baltic Sea (Cieślikiewicz and Herman, 2001,

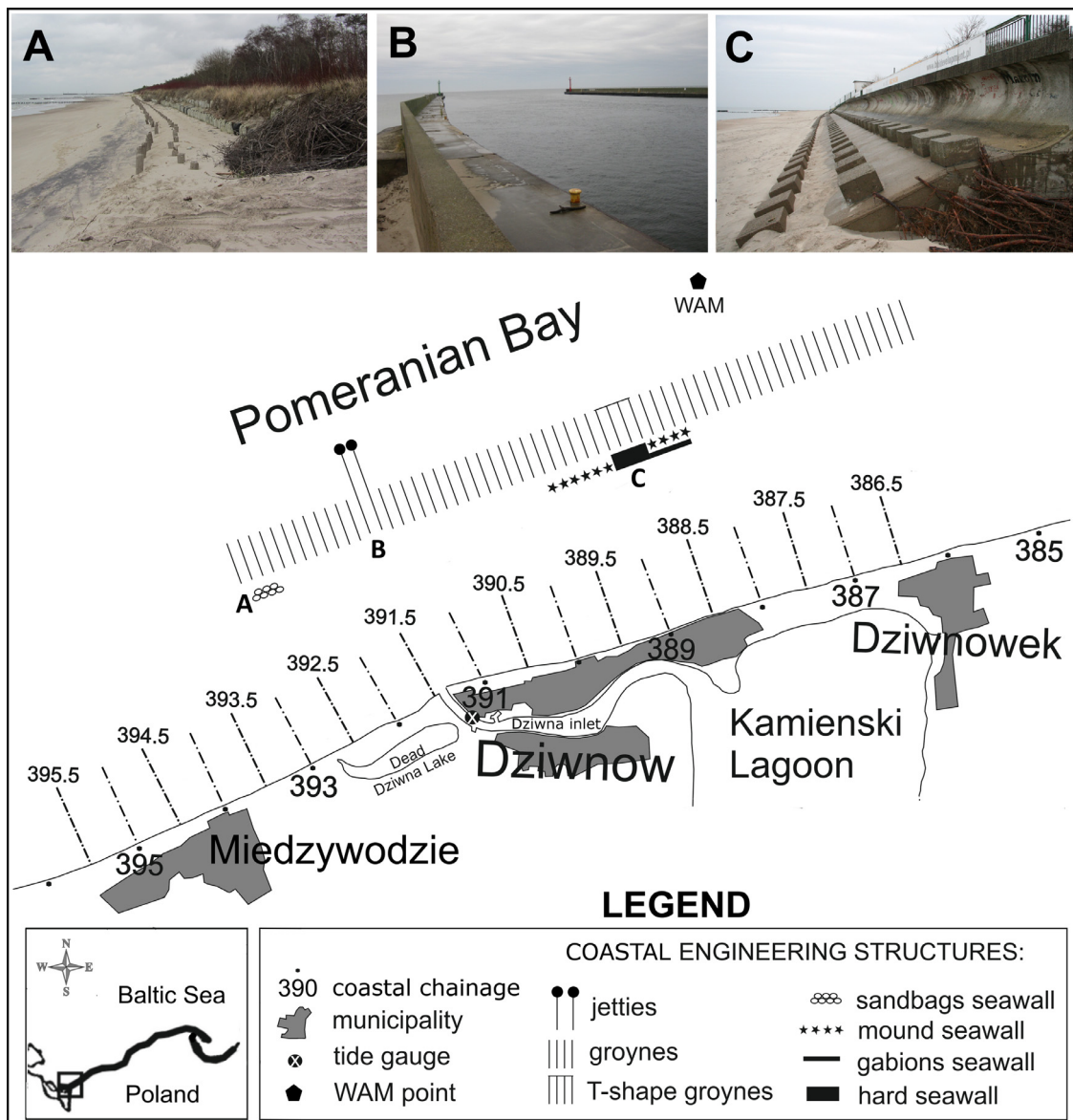


**Figure 1** Study area with the location of bathymetric-topographic profiles, hydrodynamic data and coastal engineering structures.

2002; Papińska, 1999, 2001), it was decided to use the WAM model data in this study.

This study is focused on a storm event that took place on 12–16 October 2009. It caused significant changes in a shore in the form of intense erosion of both the beach and the dunes (Furmańczyk and Dudzińska-Nowak, 2009). The maximum water level reached +0.76 m AMSL, while the maximum significant wave height ( $H_s$ ) was 3.75 m at a peak period of 11.17 s. A time series demonstrating the changes in the values of these parameters throughout the storm event is provided in Figure 2.

### 3. Methods

#### 3.1. Model performance evaluation

The performance of a model is estimated on the basis of comparison of field measurements with model simulation

results at the same location. Various measures can be used for this purpose (Sutherland et al., 2004).

The Brier skill score (BSS) is the most commonly used nondimensional measure and relies on an analytical comparison of the profile measured in the field before and after the storm and the profile after the simulation (Sutherland et al., 2004). The correlation of the measured profiles (prestorm –  $x_b$  and poststorm –  $x_p$ ) and the modeled profile ( $x_m$ ) can be expressed as follows:

$$BSS = 1 - \left( \frac{\langle |x_m - x_p|^2 \rangle}{\langle |x_p - x_b|^2 \rangle} \right)$$

The interpretation of BSS values was described by van Rijn et al. (2003). They classified the model performance as bad when  $BSS < 0$ , poor when  $BSS = 0-0.3$ , reasonable/fair when  $BSS = 0.3-0.6$ , good when  $BSS = 0.6-0.8$  and excellent when  $BSS = 0.8-1$ . Ideally, when the predicted changes are the same as the observed changes, the BSS value = 1. This indicator is sensitive to small changes

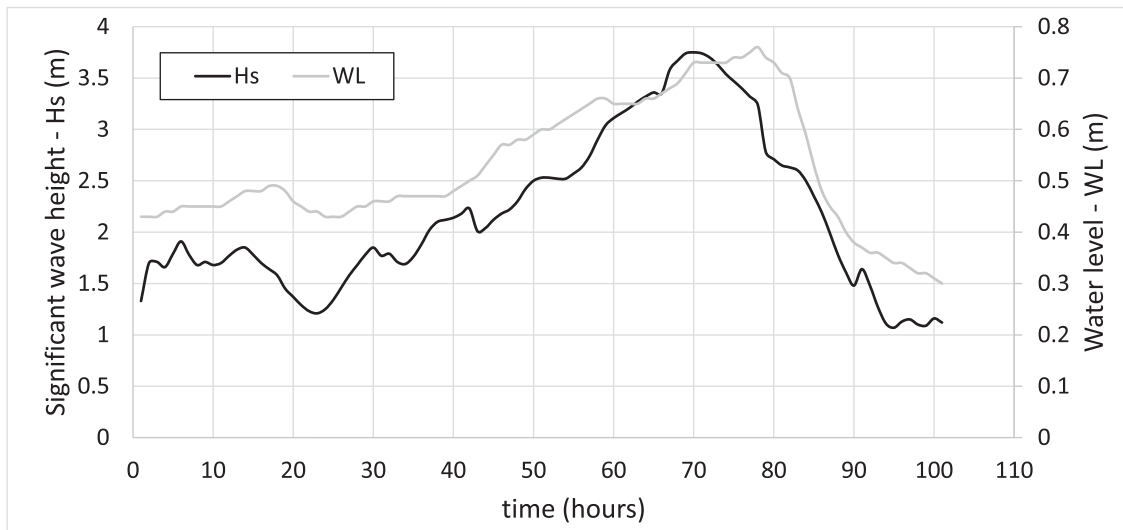


**Figure 2** Time series of 2009 storm parameters (significant wave height – Hs and water level – WL) used in the XBeach simulations.

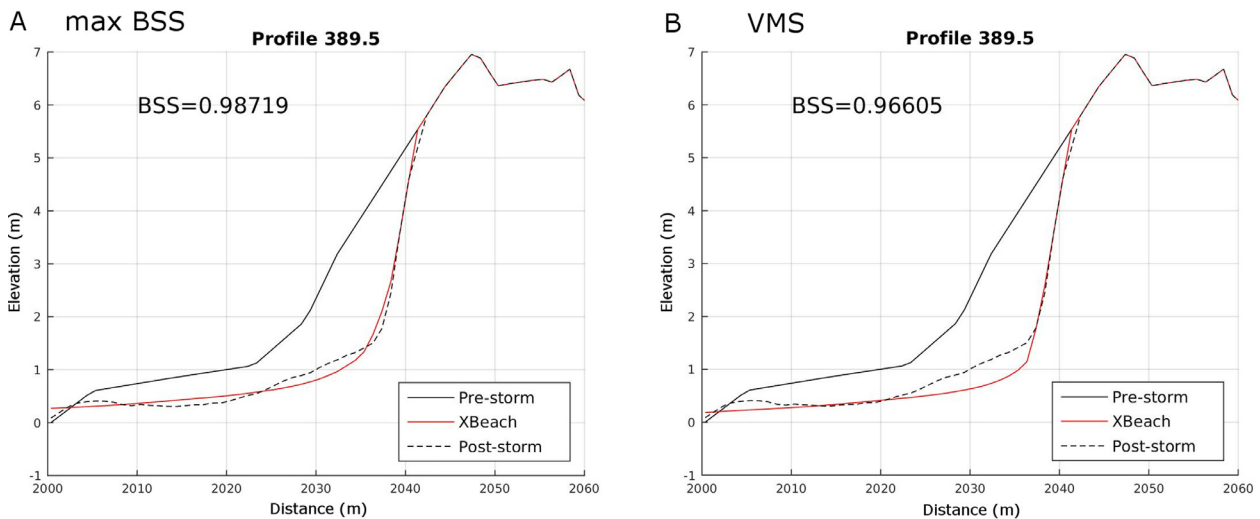


**Figure 3** Comparison of calibration results for profile 389.5 in simulations with maximum BSS (A) and based on the visual match profile shape (VMS) (B).

when the denominator takes small values. Therefore, low values of BSS can be obtained with small real changes, even if the model correctly simulates these changes (Sutherland et al., 2004). In this study, BSS values were calculated only for the land part of the profile, taking into account changes to the beach and the dunes.

The **visual match of the profile shape (VMS)** after the storm with the model result was also performed. The BSS values do not always best reflect the model fit, especially when a long time interval occurred between the storm and the poststorm measurement in the field. After the storm, a successive reconstruction of the coastal profile in the form of the beach bar and aeolian transport, especially in the area of the upper beach near the dune foot, was observed. In this case, more attention should be paid to the VMS result than to the BSS. In the current research, an assessment was carried out using both measures, BSS and VMS and a comparison of the correctness of the model calibration for the 389.5 profile is shown in Figure 3.

The simulation result for a very good match ( $BSS = 0.987$ ) and of a simulation where the modeled profile coincides with the measured one in an area located behind a beach bar toward the dune (beach lagoon) is presented in Figure 3A and 3B, respectively. The beach bar that is not included in the numerical simulation and the aeolian accumulation in the upper beach area is clearly visible. For this approach, the BSS value is slightly lower, equals to 0.966, but the simulation reflects better the actual process that was modeled; the poststorm survey took place approximately 1.5 months after the storm event.

Moreover, the accuracy of the determination of the volumetric changes on the coast was also calculated. XBeach was used to calculate the volumetric changes caused by the storm event conditions. Therefore, two additional measures were applied to assess the model performance: the absolute error and the relative error of volumetric changes.

**The absolute error of volumetric changes ( $m_b$ ).** The sum of changes in the height of the profiles multiplied by 1 m of alongshore distance was used as the volumetric change in these profiles. The error is calculated on the basis of the volumetric change in the coast between the profiles measured in the field before and after the storm and the modeled volume changes in the profile and is expressed in the absolute values of the following difference:

$$m_b = |x_i - x_m|$$

where  $x_i$  is the measured volume and  $x_m$  is the modeled volume.

**Relative error of volumetric changes ( $m_w$ ).** This is the ratio of the absolute error to the measured volumetric changes. It can be expressed as a percentage:

$$m_w = \frac{m_b}{x_i} \times 100\%$$

where  $m_b$  is the absolute error and  $x_i$  is the measured volume.

### 3.2. XBeach model calibration parameters

The XBeach model was developed to simulate the impact of extreme events on dune coasts. It is a process-based model, which makes it more complex and computationally more intense than equilibrium-type models (Ciavola et al., 2014). The XBeach (*Easter release*) was used in this study. It has approximately 100 parameters that can be significant and that should be specified in the calibration process. The default values for most parameters were used, as suggested in the model manual (Roelvink et al., 2010). However, taking into account the results obtained in previous studies on the application of XBeach on the Polish coast (Bugajny et al., 2013, 2015) and the changes in the default values of parameters in the version of the model used in this work, particular attention was paid to the following parameters:

- *wetslp*, critical wet slope, is a parameter related to the dune erosion algorithm. As the critical slope between two neighboring cells of the calculation grid is exceeded, sediment is transported between these cells until the critical slope is reached. The algorithm is a relatively simple tool for describing the complex process of dune erosion (van Thiel de Vries, 2009). The default value of the *wetslp* parameter is 0.3, which results from a study on the profile of equilibrium for a seashore by Vellinga (1986), tests performed at Oregon State University and the Zwin experiment (Roelvink et al., 2009, 2010).
- *facua* ( $u_a$ ), a dimensionless calibration parameter, was introduced into the model to take into account the size of sediment transported due to the wave shape. It can take values from 0 to 1. High values of *facua* lead to higher onshore flow, which results in greater sediment transport in this direction. Therefore, *facua* = 0.5 is suitable for medium wave conditions, whereas *facua* = 0 or low values correspond to storm conditions (Voukouvalas, 2010). The default value of this parameter was set at 0.1 on the basis of studies carried out by van Thiel de Vries (2009).
- *morfac*, the morphological acceleration factor, is a parameter that accelerates the morphological time scale in

relation to the hydrodynamic scale. This parameter can take values from 0 to 1000 (Roelvink et al., 2010). In this research, a value of 10 was used, similar to those in the work of McCall et al. (2010), Ranasinghe et al. (2011) and Pender and Karunaratna (2013).

- *smax*, is a parameter specifying the maximum value of the Shields coefficient. It was introduced into the model to balance the overestimation of dune erosion observed in McCall et al. (2010). As a result of the recommendation of McCall et al. (2010), that an *smax* between 0.8–1.2 results in small differences in BSS, this parameter was set at a constant value of 1 in this study.

### 3.3. XBeach model setup

The storm event that took place on 12–16.10.2009 was used for model calibration. This event caused significant changes to the coast, such as intense dune and beach erosion (Furmańczyk and Dudzińska-Nowak, 2009). A simulation of the storm event of 2009 was run for 19 cross-shore profiles (395.5, 395, 394.5, 394, 393.5, 393, 392.5, 392, 391.5, 391, 390.5, 390, 398.5, 389, 388.5, 388, 387.5, 387, and 386.5 km) located every 500 m along the study area (Figure 1).

For each profile, a variable computational grid was created with a cell size of approximately 20 m offshore and 1 m onshore. The application of this variable grid minimized the computing time.

The wave boundary conditions were implemented as a time series of hourly JONSWAP spectra (instat=41) perpendicular to the coast. The average spectral parameters for the Baltic Sea, obtained in Papińska (1994), did not differ much from those adopted for the North Sea, which confirmed the possibility of using the JONSWAP spectrum to describe the wind waves in the Baltic Sea. In addition, the water level at the model boundary was assumed to be the same as that recorded by a tide gauge at the mouth of the Dziwna River (Figure 1). Furthermore, average values of  $D_{50} = 0.25$  mm and  $D_{90} = 0.375$  mm for medium-sized sand were adopted.

The boundary conditions for flows at both the offshore and the onshore boundaries were set to absorbing-generating ones, while at the lateral boundaries, they were set to no flow (wall). Directional wave propagation was not taken into account in this case.

In this study, the accuracy of the volumetric change calculations performed by the XBeach model was assessed on the basis of the four measures described earlier. For each of the 19 profiles located in the study area, using the ‘trial and error’ approach for model calibration, approximately 300 simulations were run, changing the values of *wetslp* from 0.3 to 0.6 by increments of 0.05 and of *facua* from 0 to 1 by increments of 0.1. The *morfac* parameter was set to 10, and the *smax* parameter was set to 1 for all simulations. The remaining parameters were introduced with their default values. Next, on the basis of the BSS obtained from the simulations for particular profiles, the profiles with the highest BSS (max BSS) values were selected. Furthermore, the visual match of the profile shape (VMS) was assessed for those profiles to identify those in which the shape after the simulation better matched the morphological changes.

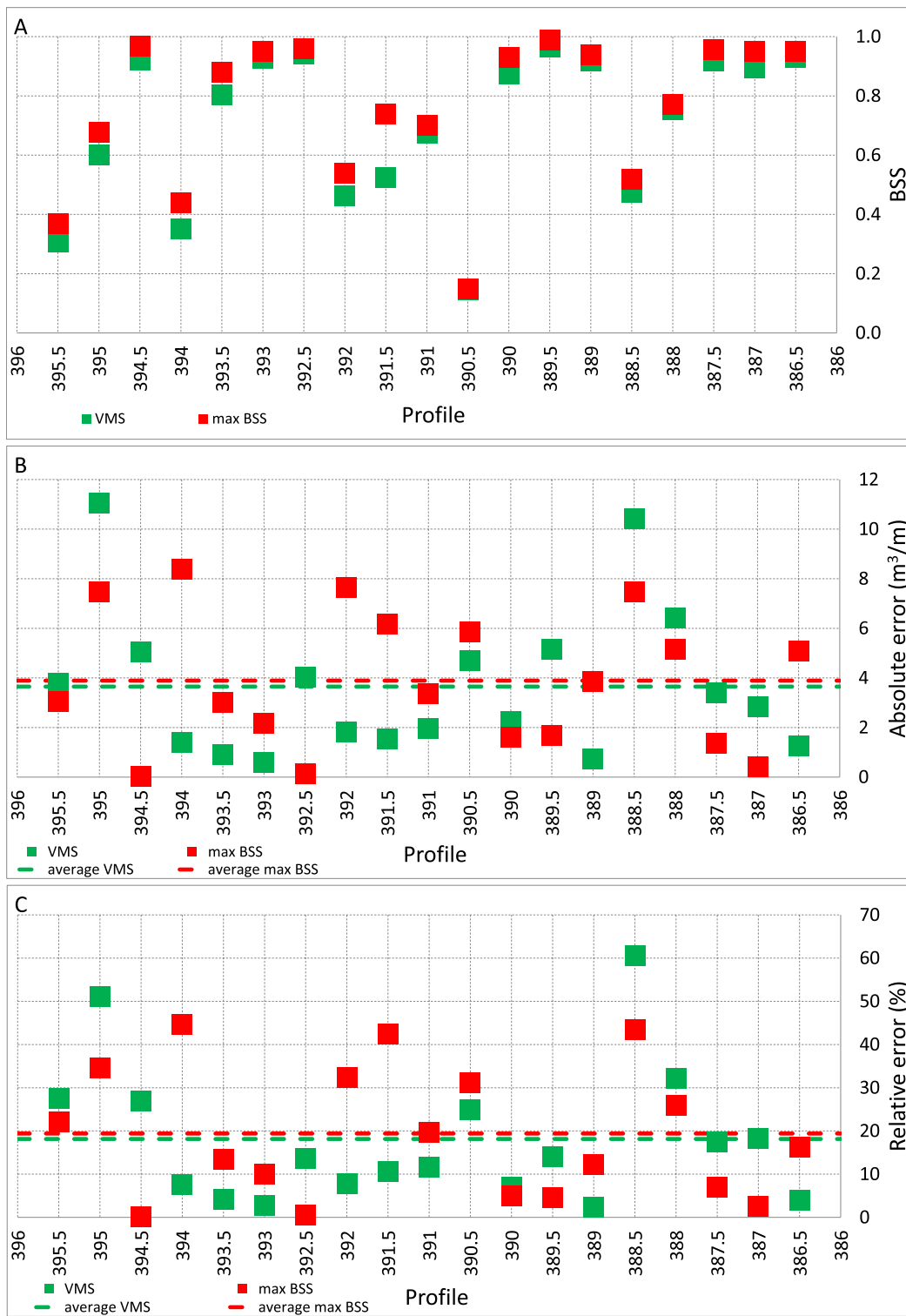


**Figure 4** XBeach 1D calibration results for particular profiles. A: Model match in line with BSS; B: Absolute error of volumetric changes for max BSS and best VMS simulations; C: Relative error of volumetric changes for max BSS and best VMS simulations.

## 4. Results

### 4.1. Model performance and accuracy

The results of model calibration using BSS values for individual profiles are shown in Figure 4. The BSS values for simu-

lations with the maximum BSS value are marked in red (max BSS), while those that are in line with the VMS are marked in green. In Figure 4A, for maximum values of the BSS, 10 profiles take values  $\geq 0.8$ , which means a ‘perfect’ fit.

For four profiles, the fit of the model varies in the range of 0.6–0.8, which means a ‘good’ fit, and four profiles are at

the ‘reasonable’ level in the range of 0.3–0.6. Only one profile (390.5) displayed a BSS of  $< 0.3$ , which means a ‘weak’ fit. In turn, the BSS values identified as being in line with the visual match of the profile shape (VMS) do not differ much from those with the maximum BSS; moreover, they reflect the profile shape better. The distinction of BSS values for max BSS and VMS simulations for each profiles is presented in Figure 4A. It is evident that values of BSS for VMS approach are lower.

The distribution of the absolute error of the volumetric changes is shown in Figure 4B. For simulations with a maximum BSS (max BSS), this error takes values from  $0.04 \text{ m}^3/\text{m}$  to  $8.38 \text{ m}^3/\text{m}$ , with an average value of  $3.89 \text{ m}^3/\text{m}$ . However, for the VMS simulations, this error ranges from  $0.59 \text{ m}^3/\text{m}$  to  $11.04 \text{ m}^3/\text{m}$ , and its average value is  $3.65 \text{ m}^3/\text{m}$ , which is slightly lower than that for max BSS. The high error values in the 388.5 profile result from its proximity to a heavy concrete seawall located in Dziwnów.

The analysis of the distribution of the relative error of volumetric changes (%) in individual profiles (Figure 4C) showed that the error ranges from 0.20% up to 44.69% for simulations with max BSS, and its average value is 19.40%. For VMS simulations, this error can be up to 60.64%, with an average value of 18.14%. Thus, it is concluded that simulations based on the maximum BSS value or the visually matched profile shape VMS give somewhat similar results, with an average relative error of approximately 20%.

Taking into account the absolute error, for simulations carried out on the basis of the max BSS, in 8 out of 19 profiles, the absolute error values are higher than the average error. For simulations performed on the basis of VMS, only 6 out of 19 profiles have higher error values than average. Similarly, the relative error values for simulations based on the max BSS are higher than the average in 8 out of 19 profiles, while for simulations based on VMS, only 6 out of 19 profiles obtained error values higher than average.

Analyzing the absolute and relative error values of the volumetric changes, it can be seen that there may be several reasons for this situation. The XBeach model is a short-term model used to simulate the volumetric changes to the coast that occur under the influence of hydrodynamic conditions such as storm events. This model is not able (using calibration parameters that are constant in simulation time) to simulate the accumulation process, which usually occurs during the storm calming and is represented by a beach bar.

Ideally, the data before and after the storm should be collected in the shortest possible time from the event. However, for calibration purposes, the only available survey data were data collected approximately 1.5 months before and after the event. Fortunately, the accumulated beach bar is very visible in most of these profiles. Apart from the accumulation related to storm calming, the shape of the cross-shore profile and thus its volume are affected by aeolian accumulation. The effects of aeolian accumulation may be observed in different parts of a beach profile. The XBeach model does not include aeolian accumulation in its simulation. Similarly, alongshore sediment transport is also not considered. Small waves and changes in water level that occur outside the time of the storm also affect the final shape of the profile.

In summary, it can be stated that the calibration of the model for each profile was carried out optimally. Simulations performed on the basis of VMS show slightly smaller absolute and relative error values than those based on the max BSS. Therefore, the simulation results from VMS were used in the further analyses in this work. The calibration results for each profile are presented individually in Table 1 as a set of *facua* and *wetslp* parameters.

#### 4.2. Impacts of the calibration parameter set: profile-specific vs. site-specific

Another aspect analyzed in the research was the impact of the adopted set of calibration parameters (*facua* and *wetslp*) on the predicted volumetric changes on the coast. Based on the VSM simulation results, parameter sets (*facua* and *wetslp*) were obtained for each of the 19 profiles; these sets are shown in Table 1. The *facua* parameter values range from 0.16 to 0.40, while the *wetslp* parameter values range from 0.35 to 0.60. Their average values are 0.27 and 0.57, respectively. The varying parameter values result from the research area, which is a complex coastal system where natural processes are modified by various coastal protection measures (Figure 1).

The most common approach for 1D modeling is to determine the optimum model parameters for one profile (surveyed before and after the storm event) and to apply them to the selected coast section as long as the alongshore characteristics are sufficiently uniform. In the case of the study area, many natural and anthropogenic conditions could affect the optimum values of the parameters. Therefore, we examined how the adoption of one set of optimum parameters (*facua* and *wetslp*) affects the level of the relative error of the modeled volumetric changes along the study area for all 19 profiles. Based on the VMS simulation (Table 1), the average values of the *facua* and *wetslp* parameters were calculated from all profiles (0.27 and 0.57, respectively), and these became set no. 1 for further research (Table 2).

Theoretically, each of the 19 profiles could be taken separately and its parameters used as the optimum model parameters (*facua* and *wetslp*) for the study area. The values of *facua* and *wetslp* parameters for each profile calibration (Table 1) were applied to all other profiles in each combinations, creating 361 simulations. BSS values were then calculated for these simulations. The profile sensitivity to changes in model parameters, on the base of the average, minimum and maximum BSS values for particular profiles with the application of sets of parameters that are optimal for other profiles is presented in Figure 5A. It can be seen that five profiles with average BSS values close to 0 or negative (395.5, 394, 390.5, 388.5 and 388) are very sensitive (least resistant) to changes in model parameters.

In sum, profiles with little BSS amplitude are stable; for these profiles, the application of an optimal set of parameters from other profiles did not affect the obtained results. On the other hand, profiles of high amplitude and low average BSS values that are located either near coastal engineering structures or at a different type of shore show improved results after the application of optimal sets, but only by a small increase in BSS value, since the specific features of their location are not included in the simulations.



**Table 1** The values of *facua* and *wetslp* parameters for the ‘visual matching profile shape (VMS)’ simulation for individual profiles with the average value (Figure 4A).

Profile	395.5	395	394.5	394	393.5	393	392.5	392	391.5	391	390.5	390	389.5	389	388.5	388	387.5	387	386.5	average
<i>facua</i>	0.40	0.37	0.20	0.27	0.26	0.24	0.17	0.23	0.24	0.27	0.31	0.19	0.16	0.19	0.40	0.32	0.30	0.30	0.23	0.27
<i>wetslp</i>	0.55	0.60	0.60	0.60	0.60	0.60	0.55	0.60	0.60	0.45	0.35	0.60	0.60	0.60	0.60	0.60	0.60	0.55	0.55	0.57

**Table 2** Parameter sets used for all profiles at once.

Set no.	Profile no.	BSS	<i>facua</i>	<i>wetslp</i>	Description
1	all	0.70	0.27	0.57	profile calibration average parameters (VMS, Table1)
2	387	0.62	0.30	0.55	the highest average BSS
3	387.5	0.62	0.30	0.60	the highest average BSS
4	388	0.61	0.32	0.60	one of the highest average BSS
5	390.5	0.61	0.31	0.35	one of the highest average BSS
6	389.5	-0.41	0.16	0.60	the lowest average BSS
7	all	-2.42	0.10	0.30	default average BSS

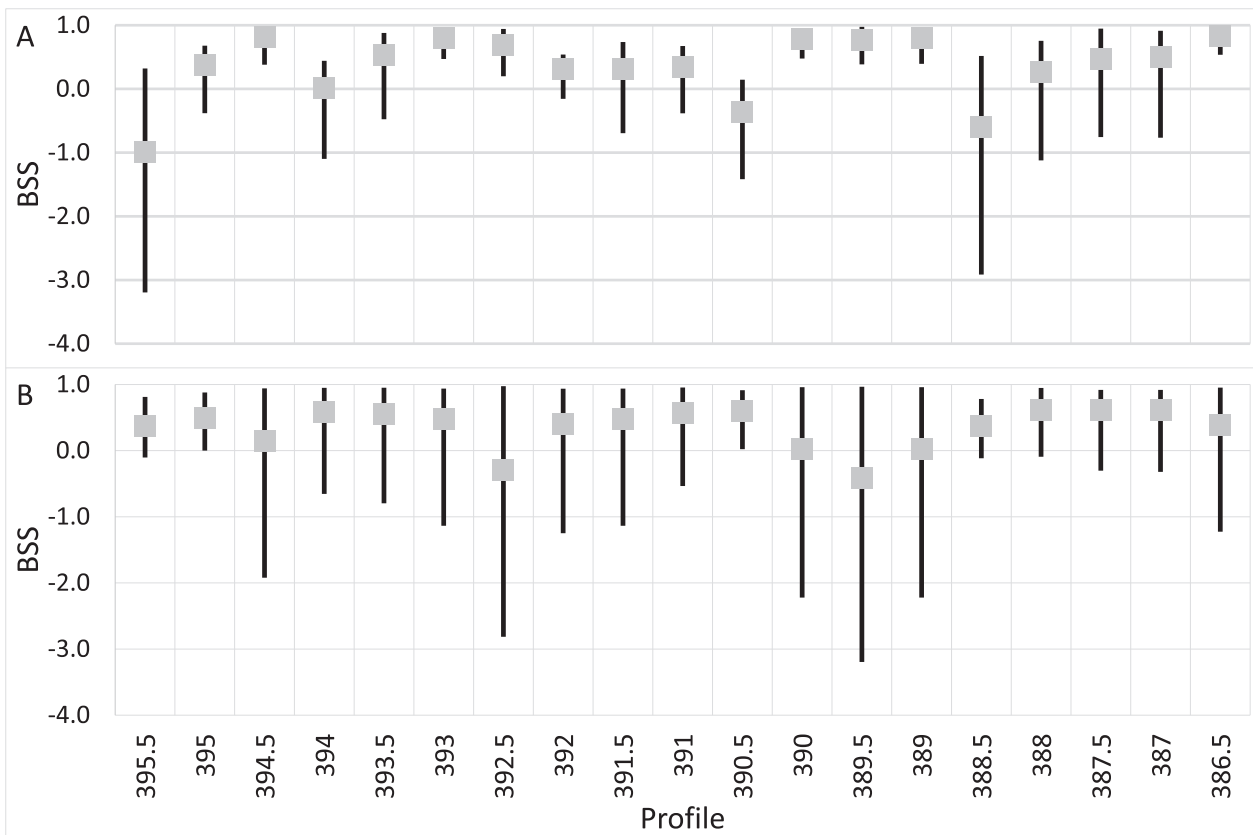


**Figure 5** Average, minimum and maximum BSS values for particular profiles with the application of sets of parameters that are optimal for other profiles. A: Profile sensitivity to changes in model parameters. B: Transferability of calibration parameters along the study area.

Moreover, average BSS values for all profiles from a given set of model parameters (profile optimum) were also calculated to find the optimum parameters by site. The average BSS value and its amplitude along the study area is shown in Figure 5B. It can be seen that the five profiles with the smallest average BSS values and their largest span (394.5, 392.5, 390, 389.5 and 389) very strongly affect

the simulations of other profiles, while others have a small impact.

Therefore, if we were looking for the answer to the question: what should the representative profile of the examined edge section be characterized by, we could assume that its calibration parameters should have the least impact on the simulations of other profiles and at the same time its sim-

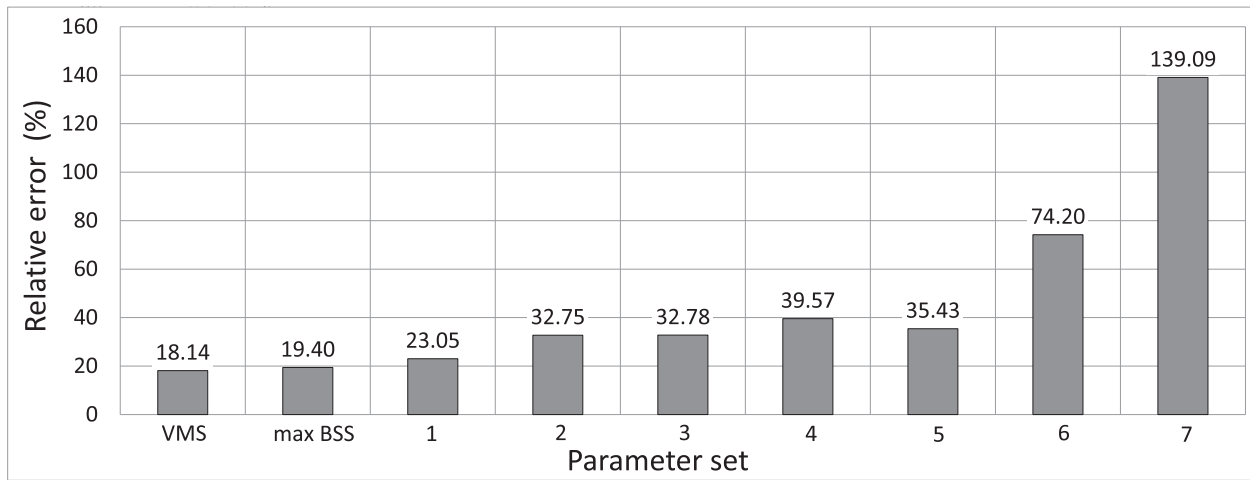


**Figure 6** Average value of the relative error for individual parameter sets: no. 1–7 (Table 2); max BSS and VMS (from Figure 4C).

ulations should be the most resistant to changes in parameters. In our case, these are the other profiles: 395, 393.5, 393, 392, 391.5, 391, 387.5, 387 and 386.5. Among the most favorable profiles in this respect, their location does not show special variation. On this basis, it is difficult to clearly define the criterion for choosing a single, representative profile.

The highest average BSS values were 0.62 and 0.61. This means that the application of the optimum parameters presented by profiles 390.5, 388, 387.5 and 387 to all 19 profiles will produce the highest average BSS values. These profiles were used to select the next sets of parameters (no. 2, 3, 4 and 5), for which the *facua* and *wetslp* values are shown in Table 2. Sets no. 2 and 3, which obtained an average BSS = 0.62, are characterized by the following values: *facua* = 0.3 and *wetslp* = 0.55 and *facua* = 0.3 and *wetslp* = 0.6, respectively. Sets no. 4 and 5, with an average BSS value = 0.61, had the values *facua* = 0.32 and *wetslp* = 0.6 and *facua* = 0.31 and *wetslp* = 0.35, respectively (Table 2). For comparison, two more sets were adopted: no. 6 and 7. Set no. 6 contains parameters optimized for profile 389.5. When these values were applied to all profiles, they produced the lowest average BSS values for all profiles (= -0.41). Last, set no. 7 is the model parameters set to their default values.

For each of the 19 profiles located in the research area, 7 simulations characterized by different values of the *facua* and *wetslp* parameters were run. They were run using the particular parameter sets shown in Table 2. Next, the mean values of the relative volumetric errors for each parameter set were calculated and are presented in Figure 6. For comparison, the mean values of the relative volumetric error that were calculated on the basis of the 19 profiles with the max BSS and VMS values are also presented (Figure 4C); these values were 19.4% and 18.14%, respectively.

It seems reasonable to use a set of averaged parameters from all profiles simultaneously (sets no. 1–5) because the relative error rate of these sets varies between 20 and 40%. In nonexperimental conditions, where one randomly located calibration profile is typically used, a relative error of volume changes of at least 40% should be expected; in particularly unfavorable cases, even 75% relative error can occur. At the same time, the use of a noncalibrated model is not

recommended because the relative error can reach up to 140% in these cases.

### 4.3. Influence of the prestorm bathymetry

Morphological data in the form of bathymetric-topographic profiles are usually created as combined profiles, i.e., the final shape is a result of various survey methods used for the underwater part (echosounder) and the subaerial part (geodetic methods, GPS, LIDAR) (see the morphological and hydrodynamic data subsection). Additionally, the data collection times for one profile are not the same, and the bathymetric data are usually shifted in time in relation to the topographic data. This generates errors, especially in the shallow area (up to a depth of 1 meter), where it is necessary to combine topographic and bathymetric data.

This study uses data provided by the Maritime Office in Szczecin in the form of bathymetric profiles that cover depths from -1 m to approx. -15 m from 2006, 2008, 2010 and 2012 for 19 profiles (every 500 m along the coast) and from 2004 for 10 profiles (395.5, 394.5, 393.5, 392.5, 391.5, 390.5, 389.5, 388.5, 387.5 and 386.5). On this basis, a computational grid was created in accordance with the conditions described in the section on the calibration of the model. As input data for the model, bathymetric data (from approx. -12 m to approx. -1 m) from a given year were linked with prestorm subaerial data from 2009 (from -1 m to the shore and the subaerial part).

Five combinations of prestorm input profiles were created for each of the 19 profiles (10 profiles for 2004). A simulation of the storm event of 2009 was performed using these input profiles and set no. 1 of the model parameters, which was determined as the best set (Table 2). The values and spatial distributions of the relative error (%) for simulations with different input bathymetry data is shown in Figure 7.

The high diversity in the value of the relative error of the volumetric changes depending on the accepted prestorm bathymetry is visible in Figure 7. In the worst case, the error is 70%. However, regardless of the accepted prestorm bathymetry, this error does not exceed 35% in 14 out of 19 profiles and it is lower than 30% in 11 profiles. Comparing these results with values of relative errors associated with

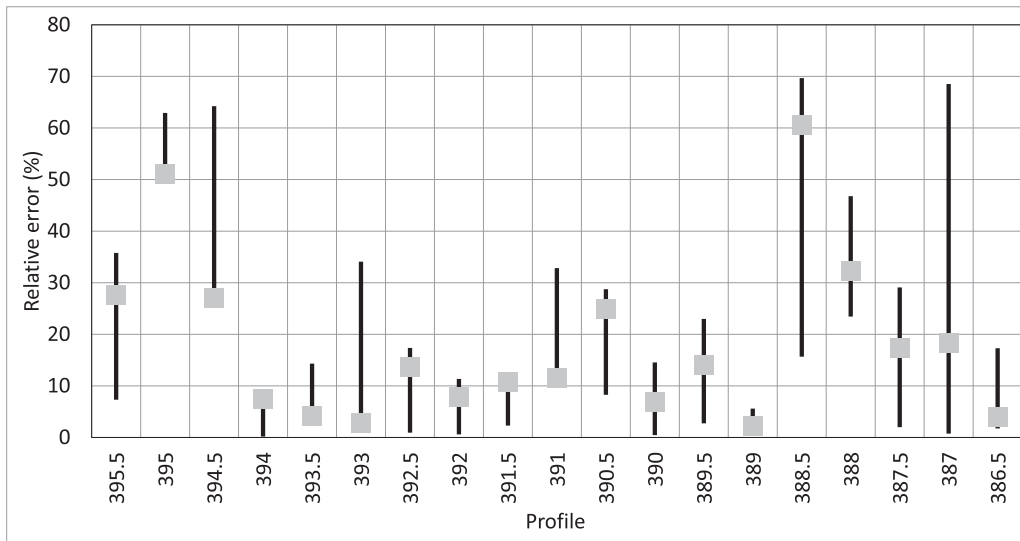


**Figure 7** The relative error for the 2009 storm event simulation with different input bathymetry data. Squares depict the 2009 bathymetry, while lines show the error range of the variations in bathymetry.

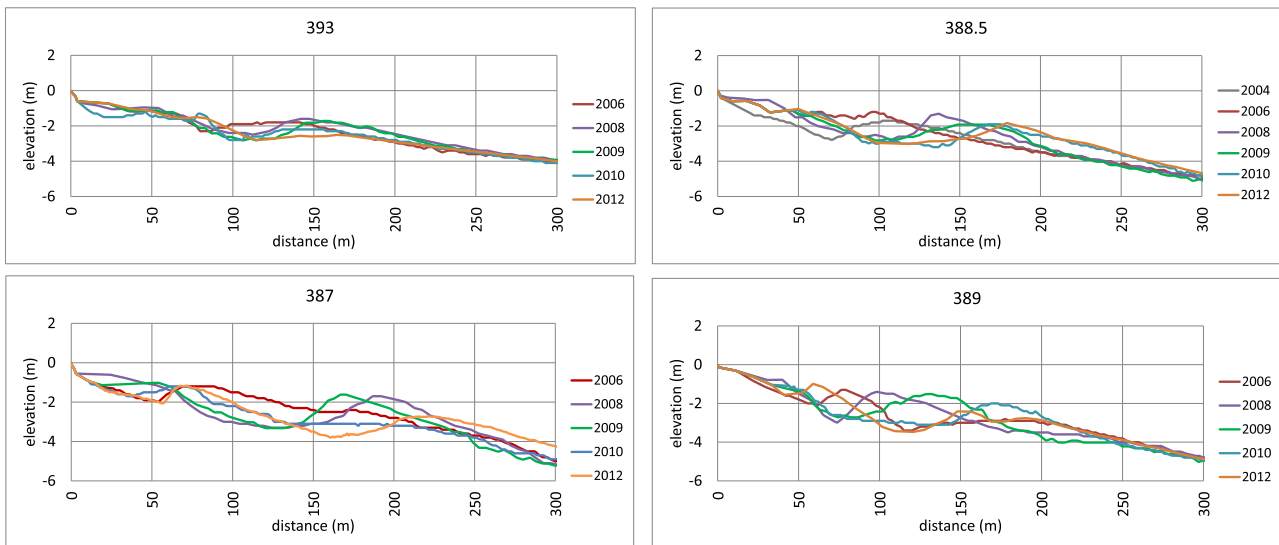


**Figure 8** Bathymetric survey in particular years for selected coastal profiles.

the selection of calibration parameters for the model (30–40%), it can be concluded that, except in a few of profiles, up-to-date prestorm bathymetry does not impact accuracy to a greater extent than the proper selection of a set of calibration parameters.

To demonstrate the various shapes and variability of profiles in particular years, 4 profiles (387, 388.5, 389, 393) were chosen and they are illustrated in Figure 8. Analysis of the profile shapes in the nearshore shows that profile 387 features a variety of shapes, which translates to a high amplitude of relative error (ca. 70%; Figure 7), whereas profile 389, in which the shapes from different years are almost the same, reveals a low amplitude of relative error (5%; Figure 7).

In the next steps, an attempt was made to determine the characteristic features of the shore profile that have the greatest impact on the determination of subaerial volumetric changes. Calculations were performed for each pro-

file for each considered year, including the seabed slope and nearshore volume every 10 m from the shoreline (from 0–10 m up to 0–150 m). The difference was calculated consecutively between the values calculated for particular years and the values of the 2009 profile that were used for calibration. Furthermore, the differences between these seabed slopes were correlated with the differences in the subaerial volumetric changes obtained from simulations with prestorm bathymetry from different years in relation to the volumetric changes modeled with the 2009 bathymetry. The results are shown in Figure 9.

The correlation coefficient (R) between the seabed slope and the differences in modeled changes in the nearshore increases from 0.48 to 0.74 in the first 40 m from the shore and then decreases to 0 at 80–100 m offshore. At greater depths, the coefficient is insignificant, as it equals not more than 0.2. In turn, the correlation coefficient between differences in the nearshore volume and differences in the mod-

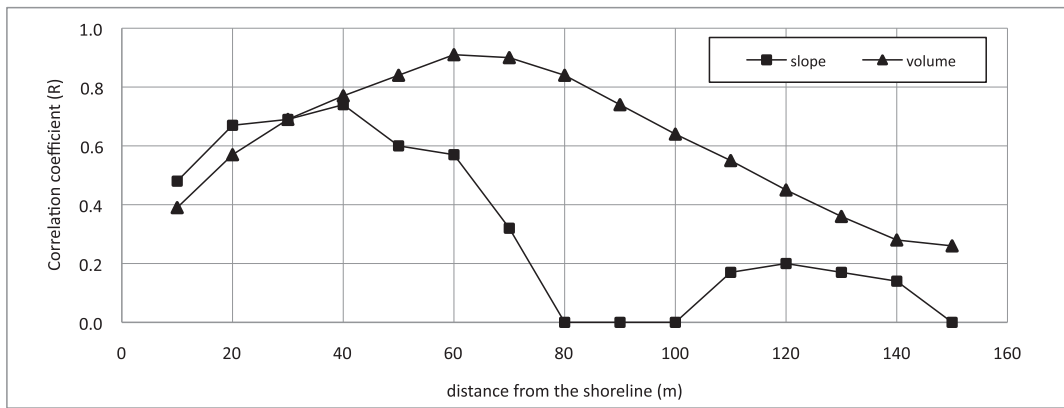


**Figure 9** Correlation coefficient (R) of the modeled differences in subaerial volumetric changes with seabed slope changes and nearshore volumetric changes between 2009 and other considered years (see detailed description in the text).

eled changes in the subaerial part rises from 0.39 in the first 10 m to 0.91 at a distance of 60 m from the shoreline. Then, a progressive decrease is observed to about 0.25 at a distance of 150 m from the shoreline.

The conclusion is that changes in the seabed slope up to 40 m off the shoreline and changes in the nearshore volume up to 60 m off the shoreline are the most significant bathymetry-related factors for modeling changes in the subaerial part of the profile. The correlations between these aforementioned differences (for seabed slope at 0–40 m and for nearshore volume at 0–60 m) are shown in Figure 10. An increase in the seabed slope by 2% can result in an increase in the difference in the volume of the subaerial part of up to 8 m<sup>3</sup>/m, while a decrease by ca. 1% may decrease that difference to –6 m<sup>3</sup>/m (Figure 10A). On the other hand, an increase in the nearshore volume by ca. 20 m<sup>3</sup>/m will result in a negative volume in the subaerial part of the profile of –6 m<sup>3</sup>/m, while a decrease of 30 m<sup>3</sup>/m will decrease the difference to –8 m<sup>3</sup>/m (Figure 10B). It is worth mentioning that in the study area, i.e., the Dziwnów Spit, the depth at a distance of 40 m off the shoreline is 1.5 m on average (min. is 0.8 m and max. is 2 m), while at 60 m off the shoreline, the depth is 2 m, on average (min. 1 m, max. 2.5 m).

In summary, the impact of the bathymetry on modeling the subaerial volumetric changes is observed in the first 40 m off the shoreline in terms of the seabed slope and in the first 60 m in terms of the nearshore volume. The greater the slope, the more the nearshore volume decreases. In these situations, the volumetric changes increase, in contrast to the opposite situation – if the slope is gentler, it makes the nearshore volume larger, which will result in smaller changes in the subaerial part.

## 5. Discussion

In the first stage of this study, an adaptation of the model in profile mode (1D) was carried out for 19 coastal profiles located over the entire length of the study area, 500 m apart (395.5–386.5 km). The calibration was performed for a storm event in 2009 that caused significant changes to the dune and the beach. An evaluation of the correctness of the modeled volumetric changes was performed on the basis of

several parameters: Brier skill score (BSS), absolute error of volumetric changes (m<sup>3</sup>/m), relative error of volumetric changes (%) and visual match of the profile shape (VMS).

The study of the model calibration involved the following parameters: critical wet slope (*wetslp*), sediment transport parameter for different wave shapes (*facua*), morphological acceleration factor (*morfac*) and Shields coefficient (*smax*). The two latter parameters were set as constant values of 10 and 1, respectively, while the values of the first two ranged from 0 to 1 for *facua* and from 0.3 to 0.6 for *wetslp*, with 0.05 increments. The other calibration parameters remained at their default values. The best calibration results for the 19 coastal profiles were obtained when the value of *facua* was between 0.16 and 0.40 and the value of *wetslp* was between 0.35 and 0.60. These values for *facua* correspond or are slightly higher than those used by Splinter and Palmsten (2012), Vousdoukas et al. (2012) and Elsayed and Oumeraci (2017), where *facua* values varied between 0.1 and 0.3. According to Voukouvalas (2010), *facua* = 0.5 is relevant for moderate wave conditions, while *facua* = 0 or a low value generally corresponds to storms. However, the cited studies referred to tidal areas that feature stronger wave dynamics than their southern Baltic counterparts. For the southern Baltic Sea, in terms of wave action, a storm is understood as a period of time when the significant wave height exceeds 1 m for at least 6 hours (Robakiewicz, 1991). Therefore, accepting slightly higher values of *facua* seems to be appropriate. Furthermore, Elsayed and Oumeraci (2017) correlate the value of *facua* with the mean coastal slope, which in the case of Polish study area characterized by a rather narrow beach compared to tidal coasts, requires the application of slightly higher values of this parameter.

The calibration of the model for particular profiles led to a good coherence between the real and the modeled volumetric changes, as the mean absolute error was ca. 4 m<sup>3</sup>/m, and the mean relative error amounted to ca. 20% for a single profile. The worst results were obtained for profiles located near coastal engineering structures. The absolute error there reached as high as 10 m<sup>3</sup>/m, while the relative error reached 60%. One disadvantage of 1D model adaptation is the lack of options for taking such structures into consideration, which means that the modification of coastal processes that they induce is overlooked.

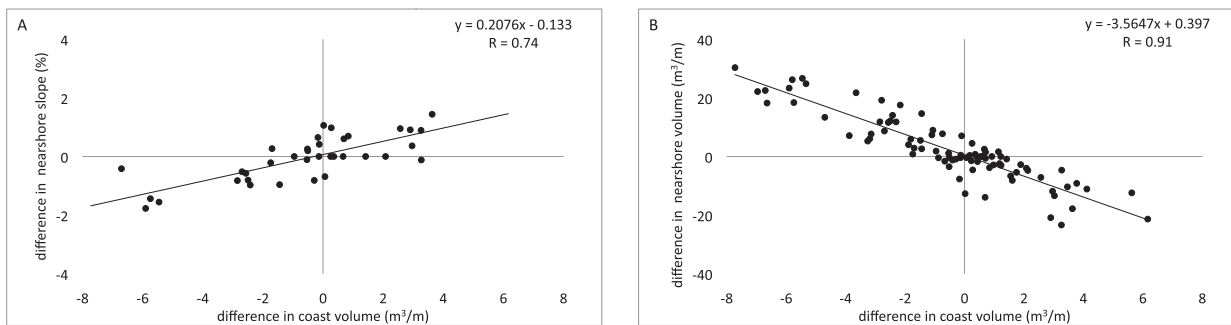


**Figure 10** Correlation charts A: differences in seabed slope (40 meters) vs differences in the subaerial part; B: differences in nearshore volume (60 meters) vs differences in the subaerial part.

In the next stage of the study, a verification of whether one set of parameters can be used for all profiles was carried out. This can be very useful if the model is deployed in more sophisticated online tools, such as early warning systems (Haerens et al., 2012). The study revealed that it was possible to apply one set of *facua* and *wetslp* parameters for all profiles at once, previously calibrated for the storm of 2009 within the Dziwnów Spit area. Simmons et al. (2017) noted that optimal parameters for the area of study should be identified after an evaluation of the uniformity of alongshore coastal processes (e.g., the same storm impact regime). In this case, all profiles were identified as a collision regime (when total water level exceeds dune toe and dune erosion occurs) according to the storm impact scale by Sallenger (2000), making the application of one parameter set possible.

However, the increase in the error values for the modeled volumetric changes should be considered. For example, among the tested sets, the lowest mean relative error (25%) was obtained for *facua* = 0.27 and *wetslp* = 0.57; the mean relative error rose to 40% when the parameter values were changed to *facua* = 0.32 and *wetslp* = 0.60. This increase is caused by the construction of a variety of coastal defense structures that modify how natural processes occur. The studies of Simmons et al. (2019) on the changeability and transferability of calibration parameters along shorelines showed that, in cases of missing data for model calibration, the lowest errors were achieved by transferring the parameters from the nearest profiles. However, these studies were conducted on embayment beaches. In the Polish study area, which is fairly straight but includes various coastal defenses, making the system quite complicated, such an approach is somewhat unsatisfactory. The results of this study indicate that the application of an average set of calibration parameters is a reliable alternative.

The last stage of the study of the application of the 1D XBeach model consisted of an investigation of how the bathymetry data recorded before the storm influence the volumetric changes determined by the model. This aspect is crucial due to the substantial difficulty of obtaining data just before and after storm events. In Poland, such data are recorded by the Maritime Offices usually once a year during the summer as a part of the coastal zone monitoring program. Another idea behind this study was to verify whether updating the bathymetric data exported to operational online early warning systems has an impact on the determina-

tion of volumetric changes. Therefore, to achieve the goal of this study, all the available bathymetric data were collected, and a simulation of the storm event of 2009 was carried out using the combined data: the prestorm topography recorded prior to that storm event and the bathymetry data from 2004, 2006, 2008, 2010 and 2012.

This study revealed that the impact of the bathymetry on modeling volumetric changes was evident up to 100 m off the shoreline and to a depth of 2 m. A change in the seabed slope of 1–2% within the first 40 m off the shoreline, and hence a change in the nearshore volume of 20–30 m<sup>3</sup>/m in the first 60 m, may increase the difference between the real and modeled changes in the volume of the subaerial part in profile by ca. 6–8 m<sup>3</sup>/m. The obtained results are in line with those of studies conducted by Splinter et al. (2011). In studies on the possibility of predicting dune erosion induced by a storm event without knowing the prestorm bathymetry, it was revealed that less dune erosion is observed for profiles with gentler seabed slopes, whereas steeper sea bed profiles induce greater erosion in the subaerial part of the profile.

## 6. Conclusion

The application of the XBeach numerical model to determine the volumetric changes to the southern Baltic dune coast using the example of the Dziwnów Spit allowed us to define:

- the calibration parameters of the 1D model;
- the possibility of using a set of parameters for all profiles at the same time with the determination of related errors; and
- the impact of prestorm bathymetry on the modeled volumetric change.

The morphology of the coast before and after a storm event should be recorded as late as possible and as soon as possible before and after the storm event, respectively. The storm calming period is characterized by the accumulative of coastal and aeolian processes, which the XBeach model does not take into account. These factors affect the volume of the profile and the calibration results. In such cases, the popular BSS indicator should be replaced with the VMS approach. Simulations conducted on the basis of

the VMS showed slightly lower absolute and relative error values than those performed on the basis of the best BSS (max BSS).

Good correspondence between the measured and modeled volume changes was obtained. The mean absolute error from all profiles was approximately  $4 \text{ m}^3/\text{m}$ , while the mean relative error was approximately 20%. The poorest results were recorded in the vicinity of coastal engineering structures. In these cases, the absolute error was up to  $10 \text{ m}^3/\text{m}$ , while the relative error was 60%. The disadvantage of the use of this model in 1D mode is its lack of ability to take into account coastal engineering structures and the modification of natural processes that they induce. In this case, the calibration with an extended range of calibration parameters or the application of a 2D model should be applied.

Under the described conditions, it is possible to apply one set of *facua* and *wetslp* parameters for all profiles at the same time; however, the increase in the error values when determining the volumetric change should be expected. It is reasonable to use the averaged parameters from all profiles because in that case, the relative error varies between 20 and 40%. When a single randomly located calibration profile is used, the relative error for the volume changes can be at least 40%, while in particularly unfavorable cases, it may rise to 75%. The use of a noncalibrated model is also not recommended because the relative error can reach up to 140%.

The influence of prestorm bathymetry on modeling volumetric changes is most evident in the area up to approximately 100 m from the shoreline. Changing the seabed slope by 1–2% up to 40 m off the shoreline and changing the nearshore volume by 20–30  $\text{m}^3/\text{m}$  to 60 m off the shoreline can increase the difference between the measured and the modeled volume change by approximately 6–8  $\text{m}^3/\text{m}$ . At higher slopes, the nearshore volume decreases. In these situations, the volumetric changes increase; in the opposite situation, when the slope is gentler, the nearshore volume is larger, which results in smaller changes in the sub-aerial part. Therefore, it seems necessary that the monitoring of the maritime coastal zone in the form of bathymetric and topographic measurements performed only once a year should be extended by measurements performed both before and after the storm.

However, regardless of the prestorm bathymetry used, the relative error of the volumetric changes on the shore is in the range of 30–35%. Comparing these results with the magnitude of the relative errors associated with the selection of model calibration parameters, which were 30–40%, it can be concluded that except in a few profiles, the prestorm bathymetry and the randomness of the selection of the calibration parameters have similar effects on the accuracy of predictions of volumetric changes.

## Data availability

The data used for the research described in this article were obtained from the Maritime Office in Szczecin and the Interdisciplinary Centre for Mathematical and Computational Modeling, University of Warsaw. The data supporting the findings of this study are available from the corresponding author N.B. on request.

## Acknowledgments

This research was conducted and financed within the framework of statutory research at the University of Szczecin and as a part of the SatBałtyk project funded by the European Union through the European Regional Development Fund – contract No. POIG.01.01.02-22-011/09, project entitled ‘Satellite Monitoring of the Baltic Sea Environment’.

## Declaration of competing interest

The authors declare that they have no known competing financial interests or personal relationships that could have appeared to influence the work reported in this paper.

## References

- Armaroli, C., Grottoli, E., Harley, M.D., Ciavola, P., 2013. Beach morphodynamics and types of foredune erosion generated by storms along the Emilia-Romagna coastline, Italy. *Geomorphology* 199, 22–35. <https://doi.org/10.1016/j.geomorph.2013.04.034>
- Barnard, P.L., van Ormondt, M., Erikson, L.H., Eshleman, J., Hapke, C., Ruggiero, P., Adams, P.N., Foxgrover, A.C., 2014. Development of the Coastal Storm Modeling System (CoSMoS) for predicting the impact of storms on high-energy, active-margin coasts. *Nat. Hazards* 74, 1095–1125. <https://doi.org/10.1007/s11069-014-1236-y>
- Bruun, P., 1954. *Coast erosion and the development of beach profiles*. Beach Erosion Board, U.S. Army Corps of Engineers Technical Memorandum No. 44.
- Bugajny, N., Furmańczyk, K., 2017. Comparison of Short-Term Changes Caused by Storms along Natural and Protected Sections of the Dziwnow Spit, Southern Baltic Coast. *J. Coast. Res.* 33, 775–785. <https://doi.org/10.2112/JCOASTRES-D-16-00055.1>
- Bugajny, N., Furmańczyk, K., Dudzińska-Nowak, J., 2015. Application of XBeach to model a storm response on a sandy spit at the southern Baltic. *Oceanol. Hydrobiol. Stud.* 44, 552–562. <https://doi.org/10.1515/ohs-2015-0052>
- Bugajny, N., Furmańczyk, K., Dudzińska-Nowak, J., Paplińska-Swerpel, B., 2013. Modelling morphological changes of beach and dune induced by storm on the Southern Baltic coast using XBeach (case study: Dziwnow Spit). *J. Coast. Res.* 65, 672–677. <https://doi.org/10.2112/SI65-114.1>
- Ciavola, P., Ferreira, O., Van Dongeren, A., Van Thiel de Vries, J., Armaroli, C., Harley, M., 2014. Prediction of Storm Impacts on Beach and Dune Systems. In: Quevauviller, P (Ed.), *Hydrometeorological Hazards: Interfacing Science and Policy*. John Wiley & Sons, Ltd, 227–252.
- Cieślakiewicz, W., Herman, A., 2001. Modelowanie falowania wiatrowego Morza Bałtyckiego i Zatoki Gdańskiej. *Inżynieria Morska i Geotechnika* 22 (4), 173–184.
- Cieślakiewicz, W., Herman, A., 2002. Wave and current modelling over the Baltic Sea. In: Smith, J.M. (Ed.), *Proc. 28th Intern. Conf. Coastal Engng Conf., ICCE 2002*. World Scientific, Cardiff, 176–187.
- Dean, R.G., Maurmeyer, E.M., 1983. Models for beach profile response. In: Komar, P. (Ed.), *Handbook of Coastal Processes and Erosion*. CRC Press, Boca Raton, 151–165.
- Dissanayake, P., Brown, J., Karunaratna, H., 2014. Modelling storm-induced beach/dune evolution: Sefton coast, Liverpool Bay, UK. *Mar. Geol.* 357, 225–242. <https://doi.org/10.1016/j.margeo.2014.07.013>

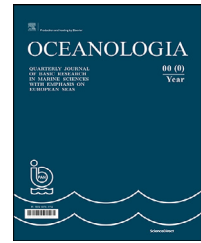
- Dobracki, R., Zachowicz, J., 2005. Mapa Geodynamiczna Polskiej Strefy Brzegowej Bałtyku. Szczecin, Państwowy Instytut Geologiczny. Oddział Pomorski, scale 1:10,000, 2 sheets.
- Dudzińska-Nowak, J., 2015. Metody ochrony zachodniego wybrzeża Polski i ich wpływ na zmiany brzegu w latach 1938-2011. Metody ochrony zachodniego wybrzeża Polski i ich wpływ na zmiany brzegu w latach 1938-2011. Wydawnictwo Naukowe Uniwersytetu Szczecińskiego, Szczecin.
- Dudzińska-Nowak, J., 2006a. Coastline long-term changes of the selected area of the Pomeranian Bay. In: Tubielewicz, A. (Ed.), Coastal Dynamic, Geomorphology and Protection. Gdańsk University of Technology, Gdańsk, 163–170.
- Dudzińska-Nowak, J., 2006b. Wpływ metod ochrony brzegu morskiego na zmiany położenia linii podstawy wydmy na wybranym przykładzie. In: Koźmiński, Cz., Dutkowski, M., Radziejewska, T. (Eds.), Człowiek i środowisko przyrodnicze Pomorza Zachodniego: III. Środowisko przyrodnicze i problemy społeczno-ekonomiczne, Szczecin, 91–98.
- Dudzińska-Nowak, J., Wężyk, P., 2014. Volumetric changes of a soft cliff coast 2008–2012 based on DTM from airborne laser scanning (Wolin Island, southern Baltic Sea). *J. Coast. Res.* 70, 59–64. <https://doi.org/10.2112/si70-011.1>
- Edelman, T., 1972. Dune erosion during storm conditions. In: Proceedings of the 13th Coastal Engineering Conference. ASCE, 1305–1311.
- Elsayed, S.M., Oumeraci, H., 2017. Breaching of coastal barriers under extreme storm surges and implications for groundwater contamination: Improvement and Extension of the XBeach Model to Account for New Physical Processes. Internal Report no 1073/17, Leichtweiß-Institut für Hydraulic Engineering and Water Resources, TU, Braunschweig.
- Furmańczyk, K., Andrzejewski, P., Benedyczak, R., Bugajny, N., Cieszyński, Ł., Dudzińska-Nowak, J., Giza, A., Paprotny, D., Terefenko, P., Zawiślak, T., 2014. Recording of selected effects and hazards caused by current and expected storm events in the Baltic Sea coastal zone. *J. Coast. Res.* 70, 338–342. <https://doi.org/10.2112/SI70-057.1>
- Furmańczyk, K., Dudzińska-Nowak, J., 2009. Effects of extreme storms on coastline changes: A southern Baltic example. *J. Coast. Res.* 56, 1637–1640.
- Furmańczyk, K.K., Dudzińska-Nowak, J., Brzezowska, N., Furmańczyk, K.A., Papińska-Swerpel, B., 2011. Dune erosion as a result of the significant storms at the western Polish coast (Dziwnow Spit example). *J. Coast. Res.* 64, 756–759.
- Haerens, P., Ciavola, P., Ferreira, Ó., van Dongeren, A., van Koningsveld, M., Bolle, A., 2012. Online Operational Early Warning System Prototypes to Forecast Coastal Storm Impacts (CEWS). In: Proc. 33rd Conf. Coast. Eng. 2012, 1142–1149. <https://doi.org/10.9753/icce.v33.management.45>
- Harley, M., Armaroli, C., Ciavola, P., 2011. Evaluation of XBeach predictions for a real-time warning system in Emilia-Romagna, Northern Italy. *J. Coast. Res.* 64, 1861–1865.
- Karunaratna, H., Pender, D., Ranasinghe, R., Short, A.D., Reeve, D.E., 2014. The effects of storm clustering on beach profile variability. *Mar. Geol.* 348, 103–112. <https://doi.org/10.1016/j.margeo.2013.12.007>
- Kriebel, D.L., Kraus, N.C., Larson, M., 1991. Engineering methods for cross-shore beach profile response. In: Proceedings of Coastal Sediments '91. ASCE, 557–571.
- Larson, M., Kraus, C.N., 1989. SBEACH: Numerical model for simulating storm-induced beach change. Report 1, Empirical foundation and model development. Technical Report CERC-89-9, Coast Eng. Research Center, U.S. Army Engineer Waterways Experiment Station, Vicksburg, Mississippi.
- McCall, R.T., Van Thiel de Vries, J.S.M., Plant, N.G., Van Dongeren, A.R., Roelvink, J.A., Thompson, D.M., Reniers, A.J.H.M., 2010. Two-dimensional time dependent hurricane overwash and erosion modeling at Santa Rosa Island. *Coast. Eng.* 57, 668–683. <https://doi.org/10.1016/j.coastaleng.2010.02.006>
- Musielak, S., Furmańczyk, K., Bugajny, N., 2017. Factors and processes forming the Polish Southern Baltic Sea coast on various temporal and spatial scales. In: Harff, J., Furmańczyk, K., von Storch, H. (Eds.), *Coastline changes of the Baltic Sea from South to East: past and future projection*, Vol. 19. Coastal Research Library, 69–86.
- Musielak, S., Łabuz, T., Wochna, S., 2007. Procesy morfodynamiczne strefy brzegowej Mierzei Dziwnowskiej. In: Florek, W. (Ed.), *Geologia i geomorfologia Półwyspu Bałtyckiego*, Wydaw. PAP, Słupsk, 63–75.
- Palmsten, M.L., Splinter, K.D., 2016. Observations and simulations of wave runup during a laboratory dune erosion experiment. *Coast. Eng.* 115, 58–66. <https://doi.org/10.1016/j.coastaleng.2016.01.007>
- Papińska, B., 1994. Weryfikacja widma JONSWAP dla Bałtyku w oparciu o pomiary falowania. In: Pruszk, Z., Wilde, P. (Eds.), *Budownictwo morskie a środowisko. Materiały sympozjum*. Wydawnictwo IBW PAN, Gdańsk, 73–84.
- Papińska, B., 1999. Wave analysis at Lubiatowo and in the Pomeranian Bay based on measurements from 1997/1998 - comparison with modelled data (WAM4 model). *Oceanologia* 41 (2), 241–254.
- Papińska, B., 2001. Specific features of sea waves in the Pomeranian Bay. *Archives of Hydro-Engineering and Environmental Mechanics* 48, 55–72.
- Papińska, B., Reda, A., 2001. Regional variability of the wave climate at the Polish coast of the Baltic Sea. In: Szmidt, K. (Ed.), *Zastosowania mechaniki w budownictwie lądowym i wodnym. Księga Jubileuszowa poświęcona 70-leciu urodzin Profesora Piotra Wilde*. Wydawnictwo IBW PAN, Gdańsk, 191–215.
- Pender, D., Karunaratna, H., 2013. A statistical-process based approach for modelling beach profile variability. *Coast. Eng.* 81, 19–29. <https://doi.org/10.1016/j.coastaleng.2013.06.006>
- Racinowski, R., Seul, C., 1999. Brzeg i podbrzeże Mierzei Dziwnowskiej. In: Borówka, R.K., Młynarczyk, Z., Wojciechowski, A. (Eds.), *Ewolucja geosystemów nadmorskich południowego Bałtyku*. Bogucki Wyd. Nauk., Poznań-Szczecin, 115–120.
- Ranasinghe, R., Swinkels, C., Luijendijk, A., Roelvink, D., Bosboom, J., Stive, M., Walstra, D.J., 2011. Morphodynamic upscaling with the MORFAC approach: Dependencies and sensitivities. *Coast. Eng.* 58, 806–811. <https://doi.org/10.1016/j.coastaleng.2011.03.010>
- Robakiewicz, M., 1991. Analiza długoterminowej zmienności ekstremalnych warunków falowych na Bałtyku Południowym na przykładzie rejonu Półwyspu Helskiego. IBW PAN PhD. thesis.
- Roelvink, D., Reniers, A., van Dongeren, A., van Thiel de Vries, J., Lescinski, J., McCall, R., 2010. XBeach Model Description and Manual. Unesco-IHE Institute for Water Education. Delft and Delft University of Technology.
- Roelvink, D., Reniers, A., van Dongeren, A., van Thiel de Vries, J., McCall, R., Lescinski, J., 2009. Modelling storm impacts on beaches, dunes and barrier islands. *Coast. Eng.* 56, 1133–1152. <https://doi.org/10.1016/j.coastaleng.2009.08.006>
- Sallenger, A.H.J., 2000. Storm impact scale for barrier islands. *J. Coast. Res.* 16, 890–895.
- Steezel, H.J., 1993. Cross-shore transport during storm surges. Delft Technical University, PhD thesis.
- Simmons, J.A., Harley, M.D., Marshall, L.A., Turner, I.L., Splinter, K.D., Cox, R.J., 2017. Calibrating and assessing uncertainty in coastal numerical models. *Coast. Eng.* 125, 28–41. <https://doi.org/10.1016/j.coastaleng.2017.04.005>
- Simmons, J.A., Splinter, K.D., Harley, M.D., Turner, I.L., 2019. Calibration data requirements for modelling subaerial beach storm erosion. *Coast. Eng.* 152, 103507. <https://doi.org/10.1016/j.coastaleng.2019.103507>

- Splinter, K.D., Palmsten, M.L., 2012. Modeling dune response to an East Coast Low. *Mar. Geol.* 329–331, 46–57. <https://doi.org/10.1016/j.margeo.2012.09.005>
- Splinter, K.D., Strauss, D., Tomlinson, R.B., 2011. Can we reliably estimate dune erosion without knowing pre-storm bathymetry? In: *Coasts and Ports 2011: Diverse and Developing: Proceedings of the 20th Australasian Coastal and Ocean Engineering Conference and the 13th Australasian Port and Harbour Conference*. Engineers Australia, 694–699.
- Sutherland, J., Peet, A.H., Soulsby, R.L., 2004. Evaluating the performance of morphological models. *Coast. Eng.* 51, 917–939. <https://doi.org/10.1016/j.coastaleng.2004.07.015>
- Sztobryn, M., Stigge, H.J., Wielbińska, D., Weidig, B., Stanisławczyk, I., Kańska, A., Krzysztofik, K., Kowalska, B., Letkiewicz, B., Mykita, M., 2005. Storm surges in the southern Baltic (western and central parts). Rep. No. 39, *Berichte des Bundesamtes für Seeschifffahrt und Hydrographie*, Hamburg-Rostock.
- van Rijn, L.C., Wasltra, D.J.R., Grasmeyer, B., Sutherland, J., Pan, S., Sierra, J.P., 2003. The predictability of cross-shore bed evolution of sandy beaches at the time scale of storms and seasons using process-based profile models. *Coast. Eng.* 47, 295–327. [https://doi.org/10.1016/S0378-3839\(02\)00120-5](https://doi.org/10.1016/S0378-3839(02)00120-5)
- van Thiel de Vries, J.S.M., 2009. *Dune Erosion During Storm Surges*. Dune Erosion During Storm Surges. IOS Press, Amsterdam.
- Vellinga, P., 1986. Beach and dune erosion during storm surges. Delft Hydraulics Comm. No. 372, Delft Hydraulics Laboratory, Delft, The Netherlands.
- Voukouvalas, E., 2010. Coastal response during the 1953 and 1976 storm surges in the Netherlands. Field data validation of the XBeach model. Delft University of Technology. Master thesis.
- Vousdoukas, M., Almeida, L., Ferreira, Ó., 2011. Modelling storm-induced beach morphological change in a meso-tidal, reflective beach using XBeach. *J. Coast. Res.* 64, 1916–1920.
- Vousdoukas, M.I., Ferreira, Ó., Almeida, L.P., Pacheco, A., 2012. Toward reliable storm-hazard forecasts: XBeach calibration and its potential application in an operational early-warning system. *Ocean Dyn.* 62, 1001–1015. <https://doi.org/10.1007/s10236-012-0544-6>
- WAMDI Group, 1988. The WAM model—a third generation ocean wave prediction model. *J. Phys. Oceanogr.* 18, 1775–1810.
- Williams, J.J., Esteves, L.S., Rochford, L.A., 2015. Modelling storm responses on a high-energy coastline with XBeach. *Model. Earth Syst. Environ.* 1, 3. <https://doi.org/10.1007/s40808-015-0003-8>
- Zawadzka-Kahlau, E., 1999. *Tendencje rozwojowe polskich brzegów Bałtyku południowego*. Gdańskie Towarzystwo Naukowe, Gdańsk, 147 pp.
- Zeidler, R.B., Wróblewski, A., Miętus, M., Dziadziuszko, Z., Cyberski, J., 1995. Wind, wave, and storm surge regime at the Polish Baltic coast. In: Rotnicki, K. (ed.), *Polish Coast: Past, Present and Future*. *J. Coast. Res.* 22, 22–55.



Available online at [www.sciencedirect.com](http://www.sciencedirect.com)

ScienceDirect

journal homepage: [www.journals.elsevier.com/oceanologia](http://www.journals.elsevier.com/oceanologia)

## ORIGINAL RESEARCH ARTICLE

# Temporal variations of phytoplankton community and their correlation with environmental factors in the coastal waters of the Çanakkale Strait in 2018

Egemen İnan Demir, Muhammet Turkoglu\*

Faculty of Marine Sciences and Technology, Canakkale Onsekiz Mart University, Canakkale, Turkey

Received 19 March 2021; accepted 15 October 2021

Available online 23 November 2021

**KEYWORDS**

Çanakkale Strait;  
Phytoplankton;  
Biodiversity;  
Chlorophyll *a*;  
Environmental  
parameters

**Abstract** In order to investigate temporal variations in phytoplankton connected with hydrography, high-resolution (twice a week) samplings were carried out between January and December 2018 at a single, shallow water station in the Dardanelles. Diatoms dominated in early and mid-winter, late spring and early summer, and between August and October. Whereas dinoflagellates dominated in the period from mid-February to the end of the third week of May, mid-summer, and late autumn. Other groups were generally more abundant in the early summer and mid-autumn than any other period. Late spring and early summer, mid-autumn and middle winter were the important bloom periods. The average contribution of diatom abundance ( $5.00 \times 10^5 \pm 7.80 \times 10^5$  cells  $L^{-1}$ ) to average total phytoplankton abundance ( $9.63 \times 10^5 \pm 7.88 \times 10^5$  cells  $L^{-1}$ ) was above 50% (average: 51.88%) during the year except spring (34.32%). However, the average contribution of dinoflagellates (43.32±20.69%) and others (4.81±6.99%) to the total phytoplankton abundance were lower than the abundance of the diatoms (51.88±21.61%). The study revealed a decrease both in the total number of algal blooms which also included HABs and their densities in the region compared to the previous findings. These observations seem to evidence environmental status improvement of the investigated area, manifested in an average chlorophyll *a* concentration ( $0.71 \pm 0.52 \mu g L^{-1}$ ) and quantitative phytoplankton structure ( $10^3$  to  $10^5$  cells  $L^{-1}$ ).

© 2021 Institute of Oceanology of the Polish Academy of Sciences. Production and hosting by Elsevier B.V. This is an open access article under the CC BY-NC-ND license (<http://creativecommons.org/licenses/by-nc-nd/4.0/>).

\* Corresponding author at: Canakkale Onsekiz Mart University, Faculty of Marine Sciences and Technology, Department of Fisheries Basic Sciences, Marine Biology Sec., Terzioğlu Campus, 17020 Canakkale, Turkey.

E-mail address: [mturkoglu@comu.edu.tr](mailto:mturkoglu@comu.edu.tr) (M. Turkoglu).

Peer review under the responsibility of the Institute of Oceanology of the Polish Academy of Sciences.



<https://doi.org/10.1016/j.oceano.2021.10.003>

0078-3234/© 2021 Institute of Oceanology of the Polish Academy of Sciences. Production and hosting by Elsevier B.V. This is an open access article under the CC BY-NC-ND license (<http://creativecommons.org/licenses/by-nc-nd/4.0/>).

## 1. Introduction

The Turkish strait system including the Bosphorus, the Sea of Marmara and the Dardanelles is a very important water passage between the Aegean Sea and the Black Sea. However, as an important waterway between the boundary of Europe and Asia, TSS carries not only ships but also biogeochemically different waters. Higher density waters (38.0 ppt) coming from the Aegean Sea flows into the Black Sea and lower density waters (18.0 ppt) coming from the Black Sea flows into the Aegean Sea. Therefore, the Sea of Marmara, located in between these two waterways, is under the constant influence of both systems (Turkoglu et al., 2004, 2006) which in turn dynamically effect all marine life in this region.

The Sea of Marmara is subject to domestic and industrial wastewater inputs from the east/northeast coasts, as well as from the Bosphorus Strait and other discharge systems. Typical indications of high nutrient inputs such as formation of harmful algal blooms (HABs) and mucilage accumulation have been reported more frequently (Balkis et al., 2010; Tufekci et al., 2010). It has been reported that HABs are stronger in semi-closed systems like the Sea of Marmara than in other systems (Turkoglu, 2008, 2010a, 2013, 2015; Turkoglu et al., 2018; Turkoglu and Koray, 2002). Moreover, Ministry of Agriculture and Forestry, General Directorate of Meteorology (TR-MAF-GDM) recently reported that the mean winter surface water temperature (11.5°C) in the last five years (2016–2021) was higher than those between 1970 and 2016 (7.90°C) (TR-MAF-GDM, 2021). The mean annual water temperature in the Sea of Marmara increased from 15.0 to 17.2°C during 1970–2020 confirming that temperature increase has been above 2°C in the last fifty years (TR-MAF-GDM, 2021). Both eutrophication and increase in surface water temperature in the Sea of Marmara have resulted in more frequent HAB events during the recent years. Even in the winter, significant HAB events of the coccolithophore *Emiliania huxleyi* (Lohmann) Hay & Mohler 1967, dinoflagellates *Noctiluca scintillans* (Macartney) Kofoid & Swezy 1921 and *Prorocentrum* spp., especially *Prorocentrum micans* Ehrenberg 1834 have been reported in the region (Turkoglu et al., 2004, 2008, 2010a, 2010b, 2016a; Turkoglu and Oner, 2010; Unsal et al., 2003).

There are more than 200 phytoplankton species belonging to different taxonomic groups in the Turkish Straits System (Balkis and Tas, 2016). In the Dardanelles, 4–6 dinoflagellate taxa and 6–8 diatom taxa dominate phytoplankton species diversity (Turkoglu et al., 2004; Turkoglu, 2010a, 2010b, Turkoglu and Erdogan, 2010; Turkoglu and Oner, 2010). Main phytoplankton groups in the Dardanelles are dinoflagellates, diatoms and coccolithophores. Although dinoflagellates and diatoms are very important phytoplankton groups both qualitatively and quantitatively, coccolithophores are important only quantitatively. Dinoflagellates, *N. scintillans* and *P. micans* Ehrenberg 1834, diatoms *Dactyliosolen fragilissimus* (Bergon) Hasle in Hasle & Syvertsen 1996, *Leptocylindrus minimus* Gran 1915, *Pseudonitzschia pungens* (Grunow ex Cleve) Hasle 1993, *Proboscia alata* (Brightwell) Sundström, 1986, *Pseudosolenia calcaravis* (Schultze) Sundström 1986, and the coccolithophore *E. huxleyi* form extensive blooms in the Dardanelles. Generally, a four-stage phytoplankton bloom sequence is observed

in the area throughout the year. Diatoms tend to dominate in March–April and July–August, dinoflagellates (particularly *N. scintillans*) in April–May, and the coccolithophore *E. huxleyi* with a typical turquoise bloom tend to dominate in May–June (Turkoglu et al., 2004; Turkoglu, 2008, 2010a, 2010b, 2013; Turkoglu and Oner, 2010). In addition, in some regions of the sea of Marmara, especially in Izmit and Bandırma Bays, excessive mucilage formation, especially in late spring and early autumn (Balkis et al., 2010; Tufekci et al., 2010), was reported, as was in the Adriatic Sea (Riccardi et al., 2007; Totti et al., 2005).

As is known while the brackish waters of the Black Sea have relatively rich nitrate and phosphate contents in the winter, their concentrations dropped to minimum levels in late summer and autumn (Turkoglu and Koray, 2000, 2002, 2004; Turkoglu and Tugrul, 2013; Uysal, 1995). However, the high nutrient contents originating from the Black Sea decrease both by the photosynthetic activities of phytoplankton and by sedimentation in the Sea of Marmara. As a result, the initially nutrient-rich brackish waters of the Black Sea enter the Dardanelles Strait having altered biochemical properties, i.e. lower nutrient content (Besiktepe et al., 1994; Polat and Tuğrul, 1996). Such variations in nutrient levels have profound effects on phytoplankton communities in the Dardanelles, compared those in the Bosphorus and the Sea of Marmara.

This study was carried out to investigate phytoplankton composition, community structures and harmful algal bloom (HAB) events, between January 2018 and January 2019 in the surface waters (0.5 m) off Çanakkale Seaport, Dardanelles. In this study, we also tried to explore interactions between phytoplankton communities and environmental characters throughout the year.

## 2. Material and method

### 2.1. Sampling area

According to a typical salinity distribution model in the Turkish Strait System (Figure 1), the upper layer of the Çanakkale Strait carries the brackish waters of the Black Sea to the North Aegean Sea, whereas the lower layer carries salty waters of the Mediterranean Sea first to Sea of Marmara and then from the Bosphorus to the Black Sea. However, the lower layer water flow in the Dardanelles is interrupted by a ridge between Eceabat and Canakkale at NE/SW direction which is the narrowest part of the Strait. For this reason, a topographic upwelling event occurs in this region and thus the deep waters mix with the surface waters. In addition to the ridge, there is a bend in the ‘Cape Nara’ region where the Strait turns toward north-east. In this region, the lower layer water flow is more interrupted than in the ridge which is the narrowest part of the Strait. Therefore, both contraction and bending of the Dardanelles cause different surface temperature and salinity levels in the NE and SW parts of the Cape Nara (Baba et al., 2007; Besiktepe et al., 1994; Polat and Tuğrul, 1996; Turkoglu et al., 2006). The surface layer waters in the SW part of the Dardanelles are also saltier than the surface layer waters in the NE of the Strait, especially in the spring and winter (Baba et al., 2007; Turkoglu et al., 2004, 2006;

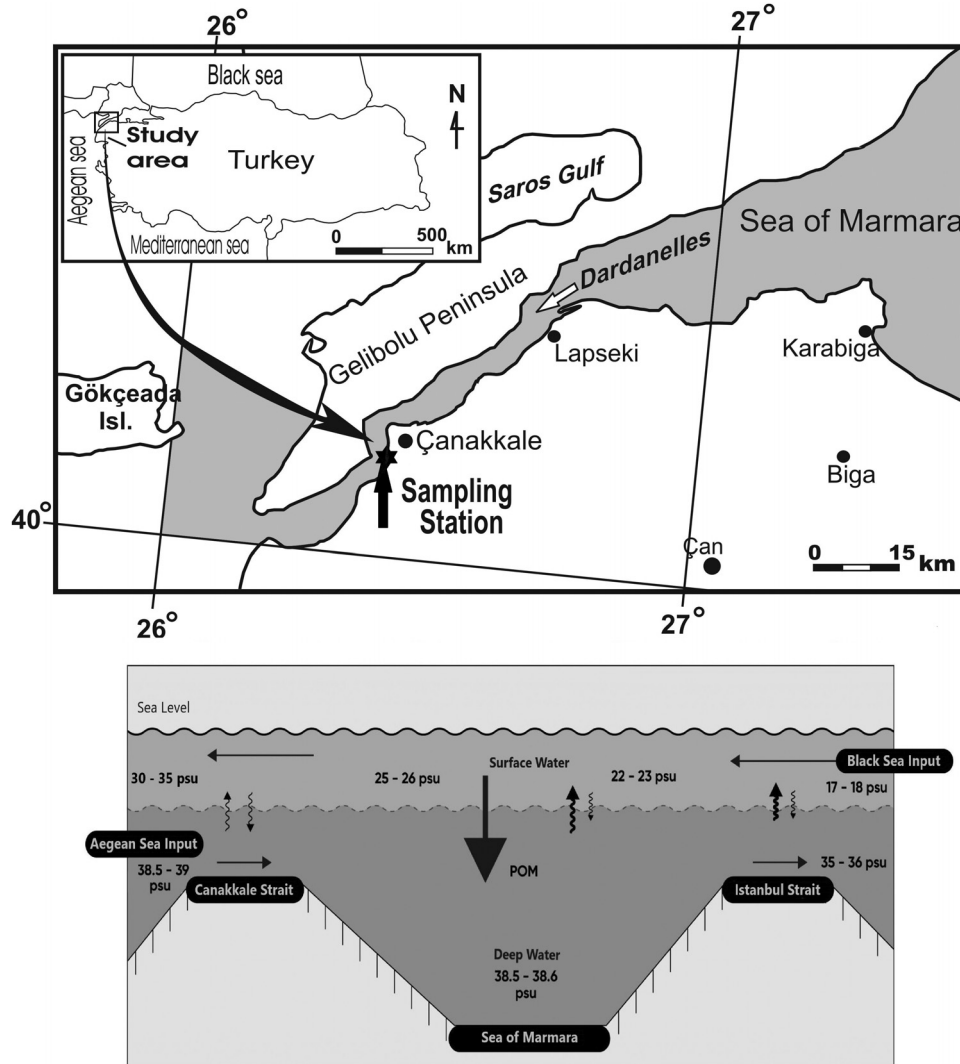


**Figure 1** Sampling station in the Dardanelles Strait and a typical salinity distribution model in the Turkish Strait System. The bottom picture has been revised after Polat-Beken (2000).

Unsal et al., 2003). In conclusion, the SW region of the Dardanelles which contains the fixed sampling station for this study is much richer in terms of the phytoplankton abundance compared to NE region due to its mixing zone (Turkoglu, 2010a, 2010b, 2010c, 2016a; Turkoglu et al., 2004; Turkoglu and Erdogan, 2010; Turkoglu and Oner, 2010).

The sampling station which is used as a monitoring station since 2001 is located at a depth of 5 m off city center (40°09'08.75"N and 26°24'13.00"E). Although the sampling station is an area affected by the general characteristics of the Dardanelles, it is close to the influence zone of the ferry port (Turkoglu and Erdogan, 2010; Turkoglu and Turgul, 2013). However, since the sampling station is located on the outer side of the jetty, it is mostly affected by the open waters. Water samples were taken from the surface (0.50 m). In each sampling, a total of 7 L of sea water was taken (3 L for phytoplankton analysis, 2 L for chlorophyll a analysis, 2 L for TSS analysis).

## 2.2. Study period and sampling interval

Samples were collected twice a week from January 2018 to January 2019 using a Niskin bottle. Throughout the study period a total of 62 samples were collected.

## 2.3. Probe (CTD) measurements

CTD values were measured *in situ* with YSI 556 MPS.

## 2.4. Total Suspended Solids (TSS)

For TSS (Total Suspended Solids), 2 L of sampled seawater were filtered through 0.45  $\mu\text{m}$  fiberglass filters. Before and after filtration, filters were dried at 105°C for one hour and the amount of TSS was determined by weighing (TUBITAK, 1989).

## 2.5. Chlorophyll *a* analysis

For chlorophyll *a* analysis, 2 L seawater sample was filtered through GF/F filter papers and 2 mL of 5% MgCO<sub>3</sub> was added at the end of the filtration. Samples filtered with GF/F were wrapped in aluminium foil to protect the samples from light exposure. These samples were stored in a deep freezer at –21.0°C until analysis. Chlorophyll *a* analyses were performed according to spectrophotometric method using Jasco V-530 UV-VIS (TUBITAK, 1989).

## 2.6. Quantitative phytoplankton analysis

For quantitative phytoplankton analysis, dark brown cylindrical glass bottles of 3 L volume were filled with 3 L of seawater and fixed with acidic lugol solution (7.50 cc lugol for 3 L sample). Samples were transported to the laboratory and left for sedimentation for a period of 10 days. At the end of the main and intermediate sedimentation, samples were reduced to 15–20 ml (Sukhanova, 1978). These samples were transferred to cylinder glass tubes with a volume of 25 ml. These samples were re-fixed with formaldehyde at a concentration of 2–4%, as lugol solution was lost during the sedimentation processes. These quantitative phytoplankton samples were preserved at 4°C until microscopic analysis (Venrick, 1978). For cell counts, the samples were firstly reduced to volume of 5–10 ml according to the amount of sedimentation in the plankton tubes and then they were homogenized (Semina, 1978). Phytoplankton cells in homogenized samples were counted using both the "Neubauer Counting Camera" (Hasle, 1978) and "Sedgwick-Rafter Counting Camera" (Venrick, 1978) under the "Olympus-BX-50 / PHD Advanced Phase-contrast Research Microscope".

## 2.7. Statistical analyses

Analyses of phytoplankton species distribution, Bray-Curtis cluster analysis, Shannon H Log Base 10 Diversity Index and Simpson D Diversity Index were conducted using Biodiversity Pro/BD2.bdp (McAlecece et al., 1999). Descriptive statistical analyses and Pearson correlations of data groups were conducted by IBM SPSS Statistics 19 (IBM SPSS, 2010).

## 3. Results

### 3.1. CTD variations

Throughout the year, the temperature of surface water (0.50 m) varied between 7.80 (30 January 2018) and 25.25°C (03 August 2018), and the mean temperature was 14.84±5.96°C (Table 1). Temperature variations were considered as normal for the Dardanelles. (Figure 2A). Salinity ranged between 23.69 (31 July 2018) and 35.50 ppt (11 January 2019) (Table 1 and Figure 2B) with a mean value of 27.36±2.68 ppt (Table 1).

Throughout the year, total dissolved solids (TDS) in surface water (0.50 m) ranged from 24.30 (26 June 2018) to 35.80 mg L<sup>-1</sup> (11 January 2019), with a mean TDS value of 27.74 ± 2.54 mg L<sup>-1</sup> (Table 1 and Figure 2C). The measured TDS values were slightly higher than the salinity values

(Table 1). This is due to the extra contribution of salinity (98–99%) and other anions and cations (1–2%) to TDS, which affects most of the TDS. Dissolved oxygen (DO) in surface waters (0.50 m) varied between 5.94 (23 July 2018) and 9.78 mg L<sup>-1</sup> (16 January 2018), with a mean DO value of 7.81 ± 0.86 mg L<sup>-1</sup> (Table 1 and Figure 2D).

Dissolved oxygen (DO) in surface waters (0.50 m) varied between 5.94 (23 July 2018) and 9.78 mg L<sup>-1</sup> (16 January 2018), with a mean DO value of 7.81 ± 0.86 mg L<sup>-1</sup> (Table 1 and Figure 2D).

### 3.2. Total Suspended Solid (TSS) and chlorophyll *a*

During the year, while total suspended solids (TSS) ranged from 2.00 (06 June 2018) to 80.15 mg L<sup>-1</sup> (07 March 2018), with an average of 10.45±12.96 mg L<sup>-1</sup>, chlorophyll *a* ranged from 0.112 (06 April 2018) to 2.865 L<sup>-1</sup> (06 May 2018), with an average of 0.714±0.515 µg L<sup>-1</sup> (Table 1). Temporal variations in TSS revealed lower fluctuations (2.00–15.40 mg L<sup>-1</sup>) during the year, except for the periods of 07 March 2018 (85.2 mg L<sup>-1</sup>), 30 January 2018 (57.6 mg L<sup>-1</sup>) and 15 May 2018 (38.4 mg L<sup>-1</sup>) (Figure 3A). The study showed that there was similarity in annual distribution neither between TSS and total phytoplankton nor between TSS and chlorophyll *a* (Figure 3A–C). This situation was also supported by Pearson correlation results between TSS and total phytoplankton ( $R = 0.012$ ) and TSS and chlorophyll *a* ( $R = -0.027$ ) (Table 2). Positive correlations found between total phytoplankton and chlorophyll *a* ( $R=0.404$ ;  $p\leq 0.01$ ) and between diatoms (Bacillariophyceae) and chlorophyll *a* ( $R=0.334$ ;  $p\leq 0.01$ ) (Table 1) revealed that the contribution to chlorophyll *a* level during the study was from diatoms ( $R=0.334$ ;  $p\leq 0.01$ ) rather than dinoflagellates ( $R=0.178$ ;  $p\leq 0.01$ ) (Table 2).

When the variations of chlorophyll *a* during the year were examined, it was observed that the highest chlorophyll *a* concentration in the first and the second stages of phytoplankton production occurred in the middle and late spring (April and May) and late winter (January–February) respectively (Figure 3B–C). However, there is a mismatch between the maximum peaks of chlorophyll *a* and total phytoplankton abundance (Figure 3B–C). This is a common situation due to fact that the maximum chlorophyll *a* will have been affected by domination of the pico- and smallest nano-plankton and macroalgal fragments, and so contributing to the total pigment content but not observable in microscopic analysis.

### 3.3. Phytoplankton

#### 3.3.1. Phytoplankton biodiversity

A total of 95 phytoplankton species were identified, including 2 taxa Cyanophyceae (blue-green algae), 32 taxa Dinophyceae (dinoflagellates), 1 taxon Prymnesiophyceae (coccolithophores), 3 taxa Dictyochophyceae (silicoflagellates), 56 taxa Bacillariophyceae (diatoms) and 1 taxon Euglenophyceae (euglenoids) throughout the year (Table 3). On the other hand, when the distribution frequencies of different taxonomic groups, especially of Dinophyceae and Bacillariophyceae are examined, the contribution of dinoflagellates (32 taxa; 33.68%) to total phytoplankton (total

**Table 1** Some descriptive statistical results in CTD parameters (e.g., temperature and salinity), TSS (Total Suspended Solid) and chlorophyll *a* in the surface water (0.50 m) of the Dardanelles in January 2018–January 2019.

Period	Environmental Parameters	Descriptive Statistical Results				
		N	Min.	Max.	Means	SD
January 2018 – January 2019	Temperature (°C)	62	7.80	25.25	14.84	5.96
	Salinity (ppt)	62	23.69	35.50	27.36	2.68
	Total Dissolved Solid (mg L <sup>-1</sup> )	62	24.30	35.10	27.74	2.54
	Conductivity (mS cm <sup>-1</sup> )	62	30.18	40.07	34.02	2.30
	Sp. Conductivity (mS cm <sup>-1</sup> )	62	37.38	53.99	42.62	3.87
	Dissolved Oxygen (mg L <sup>-1</sup> )	62	5.940	9.780	7.810	0.86
	TSS (mg L <sup>-1</sup> )	62	2.000	80.15	10.45	12.96
	Chlorophyll <i>a</i> (µg L <sup>-1</sup> )	62	0.112	2.865	0.714	0.515

**Table 2** Pearson correlation results between phytoplankton and other environmental variables in the surface water (0.50 m) of the Dardanelles in January 2018–January 2019 (N: 62).

Pearson correlation levels between data groups		Temp.	Salin.	DO	TDS	TSS	Chla	Dinop.	Bacill.	Others	Tot. Phyto
<b>Temperature</b>	Pearson	1	<b>-.883**</b>	<b>-.658**</b>	<b>-.890**</b>	-.136	-.038	-.231	.070	.098	-.018
	Correlation Sig. (2-tailed)		.000	.000	.000	.294	.769	.070	.589	.450	.892
<b>Salinity</b>	Pearson	<b>-.883**</b>	1	<b>.579**</b>	<b>.999**</b>	.097	-.117	.083	-.131	-.173	-.114
	Correlation Sig. (2-tailed)	.000		.000	.000	.454	.366	.520	.311	.178	.379
<b>DO (Dissolved Oxygen)</b>	Pearson	<b>-.658**</b>	<b>.579**</b>	1	<b>.583**</b>	.063	.016	.067	.002	-.056	.024
	Correlation Sig. (2-tailed)	.000	.000		.000	.629	.903	.606	.989	.667	.854
<b>TDS (Total Dissolved Solid)</b>	Pearson	<b>-.890**</b>	<b>.999**</b>	<b>.583**</b>	1	.104	-.124	.097	-.135	-.170	-.111
	Correlation Sig. (2-tailed)	.000	.000	.000		.422	.335	.453	.296	.187	.388
<b>TSS (Total Suspended Solid)</b>	Pearson	-.136	.097	.063	.104	1	-.027	.203	-.072	-.022	.012
	Correlation Sig. (2-tailed)	.294	.454	.629	.422		.832	.114	.579	.868	.924
<b>Chlorophyll <i>a</i> (Chla)</b>	Pearson	-.038	-.117	.016	-.124	-.027	1	.178	<b>.334**</b>	-.017	<b>.404**</b>
	Correlation Sig. (2-tailed)	.769	.366	.903	.335	.832		.166	.008	.896	.001
<b>Dinophyceae (Dinop.)</b>	Pearson	-.231	.083	.067	.097	.203	.178	1	-.207	.105	.230
	Correlation Sig. (2-tailed)	.070	.520	.606	.453	.114	.166		.106	.415	.072
<b>Bacillariophyceae (Bacill.)</b>	Pearson	.070	-.131	.002	-.135	-.072	<b>.334**</b>	-.207	1	-.030	<b>.898**</b>
	Correlation Sig. (2-tailed)	.589	.311	.989	.296	.579	.008	.106		.817	.000
<b>Other Phyto Groups</b>	Pearson	.098	-.173	-.056	-.170	-.022	-.017	.105	-.030	1	.128
	Correlation Sig. (2-tailed)	.450	.178	.667	.187	.868	.896	.415	.817		.322
<b>Total Phyto</b>	Pearson	-.018	-.114	.024	-.111	.012	<b>.404**</b>	.230	<b>.898**</b>	.128	1
	Correlation Sig. (2-tailed)	.892	.379	.854	.388	.924	.001	.072	.000	.322	

\*\* Correlation is significant at the 0.01 level (2-tailed).

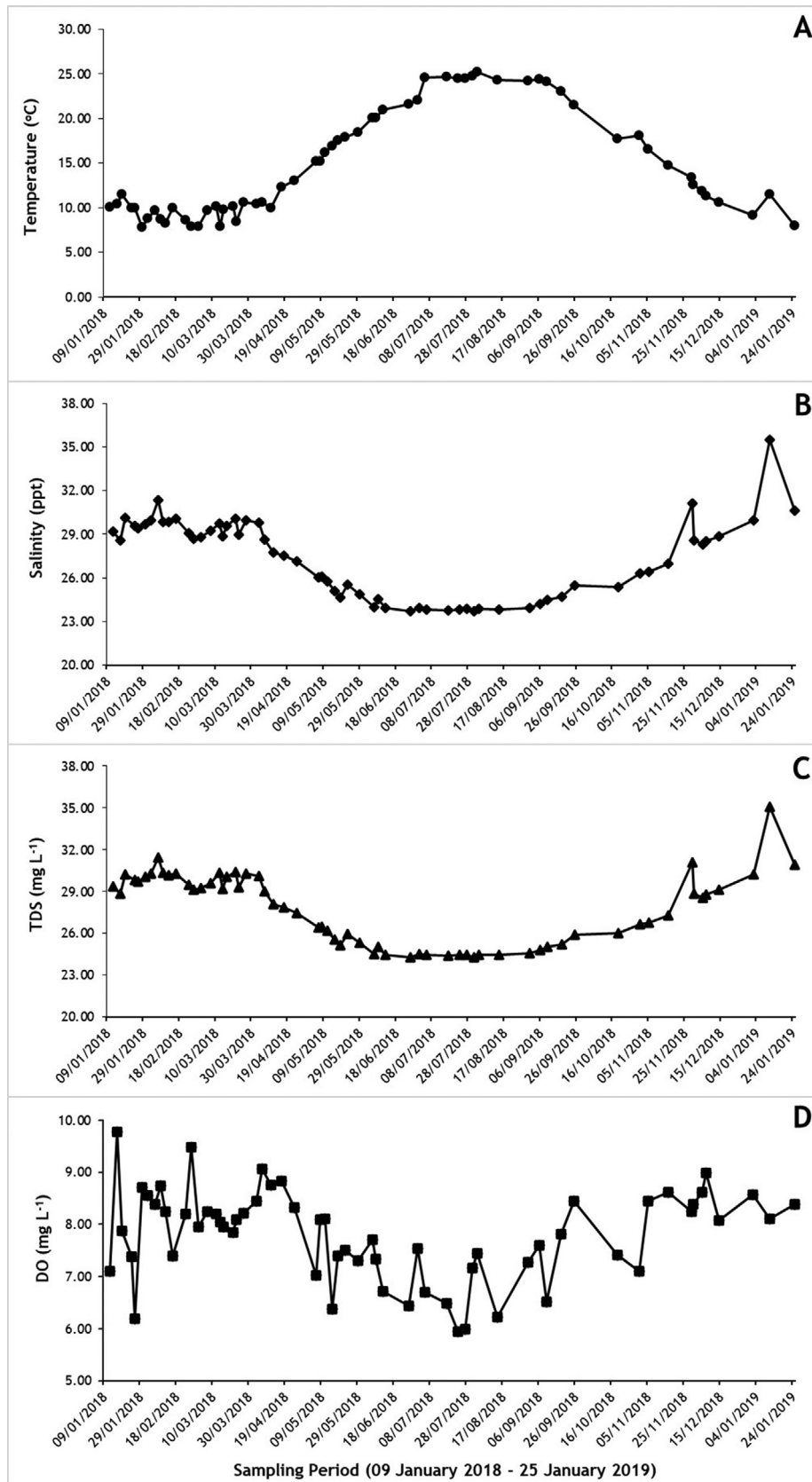


**Figure 2** Temporal variations of temperature (A), salinity (B), total dissolved solids – TDS (C) and dissolved oxygen – DO (D) in the surface water (0.50 m) of the Dardanelles in January 2018–January 2019.

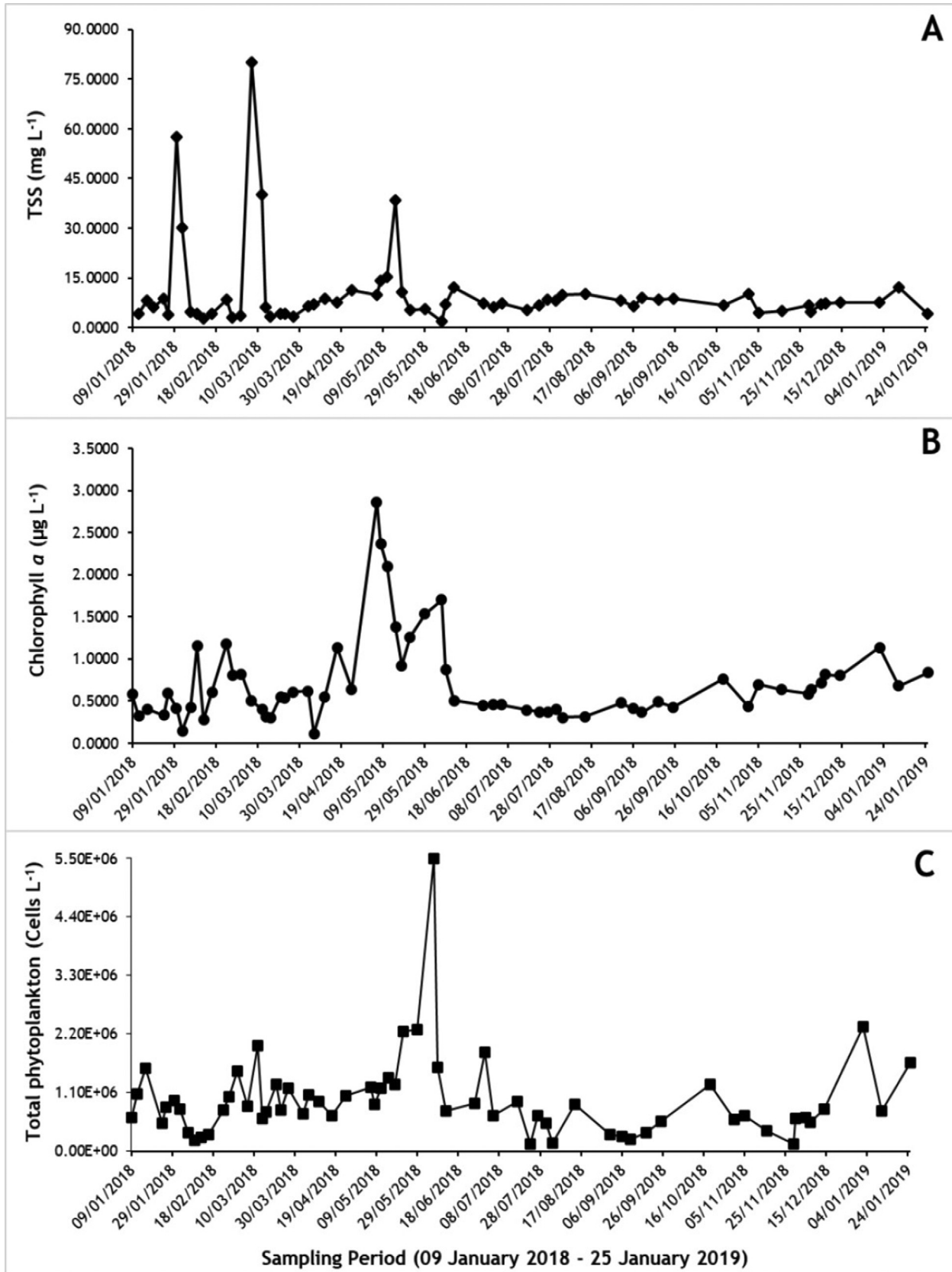


Figure 3 Temporal variations of TSS (Total Suspended Solid) (A), chlorophyll *a* (B) and total phytoplankton (C) in the surface water (0.50 m) of the Dardanelles in January 2018–January 2019.

**Table 3** Phytoplankton taxonomic composition in the surface water (0.50 m) of the Dardanelles in January 2018–January 2019 (N: 62).

Class	Genus	Species	Variety	Forma	Taxon	f (%)
Cyanophyceae	2	2	0	0	2	2.11
Dinophyceae	14	32	0	0	32	33.68
Prymnesiophyceae	1	1	0	0	1	1.05
Dictyochophyceae	1	1	1	1	3	3.16
Bacillariophyceae	35	56	0	0	56	58.95
Euglenophyceae	1	1	0	0	1	1.05
<b>Total</b>	<b>54</b>	<b>93</b>	<b>1</b>	<b>1</b>	<b>95</b>	<b>100</b>

95 taxa) was lower than that of diatoms (56 taxa; 58.95%) and other taxa (4 taxa; 7.37%) (Table 3). Despite the eutrophic condition of the Sea of Marmara, diatoms (56 taxa) outnumbered dinoflagellates (32 taxa) in the study area.

In terms of biodiversity, except for the sampling periods of January 30, 2018 (Simpson Diversity Index: 0.633, Shannon H Index: 0.405) and June 06, 2018 (Simpson D Index: 0.734, Shannon H Index: 0.302), phytoplankton species diversity was high (Simpson Diversity Index: 0.082–0.306, Shannon H Index: 0.649–1.152) (Figure 4A–B). However, since the Shannon H-Log Base 10 diversity value (1.152) was well below the 5-index value, the phytoplankton species diversity was not very high (Figure 4A–B).

### 3.3.2. Phytoplankton succession

According to the quantitative phytoplankton succession during the year, dinoflagellates dominated during the period from late winter to the end of the third week of May, middle summer and late autumn (Figure 5A), whereas diatoms predominated in mid-winter (January 2018 and January 2019), late spring (May 22–31, 2018) and early summer (June 1–10, 2018), and late summer (August 14, 2018) and middle autumn (October 19, 2018) (Figure 6B). Other groups (especially Dictyochophyceae species) were generally more dominant in the early summer and mid-autumn (Figure 5C). Total phytoplankton reached its maximum cell concentration ( $5.50 \times 10^6$  cells L<sup>-1</sup>) in early summer (June 06, 2018). Other important proliferation periods for total phytoplankton growth were full spring (March–May), mid-autumn (October) and winter (December and January). However, there were some interruption periods for phytoplankton proliferation such as late winter (February 6–16, 2018) and early autumn (September 1–10, 2018) (Figure 5D). The sampling periods of July 23 and November 29 were considered as the minimum proliferation periods for total phytoplankton ( $1.40 \times 10^5$  cells L<sup>-1</sup>) (Figure 6D).

In terms of average values, dinoflagellates reached the highest average cell abundance level in the spring ( $7.43 \times 10^5$  cells L<sup>-1</sup>), however, the average abundance of dinoflagellates in the winter was equal ( $2.97 \times 10^5$  cells L<sup>-1</sup>) to that of summer ( $2.98 \times 10^5$  cells L<sup>-1</sup>) (Table 4). It was observed that the highest mean diatom production was in summer ( $7.71 \times 10^5$  cells L<sup>-1</sup>) rather than in winter ( $3.86 \times 10^5$  cells L<sup>-1</sup>) and spring ( $4.07 \times 10^5$  cells L<sup>-1</sup>). On the other hand, silicoflagellates reached their highest mean level in summer ( $7.54 \times 10^4$  cells L<sup>-1</sup>). During the study period, densities of the main groups of

dinoflagellates and diatoms ranged from  $4.00 \times 10^4$  to  $1.62 \times 10^6$  cells L<sup>-1</sup> (average:  $4.17 \times 10^5 \pm 3.34 \times 10^5$  cells L<sup>-1</sup>) and  $2.00 \times 10^4$  to  $5.46 \times 10^6$  cells L<sup>-1</sup> (average:  $5.00 \times 10^5 \pm 7.80 \times 10^5$  cells L<sup>-1</sup>), respectively. Total phytoplankton ranged from  $1.40 \times 10^5$  to  $5.50 \times 10^6$  cells L<sup>-1</sup> (average:  $9.63 \times 10^5 \pm 7.88 \times 10^5$  cells L<sup>-1</sup>) throughout the year (Table 4). However, phytoplankton abundance throughout the year was mostly between  $1.00 \times 10^3$  and  $1.00 \times 10^5$  cells L<sup>-1</sup>.

In the present study, the contribution of diatoms to the total phytoplankton abundance (min-max: 6.78–99.3%, average: 51.9±25.84%) was higher than those of dinoflagellates (min-max: 0.730–89.83%, average: 43.3±25.8%) and other phytoplankton groups (min-max: 0.00–40.0%, average: 4.81±2.60%) (Figure 6). Contribution of diatoms to total phytoplankton was over 50% in all sampling periods except in spring (34.32%) (Figure 6). The high contribution level of diatoms to total phytoplankton was also confirmed by the correlation level (R=0.898; p<0.01) (Table 2). The dominance of diatoms in view of quantitative distribution was supported by qualitative distribution (diatoms: 58.95%; dinoflagellates: 33.68%; others: 7.37%) (Table 3).

Bray-Curtis analysis of temporal phytoplankton community structure showed high similarity between collected samples and looking at previous studies, this similarity tends to increase in the study area since beginnings of 2000s. However, the highest similarity for temporal quantitative phytoplankton distributions were observed between 21 March 2018 and 27 March 2018 (75.41% similarity), whereas the lowest similarity was observed between 06 June 2018 and 25 September 2018 (32.69% similarity) (Figure 7).

### 3.3.3. Bloom-forming phytoplankton species including harmful algae

Although bloom-forming phytoplankton species qualitatively showed great variabilities, there was no bloom-forming dinoflagellate species at densities >  $1.00 \times 10^6$  cells L<sup>-1</sup>. However, *P. micans* exhibited almost uninterrupted state of reproduction during the study period, especially its cell abundance was above  $5.00 \times 10^5$  cells L<sup>-1</sup> in March and reached a maximum on March 12, 2018 ( $8.80 \times 10^5$  cells L<sup>-1</sup>). Besides, *Prorocentrum cordatum* (Ostenfeld) J.D.Dodge, 1975 in May ( $2.60 \times 10^5$  cells L<sup>-1</sup>) and July (max.  $3.80 \times 10^5$  cells L<sup>-1</sup>), *Prorocentrum scutellum* Schröder, 1900 in January (max.  $1.20 \times 10^5$  cells L<sup>-1</sup>), *Tryblionella compressa* (Bailey) Poulin 1990 in October and November (max.  $2.20 \times 10^5$  cells L<sup>-1</sup>), *Tripos fusus* (Ehrenberg)



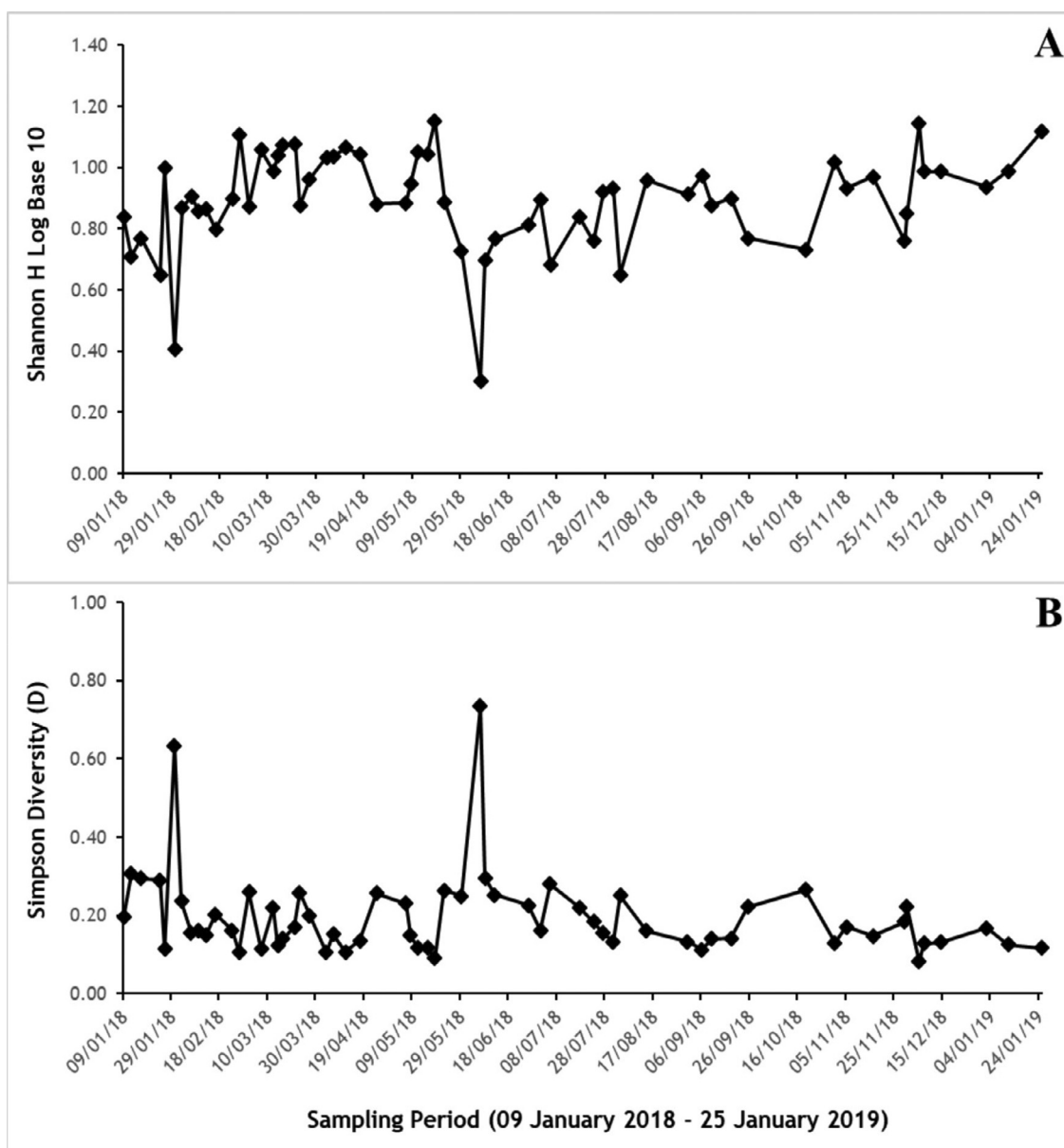


**Figure 4** Phytoplankton species diversity index variations (A: Shannon H Log Base 10; B: Simpson D) in the surface water (0.50 m) of the Dardanelles in January 2018–January 2019.

(Ehrenberg) F. Gómez, 2013 between January and March (max.  $1.60 \times 10^5$  cells  $L^{-1}$ ), *Tripes furca* (Ehrenberg) F. Gómez 2013 in March (max.  $1.20 \times 10^5$  cells  $L^{-1}$ ), *Gonyaulax* spp. in May (max.  $1.80 \times 10^5$  cells  $L^{-1}$ ) and *Gymnodinium* sp. in May (max.  $1.60 \times 10^5$  cells  $L^{-1}$ ) were other dinoflagellates to bloom in the region. Other dinoflagellates that rarely exceed  $10^5$  cells  $L^{-1}$  at different periods of the year were *Hermesinum adriaticum* Zacharias 1906, *Oxytoxum scolopax* F. Stein 1883, *Protoceratium reticulatum* (Claparède & Lachmann) Bütschli 1885, *Protoperidinium* spp., *Protoperidinium longipes* Balech 1974 and *Pyrophacus horologium* F. Stein 1883. Although these dinoflagellates may not reach to notable bloom numbers during the study, it is likely they may create HAB risk for the following years, looking at the higher bloom levels in previous years.

In this study, *Leptocylindrus minimus* Gran 1915 (max.  $4.70 \times 10^6$  cells  $L^{-1}$  in June 06, 2018) and *Cylindrotheca closterium* (Ehrenberg) Reimann & J.C.Lewin, 1964 (max.  $1.08 \times 10^6$  cells  $L^{-1}$  in May 22, 2018) were found to form excessive blooms above  $1.00 \times 10^6$  cells  $L^{-1}$ . Another potential algal bloom formation period for *L. minimus* was January (max.  $5.80 \times 10^5$  cells  $L^{-1}$ ). Furthermore, May–June was the bloom period for *C. closterium*. Apart from these two species, no other diatom species was found to form blooms over the  $10^6$  cells  $L^{-1}$  throughout the year. However, *Asterionellopsis glacialis* (Castracane) R.M. Crawford & D.G. Mann 1990 (max.  $1.10 \times 10^5$  cells  $L^{-1}$  in October), *Cerataulina pelagica* (Cleve) Hendeby 1937 (max.  $5.20 \times 10^5$  cells  $L^{-1}$  in May and June), *Chaetoceros* spp. (max.  $2.60 \times 10^5$  cells  $L^{-1}$  in January and November–December), *Climacosphenia moniligera* Ehrenberg 1843 (max.  $1.00 \times 10^5$  cells  $L^{-1}$  in

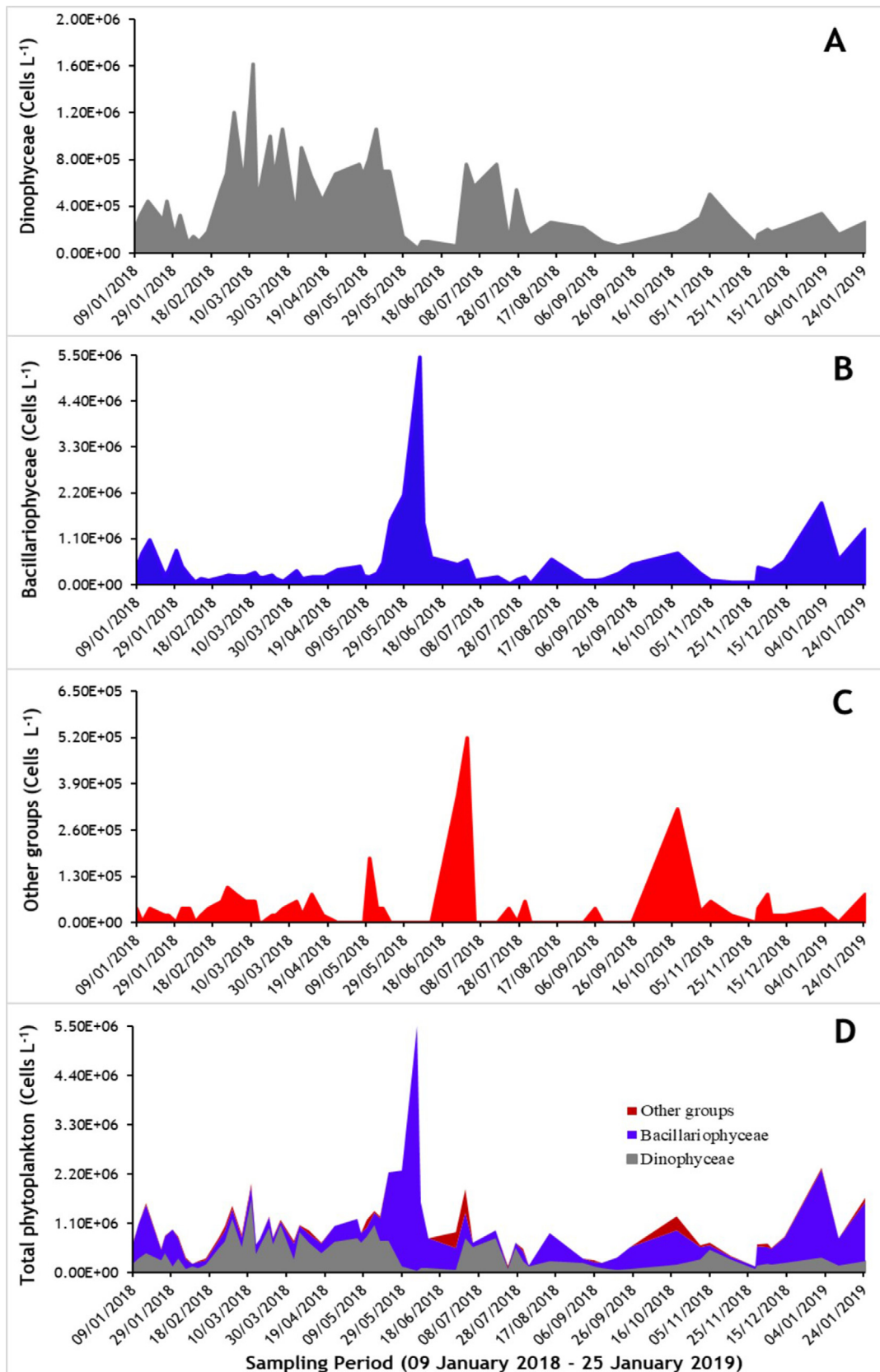


**Figure 5** Temporal variations in cell densities of dinoflagellates (A), diatoms (B), other phytoplankton groups (C) and total phytoplankton according to different taxonomic groups (D) in the surface water (0.50 m) of the Dardanelles in January 2018–January 2019.

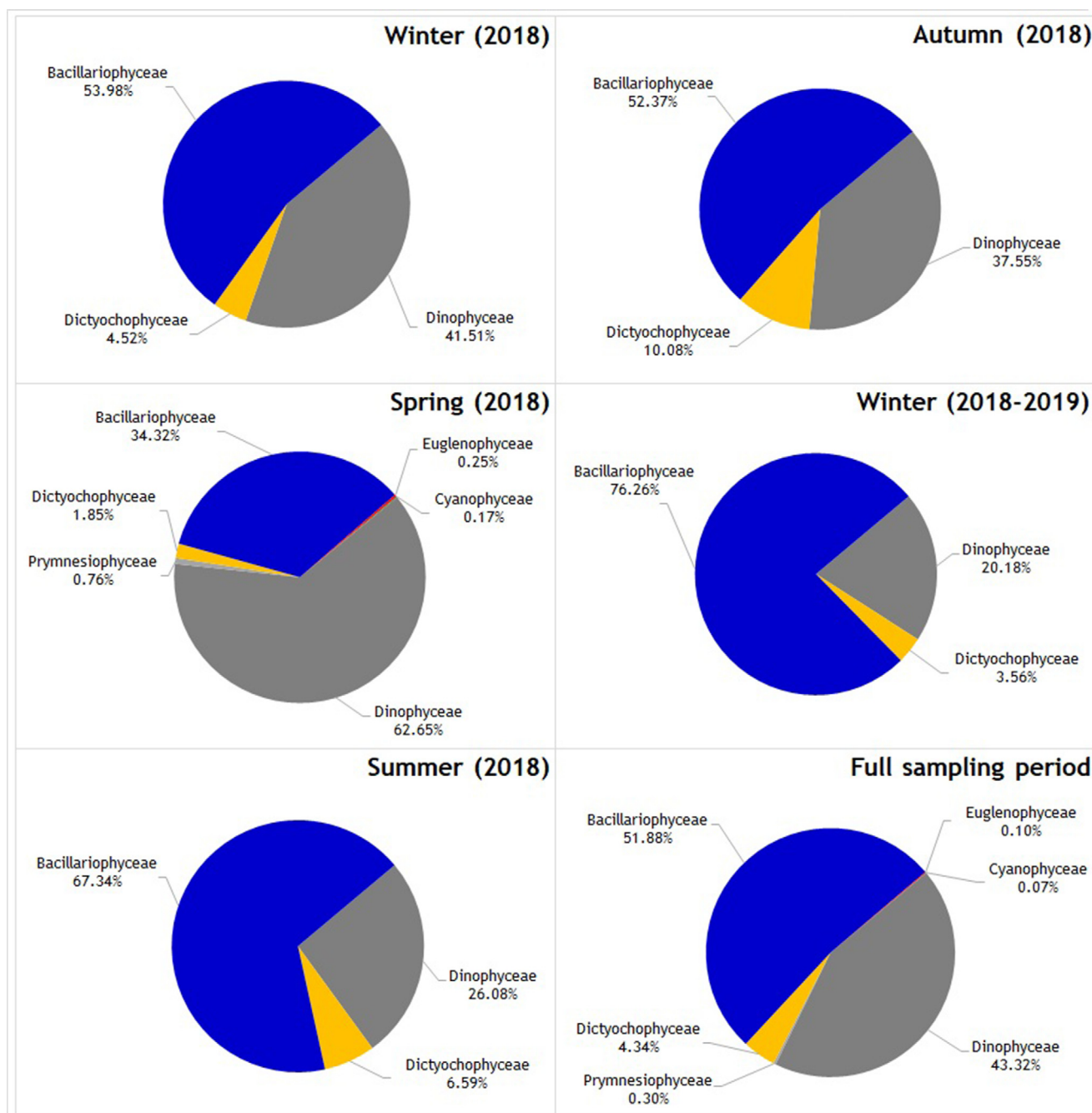


**Figure 6** Average contributions (%) of different taxonomic groups to total phytoplankton in the surface water (0.50 m) of the Dardanelles in January 2018–January 2019.

April), *Dactyliosolen fragilissimus* (Bergon) Hasle in Hasle & Syvertsen 1996 (max.  $1.80 \times 10^5$  cells  $L^{-1}$  in June), *Grammatophora marina* (Lyngbye) Kützing 1844 (max.  $2.80 \times 10^5$  cells  $L^{-1}$  in July–August and max.  $3.20 \times 10^5$  cells  $L^{-1}$  in January), *Guinardia striata* (Stolterfoth) Hasle in Hasle & Syvertsen 1996 (max.  $2.20 \times 10^5$  cells  $L^{-1}$  in September), *Hemiaulus hauckii* Grunow ex Van Heurck 1882 (max.  $5.40 \times 10^5$  cells  $L^{-1}$  in October), *Leptocylindrus danicus* Cleve 1889 (max.  $1.00 \times 10^5$  cells  $L^{-1}$  in May), *Licmophora abbreviata* C. Agardh 1831 (max.  $1.00 \times 10^5$  cells

$L^{-1}$  in March and April), *Licmophora flabellata* (Greville) C. Agardh 1831 (max.  $1.20 \times 10^5$  cells  $L^{-1}$  in February), *Nitzschia longissima* (Brébisson) Ralfs 1861 (max.  $2.00 \times 10^5$  cells  $L^{-1}$  in May), *P. alata* (max.  $1.00 \times 10^5$  cells  $L^{-1}$  in January), *Pseudo-nitzschia pungens* (Grunow ex Cleve) G.R. Hasle 1993 (max.  $7.60 \times 10^5$  cells  $L^{-1}$  in January), *Skeletonema costatum* (Greville) Cleve 1873 (max.  $8.00 \times 10^5$  cells  $L^{-1}$  in January), *Thalassionema nitzschioides* (Grunow) Mereschkowsky 1902 (max.  $2.60 \times 10^5$  cells  $L^{-1}$  in June), *Thalassiosira rotula* Meunier 1910 (max.  $6.40 \times 10^5$  cells  $L^{-1}$

**Table 4** Descriptive statistical analysis results of total phytoplankton and different phytoplankton groups in the surface water (0.50 m) of the Dardanelles in January 2018–January 2019.

Period	Descriptive Statistical Analysis of Phytoplankton Abundance (Cells L <sup>-1</sup> )					
	Phytoplankton Groups	N	Min	Max	Mean	SD
<b>Winter 2018</b> (09/01/2018 – 26/02/2018)	Cyanophyceae	13	0.00E+00	0.00E+00	0.00E+00	0.00E+00
	Dinophyceae	13	8.00E+04	6.80E+05	2.97E+05	1.84E+05
	Prymnesiophyceae	13	0.00E+00	0.00E+00	0.00E+00	0.00E+00
	Dictyochophyceae	13	0.00E+00	1.00E+05	3.23E+04	2.77E+04
	Bacillariophyceae	13	6.00E+04	1.08E+06	3.86E+05	3.14E+05
	Euglenophyceae	13	0.00E+00	0.00E+00	0.00E+00	0.00E+00
	<b>Total Phytoplankton</b>	<b>13</b>	<b>2.00E+05</b>	<b>1.56E+06</b>	<b>7.15E+05</b>	<b>3.91E+05</b>
<b>Spring 2018</b> (02/03/2018 – 29/05/2018)	Cyanophyceae	20	0.00E+00	4.00E+04	2.00E+03	8.94E+03
	Dinophyceae	20	1.40E+05	1.62E+06	7.43E+05	3.34E+05
	Prymnesiophyceae	20	0.00E+00	1.40E+05	9.00E+03	3.21E+04
	Dictyochophyceae	20	0.00E+00	8.00E+04	2.20E+04	2.82E+04
	Bacillariophyceae	20	8.00E+04	2.14E+06	4.07E+05	5.10E+05
	Euglenophyceae	20	0.00E+00	4.00E+04	3.00E+03	9.79E+03
	<b>Total Phytoplankton</b>	<b>20</b>	<b>6.20E+05</b>	<b>2.28E+06</b>	<b>1.19E+06</b>	<b>4.92E+05</b>
<b>Summer 2018</b> (06/06/2018 – 31/08/2018)	Cyanophyceae	13	0.00E+00	0.00E+00	0.00E+00	0.00E+00
	Dinophyceae	13	4.00E+04	7.60E+05	2.98E+05	2.64E+05
	Prymnesiophyceae	13	0.00E+00	0.00E+00	0.00E+00	0.00E+00
	Dictyochophyceae	13	0.00E+00	5.20E+05	7.54E+04	1.66E+05
	Bacillariophyceae	13	2.00E+04	5.46E+06	7.71E+05	1.47E+06
	Euglenophyceae	13	0.00E+00	0.00E+00	0.00E+00	0.00E+00
	<b>Total Phytoplankton</b>	<b>13</b>	<b>1.40E+05</b>	<b>5.50E+06</b>	<b>1.14E+06</b>	<b>1.40E+06</b>
<b>Autumn 2018</b> (06/09/2018 – 30/11/2018)	Cyanophyceae	10	0.00E+00	0.00E+00	0.00E+00	0.00E+00
	Dinophyceae	10	6.00E+04	5.00E+05	1.92E+05	1.20E+05
	Prymnesiophyceae	10	0.00E+00	0.00E+00	0.00E+00	0.00E+00
	Dictyochophyceae	10	0.00E+00	3.20E+05	4.85E+04	8.52E+04
	Bacillariophyceae	10	6.00E+04	7.60E+05	3.01E+05	2.16E+05
	Euglenophyceae	10	0.00E+00	0.00E+00	0.00E+00	0.00E+00
	<b>Total Phytoplankton</b>	<b>10</b>	<b>1.40E+05</b>	<b>1.26E+06</b>	<b>5.42E+05</b>	<b>2.91E+05</b>
<b>Winter 2018-2019</b> (05/12/2018 – 25/01/2019)	Cyanophyceae	6	0.00E+00	0.00E+00	0.00E+00	0.00E+00
	Dinophyceae	6	1.60E+05	3.40E+05	2.27E+05	6.53E+04
	Prymnesiophyceae	6	0.00E+00	0.00E+00	0.00E+00	0.00E+00
	Dictyochophyceae	6	0.00E+00	8.00E+04	4.00E+04	3.35E+04
	Bacillariophyceae	6	3.40E+04	1.96E+06	8.75E+05	6.48E+05
	Euglenophyceae	6	0.00E+00	0.00E+00	0.00E+00	0.00E+00
	<b>Total Phytoplankton</b>	<b>6</b>	<b>5.40E+05</b>	<b>2.34E+06</b>	<b>1.12E+06</b>	<b>7.18E+05</b>
<b>Full Sampling Period</b>	Cyanophyceae	62	0.00E+00	4.00E+04	6.45E+02	5.08E+03
	Dinophyceae	62	4.00E+04	1.62E+06	4.17E+05	3.34E+05
	Prymnesiophyceae	62	0.00E+00	1.40E+05	2.90E+03	1.84E+04
	Dictyochophyceae	62	0.00E+00	5.20E+05	4.18E+04	8.78E+04
	Bacillariophyceae	62	2.00E+04	5.46E+06	5.00E+05	7.80E+05
	Euglenophyceae	62	0.00E+00	4.00E+04	9.68E+02	5.64E+03
	<b>Total Phytoplankton</b>	<b>62</b>	<b>1.40E+05</b>	<b>5.50E+06</b>	<b>9.63E+05</b>	<b>7.88E+05</b>

in May) were other diatom species with a potential to bloom in the region. As stated above, these diatom species provided an important contribution to the total phytoplankton in different periods of the year at abundance levels ranging from 10<sup>5</sup> to 10<sup>6</sup> cells L<sup>-1</sup> (Table 5).

Apart from dinoflagellates and diatoms, other phytoplankton species with bloom-forming potential in the region include coccolithophore *Emiliania huxleyi* (Lohmann) W.W. Hay & H.P. Mohler, 1967 (max. 1.40 × 10<sup>5</sup> cells L<sup>-1</sup> in May) and silicoflagellate *Dictyocha fibula* var. *aculeata* Lemmer-

mann (max. 5.20 × 10<sup>5</sup> cells L<sup>-1</sup> in July and 3.20 × 10<sup>5</sup> cells L<sup>-1</sup> in October).

In this study, the contribution of dinoflagellates to total phytoplankton abundance varied between 0.73% (June 06, 2018) and 89.8% (March 27, 2018). The highest contribution to total dinoflagellate abundance was provided by *P. micans* (0–48.7%), *P. cordatum* (0–45.5%), *T. compressa* (0–37.5%), *O. scolopax* (0–16.1%), *T. furca* (0–15.4%), *P. scutellum* (0–15.8%), *T. fusus* (0–14.3%), *Gymnodinium* spp. (0–13.6%), *Protoceratium* sp. (0–12.7%), *Protoperidinium* spp.

**Table 5** Dominant and some bloom-forming phytoplankton species and their contribution (%) to own major taxonomic groups and to the total phytoplankton density in the surface water (0.50 m) of the Dardanelles in January 2018–January 2019 (Dinop.: Dinophyceae, Bacill.: Bacillariophyceae) (N: 62).

Date D/M/Y	Dinop. (%)	Contributions (%) of Dinoflagellate Species	Bacill. (%)	Contributions (%) of Diatom Species	Other Groups (%)	Contributions (%) of Others	Total Phytop. Cells (L <sup>-1</sup> )
09/01/18	31.25	<i>T. fusus</i> (12.50%), <i>P. micans</i> (6.25%), <i>P. scutellum</i> (6.25%), <i>T. compressa</i> (6.25%)	62.50	<i>P. pungens</i> (37.50%), <i>Thalassiosira</i> spp. (12.50%)	6.25	<i>D. fibula</i> var. <i>aculeata</i> (6.25%)	6.40E+05
12/01/18	29.63	<i>P. micans</i> (11.11%), <i>T. fusus</i> (11.11%)	70.37	<i>P. pungens</i> (51.85%), <i>S. costatum</i> (7.41%)	0.00		1.08E+06
16/01/18	28.21	<i>P. micans</i> (10.26%), <i>P. longipes</i> (5.13%)	69.23	<i>S. costatum</i> (51.28%), <i>Cheiloceros</i> spp. (10.26%), <i>P. pungens</i> (5.13%)	2.56	<i>D. speculum</i> (2.56%)	1.56E+06
24/01/18	53.85	<i>P. micans</i> (30.77%), <i>P. cordatum</i> (7.69%), <i>P. scutellum</i> (7.69%)	42.31	<i>P. pungens</i> (42.31%)	3.85	<i>D. speculum</i> (3.85%)	5.20E+05
26/01/18	53.66	<i>P. cordatum</i> (17.07%), <i>P. micans</i> (9.76%), <i>T. fusus</i> (9.76%)	43.90	<i>P. pungens</i> (17.07%), <i>C. peruvianus</i> (12.20%), <i>Thalassiosira</i> spp. (9.76%)	0.00		8.20E+05
30/01/18	14.58	<i>T. furca</i> (4.17%), <i>T. compressa</i> (4.17%), <i>P. micans</i> (2.08%), <i>P. cordatum</i> (2.08%), <i>T. fusus</i> (2.08%)	85.42	<i>P. pungens</i> (79.17%)	0.00		9.60E+05
02/02/18	40.00	<i>P. micans</i> (12.5%), <i>T. compressa</i> (7.50%)	55.00	<i>P. pungens</i> (45.00%)	5.00	<i>D. fibula</i> var. <i>aculeata</i> (2.50%), <i>D. speculum</i> (2.50%)	8.00E+05
06/02/18	23.53	<i>O. scolopax</i> (11.76%), <i>P. micans</i> (5.88%), <i>T. fusus</i> (5.88%)	64.71	<i>P. pungens</i> (29.41%), <i>Thalassiosira</i> spp. (17.65%)	11.76	<i>D. fibula</i> var. <i>aculeata</i> (5.88%), <i>D. speculum</i> (5.88%)	3.40E+05
09/02/18	70.00	<i>P. micans</i> (30.00%)	30.00	<i>Coscinodiscus</i> spp. (10.00%), <i>S. unipunctata</i> (10.00%), <i>Thalassiosira</i> spp. (10.00%)	0.00		2.00E+05
12/02/18	38.46	<i>P. micans</i> (15.38%), <i>T. furca</i> (15.38%)	53.85	<i>P. pungens</i> (29.41%), <i>Coscinodiscus</i> spp. (15.38%)	7.69	<i>Dictyocha fibula</i> f. <i>cannopilea-hexacantha</i> (7.69%)	2.60E+05
16/02/18	56.25	<i>P. micans</i> (37.50%), <i>T. furca</i> (12.50%)	31.25	<i>L. flabellata</i> (12.50%), <i>Coscinodiscus</i> spp. (6.25%), <i>C. moniligera</i> (6.25%), <i>P. pungens</i> (6.25%)	12.50	<i>D. speculum</i> (12.50%)	3.20E+05
23/02/18	69.23	<i>P. micans</i> (30.77%), <i>T. fusus</i> (12.82%), <i>T. furca</i> (10.26%),	23.08	<i>L. flabellata</i> (15.38%), <i>M. rigida</i> (5.13%)	7.69	<i>D. speculum</i> (7.69%)	7.80E+05

(continued on next page)

Table 5 (continued)

Date D/M/Y	Dinop. (%)	Contributions (%) of Dinoflagellate Species	Bacill. (%)	Contributions (%) of Diatom Species	Other Groups (%)	Contributions (%) of Others	Total Phytop. Cells (L <sup>-1</sup> )
26/02/18	66.67	<i>P. micans</i> (23.53%), <i>T. fusus</i> (13.73%), <i>T. compressa</i> (7.84%)	23.53	<i>P. pungens</i> (9.80%), <i>P. alata</i> (3.92%), <i>L. flabellata</i> (3.92%)	9.80	<i>D. speculum</i> (5.88%), <i>D. fibula</i> var. <i>aculeata</i> (1.96%), <i>D. fibula</i> f. <i>cannopilea-hexacantha</i> (1.96%)	1.02E+06
02/03/18	80.00	<i>P. micans</i> (48.00%), <i>T. fusus</i> (10.67%), <i>P. cordatum</i> (9.33%)	14.67	<i>Coscinodiscus</i> spp. (5.33%)	5.33	<i>D. speculum</i> (2.67%), <i>D. fibula</i> var. <i>aculeata</i> (2.67%)	1.50E+06
07/03/18	66.67	<i>P. micans</i> (23.81%), <i>T. fusus</i> (14.29%), <i>P. cordatum</i> (9.52%)	26.19	<i>P. alata</i> (7.14%), <i>L. flabellata</i> (4.76%), <i>Coscinodiscus</i> spp. (4.76%), <i>C. moniligera</i> (4.76%)	7.14	<i>D. speculum</i> (4.76%), <i>Euglena</i> sp. (2.38%)	8.40E+05
12/03/18	81.82	<i>P. micans</i> (44.44%), <i>P. cordatum</i> (7.07%), <i>T. furca</i> (6.06%)	15.15	<i>L. abbreviata</i> (5.05%), <i>Coscinodiscus</i> spp. (3.03%)	3.03	<i>D. fibula</i> var. <i>aculeata</i> (2.02%), <i>D. speculum</i> (1.01%)	1.98E+06
14/03/18	67.74	<i>P. micans</i> (25.81%), <i>O. scolopax</i> (16.13%), <i>T. furca</i> (9.68%)	32.26	<i>L. abbreviata</i> (6.45%), <i>P. alata</i> (6.45%)	0.00		6.20E+05
16/03/18	78.38	<i>P. micans</i> (32.43%), <i>P. dentatum</i> (10.81%)	21.62	<i>Coscinodiscus</i> spp. (5.41%), <i>T. frauenfeldii</i> (5.41%)	0.00		7.40E+05
21/03/18	79.37	<i>P. micans</i> (38.10%), <i>T. fusus</i> (7.94%), <i>T. furca</i> (7.94%)	19.05	<i>Coscinodiscus</i> spp. (3.17%), <i>P. alata</i> (3.17%), <i>L. danicus</i> (3.17%)	1.59	<i>D. speculum</i> (1.59%)	1.26E+06
23/03/18	79.49	<i>P. micans</i> (48.72%), <i>P. cordatum</i> (5.13%), <i>P. dentatum</i> (5.13%), <i>Gymnodinium</i> sp. (5.13%), <i>T. furca</i> (5.13%)	17.95	<i>Coscinodiscus</i> spp. (5.13%), <i>N. longissima</i> (5.13%)	2.56	<i>D. speculum</i> (2.56%)	7.80E+05
27/03/18	89.83	<i>P. micans</i> (40.68%), <i>T. fusus</i> (10.17%), <i>T. furca</i> (10.17%)	6.78	<i>Coscinodiscus</i> spp. (1.69%), <i>P. alata</i> (1.69%), <i>P. pungens</i> (1.69%)	3.39	<i>D. speculum</i> (3.39%)	1.18E+06
03/04/18	42.86	<i>P. micans</i> (17.14%), <i>T. fusus</i> (11.43%)	48.57	<i>L. abbreviata</i> (14.29%), <i>L. danicus</i> (11.43%)	8.57	<i>D. speculum</i> (8.57%)	7.00E+05
06/04/18	84.91	<i>P. micans</i> (33.96%), <i>T. fusus</i> (9.43%), <i>Gymnodinium</i> spp. (7.55%)	13.21	<i>L. danicus</i> (3.77%)	1.89	<i>D. fibula</i> var. <i>aculeata</i> (1.89%)	1.06E+06
11/04/18	70.21	<i>P. micans</i> (19.15%), <i>P. cordatum</i> (17.02%), <i>O. Scolopax</i> (8.51%)	21.28	<i>C. moniligera</i> (10.64%), <i>P. alata</i> (4.26%)	8.51	<i>D. speculum</i> (8.51%)	9.40E+05

(continued on next page)

Table 5 (continued)

Date D/M/Y	Dinop. (%)	Contributions (%) of Dinoflagellate Species	Bacill. (%)	Contributions (%) of Diatom Species	Other Groups (%)	Contributions (%) of Others	Total Phytop. Cells (L <sup>-1</sup> )
17/04/18	66.67	<i>P. micans</i> (30.30%), <i>P. cordatum</i> (12.12%), <i>Gymnodinium</i> spp. (9.09%)	30.30	<i>P. pungens</i> (6.06%), <i>T. frauenfeldii</i> (6.06%)	3.03	<i>D. fibula</i> var. <i>aculeata</i> (3.03%)	6.60E+05
24/04/18	65.38	<i>P. micans</i> (48.08%), <i>T. fusus</i> (3.85%), <i>Gonyaulax</i> spp. (3.85%)	34.62	<i>N. longissima</i> (11.54%), <i>L. danicus</i> (5.77%), <i>C. placentula</i> (3.85%)	0.00		1.04E+06
06/05/18	63.33	<i>P. micans</i> (43.33%), <i>P. cordatum</i> (6.67%)	36.67	<i>N. longissima</i> (16.67%), <i>L. flabellata</i> (3.33%), <i>P. pungens</i> (3.33%), <i>Coscinodiscus</i> spp. (3.33%)	0.00		1.20E+06
08/05/18	75.00	<i>P. micans</i> (25.00%), <i>P. cordatum</i> (22.73%), <i>Gonyaulax</i> spp. (11.36%)	25.00	<i>N. longissima</i> (6.82%)	0.00		8.80E+05
11/05/18	67.80	<i>P. micans</i> (23.73%), <i>Gymnodinium</i> spp. (13.56%), <i>P. horologium</i> (10.17%)	16.95	<i>C. closterium</i> (6.78%), <i>N. longissima</i> (3.39%)	15.25	<i>E. huxleyi</i> (11.86%), <i>Euglena</i> sp. (3.39%)	1.18E+06
15/05/18	76.81	<i>P. micans</i> (21.74%), <i>P. cordatum</i> (18.84%), <i>Gymnodinium</i> spp. (8.70%)	20.29	<i>L. danicus</i> (7.25%), <i>Navicula</i> spp. (5.80%)	2.90	<i>E. huxleyi</i> (2.90%)	1.38E+06
18/05/18	55.56	<i>P. micans</i> (19.05%), <i>Protoceratium</i> sp. (12.70%), <i>P. cordatum</i> (7.94%)	41.27	<i>T. rotula</i> (9.52%), <i>C. closterium</i> (7.94%)	3.17	<i>Oscillatoria</i> spp. (3.17%)	1.26E+06
22/05/18	31.25	<i>Gonyaulax</i> spp. (8.04%), <i>P. cordatum</i> (6.25%), <i>Protoceratium</i> sp. (5.36%), <i>P. micans</i> (1.17%)	68.75	<i>C. closterium</i> (48.21%), <i>Navicula</i> spp. (5.36%)	0.00		2.24E+06
29/05/18	6.14	<i>P. micans</i> (1.75%), <i>P. cordatum</i> (1.75%), <i>T. compressa</i> (1.75%)	93.86	<i>Leptocylindrus</i> spp. (32.46%), <i>C. closterium</i> (29.82%), <i>C. pelagica</i> (22.81%)	0.00		2.28E+06
06/06/18	0.73	<i>P. cordatum</i> (0.36%), <i>T. compressa</i> (0.36%)	99.27	<i>L. minimus</i> (85.45%), <i>C. pelagica</i> (4.00%)	0.00		5.50E+06
08/06/18	6.33	<i>P. micans</i> (2.53%), <i>P. cordatum</i> (1.27%), <i>C. tripos</i> (1.27%), <i>O. scolopax</i> (1.27%)	93.67	<i>L. minimus</i> (49.37%), <i>C. closterium</i> (15.19%), <i>T. nitzschioides</i> (11.39%)	0.00		1.58E+06
12/06/18	13.16	<i>T. compressa</i> (5.26%), <i>Oxytoxum</i> spp. (5.26%)	86.84	<i>C. closterium</i> (39.47%), <i>T. nitzschioides</i> (28.95%)	0.00		7.60E+05

(continued on next page)

Table 5 (continued)

Date D/M/Y	Dinop. (%)	Contributions (%) of Dinoflagellate Species	Bacill. (%)	Contributions (%) of Diatom Species	Other Groups (%)	Contributions (%) of Others	Total Phytop. Cells (L <sup>-1</sup> )
26/06/18	6.67	<i>P. micans</i> (4.44%), <i>T. compressa</i> (2.22%)	53.33	<i>T. nitzschioides</i> (28.89%), <i>L. danicus</i> (6.67%), <i>Navicula</i> spp. (6.67%)	40.00	<i>D. fibula</i> var. <i>aculeata</i> (35.56%), <i>D. speculum</i> (4.44%)	9.00E+05
01/07/18	40.86	<i>P. cordatum</i> (16.13%), <i>T. compressa</i> (13.98%)	31.18	<i>C. closterium</i> (16.13%), <i>Leptocylindrus</i> spp. (7.53%)	27.96	<i>D. fibula</i> var. <i>aculeata</i> (27.96%)	1.86E+06
05/07/18	84.85	<i>P. cordatum</i> (45.45%), <i>P. micans</i> (18.18%), <i>T. compressa</i> (18.18%)	15.15	<i>P. alata</i> (6.06%)	0.00		6.60E+05
17/07/18	80.85	<i>P. cordatum</i> (40.43%), <i>P. micans</i> (19.15%), <i>T. compressa</i> (8.51%)	19.15	<i>T. nitzschioides</i> (6.38%), <i>Navicula</i> spp. (4.26%)	0.00		9.40E+05
23/07/18	57.14	<i>P. cordatum</i> (14.29%), <i>P. micans</i> (14.29%), <i>T. compressa</i> (14.29%)	14.29	<i>N. longissima</i> (14.29%)	28.57	<i>D. fibula</i> var. <i>aculeata</i> (28.57%)	1.40E+05
27/07/18	81.82	<i>P. micans</i> (30.30%), <i>P. cordatum</i> (15.15%), <i>Protoperidinium</i> spp. (12.12%)	18.18	<i>Leptocylindrus</i> spp. (9.09%), <i>T. nitzschioides</i> (6.06%), <i>Thalassiosira</i> spp. (3.03%)	0.00		6.60E+05
31/07/18	50.00	<i>T. compressa</i> (15.38%), <i>P. micans</i> (11.54%), <i>Protoceratium</i> sp. (11.54%)	38.46	<i>G. marina</i> (23.08%)	11.54	<i>D. fibula</i> var. <i>aculeata</i> (11.54%)	5.20E+05
03/08/18	87.50	<i>T. compressa</i> (37.50%), <i>P. micans</i> (25.00%)	12.50	<i>N. longissima</i> (12.50%)	0.00		1.60E+05
14/08/18	29.55	<i>H. adriaticum</i> (11.36%), <i>Protoperidinium</i> spp. (11.36%)	70.45	<i>G. marina</i> (31.81%), <i>Navicula</i> spp. (15.91%)	0.00		8.80E+05
31/08/18	68.75	<i>T. compressa</i> (18.75%), <i>P. micans</i> (18.75%)	31.25	<i>T. frauenfeldii</i> (12.50%)	0.00		3.20E+05
06/09/18	50.00	Dinoflagellates cysts (14.29%), <i>P. lima</i> (14.29%)	35.71	<i>Chaetoceros</i> spp. (14.29%)	14.29	<i>D. fibula</i> var. <i>aculeata</i> (14.29%)	2.80E+05
10/09/18	45.45	Dinoflagellates cysts (18.18%), <i>T. compressa</i> (18.18%)	54.55	<i>Thalassiosira</i> spp. (18.18%)	0.00		2.20E+05
18/09/18	17.65	<i>T. compressa</i> (17.65%)	82.35	<i>G. marina</i> (23.53%), <i>P. alata</i> (11.76%), <i>C. closterium</i> (11.76%)	0.00		3.40E+05
25/09/18	14.29	<i>P. micans</i> (10.71%), <i>T. compressa</i> (3.57%)	85.71	<i>G. striata</i> (39.29%), <i>D. fragilissimus</i> (17.86%), <i>Chaetoceros</i> sp. (10.71%)	0.00		5.60E+05

(continued on next page)



Table 5 (continued)

Date D/M/Y	Dinop. (%)	Contributions (%) of Dinoflagellate Species	Bacill. (%)	Contributions (%) of Diatom Species	Other Groups (%)	Contributions (%) of Others	Total Phytop. Cells (L <sup>-1</sup> )
19/10/18	14.29	<i>T. compressa</i> (7.94%), <i>P. micans</i> (4.76%)	60.32	<i>H. hauckii</i> (42.86%), <i>P. alata</i> (6.35%), <i>Thalassiosira</i> spp. (4.76%)	25.40	<i>D. fibula</i> var. <i>aculeata</i> (25.40%)	1.26E+06
31/10/18	50.00	<i>T. compressa</i> (25.00%), <i>P. micans</i> (11.67%)	45.00	<i>A. glacialis</i> (18.33%)	5.00	<i>D. fibula</i> var. <i>aculeata</i> (5.00%)	6.00E+05
05/11/18	75.76	<i>T. compressa</i> (33.33%), <i>P. micans</i> (18.18%)	15.15	<i>H. hauckii</i> (3.03%), <i>P. alata</i> (3.03%)	9.09	<i>D. fibula</i> var. <i>aculeata</i> (6.06%), <i>D. speculum</i> (3.03%)	6.60E+05
16/11/18	78.95	<i>T. compressa</i> (31.58%), <i>P. micans</i> (10.53%), <i>Oxytoxum</i> spp. (10.53%)	15.79	<i>A. glacialis</i> (5.26%), <i>C. closterium</i> (5.26%), <i>Navicula</i> spp. (5.26%)	5.26	<i>D. fibula</i> var. <i>aculeata</i> (5.26%)	3.80E+05
29/11/18	57.14	<i>T. compressa</i> (28.57%), <i>P. scutellum</i> (14.29%), Dinoflagellates cysts (14.29%)	42.86	<i>C. moniligera</i> (14.29%), <i>Navicula</i> spp. (14.29%), <i>Thalassiosira</i> spp. (14.29%)	0.00		1.40E+05
30/11/18	25.81	<i>T. compressa</i> (12.90%), <i>P. micans</i> (3.23%), <i>P. scutellum</i> (3.23%), <i>P. longipes</i> (3.23%)	67.74	<i>Chaetoceros</i> spp. (41.94%), <i>B. delicatulum</i> (12.90%)	6.45	<i>D. fibula</i> var. <i>aculeata</i> (6.45%)	6.20E+05
05/12/18	31.25	<i>P. micans</i> (15.63%), <i>T. compressa</i> (9.38%)	56.25	<i>Thalassiosira</i> spp. (9.38%), <i>P. pungens</i> (9.38%), <i>G. marina</i> (9.38%)	12.50	<i>D. fibula</i> var. <i>aculeata</i> (6.25%), <i>D. speculum</i> (6.25%)	6.40E+05
07/12/18	33.33	<i>P. micans</i> (11.11%), <i>T. compressa</i> (11.11%), <i>P. scutellum</i> (11.11%)	62.96	<i>Chaetoceros</i> spp. (25.93%)	3.70	<i>D. speculum</i> (3.70%)	5.40E+05
14/12/18	27.50	<i>P. micans</i> (7.50%), <i>T. compressa</i> (7.50%), <i>P. scutellum</i> (7.50%)	70.00	<i>Leptocylindrus</i> spp. (25.00%), <i>Chaetoceros</i> spp. (17.50%)	2.50	<i>D. speculum</i> (2.50%)	8.00E+05
02/01/19	14.53	<i>P. micans</i> (6.84%), <i>P. scutellum</i> (5.17%)	83.76	<i>Thalassiosira</i> spp. (27.35%), <i>Leptocylindrus</i> spp. (24.79%), <i>G. marina</i> (13.69%)	1.71	<i>D. fibula</i> var. <i>aculeata</i> (1.71%)	2.34E+06
11/01/19	21.05	<i>P. scutellum</i> (15.79%), <i>P. micans</i> (2.63%), <i>T. compressa</i> (2.63%)	78.95	<i>Leptocylindrus</i> spp. (25.00%), <i>S. costatum</i> (15.79%)	0.00		7.60E+05
25/01/19	15.66	<i>T. compressa</i> (3.61%), <i>T. furca</i> (3.61%)	79.52	<i>Leptocylindrus</i> spp. (27.71%), <i>D. fragilissimus</i> (12.05%)	4.82	<i>D. fibula</i> var. <i>aculeata</i> (2.41%), <i>D. speculum</i> (2.41%)	1.66E+06

(0–12.1%), *Gonyaulax* spp. (0–11.4%), *Hermesinum adriaticum* Zacharias 1906 (0–11.4%), *Prorocentrum dentatum* F. Stein 1883 (0–10.8%), *P. horologium* (0–10.2%), *Oxytoxum* sp. (0–10.5%), *P. longipes* (0–5.13%) and *Ceratium tripos* (O.F. Müller) Nitzsch 1817 (0–1.27%), in different time periods, respectively (Table 5).

As for diatoms, while their contribution to the total phytoplankton abundance varied between 6.78% (March 27, 2018) and 99.27 (June 06, 2018), the highest contribution to the total diatom abundance was provided by *L. minimus* (0–85.5%), *P. pungens* (0–79.2%), *S. costatum* (0–51.3%), *C. closterium* (0–48.2%), *H. hauckii* (0–42.9%), *Cheato-ceros* spp. (0–41.9%), *G. striata* (0–39.3%), *Leptocylindrus* spp. (0–32.5%), *G. marina* (0–31.8%), *T. nitzschoides* (0–29.0%), *Thalassiosira* spp. (0–27.4%), *C. pelagica* (0–22.8%), *A. glacialis* (0–18.3%), *D. fragilissimus* (0–17.9%), *N. longissima* (0–16.7%), *Navicula* spp. (0–15.9%), *L. flabellata* (0–15.4%), *Coscinodiscus* spp. (0–15.4%), *C. moniligera* (0–14.3%), *L. abbreviata* (0–14.3%), *Bacteri- astrum delicatulum* Cleve 1897 (0–12.9%), *Thalassionema frauenfeldii* (Grunow) Tempère & Peragallo 1910 (0–12.5%), *Chaetoceros peruvianus* Brightwell 1856 (0–12.2%), *P. alata* (0–11.8%), *L. danicus* (0–11.4%), *Striatella unipunctata* (Lyngbye) C. Agardh 1832 (0–10.0%), *T. rotula* (0–9.52%), *Manguinea rigida* (M. Peragallo) Paddock 1988 (0–5.13%) and *Cocconeis placentula* Ehrenberg 1838 (0–3.85%), in different time periods, respectively (Table 5).

Apart from dinoflagellates and diatoms, the most important contribution from other taxonomic groups came from the classes Dictyochophyceae and Prymnesiophyceae. While the sole shareholder of Prymnesiophyceae was *E. huxleyi* (0–11.9%), the major contributors to Dictyochophyceae were *D. fibula* var. *aculeata* (0–35.6%), *D. speculum* (0–12.5%) and *Dictyocha fibula* f. *cannopilea-hexacantha* Frenguelli 1935 (0–7.69%). The most important contributors to Euglenophyceae and Cyanophyceae were *Euglena* sp. (0–3.39%) and *Oscillatoria* sp. (0–3.17%), respectively (Table 5).

#### 4. Discussion

In this study, phytoplankton analysis revealed that temporal variations in phytoplankton were affected by both hydrographic and climatic factors. Although the sampling station located in a relatively shallow area, high salinity fluctuations (min-max: 23.69–35.5; average:  $27.36 \pm 2.68$  ppt) (Table 1 and Figure 3) suggested that the region was affected not only from surface waters but also from the deep waters, especially in the winter (Figure 2A–D). On the other hand, a considerable increase in surface water temperatures (up to 2–3°C) in the last 20 years and higher winter surface water temperatures (above 10°C) in recent years are notable. It is obvious that these possible fluctuations in salinity and temperature values as well as other physicochemical variables such as dissolved oxygen (DO) and nutrients may have affected variations in the phytoplankton community. The negative correlation between DO and temperature ( $R = -0.658$ ,  $p \leq 0.01$ ) confirmed this relationship, while the positive correlation between DO and salinity ( $R = 0.579$ ,  $p \leq 0.01$ ) did not (Table 2), perhaps because of the mixing of oxygen-rich Mediterranean deep waters with

surface waters in the Dardanelles. On the other hand, DO values were very close to saturation level according to the salinity and temperature of the water. The water quality differences of the two flow systems in the Dardanelles Strait which carries the low-salty waters of the Marmara Sea to the Aegean Sea and high-salty waters of the Mediterranean Sea to the Marmara Sea (Basturk et al., 1990; Besiktepe et al., 1994; Polat and Tugrul, 1995, 1996) explain the reason for the temporal DO variation during the year, as was in salinity.

In the present study, although seasonal distributions of different taxonomic groups were roughly similar to previously reported results by others, differences in peak periods of phytoplankton communities compared to those reported in earlier studies were significant. For example, maximum total phytoplankton abundance reached  $5.50 \times 10^6$  cells  $L^{-1}$  in early summer (June 06, 2018), whereas, the average total phytoplankton cell abundance ( $9.63 \times 10^5 \pm 7.88 \times 10^5$  cells  $L^{-1}$ ) in this study was considerably lower than those reported in previous studies (Unsal et al., 2003; Turkoglu et al., 2004; Turkoglu, 2008, 2010a, 2010b, 2013, 2016; Turkoglu and Erdogan, 2010; Turkoglu and Oner, 2010; Turkoglu and Ozyalin, 2015; Turkoglu, 2016a, 2016b; Turkoglu and Onal, 2016). In the present study, phytoplankton dominated during late spring-early summer, winter and mid-autumn, but in previous studies carried out by various researchers (Turkoglu, 2008, 2010b, 2013; Turkoglu and Erdogan, 2010; Turkoglu and Ozyalin, 2015), dominant periods of phytoplankton were in the spring (mainly in March and April, partly in May) and late summer (from the second half of July to the end of August). However, in this study, due to the increased temperatures in the surface waters, the winter phytoplankton production levels were higher than those reported earlier for winter. Dinoflagellates, traditionally considered as typical component of plankton in warmer seasons (late spring / summer), tend to prevail also in winter due to climate-driven increased in water temperature. Our study confirmed the significant restructuring of the classical phenological pattern, where the average winter dinoflagellates abundance ( $2.97 \times 10^5$  cells  $L^{-1}$ ) was almost equal to that of summer ( $2.98 \times 10^5$  cells  $L^{-1}$ ) (Table 4).

Chlorophyll *a* levels (min-max: 0.112–2.865; average:  $0.714 \pm 0.515$   $\mu g L^{-1}$ ) revealed that mid and late spring (April and May) and mid and late winter (January–February) had the highest chlorophyll *a* concentrations (Figure 3B–C). High production periods, which were observed in the autumn or late summer in this region in previous studies (Turkoglu et al., 2004), shifted to autumn and early winter (December) in this study (Figure 4B–C). This was also supported by the annual phytoplankton succession (Figure 3C and 5D). Phytoplankton peak periods might vary between years due to seasonal changes occurring in the region from year to year. This seasonal shift was previously demonstrated by other researchers for phytoplankton dynamics in both the Black Sea and Marmara Sea (Besiktepe et al., 1994; Oguz et al., 1996; Turkoglu and Erdogan, 2010; Turkoglu and Oner, 2010; Unluata et al., 1990).

Positive correlations between total phytoplankton and chlorophyll *a* ( $R = 0.404$ ;  $p \leq 0.01$ ) and, between diatoms (Bacillariophyceae) and chlorophyll *a* ( $R = 0.334$ ;  $p \leq 0.01$ ) (Table 2) revealed that greater contribution to chlorophyll *a* level during the study was from diatoms ( $R = 0.334$ ;  $p \leq 0.01$ ) rather than dinoflagellates ( $R = 0.178$ ;  $p \leq 0.01$ ) and



*ata*, *H. hauckii*, *L. danicus*, *L. minimus*, *L. abbreviata*, *L. flabellata*, *N. longissima*, *P. alata*, *P. pungens*, *S. costatum*, *T. nitzschioides* and *T. rotula*, with respect to cell abundance. The coccolithophore *E. huxleyi* and the silicoflagellate *D. fibula* var. *aculeata* and *D. speculum* were other species providing an important contribution for the total phytoplankton in terms of cell abundance. However, cell abundances reported in this study were lower compared to those of earlier studies (Turkoglu et al., 2004; Turkoglu, 2010b; Turkoglu and Erdogan, 2010; Turkoglu and Oner, 2010; Turkoglu and Ozyalin, 2015; Unsal et al., 2003).

Diatoms which exhibits HAB over  $10^6$  cells  $L^{-1}$  were *L. minimus* in early summer (June 06, 2018:  $4.70 \times 10^6$  cells  $L^{-1}$ ) and *C. closterium* in late spring (May 22, 2018:  $1.08 \times 10^6$  cells  $L^{-1}$ ). In addition, some dinoflagellates such as *P. micans*, *T. furca*, *T. fusus* and *T. compressa* and some diatoms such as *P. pungens*, *P. alata*, *D. fragilissimus*, *C. pelagica*, *S. costatum* and *T. nitzschioides* can be considered as important bloom species. Particularly, *P. micans* had a significant share in the dinoflagellate community in most of the studied period. These findings were similar to previous studies reported in the Dardanelles (Turkoglu, 2010b; Turkoglu and Erdogan, 2010; Turkoglu and Onal, 2016; Turkoglu and Oner, 2010; Turkoglu and Ozyalin, 2015).

Despite the eutrophic status of the sea of Marmara quantitative contribution of diatoms (average:  $5.00 \times 10^5 \pm 7.80 \times 10^5$  cells  $L^{-1}$ ) to the total phytoplankton ( $9.63 \times 10^5 \pm 7.88 \times 10^5$  cells  $L^{-1}$ ) was above 50% (average: 51.88%) for all sampling periods, except for spring (34.32%) (Figure 6). The dominance of the diatoms was also supported by qualitative phytoplankton data (diatoms: 56 taxa; 58.95%; dinoflagellates: 32 taxa; 33.68%) (Table 3). The average contribution of the dinoflagellates (min-max: 20.18–62.65%; average:  $43.32 \pm 20.69\%$ ) and others (min-max: 3.03–10.08%; average:  $4.81 \pm 6.99\%$ ) to the total phytoplankton were lower than the average contribution of the diatoms (min-max: 34.32–76.26%; average:  $51.88 \pm 21.61\%$ ). The proportionality between these groups of phytoplankton can be indicative of a good environmental status in the study area compared to previous years (Turkoglu, 2008, 2010a, 2010b, 2013; Turkoglu and Oner, 2010). Moreover, there was a decrease both in the number of HABs and their densities in the region compared to previous findings. In addition, the species diversity index values (particularly in view of Simpson D Index) calculated in this study revealed an improvement in phytoplankton species diversity compared to previous data in the Dardanelles (Turkoglu, 2008, 2010a, 2010b, 2013; Turkoglu and Erdogan, 2010; Turkoglu and Oner, 2010). The phytoplankton abundance mostly between  $10^3$  and  $10^5$  cells  $L^{-1}$  during the year also supports this. This recovery in environmental status, probably due to the decrease in frequency of algal blooms and in their abundance, and so decline in eutrophication, is also supported by lower concentrations of chlorophyll *a* (min-max: 0.112–2.865  $\mu g L^{-1}$ ; average:  $0.714 \pm 0.515 \mu g L^{-1}$ ) measured in this study compared to those reported in previous years (Mercan, 2019; Turkoglu et al., 2004; Turkoglu, 2008, 2010a, 2010b, 2010c, 2013; Turkoglu and Erdogan, 2010; Turkoglu and Oner, 2010; Turkoglu and Ozyalin, 2015; Unsal et al., 2003).

Higher Bray-Curtis Cluster Similarity Index values (>50%) between different sampling periods indicate that in the

region, the temperature was above 10°C for a long time except February (8–10°C) in the winter (TR-MAF-GDM, 2021; Turkoglu, 2016b). Various researchers reported that many phytoplankton species that may reproduce in warmer waters can develop a bloom event even at lower temperature levels just below 10°C, with sufficient availability of nutrients (Broerse et al., 2003; Turkoglu, 2010a; Sorrosa et al., 2005). Moreover, it is known that the synergistic effect of high temperature and domestic pollutants can facilitate phytoplankton blooms such as *N. scintillans* (Turkoglu, 2013), *P. micans* (Turkoglu and Oner, 2010; Turkoglu and Ozyalin, 2015) and *E. huxleyi* (Turkoglu, 2010c) also in winter, even when temperature is below 10°C (Turkoglu, 2010a). However, no *E. huxleyi* or *N. scintillans* blooms were observed throughout study period.

## 5. Conclusion

In conclusion, although the results reported in this study are consistent with earlier observations in the study area, particularly in terms of species diversity, there was a decrease in both HAB events and their cell densities during the study. The observed decrease in the accumulation of organic matter originating from HAB indicated a healthier marine environment compared to earlier reports. The number of sampling stations should be increased to better understand the status and future changes in phytoplankton composition and environmental parameters in Çanakkale Strait. Considering recent extensive mucilage occurrences in the Sea of Marmara, more studies are required for successful monitoring of phytoplankton communities in this region.

## Declaration of competing interest

The authors declare that they have no known competing financial interests or personal relationships that could have appeared to influence the work reported in this paper.

## Acknowledgements

This study is part Egemen Inan Demir's master thesis (Demir, 2020) carried out in Canakkale Onsekiz Mart University, Graduate School of Natural and Applied Sciences under the consultancy of Muhammet TURKOGLU. We thank two anonymous referees for their critical reviews on earlier versions of the manuscript and Dr. Umur ONAL for proofreading.

## References

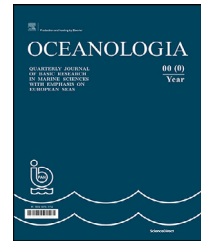
- Baba, A., Deniz, O., Turkoglu, M., Ozcan, H., 2007. Investigation of discharge offresh water in the Canakkale Strait (Dardanelles-Turkey). In: Linkov, I., Gregory, A.K., Richard, J.W. (Eds.), Environmental Security in Harbors and Coastal Areas. Environmental security in harbors and coastal areas. Springer-Verlag, Dordrecht, 421–427. <https://doi.org/10.1007/978-1-4020-5802-830>
- Balkis, N., Atabay, H., Turetgen, I., Albayrak, S., Balkis, H., Tufekci, V., 2010. Role of single-celled organisms in mucilage

- formation on the shores of Büyükkada Island (the Marmara Sea). *J. Mar. Biol. Assoc. U.K.* 91 (4), 771–781. <https://doi.org/10.1017/S0025315410000081>
- Balkis-Ozdelice, N., Tas, S., 2016. Phytoplankton of the Sea of Marmara: A review. In: Ozsoy, E., Çagatay M.N., Balkis, N., Balkis, N., Ozturk, B., (eds.), *The Sea of Marmara: Marine Biodiversity, fisheries, conservation and governance*. TUDAV, Istanbul. 42, 326–343.
- Basturk, O., Tugrul, S., Yilmaz, A., Saydam, C., 1990. Health of the Turkish Straits: Chemical and Environmental Aspects of the Sea of Marmara. METU-Institute of Marine Sciences Tech. Rep. No. 90/4, Erdemli, Mersin, Turkey, 1–69.
- Besiktepe, S., Sur, H.I., Ozsoy, E., Latif, M.A., Oguz, T., Unluata, U., 1994. The circulation and hydrography of the Marmara Sea. *Prog. Oceanogr.* 34, 285–334. [https://doi.org/10.1016/0079-6611\(94\)90018-3](https://doi.org/10.1016/0079-6611(94)90018-3)
- Broerse, A.T.C., Tyrrell, T., Young, J.R., Poulton, A.J., Merico, A., Balch, W.M., Miller, P.I., 2003. The cause of bright waters in the Bering Sea in winter. *Continent. Shelf Res.* 23, 1579–1596. <https://doi.org/10.1016/j.csr.2003.07.001>
- Demir, E.I., 2020. Short Time Series of Quantitative Phytoplankton Variations in the Seaport of the Dardanelles During the Year 2018 Master Thesis. Çanakkale Onsekiz Mart University, Graduate School of Natural and Applied Science.
- Hasle, G.R., 1978. Using the inverted microscope. In: Sournia, A. (Ed.), *Phytoplankton Manual*. Unesco, Paris, 191–196.
- IBM SPSS, 2010. IBM SPSS Statistics for Windows, Ver. 19.0 (released in 2010), IBM Corp., Armonk, NY.
- McAleece, N., Lambhead, P.J.D., Paterson, G.L.J., Gage, J.D., 1999. Biodiversity Professional Version 2 for windows program using for statistical analysis of ecological data. <http://www.nrmc.demonco.uk>
- Mercan, B., 2019. Quantitative phytoplankton variations connected with environmental interactions in southern region of the Nara cape of the Dardanelles Master Thesis, 2019 (in Turkish). Çanakkale Onsekiz Mart University, Graduate School of Natural and Applied Science.
- Oguz, T., Ducklow, H., Malanotte-Rizzoli, P., Tugrul, S., Nezlin, N.P., Unluata, U., 1996. Simulation of annual plankton productivity cycle in the Black Sea by a one-dimensional physical-biological model. *IGR Oceans* 101 (C7), 16585–16599. <https://doi.org/10.1029/96JC00831>
- Polat-Beken, C., 2000. Nutrient flows in the Turkish Straits. *Ocean Challenge* 10 (1), 31–36.
- Polat, C., Tugrul, S., 1995. Nutrient and organic carbon exchanges between the Black and Marmara seas through the Bosphorus strait. *Continent. Shelf Res.* 15, 1115–1132. [https://doi.org/10.1016/0278-4343\(94\)00064-T](https://doi.org/10.1016/0278-4343(94)00064-T)
- Polat, C., Tugrul, S., 1996. Chemical exchange between the Mediterranean and Black Sea via the Turkish Straits. In: Briand, F. (Ed.), *Dynamics of Mediterranean Straits and Channels*. Bulletin de l'Institut Oceanographique. Monaco, Special No. 17, CIESME Science Series 2, 167–186.
- Riccardi, M., Guerrini, F., Tinti, F., Boni, L., Pistocchi, R., 2007. Species-specific probe, based on 18S rDNA sequence, could be used for identification of the mucilage producer microalga *Gonyaulax fragilis* (Dinophyta). *Hydrobiologia* 580, 259–263. <https://doi.org/10.1007/s10750-006-0446-z>
- Semina, H.J., 1978. Treatment of an aliquot sample. In: Sournia, A. (Ed.), *Phytoplankton Manual*. Unesco, Paris, 182–189.
- Sorrosa, J.M., Satoh, M., Shiraiwa, Y., 2005. Low temperature stimulates cell enlargement and intracellular calcification of coccolithophorids. *Marine Biotechnology* 7 (2), 128–133. <https://doi.org/10.1007/s10126-004-0478-1>
- Sukhanova, I.N., 1978. Settling without the inverted Microscope. In: Sournia, A. (Ed.), *Phytoplankton Manual*. UNESCO, Paris, 97–98.
- TUBITAK, 1989. Handbook of Standard Methods of Measurement and Monitoring at Seas. TUBITAK, Ankara, 70 pp.
- Totti, C., Cangini, M., Ferrari, C., Kraus, R., Pompei, M., Pugnetti, A., Romagnoli, T., Vanucci, S., Socal, G., 2005. Phytoplankton size-distribution and community structure in relation to mucilage occurrence in the northern Adriatic Sea. *Sci. Total Environ.* 353, 204–217. <https://doi.org/10.1016/j.scitotenv.2005.09.028>
- TR-MAF-GDM, 2021. Sea Water Temperature Analysis of the Sea of Marmara. Turkish Ministry of Agriculture and Forestry, General Directorate of Meteorology. Available from: <http://www1.mgm.gov.tr/FILES/resmi-istatistikler/Marmara-DenizSuyu-Sicakligi-Analizi.pdf> (accessed: 14/06/2021).
- Tufekci, V., Balkis, N., Polat-Beken, C., Ediger, D., Mantıkçı, M., 2010. Phytoplankton composition and environmental conditions of the mucilage event in the Sea of Marmara. *Türk. J. Biol.* 34 (2), 199–210. <https://doi.org/10.3906/biy-0812-1>
- Turkoglu, M., Koray, T., 2000. Ecological and geographical distribution of the planktonic protista in the southern parts of the Black Sea (neritic waters of Sinop peninsula, Türkiye). *EgeJFAS* 16 (3-4), 228–244.
- Turkoglu, M., Koray, T., 2002. Phytoplankton species succession and nutrients in Southern Black Sea (Bay of Sinop). *Türk. J. Bot.* 26 (4), 235–252.
- Turkoglu, M., Unsal, M., Ismen, A., Mavili, S., Sever, T.M., Yenici, E., Kaya, S., Coker, T., 2004. Dynamics of lower and high food chain of the Dardanelles and Saros Bay (North Aegean Sea), Tubitak Project Final Report, Report No: YDABÇAG-101Y081, Canakkale, Turkey, 313 pp.
- Turkoglu, M., Baba, A., Özcan, H., 2006. Determination and evaluation of some physicochemical parameters in the Dardanelles (Canakkale Strait-Turkey) using multiple probe system and geographic information system. *Hydrol. Res.* 37 (3), 293–301. <https://doi.org/10.2166/nh.2006.012>
- Turkoglu, M., 2008. Synchronous blooms of the coccolithophore *Emiliania huxleyi* (Lohmann) Hay & Mohler and three Dinophyceae in the Dardanelles (Turkish Straits System). *J. Mar. Biol. Assoc. U.K.* 88 (3), 433–441. <https://doi.org/10.1017/S0025315408000866>
- Turkoglu, M., 2010a. Winter bloom and ecological behaviors of coccolithophore *Emiliania huxleyi* (Lohmann) Hay & Mohler, 1967 in the Dardanelles. *Hydrol. Res.* 41 (2), 104–114. <https://doi.org/10.2166/nh.2010.124>
- Turkoglu, M., 2010b. Temporal variations of surface phytoplankton, nutrients and chlorophyll-a in the Dardanelles (Turkish Straits System): A coastal station sample in weekly time intervals. *Türk. J. Biol.* 34 (3), 319–333. <https://doi.org/10.3906/biy-0810-17>
- Turkoglu, M., 2010c. Short time variations of chlorophyll a and nutrients in the Dardanelles, Turkey. *CIESM Rapp. Comm. Int. Mer. Medit.* 39, 411–411.
- Turkoglu, M., Erdogan, Y., 2010. Diurnal variations of summer phytoplankton and interactions with some physicochemical characteristics under eutrophication of surface water in the Dardanelles (Çanakkale Strait, Turkey). *Türk. J. Biol.* 34 (2), 211–225. <https://doi.org/10.3906/biy-0807-7>
- Turkoglu, M., Oner, C., 2010. Short time variations of winter phytoplankton, nutrient and chlorophyll-a of Kepez harbor in the Dardanelles (Çanakkale Strait, Turkey). *Türk. J. Fish. Aquat. Sci.* 10 (4), 537–548. <https://doi.org/10.4194/trjfas.2010.0414>
- Turkoglu, M., 2013. Red tides of the dinoflagellate *Noctiluca scintillans* associated with eutrophication in the Sea of Marmara (The Dardanelles, Turkey). *Oceanologia* 55 (3), 709–732. <https://doi.org/10.5697/oc.55-3.709>
- Turkoglu, M., Tugrul, S., 2013. Long time variations of chlorophyll a and nutrients in the coastal waters of the Sea of Marmara. *CIESM Rapp. Comm. Int. Mer. Medit.* 40 p. 900.
- Turkoglu, M., 2015. Phytoplankton in the Aegean Sea: A review. In: Katagan, T., Tokac, A., Besiktepe, S., Ozturk, B. (Eds.), *The Aegean Sea: Marine Biodiversity, Fisheries, Conservation and*

- Governance Perspectives. Turkish Marine Research Foundation (TUDAV), Istanbul, Turkey, 146–175.
- Turkoglu, M., Ozyalin, S., 2015. Çanakkale Boğazı'nın bazı liman bölgelerindeki fitoplanktonik organizmaların çevresel parametrelerle ilişkili kısa zaman serili değişimleri. ÇOMÜ-BAP, Proj. No: 2010/22, Çanakkale, Türkiye, 349 pp.
- Turkoglu, M., 2016a. First harmful algal bloom record of tytoplanktonic dinoflagellate *Prorocentrum lima* (Ehrenberg) F. Stein, 1878 in the Dardanelles (Turkish Straits System, Turkey). J. Coast. Life Med. 4 (10), 765–774. <https://doi.org/10.12980/jclm.4.2016J6-184>
- Turkoglu, M., 2016b. Bloom dynamics of *Emiliana huxleyi* (Lohmann) Hay & Mohler, 1967 in the Sea of Marmara: A review. In: Thajuddin, N., Dhanasekaran, D. (Eds.), Algae – Organisms for Imminent Biotechnology. Intech Open Access Publisher, London, UK, 29–53. <https://doi.org/10.5772/61365>
- Turkoglu, M., Onal, U., 2016. Temporal distribution of phytoplankton in Cardak Lagoon (Dardanelles, Turkey). CIESM Rapp. Comm. Int. Mer Medit. 41, 286–286.
- Turkoglu, M., Onal, U., Ismen, A., 2018. Introductory Chapter: Marine Ecology – Biotic and Abiotic Interactions. In: Turkoglu, M., Onal, U., Ismen, A. (Eds.), Marine Ecology – Biotic and Abiotic Interactions. Intech Books, IntechOpen Access, London, 1–7. <https://doi.org/10.5772/intechopen.78296>
- Unluata, U., Oguz, T., Latif, M.A., Ozsoy, E., 1990. On the physical oceanography of the Turkish Straits. In: Pratt, L.J. (Ed.), The physical oceanography of sea straits. Kluwer, Dordrecht, the Netherlands, 25–60.
- Unsal, M., Turkoglu, M., Yenici, E., 2003. Biological and physicochemical researches in the Dardanelles (Çanakkale Strait), TÜBİTAK-YDABAG-101Y075, Technical Final Report, 1–131.
- Uysal, Z., 1995. A net plankton study in the Bosphorus junction of the Sea of Marmara. Turk J. Bot. 20 (5), 321–327.
- Venrick, E.L., 1978. How many cells to count? In: Sournia, A. (Ed.) Phytoplankton Manual. Unesco, Paris, 167–180.

Available online at [www.sciencedirect.com](http://www.sciencedirect.com)

ScienceDirect

journal homepage: [www.journals.elsevier.com/oceanologia](http://www.journals.elsevier.com/oceanologia)

## ORIGINAL RESEARCH ARTICLE

# On Baltic herring morphometry and its impact on the backscattering properties.

Natalia Gorska<sup>a,\*</sup>, Jakub Idczak<sup>b</sup>

<sup>a</sup>*Institute of Oceanology, Polish Academy of Sciences, Sopot, Poland*

<sup>b</sup>*Institute of Oceanography, Faculty of Oceanography and Geography, University of Gdańsk, Gdynia, Poland*

Received 26 April 2021; accepted 20 October 2021

Available online 12 November 2021

## KEYWORDS

Backscattering;  
Target strength;  
Numerical modelling;  
Baltic herring

**Abstract** Previous studies, dedicated to backscattering properties of Baltic herring, have shown the different target strength ( $TS$  – which is a measure of fish capacity to scatter sound) values, for the same species in different regions and seasons. The intraspecies differentiation in fish physiology and morphology as well as fish swimbladder morphometry between herring aggregations, occupying various parts of the Baltic Sea, has been supposed as one of the reasons for the variability.

The paper addresses analysis of herring swimbladder morphometry and its impact on  $TS$  of individuals from ICES subdivision 26, one of the areas where Poland is responsible for herring biomass estimation. The collection of the X-rays images for 74 herring individuals, sampled in this subdivision, was created. The two-dimensional digitized dorsal images of herring swimbladder and body, as well as the angles between the swimbladder and the body longitudinal axis, were used to compute the target strength. The differentiation of herring morphometry within particular fish size classes was analysed and its consequences for the averaged target strength within the class was discussed. The difference from the previous numerical studies, in which the simplified herring morphometry was used, was also demonstrated. The computational results were considered in regard to the available in situ measured data on Baltic herring  $TS$ . The study of the Baltic herring target strength is important for increasing accuracy of acoustic biomass estimation of this ecologically and economically important species.

© 2021 Institute of Oceanology of the Polish Academy of Sciences. Production and hosting by Elsevier B.V. This is an open access article under the CC BY-NC-ND license (<http://creativecommons.org/licenses/by-nc-nd/4.0/>).

\* Corresponding author at: Institute of Oceanology, Polish Academy of Sciences, Powstańców Warszawy 55, 81–712 Sopot, Poland.

E-mail address: [gorska@iopan.pl](mailto:gorska@iopan.pl) (N. Gorska).

Peer review under the responsibility of the Institute of Oceanology of the Polish Academy of Sciences.

<https://doi.org/10.1016/j.oceano.2021.10.001>

0078-3234/© 2021 Institute of Oceanology of the Polish Academy of Sciences. Production and hosting by Elsevier B.V. This is an open access article under the CC BY-NC-ND license (<http://creativecommons.org/licenses/by-nc-nd/4.0/>).



Production and hosting by Elsevier

## 1. Introduction

Accurate information on fish biomass is critical for ecosystem-based approach to management of marine resources. The biomass, acoustically estimated, is recognized as one of the “hydroacoustic metrics” to evaluate a marine ecosystem state (Godø et al., 2014; Trenkel et al., 2011, 2016).

The central role of *Clupeids* as a link between lower and higher trophic levels makes this ecologically and economically valuable species important in a management of the pelagic ecosystem. It is recognized that biomass of herring, patchily distributed in dense aggregations, can efficiently be estimated by acoustic techniques (e.g. Fässler, 2010).

To increase the accuracy of acoustic biomass estimation, it is necessary to deepen the knowledge of the fish backscattering properties – the target strength (*TS*), a measure of individual capacity to scatter sound – and its variability. The *TS* depends on a range of factors: e.g., morphometry of fish and its swimbladder (impacted by fish physiology and behaviour), as well as acoustic frequency of the measuring device (Simmonds and MacLennan, 2005).

The variability, according to these factors, of herring from the northeast Atlantic and the North Sea has been carefully examined. *TS* measurements were based on insonification of immobilised fish (Nakken and Olsen, 1977) or active fish within a cage (Edwards and Armstrong, 1981, 1983, 1984; Edwards et al., 1984; Ona, 2003; Pedersen et al., 2009) as well as wild fish, behaving normally (Foote et al., 1986; Huse and Ona, 1996).

It was found that *TS* is strongly dependent on the herring individual tilt (Blaxter and Batty, 1990; Edwards et al., 1984; Huse and Ona, 1996; Huse and Korneliussen, 2000; Nakken and Olsen, 1977; Ona, 2001). Ona et al. (2001) demonstrated how herring *TS* is dependent on fish physiology (on the gonadosomatic indices (*GSII*)). Edwards and Armstrong (1981), Edwards et al. (1984), Ona (1990, 2003), Pedersen et al. (2009) showed the impact of depth on herring target strength. Theoretical backscatter models have helped to improve the understanding and interpretation of empirical herring *TS* data (Fässler, 2010; Gorska and Ona, 2003a, 2003b).

The findings of these empirical and theoretical studies helped to strengthen the credibility of herring *TS*-*L* relationship, which in the following form:

$$TS = 20\log_{10}(L) + b_{20} \quad (1)$$

is used in acoustic fish abundance estimates (Foote et al., 1986). Here the fish total length *L* is in cm, *TS* in dB. Consideration of the sensitivity of the intercept  $b_{20}$  to the herring physiology and behaviour allowed to improve the accuracy of the herring abundance estimates in the northeast Atlantic and the North Sea.

The situation is different for the Baltic herring, whose biomass has been assessed in acoustic survey methods since the 1980's, in line with ICES recommendations (e.g., ICES, 2017). It was justified in Fässler et al. (2008) that *TS*-*L* relationship derived for herring from the northeast Atlantic and the North Sea cannot be used for Baltic herring. The question – which *TS*-*L* relationship is appropriate to use in acoustic herring biomass estimation in the Baltic – is still open.

Direct in situ *TS* measurements were carried out in different locations (different ICES Baltic subdivisions) and different seasons (Didrikas, 2005; Didrikas and Hansson, 2004; Kasatkina, 2009; Lassen and Stæhr, 1985; Peltonen and Balk, 2005; Rudstam et al., 1988, 1999; Schmidt et al., 2011). The collected *TS* data were highly variable: it has been obtained up to 8 dB difference in the intercept  $b_{20}$ . This means the differentiation of the target strength of the same fish total length.

Unfortunately, the factors, which could impact the individual backscattering properties (fish physiology and orientation as well as the depth occupied by herring) and explain the variability, were not controlled during the measurements.

A complementary numerical *TS* modelling was also applied, providing a deeper understanding of the 8 dB difference. The variability has been partly explained by (i) different depths at which the herring aggregations could be identified during the particular measurements (Fässler and Gorska, 2009; Fässler et al., 2008), (ii) possible fish orientation difference within the studied aggregations (Fässler and Gorska, 2009; Fässler et al., 2008; Idczak and Gorska, 2016; Idczak and Książ-Kubacka, 2012) and (iii) the different acoustic frequencies used by the researchers (in the range from 38 kHz to 120 kHz) (Fässler and Gorska, 2009).

Moreover, some researchers collected *TS* data for mixed herring and sprat aggregations and analysed them as a single set (Didrikas, 2005; Didrikas and Hansson, 2004). Meanwhile, the others (Kasatkina, 2009; Peltonen and Balk, 2005; Schmidt et al., 2011) used the data gathered for single-species aggregations of herring and sprat and treated them as two independent collections. It has been found that the different approaches could also contribute to the 8 dB-variability (Fässler, 2010; Fässler and Gorska, 2009; Gorska and Idczak, 2010).

Summarizing, the *TS* modelling results have identified the difference in fish depths, tilt angle distributions, the applied acoustic frequency as well as discrepancies in the methods of data collection and analysis, as main factors responsible for the observed up to 8 dB difference in herring. However, these factors can explain only partially the 8 dB-differentiation. The final explanation remains an open question. This motivated us to look for other important factors.

Blaxter and Batty (1990), as well as Horne (2003) pointed out that in some cases, the physical environment may impact the fish physiology and morphology as well as fish swimbladder morphometry, resulting in intraspecies variability in target strength. Because of its long north–south extension (of more than 1500 km), the Baltic Sea is characterised by strong meridional differentiation in environments the herring live in, e.g. salinity value is about 1 unit for the north Baltic and 10 units for the South Baltic (Kullenberg, 1981). Moreover, there are the periods when the differentiation does intensify. This is related to the North Sea salt water inflow with more oxygenated water (Kullenberg, 1981) that improves herring living conditions in the areas which the inflow reaches. These inflows affect different areas of the Baltic Sea in different degrees. The study area (Subdivision 26) has a stronger inflow effect compared to the areas north of it and a lower impact compared to the areas west of it.

The difference in the herring living environment could result, e.g. in the differentiation over herring growth



rate (it means the differentiation in fish size and its swimbladder morphometry) as well as herring fat content and condition (Bignert et al, 2007; Cardinale and Arrhenius, 2000; Grygiel and Wyszynski, 2003; Ojaveer, 1988; Wyszynski, 1997). It could be a potential reason of the variability in Baltic herring *TS* in different parts of Baltic (Fässler and Gorska, 2008; Peltonen and Balk, 2005).

Fässler and Gorska (2008), as well as Fässler (2010) underlined that the studies of the backscattering properties of fish from different locations and at different times in the Baltic Sea are important.

Previously, Baltic herring swimbladder morphometry and its effect on the *TS* were only examined using the herring collection taken from the south-eastern (ICES subdivision 25) and eastern (ICES subdivisions 27 and 29) of Sweden during the Swedish component of the Baltic International Acoustic Survey (BIAS project) in October 2002 (Fässler et al., 2008; Fässler and Gorska, 2009; Idczak and Gorska, 2016; Idczak and Kniż-Kubacka, 2012).

It means that research of herring target strength in other particular Baltic ICES subdivisions (local approach) remains to be important. Our work focused on the study of fish morphometry and its impact on the backscattering by herring in another unexplored part of the Baltic Sea – ICES subdivision 26, one of the areas where Poland is responsible for the acoustic assessment of herring biomass. Therefore, we created our own collection of the X-rays images for 74 herring individuals sampled in the ICES subdivision 26. The morphometric features of this collection were studied (Section 3.1). The variability of herring morphometry within particular fish size classes was analysed and its impact on the averaged target strength differentiation within the classes was demonstrated (Sections 3.2, 4.1).

The previous modelling studies of Baltic herring backscattering considered a simplified body and swimbladder morphometry (Fässler et al., 2008; Fässler and Gorska, 2009; Gorska and Idczak, 2010; Idczak and Kniż-Kubacka, 2012). In our study backscatter model has been improved for Baltic herring in the ICES subdivision 26. Accurate morphometry data, defined from the X-ray images, were used to compute the dorsal backscattering cross-section of herring in this area. The distinction with the previous approach, using the simplified herring morphometry, has been also explored (Sections 3.3, 4.2).

The computational results were considered in light of the measured Baltic herring *TS* data. The herring *TS*-*L* relationship in the ICES subdivision 26 was discussed (Section 4.2).

Considering that our research was carried out only in one region of the Baltic Sea, it did not explain directly the observed 8 dB variability of Baltic herring *TS*. The explanation requires further studies in the remaining Baltic ICES subdivisions and the comparison of their results. However, our research deepened the understanding of the backscattering properties of Baltic herring and so is an important step towards solving the problem.

## 2. Material and methods

The averaged target strengths of Baltic herring were modelled using the Modal-Series-Based Deformed Cylinder Model (MSB-DCM; Stanton, 1988a,b, 1989).

The swimbladder and the body of the fish were modelled as deformed cylinders filled with gas and liquid respectively, the radius of which varies along their straight longitudinal axis. For both herring swimbladder and body, the radius at each point of the axis was half the object dorsal width at this point. The axis of the swimbladder cylinder is inclined with respect to the axis of the fish body.

The application of this approach has been justified. Firstly, the detailed analysis of the digitised X-ray images of 74 herring, caught in the Polish coastal zone (ICES subdivision 26), demonstrated that:

- herring swimbladder and body were elongated objects (the mean aspect ratios were ca. 8 and 12 for herring swimbladder and body respectively),
- the cross-sectional radius changed slowly with respect to position along the axis of these objects.

Secondly, it was assumed that also the material properties changed slowly with respect to position along the axis. Thirdly, the backscattering modelling was restricted to considering the geometries where the direction of the incident sound wave was normal or near-normal to the longitudinal straight axis of fish body and swimbladder. According to the publication (Jech et al., 2015), MSB-DCM approach could be applied.

The body and swimbladder geometry, and the angle between the swimbladder and the body longitudinal axis were defined from X-ray images of 74 specimens caught in the Polish coastal zone (ICES subdivision 26).

### 2.1. MSB-DCM Model

Following the paper of Idczak and Gorska (2016), the backscattering cross-sections of herring individual swimbladder  $\sigma_{sb}$  and body ( $\sigma_b$ ) could be presented in the form of:

$$\sigma_{sb} = \frac{L_{sb}^2}{\pi^2} \left| \int_0^1 \sum_{m=0}^{\infty} b_m^{sb} (-1)^m \times \exp[2ikL_{sb}\mu_{sb}\cos\theta_{sb}] d\mu_{sb} \right|^2 \quad (2)$$

and

$$\sigma_b = \frac{L_b^2}{\pi^2} \left| \int_0^1 \sum_{m=0}^{\infty} b_m^b (-1)^m \times \exp[2ikL_b\mu_b\cos\theta_b] d\mu_b \right|^2 \quad (3)$$

The Equations (6) and (7) from Idczak and Gorska (2016) were used. Here:  $L_b$  and  $L_{sb}$  are fish standard length and swimbladder length, respectively;  $k$  is the wave number ( $k = 2\pi f/c$ , where  $c$  is the sound speed in seawater, and  $f$  is the acoustic wave frequency). The variables  $\mu_b = x_b/L_b$  and  $\mu_{sb} = x_{sb}/L_{sb}$ , where  $x_b$  and  $x_{sb}$  are distances along the main longitudinal axis of the cylinders (the fish body and swimbladder, respectively). The angles  $\theta_b$  and  $\theta_{sb}$  are the angles between the direction of the acoustic wave incidence onto the scattering target and the longitudinal axes of the fish body and the swimbladder, respectively (Figure 1).

In Equations (2) and (3), the modal coefficient  $b_m$  is described by the equation:

$$b_m = \frac{-\varepsilon_m}{1 + iC_m} \quad (4)$$

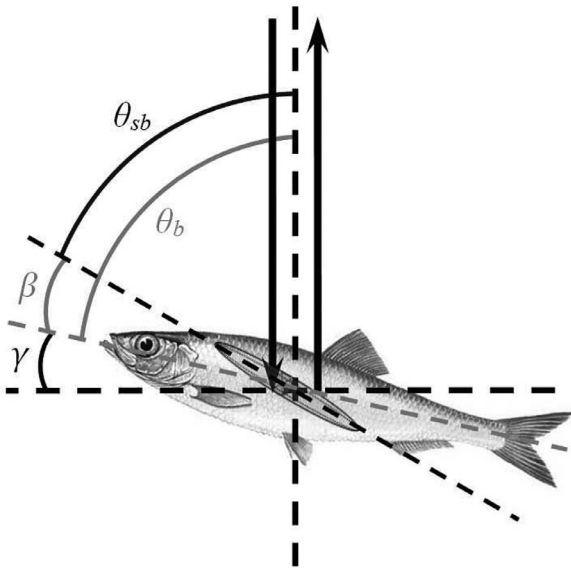


Figure 1 Geometry of acoustic wave scattering by the fish body and the swimbladder.

where  $\varepsilon_m = 1$  for  $m = 0$  and  $\varepsilon_m = 2$  for  $m > 0$ .

The coefficient  $C_m$  is defined by the equation:

$$C_m = \frac{[J'_m(K'a)N_m(Ka)]/[J_m(K'a)J'_m(Ka)] - gh[N'_m(Ka)/J'_m(Ka)]}{[J'_m(K'a)J_m(Ka)]/[J_m(K'a)J'_m(Ka)] - gh} \quad (5)$$

where: for the fish body,  $C_m = C_m^b$ ,  $a = a_b$  is a half of the body dorsal width, dependent on the coordinate  $x_b$ ; by analogy, for the swimbladder:  $C_m = C_m^{sb}$ ,  $a = a_{sb}$  is a half of the swimbladder dorsal width and are dependent on the coordinate  $x_{sb}$ .  $K = \frac{2\pi f}{c} \sin \theta$  and  $K' = \frac{K}{h}$  – inside the scattering object, where  $K = K_b$  and  $\theta = \theta_b$  for the fish body and  $K = K_{sb}$ ,  $\theta = \theta_{sb}$  for the swimbladder. The sound speed contrast  $h$  is defined by the ratio of sound speed in a scattering object and the sound speed in the ambient seawater. The density contrast  $g$  is a ratio of the target material density to the ambient seawater density. Here  $h = h_b$ ,  $g = g_b$  for the fish body and  $h = h_{sb}$ ,  $g = g_{sb}$  for the swimbladder. Functions, denoted as  $J_m(X)$  and  $N_m(X)$ , are Bessel functions of the first and second kind, respectively, of order  $m$ , whereas  $J'_m(X)$  and  $N'_m(X)$  are the respective first order derivatives relative to  $X$ . These equations, based on Equation (8) from Stanton (1989) are valid for incidence direction perpendicular to the swimbladder axis  $\pm 20^\circ$  (Jech et al., 2015).

The mean backscattering cross-sections for individual swimbladder  $\langle \sigma_{sb} \rangle$  and body  $\langle \sigma_b \rangle$  are considered to describe backscattering by aggregated herring:

$$\langle \sigma_{sb} \rangle = \int_{-\pi/2}^{\pi/2} d\gamma W_\gamma(\gamma) (\sigma_{sb}) \quad (6)$$

$$\langle \sigma_b \rangle = \int_{-\pi/2}^{\pi/2} d\gamma W_\gamma(\gamma) (\sigma_b) \quad (7)$$

where  $W_\gamma(\gamma)$  is the Probability Density Function (PDF). It describes fish distribution according to their orientation  $\gamma$ . Symbol  $\gamma$  describes the angle of the fish body longitudinal axis deviation from the horizontal plane (Figure 1).

The angle  $\gamma$  is equal zero for the horizontal position of fish body. It is positive for head up position of fish and negative for its head down position.

Basing on experimental research (e.g., Ona, 2001) and theoretical considerations (e.g., Foote and Traynor, 1988), a Gaussian PDF was assumed for fish orientation with mean  $\bar{\gamma}$  and standard deviation  $S_\gamma$ :

$$W_\gamma(\gamma) = \frac{1}{\sqrt{2\pi}S_\gamma} \exp\left(-\frac{(\gamma - \bar{\gamma})^2}{2S_\gamma^2}\right) \quad (8)$$

Following the paper by Gorska and Ona (2003b) we did not consider the swimbladder and body as a coupled system. We limited our analysis to a simple summation of the averaged backscattering cross-sections of fish body and its swimbladder. When the swimbladder is the dominant scatterer (it was confirmed by our calculations), the equation:

$$\langle \sigma_{bs} \rangle = \langle \sigma_{sb} \rangle + \langle \sigma_b \rangle \quad (9)$$

is a good description of whole-fish backscattering.

The target strength (Simmonds and MacLennan, 2005), defined as:

$$TS = 10 \log_{10} \langle \sigma_{bs} \rangle \quad (10)$$

is used in analysis and referred to as ‘averaged target strength’ in the following text.

## 2.2. Model input data

### 2.2.1. On fish sample, X-rays imaging and the morphometric data analysis

Studying fish backscattering properties, three noninvasive techniques are used for the reconstruction of the morphometric structure of fish body and swimbladder: X-rays imaging (e.g., Clay and Horne, 1994; Henderson and Horne, 2007; Sawada et al., 1999); computed tomography CT (Macaulay, 2002; Okumura and Masuya, 2004; Reeder et al., 2004), as well as magnetic resonance imaging MRI (Pena and Foote, 2008). The first method provides digitized dorsal and lateral images of a fish which could be used to present the body and swimbladder as circular or deformed cylinders (or set of short cylinders). The two other techniques generate three-dimensional images of fish anatomy. Morphometry of Baltic herring in the ICES subdivision 26 was studied, using X-rays imaging techniques.

The catch was conducted from the fishing boat HEL – 125 in early November 2011 in the Gulf of Gdańsk southeast of the Hel Peninsula (ICES subdivision 26). The coordinates of the start and end points of the transect were (54°27.026'N and 19°02.745'E) and (54°30.510'N and 18°57.036'E) respectively. While catching fish, the pelagic trawl (codend was of 11 mm mesh) moved as close to the surface as possible, vertically covering the water layer from about 5 to 25 meters deep. The trawling speed was 3.5 knots and haul duration was one and half hour.

To obtain good quality X-ray images of herring swimbladder and body, the methodology of fish capture, transportation, storage and X-raying, initiated in 2010 (Idczak et al., 2011), was used. The methodology followed the recommendations of Horne and Jech presented in the *Manual for radiographing fish* (version 24.04.2001 in Appendix B of

ICES, 2002 Report). The main concern during the fish collection, preparation and X-raying was an individual swimbladder which should remain intact and noncollapsed with a shape not substantially differing from that in the natural environment.

The methodology, developed in 2010, was not effective enough. Only for 18% of the individuals, taken from the haul, the X-ray images were of good quality, sufficient to digitize dorsal and lateral images of a fish.

Therefore, the methodology was improved in 2011, i.e. fish were:

- (i) Collected closer to the sea surface.
- (ii) Stored before the X-raying, not in the small aquarium (400 l volume), which was the case in 2010, but in the aquaculture specialized tank of 2000 l volume, with a continuous flow of seawater pumped directly from the Gulf of Gdańsk. As a result, the values of temperature, oxygen content and salinity of water were similar to the values of these parameters occurring in the natural environment. Fish were stored in the tanks 12–24 hours before the X-raying. This time allowed for the adaptation of individuals to hydrostatic pressure change. The vast majority of fish individuals were in a good state: they swam naturally throughout the entire volume of the tank and even formed small shoals.
- (iii) Transported from fishery boat to the tanks as well as from the tanks to the hospital, where the X-ray images were done, in smaller portions in the bags with more oxygenated marine water than it was in 2010.
- (iv) The multiple-fish scanning (few fish were scanned simultaneously) was conducted, reducing the waiting time for scanning for each individual. It was important to keep fish in a good condition.

This provided an increase in the rate of good quality X-ray images.

The X-ray outlines of the bladders of 31% (74 individuals) of the fish, sampled from the haul, were clearly visible and satisfactory for digitizing. The assessment of the normality of the swimbladder shape was based on the experience of X-raying of a large number of herring individuals, collected in 2010 and 2011.

We did not consider in further analysis:

- (i) Herring smaller than 15 cm in length (about 4% of the fish, sampled from the haul) that did not survive the preparation to X-ray analysis.
- (ii) Fish whose behaviour or X-ray images demonstrated that their swimbladders were damaged due to the pressure jump (38% of the haul sample).
- (iii) Fish with undamaged swimbladders, the X-ray images of which were not acceptable for the digitizing (27% of the sample). The reasons for bad quality images were of random character: e.g., some fish did not hold a proper position on the X-ray cassette during the analysis – their bodies were not perpendicular to the cassette plane.

A method for herring body and swimbladder contour digitization was developed. For the image processing, the AutoCAD LT 2013 software was used.

The digitised contours of fish swimbladders and bodies were obtained for selected 74 fish collection. Herring morphometric dimensions were then measured. The radii of swimbladder and body (both modelled as deformed cylinders), varying over the cylinder longitudinal axis and equating to half of the object dorsal width at each axis point, were defined for each fish (see Equations (2), (3), (5)).

As the target strength  $TS$  of a Baltic herring individual is primarily sensitive to the swimbladder morphometry (Fässler and Gorska, 2009; Gorska and Idczak, 2010), the analysis, presented in section 3.1.2 *Differentiation in swimbladder morphometry within particular fish size classes*, concerned mainly the swimbladder data series. Therefore, swimbladder length  $L_{sb}$  and maximum width  $w_{sb}$ , measured to the nearest 0.1 cm using good quality X-ray herring images, were chosen for the presentation. The swimbladder dorsal cross-section was determined for each individual herring using the AutoCAD LT 2013 software. In addition, the total fish length  $L$  (measured to the nearest 0.1 cm) and the angle  $\beta$  (Figure 1) between the longitudinal body and swimbladder axes (measured to the nearest 0.1 degree) were defined using good quality X-ray images.

The comparison of the Probability Density Functions (PDFs) of total fish length was done between our 74-fish collection and the herring sample (219 individuals), randomly taken from the haul during the cruise dedicated to herring biomass estimation in Polish Marine Areas. The cruise was conducted in October 2010 by National Marine Fisheries Research Institute in Gdynia (*r/v Baltica*). It was related to the Polish component of the BIAS (Grygiel et al., 2011). This comparison was reasonable because both collections were taken in the autumn season and at the same area – ICES subdivision 26. Moreover, in both selected hauls, herring was the dominant species (not less than 95% of the entire haul fish sample). The mean total lengths and their standard deviations (SD) were also compared for these two collections.

The herring X-ray images are accessible due to the project “MOST DANYCH – Multidisciplinary Open System of Knowledge Transfer – Stage II: Open Research Data”, co-financed by the European Regional Development Fund under the Operational Program Digital Poland for 2014–2020 (X-ray images of Baltic herring, 2019, DOI: <https://doi.org/10.34808/s4sj-b755>, <https://mostwiedzy.pl/pl/business/open-research-data/x-ray-images-of-baltic-herring,102102842142204-0>).

### 2.2.2. Other calculation parameters

Computations were made for acoustic frequency  $f = 38$  kHz (used in acoustic herring stock assessment in the Baltic Sea (ICES, 2017)) and sound speed in seawater  $c = 1450$  m/s (Grelowska, 2000). The density  $\rho_{sb}$  and sound speed contrasts  $h_{sb}$  of 0.00129 and 0.23, respectively, were taken for the swimbladder and 1.04 and 1.04 ( $\rho_b$  and  $h_b$ ), – for the fish body. To define the density contrast of the swimbladder, a seawater density was evaluated using an algorithm (Fofonoff and Millard, 1983) implemented in a web-based calculator (Chapman, 2006). The calculations were done for the seawater temperature varying from 10°C to 15°C and constant salinity of 7.26 (Rak and Wiczorek, 2012). This reflects the hydrographic conditions in October–November at the location, where the biological material was collected. It resulted in a seawater density variation from 1004.6 kg

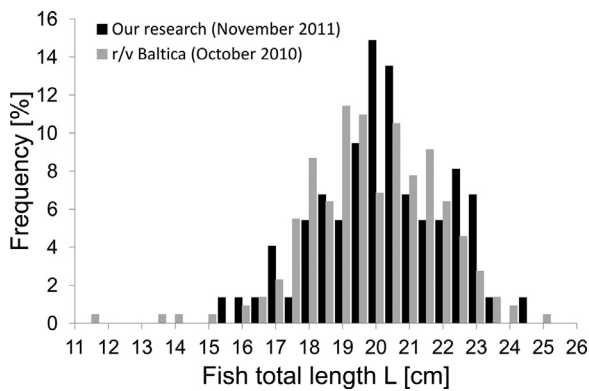


**Figure 2** PDFs of fish total length for two herring samples including 74 (black colour) and 219 (grey colour) individuals.

$m^{-3}$  to  $1005.4 \text{ kg m}^{-3}$ . The density of the swimbladder gas was assumed to be  $1.3 \text{ kg m}^{-3}$  (Brawn, 1969). The other contrasts were chosen following the papers of Gorska and Ona (2003a, 2003b).

The orientation distribution of free-swimming herring in the natural environment has not been studied in the Baltic Sea as it has been done for herring from the northeast Atlantic and the North Sea (Beltestad, 1973; Blaxter and Batty, 1990; Edwards et al., 1984; Huse and Korneliussen, 2000; Huse and Ona, 1996; Nakken and Olsen, 1977; Olsen et al., 1983; Ona, 1984, 2001). It has been obtained that the mean fish body tilt angle ( $\bar{\gamma}$ ) varied from near  $0^\circ$ -values to about  $10^\circ$ , while the standard deviation ( $S_\gamma$ ) varied from about a few degrees to about  $20^\circ$ . Just these ranges of  $\bar{\gamma}$  and  $S_\gamma$  were considered in our analysis. For all the performed calculations, selecting  $\bar{\gamma}$  and  $S_\gamma$  for the calculations, the care about the applicability of the MSB-DCM approach (the near-normal incidence) (Jech et al., 2015) was taken.

### 3. Results

#### 3.1. Input data collection

The main features of the morphometric data collection were analysed and discussed below.

##### 3.1.1. PDFs of fish total length

In Figure 2, the PDFs of fish total length for the two considered collections are compared. The first collection was acquired by us and the second one – during the *r/v Baltica* cruise (Grygiel et al., 2011). The mean total lengths were 20.21 cm and 19.85 cm for the first and second data sets respectively, while the SDs were respectively 1.90 cm and 1.95 cm. It allowed us to conclude that the PDFs of these two samples were comparable (1.7% and 2.5% difference in the mean values and SD respectively). This similarity confirms the reasonability of further analysis of our collection.

##### 3.1.2. Differentiation in swimbladder morphometry within particular fish size classes

In further analysis of the morphometry data (this subsection) as well as of the TS – differentiation in Section 3.2, the entire range of the herring total length was divided into

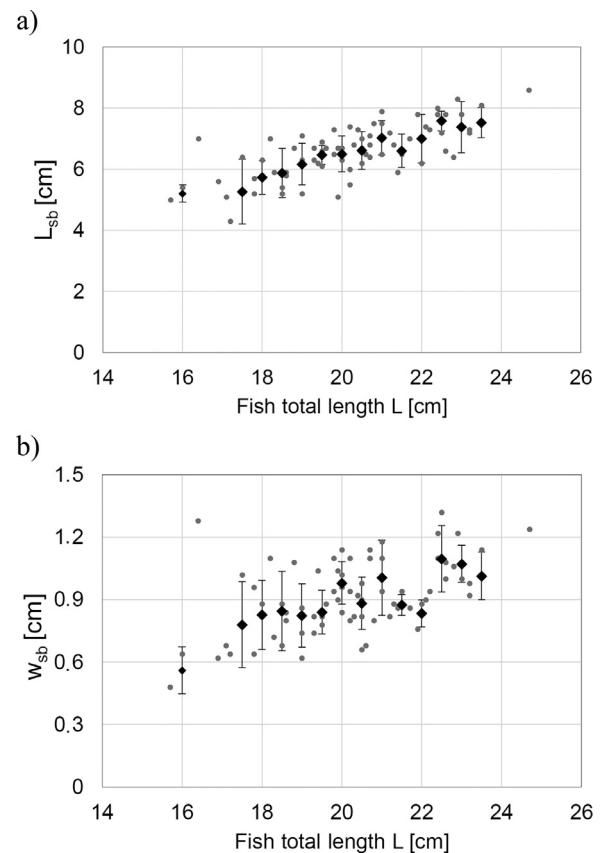


**Figure 3** The dependence of swimbladder length (plot a) and maximum width (plot b) on fish total length. Grey points at each plot correspond to the dimensions of 74 herring individuals. For each size class the mean value (black rhombs) and standard deviation (black whiskers) are presented.

0.5 cm-intervals. 14 size classes were considered. The appropriateness of 0.5 cm interval with not more than a few individuals in each one is discussed below in the Discussion section.

The results of the measurements of swimbladder length and maximum width over the entire fish total length range are presented respectively in Figures 3a and 3b. The mean values with the standard deviations were:  $6.6 \pm 0.9 \text{ cm}$  and  $0.9 \pm 0.2 \text{ cm}$  for the fish swimbladder length and width respectively.

It was demonstrated that for herring individuals of the same size class, the standard deviation could achieve up to 20% for swimbladder length and up to 27% for swimbladder maximum width (for fish size class 17–17.5 cm). The large difference between maximum and minimum dimensions in relation to mean value is also shown: this parameter varied from 16.4% (23.0–23.5 cm length class) to 46.4% (17.0–17.5 cm length class) for swimbladder length and from 13.1% (23.0–23.5 cm length class) to 61% (18.5–19.0 cm length class) for swimbladder maximum width. The mean values for all fish length classes were 25.9% and 36.3% for the swimbladder length and width, respectively.

It is also important to remind that for herring from the northeast Atlantic and the North Sea the swimbladder length is 0.26 times the total length of the fish (Gorska and Ona, 2003b). The linear approximation of the data se-

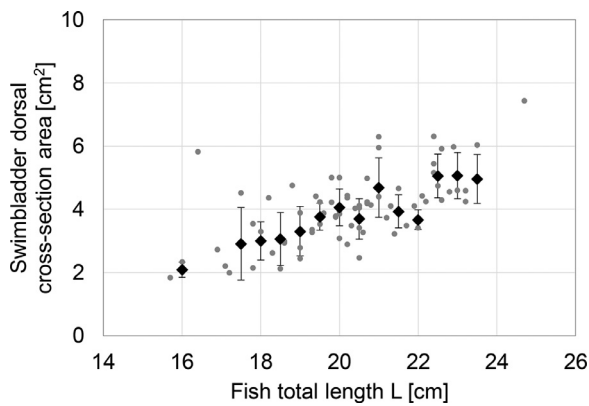


**Figure 4** The dependence of swimbladder dorsal cross-section area on fish total length. Grey points at each plot correspond to particular herring individuals. For each size class the mean value (black rhombs) and standard deviation (black whiskers) are presented.

ries presented in Figure 3a, showed that for Baltic herring the swimbladder length is 0.348 times the fish total length ( $R^2 = 0.49$ ). This is in line with the publication of Fässler et al. (2008), which showed larger dimensions of the Baltic herring swimbladder for the same total fish length in these compared herring groups.

The differentiation in swimbladder dimensions within one size class could result in the variability of the swimbladder dorsal cross-section area for individuals of the same size class. The dorsal cross-section area is an important parameter to which the backscattering could be sensitive. It determines the dimensions of swimbladder surface, as seen from the transmitting transducer, on which the echo energy depends (Simonds and MacLennan, 2005). The results of the calculation of swimbladder dorsal cross-section area are presented in Figure 4. The standard deviation, standardized by the average value of cross-section area of the size class, reaches up to 39.5% for 17–17.5 cm length class.

Figure 5 a–b shows an example of X-ray outlines illustrating the different swimbladder patterns between two individuals of the same size class, which results in the difference of their dorsal cross-section area. The dorsal cross-section areas were 2.94 cm<sup>2</sup> and 4.76 cm<sup>2</sup> for the individuals in plots a and b respectively (1.62 times difference).

In Figure 6, the result of the measurements of the angle  $\beta$  (Figure 1) between the longitudinal body and swimbladder axes is presented. It was shown that the mean standard deviation (standardization by average angle for each size class) was 39.6%, while the mean ratio of maximum to minimum angle for one fish size class was equal to 3.23.

The effect of variability of herring swimbladder morphology within particular fish size classes on the  $TS$  variability is considered in the next section, where the results of  $TS$ -modelling are presented.

### 3.2. $TS$ differentiation within particular fish size classes

The averaged target strength  $TS$  growth with fish total length is shown in Figure 7a. The calculations were made for  $\bar{\gamma} = 0^\circ$  and  $S_\gamma = 10^\circ$ . As in the previous calculations, the

entire range of the total length was divided in 0.5 cm intervals. The borders of these intervals are presented in the plot by vertical lines. We can see the difference in the averaged target strength of the individuals in particular size classes.

To evaluate this effect, the difference between the highest and lowest values of averaged target strength,  $\Delta TS_{Lclass0.5cm}$  was calculated. The results are presented in Figure 7b not only for  $\bar{\gamma} = 0^\circ$  and  $S_\gamma = 10^\circ$  (grey columns), but also for  $\bar{\gamma} = 0^\circ$  and  $S_\gamma = 5^\circ$  (black columns) and  $\bar{\gamma} = 0^\circ$  and  $S_\gamma = 20^\circ$  (white columns). In the horizontal axis of the plot b, the border length of fish size classes is presented.

The analysis of Figure 7b has shown that:

- for each size class, the larger  $S_\gamma$  (from darker to lighter columns in plot b), the smaller the difference  $\Delta TS_{Lclass0.5cm}$ ;
- the largest differences were observed for individuals of 17–17.5 cm length class: 3.1 dB; 2.8 dB and 2.7 dB for  $S_\gamma$  equalling to  $5^\circ$   $10^\circ$  and  $20^\circ$  respectively;
- over the range  $5^\circ \leq S_\gamma \leq 20^\circ$ , for six size classes the  $\Delta TS_{Lclass0.5cm}$  difference is higher than 1.5 dB.

The analysis for fixed  $S_\gamma = 10^\circ$  and  $\bar{\gamma}$  varying from  $0^\circ$  to  $10^\circ$  has been also made (results are not presented graphically). It was shown, that for most classes the  $\Delta TS_{Lclass0.5cm}$  difference increased with  $\bar{\gamma}$ . The largest differences in the  $\Delta TS_{Lclass0.5cm}$  were observed for individuals of 17–17.5 cm length class: 3.8 dB; 3.3 dB and 2.8 dB for  $\bar{\gamma}$  equalling to  $0^\circ$ ,  $5^\circ$  and  $10^\circ$  respectively. Similarly, to the case presented above for more than six size classes  $\Delta TS_{Lclass0.5cm}$  is higher than 1.5 dB.

### 3.3. Fish morphometry: effect on $TS$

In this section, the target strengths, calculated using fish and swimbladder morphometry data from the X-ray images and applying the simplified shape of swimbladder and body (prolate spheroids) (Fässler et al., 2008; Fässler and Gorska, 2009; Gorska and Idczak, 2010; Idczak and Książ-Kubacka, 2012) are compared.

In the calculations with the simplified geometrical shape, it was assumed for each fish that the lengths of swimbladder prolate spheroids to be equal to the actual values of this parameter. To calculate the width of the swimbladder prolate spheroids, it was assumed that their volumes to be equal to the true swimbladder volumes providing that the prolate spheroidal swimbladder had the appropriate volume, ensuring neutral buoyancy of the fish.

These true volumes were calculated using Equations (1)–(3) from Fässler et al. (2008) as well as the volume proportions of various fish individual components and their densities, proposed by those authors. Using the calculated swimbladder volumes and their length data and applying the formula for a prolate spheroid volume, the width of the prolate spheroids were calculated.

Results for the shapes of the fish swimbladder ( $TS$ ), as defined from the X-ray images, and from calculations for their prolate spheroid shapes ( $TS_{pr\_sph}$ ) are compared in Figure 8a. The dependence of the difference  $\Delta TS = TS_{pr\_sph} - TS$  on the fish total length is presented. The up to about 2 dB difference of averaged target strength  $\Delta TS$  was

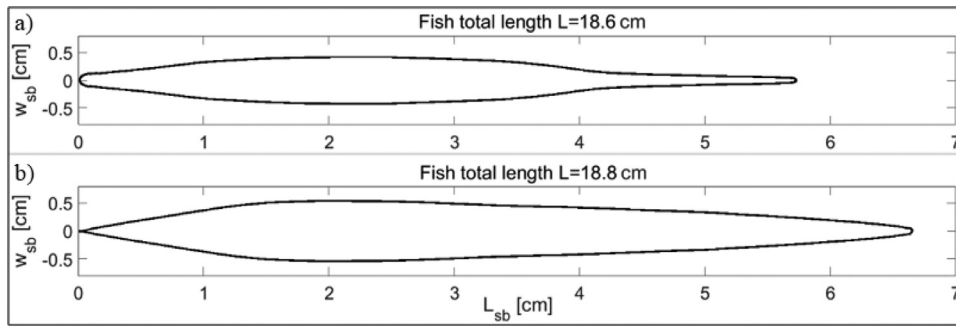


**Figure 5** The X-ray outlines of the swimbladder dorsal cross-section of two individuals of the same size class (plots a and b).

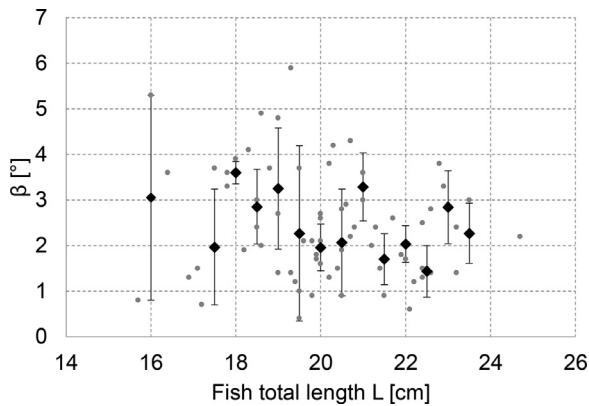


**Figure 6** The dependence of the angle  $\beta$  on fish total length. Grey points correspond to the 74 herring individuals. For each size class the mean value (black rhombs) and standard deviation (black whiskers) are presented.

demonstrated. The trend of the regression line in the plot suggests that  $\Delta TS$  increases with fish total length  $L$  from about 0.3 dB to 1.3 dB.

The effect of the angle  $\beta$  between the longitudinal axes of the swimbladder and the fish body on the averaged target strength  $TS$  is demonstrated in Figure 8b. Modelling results for values of  $\beta$ , as measured on X-ray images of the herring collection, and data from calculations for  $\beta = 0^\circ$  are compared. The dependence of the difference  $\Delta TS_\beta = TS_{(\beta \neq 0)} - TS_{(\beta = 0)}$  on the fish total length is presented. Here  $TS_{(\beta \neq 0)}$  and  $TS_{(\beta = 0)}$  denote the target strength for the measured values of the angle  $\beta$  and for the angle  $\beta = 0^\circ$  respectively. Analysing the impact of the angle on the difference  $\Delta TS_\beta$ , it can be noted that maximum observed difference between the calculation results amounted to about 3.4 dB. According to the regression line, the difference slightly depends on the fish length and amounted to about 1.35 dB.

Analysing the dependence of  $\Delta TS$  and  $\Delta TS_\beta$  on the fish total length, we considered the herring orientation distribution impact on the calculated results. The calculations demonstrated that the difference ( $\Delta TS$ ) (Figure 8a) was not sensitive to the parameters  $\bar{\gamma}$  and  $S_\gamma$  over their entire range selected for the calculations (see subsection 2.2.2). Meanwhile, the difference  $\Delta TS_\beta$  (Figure 8b) was sensitive to the mean angle of fish body orientation and its standard

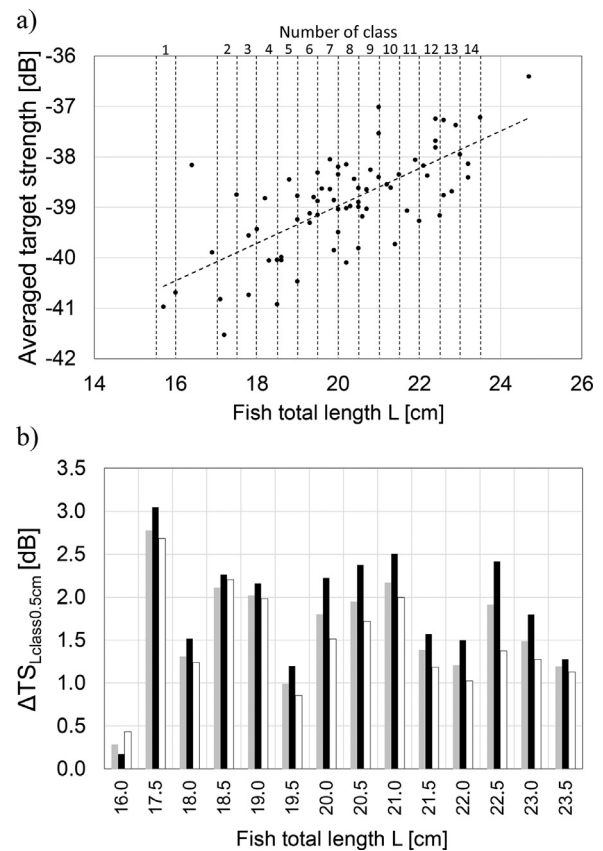


**Figure 7** Averaged target strength vs. fish total length (plot a) and the  $\Delta TS_{Lclass0.5cm}$  for each size class (plot b). A linear regression line is shown in plot a. In this plot data points correspond to calculated results for 74 herring individuals considered. The calculations assumed a mean angle of fish body orientation  $\bar{\gamma}$  equalling to  $0^\circ$ . The standard deviation of the orientation distribution  $S_\gamma$  was equal to  $10^\circ$  (plot a and grey colour in plot b) and  $5^\circ$  and  $20^\circ$  – black and white (colours respectively in plot b).  $TS$  was calculated using Equations (2)–(9).

deviation. The analysis demonstrated that the difference  $\Delta TS_\beta$  was highest for a mean angle of fish body orientation equalling to  $10^\circ$  and  $5^\circ$ -standard deviation. Just this result is presented in Figure 8b.

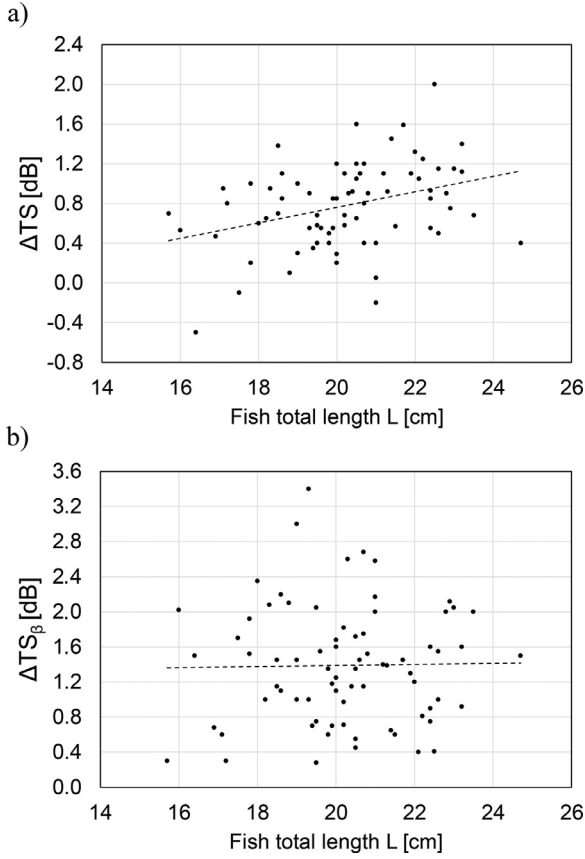


**Figure 8** The difference ( $\Delta TS$ ) between averaged target strength  $TS$  for the prolate spheroid shapes of the fish body and swimbladder and for their shapes, obtained on the basis of digitised X-ray images, relative to  $L$  (plot a). The difference  $\Delta TS_{\beta}$  between  $TS$  values obtained for the measured values of the  $\beta$  and those for  $\beta = 0^{\circ}$  (plot b). A linear regression lines are shown on both plots. Data points on both plots correspond to calculated results for 74 herring individuals considered.  $TS$  was calculated using Equations (2)–(9). The calculations assumed a mean angle of fish body orientation equalling to  $0^{\circ}$  and  $10^{\circ}$  – standard deviation of the orientation distribution (plot a) and respectively  $10^{\circ}$  and  $5^{\circ}$  (plot b).

## 4. Discussion

### 4.1. $TS$ differentiation within particular fish size classes

The finding, regarding the swimbladder geometry differentiation of the same size class individuals (Section 3.1), has been confirmed by studies reported in (Fässler et al., 2008). Figure 1 from that paper, where a relationship between the Baltic herring swimbladder volume and fish weight is presented, demonstrated a considerable scatter of swimbladder volumes in fish of the same weight (i.e. an identical total length).

Baltic herring  $TS$  is strongly sensitive to swimbladder morphometry and fish orientation (Fässler et al., 2008; Fässler and Gorska, 2009; Idczak and Gorska, 2016; Idczak and Książ-Kubacka, 2012). Therefore, the differen-

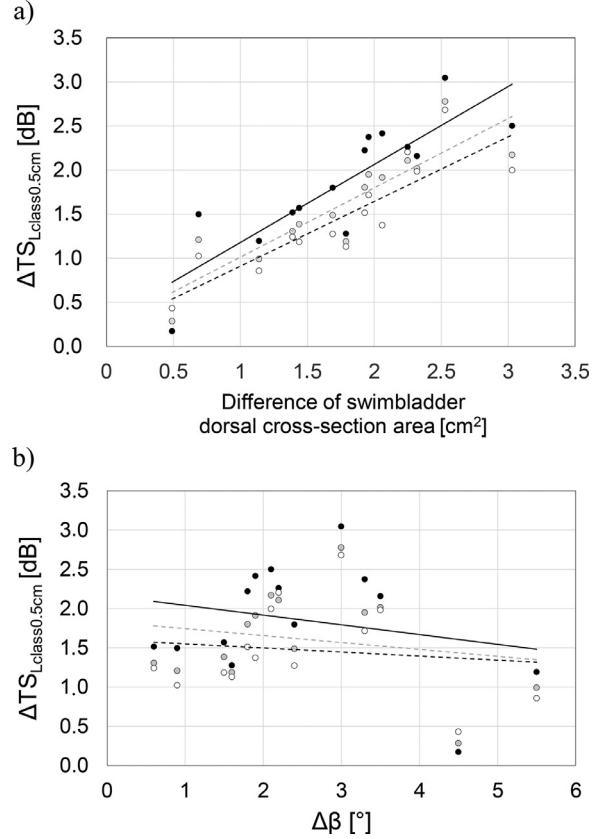


**Figure 9** Scattering plots:  $\Delta TS_{Lclass0.5cm}$  vs. the difference between the largest and smallest:

- swimbladder dorsal cross-section areas (plot a) and
- angle  $\beta$  between the longitudinal body and swimbladder axes for particular size classes. The calculations were made for a mean angle of fish body orientation  $\bar{\gamma} = 0^{\circ}$ . The standard deviation of the orientation distribution  $S_{\gamma}$  was equal to  $5^{\circ}$  (black dots and black linear regression line),  $10^{\circ}$  (grey dots and grey dotted linear regression line) and  $20^{\circ}$  (white dots and black dotted linear regression line).

tiation for fish of similar length in swimbladder morphometry (Figures 3–5) and the angle  $\beta$  between the longitudinal body and swimbladder axes (Figure 6), which defines the angle between the longitudinal axis of swimbladder and incident wave,  $\Theta_{sb}$ , governing the backscattering, could provide the differentiation of averaged  $TS$  within particular fish size classes.

To check this, the dependence of the  $\Delta TS_{Lclass0.5cm}$  on the swimbladder morphometry and the angle  $\beta$  was analysed. The obtained results are presented in Figure 9a and b for a mean angle of fish body orientation  $\bar{\gamma} = 0^{\circ}$  and the standard deviations of the orientation distribution  $S_{\gamma}$ :  $5^{\circ}$ ,  $10^{\circ}$  and  $20^{\circ}$ . In both plots a and b the results are marked by black, grey and white dots respectively. The respective linear regression lines are: black solid, grey dotted and black dotted.

In Figure 9a, the high correlation between the  $\Delta TS_{Lclass0.5cm}$  and the difference of the largest and smallest swimbladder dorsal cross-section areas for particular size classes (see Figure 4), is demonstrated. The square of cor-

relation coefficients ( $R^2$ ) were 0.73; 0.78 and 0.75 for  $S_y$ : 5°, 10° and 20° respectively. For  $S_y = 10^\circ$  and mean orientation  $\bar{\gamma}$  5° and 10° (the results were not presented in Figure 9b) the coefficient  $R^2$  was equal to 0.62 and 0.41 respectively.

In Figure 9b, the lack of correlation between the  $\Delta TS_{Lclass0.5cm}$  and the difference of the largest and smallest angles  $\beta$  for particular size classes is shown over the entire considered range of parameters of orientation distribution ( $\bar{\gamma}$  and  $S_y$ ). The  $R^2$  coefficient varies in the range from 0.005 to 0.06. The lack of correlation could be related to the smaller difference of the angles  $\beta$  in particular size classes (about a few degrees) in relation to the width of fish backscattering directivity pattern, which varies from 12.6° to 22.6° for 74-herring sample, and parameter  $S_y$  (varies from 5° to 20° in our calculations).

The sensitivity of the difference between the highest and lowest values of averaged target strength, demonstrated in Section 3.2, is related to the strong orientation sensitivity of the averaged target strength to the fish orientation distribution parameters (Idczak and Gorska, 2016). However, if averaged target strength increased by about 4 dB for some size classes with  $S_y$  growth from 5° to 20° ( $\bar{\gamma} = 0^\circ$ ) (Idczak and Gorska, 2016), the  $\Delta TS_{Lclass0.5cm}$  difference varied not more than 1 dB over this  $S_y$  range.

Analysing the target strength differentiation of individuals of the similar length, individuals were divided in 0.5-cm size classes. It was done because we would like to understand the effect on TS only of differentiation of the swimbladder morphometry of fish with a similar total length, and to eliminate the effect of the total length itself within the class.

Due to the limited number of considered fish (74) the division in 0.5-cm size classes resulted in a small number of fish in particular classes. Although this does not allow to perform deep statistical analysis for each size class, the results obtained are important. Due to different objective reasons, it is difficult to obtain morphometry data for large fish collection. As a result, in the studies of fish backscattering properties, collection of no more than ca 30 fish within a wide range of total lengths was considered (e.g. Hazen and Horne, 2003, 2004). In this approach, it is important to understand the possible difference in the swimbladder morphometry of the selected fish of the same length.

Accounting for the differentiation of the target strength within particular size classes, it could be concluded that in the TS modelling for the Baltic herring it is important to use sufficient amount of morphometric input data: one should be very careful with theoretical prediction of fish TS basing on a few fish individuals.

## 4.2. Improvement of the backscatter model for herring in the ICES subdivision 26

### 4.2.1. Fish morphometry: effect on TS

The previous modelling studies of Baltic herring backscattering used simplified body and swimbladder shapes – prolate spheroids (Fässler et al., 2008; Fässler and Gorska, 2009; Gorska and Idczak, 2010; Idczak and Książ-Kubacka, 2012). Some of the authors ignored the angle between the swimbladder and the body longitudinal axis

(Fässler et al., 2008; Fässler and Gorska, 2009). In our study, the backscatter model has been improved:

- the two-dimensional digitized dorsal images of herring swimbladder,
- the angles  $\beta$  between the swimbladder and the body longitudinal axis, defined from the images,
- were used as input data.

The effect of swimbladder shape, and the angle  $\beta$  on the averaged target strength TS have been evaluated (section 3.3). Comparing panels a and b from Figure 8 it was concluded that the effect of taking into account the actual measured values of the  $\beta$  angle on the TS is stronger than of considering the actual shape of the swimbladder:

- for 99% fish,  $\Delta TS$  is smaller than 1.6 dB, but  $\Delta TS_\beta$  exceeds this value for 35% individuals;
- the differences  $\Delta TS$  and  $\Delta TS_\beta$  could achieve up to about 2 dB and 3.4 dB (the biggest values).

The sensitivity of the averaged target strength to the angle  $\beta$  between the longitudinal body and swimbladder axes, which impact the angle between longitudinal axis of swimbladder and incident wave,  $\Theta_{sb}$ , governing the backscattering, is in line with result of the previous studies which demonstrated the strong effect of fish orientation on the TS (Idczak and Gorska, 2016).

### 4.2.2. Comparison of calculated TS with the values measured during the r/v Baltica cruise

As the next step, it was important to understand, the accuracy of the MSB-DCM approach used to describe the herring backscattering in ICES subdivision 26. Possible verifications have been made: TS modelling results were compared with the available measured data.

The two PDFs of fish total length of two herring collections: our 74-fish collection and 219-fish sample, taken during the mentioned above r/v Baltica cruise, are comparable (Figure 2). Therefore, it is reasonable to compare target strengths calculated using our herring data set with the TS measured just before the haul, from which the herring sample (219 individuals) was taken (Grygiel et al., 2011).

The dependence of the non-averaged target strength of individual fish calculated as:

$$TS = 10 \log_{10}(\sigma_{sb} + \sigma_b) \quad (11)$$

on individual orientation angle  $\gamma$  (Figure 1) is presented in Figure 10 for the 74-fish collection (thin black curves). Similar to the averaged case, due to the dominance of swimbladder in the backscattering by herring, the swimbladder and body were not considered as a coupled system. It could impact slightly the difference between theoretical and measured results presented below.

The highest measured target strength was –30 dB (top black straight line), while the lowest one –60 dB (bottom black straight line) (Grygiel et al., 2011). Meanwhile, the calculations demonstrated that the maximum target strength was –34 dB and the minimum one –63 dB. These two ranges have a common part, but the measured one is shifted towards the larger TS with respect to the calculated range.



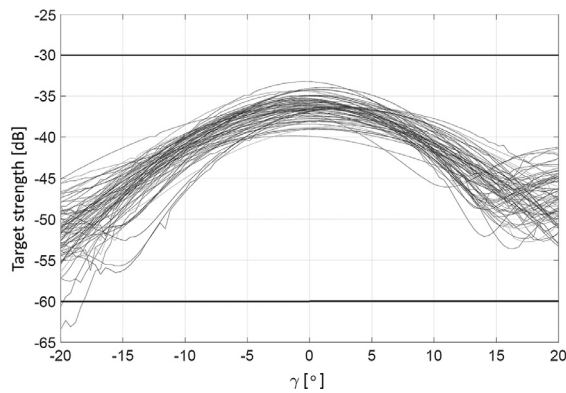


**Figure 10** The dependence of calculated fish non-averaged target strength on individual orientation angle  $\gamma$  for 74 fish collection (different curves refer to different herring individuals). Horizontal black lines indicate the limits of the measured target strength variability range. The figure is generated using the MSB-DCM (Equations (2)–(5) and Equation (11)). The angle range, from  $-20^\circ$  to  $+20^\circ$ , in which the used MSB-DCM is accurate (Jech et al., 2015), was considered.

The larger measured minimum  $TS$  ( $-60$  dB vs.  $-63$  dB) could be explained e.g., by deviating the longitudinal axis of fish from a level less than about 17 degrees for the head down-position of herring individuals. However, the larger measured maximum  $TS$  ( $-30$  dB vs.  $-34$  dB) could be explained e.g., by the presence of a small number of cod (less than 3% (Grygiel et al., 2011)) in the haul.

It could be concluded that MSB-DCM approach enabled reasonable estimation of the variability range of target strength of individual herring in ICES subdivision 26.

#### 4.2.3. Comparison of calculated and measured $TS(L)$ regressions

The herring averaged target strength as a function of the total length was calculated for the 74 herring collection within the considered ranges of a mean angle  $\gamma$  and standard deviation of fish body orientation distribution  $S_\gamma$ . For each calculated set of  $TS(L)$  data, the  $TS$ - $L$  relationship (Equation (1)) was introduced and the intercept  $b_{20}$  was determined. It was shown that the intercept changed from  $b_{20} = -67.0$  dB ( $\bar{\gamma} = 10^\circ$  and  $S_\gamma = 2^\circ$ ) to  $b_{20} = -62.6$  dB ( $\bar{\gamma} = 0^\circ$  and  $S_\gamma = 2^\circ$ ), i.e. by 4.4 dB. In this subsection, we compare the calculated intercept  $b_{20}$  with the results of measurements dedicated to ICES subdivision 26 and the adjacent subdivisions (Didrikas, 2005; Didrikas and Hansson, 2004; Kasatkina, 2009; Schmidt et al., 2011).

There is difficulty in the comparison of these modelling results with the in situ measured intercepts because the measured intercepts  $b_{20}$  were derived joining the backscattering data for different subdivisions:

- by Didrikas (2005) for subdivisions 25, 26, and 28,
- by Didrikas and Hansson (2004) for subdivisions 26 and 27
- by Schmidt et al. (2011) for subdivisions 24, 25 and 26.

Only Kasatkina (2009) analysed the data collected in the subdivision 26.

The values of the intercept  $b_{20}$ , obtained during in situ measurements, conducted by Didrikas (2005), Didrikas and Hansson (2004), and Schmidt et al. (2011), varied over the range from  $-67.8$  to  $-66.3$  dB, which is close to the lower part of the  $b_{20}$  calculated range ( $-67.0$  dB). The intercept  $b_{20}$ , equalling to  $-67.5$  dB (standard deviation 0.26 dB), obtained by Kasatkina (2009) for herring in ICES subdivision 26 at 38 kHz, is close to the minimum value ( $-67.0$  dB) in the present study.

The actual reasons for some discrepancy could be only speculated inter alia because the most important influencing factors (e.g. fish orientation, physiological condition, behaviour) were not controlled during the measurements. Moreover, some of the available data were collected in years distant from the period of our research or the other seasons (Didrikas, 2005; Didrikas and Hansson, 2004; Kasatkina, 2009).

One of the limitations of the considered approach is that the backscattering by the fish backbone has not been considered. It has been shown theoretically (Pérez-Arjona, et al., 2018) that for the dorsal aspect (our case) the backbone shadows the swimbladder that decreases the backscattering and the  $TS$  values. This theoretical result is in good agreement with measurements of Knudsen et al. (2004). It was also confirmed by the measurements comparing swimbladder fish target strength in dorsal and ventral aspects (down-looking and up-looking measurement schemes respectively) (Knudsen et al., 2004; Wanzenböck et al., 2020). The lower  $TS$  was demonstrated in the dorsal aspect in which the incident acoustic wave interacts firstly with the backbone and then with the swimbladder.

The consideration of backscattering by backbone could decrease the  $TS$  value obtained by us and could give better agreement between calculated and measured intercept  $b_{20}$ .

## 5. Conclusions and recommendations

Accounting for that research of herring target strength, in particular, Baltic ICES subdivisions (local approach) remains an important challenge, the attempt to understand the fish morphometry features and their effect on the backscattering has been made for ICES subdivision 26.

The collection of the X-rays images for 74 herring individuals, sampled in this subdivision, have been created. The differentiation in swimbladder dimensions within one size class and hence the variability of the swimbladder dorsal cross-section area (the standard deviation up to 39.5%) has been demonstrated. The differentiation increased with fish total length.

Despite the fact that we also observe the differentiation of the angle between the longitudinal body and swimbladder axes, i.e. the factor which, as well as swimbladder dimensions, may affect the dorsal backscattering, it has been shown that the differentiation of the target strength within the same size class (up to 2.8 dB) corresponds to the dorsal cross-section area variation (the correlation coefficient 0.88).

It was shown that the impact of the shape of swimbladder and angle  $\beta$  on the averaged target strength  $TS$  could be important. The greater effect of taking into account the

actual measured values of the  $\beta$  angle on the *TS* was found compared to the effect of considering the actual defined shape of the swimbladder.

The obtained modelling results have been considered in the light of the available measurement data on Baltic herring target strength that confirmed the reasonability of the approach we applied to study the herring *TS* in the selected subdivision.

The demonstrated differentiation of swimbladder morphometry within a particular herring size class as well as resulting from this *TS* variability, suggest that special concern should be given to a number of Baltic herring individuals, which morphometry supports numerical modelling of *TS*. We consider that this suggestion would be important independently of the methods (X-rays imaging, computed tomography, or magnetic resonance imaging) applied to determine the morphometry data, as well as of the studied fish species.

Our study focused on the study of fish morphometry and its impact on the backscattering by herring only in one region of the Baltic Sea – in ICES subdivision 26, so obtained results did not explain directly the observed 8 dB-variability of Baltic herring *TS*. The explanation requires research in the remaining Baltic ICES subdivisions and comparative result analysis. However, our study improves the understanding of the backscattering properties of Baltic herring and so could be considered as important for the problem solution.

Our findings confirmed that in order to obtain accurate *TS-L* relationships for Baltic herring, it is important to conduct controlled *TS* measurements, collecting data on water temperature, salinity, depth of herring occurrence, fat content and gonad state of individuals as well as herring orientation pattern.

## Declaration of competing interest

The authors declare that they have no known competing financial interests or personal relationships that could have appeared to influence the work reported in this paper.

## Acknowledgements

We greatly appreciate National Marine Fisheries Research Institute in Gdynia for sharing the measurement data. We acknowledge the comments of two anonymous Reviewers, which improved the manuscript.

## Funding

This work was partially supported by the University of Gdańsk (grant numbers: BW\G210-5-0499-0, 538-G210-0442-1 and 538-G210-B260-13); the project "Educators for the elite – integrated training program for PhD students, post-docs and professors as academic teachers at University of Gdańsk" ("Human Capital Operational Programme", financial instrument: "European Social Fund").

## References

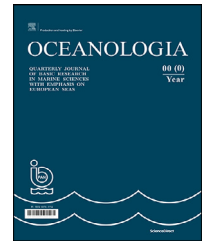
- Beltestad, A.K., 1973. Feeding behavior and vertical migration in 0-group herring (*Clupea harengus* L.) in relation to light intensity, Candidata realium thesis. University of Bergen, Norway.
- Bignert, A., Nyberg, E., Asplund, L., Eriksson, U., Wilander, A., Haglund, P., 2007. Metaller och organiska miljögifter i marin biota, trend- och områdesövervakning, Sakrapport. Swedish Museum of Natural History, Stockholm, 122 pp.
- Blaxter, J.H.S., Batty, R.S., 1990. Swimbladder "behaviour" and target strength. *Rap. Proces.* 189, 233–244.
- Brawn, V.M., 1969. Buoyancy of Atlantic and Pacific herring. *J. Fisheries Res. Board of Canada* 26, 2077–2091.
- Cardinale, M., Arrhenius, F., 2000. Decreasing weight-at-age of Atlantic herring (*Clupea harengus*) from the Baltic Sea between 1986 and 1996: a statistical analysis. *ICES J. Mar. Sci.* 57, 882–893. <https://doi.org/10.1139/f00-221>
- Chapman, R., 2006. A sea water equation of state calculator. <http://fermi.jhuapl.edu/denscalc.html>
- Clay, C.S., Horne, J.K., 1994. Acoustic models of fish: the Atlantic cod (*Gadus morhua*). *J. Acoust. Soc. Am.* 96, 1661–1668. <https://doi.org/10.1121/1.410245>
- Didrikas, T., 2005. Estimation of in situ target strength of the Baltic Sea herring and sprat, Department of Systems Ecology. Stockholm University, 1–5.
- Didrikas, T., Hansson, S., 2004. In situ target strength of the Baltic Sea herring and sprat. *ICES J. Mar. Sci.* 61, 378–382. [https://doi.org/10.1016/S1054-3139\(04\)00005-0](https://doi.org/10.1016/S1054-3139(04)00005-0)
- Edwards, J.I., Armstrong, F., 1981. Measurement of the target strength of live herring and mackerel, *ICES CM /B:26*.
- Edwards, J.I., Armstrong, F., 1983. Measurement of the target strength of live herring and mackerel. *FAO Fish* 300, 69–77.
- Edwards, J.I., Armstrong, F., 1984. Target strength experiments on caged fish. *Scottish Fisheries Bull.* 48, 12–20.
- Edwards, J.I., Armstrong, F., Magurran, A.E., Pitcher, T.J., 1984. Herring, mackerel and sprat target strength experiments with behavioural observations. *ICES CM /B 34*.
- Fässler, S.M.M., 2010. Target strength variability in atlantic herring (*Clupea harengus*) and its effect on acoustic abundance estimates. In: Fässler, S.M.M., A Thesis Submitted for the Degree of PhD at the University of St. Andrews. <http://hdl.handle.net/10023/1703>
- Fässler, S.M.M., Gorska, N., 2008. Investigation of the target strength-to-length relationship of Baltic herring (*Clupea harengus*) for use in biomass estimation. 3rd US/EU Baltic International Symposium.
- Fässler, S.M.M., Gorska, N., 2009. On the target strength of Baltic clupeids. *ICES J. Mar. Sci.* 66, 1184–1190.
- Fässler, S.M.M., Gorska, N., Ona, E., Fernandes, P.G., 2008. Differences in swimbladder volume between Baltic and Norwegian spring-spawning herring: Consequences for mean target strength. *Fish. Res.* 92, 314–321. <https://doi.org/10.1016/j.fishres.2008.01.013>
- Fofonoff, N.P., Millard, R.C., 1983. Algorithms for computation of fundamental properties of seawater, UNESCO R. M. 44. UNESCO Division of Marine Science, Paris. <http://hdl.handle.net/11329/109>
- Foote, K.G., Aglen, A., Nakken, O., 1986. Measurements of fish target strength with split-beam echo sounder. *J. Acoust. Soc. Am.* 80, 612–621. <https://doi.org/10.1121/1.394056>
- Foote, K.G., Traynor, J.J., 1988. Comparison of walleye pollock target strength estimates determined from in situ measurements and calculations based on swimbladder form. *J. Acoust. Soc. Am.* 83, 9–17.
- Godø, O.R., Handegard, N.O., Browman, H.I., Macaulay, G.J., Kaartvedt, S., Giske, J., Ona, E., Huse, G., Johnsen, E., 2014. Marine ecosystem acoustics (MEA): quantifying processes in the

- sea at the spatiotemporal scales on which they occur. ICES J. Mar. Sci. 71, 2357–2369. <https://doi.org/10.1093/icesjms/fsu116>
- Gorska, N., Idczak, J., 2010. On the acoustic backscattering by Baltic herring and sprat. *Hydroacoustics* 13, 89–100. <http://pta.eti.pg.gda.pl/journal/paper.py?id=469>
- Gorska, N., Ona, E., 2003a. Modeling the effect of swimbladder compression on the acoustic backscattering from herring at normal or near-normal dorsal incidences. ICES J. Mar. Sci. 60, 1381–1391. [https://doi.org/10.1016/S1054-3139\(03\)00142-5](https://doi.org/10.1016/S1054-3139(03)00142-5)
- Gorska, N., Ona, E., 2003b. Modelling the acoustic effect of swimbladder compression in herring. ICES J. Mar. Sci. 60, 548–554. [https://doi.org/10.1016/S1054-3139\(03\)00050-X](https://doi.org/10.1016/S1054-3139(03)00050-X)
- Grelowska, G., 2000. Prevailing patterns of the sound speed distributions in the environment of the Southern Baltic. *Arch. Acoust.* 25, 359–368. <http://acoustics.ippt.pan.pl/index.php/aa/article/view/374/312>
- Grygiel, W., Łączkowski, T., Podolska, M., Wodzinowski, T., 2011. Research report from the Baltic International Acoustic Survey (BIAS) on board of the Polish r.v. "Baltica" (20.09-08.10.2010). Working paper on the WGBIFS meeting in Kaliningrad (Russia); 21-25.03.2011, in: ICES CM 2011/SSGESST:05, REF. SCICOM, WGISUR, ACOM; Annex 9; 396–429.
- Grygiel, W., Wysztyński, M., 2003. Temporal (1980-2001) and geographic variation in the sexual maturity at age and length of herring and sprat inhabiting the southern Baltic. *Bulletin of the National Marine Fisheries Research Institute* 159 (2), 3–34.
- Hazen, E.L., Horne, J.K., 2004. Comparing the modelled and measured target-strength variability of walleye pollock, *Theragra chalcogramma*. ICES J. Mar. Sci. 61, 363–377. <https://doi.org/10.1016/j.icesjms.2004.01.005>
- Hazen, E.L., Horne, J.K., 2003. A method for evaluating the effects of biological factors on fish target strength. ICES J. Mar. Sci. 60, 555–562. [https://doi.org/10.1016/S1054-3139\(03\)00053-5](https://doi.org/10.1016/S1054-3139(03)00053-5)
- Henderson, M.J., Horne, J.K., 2007. Comparison of in situ, ex situ and backscatter model estimates of Pacific hake (*Merluccius productus*) target strength. *Can. J. Fish. Aquat. Sci.* 64 (12), 1781–1794. <https://doi.org/10.1139/f07-134>
- Horne, J.K., 2003. The influence of ontogeny, physiology, and behaviour on the target strength of walleye pollock (*Theragra chalcogramma*). ICES J. Mar. Sci. 60, 1063–1074. [https://doi.org/10.1016/S1054-3139\(03\)00114-0](https://doi.org/10.1016/S1054-3139(03)00114-0)
- Huse, I., Korneliussen, R., 2000. Diel variation in acoustic density measurements of overwintering herring (*Clupea harengus* L.). ICES J. Mar. Sci. 57, 903–910. <https://doi.org/10.1006/jmsc.2000.0057>
- Huse, I., Ona, E., 1996. Tilt angle distribution and swimming speed of overwintering Norwegian spring spawning herring. ICES J. Mar. Sci. 53, 863–873. <https://academic.oup.com/icesjms/article/53/5/863/704339>
- ICES, 2002. Report of the Study Group on Target Strength Estimation in the Baltic Sea. 28 pp. <http://www.ices.dk/sites/pub/Publication%20Reports/Expert%20Group%20Report/ftc/2002/sgtseb02.pdf>
- ICES, 2017. Manual for the International Baltic Acoustic Surveys (IBAS). Series of ICES Survey Protocols SISP 8 – IBAS, Version 2.0, 47 pp. <http://www.ices.dk/sites/pub/Publication%20Reports/ICES%20Survey%20Protocols%20SISP%29/2017/SISP%208%20IBAS%202017.pdf>
- Idczak, J., Gorska, N., 2016. Modelling of acoustic backscattering by southern Baltic herring. *Hydroacoustic* 19, 145–152. <http://pta.eti.pg.gda.pl/journal/paper.py?id=639>
- Idczak, J., Gorska, N., Arciszewski, B., 2011. Study of swimbladder morphometry of Baltic herring and sprat (development of measurement methodology). *Hydroacoustics* 14, 61–68. <http://pta.eti.pg.gda.pl/journal/paper.py?id=499>
- Idczak, J., Książ-Kubacka, N., 2012. Backscattering properties of southern Baltic herring. *Hydroacoustics* 15, 57–64. <http://pta.eti.pg.gda.pl/journal/paper.py?id=531>
- Jech, J.M., Horne, J.K., Chu, D., Demer, D.A., Francis, D.T.I., Gorska, N., Jones, B., Lavery, A.C., Stanton, T.K., Macaulay, G.J., Reeder, D.B., Sawada, K., 2015. Comparisons among ten models of acoustic backscattering used in aquatic ecosystem research. *J. Acoust. Soc. Am.* 138, 3742–3764. <https://doi.org/10.1121/1.4937607>
- Kasatkina, S.M., 2009. The influence of uncertainty in target strength on abundance indices based on acoustic surveys: examples of the Baltic Sea herring and sprat. ICES J. Mar. Sci. 66, 1404–1409. <https://doi.org/10.1093/icesjms/fsp086>
- Knudsen, F.R., Fosseidengen, J.E., Oppedal, F., Karlsen, Ø., Ona, E., 2004. Hydroacoustic monitoring of fish in sea cages: target strength (TS) measurements on Atlantic salmon (*Salmo salar*). *Fish. Res.* 69, 205–209. <https://doi.org/10.1016/j.fishres.2004.05.008>
- Kullenberg, G., 1981. Chapter 3 Physical Oceanography. Elsevier Oceanography Series 30, 135–181. [https://doi.org/10.1016/S0422-9894\(08\)70140-5](https://doi.org/10.1016/S0422-9894(08)70140-5)
- Lassen, H., Stæhr, K.J., 1985. Target strength of Baltic herring and sprat measured in-situ. ICES CM. B 41, 1–14.
- Macaulay, G.J., 2002. Anatomically detailed acoustic scattering models of fish. *Bioacoustics* 12, 275–277. <https://doi.org/10.1080/09524622.2002.9753720>
- Nakken, O., Olsen, K., 1977. Target strength measurements of fish. *Rap. Proces.* 170, 52–69.
- Ojaveer, E., 1988. Baltic Herrings. In: *Biology and Management*. Agropromizdat, Moscow, Russia, 204.
- Okumura, T., Masuya, T., 2004. Three dimensional morphometry of fish body structure by X-ray CT. *Oceans* 1, 354–356.
- Olsen, K., Angell, J., Pettersen, F., Løvik, A., 1983. Observed fish reactions to a surveying vessel with special reference to herring, cod, capelin and polar cod. *FAO Fish* 300, 131–138.
- Ona, E., 1984. Tilt measurements on herring, ICES Pelagic Fish Committee B:19. Institute of Marine Research, Bergen, Norway, 13 pp.
- Ona, E., 1990. Physiological factors causing natural variations in acoustic target strength of fish. *J. Mar. Biol. Assoc. UK* 70, 107–127.
- Ona, E., 2001. Herring tilt angles, measured through target tracking. In: Funk, F., Blackburn, J., Hay, D., Paul, A.J., Stephenson, R., Toresen, D., Witherell, R. (Eds.), *Herring: Expectations for a new millennium*. University of Alaska, Fairbanks, 509–520.
- Ona, E., 2003. An expanded target-strength relationship for herring. ICES J. Mar. Sci. 60, 493–499. <http://hdl.handle.net/11250/108201>
- Ona, E., Zhao, X., Svellingen, I., Fosseidengen, J.E., 2001. Seasonal variation in herring target strength. In: Funk, F., Blackburn, J., Hay, D., Paul, A.J., Stephenson, R., Toresen, D., Witherell, R. (Eds.), *Herring: Expectations for a new millennium*. University of Alaska, 461–487.
- Pedersen, G., Handegard, N.O., Ona, E., 2009. Lateral-aspect, target-strength measurements of *in situ* herring (*Clupea harengus*). ICES J. Mar. Sci. 66, 1191–1196. <https://doi.org/10.1093/icesjms/fsp121>
- Peltonen, H., Balk, H., 2005. The acoustic target strength of herring (*Clupea harengus* L.) in the northern Baltic Sea. ICES J. Mar. Sci. 62, 803–808. <https://doi.org/10.1016/j.icesjms.2005.02.001>
- Pena, H., Foote, K.G., 2008. Modelling the target strength of *Trachurus symmetricus murphyi* based on high-resolution swimbladder morphometry using an MRI scanner. ICES J. Mar. Sci. 65, 1751–1761. <https://doi.org/10.1093/icesjms/fsn190>
- Pérez-Arjona, I., Godinho, L., Espinosa, V., 2018. Numerical simulation of target strength measurements from near to far field

- of fish using the method of fundamental solutions. *Acta Acust. United Ac.* 104, 25–38. <https://doi.org/10.3813/AAA.919142>
- Rak, D., Wieczorek, P., 2012. Variability of temperature and salinity over the last decade in selected regions of the southern Baltic Sea. *Oceanologia* 54 (3), 339–354. <https://doi.org/10.5697/oc.54-3.339>
- Reeder, D.B., Jech, J.M., Stanton, T.K., 2004. Broadband acoustic backscatter and high-resolution morphology of fish: measurements and modelling. *J. Acoust. Soc. Am.* 116, 747–761. <https://doi.org/10.1121/1.1648318>
- Rudstam, L.G., Hansson, S., Lindem, T., Einhouse, D.W., 1999. Comparison of target strength distributions and fish densities obtained with split- and single-beam echosounders. *Fish. Res.* 42, 207–214. [https://doi.org/10.1016/S0165-7836\(99\)00047-8](https://doi.org/10.1016/S0165-7836(99)00047-8)
- Rudstam, L.G., Lindem, T., Hansson, S., 1988. Density and in situ target strength of herring and sprat: a comparison between two methods of analyzing single beam sonar data. *Fish. Res.* 6, 305–315. [https://doi.org/10.1016/0165-7836\(88\)90001-X](https://doi.org/10.1016/0165-7836(88)90001-X)
- Sawada, K., Ye, Z., Kieser, R., McFarlane, G.A., Miyanoana, Y., Furusawa, M., 1999. Target strength measurements and modelling of walleye pollock and Pacific hake. *Fisheries Sci.* 65, 193–205. <https://doi.org/10.2331/fishsci.65.193>
- Schmidt, B., Gorska, N., Szczucka, J., 2011. Target strength relationship for herring and sprat in the southern Baltic Sea. ICES Annual Science Conference, Gdańsk, Poland, 19–23 September, 2011, ICES Council Meeting 2011/R:15.
- Simmonds, E.J., MacLennan, D.N., 2005. *Fisheries Acoustics: Theory and Practice*. In: *Fish Fisheries Serie*. Blackwell Publishing, Oxford, UK, 472 pp.
- Stanton, T.K., 1988a. Sound scattering by cylinders of finite length. I. Fluid cylinders. *J. Acoust. Soc. Am.* 83, 55–63. <https://doi.org/10.1121/1.396184>
- Stanton, T.K., 1988b. Sound scattering by cylinders of finite length. II. Elastic cylinders. *J. Acoust. Soc. Am.* 83, 64–67. <https://doi.org/10.1121/1.396185>
- Stanton, T.K., 1989. Sound scattering by cylinders of finite length. III. Deformed cylinders. *J. Acoust. Soc. Am.* 86, 691–705. <https://doi.org/10.1121/1.398193>
- Trenkel, V.M., Handegard, N.O., Weber, T.C., 2016. Observing the ocean interior in support of integrated management. *ICES J. Mar. Res.* 73, 1947–1954. <https://doi.org/10.1093/icesjms/fsw132>
- Trenkel, V.M., Ressler, P.H., Jech, M., Giannoulaki, M., Taylor, C., 2011. Underwater acoustics for ecosystem-based management: state of the science and proposals for ecosystem indicators. *Mar. Ecol. Prog. Ser.* 442, 285–301. <https://doi.org/10.3354/meps09425>
- Wanzenböck, J., Kubecka, J., Sajdlova, Z., Frouzova, J., 2020. Hydroacoustic target strength vs. fish length revisited: Data of caged, free-swimming European whitefish (*Coregonus lavaretus* L.) suggest a bi-phasic linear relationship under a limited range of tilt angles. *Fish. Res.* 229, 105620. <https://doi.org/10.1016/j.fishres.2020.105620>
- Wyszyński, M., 1997. *Charakterystyka biologiczno-technologiczna śledzia południowego Bałtyku, Study and material*, Ser. B 69, National Marine Fisheries Institute, Gdynia, Poland, 94–123.

Available online at [www.sciencedirect.com](http://www.sciencedirect.com)

ScienceDirect

journal homepage: [www.journals.elsevier.com/oceanologia](http://www.journals.elsevier.com/oceanologia)

## ORIGINAL RESEARCH ARTICLE

# Bedforms evolution in the Vistula River mouth during extreme flood event, southern Baltic Sea

Aliaksandr Lisimenka<sup>a,b,\*</sup>, Adam Kubicki<sup>c</sup>, Maciej Kałas<sup>a</sup>

<sup>a</sup> Maritime Institute, Gdynia Maritime University, Gdańsk, Poland

<sup>b</sup> Institute of Oceanology, Polish Academy of Sciences, Sopot, Poland

<sup>c</sup> GEO Ingenieurservice Nord-West, Wilhelmshaven, Germany

Received 6 August 2021; accepted 20 October 2021

Available online 6 November 2021

## KEYWORDS

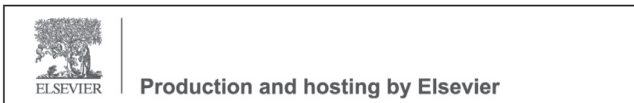
Bedform geometry;  
Bed roughness;  
Flood event;  
Anti-clockwise  
hysteresis;  
Spectral analysis;  
Vistula River mouth

**Abstract** Results of bathymetric surveys conducted to examine changes of sand dunes geometry in the Vistula River mouth before, during and after the extreme flood event are presented. A total of 2076 dunes were analysed based on a series of bed elevation profiles obtained along the centreline of about 3.3 km length. Low-steepness dunes characterized by the mean lee-side slopes milder than  $\beta < 10^\circ$  are fully dominant at low flows. In contrast, at high hydrology, nearly 50% of dunes indicate  $\beta > 10^\circ$ . Dune height and length are substantially out of phase with progressive changes of water discharge exposing a well-pronounced anti-clockwise hysteresis. Distinct behaviour of dune dimensions reflected in increasing of dune steepness  $H/\lambda$  of about 3-fold and decreasing of about 4-fold were observed during rising and falling discharges, respectively. The bed roughness due to dunes presence showed changes of about 10-fold during the both of limbs and is found to be in range of about  $k_{dunes} = (1/5 \div 3/5)H_{mean}$ . At the mesoscale region, spectra followed sufficiently by the ‘−3 power law’ for low hydrology, with steeper spectrum slopes close to ‘−4’ during moderate and high water discharges. With the development of the flood, potential of flow separation phenomena was increased of about 9-fold, from 2.2% at the flood beginning phase up to 20% at the flood peak. The obtained results could be used for the improvement of the hydraulic numerical models in sand-bed rivers to predict bed-

\* Corresponding author at: Maritime Institute, the Gdynia Maritime University, Gdańsk, Poland.

E-mail addresses: [alisimenka@im.umg.edu.pl](mailto:alisimenka@im.umg.edu.pl), [sasha@iopan.pl](mailto:sasha@iopan.pl) (A. Lisimenka).

Peer review under the responsibility of the Institute of Oceanology of the Polish Academy of Sciences.



forms evolution, flow resistance and turbulence as well as water levels for proper river system management during flood events.

© 2021 Institute of Oceanology of the Polish Academy of Sciences. Production and hosting by Elsevier B.V. This is an open access article under the CC BY-NC-ND license (<http://creativecommons.org/licenses/by-nc-nd/4.0/>).

## 1. Introduction

Bedforms, such as ripples and dunes (*sensu* Ashley, 1990), are common sedimentary structures omnipresent in alluvial river channels and seabeds. They look like a series of rhythmic undulations of bed surface, typically composed of mixture of different grain sizes ranging from sands to gravels. In response to routinely changing water flow conditions observed in natural environments, these morphological elements are in ceaseless motion triggering changes in their size, shape and cross-strata structure. Bedforms are a key features for understanding of depositional/erosional processes, changes in riverine morphodynamics and sediment transport (Wu et al., 2021). They impact functioning of habitats and often present a major problem for engineering structures (Aberle et al., 2010; Amsler and Garcia, 1997).

Due to substantial influence of dunes on flow velocity structure which, in turn, impacts directly sediment transport pattern, an appreciation of the interaction between water flow, dune geometry and dune migration is therefore fundamental to predict flow resistance, bed level adjustments as well as stratification of bed sediments (Carling et al., 2000). In fact, amongst other factors like grain resistance (or roughness), vegetation one, or resistance caused by water flow field variations in space and time, the hydraulic roughness of river channels is commonly dominated by the resistance induced by subaqueous bedforms, i.e. ripples and dunes (Warmink et al., 2007, 2012, 2013). In addition, depending on a bedform size and shape, flow separation phenomena is observed at the dune lee-side and influences significantly the energy dissipation between the overlying free water flow and the recirculating turbulent vortex shedding (Best, 2005; Cisneros et al., 2020; Lefebvre and Winter, 2016). Therefore, the the resistance coefficient of bedforms uncertainty becomes one of the main sources of errors in numerical modelling studies, and these errors increase dramatically while investigating extremely high water level conditions.

Earlier studies dealing with changes of bedform geometry performed in large sand-bed rivers during flood events showed that both, mean dune height and length increase as a function of the water discharge. Moreover, a hysteresis (loop-rating effect) can be observed for dune height and length, which indicates that, for a given water discharge, both dune size parameters are larger during the falling limb than for the period of the rising stage (e.g. Harbor, 1998; Julien and Klassen, 1995; Julien et al., 2002; Ten Brinke et al., 1999; Wilbers and Ten Brinke, 2003). Lagged response of dunes presents significant implications for flow hydraulics: in fact, dunes extract fluid momentum by form drag and therefore dune size has a significant effect on the bed friction factor, and moreover, large losses

by form drag reduce the skin friction available for sediment transport as well (Martin and Jerolmack, 2013). As noted in Warmink (2014), dune evolution during rising limb of a flood wave is quite well understood and can be successfully modelled, however, dune evolution during the falling limb remains poorly understood yet. Also, Reesink et al. (2018) underlined recently that the precise mechanisms of dunes adaption to changes in water flow and knowledge of the hydraulic variables that control dune modifications in size and shape over time and space remain still insufficiently studied. Therefore, understanding physical processes accompanying changes in bedform geometry, their migration and how one responses to a changing water flow are of particular significance for river system management aimed primarily to accurately estimate water levels during normal and extreme hydrological conditions.

The development of high-resolution measurement techniques led to the availability of bottom relief data with unprecedented accuracy and hence lots of progress have been accomplished in different aspects of subaqueous bedform studies performed in natural environments during last decades (e.g. Barnard et al., 2013; Best et al., 2010; Hu et al., 2018; Koop et al., 2020; Lyons and Pouliquen, 2004; Parsons et al., 2005; Sambrook Smith et al., 2013). These measuring techniques, however, are of limited use during the extreme events, when navigating the vessel through abnormal hydraulic conditions becomes dangerous for the crew and equipment.

In order to fill this gap, this study provides the first insight into bedform morphodynamics during the passage of flood wave on a river of the Baltic Sea basin. The paper presents results of investigations of subaqueous sand dunes geometry in the Vistula River mouth performed before, during, and after the flood event. An analysis of high-resolution bathymetric dataset that permits: to quantify the Vistula dunes dimensions (dune height and length, steepness) together with their angularity (mean stoss- and lee-side angles), to determine dune development, and to calculate bed roughness due to dunes under more energetic hydrological conditions is presented here. A parametrization of relation between flow depth and dune height and an estimation of the potential for flow separation are performed as well. In addition, the spectral analysis of the bed elevation profiles allowed distinguishing regions in the riverbed morphology of the Vistula mouth, and highlighted a distinct behaviour of the power-law spectral functions. The outcome of the study could be pivotal for improving our understanding of bedload transport processes, could help in palaeohydraulic reconstruction studies in the area, as well as could be essential for calibration of numerical models of alluvial sand-bed large rivers, aiming to predict dune dynamics, bed resistance, turbulent flow and flood water levels.

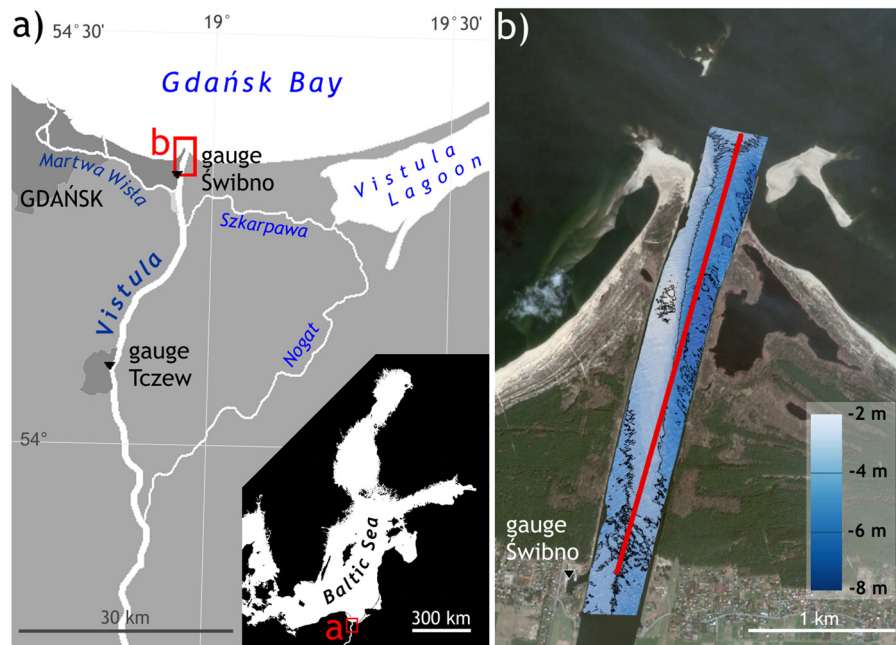


**Figure 1** a) Location of the study area ‘Przekop Wisły’ in the southern Baltic Sea; b) Bathymetry of the Przekop Wisły surveyed in March 2014 (contours every 2 m) overlying an aerial photograph of April 2, 2014, together with the red centreline of 3270 m length along which the repetitive surveys were accomplished.

## 2. Material and methods

### 2.1. Geographical setting

The measurements were carried out in the main mouth of the Vistula River (Przekop Wisły) located in southern part of non-tidal Baltic Sea (Figure 1). The Vistula (Wisła) with the total length of 1047 km and the river basin of about 194 400 km<sup>2</sup> is the largest river in the region. The Vistula plays a dominant role both regards to the quantity of discharged fresh water flowing into the Gdańsk Bay and the sediment delivery. The river supplies about 7% of entire fresh water to the Baltic Sea with the average multiyear outflow amounting to 33.3 km<sup>3</sup> (Majewski, 2013).

The Przekop Wisły is a cross-cut artificial channel which was opened in 1895 (Szymański, 1897a,b) in order to protect Gdańsk city and nearby lowlands from floods. The intermittent catastrophic floods occurring previously, were effectively terminated (Makowski, 1995).

The channel has a total length of ca. 7000 m (starting at the Martwa Wisła lock; Figure 1a), ca. 400 m width and up to 8–9 m water depth. In the final 3000 m of the channel, a submerged sandbar crossing the channel diagonally from N to S is the most distinctive morphological feature (Fig. 1b). The riverbed is covered by complex patterns of rhythmic bedforms that were investigated recently by Lisimenka and Kubicki (2017). Results of granulometric analysis of grab samples revealed that the bottom sediments are characterized here by coarse and medium-grained sands (Rudowski et al., 2017).

Due to existing locks, about 95% of total Vistula water outflows into the Baltic Sea through this channel. Based on operational data obtained from the closest gauging station located in Tczew (31.2 km upstream, Figure 1a),

which represents 99.9% of the total Vistula River catchment area (Majewski, 2018), the long-term (1921–2020) average annual water discharge reaches  $Q_{mean}=1020 \text{ m}^3/\text{s}$  (IMGW-PIB, 2020). In the time span 1921–2020, the average daily water discharge ranged between a minimum of 238 m<sup>3</sup>/s and a maximum of 9530 m<sup>3</sup>/s (recorded during the flood event in April 1924, see Figure 2). In addition, based on the multiyear hydrological observations in Tczew, the Lower Vistula has an average ratio of maximum to minimum water discharge  $\langle Q_{max}/Q_{min} \rangle = 9.4$ , where  $Q_{max}$  and  $Q_{min}$  are the water discharges representative of the highest and lowest daily flows in a particular hydrological year, respectively. Records covering one century show that there have been 36 flood events with the water discharge higher than  $Q > 4000 \text{ m}^3/\text{s}$ . Amongst these, the flood event of May 2014 with the peak wave discharge  $Q_{peak}=4110 \text{ m}^3/\text{s}$  belongs to the group of the highest high-water hydrological events ( $\approx 25^{\text{th}}$  percentile of the century-long annual maximum flow values) that occurred in the area of interest.

### 2.2. Hydrological conditions during the experiment

The time series of the Vistula River discharge values, collected at the Tczew gauge in a period of experiment between 28.02. and 16.06.2014 (Figure 3a), revealed a passage of flood wave with the maximum intensity about four times higher than that of the long-term mean annual outflow. The peak wave with the discharge  $Q_{peak}=4110 \text{ m}^3/\text{s}$  was observed in 25<sup>th</sup> of May 2014 (Figure 3b). Duration time of the observed flood wave was about 25 days (if  $Q_{mean}$  exceedance is considered), but in fact the water level stabilised after 10 days at  $Q=1500 \text{ m}^3/\text{s}$  (Figure 3) and the peak discharge occurred for a short period of

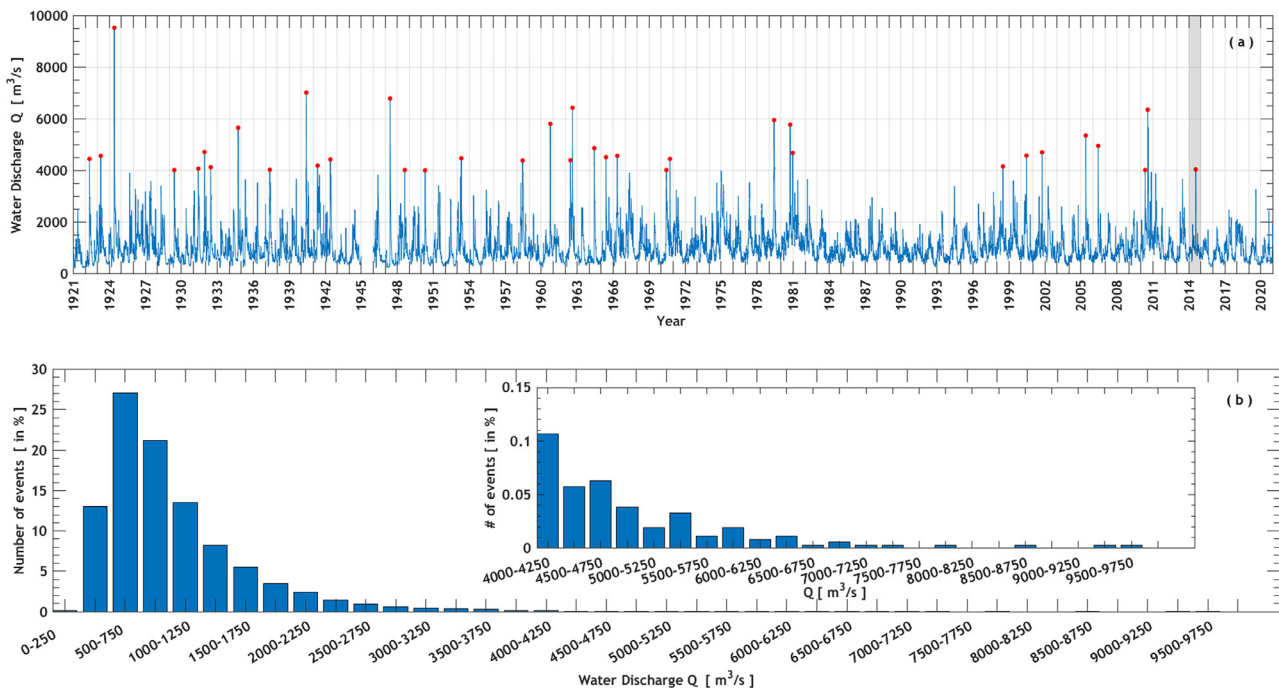


**Figure 2** a) A century-long time series of the daily water discharges of the Vistula River at the Tczew gauge (see Figure 1a for location). Red dots mark flood events with the water discharge higher than  $Q > 4000 \text{ m}^3/\text{s}$ ; b) Variations in discharges in  $250 \text{ m}^3/\text{s}$  intervals with largest discharges rescaled (IMGW-PIB, 2020).

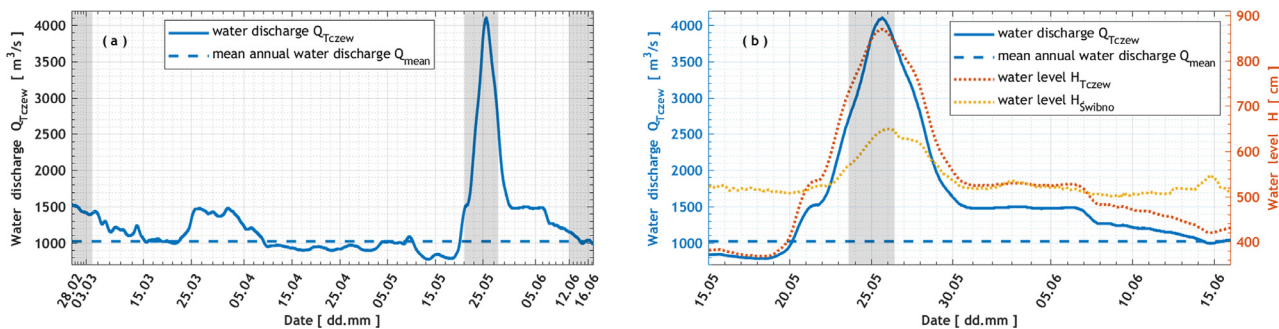


**Figure 3** a) Discharge graph in the Lower Vistula between 28.02. and 16.06.2014. Time series of hourly water discharge  $Q_{Tczew} \text{ m}^3/\text{s}$  (solid blue curve) in respect to long-term mean annual water discharge  $Q_{mean} = 1020 \text{ m}^3/\text{s}$  in Tczew (dashed blue line); b) time series of water discharge and water levels  $H$  cm at Tczew and Świbno gauges (see Figure 1 for location) in a period between 15.05. and 15.06.2014 (dotted dark and light brown curves, respectively). The grey rectangles indicate time periods of in-situ measurements (IMGW-PIB, 2020).

time, so the flood wave can be schematically classified as the sharp-peaked one. In accordance with Allen and Collinson’s (1974) formulation  $(\Delta Q/\Delta t) \cdot Q_{peak}^{-1}$  (where  $\Delta Q$  is the change of discharge in a time step  $\Delta t$ ), the characteristic rate of the rising limb between the long-term mean annual outflow  $Q_{mean}$  and the observed flood peak  $Q_{peak}$  was about of 0.125 per day. In turn, the characteristic rate of the falling stage was in the order of 0.04 per day. Essentially, such relatively fast changes in hydrological conditions are favourable to formation of superimposed bedforms, i.e., the smaller dunes overlaid on the larger ones (e.g., Allen and Collinson, 1974; Wilbers and Ten Brinke, 2003). Moreover, Paarlberg et al. (2008) observed that the shape of a flood wave influences dune dynamics in significant way. The authors underlined that the sharp-peaked flood wave

characterized by the longer duration of the rising and falling stages gives subaqueous dunes less time to adapt to the higher (peak) discharge.

Based on cross-correlation analysis (using the Matlab® xcov function) performed on water level time series, the time lag of flood wave passage between Tczew and Świbno cross-sections (over distance of 31.2 km) was estimated at  $\tau = 8$  h. Thus, an average speed of flood wave was evaluated at ca. 1.1 m/s what is in reliable agreement with the observed vessel drift speed ( $\approx 2$  knots) during the measurements. The estimated flow speed is approximately twice faster (considering also the spatial variability of the flow field across the river channel) than the depth-averaged velocities observed during normal hydrological conditions (Lisimenka et al., 2015).



### 2.3. In-situ measurements

The measuring campaign was initially a part of regular half-yearly monitoring carried out in Vistula River mouth area within the project VISTULA No PBS1/A2/3/2012. Two months after the monitoring survey of March 2014 (28.02–03.03), heavy rains in the Upper Vistula basin initiated a flood wave. Additional surveys were organised in the Vistula mouth and undertaken between May 23 (flood beginning phase) and May 26, 2014 (flood peak phase) during the passage of the flood wave. The surveys initially planned until May 29 (flood end phase), were too dangerous to perform due to significant number of large debris floating on and just below the river surface. Therefore, the survey accomplished in June, 2014 (12.06–16.06) is treated here as flood end situation.

The boat-mounted Reson SeaBat 7101 multibeam echosounder (MBES) with the nominal working frequency of 240 kHz and ping rate up to 40 pings/s was used in all bathymetric surveys. The high-resolution multibeam sonar system provides up to 511 discrete across-track sounding beams and illuminates 150° swath on the seafloor (with 1.5° along-track transmit beamwidth, 1.8° across-track receive beamwidth and depth resolution 0.0125 m). The fixed-mount sound velocity probe Reson SVP-70 was installed on the MBES head aiming to permanent monitoring of the sound speed at the depth of the sonar head. The portable sound velocity profiler Reson SVP-15 was used to obtain the sound speed profile through the whole water column. The Trimble SPS 851 GPS Receiver with RTK-positioning (ensuring centimeter-level accuracy) together with the Ixsea Hydrins inertial navigation system (with r-p-h accuracy of 0.01°) were integrated with the MBES and SVPs using the QINSy data acquisition software package. In that way, the overall measuring error is estimated within 5 cm xyz. The initial post-processing of the MBES raw data were performed in the QINSy Processing Manager according to the IHO standard procedures used in hydrography.

### 2.4. Dune geometry determination and spectral approach

Determination of crest and trough positions of individual primary bedforms (Figure 4, red and green markers respectively) for all one-dimensional bed elevation profiles (BEPs) were performed based on the approach proposed by Van der Mark and Blom (2007). For each single bedform, dune height  $H$  defined as the vertical distance between a crest and its downstream trough and dune length  $\lambda$  defined as the horizontal distance between two subsequent crests were obtained. Additionally, the relationship between dune height and flow depth  $H/Z$ , dune steepness defined as  $H/\lambda$  ratio and the mean stoss- and lee-side angles were determined using simple geometric relations (see dune schematic concept presented in Cisneros et al., 2020).

The spectral analysis of the BEPs to obtain power spectrum density (PSD) estimates was performed by using the Matlab® *periodogram* function. After subtracting the mean depth and applying the detrending procedure by fitting and removing a five-order polynomial regression model, the variance spectra were determined for each flow rates. The

smoothing of the obtained spectra was fulfilled with use of the DPSS taper function, i.e., discrete prolate spheroidal sequences or Slepian sequences, which are known as unique window functions which offer the best side-lobe suppression (Percival and Walden, 1993).

In context of the determination of the dominant dune lengths (local peaks of the spectra), the characteristic wavenumbers  $k_{ch}$  (and consequently  $\lambda_{ch}$ ) were evaluated for all measurements based on the concept introduced firstly by Young (1995) in sea surface dynamics study. For this purpose, the author proposed to calculate the weighted integral of power 4 of the spectral function. This approach was applied also by Davis et al. (2004) as well as by Lisimenka and Kubicki (2017) in bedform studies:

$$k_{ch} = \frac{\int k \cdot S^4(k) dk}{\int S^4(k) dk} \text{ and } \lambda_{ch} = \frac{2\pi}{k_{ch}} \quad (1)$$

### 3. Results

The analysis of bed elevation profiles revealed a presence of asymmetrical small (with typical spacing  $\lambda=0.6-5$  m), medium ( $\lambda=5-10$  m) and large ( $\lambda=10-100$  m) sand dunes according to the bedform classification scheme introduced in Ashley (1990).

Comparison of the successive bed elevation profiles indicated significant changes with time in conjunction with changing hydrological conditions. To start with, the number of dunes increased from  $N_1=478$  up to  $N_2=630$  in time period between the initial time step (Figure 4a) and the first survey during passage of the flood wave (Figure 4b). After that the number of individual dunes reduced considerably up to  $N_5=160$  at the final stage of the rising limb (Figure 4e), so that to reduce even more up to  $N_6=134$  at the next time step, i.e., at the beginning of the falling limb (Figure 4f), what is probably an effect of an amalgamation (merging) of the investigated bedforms. In turn, approximately the same number of dunes  $N_7=138$  was identified in the last time step, i.e., two and half weeks later, when the hydrological regime of the river returned closely to the long-term average conditions.

The relationship between dune height  $H$  and flow depth  $Z$  for each time steps (Figure 5) shows that the vast majority (about 95%) of dunes observed in low hydrological conditions  $Q < 1500$  m<sup>3</sup>/s (time steps  $Q_1$  and  $Q_7$ , standard flows) fall below  $H=0.127Z$  approximation (Figure 5, dotted line). Moreover, for relatively low/moderate hydrology with  $Q < 2500$  m<sup>3</sup>/s (including of time step  $Q_2$  corresponding to the beginning of the rising limb) there are almost no dunes with height above  $H=0.17Z$  (Figure 5, dashed line), i.e., of about 96% of bedforms are below this line at all. In turn, about 75% of dunes observed in hydrological conditions higher than  $Q > 2500$  m<sup>3</sup>/s (starting with time step  $Q_3$ ; rising limb) fall above  $H=0.17Z$ . Interestingly, for the highest hydrological conditions observed in the experiment close to  $Q \approx 4000$  m<sup>3</sup>/s, i.e., time steps  $Q_4$  (rising limb),  $Q_5$  (peak discharge) and  $Q_6$  (beginning of the falling limb), a relationship between dune height and flow depth of  $H=0.33Z$  (Figure 5, dash-dotted line, see Wignall and Best, 2000; c.f. Cisneros et al., 2020) could be assumed as an 'upper boundary condition' for approximately 50% of dunes. It should be noted also that only 6 dunes (see grey patches in Figure 4f

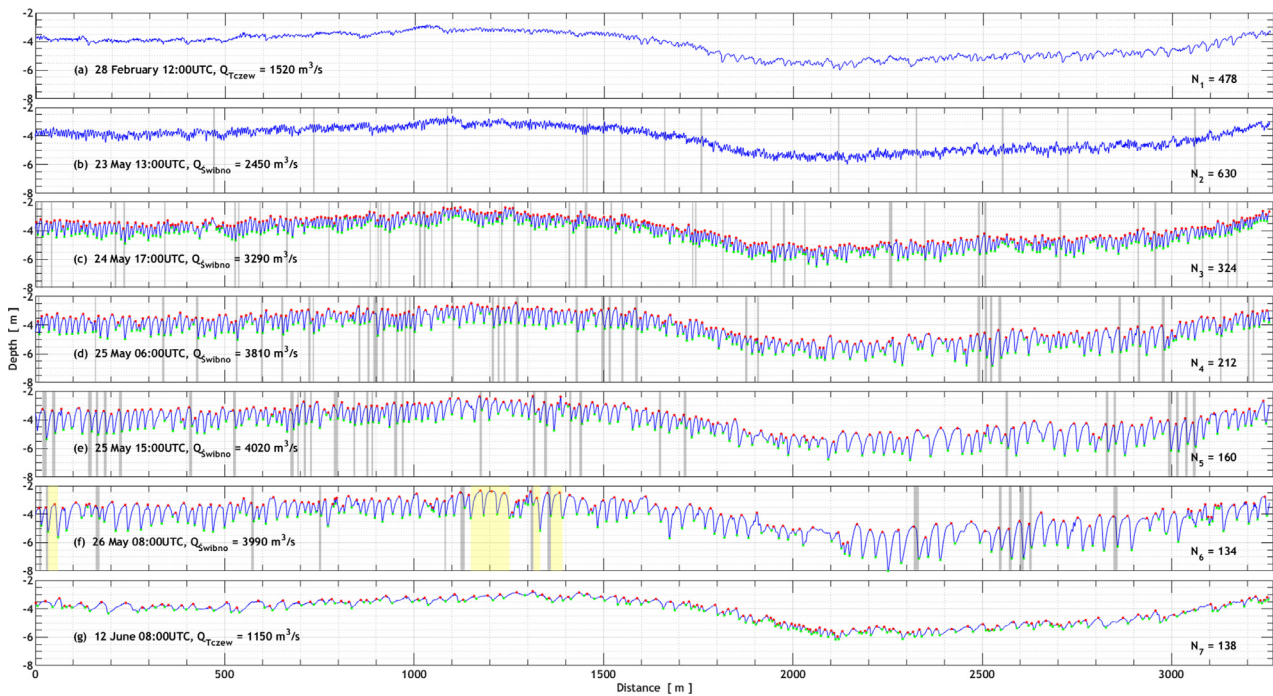


**Figure 4** Bed elevation profiles (BEPs) along the centreline of 3270 m length with the appropriate date, time, water discharge value  $Q$   $m^3/s$  and number of dunes  $N$  for all successive echosoundings. Location of crests and troughs depicted with red and green markers respectively (not shown for two first surveys due to readability). Grey patches mark lee-side slopes of the particular dunes with the potential for flow separation (based on findings of Lefebvre and Winter, 2016). Yellow patches mark six dunes with  $H/\lambda > 0.66$  (see Figure 5). Note: water discharges values  $Q_{Swibno}$  were calculated based on the obtained time lag (see Sec. 2.2).

for location) amongst the total number of 2076 examined in the whole experiment fall above  $H=0.66Z$  (Figure 5, solid line).

For clarity, further in the text, the same concept of colours representing all hydrological conditions is applied in the following figures:  $Q_1=1520$   $m^3/s$  (blue),  $Q_2=2450$   $m^3/s$  (green),  $Q_3=3290$   $m^3/s$  (magenta),  $Q_4=3810$   $m^3/s$  (black),  $Q_5=4020$   $m^3/s$  (red),  $Q_6=3990$   $m^3/s$  (yellow) and  $Q_7=1150$   $m^3/s$  (cyan).

The scatter plot of dune heights vs. lengths (Figure 6a) reveals that, the greater number of dunes falls between the global average (grey line) and upper limit trends (black line) obtained by Flemming (1988). There is, however, an exception related to the initial and the final steps (corresponding to the lowest hydrological conditions observed in the experiment), at which the vast majority of dunes fall below the global mean trend, what could suggest that these bedforms are lower at these stages (Figure 6a, blue and cyan dots, respectively).

Naturally, in the context of the dune geometry a considerable reshaping was observed with time as well (Table 1). Analysis of the mean dune height and length vs. water discharge revealed a counter-clockwise hysteresis (Figure 6b, blue and brown curves respectively). For example, after the almost 3 months period of time between the initial time step and the first survey during the flood, a significant increase in the mean value of the dune steepness  $H_{mean}/\lambda_{mean}$  of about 3 times was observed (Figure 6c, blue curve), where the mean dune height increased from  $H_1=0.16$  m

and its standard deviation  $\sigma_{H1}=0.12$  m up to  $H_2=0.35$  m ( $\sigma_{H2}=0.16$  m) while the mean dune length reduced from  $\lambda_1=6.8$  m ( $\sigma_{\lambda1}=4.7$  m) up to  $\lambda_2=5.2$  m ( $\sigma_{\lambda2}=1.4$  m). After that, during the first 28 h of the flood observation, in the course of which the water discharge increased gradually on  $\Delta Q=840$   $m^3/s$  from  $Q_2=2450$   $m^3/s$  to  $Q_3=3290$   $m^3/s$  (almost the same increase of  $Q$  value as in preceding time period), the mean dune height and length both have risen to  $H_3=0.71$  m ( $\sigma_{H3}=0.26$  m) and to  $\lambda_3=10.0$  m ( $\sigma_{\lambda3}=2.6$  m), respectively. Successively, the mean dune height and length increased up to  $H_5=1.17$  m ( $\sigma_{H5}=0.42$  m) and  $\lambda_5=20.1$  m ( $\sigma_{\lambda5}=6.4$  m) at the final stage of the rising limb with  $Q_5=4020$   $m^3/s$ . In turn, at the beginning of the falling limb, the geometrical dimensions of the dunes increased even more up to  $H_6=1.28$  m ( $\sigma_{H6}=0.6$  m) and  $\lambda_6=24.1$  m ( $\sigma_{\lambda6}=10.1$  m). Finally, after 17 days during which the hydrological conditions in the Lower Vistula returned closely to the long-term average  $Q_{mean}$  (Figure 3), a significant reducing in dune steepness was detected – the mean dune height reduced of about 4 times while the mean dune length kept almost the same (comparably stable) by comparison to the time step corresponding to the beginning of the falling limb. Thereby, the highest dynamics in dune field changes was observed at the final stage of the rising limb during which the bedforms revealed growth with average rates about of 0.02 m/h in height and about of 0.5 m/h in length respectively, while the water discharge increased from  $Q_4=3810$   $m^3/s$  to  $Q_5=4020$   $m^3/s$  during about 9 hours only. However, the latter one could be attributed to a lack of

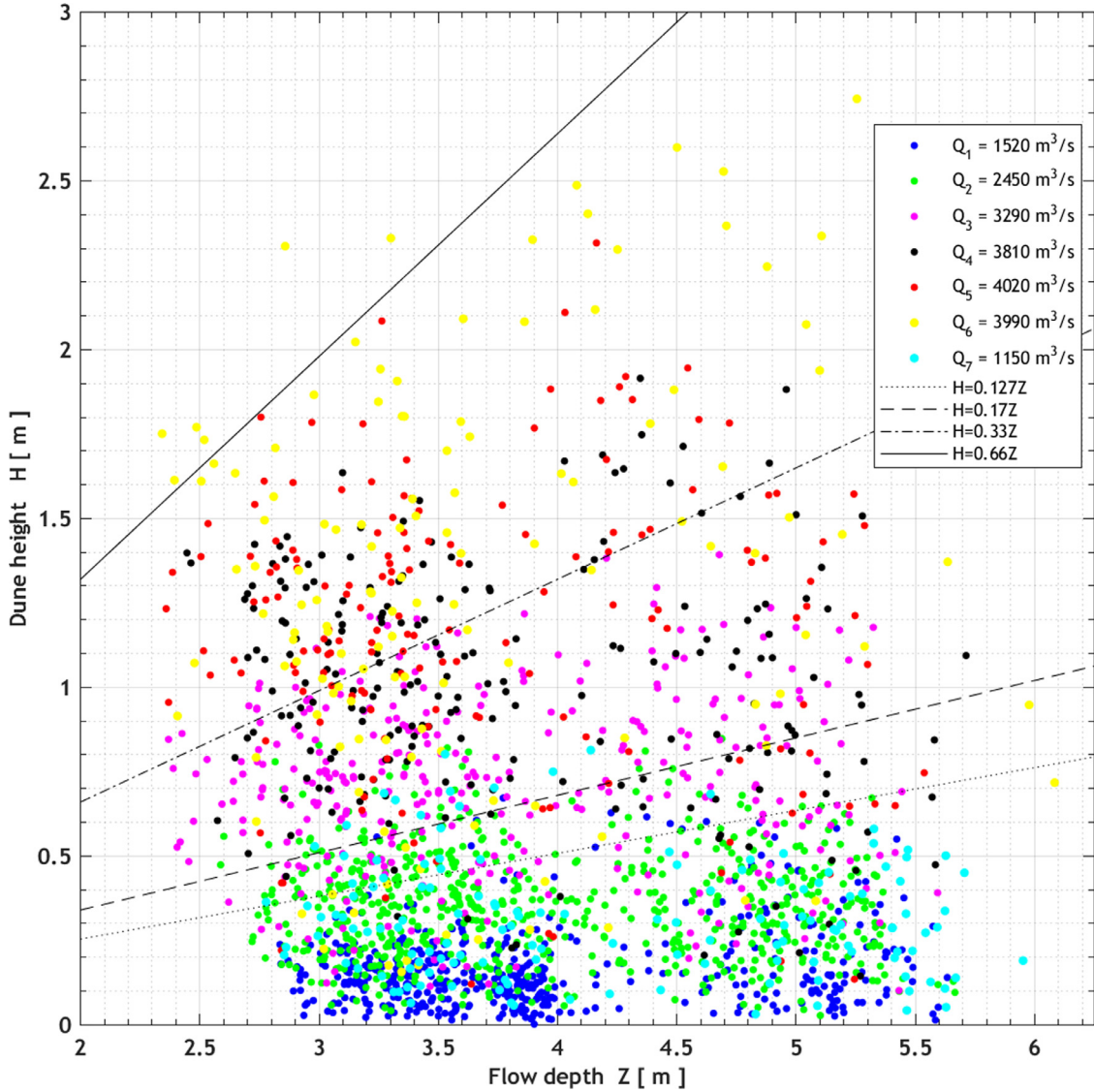


**Figure 5** Plot of dune height  $H$  m versus flow depth  $Z$  m for all dunes observed in the experiment under changing hydrological conditions. The  $H/Z$  relationships for values equal to 0.127 (dotted line), 0.17 (dashed), 0.33 (dash-dotted) and 0.66 (solid), respectively.

a sufficient number of observations during the falling limb phase.

Besides, the bed roughness  $k_{dunes}$  related to dunes was calculated based on the empirical relationship obtained by Van Rijn (1984):

$$k_{dunes} = 1.1\gamma_d H_{mean} (1 - e^{(-25H_{mean}/\lambda_{mean})}) \quad (2)$$

where  $H_{mean}$  and  $\lambda_{mean}$  – the mean dune height and length respectively, and  $\gamma_d$  is the shape factor expressing the influence of the dune form on the roughness height, taking into account that according to Van Rijn (1993),  $\gamma_d$  equals to 0.7 for dunes observed in field conditions.

As shown in Figure 6c (brown curve), the bed roughness noticeably increases with water discharge with the lag-effect, like in the case of the dune height (anti-clockwise hysteresis). It should be also noted that for moderate ( $Q > 2000 \text{ m}^3/\text{s}$ ) to high hydrological conditions, the bed roughness due to dunes is found to be of about 50%–63%

of the mean dune height value of the primary bedforms, wherein the  $k_{dunes}/H_{mean}$  ratio is higher during the rising limb of the flood wave. In contrast, one reveals values of about 22%–37% during low hydrology ( $Q < 1500 \text{ m}^3/\text{s}$ ).

The smoothed variance spectra corresponding to the particular hydrological conditions  $Q_1$ – $Q_7$  together with the appropriate locations of the characteristic wavenumbers  $k_{ch}$  (depicted with the diamond markers in according with the applied colour scheme) are presented in Figure 7.

In general, three scaling regions could be distinguished in the riverbed morphology of the Vistula mouth: the first one – the low-frequency part of the spectrum with wavenumbers below  $k < 0.015 \text{ rad/m}$  what corresponds to macroscale bedforms with lengths larger than of about  $\lambda > \approx 420 \text{ m}$ , i.e. comparable or larger than the river width  $W$ . Behaviour of all of the spectra in this low frequency range is characterized by flat spectra, what could be potentially interpreted as a lack of influence of any large scale anthro-

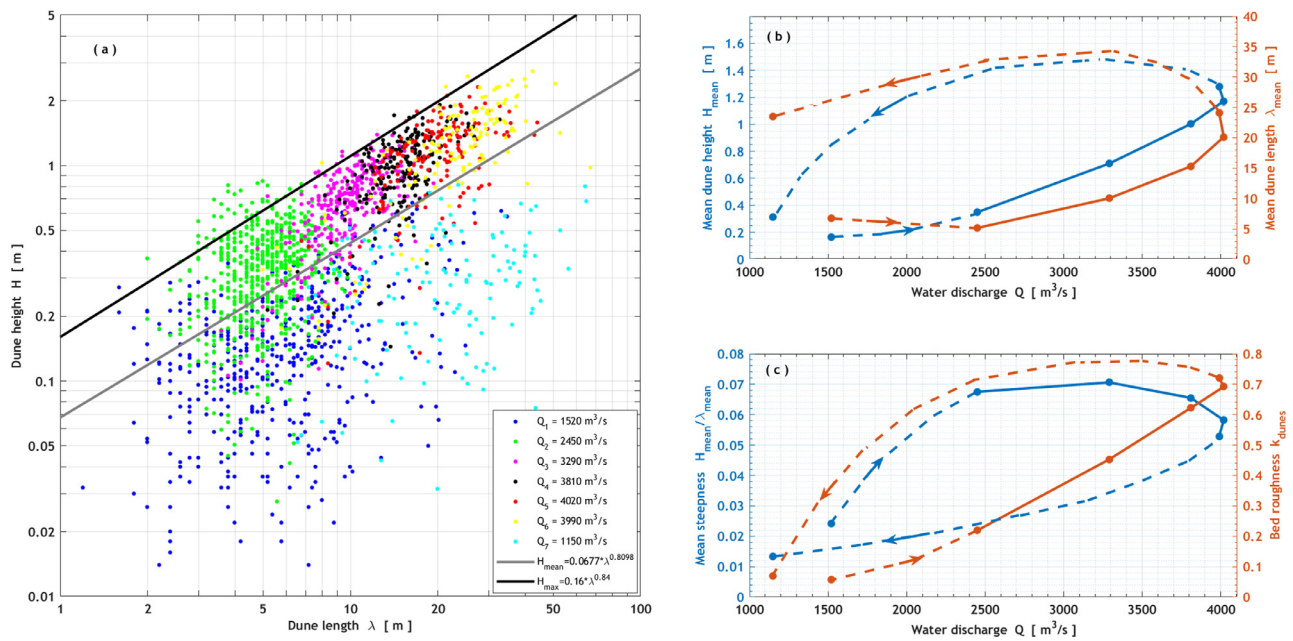


**Figure 6** a) Plot of dune height  $H$  vs. dune length  $\lambda$  under changing hydrological conditions, overlapping the global average  $H_{\text{mean}}=0.0677\lambda^{0.8098}$  (grey line) and upper limit  $H_{\text{max}}=0.16\lambda^{0.84}$  (black line) relationships obtained by Flemming (1988). Development of dunes during flood: b) mean dune height  $H_{\text{mean}}$  m (blue curve; left y-axis) and dune length  $\lambda_{\text{mean}}$  m (brown curve; right y-axis); c) mean steepness  $H_{\text{mean}}/\lambda_{\text{mean}}$  (blue curve; left y-axis); and bed roughness due to dunes  $k_{\text{dunes}}$  (brown curve; right y-axis).

pogenic factors (like river groynes or other hydrotechnical structures) on the riverbed morphology (at the investigated river stretch, the straight-segment riverbanks are strengthened by concrete and/or stony walls along the whole river channel). The second scaling region is the mesoscale one, which is characterized by a presence of a large sand dunes with lengths between of about  $1 \div 2 < \lambda < 420$  m. In turn, the third region – the high-frequency ‘tail’ corresponds to microscale surface roughness with wavenumbers  $k > 2\pi$  rad/m, i.e. small dunes (with  $\lambda < 1$  m) and ripples.

The spectra show that with the development of the flood wave, the most significant changes of the riverbed morphology were observed in the ‘mesoscale’ frequency region between  $0.094 < k < \pi/2$  rad/m (i.e., for dune lengths between of about  $2 < \lambda < 66$  m). Interestingly, in this ‘transition region’, the distinct behaviour of the spectra is observed. The ‘low hydrology’ spectra (blue and cyan curves in Figure 7) follow sufficiently well the power law function  $S(k) \sim k^\gamma$ , described by the spectrum slope  $\gamma = -3$  (Figure 7, grey dashed line). However, during the moderate and high hydrological conditions ( $Q_2$ – $Q_6$  curves in Figure 7), the spectrum slope  $\gamma$  increases and all of the spectra follow by a ‘–4 power spectral law’ (Figure 7, grey dotted line).

Analysis of the dune slope angles (the average slope of all grid samples from crest point to trough point or vice versa, for lee- or stoss-side angles respectively) revealed that greater number of dunes (83% of the total ones) are asymmetrical with the gentler stoss-side slope  $\alpha$  in comparison to the steeper lee-side one  $\beta$  (Figure 8a). In turn, only of about 2% of the observed dunes are ideally symmetrical (triangular). With the development of the flood wave, the clockwise hysteresis of the mean stoss and lee angles vs. water discharge were found (Figure 8b, black and blue curves respectively). Moreover, significant increase of

about 3 times in both of the mean angles was observed starting from the initial time step up to (in general) the final stage of the rising limb. During this period of time, the mean dune stoss- and lee-side slopes increased respectively from  $\alpha_1=2.6^\circ$  ( $\sigma_{\alpha_1}=1.1^\circ$ ) and  $\beta_1=3.6^\circ$  ( $\sigma_{\beta_1}=1.8^\circ$ ) up to values higher than about of  $\alpha_{\text{mean}} \approx 7^\circ$  and  $\beta_{\text{mean}} \approx 10^\circ$ , with the maximum values of  $\alpha_3=7.6^\circ$  ( $\sigma_{\alpha_3}=2.0^\circ$ ) and  $\beta_3=10.6^\circ$  ( $\sigma_{\beta_3}=3.3^\circ$ ) observed at the time step corresponding to the pre-final stage of the rising limb with  $Q_3=3290$   $\text{m}^3/\text{s}$ . It should be noted that the dune slope angles returned to even slightly lower values at the last time step [ $\alpha_7=1.7^\circ$  ( $\sigma_{\alpha_7}=0.8^\circ$ ) and  $\beta_7=2.5^\circ$  ( $\sigma_{\beta_7}=1.5^\circ$ )] in comparison with the initial time step during which nearly the same low hydrological conditions were observed.

## 4. Discussion

With the development of the flood wave, growth of dunes in height together with the diminishing number of individual dunes were identified in all subsequent time steps ( $Q_2$  to  $Q_6$ ), although with progressively reducing rates. The reduction can be explained by the different kinematics of the large-scale bedforms in comparison with the small-scale ones. It is well known that the reaction time needed to adapt to changes of flow conditions varies depending on bedforms geometric dimensions. Naturally, the small-scale bedforms are subjected to quick modifications, but the large-scale ones, inversely, may take longer period of time to change (e.g., Bridge, 2003; Guala et al., 2020; Venditti et al., 2016).

The presented dataset illustrates that dunes with small heights are dominant in the Vistula River mouth channel. For the overwhelming majority of dunes observed in low

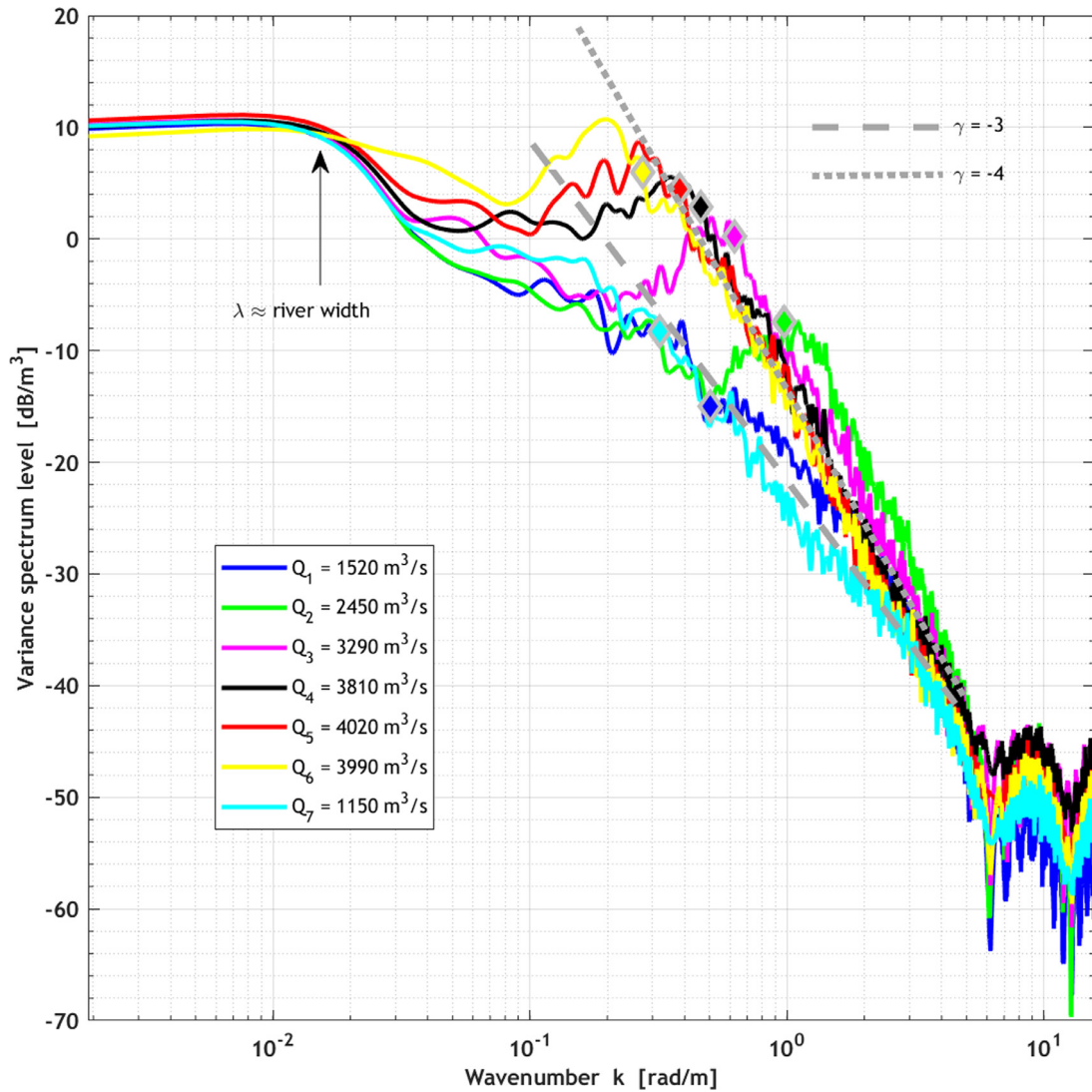


**Figure 7** Variance spectra [dB/m<sup>3</sup>] of the bed elevation profiles measured under changing hydrological conditions. Grey lines – power law functions with spectrum slopes  $\gamma=-3$  (dashed) and  $\gamma=-4$  (dotted), respectively. The black arrow appoints the scaling region corresponds approximately to the river width  $\lambda \approx W$ . The appropriate diamond markers determine the characteristic wavenumber  $k_{ch}$  obtained based on the Eq. (1).

hydrological conditions ( $Q < 1500 \text{ m}^3/\text{s}$ ), the approximation  $H < 0.127Z$  proposed recently by Cisneros et al. (2020) for deep flows ( $Z > 2.5 \text{ m}$ ) could be representative for collected dataset. In turn, a value of  $H = 0.17Z$  (Rubin and McCulloch, 1980) reflects well the maximum dune height that bedforms attain during moderate hydrology (up to  $Q \approx 2500 \text{ m}^3/\text{s}$ ). It is worth to note that the largest submerged dune heights with  $H > 0.66Z$  (with a maximum value of  $0.8Z$ ) were observed at the beginning of the falling stage of the flood hydrology ( $Q \approx 4000 \text{ m}^3/\text{s}$ ) for six bedforms only located at shallower part of the river with depths about of  $Z = 2.3\text{--}3.3 \text{ m}$ . However, due to lack of sufficient data samples related to the falling limb phase of the examined flood, it is rather difficult to establish if there were any more individual dunes with heights higher than  $H = 0.66Z$ , although some growth of dunes in height could potentially be observed at the next few time steps after the beginning of the falling limb (Figure 6b).

A noticeable anti-clockwise hysteresis (lag effect) was detected both between dune height  $H$  or length  $\lambda$  and water discharge (Figure 6b), where  $H$  and  $\lambda$  are substantially out of phase with progressive changes of  $Q$ . Such phenomena of the subaqueous dune evolution occurs only when the time scale of water discharge change is faster than the bedform adjustment time and specifically more pronounced lags are observed in the case of ‘fast flood waves’ (Martin and Jerolmack, 2013). In general, our observations are in agreement with the results of investigations performed by other authors in large sand bed rivers. The findings of earlier studies indicate that dunes are observed to grow during the rising limb, reach their maximum size after peak discharge and decay in size as the flood recedes (e.g., Amsler and Garcia, 1997; Julien and Klassen, 1995; Julien et al., 2002; Ten Brinke et al., 1999; Wilbers and Ten Brinke, 2003).

Even though there is a lack of data sets collected during the falling limb, different behaviour of the primary ge-

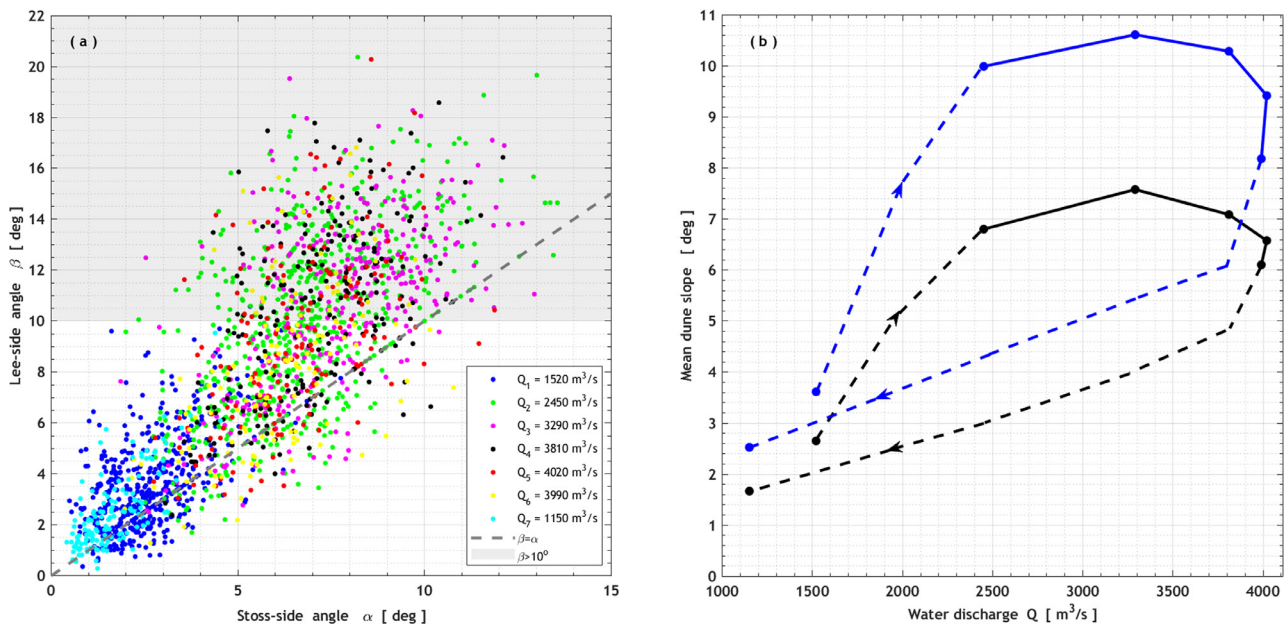


**Figure 8** a) Plot of the lee-side angle  $\beta$  vs. stoss-side angle  $\alpha$  (in degrees) under changing hydrological conditions. The dashed grey line marks dune symmetry condition  $\beta = \alpha$ . The grey patch indicates lee-side angles  $\beta > 10^\circ$ ; b) Clockwise loops for the mean dune slopes of stoss-side angle (black curve) and lee-side angle (blue curve) as a function of the water discharge.

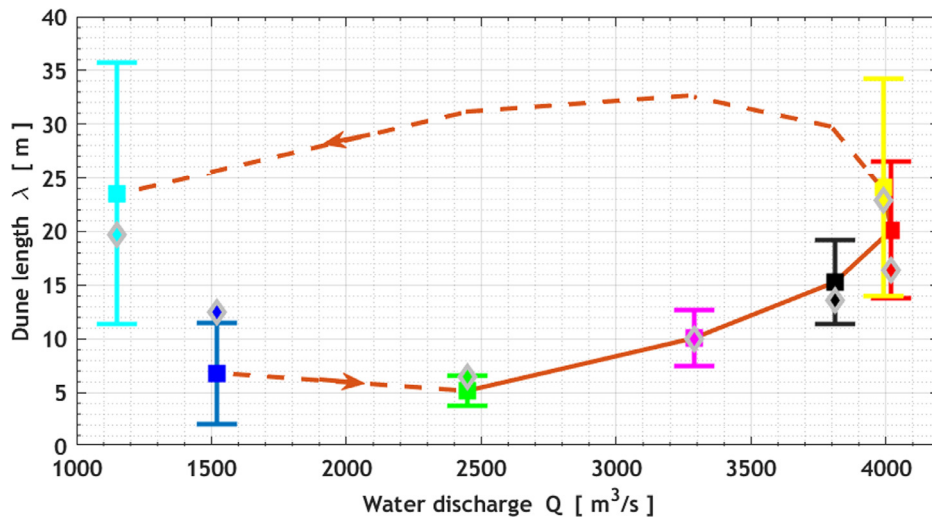


**Figure 9** Development of dune length under changing hydrological conditions. Statistically derived mean dune lengths  $\lambda_{mean}$  m (square markers) with the whiskers indicating the standard deviation. Characteristic dune lengths  $\lambda_{ch}$  m (diamond markers) derived from spectral analysis on the basis of the Eq. (1).

ometry parameters ( $H$  and  $\lambda$ ) of the Vistula dunes could be distinguished. The observed dunes show quick growth both in  $H$  as well as in  $\lambda$  when the water discharge increases, starting especially from the moderate hydrological conditions. In turn, when the hydrology starts to back close to the initial (long-term average) one,  $H$  decreases definitely with higher dynamics in comparison to  $\lambda$ . Although some indefinite growth of dunes size could be expected after the flood peak [e.g., dunes start to decrease only in size halfway through the flood falling limb according to Martin and Jerolmack (2013)],  $\lambda$  does not reveal a significant change at the final time step at all (in relation to the previous survey which corresponds to the initial stage of the

falling limb). The probable explanation could be the erosion of dune crests and subsequent deposition of the material in the dunes troughs – in that way, low dunes in height, but long in length may form. In general, it is in agreement with the field observations performed by Wilbers and Ten Brinke (2003) of sand and sand-gravel bed reaches of the Dutch Rhine. Notwithstanding, the authors did not observe the dune length change in response to the varying water discharge in the sand bed section of the Waal River characterized by nearly the same granulometric composition of river bottom sediments consisted of medium to coarse-grained sands like in the Vistula River mouth (Rudowski et al., 2017). Likewise, results of laboratory observations and numerical

**Table 1** Statistics of dune geometry during the passing flood.

# of time step	Water discharge Q [m <sup>3</sup> /s]*	Dune height H [m]				Dune length λ [m]				Dune steepness H/λ [-]				Bed roughness		Stoss-side angle α [deg]		Lee-side angle β [deg]	
		H <sub>mean</sub>	mean	median	stand.	λ <sub>mean</sub>	mean	median	stand.	H/λ <sub>mean</sub>	mean	median	stand.	α <sub>50</sub>	α <sub>mean</sub>	α <sub>50</sub>	α <sub>mean</sub>	β <sub>50</sub>	β <sub>mean</sub>
1	1520	0.16	0.14	0.12	0.12	6.8	5.6	4.7	4.7	0.029	0.025	0.021	0.06	2.6	2.5	1.1	3.6	3.3	1.8
2	2450	0.35	0.35	0.16	0.16	5.2	5.0	1.4	1.4	0.070	0.066	0.034	0.22	6.8	6.7	2.0	10.0	10.0	3.4
3	3290	0.71	0.72	0.26	0.26	10.0	10.0	2.6	2.6	0.070	0.072	0.021	0.45	7.6	7.7	2.0	10.6	11.0	3.3
4	3810	1.00	1.00	0.35	0.35	15.3	15.3	3.9	3.9	0.066	0.065	0.019	0.62	7.1	7.1	1.8	10.3	10.5	3.4
5	4020	1.17	1.20	0.42	0.42	20.1	19.3	6.4	6.4	0.060	0.060	0.019	0.69	6.6	6.6	1.8	9.4	9.1	3.5
6	3990	1.28	1.25	0.60	0.60	24.1	23.6	10.1	10.1	0.054	0.053	0.019	0.72	6.1	6.1	1.7	8.2	8.0	3.3
7	1150	0.32	0.29	0.17	0.17	23.6	21.2	12.2	12.2	0.016	0.012	0.011	0.07	1.7	1.5	0.8	2.5	2.2	1.5

\* Water discharge values Q correspond to the time steps t<sub>2</sub>–t<sub>6</sub> were calculated based on the obtained time lag τ=8 h (see Sec. 2.2).

\*\* Characteristic dune length derived from spectral analysis of the BEPs on the basis of the Eq. (1).

simulations of bedform response to flow variability accomplished by Nelson et al. (2011) also revealed that when the flow decreases back to the original discharge, H quickly decreases in response, but λ decreases much more slowly. Using an unsteady two-dimensional flow model, the authors predicted much slower rate of λ increase during the rising limb and observed that one remains essentially constant, rather than decreasing, during the final low-flow period.

The result of our observations exposes a relatively greater growth in H versus λ reflecting in significant steepening of dunes (of about 3-fold) during a period of time between the origin phase and the flood peak approaching (dunes tend to steepen from 0.024 up to ≈0.07). Subsequently, around the flood peak, slight decreasing in the mean dune steepness was found (up to 0.06) with clearly visible further tendency of H/λ to reduce crucially (of about 4-fold) forward close to the origin stage. In that way, contrary to the dune height and length lag effects, the dune steepness reveals the clockwise hysteresis (Figure 6). It is worth noting that the observed variability of dune steepness is in general agreement within the ranges obtained in other field studies (Carling et al., 2000; Julien and Klassen, 1995; Julien et al., 2002). Furthermore, the relationship  $H/\lambda_{\max}=0.16\lambda^{-0.16}$  proposed by Flemming (1988) as the maximum limit trend effectively exemplifies a range of steepness for the dunes observed in the measurements (Figure 6a, black line). Besides, dunes with steepness lower than  $H/\lambda \approx 0.06$  (Figure 6a, grey line) are either considered as a non-equilibrium bedforms (in our case, the ones observed at low hydrological conditions mainly) or, as noted in Carling et al. (2000), represent an equilibrium adjustment of the bedform, in which maximum steepness is precluded by hydraulic constraints, notably a depth limitation. On the other hand, real world observations suggest that equilibrium bedforms (the ones with consistent geometry/shape during their migration) are relatively rare in flood conditions and that subaqueous dunes evolve dramatically over the time scale of real floods (Nelson et al., 2011) what is confirmed thoroughly by our observations. In fact, tracking of the individual dunes was impossible to achieve as the latter ones were undergoing rapid changes under the varying hydrological conditions and, moreover, surveys were done rather too rarely in order to identify particular dunes on the subsequent records (see Figure 4).

By analysing the subsequent roughness spectra in context of localization of its local spectral peaks (Figure 7), the anti-clockwise hysteresis effect both for H (spectrum level) and λ (wavenumber) may be inferred by the spectral method as well, confirming in that way the considerable reshaping of the dune field with time. It is visible that the dominant local peaks of the particular spectra change its x-y positions, repeating in this manner behaviour of the primary geometry parameters H and λ (Figure 6b). Naturally, it reflects re-organization of the dune field with time – sand dunes with the smaller heights and shorter lengths are swallowed by the bigger ones, creating the new bedforms which are become appropriately higher and longer than the two initial ones. In that way, high frequency spectral peaks are gradually shifted towards the low wavenumbers (i.e. increasing of λ) with the simultaneous growth of their spectral levels (i.e. increasing of H). Finally, spectral level of the dominant local peak of the ‘end of the flood’ spectrum (Figure 7, time step

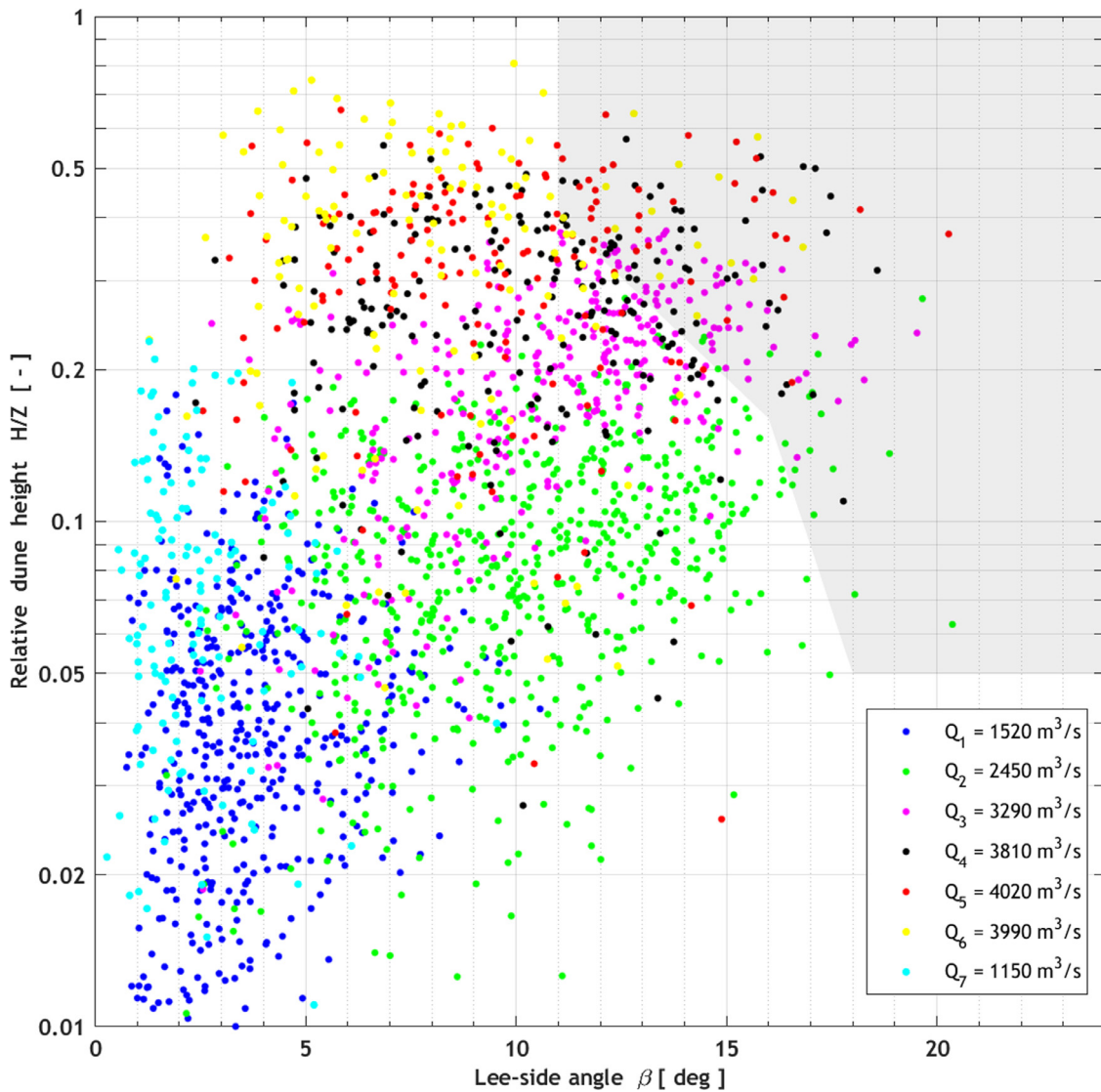


**Figure 10** The potential for flow separation. Plot of lee-side angle  $\beta$  [deg] vs. relative dune height  $H/Z$  under changing hydrological conditions. The grey area indicates the minimum boundary conditions for  $\beta$  and  $H/Z$  at which, according to Lefebvre and Winter (2016), the onset of permanent flow separation could be observed.

$Q_7$ ) is abruptly dropped with keeping its almost the same position in the wavenumber domain, confirming reducing of the dune height, but keeping the dune length (i.e. reducing the dune steepness).

Furthermore, for low flow rates (average/standard hydrological conditions), the observed spectra could be approximated by the power-law fitting functions with the spectrum slopes close to  $\gamma = -3$ , especially at the mesoscale region, where the most significant dune field reshaping was observed (Figure 7, grey dotted line). This is in general agreement with the classic findings of Hino (1968), and confirms also the results of investigations performed by other authors (e.g., Aberle et al., 2010; Nikora et al., 1997). However, with the development of the flood wave, significant deviation from the ‘-3 power law’ is observed – all of the spectra obtained at the moderate and high flows (Figure 7, time steps  $Q_2$ – $Q_6$ ) are characterized by the steeper spectrum slopes close to  $\gamma = -4$  (Figure 7, grey dashed line).

Interestingly, comparison of behaviour of the (mean) dune lengths derived statistically  $\lambda_{mean}$  and the characteristic dune lengths  $\lambda_{ch}$  obtained based on spectral analysis under changing water discharge  $Q$  (Figure 9, square and diamond markers, respectively) revealed anti-clockwise hysteresis almost the same in both cases. Dune length values derived spectrally are, in general, in full agreement with the statistical values of  $\lambda$ , taking also into account the appropriate standard deviations  $\sigma_\lambda$  for the particular time steps. Nevertheless, it should be noted that at the time step corresponds to the initial phase, the spectrally derived  $\lambda_{ch}$  is out of whiskers, what could be explained by a presence of large numbers of relatively small-scaled dunes which significantly reduce the statistical mean at this particular time step.

In the context of the angular geometry of bedforms, our results exhibit the ubiquity of low-angle dunes, in vast majority with the asymmetrical shapes. Specifically, dunes



with the mean lee-side slopes milder than  $\beta=10^\circ$  are fully dominant in low hydrological conditions (Figure 8a, time steps  $Q_1$  and  $Q_7$ ). According to the results of the numerical simulations performed by Lefebvre and Winter (2016), regardless of dune size and flow depth, a flow separation zone does not develop over such low-angle dunes (lack of a zone of permanent flow separation). It could give an answer (at least partly) to the question raised by Warmink (2014) in relation to an existence of the flow separation behind such non-equilibrium bedforms with relatively large lengths (and small heights) observed at the final stage of the falling limb (see Figures 6a, 10). Moreover, in our case, about 70% of the ‘low hydrology’ dunes are characterized by the mean lee-side angles  $\beta < 4^\circ$  what could be evidence of an absence of a hydraulic effect at all (e.g. Cisneros et al., 2020). In the case of low-angle dunes, flow field structure characterizes by lower turbulence production dominated by eddies generated along shear layer, with a much smaller velocity differential than is characteristic of shear layers caused by flow separation in the lee side of classic angle-of-repose dunes. Consequently, lower energy losses between the recirculating flow and overlying free water flow are observed what results in weakening of flow resistance caused by (low-angle) dune form roughness (Best, 2005; Best and Kostaschuk, 2002).

With the development of flood wave, number of asymmetric dunes with lee-side angles  $\beta > 10^\circ$  significantly increases. Moreover, clockwise loops are observed both for stoss- as well as lee-side angles, with higher magnitude in the case of the last ones (Figure 8). It could suggest a probable appearance of recirculating flow (at least with intermittent origin) and its impact on steepening of lee-side slopes of particular dunes (Figure 4).

Findings of Lefebvre and Winter (2016) revealed that the minimum angle at which a flow separation zone is detected depends on the relative dune height  $H/Z$ . The authors determine the range of lee-side angles at which the flow separation is found to be present from  $\beta_{\min}=11^\circ$  for  $H/Z=0.4$  to  $\beta_{\min}=18^\circ$  for  $H/Z=0.05$  and predict an absence of the one for bedforms with a relative height  $H/Z=0.16$  (Figure 10). In that way, total number of 146 dunes, which fulfil the mentioned above conditions were identified (points inside the grey polygon in Figure 10), what is of about 7% of the total number of dunes (2076 ones) examined in the experiment. It should be noted that with the development of the flood wave, the potential of flow separation increased gradually from 2.2% (at  $Q_2 \approx 2500 \text{ m}^3/\text{s}$ ), through 14.2% (at  $Q_3 \approx 3290 \text{ m}^3/\text{s}$ ), 18.4% (at  $Q_4 \approx 3810 \text{ m}^3/\text{s}$ ) up to 20% at the flood peak ( $Q_5 \approx 4020 \text{ m}^3/\text{s}$ ), in order to start to decrease to 11.1% at the beginning of the falling limb ( $Q_6 \approx 3990 \text{ m}^3/\text{s}$ ).

## 5. Conclusions

Subaqueous dunes in the mouth of the Vistula River to the non-tidal Baltic Sea share their geometric characteristics with bedforms of other large sand-bed rivers and fluvial environments. For the Vistula dunes, composed mainly by coarse and medium-grained sands, the global trend described by the exponential relationship between their height and length  $H_{\text{mean}}=0.0677\lambda^{0.8098}$  proposed by Flemming (1988) and interpreted as an equilibrium condi-

tion could be a limiting factor indicating rather lack of sufficient sediment supply from the upper parts of the river, i.e., dunes are definitely underdeveloped at low hydrological conditions. Naturally, with increasing of water flow strength, ones indicate a tendency to grow both in height as well as in length and, in turn, are in a good agreement with Flemming’s upper limit trend relationship  $H_{\text{max}}=0.16\lambda^{0.84}$ .

The present dataset reveals also that dunes with relatively small heights are absolutely dominant in the Vistula River mouth and the vast majority of rhythmic bedforms (about 95%) observed at low ( $Q < 1500 \text{ m}^3/\text{s}$ ) to moderate hydrological conditions ( $Q < 2500 \text{ m}^3/\text{s}$ ) could be characterized by the relationship between dune height against flow depth in range of  $H/Z \approx 1/8 \div 1/6$ , respectively. In turn, the relationships  $H/Z = 1/3 \div 2/3$  could be assumed as upper limits for approximately 50% of dunes observed at high hydrology ( $Q > 3800 \text{ m}^3/\text{s}$ ).

In context of the dune geometry, significant reshaping of the Vistula dune field was observed with the development of the examined flood wave. The mean dune height and length vs. water discharge revealed the anti-clockwise hysteresis (the lag effect). Based on our observations, starting from low hydrological conditions and up to the time step corresponding to the flood peak, the mean dune height and length increased successively from  $H=0.16 \text{ m}$  and  $\lambda=6.8 \text{ m}$  to  $H=1.17 \text{ m}$  and  $\lambda=20.1 \text{ m}$ , in order to increase even more up to  $H=1.28 \text{ m}$  and  $\lambda=24.1 \text{ m}$  at the beginning of the falling limb. Moreover, different behaviour of the primary geometry parameters ( $H$  and  $\lambda$ ) of the Vistula dunes could be distinguished during the rising and falling limbs. The dune height decreases definitely with higher dynamics in comparison to the dune length during the falling phase, indicating in that way a significant decrease in dune steepness. During a period of time when the river returns to the long-term average hydrological conditions after the passage of the flood peak wave, the mean dune height was reduced about 4-fold while the mean dune length was almost the same by comparison with the time step corresponding to the beginning of the falling limb.

The spectral analysis of the bed elevation profiles led to distinguishing three scaling regions that corresponded to micro-, meso- and macroscales. Specific patterns of the spectra are observed in dependence on hydrological conditions. At the mesoscale region, where the most significant dune field changes were observed, the exponent of the spectral function  $S(k) \sim k^\gamma$  is to be found close to ‘-3 power law’ for low hydrological conditions, which is in agreement with the ‘classic’ assumption obtained firstly by Hino (1968). However, during the moderate and extreme hydrological conditions, spectra are characterized definitely by the steeper spectrum slopes close to or slightly higher than  $\gamma = -4$ . Furthermore, determination of the characteristic dune length  $\lambda_{ch}$  derived ‘spectrally’ could be a good alternative to ‘the statistical approach’ aiming to get an information about dominant dune length in bed elevation profile by finding the local peak position in the wavenumber domain of the spectrum. It was shown that the characteristic (dominant) dune lengths derived ‘spectrally’ are in general agreement with the ones derived ‘statistically’ (taking into account the standard deviation), showing the same pattern of the lag-effect as well. It could confirm the usefulness of the spectral approach in dune field analysis.

Analysis of the angular geometry of the Vistula dunes revealed supremacy of low-angle bedforms, in vast majority with the asymmetrical shapes. In general, of about 83% of dunes are characterized by gentler stoss-side slope  $\alpha$  in comparison to the steeper lee-side one  $\beta$ , with only of 2% of the total number of ones which are ideally triangular. Definitely, dunes with the mean lee-side slopes milder than  $\beta=10^\circ$  are fully dominant in low hydrological conditions. What is more, of about 70% of the ‘low hydrology’ dunes are characterized by the mean lee-side angles  $\beta < 4^\circ$  what, in turn, could be a reason for weakening of flow resistance caused by dune form roughness due to a complete absence of a hydraulic effect. With the development of flood wave, clockwise loops were observed both for the mean stoss-side as well as lee-side angles, with higher magnitude in the case of the last ones. This could suggest a probable appearance of recirculating flow (at least with intermittent origin) and its impact on steepening of lee-side slopes of particular dunes (see Figure 4). Interestingly, it was observed that stoss- and lee-side angles behaviour as a function of the water discharge is the same as dune steepness taking into account clockwise hysteresis, with almost identical step-by-step analogy in evolution in the case of the stoss-side angles. In addition, based on findings of Lefebvre and Winter (2016) regarding criteria of probable appearance of flow separation, a relatively low number of dunes – of about 7% only (amongst 2076 of the total ones examined in the experiment) were identified as a fulfilling the mentioned above conditions (i.e., the appropriate range of lee-side angles  $\beta$  and relative heights  $H/Z$ ). Notwithstanding, with the increasing of flow strength, it was observed that the potential of flow separation was increased of about 9-fold, from 2.2% at the flood beginning phase up to 20% at the flood peak and dropped abruptly up to 11.1% immediately at the beginning of the falling limb. Importantly, dunes with lee-side angles  $\beta > 24^\circ$  (with a fully developed flow separation zone) were not observed at the experiment at all, independently on hydrological conditions.

The data presented in the study could be an essential basis for creation of fluid dynamics models of natural bedforms in large sand-bed river channels, aiming to predict accurately dune dimensions and their evolution, flow resistance caused by bedform roughness, turbulent flow, as well as water levels during extreme hydrological conditions, for proper river system management.

## Acknowledgements

The authors are grateful to the National Centre for Research and Development (Poland) for funding this work by grant VISTULA No PBS1/A2/3/2012. We wish to thank to our colleagues from the Department of Operational Oceanography of the Maritime Institute for their help in preparing and carrying out the bathymetric survey. Comments of two anonymous reviewers greatly enriched the manuscript.

## Declaration of competing interest

The authors declare that there is no conflict of interest with third parties and that they have no known competing finan-

cial interests or personal relationships that could have appeared to influence the work reported in this paper.

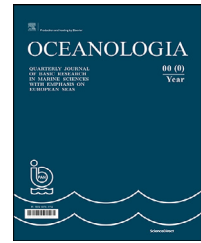
## References

- Aberle, J., Nikora, V., Henning, M., Ettmer, B., Hentschel, B., 2010. Statistical characterization of bed roughness due to bed forms: A field study in the Elbe River at Aken, Germany. *Water Resour. Res.* 46, W03521. <https://doi.org/10.1029/2008WR007406>
- Allen, J.R.L., Collinson, J.D., 1974. The superimposition and classification of dunes formed by unidirectional aqueous flows. *Sediment. Geol.* 12, 169–178.
- Amsler, M.L., Garcia, M.H., 1997. Sand-dune geometry of large rivers during floods. *J. Hydraul. Eng.* 123, 582–585.
- Ashley, G.M., 1990. Classification of large-scale subaqueous bedforms: a new look at an old problem. *J. Sediment. Res.* 60, 160–172. <https://doi.org/10.2110/jsr.60.160>
- Barnard, P.L., Erikson, L.H., Edwin, P.L., Elias, E.P.L., Dartnell, P., 2013. Sediment transport patterns in the San Francisco Bay Coastal System from cross-validation of bedform asymmetry and modeled residual flux. *Mar. Geol.* 345, 72–95. <https://doi.org/10.1016/j.margeo.2012.10.011>
- Best, J.L., 2005. The fluid dynamics of river dunes: a review and some future research directions. *J. Geophys. Res. Earth Surf.* 110, JF000218.
- Best, J.L., Kostaschuk, R., 2002. An experimental study of turbulent flow over a low-angle dune. *J. Geophys. Res. Oceans* 107 (C9), 3135. <https://doi.org/10.1029/2000JC000294>
- Best, J., Simmons, S., Parsons, D., Oberg, K., Czuba, J., Malzon, C., 2010. A new methodology for the quantitative visualization of coherent flow structures in alluvial channels using multibeam echosounding (MBES). *Geophys. Res. Lett.* 37, L06405. <https://doi.org/10.1029/2009GL041852>
- Bridge, J.S., 2003. *Rivers and Floodplains; Forms, Processes, and Sedimentary Record*. Blackwell Publ., Oxford, U.K., 600 pp.
- Carling, P.A., Götz, E., Orr, H.G., Radecki-Pawlik, A., 2000. The morphodynamics of fluvial sand dunes in the River Rhine, near Mainz, Germany. I. Sedimentology and morphology. *Sedimentology* 47, 227–252.
- Cisneros, J., Best, J., van Dijk, T., de Almeida, R.P., Amsler, M., Boldt, J., et al., 2020. Dunes in the world’s big rivers are characterized by low-angle lee-side slopes and a complex shape. *Nature Geosci.* 13, 156–162. <https://doi.org/10.1038/s41561-019-0511-7>
- Davis, J.P., Walker, D.J., Townsend, M., Young, I.R., 2004. Wave-formed sediment ripples: Transient analysis of spectral development. *J. Geophys. Res.* 109, C07020. <https://doi.org/10.1029/2004JC002307>
- Flemming, B.W., 1988. Zur Klassifikation subaquatischer, strömungstransversaler Transportkörper. *Bochum Geol. Geotechn. Arb.* 29, 44–47.
- Guala, M., Heisel, M., Singh, A., Musa, M., Buscombe, D., Grams, P., 2020. A mixed length scale model for migrating fluvial bedforms. *Geophys. Res. Lett.* 47, 2019GL086625. <https://doi.org/10.1029/2019GL086625>
- Harbor, D.J., 1998. Dynamics of bedforms in the lower Mississippi River. *J. Sediment. Res.* 68 (5), 750–762.
- Hino, M., 1968. Equilibrium-range spectra of sand waves formed by flowing water. *J. Fluid Mech.* 34, 565–573. <https://doi.org/10.1017/S0022112068002089>
- Hu, H., Wei, T., Yang, Zh., Christopher, R., Hackney, C.R., Parsons, D.R., 2018. Low-angle dunes in the Changjiang (Yangtze) Estuary: Flow and sediment dynamics under tidal influence. *Estuar. Coast. Shelf Sci.* 205, 110–122. <https://doi.org/10.1016/j.ecss.2018.03.009>
- IMGW-PIB, 2020. [www.pogodynka.pl](http://www.pogodynka.pl). Online hydrological and meteorological database of the Institute of Meteorology and Wa-

- ter Management – National Research Institute, Warsaw; Instytut Meteorologii i Gospodarki Wodnej – Państwowy Instytut Badawczy, Warszawa (accessed on 31 December 2020).
- Julien, P.Y., Klaassen, G.J., 1995. Sand-dune geometry of large rivers during floods. *J. Hydraul. Eng.* 121 (9), 657–663. [https://doi.org/10.1061/\(ASCE\)0733-429\(1995\)121:9\(657\)](https://doi.org/10.1061/(ASCE)0733-429(1995)121:9(657))
- Julien, P.Y., Klaassen, G.J., Ten Brinke, W.B.M., Wilbers, A.W.E., 2002. Case study: bed resistance of Rhine River during 1998 flood. *J. Hydraul. Eng.* 128 (12), 1042–1050. [https://doi.org/10.1061/\(ASCE\)0733-9429\(2002\)128:12\(1042\)](https://doi.org/10.1061/(ASCE)0733-9429(2002)128:12(1042))
- Koop, L., van der Reijden, K.J., Mestdagh, S., Tom Ysebaert, T., Govers, L.L., Han Olff, H., Herman, P.M.J., Snellen, M., Dick, G., Simons, D.G., 2020. Measuring Centimeter-Scale Sand Ripples Using Multibeam Echosounder Backscatter Data from the Brown Bank Area of the Dutch Continental Shelf. *Geosciences* 10, 495. <https://doi.org/10.3390/geosciences10120495>
- Lefebvre, A., Winter, C., 2016. Predicting bed form roughness: the influence of lee side angle. *Geo-Mar. Lett.* 36, 121–133. <https://doi.org/10.1007/s00367-016-0436-8>
- Lisimenka, A., Kubicki, A., 2017. Estimation of dimensions and orientation of multiple riverine dune generations using spectral moments. *Geo-Mar. Lett.* 37, 59–74. <https://doi.org/10.1007/s00367-016-0475-1>
- Lisimenka, A., Zwoliński, Z., Rudowski, S., 2015. The nature of the bed load transport in the mouth of the river to the non-tidal sea (the Vistula River, Poland), EGU General Assembly, Geophys. Res. Abst. 17 EGU2015-8955-1 (poster).
- Lyons, P., Pouliquen, E., 2004. Advances in high-resolution seafloor characterization in support of high-frequency underwater acoustics studies: techniques and examples. *Meas. Sci. Technol.* 15, R59–R72. <https://doi.org/10.1088/0957-0233/15/12/R01>
- Majewski, W., 2013. Sustainable development of the Lower Vistula. *Meteorol. Hydrol. Water Manage.* 1 (1), 33–37.
- Majewski, W., 2018. Vistula River, its characteristics and management. *Int. J. Hydrol.* 2 (4), 493–496. <https://doi.org/10.15406/ijh.2018.02.00116>
- Makowski, J., 1995. *Setna rocznica wykonania Przekopu Wisły 1885-1995*. IBW PAN, Gdańsk, 100 (in Polish).
- Martin, R.L., Jerolmack, D.J., 2013. Origin of hysteresis in bed form response to unsteady flows. *Water Resour. Res.* 49, 1314–1333. <https://doi.org/10.1002/wrcr.20093>
- Nelson, J.M., Logan, B.L., Kinzel, P.J., Shimizu, Y., Giri, S., Shreve, R.L., McLean, S.R., 2011. Bedform response to flow variability. *Earth Surf. Process. Landforms* 36, 1938–1947. <https://doi.org/10.1002/esp.2212>
- Nikora, V., Sukhodolov, A., Rowinski, P.M., 1997. Statistical sand wave dynamics in one-directional water flows. *J. Fluid Mech.* 351, 17–39. <https://doi.org/10.1017/S0022112097006708>
- Paarlberg, A.J., Dohmen-Janssen, C.M., Hulscher, S.J.M.H., Schielen, R., Termes, A.P.P., 2008. Modelling dynamic roughness in rivers during floods. In: Parsons, D.R., Garlan, T., Best, J.L. (Eds.), *MARID 2008, 3<sup>rd</sup> international workshop on marine and river dune dynamics*, 1-3 April 2008, Leeds, UK, 257–264.
- Parsons, D.R., Best, J.L., Orfeo, O., Hardy, R.J., Kostaschuk, R., Lane, S.N., 2005. Morphology and flow fields of three-dimensional dunes, Rio Paraná, Argentina: Results from simultaneous multibeam echo sounding and acoustic Doppler current profiling. *J. Geophys. Res. Earth. Surg.* 110, F04S03. <https://doi.org/10.1029/2004JF000231>
- Percival, D.B., Walden, A.T., 1993. *Spectral analysis for physical applications*. Cambridge University Press, Cambridge <https://doi.org/10.1017/CBO9780511622762>
- Reesink, A.J.H., Parsons, D.R., Ashworth, P.J., Best, J.L., Hardy, R.J., Murphy, B.J., McLelland, S.J., Unsworth, C., 2018. The adaptation of dunes to changes in river flow. *Earth-Sci. Rev.* 185, 1065–1087. <https://doi.org/10.1016/j.earscirev.2018.09.002>
- Rubin, D.M., McCulloch, D.S., 1980. Single and superimposed bedforms: a synthesis of San Francisco Bay and flume observations. *Sediment. Geol.* 26 (1–3), 207–231.
- Rudowski, S., Edut, J., Wróblewski, R., Dworniczak, J., Lisimenka, A., Jereczek-Korzeniewska, K., Galer-Tatarowicz, K., 2017. Granulometry of bottom sediments of the Przekop Wisły canal. *Bull. Maritime Inst. Gdańsk* 32 (1), 14–20. <https://doi.org/10.5604/12307424.1224050>
- Sambrook Smith, G.H., Best, J.L., Orfeo, O., Vardy, M.F., Zinger, J.A., 2013. Decimeter-scale in situ mapping of modern cross-bedded dune deposits using parametric echo sounding: A new method for linking river processes and their deposits. *Gephys. Res. Lett.* 40, 3883–3887. <https://doi.org/10.1002/grl.50703>
- Szymański, E., 1897a. The regulation of the Vistula River mouth. *Tech. Rev.* 17, 270–274 (in Polish).
- Szymański, E., 1897b. The regulation of the Vistula River mouth (continuation). *Tech. Rev.* 18, 285–289 (in Polish).
- Ten Brinke, W.B.M., Wilbers, A.W.E., Wesseling, C., 1999. Dune growth, decay and migration rates during a large-magnitude flood at a sand and mixed sand–gravel bed in the Dutch Rhine river system. In: Smith, N.D., Rogers, J. (Eds.), *Fluvial Sedimentology VI*, 15–32. <https://doi.org/10.1002/9781444304213.ch2>
- Van der Mark, C.F., Blom, A., 2007. A new and widely applicable tool for determining the geometric properties of bedforms. University of Twente, Enschede CE&M Research Report 2007R-003/WEM-002.
- Van Rijn, L.C., 1984. *Sediment transport. Part III: Bed forms and alluvial roughness*. *J. Hydr. Eng.* 110 (12), 1733–1754.
- Van Rijn, L.C., 1993. *Principles of Sediment Transport in Rivers, Estuaries and Coastal Seas*. AQUA Publications – I11, Amsterdam.
- Venditti, J.G., Lin, C.-Y.M., Kazemi, M., 2016. Variability in bedform morphology and kinematics with transport stage. *Sedimentology* 63, 1017–1040. <https://doi.org/10.1111/sed.12247>
- Warmink, J.J., Booij, M.J., Van der Klis, H., Hulscher, S.J.M.H., 2007. Uncertainty in water level predictions due to various calibrations. In: *Proc. 1st International Conference on Adaptive & Integrated Water Management, CAIWA 2007*, Basel, Switzerland, 1–18.
- Warmink, J.J., Booij, M.J., Van der Klis, H., Hulscher, S.J.M.H., 2012. Quantification of uncertainty in design water levels due to uncertain bed form roughness in the Dutch river Waal. *Hydrol. Process* 27 (11), 1646–1663. <https://doi.org/10.1002/hyp.9319>
- Warmink, J.J., Straatsma, M.W., Huthoff, F., Booij, M.J., Hulscher, S.J.M.H., 2013. Uncertainty of design water levels due to combined bed form and vegetation roughness in the Dutch River Waal. *J. Flood Risk Manag.* 6 (4), 302–318.
- Warmink, J.J., 2014. Dune dynamics and roughness under gradually varying flood waves, comparing flume and field observations. *Advances in Geosciences* 39, 115–121. <https://doi.org/10.5194/adgeo-39-115-2014>
- Wignall, P.B., Best, J.L., 2000. The Western Irish Namurian Basin reassessed. *Basin Res.* 12, 59–78.
- Wilbers, A.W.E., Ten Brinke, W.B.M., 2003. The response of subaqueous dunes to floods in sand and gravel bed reaches of the Dutch Rhine. *Sedimentology* 50, 1013–1034. <https://doi.org/10.1046/j.1365-3091.2003.00585.x>
- Wu, S., Jun Xu, Y., Wang, B., Cheng, H., 2021. Riverbed morphology of the Lowermost Mississippi River – Implications of leeside slope, flow resistance and bedload transport in a large alluvial river. *Geomorphology* 385, 107733. <https://doi.org/10.1016/j.geomorph.2021.107733>
- Young, I., 1995. The determination of confidence limits associated with estimates of the spectral peak frequency. *Ocean. Eng.* 22, 669–689. [https://doi.org/10.1016/0029-8018\(95\)00002-3](https://doi.org/10.1016/0029-8018(95)00002-3)

Available online at [www.sciencedirect.com](http://www.sciencedirect.com)

ScienceDirect

journal homepage: [www.journals.elsevier.com/oceanologia](http://www.journals.elsevier.com/oceanologia)

## SHORT COMMUNICATION

# A substantial range expansion of alien Ponto-Caspian amphipods along the eastern Baltic Sea coast

Denis Copilaş-Ciocianu\*, Eglė Šidagytė-Copilas

Laboratory of Evolutionary Ecology of Hydrobionts, Nature Research Centre, Vilnius, Lithuania

Received 24 May 2021; accepted 16 September 2021

Available online 8 October 2021

## KEYWORDS

Estonia;  
First record;  
Invasive crustaceans;  
Latvia;  
Transitional waters

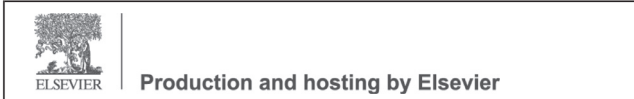
**Abstract** We report a considerable range expansion of four Ponto-Caspian amphipod species in transitional waters along the southeastern Baltic Sea coast. *Chaetogammarus warpachowskyi* and *Dikerogammarus haemobaphes* were found for the first time in Latvia, the former being common along the coast, while the latter was encountered only in the port of Riga. This indicates a 400 to 600 km expansion along the coast, assuming an origin from the Curonian or Vistula lagoons. We also officially document an expansion for *Chelicorophium curvispinum* in Latvia of ca. 300 km until Riga, confirming recent unpublished records. Moreover, we document a second invasion route of *Pontogammarus robustoides* into Estonia from nearby Latvian waters by uncovering a population at the port of Pärnu. This species was previously known in Estonia only from the Gulf of Finland (>500 km from Pärnu). With the exception of *D. haemobaphes*, all newly recorded species were represented by various life-stages and ovigerous females, indicating viable populations. Overall, our findings reveal that Ponto-Caspian amphipods are much more widespread in the Baltic area than previously known and highlight the need for more stringent monitoring.

© 2021 Institute of Oceanology of the Polish Academy of Sciences. Production and hosting by Elsevier B.V. This is an open access article under the CC BY-NC-ND license (<http://creativecommons.org/licenses/by-nc-nd/4.0/>).

\* Corresponding author at: Laboratory of Evolutionary Ecology of Hydrobionts, Nature Research Centre, Akademijos Str. 2, LT-08412 Vilnius, Lithuania.

E-mail address: [denis.copilas-ciocianu@gamtc.lt](mailto:denis.copilas-ciocianu@gamtc.lt) (D. Copilaş-Ciocianu).

Peer review under the responsibility of the Institute of Oceanology of the Polish Academy of Sciences.



Alien Ponto-Caspian species are spreading at an increasing rate in European and North American fresh- and brackish water habitats, sometimes with significant ecological and economic effects (Bij de Vaate et al., 2002; Vanderploeg et al., 2002). Amphipod crustaceans are perhaps the most diverse group of Ponto-Caspian organisms (Copilaş-Ciocianu and Sidorov, 2021), and among the most common and successful aliens of Ponto-Caspian origin (Bij de Vaate et al., 2002; Cuthbert et al., 2020). It is thought that their ecological plasticity, aggressiveness and high fecundity makes them superior competitors, often driving populations of

<https://doi.org/10.1016/j.oceano.2021.09.005>

0078-3234/© 2021 Institute of Oceanology of the Polish Academy of Sciences. Production and hosting by Elsevier B.V. This is an open access article under the CC BY-NC-ND license (<http://creativecommons.org/licenses/by-nc-nd/4.0/>).

native species to extinction (Arbačiauskas et al., 2013; Dick and Platvoet, 2000; Grabowski et al., 2007a; Šidagytė and Arbačiauskas, 2016).

The southeastern Baltic Sea region harbors eight alien Ponto-Caspian amphipod species originating from the river mouths and lagoons draining to the northwestern Black Sea. Most have spread naturally and/or by shipping after construction of artificial canals: some since or even before the early 20<sup>th</sup> century (*Chelicorophium curvispinum* (Sars, 1895) and *Chaetogammarus ischnus* (Stebbing, 1899)), while others during the last decades (*Dikerogammarus haemobaphes* (Eichwald, 1841), *Dikerogammarus villosus* (Sowinsky, 1894) and *Trichogammarus trichiatus* (Martynov, 1932)) (Arbačiauskas et al., 2011; Bij de Vaate et al., 2002; Grabowski et al., 2007b; Rachalewski et al., 2013). In the 1960s, however, three species, namely *Chaetogammarus warpachowskyi* (Sars, 1894), *Obesogammarus crassus* (Sars, 1894), and *Pontogammarus robustoides* (Sars, 1894), were deliberately introduced and successfully acclimatized in the Lithuanian Kaunas water reservoir, and then translocated into numerous Lithuanian water bodies as well as in the nearby countries such as Latvia, Estonia and Russia (Arbačiauskas et al., 2017; Jażdżewski, 1980). From the Curonian Lagoon, the Ponto-Caspian amphipods have also dispersed along the sea coast naturally or via shipping. Namely *O. crassus* and *P. robustoides* have dispersed westward, reaching Germany (Bij de Vaate et al., 2002), the latter also making its way into the Netherlands (Moedt and Van Haaren, 2018), while *C. curvispinum*, *C. warpachowskyi*, and *P. robustoides* have spread as far north as the Gulf of Finland (Berezina, 2007; Malyavin et al., 2008).

Although Lithuania and Latvia are neighboring countries with a somewhat similar history of Ponto-Caspian amphipod introductions, the latter harbors less species. Two of them, namely *D. villosus* and *P. robustoides*, are well-documented in both countries (Arbačiauskas, 2008; Arbačiauskas et al., 2011; Grudule et al., 2007; Minchin et al., 2019; Paidere et al., 2016, 2019a; Šidagytė et al., 2017). The distribution of *C. curvispinum* is well known in Lithuania (Arbačiauskas, 2008; Arbačiauskas et al., 2011), whereas in Latvia it was only reported from the Pāvilosta port half a century ago (Nikolaev, 1963), and subsequent grey literature records were reported only after 2014 (Harju et al., 2018). The remaining species, *C. warpachowskyi* and *O. crassus*, are also relatively common in Lithuania, including transitional waters (Arbačiauskas, 2008; Arbačiauskas et al., 2011), yet in Latvian inland waters they have never been officially documented (at least convincingly, see Discussion on *O. crassus* in Latvia). In Estonia the only known Ponto-Caspian amphipods are *C. curvispinum* and *P. robustoides*, occurring in a restricted area in the Gulf of Finland close to Russia (Herkül et al., 2009). Both of these species are very common in the Russian part of this gulf (Berezina, 2007; Malyavin et al., 2008).

Considering the above, a noteworthy pattern emerges. Although *C. curvispinum*, *C. warpachowskyi*, and *P. robustoides* are present in the Curonian Lagoon and the Gulf of Finland, the first two were seldom, if at all, reported in between the two regions. Such a wide distribution gap, equivalent to almost the entire Estonian and Latvian coastline, is remarkable. This pattern could be either the result of long-distance dispersal (common in invasive species) or

an artifact related to insufficient distributional knowledge. Our study agrees with the latter possibility by revealing that these amphipods are actually much more widespread than currently officially recognized, having expanded their ranges hundreds of kilometers along the eastern Baltic Sea coastline.

For this study, we collected material from 10 localities (mostly transitional waters) along the Baltic Sea coast in Latvia (8) and Estonia (2) on 11–14 August 2020 (Table 1). Samples were collected using kick-sampling with a standard benthic hand net (1 mm mesh size). All available substrates and habitats were investigated up to a depth of 1.5 m. Amphipods were fixed in 96% ethanol in the field. Specimens were dissected under a Nikon SMZ1000 stereomicroscope and identified using the keys in Bellan-Santini et al. (1982) and Copilaș-Ciocianu and Sidorov (2021). Appendages were mounted on microscope slides in glycerol and photographed using a Nikon DS-Fi2 camera attached to a Nikon SMZ1000 stereomicroscope. Previously known distribution data for the focal species was obtained from the relevant literature as well as the GBIF database (<https://doi.org/10.15468/dl.iddp60>; <https://doi.org/10.15468/dl.xmntxw>, accessed 22–23 March 2020).

Altogether we collected and identified 771 specimens belonging to seven amphipod species, five of which were aliens of Ponto-Caspian origin (*C. curvispinum*, *C. warpachowskyi*, *D. haemobaphes*, *D. villosus*, and *P. robustoides*), one of North American origin (*Gammarus tigrinus* Sexton, 1939), and one was native (*Corophium volutator* (Pallas, 1776)) (Table 1). We found that four Ponto-Caspian species (Figure 1) have expanded their previously published distribution ranges along the eastern Baltic Sea coast (Figure 2). The new findings include the first records of *C. warpachowskyi* and *D. haemobaphes* in Latvia, a new invasion route of *P. robustoides* into Estonia, and an official documentation of *C. curvispinum* expansion along the Latvian coast. Below we expand on our findings.

Our most unexpected discovery is that *C. warpachowskyi* (Figure 1A) is rather common along the Latvian coast, despite that it was never reported from this country. The previously known closest locality was in Lithuania, at the mouth of the Šventoji River (5 km from the Latvian border) (Arbačiauskas et al., 2011). We encountered this species until the port of Riga, which reveals a substantial coastal range expansion of ca. 400 km (Figure 2A). These populations were clearly established since we found male and female adults at all four localities, including ovigerous females at three of them (Table 1). Most likely *C. warpachowskyi* spread from the Šventoji river mouth or the Curonian Lagoon naturally and/or via shipping. However, it could have also spread downstream from the reservoirs on the Daugava River where it was possibly introduced during the intentional stocking campaigns in the 1960s (Arbačiauskas et al., 2017; Paidere et al., 2016). Nevertheless, despite recent sampling it has not been reported from the Daugava reservoirs (Paidere et al., 2016, 2019a, current study). Generally, *C. warpachowskyi* is among the least widespread alien Ponto-Caspian amphipods, mainly occurring in water bodies where it was deliberately introduced during the second half of the 20<sup>th</sup> century (Arbačiauskas et al., 2017, 2011; Jażdżewski, 1980).

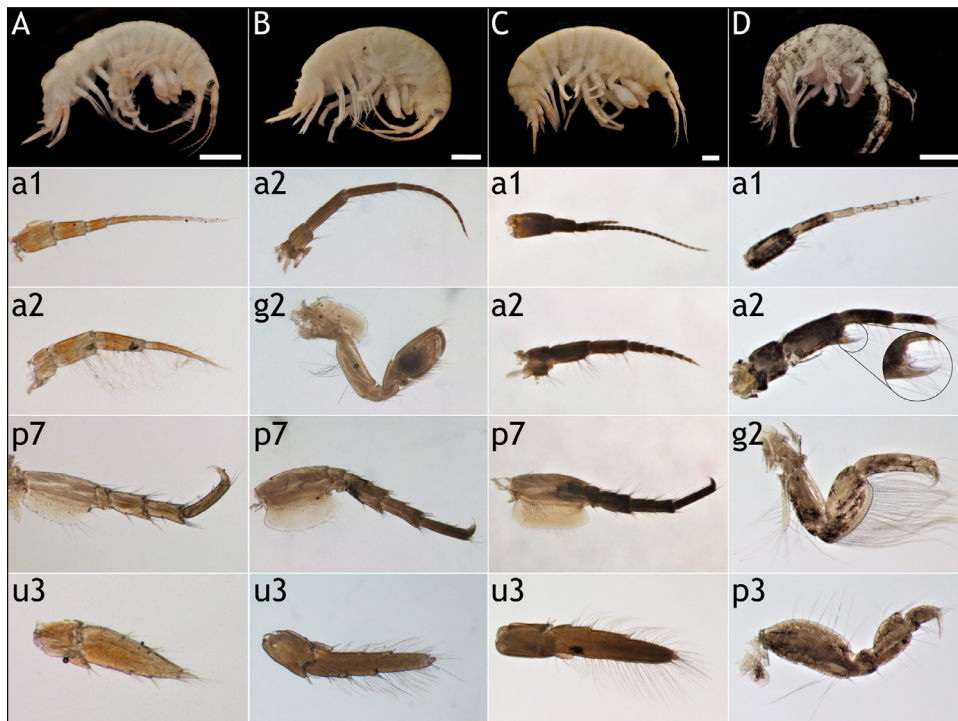


**Figure 1** Identification characteristics of the Ponto-Caspian amphipods that expanded their ranges in the Baltics. Scale bar = 1 mm. A) *Chaetogammarus warpachowskyi*, B) *Dikerogammarus haemobaphes*, C) *Pontogammarus robustoides*, and D) *Chelicorophium curvispinum*. Abbreviations: a1 – antenna 1, a2 – antenna 2, g2 – gnathopod 2, p3 – pereopod 3, p7 – pereopod 7, u3 – uropod 3.

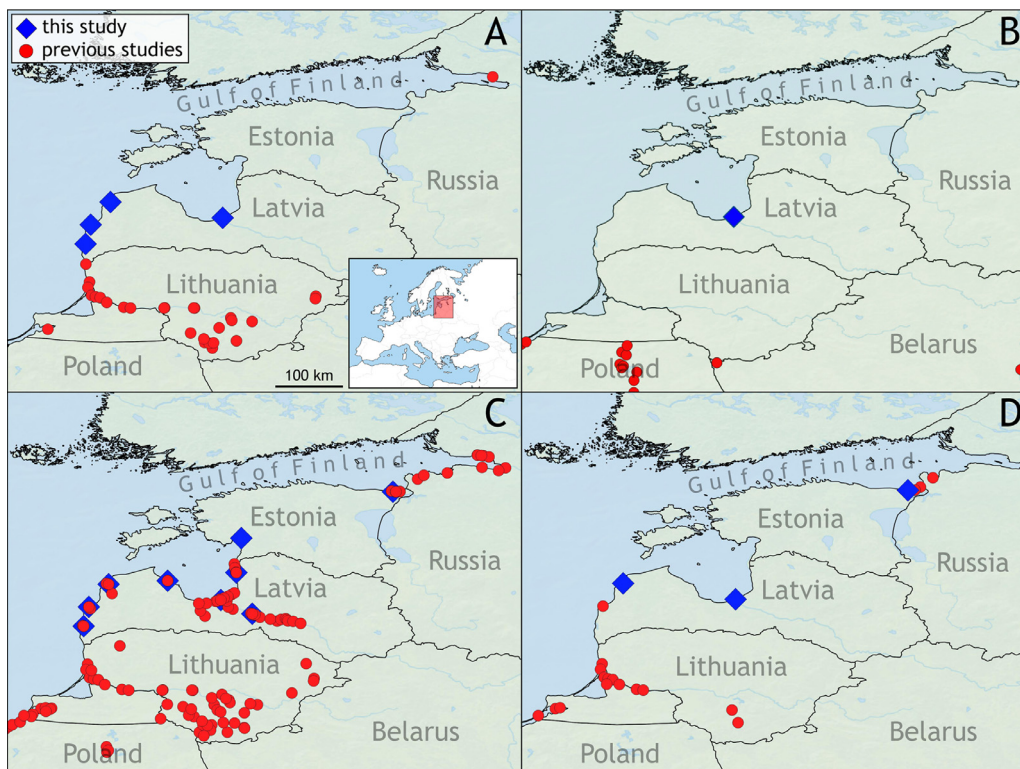


**Figure 2** Baltic distributions of A) *Chaetogammarus warpachowskyi*, B) *Dikerogammarus haemobaphes*, C) *Pontogammarus robustoides*, and D) *Chelicorophium curvispinum*. Red dots and blue diamonds indicate records from the peer-reviewed literature and current study, respectively.

**Table 1** Information about sampling localities, habitat and amphipod species collected. Country codes: EE – Estonia, LV – Latvia. Species abbreviations: CC – *Chelicorophium curvispinum*, CV – *Corophium volutator*, CW – *Chaetogammarus warpachowskyi*, DH – *Dikerogammarus haemobaphes*, DV – *D. villosus*, GT – *Gammarus tigrinus*, PR – *Pontogammarus robustoides* (Ponto-Caspian species are shown in boldface). Specimen stages: ovig. – a subset of ovigerous females, juv. – juveniles.

No.	Locality	Coordinates	Date	Habitat	Species	Number of specimens
EE 1	Sillamäe, Sõtke stream mouth	59°23'56"N, 27°46'12"E	11 August 2020	Depth: 0.1–1.5 m Substrate: stones, sand, detritus	CC GT PR	3♀, 1♂ 4 (2 ovig.)♀, 6♂ 28 (12 ovig.)♀, 29♂, 3 juv.
EE 2	Pärnu, Pärnu river mouth	58°23'17"N, 24°29'00"E	11 August 2020	Depth: 0.1–0.4 m Substrate: stones, sand	CV GT PR	2♀ 13 (8 ovig.)♀, 11♂ 32 (17 ovig.)♀, 18♂, 49 juv.
LV 1	Vitrupe, Vitrupe river mouth	57°38'13"N, 24°22'31"E	11 August 2020	Depth: 0.1–0.5 m Substrate: sand, plants	PR	8 (5 ovig.)♀, 8♂, 4 juv.
LV 2	Kegums Reservoir	56°44'21"N, 24°43'14"E	12 August 2020	Depth: 0.1–1.5 m Substrate: stones	PR	5 (2 ovig.)♀, 2♂, 6 juv.
LV 3	Riga, Daugava river mouth	57°02'18"N, 24°02'22"E	12 August 2020	Depth: 0.1–1.5 m Substrate: boulders, stones, sand, plants	CC CV CW DH DV GT PR	18 (6 ovig.)♀, 2♂ 3♀, 3♂ 2♀, 1♂ 1♀, 2♂ 4 (2 ovig.)♀, 6♂, 1 juv. 3♀, 1♂ 30 (8 ovig.)♀, 15♂, 32 juv.
LV 4	Kaltene, sea shore	57°27'34"N, 22°53'09"E	12 August 2020	Depth: 0.1–0.5 m Substrate: stones, pebbles	GT PR	47 (26 ovig.)♀, 45♂, 5 juv. 6 (1 ovig.)♀, 8♂, 5 juv.
LV 5	Ventspils, Venta river	57°22'58"N, 21°36'23"E	13 August 2020	Depth: 0.1–1 m Substrate: sand, plants, detritus	CC CV CW GT PR	8 (2 ovig.)♀, 2♂ 2♀ 35 (27 ovig.)♀, 32♂ 3♀, 3♂ 7♀, 4♂, 12 juv.
LV 6	Pāvilosta, Saka river mouth	56°53'17"N, 21°10'40"E	13 August 2020	Depth: 0.1–1 m Substrate: stones, sand, plants, detritus	CV CW DV GT PR	5 (3 ovig.)♀, 3♂, 1 juv. 11 (9 ovig.)♀, 6♂ 27 (15 ovig.)♀, 16♂, 6 juv. 1♀, 3♂
LV 7A	Liepāja, Lake Liepāja	56°30'30"N, 21°02'18"E	14 August 2020	Depth: 0.1–1 m Substrate: stones, mud	GT	9 (2 ovig.)♀, 8♂, 2 juv. 22 (9 ovig.)♀, 16♂
LV 7B	Baidzele, Lake Liepāja	56°28'08"N, 21°03'57"E	14 August 2020	Depth: 0.1–1 m Substrate: sand, plants	CW PR	15 (11 ovig.)♀, 6♂ 6 (3 ovig.)♀, 4♂, 24 juv.

The appearance of *D. haemobaphes* in the port of Riga (Figure 1B) is enigmatic since this species does not seem to occur anywhere along the Baltic coast eastwards from Poland (Figure 2B). Few individuals have been recently recorded in Belarus, close to the Lithuanian border (Lipinskaya et al., 2021), and since 2019 viable populations have been observed in the upper Lithuanian part of the Nemunas River, but never below the Kaunas Reservoir (Šidagytė-Copilas and Copilaş-Ciocianu, in preparation). Therefore, the most likely origin of the Latvian specimens remains the Vistula Lagoon, located ca. 600 km away.

However, given that we have found only three individuals (Table 1), it is unclear whether this is an established population or not. Future sampling in the area is therefore necessary. At a broad scale, *D. haemobaphes* is among the most successful and widespread Ponto-Caspian amphipods (Bacela-Spychalska and Van der Velde, 2013; Bij de Vaate et al., 2002; Jażdżewska et al., 2020). As such, its further northward dispersal is to be expected.

Within this paper, we provide the first report of *P. robustoides* from the Estonian port of Pärnu (Figure 1C). It was the most abundant amphipod at this locality and

all life stages were observed, including ovigerous females (Table 1). Almost certainly *P. robustoides* reached this area from Latvia, as it was reported a few kilometers from the Estonian border in 2011, but not from Pärnu Bay (Strode et al., 2013). This established population clearly demonstrates that the species expanded northwards by up to 70 km and exposes a second invasion route of *P. robustoides* into Estonia (Figure 2C). The previously known route was a westward dispersal from Russia along the shore of the Gulf of Finland, the invader being discovered for the first time close to the border in 2006 (Herkül et al., 2009). Herein, we further confirm its presence in this area, and also in various places throughout Latvia (Table 1, Figure 2C). At a broader geographic scale, *P. robustoides* is relatively widespread in Europe, although not nearly as much as some other Ponto-Caspian species. Its current range is a result of both natural dispersal and deliberate introductions (Arbačiauskas et al., 2011; Bij de Vaate et al., 2002; Moedt and Van Haaren, 2018).

Our study also clarifies the expansion of *C. curvispinum* in the eastern Baltic Sea (Figure 1D). In Latvia, it was first reported from the port of Pāvilosta in the 1960s (Nikolaev, 1963). Since 2014 it was reported from the ports of Liepāja, Ventspils, and Riga, however, only in the grey literature (Grudcina, 2018; Harju et al., 2018). We confirm this spread of ca. 300 km northwards along the Latvian coast, as we also observed *C. curvispinum* in Ventspils and Riga (Figure 2D). Specimens of both sexes as well as ovigerous females were collected, thus confirming its establishment (Table 1). We also confirm its presence on the Estonian shore of the Gulf of Finland (Sõtke stream mouth) where it was hitherto reported (Herkül and Kotta, 2007). Being encountered in almost all major European watersheds (Figure 2F) (Bij de Vaate et al., 2002), *C. curvispinum* is one of the most widely distributed Ponto-Caspian amphipods. Most likely its dispersal began in the early 20<sup>th</sup> century, or even earlier, and was facilitated by artificial canals that connected previously isolated watersheds (Arbačiauskas et al., 2011; Jażdżewski, 1980).

We sampled *D. villosus* only within its previously reported range (Minchin et al., 2019; Šidagytė et al., 2017), confirming its establishment with records of adult specimens, ovigerous females, and juveniles (Table 1). This dispersal stagnation is only apparent given that just a couple of years passed between our current sampling and that of the most recent study (Minchin et al., 2019). It is therefore still highly likely that *D. villosus* will spread further north, and its presence in Estonia (especially Pärnu Bay) should soon be expected.

Recently, *O. crassus* has been reported (mainly in the grey literature) from the Latvian ports of Liepāja, Ventspils, and Riga (Grudcina, 2018; Harju et al., 2018; Paidere et al., 2019b). Nevertheless, we could not confirm these reports. Firstly, we did not manage to collect this species in our current study although the sampling localities roughly coincided. Secondly, the only accessible evidence for the identification of the Latvian *O. crassus* provided by the authors is a habitus photograph of a highly damaged specimen (Harju et al., 2018), making a full validation impossible. Our doubts, of course, do not exclude the species' occurrence in Latvian waters.

Overall, our findings indicate that several Ponto-Caspian alien amphipods are substantially more widespread than previously known, inevitably dispersing northwards along the eastern Baltic Sea coast. The expanding distribution is most likely a result of natural spread combined with shipping activity. It remains to be seen whether the southern (from Latvia) and northeastern (from Russia) invasion fronts will ever meet in Estonia. We recommend more stringent monitoring activities, especially in the transitional waters, to better understand the dispersal of these species and their impact on the local biota.

## Acknowledgements

This work was supported by the Research Council of Lithuania, Contract No. S-MIP-20-26.

## References

- Arbačiauskas, K., 2008. Amphipods of the Nemunas River and the Curonian Lagoon, the Baltic Sea basin: Where and which native freshwater amphipods persist. *Acta Zool. Lit.* 18, 10–16. <https://doi.org/10.2478/v10043-008-0002-3>
- Arbačiauskas, K., Lesutienė, J., Gasiūnaitė, Z.R., 2013. Feeding strategies and elemental composition in Ponto-Caspian peracaridans from contrasting environments: Can stoichiometric plasticity promote invasion success? *Freshw. Biol.* 58, 1052–1068. <https://doi.org/10.1111/fwb.12108>
- Arbačiauskas, K., Šidagytė, E., Šniaukštaitė, V., Lesutienė, J., 2017. Range expansion of Ponto-Caspian peracaridan Crustaceans in the Baltic Sea basin and its aftermath: Lessons from Lithuania. *Aquat. Ecosyst. Heal. Manag.* 20, 393–401. <https://doi.org/10.1080/14634988.2017.1328229>
- Arbačiauskas, K., Višinskienė, G., Smilgevičienė, S., Rakauskas, V., 2011. Non-indigenous macroinvertebrate species in Lithuanian fresh waters, Part 1: Distributions, dispersal and future. *Knowl. Manag. Aquat. Ecosyst.* 402, 12. <https://doi.org/10.1051/kmae/2011076>
- Bacela-Spychalska, K., Van der Velde, G., 2013. There is more than one “killer shrimp”: Trophic positions and predatory abilities of invasive amphipods of Ponto-Caspian origin. *Freshw. Biol.* 58, 730–741. <https://doi.org/10.1111/fwb.12078>
- Bellan-Santini, D., Karaman, G.S., Krapp-Schickel, T., Ledoyer, M., Myers, A.A., Ruffo, S., Schiecke, U., 1982. *The Amphipoda of the Mediterranean*. Institut Océanographique, Monaco.
- Berezina, N.A., 2007. Invasions of alien amphipods (Amphipoda: Gammaridea) in aquatic ecosystems of North-Western Russia: Pathways and consequences. *Hydrobiologia* 590, 15–29. <https://doi.org/10.1007/s10750-007-0753-z>
- Bij de Vaate, A., Jażdżewski, K., Ketelaars, H.A.M., Gollasch, S., Van der Velde, G., 2002. Geographical patterns in range extension of Ponto-Caspian macroinvertebrate species in Europe. *Can. J. Fish. Aquat. Sci.* 59, 1159–1174. <https://doi.org/10.1139/f02-098>
- Copilaş-Ciocianu, D., Sidorov, D., 2021. Taxonomic, ecological and morphological diversity of Ponto-Caspian gammaridean amphipods: a review. *bioRxiv*, 1–36. <https://doi.org/10.1101/2021.01.21.427559>
- Cuthbert, R.N., Kotronaki, S.G., Dick, J.T.A., Briski, E., 2020. Salinity tolerance and geographical origin predict global alien amphipod invasions. *Biol. Lett.* 16, 2–7. <https://doi.org/10.1098/rsbl.2020.0354>
- Dick, J.T.A., Platvoet, D., 2000. Invading predatory crustacean *Dikerogammarus villosus* eliminates both native and exotic



- species. Proc. R. Soc. B Biol. Sci. 267, 977–983. <https://doi.org/10.1098/rspb.2000.1099>
- Grabowski, M., Bacela, K., Konopacka, A., 2007a. How to be an invasive gammarid (Amphipoda: Gammaroidea) - comparison of life history traits. *Hydrobiologia* 590, 75–84. <https://doi.org/10.1007/s10750-007-0759-6>
- Grabowski, M., Jażdżewski, K., Konopacka, A., 2007b. Alien crustacea in Polish waters - Amphipoda. *Invasions* 2, 25–38. <https://doi.org/10.3391/ai.2007.2.1.3>
- Grudcina, M., 2018. Impact of environmental characteristics on the benthic fauna in the Ports of the Baltic sea Master thesis. University of Latvia.
- Grudule, N., Parele, E., Arbačiauskas, K., 2007. Distribution of Ponto-Caspian amphipod *Pontogammarus robustoides* in Latvian waters. *Acta Zool. Litu.* 17, 28–32. <https://doi.org/10.1080/13921657.2007.10512812>
- Harju, M., Kalnina, M., Strake, S., 2018. Recent findings about benthic non-indigenous species in the ports of the southern part of the Baltic Sea. ICES Annual Science Conference. Hamburg, September 24–27.
- Herkül, K., Kotta, J., 2007. New records of the amphipods *Chelicorophium curvispinum*, *Gammarus tigrinus*, *G. duebeni*, and *G. lacustris* in the Estonian coastal sea. *Proc. Est. Acad. Sci.* 56, 290–296
- Herkül, K., Kotta, J., Püss, T., Kotta, I., 2009. Crustacean invasions in the Estonian coastal sea. *Est. J. Ecol.* 58, 313–323. <https://doi.org/10.3176/eco.2009.4.06>
- Jażdżewska, A.M., Rewicz, T., Mamos, T., Wattier, R., Baćela-Spychalska, K., Grabowski, M., 2020. Cryptic diversity and mtDNA phylogeography of the invasive demon shrimp, *Dikerogammarus haemobaphes* (Eichwald, 1841), in Europe. *Neobiota* 57, 53–86. <https://doi.org/10.3897/neobiota.57.46699>
- Jażdżewski, K., 1980. Range extensions of some gammaridean species in European inland waters caused by human activity. *Crustaceana Supplement* 6, 84–107
- Lipinskaya, T., Makaranka, A., Razlutskiy, V., Semenchenko, V., 2021. First records of the alien amphipod *Dikerogammarus haemobaphes* (Eichwald, 1841) in the Neman River basin (Belarus). *BiolInvasions Rec.* 10, 319–325
- Malyavin, S.A., Berezina, N.A., Hwang, J.-S., 2008. A finding of *Chelicorophium curvispinum* (Amphipoda, Crustacea) in the Gulf of Finland (the Baltic Sea). *Zool. Zhurnal* 87, 643–649
- Minchin, D., Arbačiauskas, K., Daunys, D., Ezhova, E., Grudule, N., Kotta, J., Molchanova, N., Olenin, S., Višinskienė, G., Strake, S., 2019. Rapid expansion and facilitating factors of the Ponto-Caspian invader *Dikerogammarus villosus* within the eastern Baltic sea. *Aquat. Invasions* 14, 165–181. <https://doi.org/10.3391/ai.2019.14.2.02>
- Moedt, S., Van Haaren, T., 2018. *Pontogammarus robustoides* (Sars, 1894), a new non-indigenous amphipod in the Netherlands (Crustacea: Amphipoda). *Lauterbornia* 85, 123–126
- Nikolaev, I.I., 1963. New recruits in the fauna and flora of the Northern Sea and the Baltic. *Zool. Zhurnal* 62, 20–27
- Paidere, J., Brakovska, A., Bankovska, L., Gruberts, D., 2019a. Changes in the distribution of amphipods in the Daugava River. Latvia. *Zool. Ecol.* 29, 96–99. <https://doi.org/10.35513/21658005.2019.2.4>
- Paidere, J., Brakovska, A., Škute, A., 2016. Ponto-Caspian gammarid *Pontogammarus robustoides* G. O. Sars, 1894 in the Daugava River reservoirs (Latvia). *Zool. Ecol.* 26, 227–235. <https://doi.org/10.1080/21658005.2016.1181847>
- Paidere, J., Brakovska, A., Vezhnavets, V., Škute, A., Savicka, M., 2019b. Effects of the environmental variables on the alien amphipod *Pontogammarus robustoides* in the Daugava River and its reservoirs. *Acta Biol. Univ. Daugavp.* 19, 169–180 [http://sciences.lv/wp-content/uploads/2020/01/Paidere\\_19\\_2.pdf](http://sciences.lv/wp-content/uploads/2020/01/Paidere_19_2.pdf)
- Rachalewski, M., Grabowski, M., Konopacka, A., Baćela-Spychalska, K., 2013. *Echinogammarus trichiatus* (Martynov, 1932) – a new Ponto-Caspian amphipod invader in Poland with remarks on other alien amphipods from the Oder River. *Crustaceana* 86, 1224–1233. <https://doi.org/10.1163/15685403-00003228>
- Šidagytė, E., Arbačiauskas, K., 2016. Resistance to low oxygen in the Ponto–Caspian amphipod *Pontogammarus robustoides* varies among lentic habitats of its northern invaded range. *Limnologia* 61, 7–13. <https://doi.org/10.1016/j.limno.2016.09.001>
- Šidagytė, E., Solovjova, S., Šniaukštaitė, V., Šiaulyš, A., Olenin, S., Arbačiauskas, K., 2017. The killer shrimp *Dikerogammarus villosus* (Crustacea, Amphipoda) invades Lithuanian waters, South-Eastern Baltic Sea. *Oceanologia* 59 (1), 85–91. <https://doi.org/10.1016/j.oceano.2016.08.004>
- Strode, E., Berezina, N.A., Kalnins, M., Balode, M., 2013. New records of the amphipods *Gammarus tigrinus* Sexton, 1939 and *Pontogammarus robustoides* G.O. Sars, 1894 in Latvian waters of the Baltic Sea. *BiolInvasions Rec.* 2, 63–68. <https://doi.org/10.3391/bir.2013.2.1.11>
- Vanderploeg, H.A., Nalepa, T.F., Jude, D.J., Mills, E.L., Holeck, K.T., Liebig, J.R., Grigorovich, I.A., Ojaveer, H., 2002. Dispersal and emerging ecological impacts of Ponto-Caspian species in the Laurentian Great Lakes. *Can. J. Fish. Aquat. Sci.* 59, 1209–1228. <https://doi.org/10.1139/f02-087>